NOAA Technical Report NOS 137 NGS 49

Proceedings of the AGU Chapman Conference on Geodetic VLBI: Monitoring Global Change

American Geophysical Union
Washington, D.C.
April 22-26, 1991

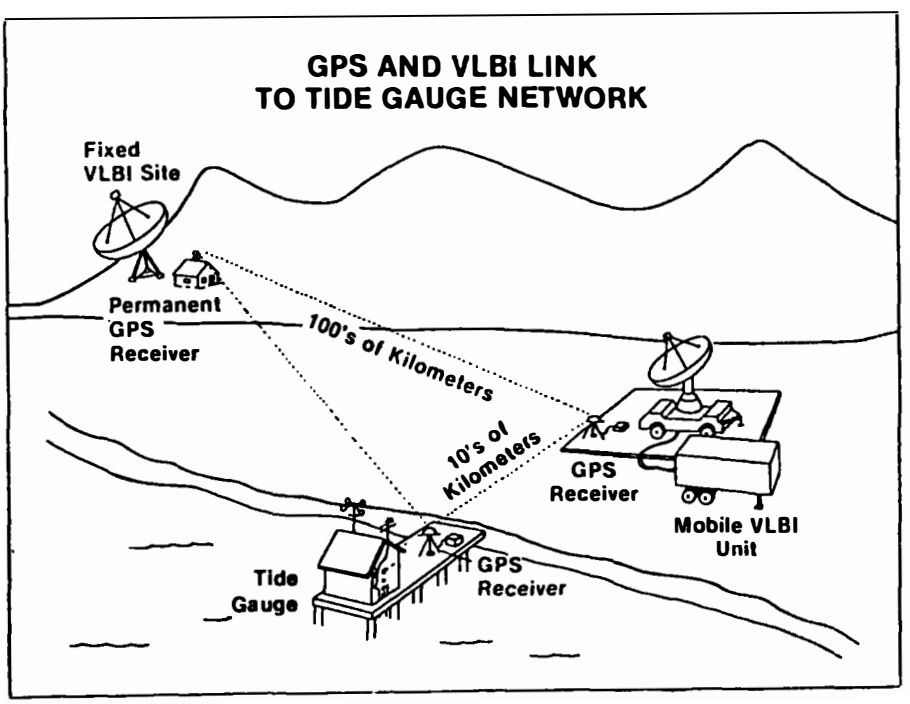

1991
U.S. DEPARTMENT OF COMMERCE
National Oceanic and Atmospheric Administration
National Ocean Service

NOAA Technical Report NOS 137 NGS 49

Proceedings of the AGU Chapman Conference on Geodetic VLBI: Monitoring Global Change

American Geophysical Union
Washington, D.C.
April 22-26, 1991

William E. Carter, Convenor
Laboratory for Geosciences

U.S. DEPARTMENT OF COMMERCE
Robert A. Mosbacher, Secretary

National Oceanic and Atmospheric Administration
John A. Knauss, Under Secretary and Administrator

National Ocean Service
John Carey, (Acting) Assistant Administrator for
Ocean Services and Coastal Zone Management

Sponsors

The National Oceanic and Atmospheric Administration

The National Aeronautics and Space Administration

The U.S. Naval Observatory

For sale by the National Geodetic Information Branch, NOS/NOAA, Rockville, MD 20852, price in U.S. dollars $20.00
(Make check payable to: National Geodetic Survey)

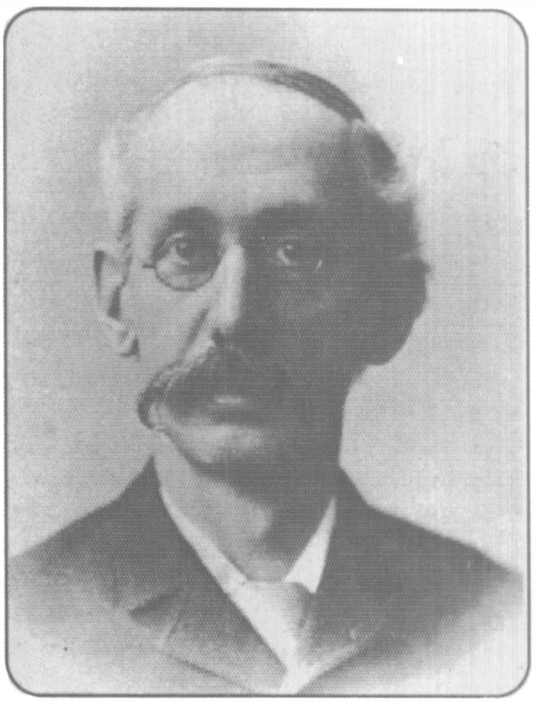

SETH CARLO CHANDLER, JR.

September 16, 1846 - December 31, 1913

These Proceedings are dedicated to the life and works of Seth Carlo Chandler Jr., the American astronomer, geodesist and actuary, on the centennial of his historical paper "On the variation of latitude, I" *(Astronomical Journal, 248,* 1891 p 59-61).

Chandler's study of the variation of latitude, i.e., the complex wobble of the surface of the Earth relative to its axis of rotation, (now referred to as polar motion) spanned nearly three decades. He published more than 25 technical papers characterizing the many facets of the phenomenon, including the two-component model with 14-month and annual terms most generally accepted today. The 14-month cycle is called the Chandler wobble in his honor. His further analysis explored multiple frequency models, variation of the frequency of the 14 month component, ellipticity of the annual component, and secular motion of the pole. His interests were much wider than this single subject however, and spanned most of the active areas of astronomical research of his era. He made substantial contributions to cataloging and monitoring variable stars, computing the orbital parameters of minor planets and comets, and improving the estimate of the constant of aberration. His publications totaled nearly 200. He served as Associate Editor to B.A. Gould and then succeeded him as Editor of the Astronomical Journal.

Recent advances in observational methods, most particularly the use of Very Long Baseline Interferometry (VLBI), have resulted in two orders of magnitude improvement in the measurement of polar motion. Renewed interest in the phenomenon has increased awareness of the pioneering and comprehensive works of Chandler. His work has withstood the test of time and it is with great pleasure and respect that we dedicate these proceedings to his memory.

PREFACE

This volume contains the proceedings of the Chapman Conference on *Geodetic VLBI: Monitoring Global Change*, held at the Herbert C. Hoover Building, Washington, DC, from April 22-28, 1991. The conference was convened by William E. Carter.

The program was organized by a technical organizing committee, composed of William E. Carter (Chairman), NOAA, Principal Coordinator for VLBI, International Earth Rotation Service; Douglas S. Robertson, NOAA, Research Geodesist; Dennis D. McCarthy, Chief, USNO, Earth Orientation Division; Miriam Baltuck, NASA, Chief, Geodynamics Branch, NASA HQ; Thomas A. Herring, Massachusetts Institute of Technology; Alan E.E. Rogers, Assistant Director, Haystack Observatory, Massachusetts Institute of Technology; Hermann Seeger, Director, Institute for Applied Geodesy, FRG; James Campbell, University of Bonn, FRG; President of IRIS Subcommission, IUGG-IAU; Koichi Yokoyama, National Astronomical Observatory at Mizusawa, Japan; Chairman, Directing Board, International Earth Rotation Service; Andrei M. Finkelstein, Director, Institute of Applied Astronomy, Leningrad, USSR, Richard D. Rosen, AER, Inc., David A. Salstein, AER, Inc.

In total, 49 papers were given. The papers were organized into six sessions, as outlined in the table of contents. Four authors failed to submit completed manuscripts for a total of six papers, and are represented here only by abstracts.

The proceedings have been assembled and published by the National Geodetic Survey of the National Oceanic and Atmospheric Administration from camera-ready copy provided by the authors. We chose this method to minimize the cost and time required to complete the proceedings, realizing that minimizing the delay in distributing the papers was particularly important in such a rapidly changing subject area.

The organizing committee would like to express its appreciation to Virginia Tippee of NOAA, Gart Westerhaut of the USNO and Miriam Baltuck of NASA for their opening remarks at the welcoming session, and to John Knauss, Undersecretary of Commerce for Oceans and Atmospheres, for his inspiring speech at the conference dinner.

The committee would also like to express its gratitude to the many other people who contributed to the success of the conference. We would like to thank Lynn Mersefelder of NOAA and the staff of the AGU, who made the detailed preparations that made the conference possible. We also thank the session chairpersons, and of course the speakers for their fine presentations and for the papers that are presented in this document.

Table of Contents

Dedication i

Preface ii

Session 1: Instrumentation Improvements to Achieve Millimeter Accuracy

Chairperson: William E. Carter

A.E.E. Rogers (Keynote Presentation)
Instrumentation Improvements to Achieve Millimeter Accuracy 1

A.R. Whitney, A.E.E. Rogers, R.J. Cappallo, J.E. Hargreaves, H.F. Hinteregger, and D.L. Smythe
The Mark 4 Data-Acquisition System 7

B.E. Corey and T.A. Clark
The RF Bandwidth Upgrade: Doubling the X-Band Spanned Bandwidth of Geodetic VLBI Receiving Systems 15

R.J. Cappallo, A.R. Whitney, A.E.E. Rogers, C.J. Lonsdale, and E.F. Nesman
The Mark 4 Correlator System 24

R.C. Walker
The VLBA as a New Tool for Geodesy 25

H. Kiuchi, S. Hama, J. Amagai, Y. Abe, Y. Sugimoto, F. Takahashi, and N. Kawaguchi
Present Status of the K-4 VLBI System 35

T. Sasao and M. Morimoto
Antennacluster-Antennacluster VLBI for Geodesy and Astrometry 48

F. Takahashi, T. Yoshino, Y. Sugimoto, Y. Takahashi, N. Kurihara, and A. Kaneko
The Roles of IERS VLBI Technology Development Center of CRL, Japan 63

N. Umarbaeva, A. Diakov, A. Egorov, and G. Krasinsky
"Syrius-A" Observes NAVSTAR in the Campaign "GIG-91" 71

N. Kawaguchi, T. Miyaji, T. Sasao, T. Hara, S. Kuji, K-H Sato, Y. Tamura, K. Asari, O. Kameya, K. Iwadate, S. Abe, S. Yasuda, and K. Matsumoto
A High Performance Transportable VLBI Correlator 82

W.T. Petrachenko, P. Mathieu, J. Popelar, W.H. Cannon, and J.L. Yen
The Canadian Geophysical Long Baseline Interferometry System Design 90

Session 2: Data Processing and Modeling to Achieve Millimeter Accuracy

Chairperson: Joseph Engeln

T.A. Clark (Keynote Presentation)
Progress to Millimeter Accuracy VLBI: Synergism of Many Factors 98

J.W. Ryan, C. Ma, and W.E. Himwich
NASA Crustal Dynamics Project Results: Sensitivity of Geodetic Results to Clock and Atmosphere Estimation Models 99

W.E. Himwich, D.S. MacMillan, T.A. Herring, C. Ma, and J.W. Ryan
Consistency of Geodetic Information from Kalman Filtering and Batch Least-Squares 106

S. Manabe, T. Sato, S. Sakai, and K. Yokoyama
Atmospheric Loading Effect on VLBI Observations 111

J.R. Ray and B.E. Corey
Current Precision of VLBI Multi-Band Delay Observables 123

C.E. Kuehn and D.S. MacMillan
Sensitivity of Geodetic Parameter Estimates to the Assumed Distribution of the "Wet" Troposphere 135

A.E. Niell
Vertical Change and Atmosphere Correction in VLBI 147

C.S. Jacobs
Modeling Antenna Effects for mm Level VLBI 159

T.M. Eubanks, D.N. Matsakis, D.D. McCarthy, and B.A. Archinal
Comparison of Two Different Scheduling Philosophies for Earth Orientation Measurements Using Very Long Baseline Interferometry 160

S.T. Lowe and R.N. Treuhaft
Applications of Sub-Milliarcsecond Astrometric Techniques to Geodetic Measurements 161

Session 3: Relativistic Effects on VLBI Observables and Data Processing Algorithms

Chairperson: Irwin I. Shapiro

R.W. Hellings, B. Shahid-Saless, and N. Ashby (Keynote Presentation)
Relativistic Effects on VLBI Observables and Data Processing Algorithms 164

I.I. Shapiro
Relativity and VLBI 175

M.H. Soffel, J. Mueller, X. Wu, and C. Xu
Consistent Relativistic VLBI Theory with Picosecond Accuracy 179

S.A. Klioner
General Relativistic Model of VLBI Observables 188

D.S. Robertson, W.E. Carter, and W.H. Dillinger
A New Measurement of Solar Deflection of Radio Signals Using VLBI 203

Session 4: Earth Orientation I: UT1, Earth-Atmosphere-Ocean Momentum Exchange

Chairperson: David A. Salstein

R.D. Rosen (Keynote Presentation)
Studies of the Earth-Atmosphere-Ocean Momentum Exchange: Status and Prospects 213

E. Kalnay
The NMC Global Analysis and Forecast System: Where Are We Going? 221

D.A. Salstein and D.M. Kann
Developments at the Sub-Bureau for Atmospheric Angular Momentum of the IERS 228

R.S. Gross, J.A. Steppe, and J.O. Dickey
The Running RMS Difference Between Length-of-Day and Various Measures of Atmospheric Angular Momentum 238

J.O. Dickey
High Time Resolution Measurements of Earth Rotation 259

G.H. White
Mountain and Surface Stress Torques in NMC Analyses 262

R.M. Ponte
Angular Momentum in the Ocean and Mechanisms of Exchange with the Atmosphere and Solid Earth 270

A.P. Freedman and J.O. Dickey
Intercomparison of AAM Analysis and Forecast Data in UT1 Estimation and Prediction 279

B.F. Chao and A.Y. Au
Atmospheric Excitation of the Earth's Annual Wobble: 1980-1988 294

Session 5: Earth Orientation II: Polar Motion, Nutation, Terrestrial and Celestial Reference Frame

Chairperson: Douglas S. Robertson

T.A. Herring and D. Dong (Keynote Presentation)
Current and Future Accuracy of Earth Orientation Measurements 306

J.C. Davis and R.E. Packard
The Superfluid Helium Gyroscope: An Emerging Technology for Earth Rotation Studies 325

R.S. Gross and J.A. Steppe
The Stability of the Terrestrial Reference Frame Inferred from Earth Orientation Series 335

A. Nothnagel and J. Campbell
Polar Motion Observed by Daily VLBI Measurements 345

E. Groten and S.M. Molodensky
On the Damping of the Nearly Diurnal Free Wobble 355

Session 5: Earth Orientation II: Polar Motion, Nutation, Terrestrial and Celestial Reference Frame (Continued)

C. Ma, J.W. Ryan, and W.E. Himwich
VLBI Reference Frames 376

D.D. McCarthy and B.J. Luzum
Comparison of VLBI Observations 386

D. Zheng, S. Luo, and Z. Xie
Monitor of Oceanic Activities from Observations of Earth Rotation 391

Session 6: Global Change: Sea Level, Crustal Motion, Geodynamics

Chairperson: Herman Seeger

W.E. Carter and D.S. Robertson (Keynote Presentation)
Geodetic VLBI: Monitoring Global Change 398

H. Seeger
IFAG Plans to Support VLBI in the Southern Hemisphere 411

N. Kurihara, T. Kondo, Y. Takahashi, F. Takahashi, and M. Ejiri
The Results of the Test VLBI Experiments with the Syowa Station in Antarctica and Its Future Plans 419

T.A. Clark, D.B. Shaffer, R.M. Allshouse
A New Transportable VLBI System 427

D.S. MacMillan and J.R. Ray
Current Precision of VLBI Vertical Determinations 428

T.M. Eubanks
Global Warming Signals in Earth Rotation 437

Appendix: List of participants 438

Instrumentation Improvements to Achieve Millimeter Accuracy

Alan E.E. Rogers
MIT Haystack Observatory, Westford, MA 01886

23 April 1991

Abstract

The Mark III system was upgraded at Fairbanks, Westford, Haystack and Mojave for special research and development experiments designed to achieve millimeter accuracy. These upgrades include an increase in the spanned bandwidth from 360 to 720 MHz at X-band; doubling the recorder bandwidth from 2 to 4 MHz per baseband channel; improvement in the receiver system temperatures and new calibration electronics. Other improvements include temperature control of the electronics to reduce the temperature sensitivity of instrumental delay calibration; better feed polarization purity; and lower recorder error rates.

These upgrades have reduced the instrumental error sources and the system noise. Experiments with the upgraded systems, which were started in 1989, have achieved repeatability in baseline length of a few millimeters. Estimates of the magnitudes of the remaining instrumental error sources are summarized and performance projections made for future instrumentation improvements.

Introduction

While system noise is thermal and completely random other error sources are at best only quasi-random. Thermal noise decreases with the square root of the number of observations while instrumental error sources will not all average out and will therefore produce a measurement error floor. (See paper by Ray and Corey in this report for observed measurement floor.)

Table 1 lists those instrumental error sources which result in differences between the phase and group delay, as measured by bandwidth synthesis (BWS). The error in BWS delay is computed from:

$$\frac{\textit{phase difference between highest and lowest channels}}{2\pi\ (\textit{frequency difference between highest and lowest channels})}$$

and the r.m.s. value is assumed to be ¼ of the peak to peak value. Many of the instrumental deficiencies result in phase errors which are independent of frequency channel and hence produce a BWS error which decreases with spanned bandwidth. Some error sources, however, like the cross-polarization response produce BWS errors which are more or less constant with spanned bandwidth and will even increase if spanned bandwidth is pushed beyond the limits of good feed performance.

Correlation Errors

Table 2 shows the correlation errors in more detail. The worst errors are the result of unequal data acceptance among the result of unequal data acceptance among the frequency channels which make instrumental dispersion and atmospheric phase fluctuations couple into BWS errors. These errors can be reduced, in the future, by more sophisticated data filtering and better recorder playback performance.

BBC Filters

The baseband (also knows as video) converters have about 400 ns delay at the center of the 4 MHz bandwidth. 2.5% variation between filters results in 10 ns error or 7 degrees phase error at 2 MHz, which in turn produces 50 ps BWS error. Most of the error is constant, although some of this error (probably about 5 ps) will be slowly varying with the ambient temperature changes. These filter errors can be reduced in the future by processing a phase calibration signal close to the center of the baseband.

Spurious Signals

Spurious signals result from harmonics of 5 MHz, harmonics of the sample clock, harmonics of 72 MHz, leakage from the recorder electronics and L.O.s and their harmonics. The signals corrupt the phase calibration phases. At -40 dB the phases are corrupted by 0.6 degrees or 4 ps BWS error in 360 MHz. The spurious signal levels can be checked by turning off the phase calibrator and measuring the residual signals.

Intermodulation Products

Intermodulation products between phase calibration rails result from amplifier and mixer saturation during the phase calibration pulse. At -40 dB these produce 4 ps BWS error in 360 MHz. The level of intermodulation can be checked by unlocking the L.O.s and measuring the residual signals.

Receiver Images

Images are another source of spurious signals. At the -50 dB specification for the front-end image filters the BWS error is 1 ps in 360 MHz. The image performance can be measured by offsetting the first L.O.

Multiple Reflections

Multiple reflections in the antenna system corrupt the radio source phases and hence the BWS delay. For example, multiple reflections from the main reflector to the subreflector on the Haystack antenna are at the -34 dB level and could result in a BWS error as large as 8 ps. However most of the error will be constant and hence an error of 1 ps or less is more likely. Multiple reflections can be significantly reduced by using a "spoiler". On Haystack a spoiler is used to eliminate reflections on the main reflector in the region shadowed by the subreflector. On prime focus systems a spoiler can be placed on the vertex to deflect reflections in the area shadowed by the feed.

Antenna Dispersion

A defocussed parabolic system becomes dispersive owing the frequency dependence of the illumination. Figure 1 shows the small amount of dispersion as a function of the focus. On large antennas the focus can change significantly with elevation angle and might result in BWS delay errors of about 4 ps independent of spanned bandwidth.

Antenna Polarization Impurities

The normalized response of a single baseline to an unpolarized radio source is

$$1 + x_1 x_2^* \; e^{-2i(\theta_2 - \theta_1)}$$

where $x_1 x_2$ are the unwanted LCP voltage responses for antennas 1 and 2

θ_1, θ_2 are feed position (or parallactic) angles

A BWS error of

$$\frac{\partial}{\partial w} \, Im \, (x_1 x_2^* \, e^{-2i(\theta_2 - \theta_1)})$$

results from the frequency dependence of x_1 and x_2. For many of the S/X feeds used in geodetic VLBI the unwanted LCP response is about -15 dB which is large enough to produce about 14 ps error in BWS delay. Linearly polarized radio sources produce additional BWS errors at a somewhat lower level for 10% polarization. These errors can be removed by improving the feeds or making appropriate calibrations.

Summary of Combined Errors

The root sum square of all the instrumental error sources listed with 720 MHz BWS in Table 1 are

≈ 17 ps (5mm) r.m.s. at present
≈ 7 ps (2mm) r.m.s. with polarization calibration

In the future it should be possible to reduce instrumental errors to

≈ 3 ps (1mm) r.m.s. with calibration, and improved correlation

Other instrumental error sources are generally not dispersive and in many cases cannot be separated from clock drifts. The temperature sensitivity of the calibrated electronics, with the new phase calibrator, should be less than 1 ps/°C. Antenna deformation with gravity is largely repeatable leaving local site stability and changes in the antenna axis locations with thermal expansion as remaining concerns as we improve methods of solving for atmospheric parameters to correct the dominant atmospheric delay.

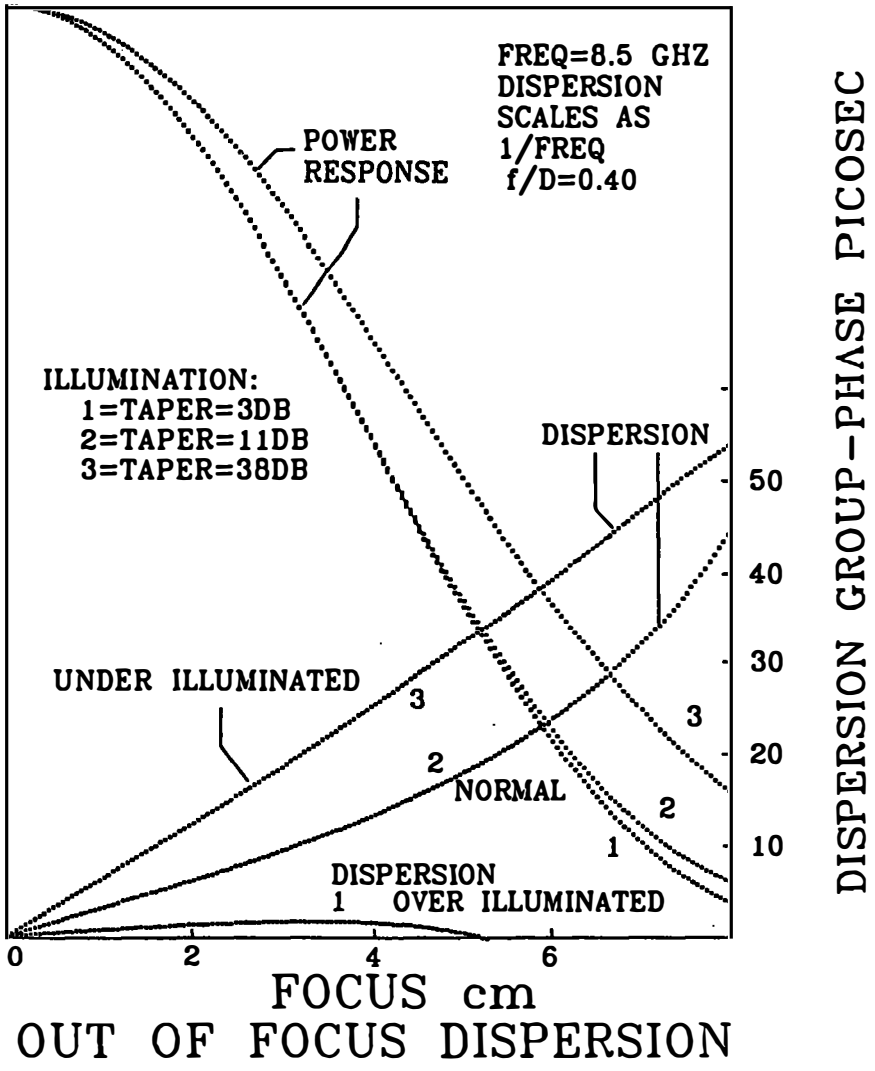

Figure 1

List of Instrumental Error Sources in Bandwidth Synthesis VLBI (which need to be verified by special tests and experiments)			
Error Source	Delay Bias ps	Variable ps rms	Comments Peak-Peak=4xrms
ELECTRONICS:			
Correlator (1 deg.)	8	8	Random (COREL + FRNGE Accuracy)
BBC Filters (7 deg.)	50	5	Constant + 10% Slowly Variable
Spurious Signals (-40 dB)	4	4	Quasi-Random
Intermodulation (-40 dB)	4	4	Slowly Variable
Receiver Images (-50 dB)	1	1	Quasi-Random
ANTENNA and FEED:			
Multiple Reflections	8	1	Mostly constant but may vary with pointing and focus.
Multiple Reflections in the Feed (Refl. = 0.1)	44	1	Mostly constant but may vary with pointing and focus.
Out-of-focus Dispersion	10	4*	Varies with focus and antenna deformation.
Cross-Polarization (-15 dB) on unpol. Sources	14	14*+	Depends on difference in feed position angles.
Cross-Polarization on pol. (10%) Sources	8	8*	Depends on feed position angles at both sites
RSS (of Variable Portion of Error Sources)		20	360 MHz Spanned Bandwidth
		17	720 MHz Spanned Bandwidth
		14	360 MHz Haystack-Westford
		11	720 MHz Haystack-Westford
		7	720 MHz + Cross-Pol Calibration

Notes: 1] All entries assume 360 MHz spanned bandwidth - those marked with * are independent of spanned bandwidth.
2] + Error is zero for Haystack-Westford.
3] Entries are current estimates only (AEER Mar 1991)

Table 1

Correlation Errors	
Bandpass Offsets	≈0.1 Degree
Phase cal (10 KHz 1-bit sine/cos) Extraction Errors	≈0.2 Degree
Phase Rotation Errors	≤0.1 Degree
FRNGE Program Accuracy	≤0.1 Degree
Unequal Data Acceptance 10% with 10 Degree Dispersion	≈1 Degree
Unequal Data Acceptance 10% with 10 Degree Atmos. Curvature	≈1 Degree
10^{-2} Bits out of Sync (VLBA spec. is 10^{-3})	≤0.9 Degree
1 Degree ≈8 ps rms in BWS with 360 MHz	

Table 2

The Mark 4 Data-Acquisition System

A. R. Whitney
A. E. E. Rogers
R. J. Cappallo
J. E. Hargreaves
H. F. Hinteregger
D. L. Smythe

MIT Haystack Observatory, Westford, MA 01886

Abstract

Continued sustained progress in both astronomical and geodetic VLBI efforts demands ever-increasing sensitivity. Recent demonstrations of the feasibility of a fourfold increase in VLBA/Mark IIIA data recording rates to the order of 1-Gbit/sec demonstrate the cost effectiveness of this approach to doubling existing VLBI sensitivity. Such a sensitivity increase could be crucially important for geodetic programs pushing towards 1-mm precision or incorporating small transportable antennas on long baselines.

A program is now in place, with broad support from many agencies, to upgrade existing Mark IIIA recording systems to 1024 Mbits/sec. The main elements of this upgrade are 1) a new plug-compatible formatter with full Mark IIIA and VLBA compatibility, 2) upgrade of existing Mark III video converters to an 8-MHz channel bandwidth, and 3) upgrade of the Mark IIIA recorder to write 64 tracks at 16 Mbits/sec/track. Once engineered, the upgrade cost of a Mark IIIA system to Mark 4 capability is expected to be relatively modest. Completion of a prototype Mark 4 system, including a 2-station VLBI experiment, is expected in early 1993.

1. Introduction

The progress of geodetic VLBI over the last decade has been truly dramatic. Following is a partial list of a few of the many advances that have been made:

- Distances between radio telescopes distributed widely over the world are routinely measured to the order of 1 cm, meeting and exceeding the original goals of the NASA Crustal Dynamics Project. As a result, the motion of tectonic plates, typically a few cm/year, has been measured directly for the first time, and a new goal of mm-level measurements has been set.
- Specially-instrumented and conducted R&D experiments in the fall of 1989 showed measurement precision and repeatability of ~3 mm on baselines thousands of kilometers in length.
- VLBI routinely provides the most precise measurements available of the earth's rotation rate and spin-axis orientation.

These advances have been largely fueled by a broad spectrum of technological advances. Among these are:

- Routine use of the Mark III system beginning in the early eighties increased the recording bandwidth of VLBI data from 4 Mbits/sec of the Mark II system to more than 200 MBits/sec, improving the basic sensitivity of continuum observations by more than a factor of 7.
- Development of the Mark III and Mark IIIA correlators have allowed unprecedented volumes of VLBI data to be routinely processed. In the ten years from 1980, an estimated 3 million observations have been processed.
- Improved receiver systems with lower noise and wider-bandwidths
- Improved phase-calibration systems and cable-calibration systems to remove small instrumental effects
- Improved data-analysis techniques and software

Though the advances both scientifically and technologically have been impressive, there is still much room for growth. In this paper, we will attempt to lay a sound plan for cost-effective continued growth in VLBI data-recording technology in the 90's based on the clear requirements of yet-increased measurement precision

2. The Need for Greater Sensitivity

As scientists continue to pursue ever more precise geodetic VLBI measurements covering more of the globe, the present VLBI system is being pushed to its limits. There are several reasons for this --among them:

- the push to mm-level baseline precision requires observing strategies which currently are marginally acceptable, specifically that many radio sources spread over large angles in the sky must be observed in quick succession
- an ideal spacing of radio sources across the sky is rarely achieved due to a lack of sufficiently strong radio sources in all areas of the sky
- due to the short observation time on each source, signal-to-noise ratios of the resulting observations are often too low to identify potentially-significant systematic trends in single observations

Clearly, the potential set of natural radio sources which may be used by VLBI is fixed in strength and location by Mother Nature. The ability of VLBI to use these sources is by and large set by the *sensitivity* of the VLBI equipment, which includes everything in the equipment chain from antennas to receivers to data-recorders. Since the number of usable natural radio sources increases steeply with a decline in the minimum usable source strength, the advantage of increasing system sensitivity is undeniable. A factor of two increase in sensitivity typically quadruples the number of usable natural radio sources. Such a sensitivity increase dramatically broadens the options open to the VLBI scientist. Depending on the goals of a particular experiment, either more sources may be observed in more optimum locations around the sky, or an existing set of sources may by observed for shorter periods of time in order to move around the sky more quickly. Alternatively, in certain cases, a set of observations may be carried out with smaller antennas.

3. The Means To Greater Sensitivity

VLBI sensitivity may, in general, be increased in only three ways:

- **Increase antenna size.** For any given observation, the signal-to-noise ratio increases directly as the geometric mean of the effective collecting area.
- **Lower receiver noise.** For any given weak-signal observation, the signal-to-noise ratio improves inversely to the geometric mean of the receiver temperatures.
- **Increase bit-rate on tape.** The signal-to-noise ratio improves essentially as the square root of the bit rate. Actual recorded bandwidth may be traded off against #bits/sample, but the SNR remains basically the same for a given bit rate on tape for either the cases of 1 or 2 bits/sample.

In the case of geodesy, the measurement precision of group delay is also related to the total *spanned* bandwidth as well as the signal-to-noise ratio. Recent experiments have pushed the spanned-bandwidth of geodetic measurements to 10% of the observing frequency, which is approaching the practical limit.

4. The Case for Increasing Recorded Bit Rate

Of the three possible options to increase sensitivity, increasing the recorded bit rate is the most cost effective in the current climate of VLBI technology. The reasons are as follows:

- A recent demonstration has been made at MIT Haystack Observatory of a 1-Gbit/sec recording capability using a VLBA recorder[1] very similar to the Mark IIIA VLBI recorder. This was done by simply adding headstacks to existing unused positions on the tape transport and then driving all heads simultaneously. The maximum bit rate was increased a factor of fourfold from 256 Mbits/sec to 1024 Mbits/sec, increasing the overall fundamental sensitivity by a factor of 2. No new technology is involved.
- General consensus is that antenna costs increase roughly as the cube of the diameter. Even for small antennas, the cost of increasing the diameter by a factor of $\sqrt{2}$ is likely to be in excess of $100k, and often impossible for transportable systems; for large antennas, it is completely uneconomical. For an SNR improvement of 2, the diameter of *both* antennas of a baseline must be increased by $\sqrt{2}$ in diameter, or a single antenna by a factor of 2. Also, additional costs must normally be incurred to make larger antennas slew with sufficient rate to support geodetic/astrometic schedules.

---

[1]The VLBA recording system was designed by Haystack Observatory, under contract to the National Radio Astronomy Observatory, for use in the Very-Long Baseline Array (VLBA) project. It uses the same basic tape transport and headstack as the Mark IIIA system, but employs significantly-modernized control and signal electronics; a number of new recording modes are available on the VLBA system, although it supports backward compatibility with some modes of the Mark IIIA recording system.

- Although receiver technology continues to improve, practical limits are being reached, particularly in wavelengths in the cm range. In any case, all VLBI receivers at *every* frequency would have to be improved by a large margin to gain the same benefit that increased bit-rate-to-tape will gain automatically for *all* frequencies.

Of course, increasing bit rate on tape also imposes additional loads on correlators, which must also be taken into account. As a rule of thumb, correlators have been designed for a given total bit-rate throughput, so that increasing that data rate by a factor of 4 will in general cause the data throughput rate of a given correlator to drop by the same factor. Nevertheless, although it will be necessary to increase correlator capacity in order to keep up with an increased data rate, such correlator costs are virtually guaranteed to be smaller than the alternatives to gain the same basic sensitivity.

5. The 1-Gbit/sec Feasibility Demonstration

The VLBA recorder normally operates with a single headstack with a maximum formatted data rate of 256 Mbits/sec. However, the transport has positions for up to four headstacks, three of which are vacant for a standard VLBA recorder. For a special feasibility demonstration of very-high-data-rate recording, a standard VLBA tape recorder was outfitted with four standard headstacks to occupy all headstack-positions available on the Honeywell 96 tape transport. A standard VLBA formatter was used to drive the 36 tracks on each headstack at a bit rate of 9 Mbits/sec/track for a total of 1.296 Gbits/sec total data rate. With the normal formatting overhead of 9/8, this corresponds to a 1.152 Gbits/sec data rate for formatted VLBI data. Data were recorded for several adjacent passes on the tape to simulate a portion of an actual experiment. For compatibility with the Mark IIIA correlator, data was recorded in Mark IIIA format at 33,000 bits/inch along each track.

Following recording of the data, the Mark IIIA correlator at Haystack was used to auto-correlate the recorded tape (in several passes) to verify the quality and validity of the data. All data were read properly and the processing through the correlator produced nominal results.

6. The Mark 4 Data-Acquisition System

Over the past dozen or so years, over 35 Mark III and Mark IIIA data-recording systems have been installed around the world. Most of the original Mark III systems have now been upgraded to the high-density Mark IIIA system, which provides for much higher-density recording but does not increase the maximum (formatted) recording-rate capability of 224 Mbits/sec. The original design of the Mark IIIA system envisioned an eventual upgrading of the design to accommodate much higher data rates as the required electronics becomes smaller, cheaper, and more reliable. With the definitive demonstration of 1 Gbit/sec capability on the similar VLBA recording system, the expansion path of the Mark IIIA system has also been validated. Accordingly, we propose to significantly upgrade Mark IIIA capability by quadrupling the maximum date rate to 1024 Mbits/sec. At the same time, a general upgrade of the recording-

system electronics will incorporate newer technology for *higher reliability and lower maintenance costs*.

The Mark IIIA recording system uses exactly the same Honeywell tape transport and headstack assembly as the VLBA recorder used in the 1-Gbit/sec demonstration; therefore, the Mark IIIA data-recording system may be upgraded in a similar fashion to that demonstrated in the 1-Gbit/sec demonstration, provided the necessary formatter and write electronics are provided.

The standard Mark IIIA data-acquisition-system configuration provides 14 video converters, each with independent upper and lower-sideband channels of 4 MHz bandwidth maximum each, for a total maximum bandwidth of 112 MHz. The existing formatter provides 28 channels of data at 1-bit/sample, at a maximum sample rate of 8 Mbits/sec/channel, for a total maximum date rate of 224 Mbits/sec. Two identical standard high-density headstacks are mounted in the Mark IIIA recorder, one headstack dedicated to writing and the other to reading. Of the 36 tracks available in each headstack, only 28 are used by the Mark IIIA system, each track independently carrying data from a single video-converter sideband.

The following actions will be necessary to increase the maximum data rate of the Mark IIIA to 1024 Mbits/sec (more than factor of 4 increase):

- Increase the number of video-converters from 14 to 16; this will be done by utilizing an existing rack-mounted spare and adding one more video-converter to the rack.
- Increase the maximum bandwidth of a video-converter sideband to 8 MHz by replacing one of the existing unused (or seldom-used) internal filters with an 8 MHz filter and changing the gain-compensation resistors.
- Design a new formatter with the following characteristics -
    - Plug-in replacement for existing formatter
    - 32 channels @ 16 Msamples/sec (and lower rates)
    - 1 or 2 bits/sample
    - channel-to-head cross-point matrix switch
    - support of many VLBA-compatibility modes
- Replace existing write interfaces with VLBA-style read/write interfaces which use the same heads for read and write
- Use both existing headstacks for both reading and writing, for a total of 64 available tracks
- Add necessary write electronics to support 64 heads

The **Mark 4** data-recording system will have the following characteristics:

- 64 tracks at 16 Mbits/sec/track for a total of **1024 Mbits/sec formatted data**
- Will use the same 16 micron-thick tape chosen by the VLBA:
    - 18000' of tape on standard 14" reel
    - longitudinal density: 56,000 bits/inch/track
    - tape speed: 320 ips (16 Mbits/sec/track)
    - record time per pass: 11.25 minutes
    - record time per tape (6 passes): 67.5 minutes

- ~95% SNR improvement over present maximum-data-rate Mark IIIA
- Full backward compatibility to all standard Mark IIIA operating modes, as well as compatibility with as many VLBA modes as possible

Based on current projections, the estimated materials and services (only) cost per Mark IIIA system upgrade is:

• New formatter	$10K
• Additional video converter	$3K
• 8 MHz filters (32 per system)	$3K
• New write drivers	$3K
• New read module	$1K

The only major new design work necessary for the upgrade to Mark 4 is the new formatter, which is estimated to require ~2 man-years of engineering time. In the new formatter design we expect to also support many of the VLBA data-multiplexing modes currently unsupported by the Mark IIIA system, although we do not propose to support the 'non-data-replacement' tape format which is supported by the VLBA formatter.

7. Compatibility Between Various Recording Systems

The subject of compatibility between various VLBI data-acquisition system and correlators is a very complex one. In this section we will only attempt to summarize the salient similarities and differences of the various systems; a complete discussion is beyond the scope of this document. The major differences between the Mark IIIA, Mark 4, and VLBA system can be summarized as follows:

- the Mark IIIA has 14 video converters, each with a maximum bandwidth of 4 MHz/sideband, supports only 1 bit/sample, data-replacement format only, and maps data from one VC sideband to one tape-track (i.e. no data-multiplexing or 'barrel-rolling'), with a maximum data rate of 224 Mbits/sec on 28 tracks
- the Mark 4 has 16 video converters, each with a maximum bandwidth of 8 MHz/sideband, supports 1 or 2 bits/sample, data-replacement format only, support several modes of multiplexing, with a maximum data rate of 1024 Mbits/sec on 64 tracks
- a single standard VLBA data-acquisition system has 8 video converters, each with a maximum bandwidth of 16 MHz/sideband, supports 1 or 2 bits/sample, data-replacement or non-data-replacement format, many mode of multiplexing and barrel-rolling, with a maximum data rate of 256 Mbits/sec on 32 tracks; each VLBA station will (eventually) be equipped with 2 standard VLBA DAS's; on special order, a VLBA DAS may be equipped with 14 VC's

Table I shows a comparison of the data-recording capabilities of the Mark IIIA, the Mark 4, and 'standard' and 'augmented' VLBA data-acquisition systems. The major differences to note are numbers of channels and channel bandwidths. As you can see from an examination of Table I, there are many compatible modes between Mark 4 and VLBA, though the reader is referred to official VLBA documentation for a complete discussion of the capabilities of the VLBA DAS.

8. Proposed Plan of Action

A straightforward, two-step plan is suggested for implementation of the Mark 4 recording system:

- **Build a prototype system and test in a real VLBI experiment.** A new formatter will be designed, and two existing Mark IIIA systems will be fully upgraded to Mark 4 capability. A 'full-up' test experiment then will be conducted between two sites and the data processed on the correlator at Haystack Observatory. Estimated cost for this development and test effort is ~$500K over two years. Multi-agency support is proposed to make this development cost effective for all applications.
- **Develop a kit for upgrade from Mark IIIA to Mark 4.** As in the past, Haystack will transfer the Mark 4 design to other interested colleagues in the U.S. and around the world, as well as to industry. Replication of the upgrade kit can be made by all interested parties.

This strategy has proven effective in the past for several major VLBI sub-systems, and should prove equally effective in this case.

9. Summary

Achievement of significant improvements in geodetic measurement accuracy and precision is closely tied to continued improvements in VLBI technology, including system sensitivity. The most cost effective approach to improving system sensitivity is to increase the recorded VLBI data rate.

In this document, we have outlined a straightforward approach to improving Mark IIIA sensitivity by a factor of 2 by quadrupling the maximum date rate from 224 Mbits/sec to 1024 Mbits/sec. The path to this improved system is clear and surprisingly straightforward. The cost is kept relatively modest through upgrading of existing hardware and software in most cases, and the technology is existing and well-proven. The result will be a system with *significantly* enhanced capabilities at a small fraction of the cost of a new system.

We have laid out a step-by-step plan of action to accomplish these goals, structured in such a way so as to gain the maximum benefit of each element within the existing system as soon as possible. Importantly, full backward compatibility is maintained to the existing Mark IIIA system throughout the Mark 4 development program.

Since the usage of many VLBI systems is already shared between several agencies, a coordinated multi-agency program of support for the proposed upgrades would mutually benefit all, at a modest cost to each.

DATA-ACQUISITION-SYSTEM CAPABILITY COMPARISON

		Mark IIIA		Standard VLBA[1]		Augmented VLBA[2]		Mark 4	
		# chans	Mb/s	# chans	Mb/s	# chans	Mb/s	# chans	Mb/s
4 Msamples/sec	1 bit	14x2	112	8x2	64	14x2	112	16x2	128
	2 bit	-	-	8x2	128	14x2	224	16x2	256
8 Msamples/sec	1 bit	14x2	224	8x2	128	14x2	224	16x2	256
	2 bit	-	-	8x2	256	14x1	224	16x2	512
16 Msamples/sec	1 bit	-	-	8x2	256	14x1	224	16x2	512
	2 bit	-	-	8x2	512	8x1	256	16x2	1024
32 Msamples/sec	1 bit	-	-	8x2	512	8x1	256	-	-
	2 bit	-	-	8x1	512	4x1	256	-	-

[1]Standard VLBA - 8 video converters, 2 formatters, 2 recorders
[2]Augmented VLBA - 14 video converters, 1 formatter, 1 recorder

Table I

The RF Bandwidth Upgrade: Doubling the X-band Spanned Bandwidth of Geodetic VLBI Receiving Systems

Brian E. Corey
Haystack Observatory, Westford, MA

and

Thomas A. Clark
NASA Goddard Space Flight Center, Greenbelt, MD

Modifications to the standard S/X receivers and to the MkIII data acquisition terminal have been developed to increase the instantaneous RF and IF bandwidths to >700 MHz at X-band and to 240 MHz at S-band. This upgrade permits a doubling of the X-band spanned bandwidth of observation, and hence an approximately twofold improvement in the precision of the group delay observable. The hardware modifications include minor changes in the receiver and the addition of a new "IF3" module to the MkIII terminal. The modifications and new observing frequencies are fully compatible with the capabilities supported by the 10-station Very Long Baseline Array being built by the National Radio Astronomy Observatory.

As of April 1991, the new equipment has been installed at 6 stations that regularly participate in geodetic VLBI programs. Within the next year we anticipate that another 10 stations will be upgraded. The wideband hardware was used during the October 1989 Extended R&D Experiment (ERDE) in a 5-station network (Haystack MA, Westford MA, Mojave CA, Fairbanks AK, and Pie Town NM) that produced VLBI data with repeatability of ~1 mm horizontal and ~7 mm vertical [*MacMillan and Ray*, 1991].

1. INTRODUCTION

In the 22 years since the first "high-precision" geodetic VLBI experiments, the precision of the best VLBI measurements has improved by roughly three orders of magnitude, from a few meters [*Hinteregger et al.*, 1972; *Cohen and Shaffer*, 1971] to a few millimeters [*MacMillan and Ray*, 1991]. One of the critical elements contributing to this improvement has been increased precision of the geodetic observables themselves, including particularly the multiband delay, or group delay, which is the primary observable used in present-day geodetic VLBI.

The current standard practice in geodetic VLBI is to record signals in several relatively narrow (a few MHz wide) frequency channels that are spread over a large RF frequency range (several hundred MHz). The standard error σ_τ of the multiband delay depends on the overall signal-to-noise ratio SNR and the rms value $\Delta\nu_{rms}$ of the channel frequencies *via* the following relation:

$$\sigma_\tau = \frac{1}{2\pi \ \mathrm{SNR} \ \Delta\nu_{rms}} \quad . \tag{1}$$

In order to decrease σ_τ, one must exercise one (or both) of the following two options:

1. **Increase the SNR.** For a pointlike radio source, the SNR is proportional to

$$\frac{\text{antenna temperature}}{\text{system temperature}} \times \sqrt{(\text{bit rate}) \times (\text{integration time})} \quad .$$

Past efforts to increase the SNR through system improvements have concentrated on increasing the recorded bit rate (the MkIII system supports a maximum bit rate more than two orders of magnitude higher than that of the MkI system used in the early geodetic experiments), and on lowering the system temperature of the S/X-band receivers (the X-band system temperatures of our present receivers, which utilize cryogenically cooled HEMT or FET RF amplifiers, are a factor of 2–3 lower than those of older receivers employing room-temperature parametric amplifiers). These efforts continue, the most notable example being the MkIV system [*Whitney et al.*, 1991; *Cappallo et al.*, 1991] now under development.

2. **Increase the rms bandwidth.** In the earliest X-band geodetic VLBI observations that made use of the multiband delay [*Hinteregger et al.*, 1972], the total spanned bandwidth was 36 MHz, and the rms bandwidth was 12.3 MHz. Improvements in both RF and IF electronics in the years since then have permitted an increase in the bandwidth by roughly an order of magnitude. Further widening of the bandwidth is the subject of this paper.

Equation (1) takes account of only the thermal noise contribution to the group delay error. There are a number of instrumental error sources in our geodetic systems that can further limit the delay precision [*Rogers*, 1991]. All the instrumental errors listed in *Rogers's* Table 1 are independent of SNR, but many (*e.g.*, those listed under the "Electronics" heading) should be proportional to $\Delta\nu_{rms}^{-1}$. Hence the latter errors should be reduced by widening the bandwidth.

The system improvements listed above (higher bit rate, lower system temperature, and wider bandwidth) may of course be used for purposes other than decreasing the group delay error of individual observations. For instance, smaller antennas may be employed without increasing the delay error. Or, one may trade off SNR for rms bandwidth: with the wider bandwidth, more observations of shorter duration can be scheduled in a given time span, thereby permitting better sampling of the atmospheric mapping function.

The bandwidth upgrade described in this paper was designed for the S/X receivers and MkIII data acquisition terminals employed by the NASA Crustal Dynamics Project (CDP) in its observing program. The primary objective of the upgrade is to widen the X-band bandwidth of the receivers and MkIII terminals enough that the rms bandwidth of the observing frequencies can be doubled. Widening the S-band bandwidth is also an objective.

The spanned bandwidths of the standard observing frequency sequences employed over the past decade are 360 MHz at X-band and 85 MHz at S-band. These values are close to the limits imposed by the equipment: The S/X receivers, as originally constructed, support a maximum spanned bandwidth of 400 MHz at X-band and 140 MHz at S-band, and the MkIII terminal has an upper limit of 400 MHz for the bandwidth of a single IF channel. As a concrete goal for the upgrade, we chose to double the X-band spanned bandwidth of the equipment, from 400 to 800 MHz, and to increase the S-band bandwidth to 240 MHz. The X-band upgrade therefore entails changes to both the receiver and the MkIII terminal.

In the next section we describe the hardware aspects of the upgrade. In section 3, we review the accomplishments to date, and discuss two problems that have been encountered. In the final section we speculate on the future.

2. METHOD OF IMPLEMENTATION

Because the equipment changes necessary to widen the S-band bandwidth are trivial, we concentrate in this section on the X-band upgrade.

In addition to the usual considerations of cost and development time, the following goals were kept in mind during the design phase:

- Maintain compatability with existing geodetic systems. The desire for backward compatability argued against a change in the receiver LO frequencies.
- Make the RF frequency coverage compatible with that of the Very Long Baseline Array (VLBA) being constructed by the National Radio Astronomy Observatory (NRAO). The VLBA will produce high-quality geodetic and astrometric results. Joint experiments between VLBA and CDP stations will be extremely useful for tying the two reference systems together, for filling in gaps in the geographic coverage of one or the other array, and for checking the performance of the two arrays.
- Minimize the extent of the changes to the receiver hardware. At most sites, it is far easier to make hardware changes (or repairs!) in the control room equipment than in the receiver.

In light of these considerations, we chose to do the upgrade simply by expanding the frequency coverage at the upper end of the present S- and X-band ranges, without changing receiver LO frequencies or adding an additional IF channel in the receiver. At S-band, the only modification to the existing hardware that is needed is to replace the image rejection filter in the receiver with a wider-bandwidth model. At X-band, the upgrade is done in the following manner:

1. In the receiver, replace a few of the components (image rejection filter, mixer/preamplifier, and IF amplifier) with wider-bandwidth components. Otherwise, make no changes in the receiver. The new RF frequency coverage is added at the upper end of the present range. Because the receiver mixer does an upper sideband (USB) conversion, the IF frequency range is also expanded at its upper end, from the present 100–500 MHz, to the upgraded 100–900 MHz.
2. Build a new module, poetically dubbed the "IF3" module, for the MkIII terminal. The purpose of the module is to make the upper portion of the wider X-band IF available to the MkIII video converters, whose input signals must lie in the range 100–500 MHz.

With this arrangement, stations may switch from "wideband" observations to "standard" observations (which use frequency sequences with pre-upgrade bandwidths), or *vice versa*, simply by reconfiguring the MkIII terminal, without having to make changes in the receiver.

Table 1 gives the RF frequency coverage of the standard and wideband systems. The 100-MHz gap in the X-band wideband frequency coverage arises in the IF3 module (see below) – there is no such gap in the IF signal coming from the receiver.

Table 1. Frequency Coverage Supported by Standard and Wideband Geodetic Systems
(All frequencies are in MHz.)

System	*S-band RF*	*X-band RF*	*S-band IF(*)*	*X-band IF(*)*
Standard	2210–2350	8180–8580	190–330	100–500
Wideband	2210–2450	8180–8580 & 8680–8980	190–430	100–500 & 600–900

(*) For receiver LO frequencies of 2020 and 8080 MHz.

A slight conflict exists between the X-band frequency range of the wideband system given in Table 1 and that of the VLBA receivers. The advertised VLBA passband is 8000–8800 MHz. The 3-dB passband of the VLBA X-band filters is much wider, however: 7850–8950 MHz. Discussions with NRAO staff led us to conclude that the VLBA sensitivity should not degrade significantly between 8800 and 8950 MHz, so we proceeded with the design as outlined above.

The IF3 module functions much like one channel of the MkIII IF distributor, except that the former includes a mixer stage. Figure 1 shows a simplified block diagram of the IF3 module. The X-band IF signal from the receiver is first attenuated by the amount needed to bring the IF3 output level into the proper range for the MkIII video converters, and it is then amplified. Depending on the setting of a double-pole/double-throw (DPDT) switch, the signal is then either (1) down-converted in frequency by 500.1 MHz, or (2) bandpass filtered, with no frequency conversion. Option (1) converts the 600–900 MHz portion of the original IF to 100–400 MHz, which can then be passed to the video converters. Option (2) is included to allow easy changeover from wideband to standard frequency observations. Following the second pole of the switch, the IF3 signal is further amplified and then sent to a 4-way power splitter, from which the signals can be routed to the video converters. The 500.1-MHz LO, which is generated by a VLBA-style baseband converter oscillator designed by Alan Rogers (Haystack), is phase-locked to a 5 MHz signal from the MkIII 5 MHz distributor. The LO frequency is offset from an integral number of MHz in order to reject strongly the image phase cal tones in the mixing process.

Not shown in Figure 1 are a digital interface circuit and a MkIII-specific Microprocessor Ascii Transceiver (MAT), which together allow computer control of the attenuator setting and DPDT switch state. They also permit remote reading of the output power level (measured with the square-law detector), attenuator setting, switch state, and LO frequency setting. In addition, they can control an external set of single-pole/double-throw RF switches that serve as general-purpose switches to change the input IF signals sent to individual video converters. The IF3 module may also be operated manually *via* front-panel switches.

The 100-MHz gap in the X-band IF coverage, while unesthetic, has not proven to be a limitation. Most candidate frequency sequences considered for use with the wideband system have naturally contained a gap larger than 100 MHz in the appropriate frequency range. In order to eliminate the gap in the present design, the LO frequency would have to be dropped to 400 MHz, in which case spurious signals would appear in the IF3 output due to LO leakage and $3\nu_{LO} - \nu_{RF}$ harmonic mixer products. Other IF3 designs were considered and rejected as being too complex (two frequency converters) or as requiring modifications to the processing software that are too extensive (single high-side mixer stage).

Table 2 lists the frequency sequences used in most pre-upgrade geodetic experiments (CDP, IRIS,

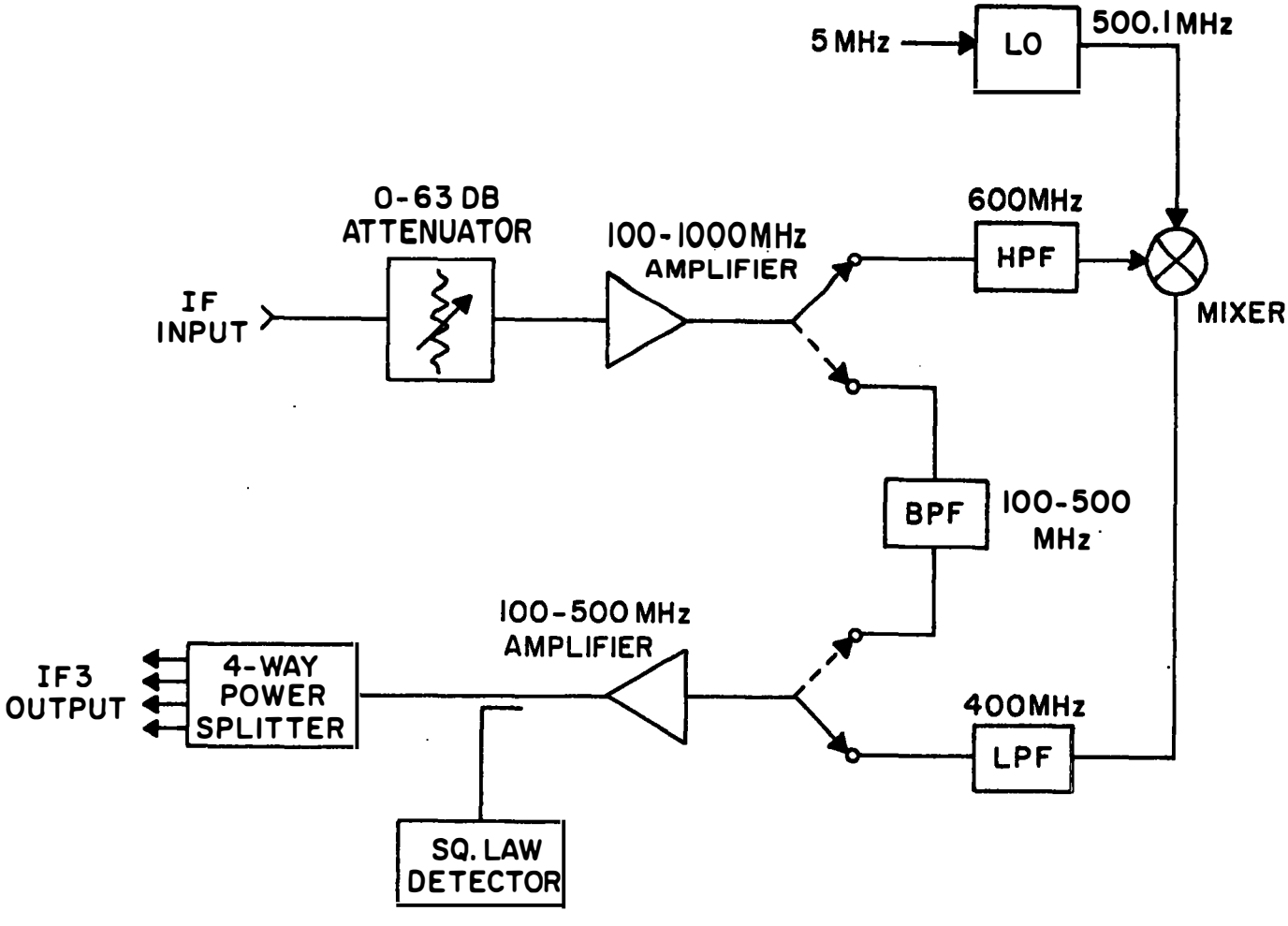

Figure 1. Simplified block diagram of the analog electronics of an IF3 module. Notation: BPF = bandpass filter, HPF = highpass filter, LPF = lowpass filter.

etc.) and in the wideband experiments conducted since 1989. The X-band wideband sequence is the same as the standard except that all frequency spacings have been doubled, and the sequence has been flipped upside down to accommodate the 100-MHz gap. We did not attempt to double the rms bandwidth at S-band because it is not possible to do so while both (a) keeping the sidelobe levels in the group delay resolution function sufficiently low, when only six frequency channels are used; and (b) maintaining a group delay ambiguity large enough (of order 200 ns) to ensure proper ambiguity resolution during periods of high solar activity. Because the S-band delay normally makes only a small contribution to the total error in the ionosphere-free delay constructed from the X- and S-band delays, the modest 53-percent increase in S-band rms bandwidth was deemed sufficient.

Table 2. Standard and Wideband S/X Frequency Sequences
(All frequencies are in MHz.)

	S-band standard	*S-band wideband*	*X-band standard*	*X-band wideband(*)*
Channel freqs.(†)	2217.99	2220.99	8210.99	8212.99
	2222.99	2230.99	8220.99	8252.99
	2237.99	2250.99	8250.99	8352.99
	2267.99	2305.99	8310.99	8512.99
	2292.99	2340.99	8420.99	8732.99
	2302.99	2345.99	8500.99	8852.99
			8550.99	8912.99
			8570.99	8932.99
Spanned bandwidth	85.0	125.0	360.0	720.0
RMS bandwidth	33.1	50.7	140.2	280.4

(*) In the CDP R&D experiments, the VLBA stations do not record X-band channels 4 (8512.99 MHz) and 6 (8852.99 MHz). See *Ray and Corey* [1991] for details.

(†) The channel frequencies are the sky frequencies corresponding to DC at baseband. They lie at the lower edge of the channel bandwidth of 2 MHz (standard) or 4 MHz (wideband).

3. PROGRESS AND PROBLEMS

The bandwidth upgrade has undergone minor changes since its initial design in early 1989. The first IF3 modules did not include the computer interface or the DPDT switch. In addition, lessons learned with the early hardware led us to make some other, minor changes, which we describe later in this section.

The first four upgrade kits (receiver hardware and IF3 module) were installed in July 1989 at the geodetic VLBI stations at Fairbanks (AK), Mojave (CA), Westford (MA), and Haystack (MA). Their installation was the final step in a series of system improvements made at these sites during the first half of 1989. The other hardware modifications included:

- The phase calibrators in the receivers were replaced with new, more compact units designed by Alan Rogers. The output power of the new units is much flatter with frequency, and the temperature stability of the pulse epoch relative to the incoming 5 MHz is improved (< 2 ps/°C). In order to reduce further any drifts in the pulse epochs, the calibrators were enclosed in temperature controllers built by Bendix Field Engineering.

- For those receivers whose internal air temperature is not well regulated, Bendix-built temperature controllers were added to the local oscillators to reduce the temperature-driven LO phase drifts.
- In order to support "double-speed" (8 Mbps) recording, all 14 MkIII video converters at each site were outfitted with 4-MHz video filters.

Starting in July 1989, these four stations, together with the VLBA station at Pie Town (NM), participated in monthly, 24-hour-long, geodetic experiments organized by the CDP under the series name "R&D". These experiments utilized the wideband frequency sequence of Table 2, with 4-MHz channel widths and double-speed recording, and a new observing schedule written by Arthur Niell (Haystack). This schedule emphasizes rapid and thorough sampling of all azimuths and elevations at each site, including particularly the lowest possible elevations. Such sampling is achieved through extensive subnetting and by keeping individual scan durations no longer than needed to give delay standard errors of ~20 ps.

Shortly after the first stations were upgraded, two problems related to the upgrade were discovered in the correlator output from the fringe tests and initial R&D experiments:

1. The fringe amplitude on all baselines dropped significantly above 8.6 GHz, with the largest drop at the highest frequencies. On non-Haystack baselines the rolloff was 20–30 percent, and on Haystack baselines it was as much as 50 percent. The performance of the Haystack feed and receiver, both of which differ from the CDP norms, was known to degrade above 8.6 GHz, so weaker amplitudes on Haystack baselines at the higher X-band frequencies were expected. The 20–30 percent rolloff on the other baselines was not anticipated, however.

   System tests at Westford showed conclusively that the fault lay with the receiver/feed sensitivity, and not in the IF3 module (through which pass all signals whose sky frequency is above 8.6 GHz). Potential causes for reduced sensitivity are lower aperture efficiency (due to, for example, underillumination of the primary reflector by the feed or higher return loss within the feed) and higher system temperature. Further measurements at Fairbanks, Mojave, and Westford showed both effects to be present, but the dominant one appeared to be higher system temperatures. Roger Allshouse and Hollys Allen (Bendix) have found that the cooled X-band HEMT amplifiers need to be retuned for optimum noise performance over the wideband frequency range. We are currently in the process of installing such retuned amplifiers at the R&D stations. Meantime we continue to study other sources of the higher system temperature and of the degraded aperture efficiency.

   Although certainly undesirable, a 30-percent drop in the fringe amplitude at the highest X-band frequencies is not a serious problem. For non-Haystack baselines, the worst-case rolloff causes the group delay standard error to be about 20 percent higher than it would be with no rolloff.

2. Evidence of strong (−20 dB relative to phase cal) spurious signals, nearly coherent with the true phase cal tones, was seen in the correlator output for the lower X-band frequencies at non-VLBA sites. Checks at the stations confirmed these findings: when the receiver LO was unlocked, the X-band phase cal level measured at the MkIII terminal dropped by only ~20 dB in the low-frequency channels. A spurious signal of this level can cause slow apparent drifts

of ±6° in the measured phase of the phase cal tone. Over a 720-MHz spanned bandwidth, such a phase change corresponds to a group delay error of ±22 ps.

These spurious signals result from overdriving the receiver mixer/preamp when the phase cal pulse is on. (During the ~1 ns when each X-band pulse is on, the phase cal power exceeds the receiver noise by 10 dB or more.) Such signals were present in the receivers before the bandwidth upgrade, but at much lower levels. The upgrade hardware exacerbated the problem due to the doubled bandwidth (which increases the amplitude of the phase cal pulse) and, more significantly, due to poor design of the IF amplifier part of the mixer/preamp. As an interim fix, in September 1989 the spurious levels at the CDP stations were reduced by decreasing the RF gain ahead of the mixer/preamp, and by attenuating the X-band level out of the phase calibrator. Since then we have identified other mixers and IF amplifiers that can meet the goal of spurious levels >50 dB below phase cal with normal RF gain and phase cal levels. Such equipment was installed at Wettzell and Kokee Park when they were upgraded in early 1991, and the performance on the antennas has confirmed our lab tests.

In October 1989, the five R&D stations conducted the 12-day Extended R&D Experiment (ERDE), which used the same frequency sequence and daily observing schedule as the monthly R&D experiments, but fit 12 days of observations into a 17-day span. The purposes of the experiment included: (1) with the best geodetic equipment available, determining baseline precision from repeated, intensive measurements over a short time span; (2) continuous monitoring of UT1 and pole position over multi-day arcs; and (3) providing a large, homogeneous data set for studies of the effect of the neutral atmosphere on geodetic VLBI measurements.

The geodetic precision in ERDE is among the best ever achieved: *MacMillan and Ray* [1991] find that the ERDE baseline repeatability is approximately 1 mm rms in the horizontal coordinates and 7 mm rms in the vertical. *Ray and Corey* [1991] analyze the precision of the ERDE group delay observables themselves, and find that the bandwidth upgrade did in fact improve the delay precision significantly. The precision of the highest-SNR observations is still limited by instrumental error sources, however.

The monthly R&D experiments resumed after ERDE, and they continue today, but with a different set of stations. The R&D network as of April 1991 comprises Fairbanks, Mojave, Westford, Wettzell (Germany), Kokee Park (HI), and the VLBA station at Los Alamos (NM).

4. THE FUTURE

Upgrade kits for another 10 stations are presently under construction and will be available within a year. Because many non-CDP geodetic stations have MkIII terminals and S/X receivers of design similar to CDP receivers, the usefulness of the upgrade is not limited to CDP sites. We anticipate that, by the end of 1992, most geodetic observing will be done with a wideband frequency sequence.

Further significant widening (by a factor of 2, say) of the instantaneous X-band bandwidth is easy in principle (simply double the bandwidths of the receiver components again, and build IF4 modules for the MkIII terminals), but difficult in practice. Two receiver components that did not need major modifications for the upgrade described here, the antenna feed and the X-band RF amplifier, will almost certainly limit the effective bandwidth to well under 2 × 800 MHz if they are

not redesigned: At the edges of a 1600-MHz band, the gain of the present amplifiers will be low, and the noise temperature high; similarly, the feed return loss will likely be high, and the polarization purity poor. The amplifier problem is soluble, either with wider-bandwidth circuits or by using two parallel X-band channels with center frequencies offset by 800 MHz. Broadening the feed bandwidth will probably be more difficult. Most feeds show good performance only over a bandwidth of ~10 percent of the center frequency. A technically simple but operationally nightmarish solution is to move the X-band channel up to 15–16 GHz, where 1600 MHz is a 10-percent bandwidth. Not only would such a change cause serious backward compatability problems, but also the aperture efficiency at 16 GHz on many geodetic antennas is poor. A less drastic solution may be to add an "outlier" frequency channel to the receiver, close enough to our present X-band frequencies to allow estimation of a single group delay, but far enough removed to make the feed design feasible. In any event, feed design will surely be a major part of the next bandwidth upgrade.

Acknowledgements: We thank Roger Allshouse, Ed Himwich, Dave Shaffer, Nancy Vandenberg, and especially Alan Rogers, for important contributions to the design of the upgrade; the staffs at the Fairbanks, Mojave, Wettzell, and Kokee Park stations, for installing the new equipment and for their indispensable aid in shaking it down and running test after test, all with seeming eagerness; Roger Allshouse and Hollys Allen, for performing critical receiver tests and for upgrading the Kokee Park receiver; Viet Tran, for designing the IF3 digital interface; and Pat Morrison, for building everything.

REFERENCES

Cappallo, R.J., A.R. Whitney, A.E.E. Rogers, C.J. Lonsdale, and E.F. Nesman, The Mark 4 correlator system, this volume, 1991.

Cohen, M.H., and D.B. Shaffer, Positions of radio sources from long-baseline interferometry, *Astron. J.*, *76*, 91–100, 1971.

Hinteregger, H.F., I.I. Shapiro, D.S. Robertson, C.A. Knight, R.A. Ergas, A.R. Whitney, A.E.E. Rogers, J.M. Moran, T.A. Clark, and B.F. Burke, Precision geodesy via radio interferometry, *Science*, *178*, 396–398, 1972.

MacMillan, D.S., and J.R. Ray, Current precision of VLBI vertical determinations, this volume, 1991.

Ray, J.R., and B.E. Corey, Current precision of VLBI multi-band delay observables, this volume, 1991.

Rogers, A.E.E., Instrumentation improvements to achieve millimeter accuracy, this volume, 1991.

Whitney, A.R., A.E.E. Rogers, H.F. Hinteregger, D.L. Smythe, and J.E. Hargreaves, The Mark 4 data-acquisition system, this volume, 1991.

The Mark 4 Correlator System

R J Cappallo, A R Whitney, A E E Rogers, C J Lonsdale, and E F Nesman (All at: MIT Haystack Observatory, Westford, MA 01886)

The development of the Mark 4 VLBI data-acquisition system, with data rates up to 1024 Mbits/sec, requires the complementary development of a new correlator system to take advantage of its many new capabilities. In order to process data from the Mark 4 recording system, a correlator will be constructed to meet the following design goals:

1. A baseline-oriented architecture similar to the Mark IIIA correlator.
2. A new playback-machine design based upon the VLBA transport, which was developed by Haystack.
3. Expansion from 28 to 32 tracks per tape drive.
4. New correlator modules which are based on the widely-used 'Bos' correlator chip. Module cost will be lowered by incorporating modern gate arrays, semi-custom IC's, and microprocessors.
5. Improved modelling capabilities to further reduce any systematic errors.
6. Operation at data rates up to 32 Mbits/sec/channel.
7. Compatibility with Mark IIIA, Mark 4, and some VLBA-format modes.
8. Significantly-improved computer support utilizing the Unix operating system on a modern platform.
9. Full real-time capability integrated into the design in anticipation of real-time VLBI processing in the future.
10. Improved hardware reliability and ease of maintenance.

Design and development work are expected to extend approximately 3 years, with the first operational systems to be placed at the U.S. Naval Observatory and Haystack Observatory.

THE VLBA AS A NEW TOOL FOR GEODESY

R. Craig Walker
National Radio Astronomy Observatory*
Socorro, NM 87801

VLBA OVERVIEW

The Very Long Baseline Array (VLBA) is a major new national facility for astronomy. It is being built by the National Radio Astronomy Observatory (NRAO) with funding from the National Science Foundation. The primary use of the VLBA will be for high resolution imaging of high brightness radio sources in order to study their structure and evolution. The VLBA is also expected to serve as a premier instrument for astrometry. Since the techniques and requirements of astrometry and geodesy are essentially the same, the VLBA will also be a powerful instrument for geodetic applications. Astrometric and geodetic requirements on the performance and stability of the instrument are, in many ways, stricter than those of pure imaging and have therefore set many of the design specifications of the VLBA.

The VLBA will consist of 10 antennas on United States territory plus an Array Operations Center (AOC) in Socorro, New Mexico. The antennas are 25 m in diameter and will be outfitted with receivers and feeds for observing in 9 bands between 327 MHz and 43 GHz. The observing band can be changed in seconds by rotating the subreflector. The antenna structures are sufficiently stiff for use at 86 GHz and systems at that frequency will be added eventually, although pointing improvements will be required. Each site will be outfitted with a hydrogen maser and a VLBA tape recording system including 2 tape drives. The computer at each site will control the antenna pointing, the electronic configuration, and the tape system. It will follow schedules distributed from the operations center and will be monitored from that center. Each site will have a minimal local staff of 2 people and will be operated unattended most of the time. The local staff will change tapes and maintain the site and equipment. Any serious problems will be handled by module swaps and infrequent visits by staff from the AOC. In order to limit tape changes to once per day with 2 drives, long (thin) tapes will be used which allow the recording of 12 hours of data per tape at the nominal rate of 128 Mbps.

Most of the personnel and activity of the array will be located at the AOC. The antennas will be controlled from there mainly by means of preplanned schedules, although some limited interactive use is possible. The array will be monitored around the clock by operators at the AOC. The maintenance labs and a staff of engineers and technicians will also be located there. Modules will be repaired there and most problems that occur on the array will be diagnosed from there. As with all NRAO instruments, development of new equipment will be spread among the NRAO sites. The AOC is located in Socorro in

* The National Radio Astronomy Observatory is operated by Associated Universities, Inc. under cooperative agreement with the National Science Foundation.

order to combine operations with the Very Large Array (VLA) which will remain NRAO's largest instrument.

A major component of the operations center will be the correlator. A large correlator is required to keep up with the array since the array will be observing full time and will often work in conjunction with other telescopes. The VLBA correlator will have 24 input tape transports and be capable of correlating all baselines for a 20 station experiment. It will have subarray capabilities that allow almost any combination of smaller experiments with a total of up to 20 stations. The inevitable processing inefficiencies caused by experiments that require more than one pass or by problems with correlation must be balanced with the faster-than-real-time processing that is allowed by playing tapes at twice the normal record rate and by correlating more than one experiment at a time. The correlator architecture is of the innovative FX type first used in a major instrument by the Nobeyama mm Array in Japan. In an FX correlator, the input data are Fourier transformed on input to form voltage spectra which are then cross multiplied channel by channel. For a large correlator with many spectral channels and many stations, this architecture requires considerably less electronics than the standard XF architecture used on all previous VLBI correlators. The FX architecture has the additional advantages that it is relatively easy to avoid the fringe rotation and delay stepping losses often associated with VLBI.

Most of the data processing facilities and scientific staff associated with the VLBA will be located in the AOC, although there will be related facilities on a smaller scale in Charlottesville, Virginia at the NRAO headquarters. The data processing facilities will be some combination of workstations and much larger number crunching machine(s) which has not yet been specified exactly. The purchase of this equipment has been postponed as long as possible in order to get the most compute power for the money in this rapidly changing market. The data processing will be done with the same software and on the same machines as for the VLA.

The VLBA, as all NRAO instruments, will be operated as a national facility open to all users regardless of institution or nationality. Observing time will be assigned on the basis of scientific proposals reviewed by outside referees. The staff has no special access to the instrument for scientific purposes, although time is assigned outside the review process for instrumental tests. The VLBA will present a special challenge for scheduling relative to other NRAO instruments because, with both astronomy and geodesy, it will support two very different kinds of science. Direct ranking of proposals will be difficult. Since the VLBA is being built and operated with funding designated for astronomy at NSF, astronomical projects are likely to be favored. This could modified if the geodetic funding agencies were to contribute to operations.

The astronomical and geodetic communities have rather different scientific styles which are likely to require that different criteria be used to rank proposed observing projects. Astronomers tend to do complete projects individually or in small groups. Each astronomer is involved in taking the data and analyzing it. There is relatively little sharing of data at stages prior to publication. The geodetic VLBI community tends to have large operational groups that gather large quantities of data in regular observing programs. They do the initial editing and calibration of these data and enter them into data bases containing essentially the whole history of geodetic VLBI. These data bases are then shared by a wide

range of scientists for a variety of purposes. The same data might be used by different persons to study tectonic plate motions, tidal effects, general relativistic light bending, better processing algorithms and many other topics. While the priority of an astronomical observation can be evaluated on the basis of the expected end product of that observation, a geodetic project may have to be evaluated more on the basis of its contribution to the overall effort.

More information about the VLBA can be found in Kellermann and Thompson (1985). Technical details can be found in the VLBA Project Book which is available from the VLBA Project Office in Socorro, NM.

SPECIAL FEATURES FOR GEODESY/ASTROMETRY

The design of the VLBA was influenced in many ways by the requirements for the high accuracy delay measurements used in geodesy and astrometry. Some of the specifications driven by these needs are:

1. Low Elevation Limits. For imaging and most astronomical applications, there is little need or desire to observe at elevations much below about 10 degrees. At such low elevations, the atmosphere distorts the amplitudes and phases so much that the data are of relatively little use. The VLA, for example, has an elevation limit of 8 degrees and this causes little complaint. For high accuracy work, however, the atmosphere is one of the major limiting factors in the ultimate accuracy of the observations and it is widely believed that observations at very low elevations are important in calibrating the atmosphere (see other papers in this volume). For this reason, the VLBA antennas were designed to reach an elevation of just over 2 deg. This required the use of a large axis offset and a somewhat asymmetric support structure that might not have been used otherwise. Low horizons were also among the selection criteria for VLBA sites.

2. High Slew Speeds. The VLA has maximum slew speeds of 20 degrees per minute in elevation and 40 degrees per minute in azimuth. Imaging applications on the VLBA would be well served by such slew speeds and the original design concept did no better. However the desire of geodetic and astrometric observers to obtain observations all over the sky in the minimum possible time drove the project to specify higher speeds. The final specification is 40 degrees per minute in elevation and 90 degrees per minute in azimuth. Even higher speeds were advocated by some in the geodetic community, but the VLBA engineers felt that this was the maximum possible without considerable increase in complexity and without compromising the tracking accuracy.

3. Dual Frequency S/X System. Accurate delay measurements require calibration of the ionosphere. This can be done very well if delay measurements are made at two well separated frequencies, thanks to the dispersive nature of the ionospheric delay. The geodetic community has traditionally used the S/X combination (13 and 4 cm wavelengths) established by the availability of that combination on NASA deep space tracking antennas. The VLBA has the ability to observe simultaneously in the S and X bands. On the VLBA antennas, the feeds and receivers for all frequencies above 1 GHz are arranged in a circle at the cassegrain focus so that the observing band in use can be changed by rotating the asymmetric subreflector. For dual frequency observations, a dichroic plate is fastened over the 13 cm feed. This plate passes the 13 cm radiation, but reflects radiation at 4 cm to an

ellipsoidal reflector positioned over the 4 cm feed. Thus both frequencies can be observed simultaneously when the subreflector is positioned over the 13 cm feed.

The dichroic/ellipsoid system causes a loss of sensitivity at both 13 and 4 cm of about 15 to 20 percent. The 4 cm band is the one at which some of the most sensitive astronomy observations can be made using the VLBA in conjunction with the VLA, the Deep Space Network and other stations. Therefore, the ellipsoid has been attached to a positioning device that allows it to be moved out of the way when not required so that 4 cm observations can be made with full sensitivity. However, the dichroic plate is not designed to be moved so single frequency astronomy observations at 13 cm will always suffer a loss of sensitivity.

Other frequency pairings are possible given the layout of the feed circle. None are in the construction plan, but some might be installed at a later date. At the moment, the ones thought to be of most interest are between the 43 GHz or 86 GHz systems and lower frequencies between 8 and 22 GHz. Here the primary purpose would be to try to extend the coherence time at the high frequency. However there may be interest in doing geodetic observations with other pairs. The planned 12-15 GHz receiver, for example, spans a far wider bandwidth than the 4 cm system so it might prove to be of interest for bandwidth synthesis.

4. Number of Channels. The VLBA proposal calls for 4 independently settable channels — the same number used in the VLA. It was proposed that bandwidth synthesis be done using frequency switching. This keeps the hardware and imaging software relatively simple and saves the cost of many Baseband Converters (BBC's — equivalent to Mark III Video Converters), a fairly expensive item. Under pressure from the geodetic community, the design was modified to include 8 BBC's, thought to be the minimum that would allow bandwidth synthesis to be done without frequency switching. For the extra wide spanned bandwidths that have come into use since the design was set, 8 BBC's is only adequate without frequency switching if the single band delays are used. A viable observing mode for VLBA geodetic observing is proposed in a later section. Joint observations with Mark III stations are likely to require frequency switching, as is now done when VLBA sites participate in the CDP R&D observations, until the Mark IV upgrades provide wider individual channel bandwidths.

5. Cable Measuring System. Traditional imaging observations only constrain the phase stability of the antennas in the sense that the maximum possible coherence time is desired while tracking a source. There is little concern about being able to relate phases or delays measured on different sources. For such observations, if the delay through the cables between the receivers and the samplers changes as the antenna moves, there is little problem as long as the changes are not excessive. This is not true for geodetic and astrometric observations (or even for phase connection imaging) where results from observations of many sources all over the sky are used to get antenna and source positions. For these observations, it is important to both minimize the cable delay changes as the antenna is moved and to measure the changes that do occur. The VLBA system measures the electrical length of the cable that carries the LO signals from the site building to the receivers. This LO system will also be the source of the signals that drive the phase cal system so the monitoring system is equivalent to the cable cal system associated with the

phase cal system on the geodetic antennas.

6. Phase Stable Cable Wrap Design. A number of things have been done to try to stabilize the electrical lengths of the cables from the site building to the receivers and associated electronics. The cables are protected from the sun and special high-stability cables are used at the elevation and azimuth wraps. The worst problems typically occur at the azimuth wrap since it must cover about 6 times the angular range of the elevation wrap. There a special "watch spring" design is used to avoid cable twists. The results of these efforts show up in the range of cable lengths measured during observations. They are typically much lower than that seen at typical geodetic sites.

7. Phase Stable Electronic Designs. At all stages of the signal path, attention has been paid to phase stable designs. Also efforts have been made to maintain stable operating environments. In the original design efforts, some engineers felt that, by being careful, the phase stability could be made to be sufficiently good that use of a phase cal system would only introduce added noise. This is no longer being relied upon, but efforts are still being made to make the system as stable as possible. While much success in this area has been achieved, this is an area where much testing remains to be done and where improvements will undoubtably be made.

8. Multi-tone-per-Band Phase Cal. The final VLBA phase cal system is still under design, partly because of the earlier feeling that it might not be needed. One of the capabilities that it will have is the ability to measure several tones per band. This will allow the single band delays to be related directly to the multi-band delay, a necessary condition if 8 channels are to be used effectively for bandwidth synthesis observations with the widest spanned bandwidths. The system will deviate from the Mark III system in that the phase cal phases will be measured at the antenna, not in the correlator. This decision was driven by details of the correlator design that made measurement at the correlator difficult. It has the advantage that the detected phase cals can serve as a very good diagnostic of system performance during observing. However it has the effect that extra effort will be required at the correlator to measure the phases from non-VLBA antennas unless on-site measuring schemes become more widespread.

9. Accountable Correlator Model. In order to do high accuracy work, especially when combining results from many observations, it is necessary to know exactly what has been done to the data. In the language of the geodetic community, it must be possible to recover the raw observables - the delay, delay rates etc. For imaging, this is not so necessary as one works with the residuals. The VLBA data system will maintain a record of results of the model used on the correlator so that it can be removed to get the raw observables to high accuracy. Unlike the current Mark III/geodetic system, the raw observables are not kept explicitly because imaging is still expected to be the dominant work on the array and a great deal of model recalculation can be saved by storing the residuals.

THE VLBA AS A GEODETIC TOOL

In addition to the above listed special features for geodesy, the VLBA has a number of properties that are useful for geodetic observations.

With 25 m antennas and receivers with system temperatures typically between 30 and 40 degree K, the VLBA systems are very sensitive relative to most other geodetic systems.

The typical system equivalent flux density (SEFD) is on the order of 350 K at S and X bands with the dual frequency system in place (better for single bands). It should be possible to do geodetic observations with 90 sec scans with the same SNR that is now used for the NASA R&D runs with sources as weak as 0.2 Jy. There is a flat spectrum source of this strength approximately every 4 degrees on the sky which would give much enhanced scheduling flexibility. A VLA project is already in progress identify and get good positions for thousands of such sources for use as calibrators by MERLIN and VLBI (Patniak *et al.*, 1991). The high sensitivity of the VLBA should also make the antennas useful base stations for use with small mobile systems. Sensitivity is an area where improvements will continue to be made since it is an area of great concern for astronomy. While the VLBA antennas are very sensitive by geodetic standards, they are rather small by the standards of the astronomy community so there will always be great demand for improvements.

With 10 antennas, the VLBA can provide a large number of FLINN sites well equipped for VLBI and able to host other types of observations. The positions of the antennas will be known and monitored both by the VLBA staff and, most likely, by the geodetic community. The sites have maser based time keeping, power, a secure fenced yard and a building that can house some equipment for visiting groups. For use as FLINN sites, monuments would have to be installed in the vicinity and surveyed relative to the antenna. Geodetic grade GPS equipment would have to be installed. The current GPS receivers are intended for timekeeping only. It would be desirable to have regional GPS experiments done near each antenna to determine any local motions of the antenna relative to the surrounding territory.

The large correlator should allow classes of experiments that are not considered today. It seems that a 7 station experiment is now considered large for geodetic work. In astronomy, a 7 station experiment is already considered small and experiments twice that size are common. Larger experiments give far more source information and much improved station calibration. It seems reasonable to assume that some of the same advantages will be seen for geodetic observations as they get larger. With the large correlator, such experiments will not impose a strain on the correlation resources, as they do today.

The VLBA recording system will use a barrel roll mechanism to avoid total loss of any single channel if a recording track fails. This can happen, for example, when a head clogs or fails. For the barrel roll, the channel-track assignment will change each frame. If a track is lost, the integration time on several channels will be reduced, but no single channel will be lost completely. This preserves the frequency sampling required for the bandwidth synthesis.

There are also some complications for geodetic observations imposed by the VLBA design.

The limitation to 8 channels will require that experiments with the VLBA be done somewhat differently from ones done with Mark III sites. The observing mode proposed below relies on use of wide individual bandwidths which may not be available at other sites, at least until the Mark IV system is available. Until then, either frequency switching on the VLBA, or multiple Mark III bands within a VLBA band (a mode that may be supported on the VLBA correlator) must be used.

The decision to detect phase cal at the stations will complicate processing of experiments involving Mark III systems that have not been modified for on-site detection. An

extra pass through the correlator, or some loss of observing time, must be used to detect phase cal tones.

PROPOSED GEODETIC OBSERVING MODE

After a study of possible observing modes for geodetic and astrometric observations, Walker (1990) proposed a mode for use with the VLBA system. This mode provides high sensitivity, little problem with ambiguities, and uses only 8 BBC's without frequency switching. In this mode, individual channel bandwidths of 16 MHz would be used with 3 channels at S band and 5 channels at X band. The spanned bandwidths would be at least as great as those used in the CDP R&D runs which are 125 MHz at S band and 720 MHz at X band. At least 2 phase cal tones would be detected in each channel in order to relate the single band and synthesized delays.

The maximum delay sidelobe in the delay synthesis can be kept below about 70 percent with the 3 channels at S band and 5 at X band with the R&D spanned bandwidths if the single band delays can be used to constrain the delay to better than about 30 ns. With 16 MHz channels, this will be possible with SNR's above about 5, which is lower than would ever need to be used for geodesy and would allow astrometric observations of rather weak sources of astronomical interest. Since the single band delays are not subject to delay ambiguities and are used to constrain the synthesized delay to one of the possible values, there should be no problem with delay ambiguities.

In the above observing mode with 1 bit digitization, the record rate is 256 Mbits per second. This is twice the rate that can be sustained by the VLBA recording system and still meet the 12 hours per tape constraint imposed by the small staff at each station. This is not a problem if the tape is stopped half the time. The sensitivity of the systems will probably cause geodetic observers to use the shortest possible scan lengths consistent with reliable playback, perhaps 60 or 90 seconds. Slews to new sources will probably also take about this long on average. If the tape is stopped during the slews, the tape consumption rate will stay within the required bounds.

CONSTRUCTION STATUS

The following list gives the status of each antenna of the VLBA as of June, 1991.

Pie Town: The antenna near Pie Town, New Mexico, was the first constructed and is still the test site. Any equipment developed for the VLBA is installed and tested first at Pie Town. Pie Town was also the site used with the CDP R&D experiments until recently. It participated in the intensive session in Oct 89 and produced some very good results as are described elsewhere in this volume. Recently, the main VLBA site used for the CDP has been moved to Los Alamos to free Pie Town for other testing.

Kitt Peak: Kitt Peak, Arizona, has most of the final receivers and other hardware and is fully staffed.

Los Alamos: The antenna at Los Alamos, New Mexico is also has most of the final equipment and is fully staffed. Los Alamos is now the primary VLBA antenna participating in the CDP programs.

Fort Davis: The major concern at the Fort Davis, Texas, site recently has been to obtain an accurate baseline between the old George R. Agassiz antenna and the VLBA

antenna. This now seems well in hand after a few teething problems. The site is now fully staffed and outfitted with most of the final equipment.

North Liberty: This site, located at the old North Liberty Radio Observatory grounds in Iowa, is in operation with many of the final receivers and both VLBA and Mark II recording systems. However Mark III observations are still limited by the presence of only 2 BBC's. The second site technician has just been hired and is in training.

Owens Valley: The VLBA antenna in the Owens Valley is located very close to the Owens Valley Radio Observatory. First fringes were found very recently. The antenna is being used to cover the VLBI Network Mark III observations in June 1991.

Brewster: The Brewster, Washington antenna is complete and astronomical testing has just begun.

Hancock: Erection of the antenna in Hancock, New Hampshire is nearly complete. Electronic outfitting will begin soon.

St. Croix: The Virgin Islands antenna is being erected. The structure is complete and some surface panels are in place.

Mauna Kea: The road, building, and antenna foundation are under construction at the last site in Hawaii. Antenna erection should begin soon after the eclipse in the summer of 1991. This antenna should be ready for initial operations by mid 1992.

As of the Fall of 1991, Pie Town, Kitt Peak, Los Alamos, Fort Davis and North Liberty should have sufficient equipment to do geodetic style observations. Owens Valley will have sufficient BBC's but will not have an S band system.

The AOC is mostly complete and has been occupied for about 2.5 years. When initially occupied, a significant amount of space was left unfinished. That area is now being completed and will be occupied soon.

The correlator is moving forward rapidly now that problems with the custom chip have been overcome. The chip problem was a design flaw in the commercial part of the chip as provided by the manufacturer and affected a number of customers besides NRAO. In the end, the NRAO project had to be moved to a different gate array product. Essentially all of the hardware has now been purchased and much has been assembled. First fringes are expected during the summer of 1991. A significant subset of the correlator (minimum 7 station, 2 channel, but probably much more) will be carefully checked out in Charlottesville and then shipped to the AOC in very early 1992. Correlator operation will ramp up during 1992 to the point where, by late in the year, most VLBI Network experiments and all pure VLBA experiments will be processed in Socorro.

VLBA construction funding ends after 1992. By the end of that year, the instrument should be very close to full operation with all hardware in place.

CONSTRUCTION ZONE

During the construction and checkout phase of any instrument, attempts to do routine observations can be difficult because of incomplete equipment and performance problems that have not yet been identified or fixed. Also operations procedures and software are incomplete and staffing is below final levels. Most of the staff that is available is more concerned with the on-going construction than with operations. For most instruments, this is obvious to early users. The VLBA has been in something of a special position

in this regard. As VLBA antennas come into operation, they are inserted into ongoing Network and CDP operations where most of the other participating observatories are well "broken in". The users schedule the VLBA antennas and wait for data to arrive without really being aware of the construction project. They tend to expect the same level of reliability as at other stations, which just does not happen. As a result there is much frustration. We only ask that early VLBA users be patient. Smooth, reliable, routine operation is the ultimate goal; it will come in time.

SUMMARY

The Very Long Baseline Array will be complete in less than two years. It will be a major new instrument for astronomy and has the potential to make major contributions to the worldwide geodetic effort if properly used. Initial experiments with Pie Town have shown some of the geodetic potential of the eventual instrument, if a bit painfully because they were done context of the construction project. Soon the full potential should begin to be apparent as several VLBA sites are sufficiently equipped for geodetic observations and the VLBA correlator becomes available with the capability to process recordings made in the VLBA modes.

There are a number of ways in which the VLBA can contribute significantly to the geodetic efforts:

1. It is the natural instrument with which to maintain the source catalogs used for geodetic observations. Source structures can be monitored and the necessary astrometry can be done. The source catalogs can be extended through projects to investigate large numbers of possible candidates. All of this work is very close to the main astronomical goals of the Array and will fit in very well.

2. The VLBA can provide up to 10 FLINN sites well equipped for VLBI and able to host observations of other kinds.

3. It is expected that very frequent, short observations will be done for purposes of array calibration. With appropriate communication and experiment design, these observations might be able to contribute to such routine projects as monitoring of UT and polar motion.

4. The VLBA sites can serve as base stations for regional experiments using mobile systems, as long as such observations do not require too large a fraction of the total observing time.

5. The VLBA should be very good for experiments that test observing methods in the ongoing efforts to improve the accuracy of VLBI. The combination of the high sensitivity, low elevation limits, high slew speeds, multiple observing bands, and continuous operation make possible experiments that would be difficult or impossible elsewhere.

6. The VLBA will have a very large correlator which could be used to process experiments that use far more antennas than is typical in current experiments. It will be interesting to see if geodetic observations profit from large numbers of stations to anywhere near the extent that is seen in imaging observations.

The challenges that must be overcome to obtain the best possible use of the VLBA for geodetic applications will be both technical and organizational. Technically, the best methods to obtain geodetic observations with a system optimized for astronomy must be

found. This will be most difficult when experiments are done between Mark III sites that don't have the wide channel bandwidths of the VLBA and VLBA sites that don't have the large number of channels of the Mark III. The organizational issues involve the allocation time between very different kinds of science performed by communities with very different scientific styles. As always in this time of limited and strained budgets, the greatest challenges are likely to involve funding. None of these challenges appear especially difficult so the VLBA should make a strong contribution to geodesy over the next few decades.

REFERENCES:

Kellermann, K. I., A. R. Thompson, 1985. The Very Long Baseline Array, **Science, 229**, 123-130.

Patniak, A. R., I. W. A. Browne, P. N. Wilkinson, and J. M. Wrobel, 1991. Phase Calibrators for MERLIN. In: **Radio Interferometry: Theory Techniques, and Applications, IAU Colloquium 131** (ed. T. J. Cornwell and R. A. Perley), The Astronomical Society of the Pacific, San Francisco, (in press).

Walker, R. C., 1990. Frequency Sequences for Bandwidth Synthesis on the VLBA, **VLB ARRAY MEMO No. 674**.

Present Status of the K-4 VLBI System

by

H. Kiuchi, S. Hama, J. Amagai, Y. Abe, Y. Sugimoto, F. Takahashi, and N.Kawaguchi*

Kashima Space Research Center, CRL, 893-1 Hirai, Kashima, Ibaraki, 314 Japan

*Nobeyama Radio Observatory, NAO

1. Introduction

A new data acquisition system, called K-4, has been developed by the Communications Research Laboratory (CRL, Japan) as the next generation VLBI system. We had developed K-1, K-2, K-3 VLBI systems and K-3 system succeeded to measure the plate motion. In K-4 system, the adoption of a rotary-head type recorder using a cassette tape makes the system smaller and easier to operate. The K-4 is a compact VLBI terminal, one forth in weight, one fifth in size of Mark-III and K-3 system. The K-4 system can be used as fully compatible on output data with the Mark-III and the K-3 VLBI system by using Input and Output Interface Units. The measured coherence loss of the K-4 system is less than 5%, which shows that the K-4 system performs well enough for the VLBI experiments. It was confirmed that the geodetic result on the 55km baseline (Kashima-Tsukuba) of the K-4 system agreed with that of K-3 system, within a discrepancy of only a few millimeters in vector. In 1990, this system had been operated in Antarctica, and the good geodetic results ware obtained(1).

2. The K-4 system

The K-4 VLBI system is being developed at the CRL as the next-generation system. In this system a rotary-head type recorder using a cassette tape (American National Standard 19 mm Type ID-1 Instrumentation Digital Cassette Format) is adopted for making the system smaller and easier to be operated. The interfaces were designed to be compatible with that new recorder. Two Interface Units are used to get compatibility with other VLBI equipments, Input Interface Unit is established between the Video Converter and the Recorder and Output Interface Unit is established between the Recorder and the data processing system. We make the system smaller, the functions necessary for the observation and those necessary for the data processing are housed in separate units. The K-4 system consists of the following five equipments; (1) Local Oscillator, (2) Video Convertor, (3) Input Interface Unit, (4) Output Interface Unit, and (5) Data Recorder.

Fig.1a shows the K-4 system. The block diagram is shown in Fig. 1b and 1c. The Local Oscillator synthesizes the local frequency signal for Video Convertor. The Video Convertor converts a window in the IF signal (100-500MHz) input to video signal (0-2 or 4 MHz). The frequency conversion is made using Image Rejection Mixer of single side band conversion. The functions are equivalent to the IF distributor, Video Convertors(16ch) and Reference distributor of the Mark-III or K-3 VLBI system. The Input Interface Unit is to be used for the data acquisition

and recording at the VLBI observing station (Fig.1b). It samples the video signal from the Video Converter, and sends the digital data to the Data Recorder together with the time data which is derived from the external time standard signal.

The Output Interface Unit is to be used at the data processing station (Fig.1c). It converts the reproduced data into the appropriate output format, and sends them to the Correlator. The format of Output Interface Unit is compatible to the Mark-III format. Besides this format, another format is also provided for future correlator system, this signal is only digitized raw data. When multi baseline correlation was processed, all the Output Interface Units are daisy-chain connected through GP-IB, so that the tape position data and status data of all the Data Recorders can be exchanged. The Main (Reference) Output Interface supplies the timing clock to Sub Output Interfaces. The delay bit between the Main and Sub Output Interface Units is calculated in the each Sub Output Interface Unit, using the time data which is inserted in the recorded data at certain times.

It is possible to interface with the current VLBI system through those two Interface Units. Table.1 shows the size of the K-4 system. The K-4 is a compact VLBI terminal, one forth in weight, one fifth in size of the Mark-III or K-3 system. We introduce the data acquisition parts of K-4 system :Local oscillator, Video converter, Input Interface, Output interface, and Data recorder.

2.1. Local Oscillator

This unit is to be used at the VLBI observing station, and consists of the following sections.

(1)Reference signal distribution section

(2)10kHz step synthesizer (& auto gain controller) section

(3)System controller

The block diagram is shown in Fig. 2. The Local Oscillator is specially designed to use with the K-4 Video Converter. It supplies frequency and phase references to the converter which extracts video signals (whose bandwidth is 2MHz or 4MHz) from the IF signal which spans from 100 MHz to 500 MHz. The Local Oscillator outputs sixteen local signals, the frequency of which can be set in local or remote control. The frequency range and the frequency step are fully compatible with an current VLBI system such as the Mark-III or the K-3 system. Communications with a computer for the remote control are made through a standard GP-IB interface. User-friendly message words for the communication are prepared.

(1)Reference signal distribution section

Geodetic VLBI achieves precise results by using the Bandwidth Synthesis method(8). It is necessary to distribute the reference signal (10 MHz) from hydrogen maser in keeping coherence in each 10kHz step synthesizer. The coherent 5MHz signal made from 10MHz reference which is required for phase calibrator. This section has five 10MHz outputs and two 5MHz outputs for auxiliary.

(2)10kHz step synthesizer section

The 10 MHz reference signal from reference signal distribution section is divided and its phase is compared with the divided VCO signal, whose frequency is under controlled CPU in system controller. The output signal frequency is possible to select in 10kHz step. This section supplies the local signals which are phase locked to the reference signal and are stable in phase noise. The selectable frequency range is from 100MHz to 500MHz. Usually, this frequency is selected by the experiment organizer, according to the minimum redundancy theory of the bandwidth synthesis. The 10kHz step frequency selection is necessary because the phase calibration signal detection is made in 10kHz in the correlation processor but the phase calibration signal is composed every 1MHz in IF signal, which is controlled to 10kHz in Video signal by the synthesized local signal. The IF signal range is covered by two VCOs of this synthesizer. The output of VCO is protected from the influence of the load impedance with automatic gain controller.

(3)System controller

Execution commands and status data are sent to the host computer through GP-IB. The local frequency is set by computer through GP-IB.

2.2. Video Convertor

This unit is to be used at VLBI observing station, and consists of the following sections.

(1)Power detection and attenuator

(2)Filterand amplifier

(3)Image Rejection Mixer (IRM) section

(4)System controller

The block diagram is shown in Fig. 3. The Video Converter is a compact unit in which an IF distributor and sixteen single side band converters are assembled. With the use of the local oscillator (section 2.1), all analog devices required in VLBI observations are performed. In an current VLBI system such as the Mark-III or the K-3, all these units are separated and rack mounted. It is very easy to transport the K-4 unit to a VLBI site and to make operations. Communications with this unit can be made with a computer through a GP-IB interface. User-friendly words are prepared for the communications. Two types of operation are supported, one of them is one IF input and 16 video outputs, and the other is two IF inputs and two groups outputs, are supported. In addition, four IF inputs and four groups of four video outputs are available for dual frequency bands and dual polarization VLBI observations. The video outputs are fully compatible with the Mark-III and the K-3.

(1)Power detection and attenuator

Power detection of four input IF signals is mentioned in this section. The each IF input signal is divided to four channels. Their powers are detected and are sent to system controller section and displayed on the front panel. Operator sets the attenuators value from 0 to 15dB, in order to keep the detected (displayed) value from 10 to 90 on the front panel, the linearity is gallanted within this range.

(2)IF filter and amplifier

Two kinds of band pass filters are equipped on each channel. One filter has the pass band of 100-230MHz and the other has 200-520MHz, the role of these filters is to eliminate influence of the 3rd order harmonics in local oscillator. It is possible to select the Lo-IF or Hi-IF filter from front panel on local mode or from host computer on remote mode.

(3)Image Rejection Mixer (IRM) section

Image Rejection Mixers are integrated networks composed of an in-phase power divider, two double balanced mixers and two 90 degree quadrature hybrids (or ±45 degree networks). The primary function of the circuit is to separate a desired signal from its image signal. The image occurs during mixing when both the sum and difference output signals appear in the video band. In the image rejection mixer the image (undesired) signal is separated from the desired signal by vector subtraction. In K-4, this ratio is better than 20dB. These low pass filters are located on after IRM section. The filter consists of 7-pole Butterworth filter circuit, as same as Mark-III or K-3 VLBI system. The location of 3dB point is selected by 91% of the video band maximum frequency. The coherence loss resulting from the imperfect bandpass shape and foldover is about 3%.

(4)System controller

Execution commands and status data are sent to the host computer through GP-IB. Input attenuators adjustment and IF filter selection are possible to remote from host computer, the power detected value is sent to host computer through GP-IB.

2.3.Input Interface Unit

This unit is to be used at VLBI observing station, and consists of the following sections.

(1)Sampling Section
(2)Time Code Generator
(3)Phase Calibration Signal (Pcal) Detector
(4)Datarecorderinterface
(5)Software Control Section

The block diagram is shown in Fig. 4.

(1)Sampling Section

This section quantizes (1-bit) the 16-channel 2MHz (4MHz) video bandwidth input signal with a 4 MHz (8MHz) clock, and produces a 64 Mbps (128Mbps) data train.

(2)Time Code Generator

This section produces all the clock signals necessary for the interface and the time data using the 10 MHz standard frequency signal supplied from the hydrogen maser atomic frequency standard and the external 1 PPS signal which is the basis of the UTC time. The time data are backed up by an built-in battery. The phase of this internal 1 PPS signal is always compared with the leading edge of the external 1 PPS signal, and the error is generally within ± 3 clock lengths in

terms of the 10 MHz clock. The alarm comes up if the error exceeds that criterion. The status can be sent to the host computer through GP-IB. The time data are generated from the internal 1 PPS signal. They are in the form of YYDDDHHMMSS (BCD), and are overwritten upon the data train every second.

(3)Phase Calibration Signal (Pcal) Detector

This section measures the amplitude and phase of the 10kHz phase calibration signals, which are included in the video signals, by product-detecting them with a set of phase-quadrature 10 kHz signals which are derived from the external 10 MHz reference signal (Fig.5). Any 2ch out of 16ch are selected to monitor. They can be selected from the host computer as well as from the panel. Amplitude is displayed in [%] and phase is displayed in [degrees]. The measured data can be sent to the host computer through GP-IB.

(4)Data recorder interface

The signal data train of the 16 channels sent from the sampling section has a 16-bit format. This Data Output section translates into an 8-bit format and adds the time data and a (4-byte) sync code. The logic level is converted from TTL to ECL.

(5)Software Controlling Section

The following controls are performed by the mounted CPU (Z80).

(i)Interface with the host computer.

Execution commands and status data are sent to the host computer through GP-IB. The functions are;

a) interpret the commands from the host computer

b) control the Data Recorder accordingly

c) sends the status data (time data, phase calibration data)

d) status data of the Data Recorder back to the host computer.

Also to remote the protocol errors, device alarm of the Data Recorder, and status of the Data Recorder to the host computer through SRQ.

(ii)Interface with the Data Recorder

The remote control of the data recorder, the status of the operations and error status are exchanged through the RS-422 interface. It is possible to read the error rates of the data recorder during recording and replaying, and it is possible to send those data to the host computer. The data recorder records a signal which indicates the tape position (23-bit binary data) as well as the sampled data, and the remote control of its set / reset is possible. The recorded position data (ID NUMBER) can be read.

2.4. Output Interface Unit

This unit is used with the Data Recorder at the correlation station. It consists of the following sections.

(1)Buffer memory

(2)Formatting Section (Mark-III format)

(3)External 1PPS Phase Compare Section

(4)Software Control Section

The block diagram is shown in Fig.6.

(1)Buffer memory

The replayed data from the Data Recorder is written into the buffer memory. The Main replay system (the Main Output Interface Unit and the Data Recorder) and the Sub replay system (the Sub Output Interface Unit and the Data Recorder) are possible to be synchronized in one-bit step. The delay adjustment is done by controlling the buffer memory (4 Mbits) and subsequent programmable shift registers (PSR) using the information from the host computer.

(2)Formatting Section (Mark-III format)

The header data (SYNC, time data, AUX data, and CRC codes) is generated in output interface, which is inserted into the 16-channel observational data, adds the parity bits (at every 8 bits) in accordance with the Mark-III format. As a result, the output data rate becomes 4.5 Mbyte / sec in each channel while the input data rate is 4 Mbyte / sec. And the other unformatted signal (raw data), which is provided for the future correlator.

(3)External 1 PPS Phase Compare Section

The measured phase difference between the replayed 1pps and the external 1pps sent from the Main Replay system, by counting the 4 MHz clock. Those measured data are sent to the Main Replay system, and used to make the bit synchronization (fine sync.) between the Main and Sub Replay systems.

(4)Software Control Section

A CPU (Z80) provided in this Output Interface Unit performs the following controls.

(I)Interface with the host computer

The interface with the host computer is made through GP-IB. More than one Output Interface Units can be star-connected to the host computer, the host computer can nominate a particular Output Interface Unit as the Main Unit and synchronizing operations are performed using that Main as the reference.

(ii)Interface with the Data Recorder

The communication to the Data Recorder is made through the RS-422 serial interface. The Data Recorder is remote controlled by the command from the Output Interface Unit . The tape position data (ID NUMBER) is recorded on the tape, those of sub are sent through the Output Interface Unit concerned to the Main Output Interface Unit for the synchronization between the Output Interface Units. It is possible to read the amount of the error in the Data Recorder during the replay and to send them to the host computer.

(iii)Control of buffer memory

Buffer memory is provided in the Output Interface Unit for data synchronization and the delay of the data can be adjusted at one-bit step by changing the read address of this buffer memory.

(iv)Data communication between Output Interface Units

All the Output Interface Units are daisy-chain connected through GP-IB, So that the tape position and status of all the Data Recorders can be exchanged. The delay bit between the Main and Sub Output Interface Units is calculated using the time data inserted in the recorded data at certain times.

(v)Control of the Front Panel

The replayed time data are displayed on the Front Panel.

2.5.Data recorder

A rotary-head type recorder using a cassette tape (American National Standard 19 mm Type ID-1 Instrumentation Digital Cassette Format) is adopted. In Fig.7, it shows the tape format. It is possible to read the error rates of the Data Recorder during recording and replaying through the host computer. Helical scan recording is used to record high rate digital signals. With an L-size cassette (16 μm), the K-4 recorder provides up to 770Gbits of data storage capacity, which is equivalent to 7.7 reels of conventional Mark-III magnetic tapes. Recording time is 200 min (L-size cassete, 16μm) with 64 Mbit/sec recording rate. Recording and playback are possible at different data rates: 256, 128, 64, 32, 16, 10.7, (Mbps), making the data recorder suitable for many different applications. For example, it is possible to record data at an extremely high speed and then play it back at a slower speed which is suitable for computer processing. Reed-Solomon error correction is performed by the use of customized encoder and decoder chips to permit powerful error correction. The playback heads are placed so that the recorded data is immediately played back during recording. This Read-after-Write facility makes it possible to monitor the error conditions of recording in real time. After correction, a bit error rate of better than $1x\ 10^{-10}$ is achieved. In addition to the helical data tracks, two longitudinal tracks are recorded with AC bias as annotation channels. These are provided to record auxiliary information such as oral comments, time code, etc. The Track Set ID numbers recorded on the control track can be read at any tape speed during fast forward or rewind. When the search function is executed via the remote control interface or on the front panel, a marked search point can be found quickly and automatically by using Track Set ID. The data recorder is equipped with three different types of communication port: RS-422, IEEE-488 (GP-IB), and RS-232C.

The data recorder employs a built-in diagnostic system, which is designed to detect an operation error or hardware fault. An error message or warning information is fed to host computer via the remote control interface, as well as to the front panel display.

2.6.Data synchronization

(1)Course Synchronization

The Track Set ID numbers recorded on the control track can be read at any tape speed regardless of tape direction. When the course synchronization or pre-roll is executed via the

remote control interface or on the front panel, a marked search point can be found quickly and automatically by using Track Set ID.

(2)Fine Synchronization

The measured phase difference between the replayed 1pps and the external 1pps sent from the Main Replay system, by counting the 4 MHz clock. Those measured data are sent to the Main Replay system, and used to make the bit synchronization (fine sync.) between the Main and Sub Replay systems. The delay bits between the Main and Sub Output Interface Units can be calculated using the time data inserted in the recorded data at certain times. To synchronize the Main replay system and the Sub replay system is possible to adjust the delay in one-bit step. The delay adjustments are done by controlling the buffer memories and subsequent programmable shift registers using the information from the host computer.

3.Overall coherence check of the total K-4 VLBI system

i)measurement method

We made an overall coherence check using K-4 system and antenna system. We used two independent interrelated groups, called "system A" and "system B". It is possible to change S/N, so it is obtained the relationship between correlated amplitude and S/N. The signal source is a noise generator, this signal is divided to inject to "system A" and "system B" through 40 dB directional coupler at the input port of low noise amplifier (LNA). X-band sky noise is used as noise source for "system A" and S-band sky noise is used for "system B". The coefficient of cross correlation function ρo estimated from system temperature is given by next function.

$$\rho o=\sqrt{\frac{\{S1*S2\}}{\{(N1+S1)*(N2+S2)\}}} \qquad (1)$$

where S1 : signal temperature in "system A"

S2 : signal temperature in "system B"

N1 : system noise temperature in "system A"

N2 : system noise temperature in "system B"

It is possible to estimate the coherence by using next equation. ρ1 is the coefficient of cross correlation function from the correlation processor after 1 bit sampling correction.

$$\text{coherence loss} = 1 - \frac{\rho 1}{\rho o} \qquad (2)$$

ρ1 is larger than ρo in appearance. ρ1/ρo shows coherence. If ρ1/ρo is 1, then coherence is 1. In this measurement, ρ1/ρo =0.975 is obtained. The overall coherence loss is 2.5 % in 250 MHz, but it does not include the loss of aliasing noise cause by there is no fringe rotation. Table 2

shows the summary of coherence loss. The estimated total coherence loss is less than 5% in K-4 VLBI data acquisition system, but this value does not include the correlation processing loss or atmosphere loss, fringe stopping, phase scintillation etc.. We estimate the coherence of the K-4 system. The measured coherence loss of the K-4 system is less than 5%, which shows that the K-4 system performs well enough for the VLBI experiments.

4.Performance check of K-4 system

Domestic VLBI experiment between Kashima and Tsukuba was carried out on 15 JUN 1989. In this experiment, the K-3 and K-4 acquisition systems were used in both stations to compare the results and the performances. It was confirmed the geodetic solution of the K-4 system agreed with that of K-3 system, with only a few millimeters in vector. The result is shown in Table 3. The residual delay is 0.091 nsec, residual rate is 0.151 ps/s. They denote the K-4 system has better performances than K-3 system. In addition, to make 24 hours experiment 8 medium size cassette tapes were used in K-4 system on the other hand 30 tapes were used in K-3 system, it makes easy operation. It is possible to cover this experiment with 3 or 4 of large size tapes.

5.Conclusion

The measured coherence loss of the K-4 and K-3 system is less than 5%, which shows that the K-4 system performs well enough for the VLBI experiments. It is confirmed that the geodetic solution on the 55km baseline (Kashima-Tsukuba) using the K-4 system agreed with that of K-3 system, with only a few millimeters of difference in vector. The K-4 system is already used in domestic VLBI experiments in remote islands and Antarctica VLBI experiment.

Acknowledgement

We would like to express our thanks to staff of SONY and Nihon Tsushinki Co. and staff of Kashima Space Research Center. We are indebted to the staff members of Geographical Survey Institute in the domestic experiment.

reference

(1)N.Kurihara, et.al.; "The result of the test VLBI experiments with the Syowa Station in Anterctica and its future plans", in this issue.

(2)A.E.E. Rogers; "Coherence Limits for Very-Long-Baseline Interferometry", IEEE trans., IM-30, 4, 283-286, Dec.1981.

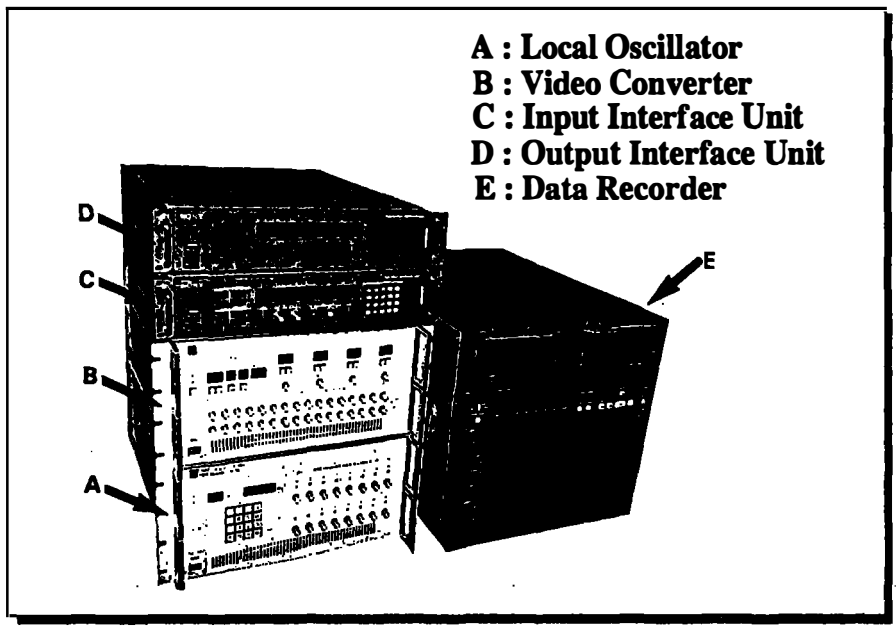

Fig. 1a. Picture of K-4 system

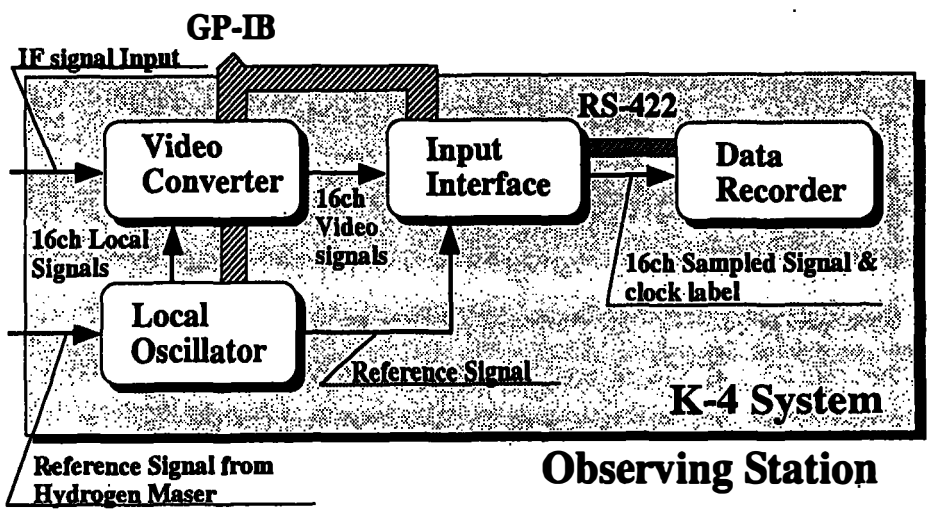

Fig. 1b. K-4 system block diagram (observing station)

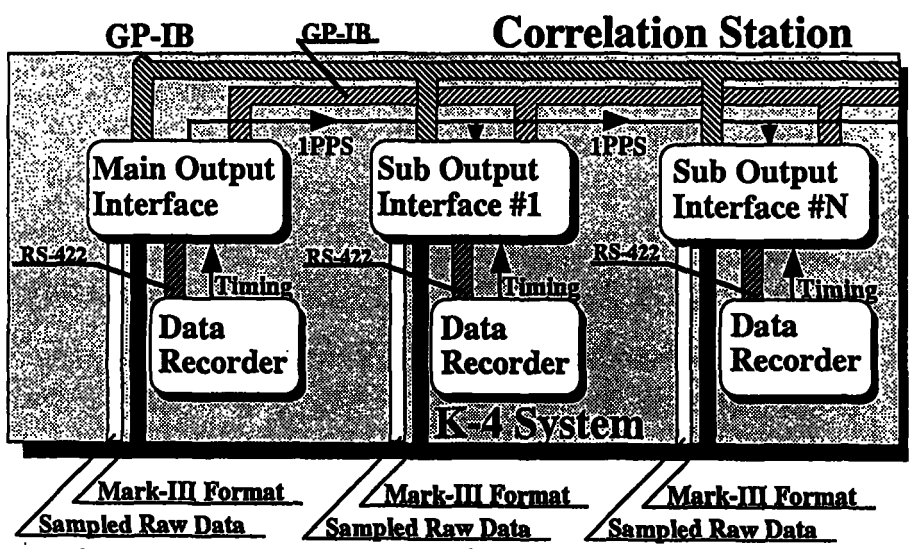

Fig. 1c. K-4 system block diagram (correlation station)

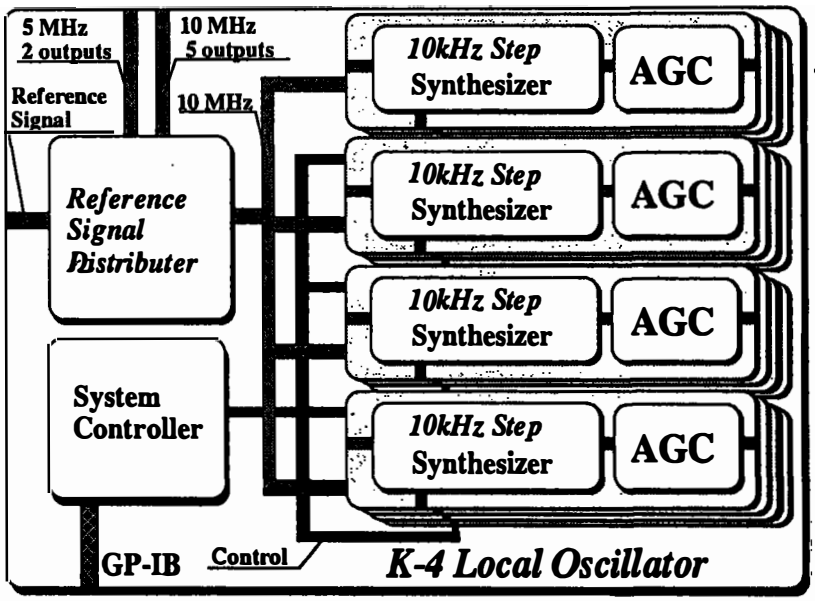

Fig. 2. Local oscillator block diagram

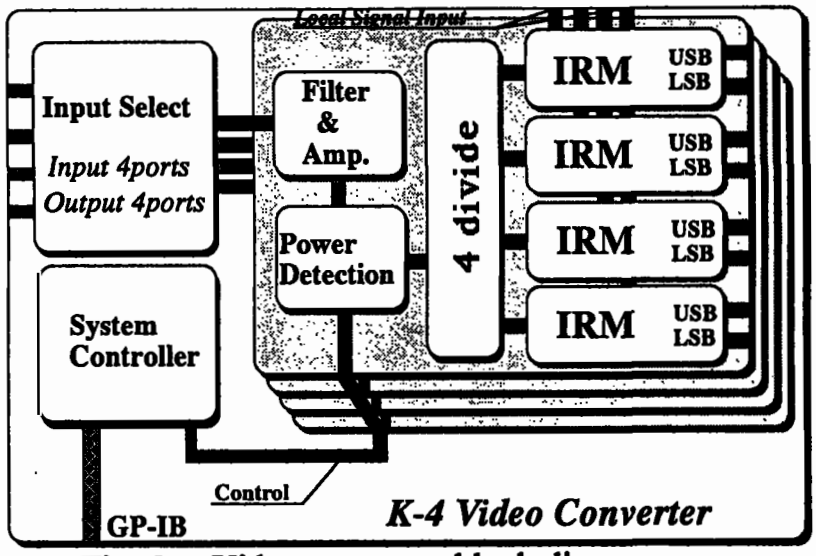

Fig. 3. Video converter block diagram

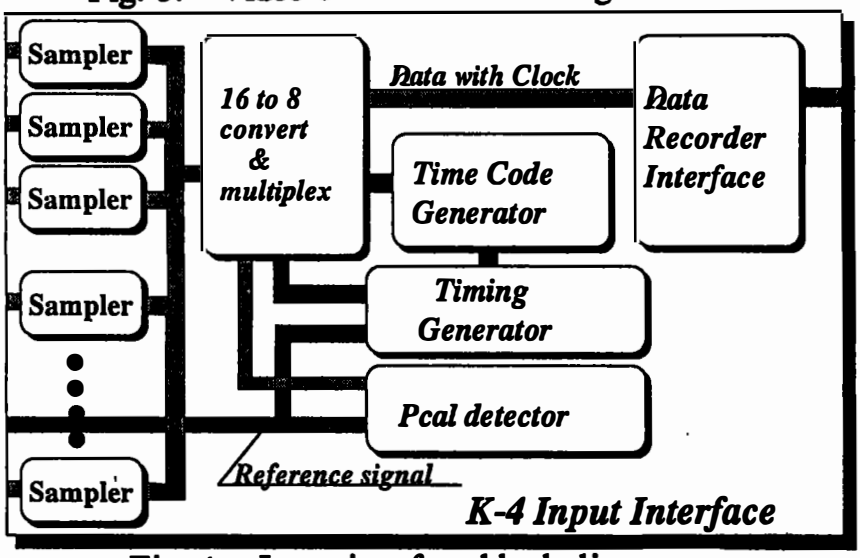

Fig. 4. Input interface block diagram

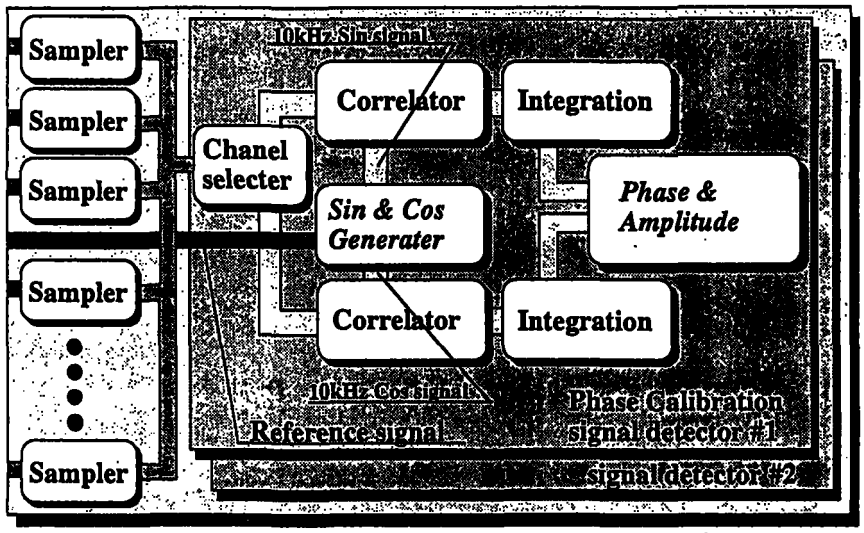

Fig. 5. Pcal detection *K-4 Input Interface*

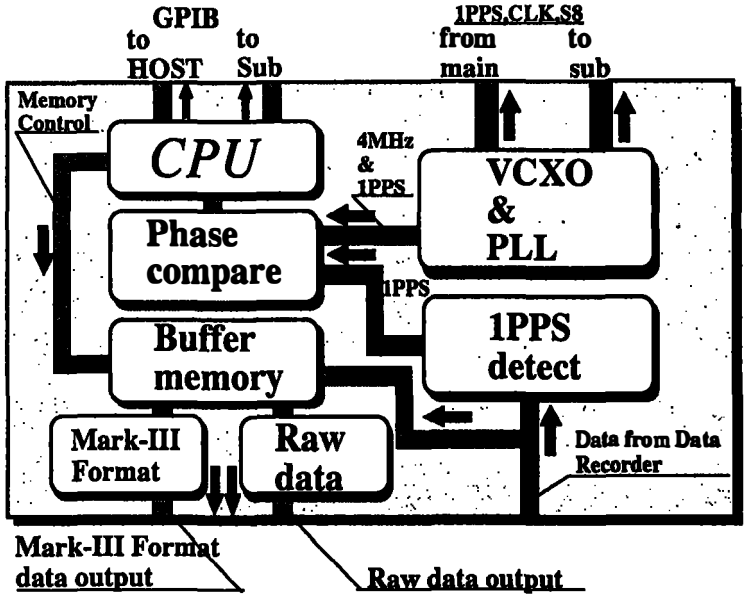

OUTPUT INTERFACE UNIT

Fig. 6. Output interface block diagram

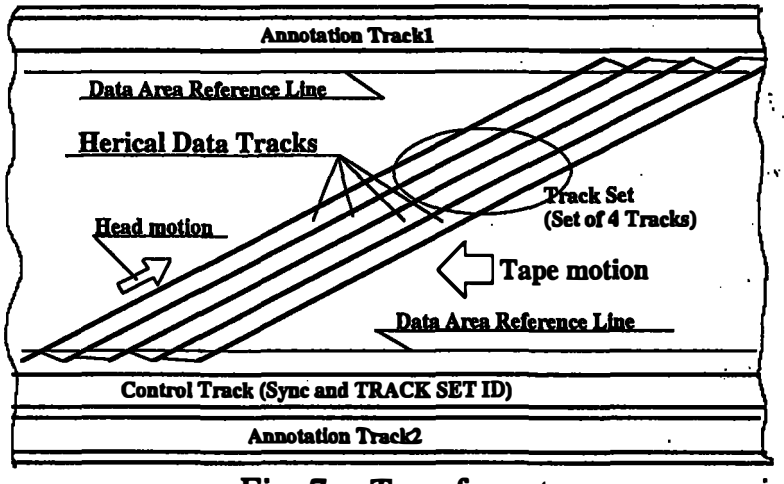

Fig. 7. Tape format

Table.1. Size of K-4 VLBI data acquisition system

K-4 System	size in mm W,H,D	weight in kg
Local Oscillator	480x199x590	36
Video Converter	480x199x590	35
Input Interface	424x 88x550	13
Output Interface	424x 88x550	13
Data Recorder	436x432x635	67
Total		164

Table.2. The summary of coherence loss

Estimated Loss in worst case		
Coherence Loss Factors	Fringe Rotation	Without Fringe Rotation
Local Phase Noise (3.1 deg.)	0.23 %	0.23 %
Imperfect Image rejection (23dB)	0.72 %	0.12 %
Imperfect Filtering	1.28 %	1.28 %
Aliasing Loss	1.99 %	———
Clipping Loss	0.36 %	0.36 %
Total	4.58 %	1.99 %

Table.3.The results of baseline analysis in Kashima-Tsukuba VLBI experiment

	K-3 system		*K-4 system*		
	Length in [m]	σ in [m]	Length in [m]	σ in [m]	Difference in [m]
X element	40719.331	0.020	40719.327	0.019	-0.004
Y element	33656.704	0.017	33656.713	0.016	0.009
Z element	13590.709	0.022	13590.716	0.018	0.007
Baseline Length	54548.556	0.007	54548.561	0.005	0.005

Antennacluster-Antennacluster VLBI for Geodesy and Astrometry

Tetsuo Sasao and Masaki Morimoto
National Astronomical Observatory, Japan

Table of Contents

1. Introduction
2. Basic Concepts of Antennacluster-Antennacluster VLBI System
3. Baseline Vector Determination
4. High-Time Resolution Earth Orientation Series
5. Radio Source Positions Independent of Earth Rotation Models
6. Unification of Global VLBI Networks
7. Multi-View Differential VLBI
8. Differential Fringe Search and Phase Referencing
9. Tying Maser Source Positions with Quasar Positions
10. Japanese Project VERA

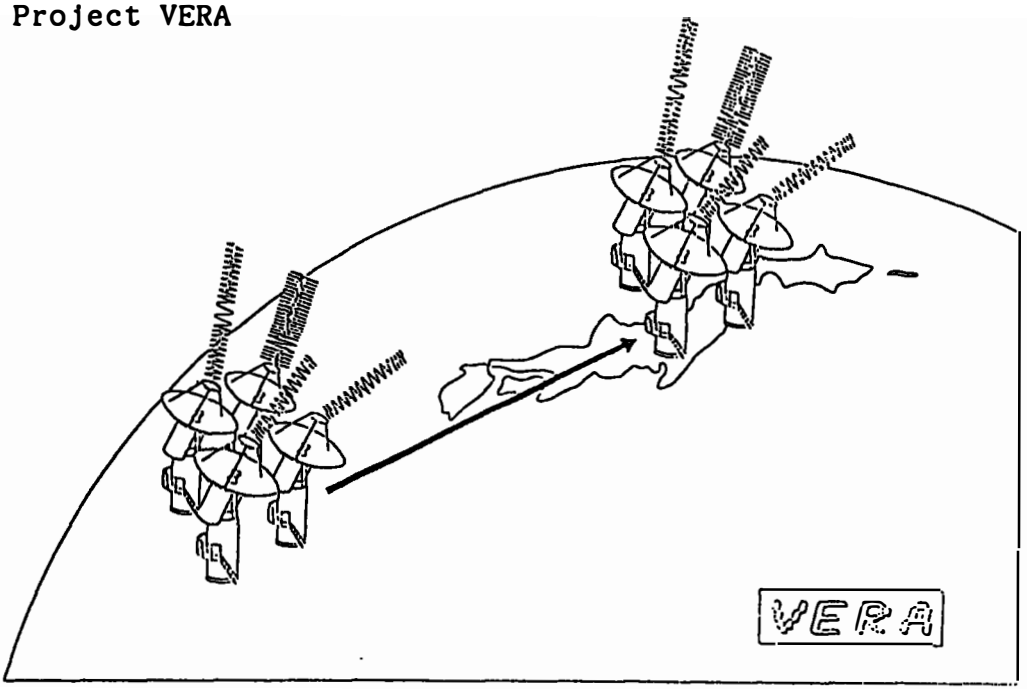

(To be published in Proceedings of Chapman Conference on Geodetic VLBI: Monitoring Global Change, April 22-26, 1991, Washington, D.C., USA)

Antennacluster-Antennacluster VLBI for Geodesy and Astrometry

T Sasao (Mizusawa Astrogeodynamics Observatory/NAO, Hoshigaoka, Mizusawa, Iwate, 023 Japan; Tel: 81-197-24-7111, Fax: 81-197-25-6619)
M Morimoto (Nobeyama Radio Observatory/NAO, Minamimaki, Minamisaku, Nagano, 384-13 Japan; Tel: 81-267-63-4372, Fax: 81-267-98-2884)

Abstract

If each end of a VLBI baseline is composed of at least 4 identical antennas with well-monitored relative positions and reference signals fed from a common frequency standard, then such a cluster-cluster VLBI system would allow us

1) to determine 3 spatial components of the baseline vector and the clock offset at once, by simultaneously observing 4 radio sources with known positions;

2) to derive the Earth orientation parameters for every 10 minutes or so, by participating in a global VLBI network with a baseline of known spatial direction;

3) to measure radio source positions in direct reference to other sources, without invoking any precession-nutation model or equatorial system; and

4) to yield precise relative positions and proper motions of close radio sources, in terms of the multi-element (or multi-view) differential VLBI and phase referencing techniques.

Japanese project VERA (VLBI for the Earth Rotation study and Astrometry), originally conceived as a classical 2 element VLBI, is now being reconsidered on the basis of the above concept.

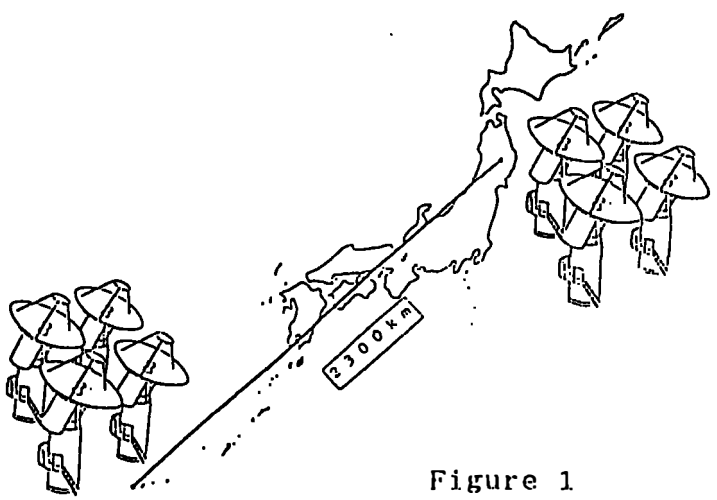

Figure 1

1. Introduction

VLBI geodesy and astrometry have achieved unprecedented measurement accuracy and made spectacular discoveries in many fields of sciences within the past decade. Now the wide scientific prospects opened by the VLBI themselves demand even further improvements in the observational capability of the technique. In fact, finer accuracy and higher time resolution are required in such research objectives like global sea-level change, plate dynamics, angular-momentum exchange on the surface of the Earth, structure and physics of the core-mantle boundary, cosmic distance measurements, three-dimensional velocity field of our Galaxy, and link of radio and optical reference frames.

Specifically, current observational goals of the VLBI geodesy and astrometry could be summarized as follows,

1) mm-level geodesy,
2) 0.1 milliarcsecond Earth orientation parameters,
3) high-time resolution Earth orientation series,
4) 0.1 milliarcsecond radio-source refernce frame,
5) mm-level terrestrial reference frame,
6) wider use of differential VLBI for microarcsecond-level astrometry, and
7) long-time integration via the phase referencing technique.

We propose here a new design of VLBI system, which we call 'antennacluster-antennacluster VLBI', in order to meet the above requirements (Figure 1).

2. Basic Concepts of Antennacluster-Antennacluster VLBI System

Major features of the proposed system are the followings.

1) Each component station of the system is composed of clustered antennas. In other words, there are at least 4 antennas and receiving systems at each station. They must be manufactured as identically as possible.

2) Relative positions of antenna reference points are monitored with great precision in terms of ground geodetic measurements.

3) Reference signals for both receiving and recording systems are fed from a common frequency standard at each station.

4) Instrumental phases inside the antennas and transmission systems are monitored and calibrated as precisely as possible.

5) GHz-wideband recording systems, presumably K-4 type 1 (or Mark IV), are equipped for each of the antennas (Kawaguchi, 1988; Whitney et al.,

1991).

6) Antenna slew speed is high enough to facilitate quick switching from one source to another.

Such a system (Figure 2) will enable us to realize a series of new VLBI observing modes described below, which could be powerful new tools of our sciences.

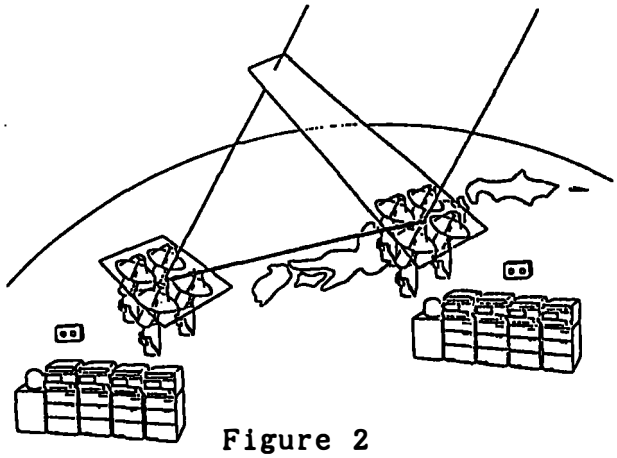

Figure 2

3. Baseline Vector Determination

The cluster-cluster system may look like a highly elongated interferometer array. However, contrary to an usual array aiming at observing a single source with many baselines, our system can be used just in an opposite sense, namely for determining a baseline vector by observing many radio sources at once (Figure 3). The baseline vector here implies a vector connecting geometrical centers of the two antennaclusters.

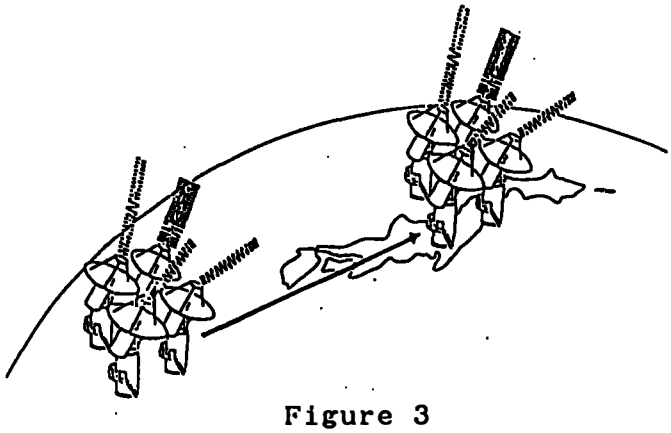

Figure 3

Indeed, the well-known expression of the group delay observable τ_G:

$$\tau_G = D \cdot s / c + \tau_c + \tau_a + \tau_i, \qquad (1)$$

where D is a baseline vector, s is a source vector, c is the light velocity, τ_c is a clock offset, τ_a is an atmospheric propagation delay, and τ_i is an instrumental delay, and simple geometry of observations with 4 VLBI pairs in Figure 4, show that we can determine 3 spatial components of the baseline vector D and the clock offset τ_c at once by

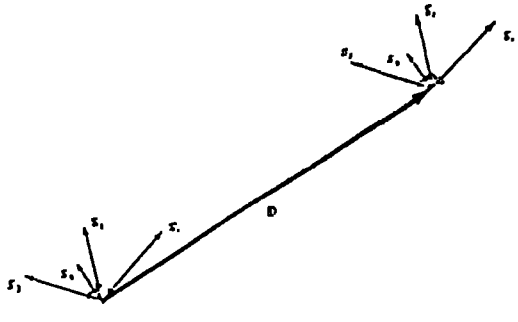

Figure 4

simultaneously observing at least 4 sources with known celestial coordinates, as far as small atmospheric and instrumental delays are neglected or calibrated. Thus a single observation lasting only a few minutes will yield a value for the physically meaningful quantity, the baseline vector, with the cm-level accuracy.

Although the atmospheric effects will remain as major error sources unless substantial progresses are made in remote-sensing of water vapor contents, our system may improve modeling of the effects by providing simultaneous delay values at several directions of the sky. Furthermore, the instrumental delays could be well measured and calibrated either by using the phase and delay calibrator units or by periodically observing a calibration source with all 4 VLBI pairs. Since the unmodeled atmospheric effects are largely random, statistical analyses of hourly data will be sufficient to provide mm-level estimations.

Kawaguchi(1989) proposed a similar method of baseline vector determination with the aid of single antennas of very high slew speed and quick recording of the super-wideband burst-sampled data.

4. High-Time Resolution Earth Orientation Series

It is evident from Figure 5 that the rotational ambiguity around the source vector, which is inevitable in conventional global geodetic VLBI networks, will disappear provided that spatial components of at least one member baseline vector are known. Therefore, the cluster-cluster system will make significant contributions to the high-time resolution study of the Earth rotation and atmospheric angular momentum, which is accepted as a major research area for the 1990's (Dickey, 1991). The only thing needed is to observe every schedule source of the network as one of the 4 simultaneously observed sources. Then, the pole coordinates and UT1 will be determined with the milliarcsecond-level accuracy with time intervals as short as 10 minutes or so without tedious time-series analyses.

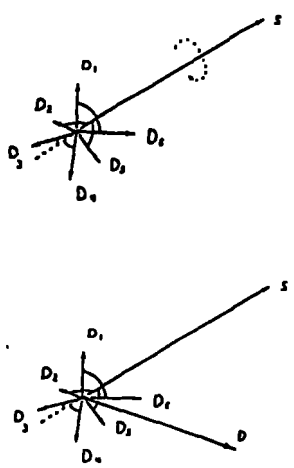

Figure 5

If there is only one cluster-cluster baseline in the network, terrestrial coordinates and clock parameters for the rest of stations must be assumed or estimated in the conventional way. It is much more desirable instead to have many clustered antennas spread over the world.

In that case, we could precisely monitor both rotation and deformation of the Earth with the high-time resolution.

5. Radio Source Positions Independent of Earth Rotation Models

Conventional estimations of VLBI radio source positions are based on time-series analyses of group delay data and need an Earth rotation model, especially of the precession and nutation (Figure 6). The situation causes some discrepancies of the submilliarcsecond-level among existing VLBI source catalogues compiled for different data sets and different models (for example, see Arias and Feissel, 1990).

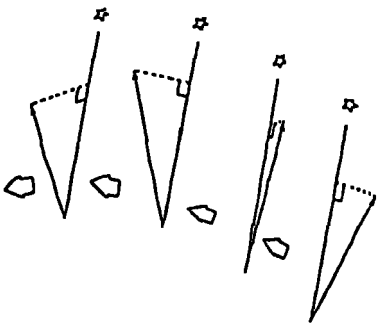

Figure 6

Now if the baseline vector is precisely known, either by simultaneous determination or by interporation from successive observations with the cluster-cluster system, in principle two group delay values are sufficient to determine the source position (Figure 7). In that case, the new position is determined in direct reference to positions of those sources which are used for the baseline vector determination. Therefore, no precession-nutation model is needed in this method. Even the concept of the equatorial coordinate system itself seems no longer necessary.

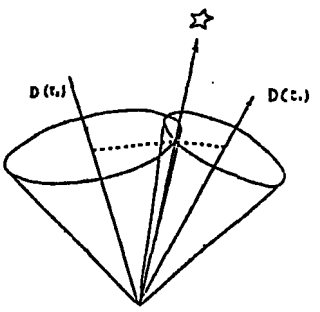

Figure 7

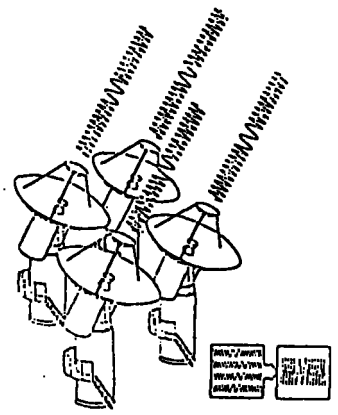

Figure 8

The cluster-cluster system can increase its sensitivity by forming a phased array (Figure 8). This will be particularly useful in position measurements of fainter sources. Note that our system will not suffer much from the difficulties associated with antenna deformations due to self-gravity, heat or wind inherent to a bigger telescope of equal collecting area.

6. Unification of Global VLBI Networks

A precise terrestrial reference frame is crucial for such studies like sea-level monitoring (Carter et al., 1986). At present, however, the world geodetic VLBI network is split into several independent pieces to meet the mutual visibility requirements and results of observations obtained in separate networks often show systematic differences (Yokoyama et al., 1988). It is therefore important to combine those global networks to make a uniform terrestrial reference system.

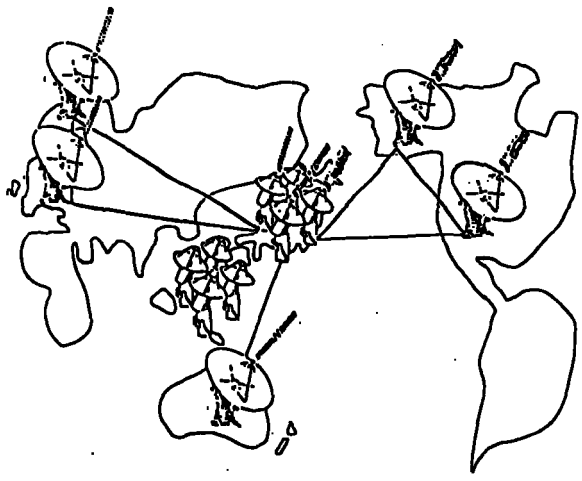

Figure 9

The cluster-cluster system may serve as a corner stone for that purpose, because, if observation schedules are well adjusted, the system can simultaneously participate in several networks (Figure 9). In that case, the cluster-cluster baseline vector will be common for all the networks. This will impose a good constraint for their unification.

7. Multi-View Differential VLBI

Another important application of the cluster-cluster system will be the multi-view differential VLBI (Figure 10).

Differential VLBI is a powerful method which enables us to use the full microarcsecond-level accuracy, inherent in the long baseline, in terms of measuring relative fringe phases of closely spaced sources and thus effectively eliminating destructive phase fluctuations due to the atmosphere and frequency standards (see, for example, Thompson, Moran and Swenson, 1986). The differential measurements are particularly successful, and in fact microarcsecond-level results are reported, when the sources are close enough that both fall within the antenna beams (Marcaide and Shapiro, 1983; Bailes, et. al., 1990). For

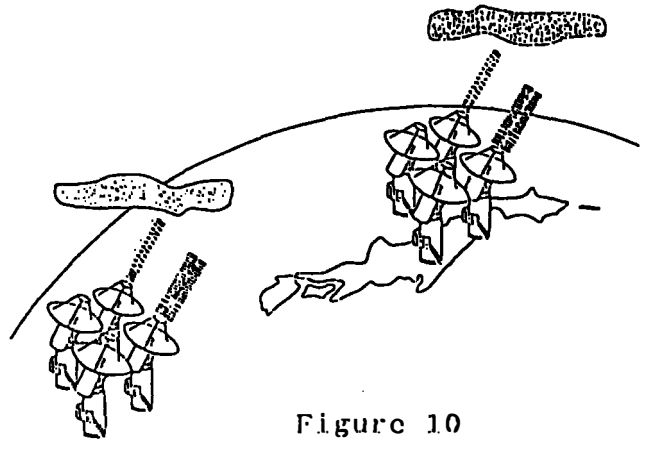

Figure 10

sources with wider separations, two methods are available, namely the switching method based on the periodic nodding of antenna beams between two sources and the multi-view method using multiple antennas at each station one tracking each source.

The switching method has been used rather widely and yielded many interesting discoveries (Bartel et al., 1986; Gwinn et al., 1986; Lestrade et al., 1990), especially in those applications where the ordinary group delay observations are not effective. However, quated accuracies tend to be less impressive and sometimes even lower than the useful level as source separations increase (Greenhill, 1990).

On the other hand, the multi-view technique has been successfully demonstrated by Counselman et al. (1974) in the well-known 4 element VLBI experiment to measure solar gravitational deflection of radio waves, which achieved milliarcsecond-level accuracy in the era of Mark I recording system. Unfortunately, similar experiments have not been pursued, perhaps because of the brilliant successes of the group delay measurements (for example, see Robertson et al., 1991) and lack of suitable instruments.

We believe that now is the time to revive the multi-view idea on the following grounds.

From the well-known formula for the RMS thermal phase noise

$$\sigma_{\phi} = 1 / SNR , \qquad (2)$$

where SNR stands for the signal-to-noise ratio (Thompson, Moran and Swenson, 1986), we see that the phase delay difference and angular separation of the two closely spaced sources can be estimated with accuracies of the order of

$$\sigma_{\Delta\tau} \sim \sqrt{2}\,\sigma_{\phi} / (2\pi f) = \sqrt{2} / (2\pi f \cdot SNR) , \qquad (3)$$

and

$$\sigma_{\theta} \sim c\,\sigma_{\Delta\tau} / D , \qquad (4)$$

where f is the center frequency of the RF band and D is the baseline length, provided that the phase fluctuations due to the atmosphere and frequency standards are well compensated (here we assume, for simplicity, that SNR's for two sources are nearly equal). One could easily confirm, that the accuracy might really be as high as microarcsecond-level if we use an intercontinental baseline with high observing frequency (>10 GHz) and large SNR (>10).

For the switching method, it is impossible to expect complete compensation of the phase fluctuations, because the phase error is accumulated during the switching cycle (slewing and recording). The accumulation of the phase error is roughly described by a formula

$$\Delta \phi = 2 \pi f \sigma_y \Delta t , \qquad (5)$$

where σ_y is Allan standard deviation of the phase fluctuations and Δt is the duration of time (Thompson, Moran and Swenson, 1986; for an observational evidence of the formula, see Lestrade et al., 1990). Demanding that the accumulated phase error $\Delta \phi$ must be less than the thermal phase noise σ_ϕ of equation (2), we obtain upper limit Δt_{max} for half switching cycle during which the nodding does not degrade the phase measurement:

$$\Delta t_{max} = 1 / (2 \pi f \sigma_y SNR) . \qquad (6)$$

Assuming that Allan standard deviation of the atmospheric phase fluctuation is $\sigma_y \sim 10^{-13}$ for time scales less than 100 sec (Rogers and Moran, 1981), we get results for Δt_{max} shown in Table 1.

SNR \ f	8 GHz	22 GHz	43 GHz
10	20	7	4
20	10	4	2
40	5	2	1

Table 1. Upper limit for the half switching cycle (in second).

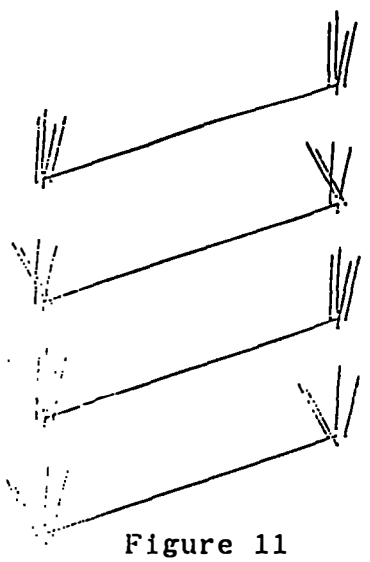

Figure 11

The table evidently shows that the switching method cannot provide desired accuracy, unless one is allowed to shake telescopes with periods less than a few seconds or so. The simultaneous observations in the multi-view method seem definitely superior in this respect.

On the other hand, precise calibration of instrumental phases in the individual antennas and transmission systems is crucial for the

multi-view method. Fortunately, the world experiences with modern connected-element interferometer arrays apparently indicate that the instrumental phases can be calibrated at a few degree-level, by means of the high-precision phase and delay calibrator units and proper calibration observations. If there are 4 antennas at each station, 2 VLBI pairs can be used to observe object sources while other two observe a strong calibration source (Figure 11). So, in effect, we would be in almost the same situation with the case where the two sources happen to appear within the same antenna beams. Note that the calibration sources must be strong for the short baselines inside a station only. Therefore, we will have a lot of such sources.

Thus, we have a real possibility to apply the microarcsecond-level phase measurements to much wider fields of astrometry, and perhaps to geodesy as well (Jacobs, 1991; Lowe and Treuhaft, 1991), by means of the cluster-cluster VLBI system and the modern interferometry techniques which have advanced in a great deal since the 1970's.

8. Differential Fringe Search and Phase Referencing

Results of multi-view differential VLBI observations could be processed in terms of a new 'differential' fringe search algorithm.

An output of a n-lag complex correlator is expressed by a matrix:

$$\begin{array}{cccc} & \longleftarrow \text{time } t \longrightarrow & & \\ R_1(\tau_1), & R_2(\tau_1), \cdots\cdots, & R_N(\tau_1) & \\ R_1(\tau_2), & R_2(\tau_2), \cdots\cdots, & R_N(\tau_2) & \\ \vdots & & \vdots & \\ R_1(\tau_n), & R_2(\tau_n), \cdots\cdots, & R_N(\tau_n) & \end{array} \quad \text{lag } \tau \qquad (7)$$

where n is number of lags, N is number of accumulation periods in an observation, $R_j(\tau_k)$ is a complex cross-correlation, j is accumulation period number, and k is lag number. The accumulation period is the 'hardware integration time' of the order of a few seconds.

Let results of a multi-view differential VLBI observation of point sources A and B be represented by two sets of such matrices $R_A(\tau, t)$ and $R_B(\tau, t)$. Here we denote an analogue equivalent of $R_j(\tau_k)$ by $R(\tau, t)$. For their cross-power spectra at each accumulation period, we have

$$S_A(\omega, t) = \int_{-\infty}^{\infty} R_A(\tau, t) \exp(-i\omega\tau)\, d\tau = A_A \exp[-i\Phi_A(\omega, t)],$$
$$S_B(\omega, t) = \int_{-\infty}^{\infty} R_B(\tau, t) \exp(-i\omega\tau)\, d\tau = A_B \exp[-i\Phi_B(\omega, t)]. \quad (8)$$

The phases Φ_A and Φ_B of the cross-power spectra are expressed as

$$\Phi_A = \omega(\tau_{gA} + \tau_a) + (\omega - \omega_0)\tau_c + \phi_l + \phi_A,$$
$$\Phi_B = \omega(\tau_{gB} + \tau_a) + (\omega - \omega_0)\tau_c + \phi_l + \phi_B, \quad (9)$$

apart from random noise and $2n\pi$ ambiguity (Thompson, Moran and Swenson, 1986). Here ω is RF frequency, τ_{gA}, τ_{gB} are geometrical delays of two sources ($\tau_g = D \cdot s / c$), τ_a is the atmospheric delay, τ_c is the clock offset, ω_0 is local oscillator frequency, ϕ_l is LO phase difference, and ϕ_A, ϕ_B are instrumental phases of two antennas. The atmospheric effects are assumed to be common to the two sources.

Now taking complex conjugate of one of the spectra and forming a cross-product, we get

$$S_A(\omega, t)\, S_B^*(\omega, t) = A_A A_B \exp[-i(\Phi_A - \Phi_B)]. \quad (10)$$

The phase difference in the exponential function must be expressed as

$$\Phi_A - \Phi_B = \omega(\tau_{gA} - \tau_{gB}) + 2n\pi + \text{thermal noise}, \quad (11)$$

after calibration of the instrumental phases, since common terms are mutually compensated. Using the product, we form a new search function:

$$f(\delta\tau, \delta\dot{\tau}) = \frac{1}{2\pi T} \int_{t_0 - \frac{T}{2}}^{t_0 + \frac{T}{2}} \int_{\Delta\omega} S_A(\omega, t) S_B^*(\omega, t) \exp\{i\omega[\delta\tau + \delta\dot{\tau}(t - t_0)]\}\, d\omega\, dt, \quad (12)$$

where $\delta\tau$ and $\delta\dot{\tau}$ are trial values for delay- and delay-rate differences, T is duration of an observation, t_0 is epoch of the observation, and $\Delta\omega$ is receiving bandwidth. Then, finding values of $\delta\tau$ and $\delta\dot{\tau}$ which make amplitude of the search function maximum, we get precise estimates for the group-delay- and delay-rate differences:

$$\delta\tau = \tau_{gA} - \tau_{gB}, \quad (13)$$
$$\delta\dot{\tau} = \dot{\tau}_{gA} - \dot{\tau}_{gB}. \quad (14)$$

and for the fringe-phase difference:

$$\mathrm{Arg}\,[\,f\,(\delta\tau\,,\delta\dot{\tau}\,)\,] = \omega\,(\tau_{gA} - \tau_{gB}) + 2n\pi. \qquad (15)$$

From equation (15), we can estimate the phase-delay-difference with the accuracy given in equation (3) after removing the $2n\pi$ ambiguity with the aid of the group-delay- or delay-rate-difference observable.

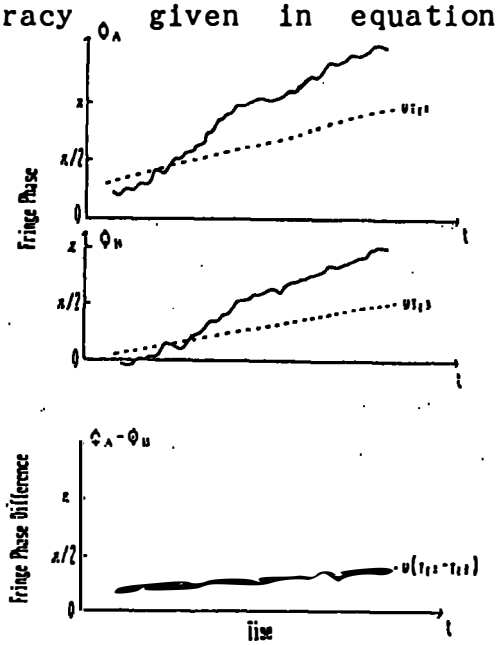

Figure 12

A diagram of Figure 12 schematically shows that, with the above new search algorithm, we can extend coherent integration well beyond the ordinary VLBI coherence time. This is nothing but the long time integration with the phase referencing technique (Lestrade et al., 1988; Lestrade et al., 1990; Lestrade et al., 1991). Note that the phase referencing is realized here in a natural and symmetric way.

We see two possible advantages in the above algorithm.

First, since fringe peaks are searched for during the full integration time, reference sources may not be strong enough to be detected within the VLBI coherence time of the order of a few minutes. This might be important in practical setups of observations.

Second, since atmospheric phase fluctuations are compensated within time intervals as short as an accumulation period, we expect that the delay-rate-difference observable of equation (14) will be as accurate as (or, even more accurate than, as integration time increases) the group-delay observable (Thompson, Moran and Swenson, 1986).

9. Tying Maser Source Positions with Quasar Positions

The differential fringe search algorithm will enable us to apply the 'fringe frequency mapping' technique (Moran et al., 1968) to tye a maser source position with a quasar position. For that purpose, we will simultaneously observe closely spaced maser and quasar sources. The search function of equation (12) should be slightly changed in view of the line spectrum nature of the maser emission. We look for now values of $\delta\tau$ and $\delta\dot{\tau}$ which maximize the amplitude of a modified search

function:

$$f(\delta\tau, \delta\dot{\tau}) =$$

$$= \frac{1}{2\pi T} \int_{t_0-\frac{T}{2}}^{t_0+\frac{T}{2}} R_m^*(\tau, t)\left[\int_{\Delta\omega} S_q(\omega, t)\exp\{i\omega[\delta\tau + \delta\dot{\tau}(t-t_0)]\}d\omega\right]dt, \quad (16)$$

where $S_q(\omega, t)$ is a cross-power spectrum of the quasar and $R_m(\tau, t)$ is a cross-correlation of a single line component (a spot) of the maser source, which could be reduced from an original cross-correlation function, usually corresponding to many maser spots, by means of a suitable filtering. The bandwidth $\Delta\omega$ here must be centered at the frequency of the maser line. Note that amplitude of cross-correlation of a line source is almost independent of τ. The $\delta\tau$ and $\delta\dot{\tau}$ thus obtained give us estimates for the group delay of the quasar and the delay-rate difference between the maser and quasar sources, respectively. Thus we will get the position of the maser source relative to the reference quasar using the delay-rate-difference observable, which is likely to be accurate enough to remove $2n\pi$ ambiguity in the more accurate fringe-phase-difference data (Marcaide and Shapiro, 1983).

10. Japanese Project VERA

Japanese domestic VLBI project VERA (VLBI for the Earth Rotation study and Astrometry), which was originally conceived as a classical 2 element VLBI (Fujishita and Hara, 1988; Hara et al., 1988), is now being reconsidered on the basis of the cluster-cluster concept.

Currently, we are thinking to construct 4 and 4 antennas in the southwest and northeast of Japan, forming a baseline longer than 2000 km. Although a third station is highly desirable, it is difficult to find a suitable location within the terretory of Japan.

Diameter of each antenna is thought to be of 15± 5 m class. Larger antennas, though attractive in many respects, might be too expensive and too flexible for precision geodesy and astrometry.

Major receiving frequencies will be 2GHz, 8GHz, 22GHz and 43GHz. Special emphases will be made on the super-wideband geodesy at 22GHz and maser line observations.

Presumably, high cost of the 8 antennas will be the primary obstacle for realization of the project. We would like to accentuate

that 4 and 4 sets of 15 m antennas must be significantly less expensive than two 30 m antennas of the same sensitivity, and will be, as we believe, far more productive in science.

The antennas can be located within areas of 50 m × 50 m or so, therefore the land will not be a big problem.

The project is now in a feasibility study phase and, if successful, could be funded in later half of the 1990's.

References

Arias, E.F., and Feissel, M., The Celestial System and Frame of IERS, Proc. of IAU Coll. No.127, "Reference Systems", preprint, 1990.

Bailes, M., Manchester, R.N., Kesteven, M.J., Norris, R.P., and Reynolds, J.E., The Parallax and Proper Motion of PSR1451-68, Nature, 343, 240-241, 1990.

Bartel, N., Herring, T.A., Ratner, M.I., Shapiro, I.I., and Corey, B.E., VLBI Limits on the Proper Motion of the 'Core' of the Superluminal Quasar 3C345, Nature, 319, 733-738, 1986.

Carter, W.E., Robertson, D.S., Pyle, T.E., and Diamante, J., The Application of Geodetic Radio Interferometric Surveying to the Monitoring of Sea-level, Geophys. J. R. astr. Soc., 87, 3-13, 1986.

Counselman, C.C., III, Kent, S.M., Knight, C.A., Shapiro, I.I., Clark, T.A., Hinteregger, H.F., Rogers, A.E.E. and Whitney, A.R., Solar Gravitational Deflection of Radio Waves Measured by Very Long Baseline Interferometry, Phys. Rev. Lett., 33, 1621-1623, 1974.

Dickey, J.O., High-Time Resolution Measurements of Earth Rotation, this volume, 1991.

Fujishita, M., and Hara, T., Japanese VLBI Project-VERA, Proc. of IAU Symp. No.129, The Impact of VLBI on Astrophysics and Geophysics, eds. M.J. Reid and J.M. Moran, 483-484, 1988.

Greenhill, L.J., Observation of Extragalactic Water Vapor Masers, PhD Thesis, Harvard University, 1990.

Gwinn, C.R., Taylor, J.H., Weisberg, J.M., and Rawley, L.A., Measurement of Pulsar Parallaxes by VLBI, Astron. J., 91, 338-342, 1986.

Hara, T., Okamoto, I., and Sasao, T., The Japanese VLBI Project VERA (VLBI for the Earth Rotation study and Astrometry), Proc. Fourth Asian-Pacific Regional Meeting of IAU, eds. J.B. Hearnshaw and Z. Erhe, 647-652, 1988.

Jacobs, C.S., Modeling Antenna Effects for Millimeter-Level VLBI, this

volume, 1991.

Kawaguchi, N., private communication, 1988.

Kawaguchi, N., private communication, 1989.

Lestrade, J.-F., Rogers, A.E.E., Niell, A.E., and Preston, R.A., Astrometry of Millijansky Sources Using a Phase Reference VLBI Technique, Proc. of IAU Symp. No.129, The Impact of VLBI on Astrophysics and Geophysics, eds. M.J. Reid and J.M. Moran, 323-324, 1988.

Lestrade, J.-F., Rogers, A.E.E., Whitney, A.R., Niell, A.E., Phillips, R.B., and Preston, R.A., Phase-Referenced VLBI Observations of Weak Radio Sources. Milliarcsecond Position of Algol, Astron. J., 99, 1663-1673, 1990.

Lestrade, J.-F., Preston, R.A., Gabuzda, D.C., and Phillips, R.B., VLBI Astrometry and the HIPPARCOS Link to the Extragalactic Reference Frame, Adv. Space Res., 11, 129-132, 1991.

Lowe, S.T., and Treuhaft, R.N., Application of Sub-Milliarcsecond Astrometric Techniques to Geodetic Measurements, this volume, 1991.

Marcaide, J.M., and Shapiro, I.I., High Precision Astrometry via Very-Long-Baseline Radio Interferometry: Estimate of the Angular Separation between the Quasars 1038+528A and B, Astron. J., 88, 1133-1137, 1983.

Moran, J.M., Burke, B.F., Barrett, A.H., Rogers, A.E.E., Ball, J.A., Carter, J.C., and Cudaback, D.D., The Structure of the OH Source in W3. Astrophys. J. (Lett), 152, L97-L101, 1968.

Robertson, D.S., Carter, W.E., and Dillinger, W.H., New Measurements of Solar Gravitational Deflection of Radio Signals Using VLBI, Nature, 349, 768-770, 1991.

Rogers, A.E.E., and Moran, J.M., Coherence Limits for Very-Long-Baseline Interferometry, IEEE Trans. Instrum. Meas., IM-30, 283-286, 1981.

Thompson, A.R., Moran, J.M., and Swenson, G.W., Interferometry and Synthesis in Radio Astronomy, John Wiley, New York, 1986.

Whitney, A.R., Rogers, A.E.E., Hinteregger, H.F., Smythe, D.L., and Hargreaves, J.E., The Mark 4 Data-Acqusition System, this volume, 1991.

Yokoyama, K., Manabe, S., Hara, S., Yoshino, T., Takahashi, Y., and Kawaguchi, N., The Earth Rotation Parameters Determined with the New IRIS-P VLBI Network, Vistas in Astronomy, 31, 657-662, 1988.

The Roles of IERS VLBI Technology Development Center of CRL, Japan

by

F. Takahashi and T. Yoshino
(CRL, Nukui-Kitamachi, Koganei-shi,Tokyo, 184 Japan)

and
Y. Sugimoto, Y. Takahashi, N. Kurihara and A. Kaneko
(KSRC, CRL, Hirai, Kashima-machi, Ibaraki, 314 Japan)

Introduction

The IERS is responsible for the science and technology with respect to the development of the observation system of the earth and space sciences in the long scale of time. The technical innovations of the observation system should be always essential for the IERS programs. CRL plans to proceed the following activities as the VLBI Technology Development Center (TDC). CRL will contribute to IERS under the cooperation with another center of Haystack Observatory, a big senior center of VLBI technologies, and also with Japanese relating institutes such as National Astronomical Observatory (NAO; Nobeyama, Mizusawa), National Institute of Polar Research (NIPR) and Geographical Survey Institute (GSI).

1) Development and demonstration of K-4 VLBI system.
2) Realization of single-frequency VLBI with dual-frequency GPS TEC measurements.
3) Collocations among the space techniques, e,g., VLBI, SLR, GPS and two-way time transfer.
4) Improvement of data reduction and analysis of VLBI experiments.
5) Participation in IRIS -P and DOSE global VLBI experiments.

When Japan will start the formal Antarctic VLBI program by NIPR, we CRL contribute to the IERS works by using the southern hemisphere VLBI network data linked with Japanese Syowa Station.

Background

After the completion of K-3 VLBI system, which was developed in Communications Research Laboratory (CRL) and is compatible with Mark-III VLBI system of NASA, CRL has started international VLBI Experiments since 1983. Major part of CRL's international experiments was performed under US-Japan joint VLBI experiments. CRL has participated in NASA's Crustal Dynamics Project(CDP) for more than seven years. US-Japan experiments has brought us many kinds of advanced and fruitful results in the study of crustal plate motions, earth rotations, time transfers and satellite VLBI.

Besides US-Japan cooperation, CRL now performs several bilateral government-level cooperations with, for example, China, Australia, Germany,

Canada, and Sweden. These cooperations contribute to the important geodetic results from the joint VLBI experiment in 1980's.

In 1990's the major target of CRL's VLBI project has shifted to the works relating to both the importance of Japan Standard Time of CRL and International Earth Rotation Service (IERS).

Facilities for IERS Works

CRL can provide major space geodetic facilities for IERS works. Two large aperture antennas and three transportable antennas are available. Particularly our major 34m antenna, as shown in Fig.1(a), covers from VHF to mm-wave and it is applicable to several important research work of technical development as IERS/TDC, such as mm-wave VLBI and high precision VLBI using wide bandwidth. Three transportable antennas are also available for IERS/TDC as Japanese " Western Pacific VLBI network".

CRL can provide a new SLR system with 1.5m telescope, as shown in Fig.1(b), in Tokyo. Tokyo SLR system has participated in the ETALON Campaign in 1990 which was promoted by IERS. The global position of Tokyo SLR system is now determined with the precision of better than a few centimeters.

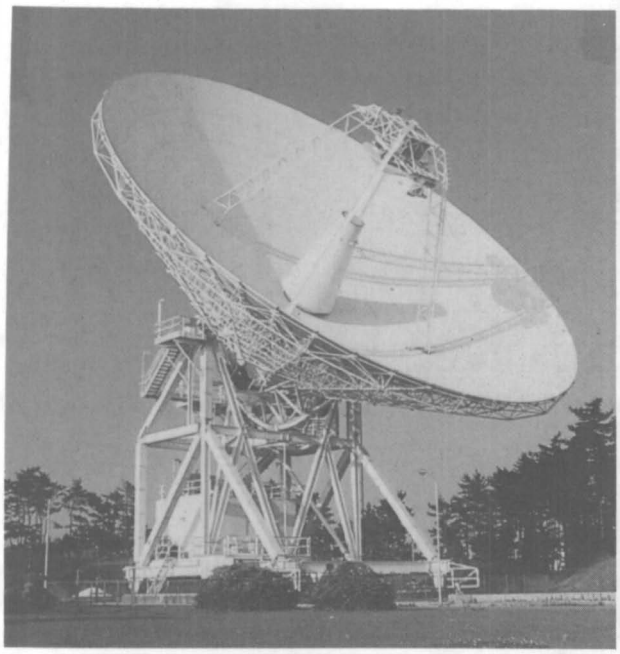

Fig.1(a) 34m antenna at Kashima, CRL

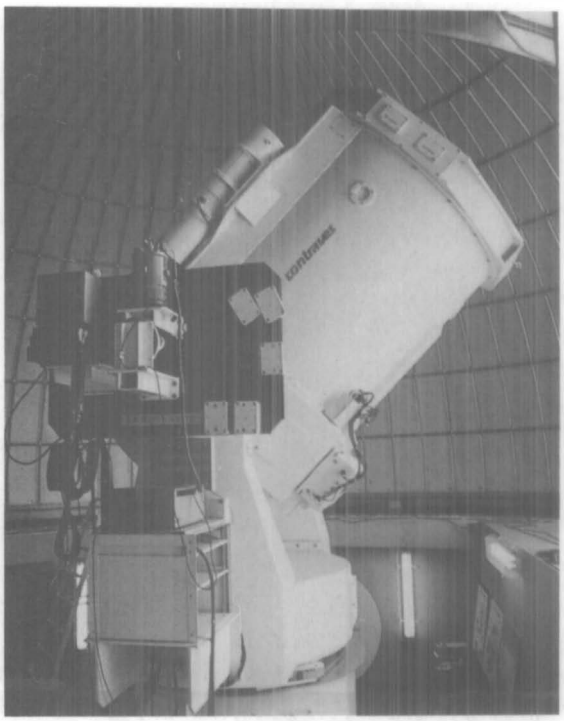

Fig.1(b) 1.5m SLR telescope at Tokyo

Major Funds

As the IERS TDC, CRL now proceeds following two works: one is the long-term bureaucratic works to keep TDC financially and another is the research and development works. Latter works will be mentioned in the following sections.

The CRL's major fund for TDC is the contribution to the national time and frequency standards. CRL is responsible to keep and disseminate the standard time in Japan. Fig.2 shows the international scheme of standard times. Three categories are relating to them. Until 1987, BIH played a comprehensive role of the service of UT1 and Atomic Time. Since 1988, when IERS has started, respective schemes of TAI and UT1 have been separated. TDC of CRL, however, pursues the linkage research between TAI and UT1 now and this linkage could be the major source of the funds for CRL's VLBI activities.

Other fund are regarding the earthquake prediction research and the environmental budgets for the mean sea-level change. And TDC of CRL now strongly promote Science and Technology Agency (STA) fellowship to invite space geodetic researchers to Japan.

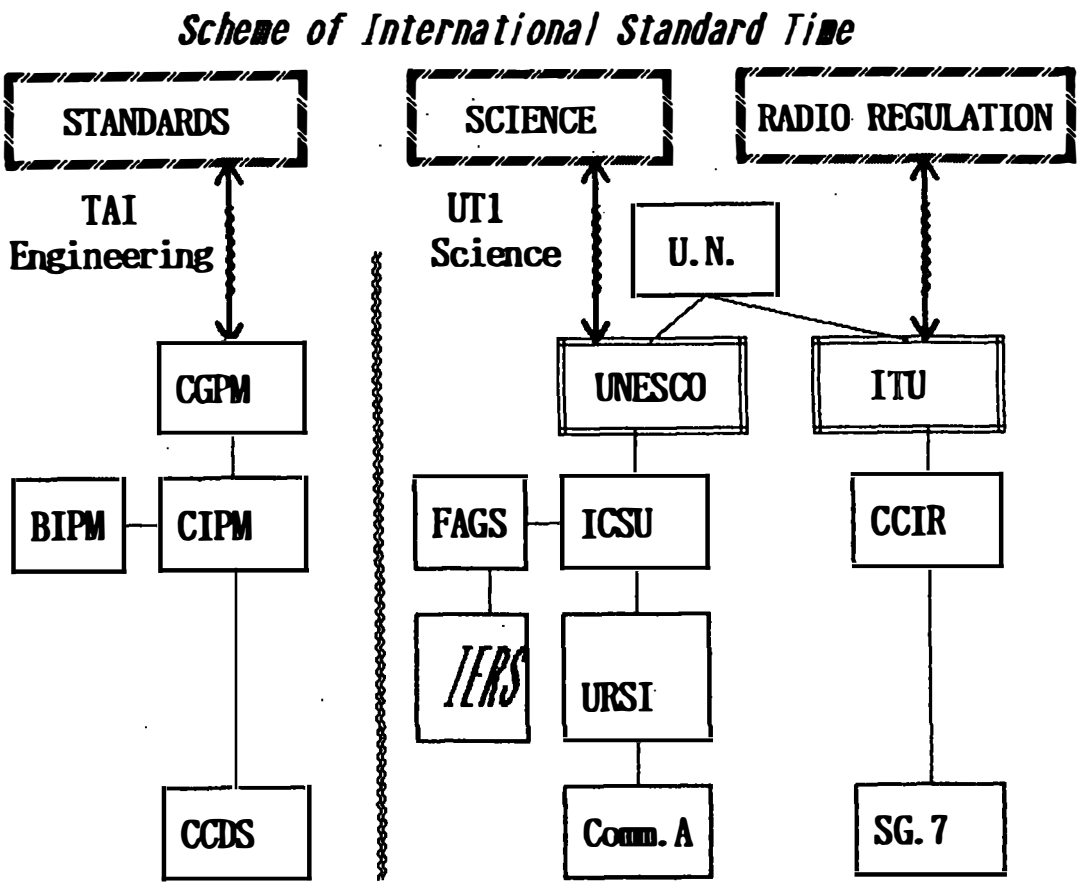

Fig.2 International scheme of Standard Time/Frequncy since 1988

Development of K-4 VLBI system

A new data acquisition system, called K-4, has been developed by CRL[1]. A large capacity data could be recorded with high-recording density. High-speed recording rate is one of the most important developing items of the VLBI system. The adoption of a rotary-head recorder using a cassette tape (Instrumentation Digital Cassette Format) makes the system reliable, smaller and easier to operate. Their interface units make the K-4 system fully compatible with the Mark-III and the K-3 VLBI system. On reproducing the VLBI data, the perfect synchronization is accomplished the K-4 Data Record and Interface units. The synchronization control of the recorders is much easier than the open reel Honeywell recorder for correlation processing.

TIME/VLBI Collocation

One of the major reason of the vertical component error of VLBI experiments is the parameter correlations between the baseline components and the time polynomials. If we can measure and determine the clock difference between two stations by other methods (TIME/VLBI Collocations), we can concentrate on the adjustment of baseline parameters themselves. Fig.3 shows the system diagram of TIME/VLBI Collocation assumed in this simmulation.

The simulation was performed to show the improvement of the vertical component error of trans-pacific baseline by using the two-way time transfer method. The simulation results in Table 1 shows that in the Kashima-Mojave (almost completely east-west) baseline case, X and Z components errors were dramatically improved by this method. These component are considered almost along the vertical components of this baseline.

In our simulation, we adopted the value of 0.4 ns as the two-way time transfer error. If we can improve the two-way precision, much more important and significant results will be available, we expect.

Table 1 Results from the simulation of TIME/VLBI colocation

		case 1			case 2			case 3		
Parameters	a'pri	adjst	delta	rms	adjst	delta	rms	adjst	delta	rms
x-cmp (cm)	30.0	28.5	1.5	1.3	28.3	1.7	4.2	29.8	.2	4.3
y-cmp (cm)	30.0	30.7	-.7	2.4	32.1	-2.1	2.6	31.1	-1.1	2.6
z-cmp (cm)	30.0	29.8	.2	1.5	31.3	-1.3	4.6	29.6	.4	4.6
c10 (ns)	1.00				1.09	-.09	.54	.87	.13	.63
c11 (ns/d)	1.00				-.24	1.24	1.25	3.23	-2.23	3.41
c12 (ns/d/d)	1.00				2.08	-1.08	1.20	-3.12	4.12	6.52
c20 (ns)	1.00							-5.82	6.82	3.70
c21 (ns/d)	1.00							11.81	-10.81	9.89
c22 (ns/d/d)	1.00							-9.29	10.29	6.54

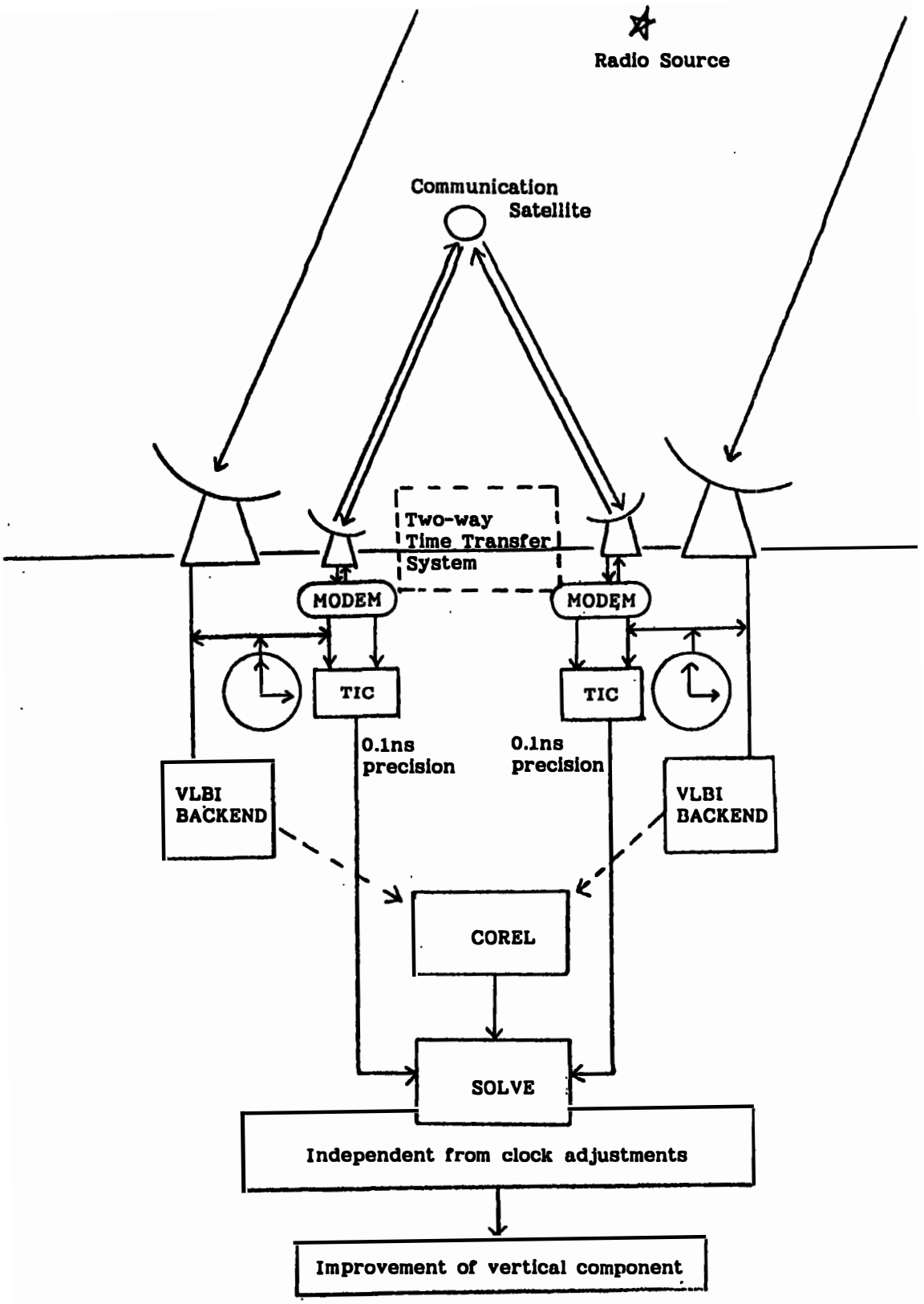

Fig.3 Assumed system diagram for the simulation of TIME/VLBI colocation

Fig.4 shows the relation between S/N ratio and expected precision about two-way time transfer experiment. CRL already performed the ranging test between CRL and pacific INTELSAT and we attained 0.4 ns. for Ku-band and ranging measurements.

We have prospects to improve the precision up to 0.1 ns by increasing the S/N of two-way signals. This simulation clearly shows that VLBI is the most precise time delay mesurement and the research about the clock behavier as the reference of the delay should be done much more.

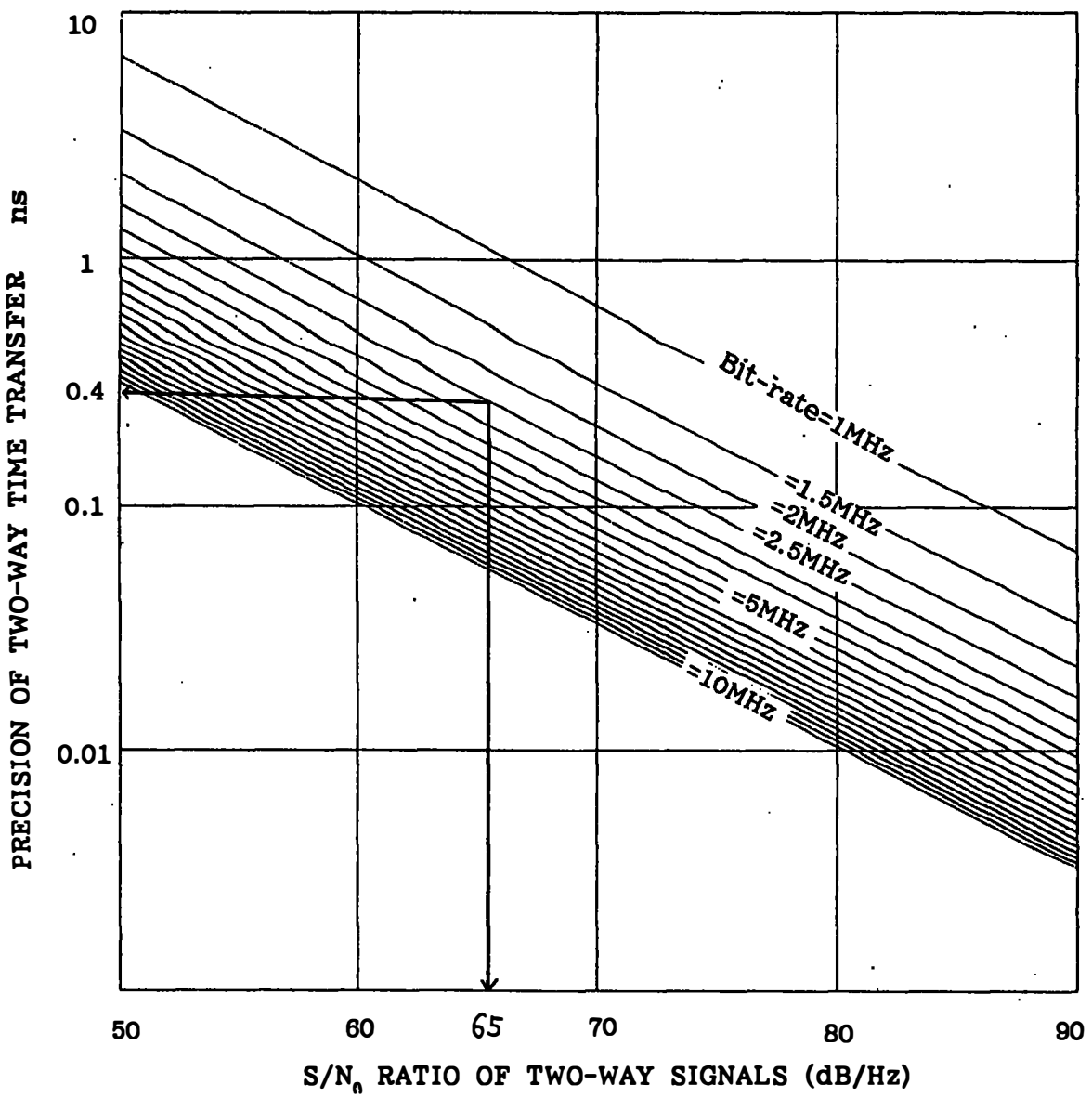

Fig.4 Relation between S/N ration and expected precision of two-way time transfer. Present case:bit-rate=2.5MHz and S/N_0=65dB/Hz, then precision better than 0.4 ns is available. If they will be improved, precision better than 0.1 ns would be possible

Single Frequency VLBI

The new total election content(TEC) measurement system (TECmeter) is developed by CRL and manufactured by Nihon Tsushinki Inc. This system utilizes the coherent P code modulation of two L band signals transmitted from GPS satellites. It does not require the knowledge of the P code itself but only uses the cross-correlation of P code modulation of respective L band signals. The observed value of TEC can be obtained from the measurement of the correlation amplitude, which is related to the dispersive delay between two P code modulation.

The test experiment of single frequency VLBI was carried out at Kashima and Chichijima simultaneously from Nov.25 to Dec.9, 1989 by using TECmeter. Multi-directional observations of slant TECs at a station enable us to depict a vertical TEC distribution around the VLBI station with a simplified ionospheric model. By combining the data observed at two stations, it is possible to extend a TEC mapping area.

TECmeter gives us the ionospheric propagation delay with the precision of less than 1 ns in 1.5 GHz. It corresponds to the 30 ps precision in 8 GHz, which is sufficient for the ionospheric compensation of the geodetic VLBI observations.

Domestic cooperations.

Fig.5 shows the Japanese major institutes relating for IERS. Mizusawa/NAO has been contributing to IERS as the VLBI data analysis and observation centers. MSA is contributing as the SLR observing site. And CRL has started the works of VLBI TDC and non-regular SLR observations for IERS. It is important to coordinate the cooperation among the centers and observation sites. CRL now prepares and will start the domestic committee of IERS TDC specialists to proceed the TDC work regularly. This committee will contribute to the research and development of space geodesy both for IERS and for NASA's new DOSE program.

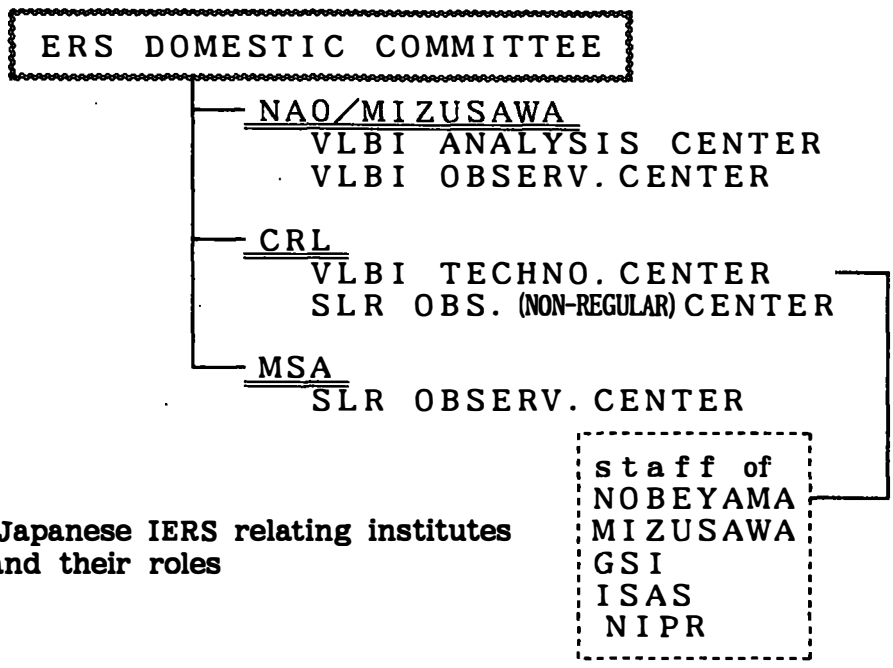

Fig.5 Japanese IERS relating institutes and their roles

New experiment

Japanese Science & Technology Agency(STA) now starts the new project for the Tokyo-metropolitan earthquake research. In recent several years, modern geodetic measurement station such as VLBI and SLR was installed around Tokyo metropolitan region. These new facilities are very important for the geodetic fiducial points for conventional and GPS geodetic networks. Fig.6 shows that by using fiducial points, the network accumulation error will be improved to better than a few centimeters from a decimeter level. This means that the measurement of crustal motion will be performed more effectively for the earthquake research.

ISAS and NAO group now proceed the first space VLBI program. The VSOP satellite will be launched early in 1995. Since the satellite does not have an on-board atomic standard, ground stations should transfer the standard frequency and time to the satellite. The dynamic phase-lock loop with the dead time of about 0.1 sec should be accomplished to keep the on-board clock coherent to ground H-maser. This experiment is also one good example of TIME-VLBI links applications.

National Institute of Polar Research (NIPR) has a new plan of Antarctic VLBI experiments. A series of test VLBI experiments among Syowa station in Antarctica, Kashima and Tidbinbilla were carried out from Jan.16 to 25, 1990, for the first antarctic experiments in the world[2]. The data were successfully recorded at all stations. After the data processing, the global position of Syowa station was determined with the precision of 20cm.

Conclusion

CRL now starts the new technical developments and research works, just above mentioned, under the name of IERS VLBI Technology Development Center. We expect that CRL's activities will contribute the improvement of the results from IERS works, because VLBI is the most precise time delay measurement and the research about the clock behavior as the reference of the delay are suitable works for CRL.

References

(1) Kiuchi, H., S. Hama, J. Amagai, Y. Abe, Y. Sugimoto and F. Takahashi, "Present status of the K-4 VLBI system", in this issue, 1991

(2) Kurihara, N. T. Kondo, Y. Takahashi, F. Takahashi, M. Ejiri, "The result of the test VLBI experiments with the Syowa Station in Antarctica and its future plans", in this issue, 1991

"SYRIUS-A" - Observes NAVSTAR in the Campaign "GIG-91"

N. Umarbaeva, A. Diakov, A. Egorov, G. Krasinsky.

Institute of Applied Astronomy USSR Academy of Sciences,
8, Zhdanovskaya st., Leningrad, 197042 USSR.
Phone (812)2307414; Fax (812)2307413; Telex 121391 IPA

The Institute of Applied Astronomy took part in the campaign **"GIG-91"** (First **G**PS **I**ERS and **G**eodynamics Experiments).

The VLBI observations of NAVSTAR satellites with system "SYRIUS-A" were carried out in January 23 - February 3 at 4 stations of network "QUASAR" (fig.1). Distances between stations are shown in Table 1.

"SYRIUS-A" (**SY**stem **R**adio**I**nterferometrical **U**niversal for **S**atellites observations) has been developed for determination of geocentric coordinates of sites and orbit elements of NAVSTAR and GLONASS [1].

"SYRIUS-A" may be used in the two regimes - as a two frequency VLBI system (in L1 and L2 bands) or as a set of GPS-type receivers (in L1 band).

The system "SYRIUS-A", is an interferometric system, which accept a satellite signal as a noise.

The system is based on a satellite communications earth station "Volna-S".

This station operates in INMARSAT system in a frequency range 1.54-1.64 GHz, what is very close by to NAVSTAR and GLONASS frequency range (1.2 and 1.6 GHz)[2]. So it was possible to use main equipment of the station (antenna and receiver) with a slight modernization. The system "SYRIUS-A" can be used for observation both NAVSTAR and GLONASS satellites.

"SYRIUS-A" consist of 3 modules: 1.3 m antenna (fig.2), a two channels receiver (fig.3) and data recorder (fig.4). The characteristics of the "SYRIUS-A" are summarized in Table2. Fig.5 and fig.6 show the simplified functional block diagram of receiver and data recorder.

Antenna, UHF amplifier and converter are protected by radome (fig.7).

Antenna is automatically operated though a computer program or by a signal of Satellite.

Two-channels receiver satisfies the requirements usual for VLBI. Effective width of each channel is 10 MHz. The system noise temperature is about 200 K.

Output signals from two channels receiver are recorded digitally on magnetic tape SM5309 in MARK-I format. Bandwidths of the registration can be 10.0 or 5.0 or 0.25 MHz. For very long baseline a delay can be compensated on range from 0 to 99 ms with step 1 ms. The data can be transmitted from any site through satellite link to central facility for real-time processing (fig.7). Both testing of all equipment and observations are controlled by computer.

One observation in a set lasted 50 ms. Interval between two adjacent observations was 2 minutes. Duration of a set was ten days. Fig.8 shows functions of correlation of satellites NAVSTAR and GLONASS (first channel).

Due to high signal/noise ratio it appeared possible to restrict the averaging time by the value 50 ms only (about one million samples) and to use refined algorithms of signal processing for general purpose computers (VAX-type in our case). Accurate procedure of fractional bit correction and proper compensating of fringe rotation have diminished the loss of the correlation to the level of 1%-2% (see Fig. 9,10). The testing has proved that the group delays may be determined with the error about 2% of time interval between the samples (0.5 - 0.8 ns) and the interferometric phases with the errors which do no exceed 5 degrees (see Fig 11). Thus it appeared possible to control the phase variations after two-minute time intervals elapsed between the consequent observations and to resolve the phase ambiguities for the synthesized wide band (the ambiguity 2.8 nsec) as well as for each of L1 and L2 bands (the ambiguities 0.7 - 0.8 ns; see Fig 12). By comparing the group delays for L1 and L2 channels the time behavior of the ionospheric corrections was studied (see Fig. 13). These corrections in time delays appeared to be as large as 50 ns.

As a by-product the ionosphere contribution may be estimate with r.m.s. < 1.5 ns for each observation. Besides the data recorded on each site being independently processed made it possible to obtain observables for GPS receiver - they are the pseudoranges (r.m.s. < 1 ns) and the phases (r.m.s. < 10 deg).

The experiment of the combined processing of the both type observations shaw that the system is useful tool for determining both the accurate site positions and orbital elements.

1. Gubanov V.S. and Umarbaeva N.D.,1989, Determination of satellite orbit elements and geocentric coordinates of station from VLBI-observation, Preprint N5, Institute of Appiled Astronomy USSR AS, Leningrad.
2. Zhilin V.A., 1988, Mezhdunarodnoj Sputnikovaj systema morskoj svajzi INMARSAT (spravochnik), Leningrad, Sudostroenie.

Table 1

Distances in kilometers between sites of the "GIG-91" observations of "SYRIUS-A"

	Zelentchukskaj	Badary	Firyuza (Ashkhabad)
Svetloe (near Leningrad)	2013	4273	3156
Zelentchukskaj (Northern Caucasus)		4398	1518
Badary (Eastern Siberia near Lake Baikal)			3687

Table 2

Characteristics of "SYRIUS-A"

Equipment Characteristics

System noise temperature	200 K
Frequency range	
I channel	1.57-1.62 GHz
II channel	1.22-1.26 GHz
Antenna type	parabolic dish
diameter	1.3 m
gain	22 dB
tracking	program-driven
Receiver	
pre-amplifier	uncooled transistor
noise temperature	100-150 K
gain	25 dB
amplifier and converter	up to 2 identical units
band width	10 MHz
synthesizer	up to 2 identical units program-driven
Data Recorder	
channel	up to 2 identical units
frequency band	10.0 or 5.0 or 0.25 MHz
sampling	20.0 or 10.0 or 0.5 MHz
capacity buffer memory	2 Mbit
compensating delay	range 0-99 ms step 1 ms
storage data	magnetic tape or satellite link
control computer	DVK 3M
Total systematic error	
for VLBI mode (L1 and L2)	
group delays	< 1 ns
phase delays	< 0.1 ns
phase	< 3 deg
for GPS	
mode (L1) ranges rate	< 1 ns
phase	< 10 deg

Fig 1. Situation of sites network "Quasar" in the campaign "GIG-91"
(1 - Svetloe, 2 - Zelentchukskaj, 3 - Firyuza, 4 - Badary)

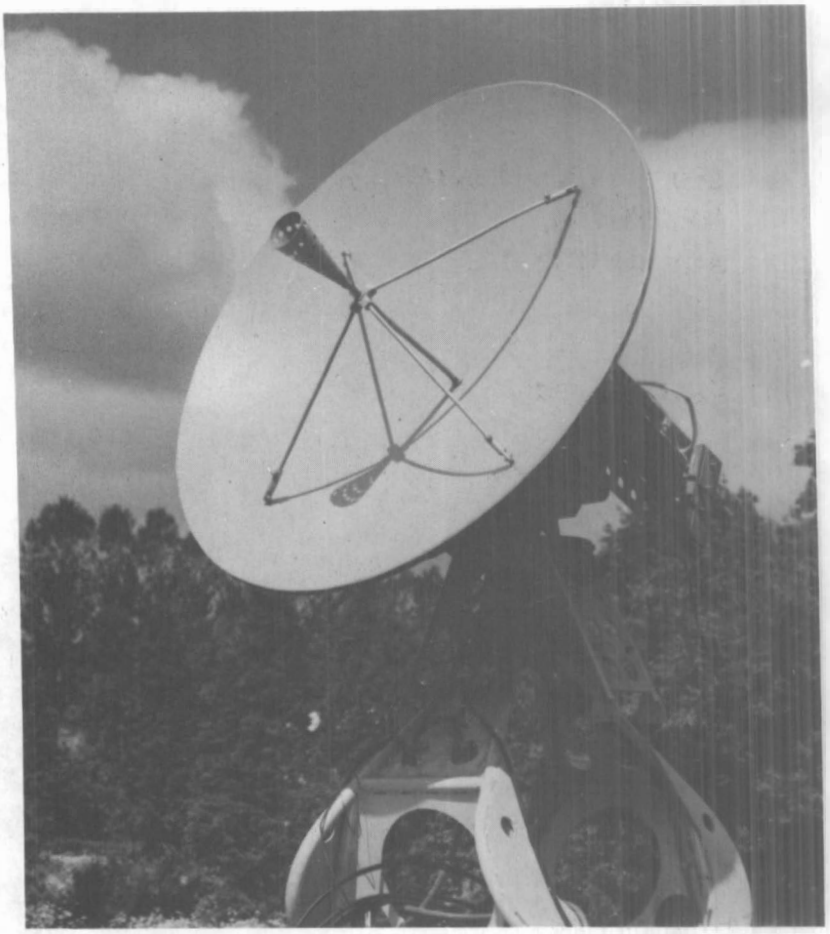

Fig 2. Antenna of "SYRIUS-A".

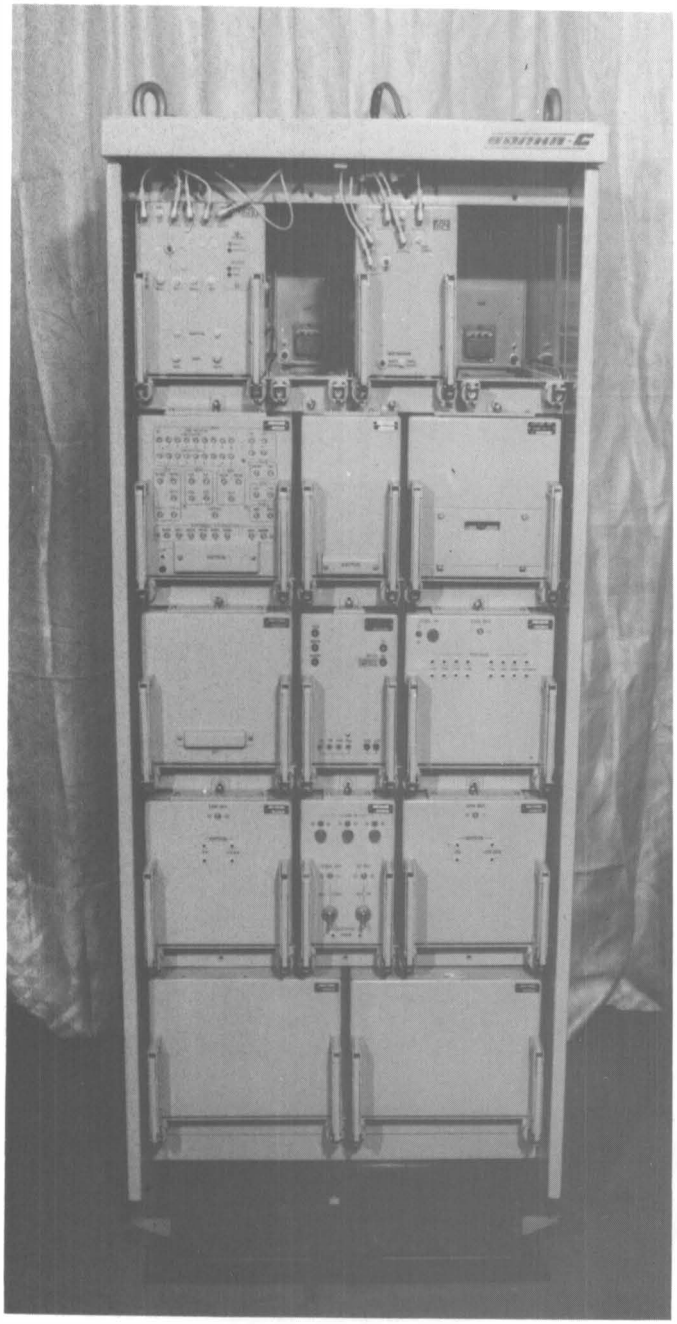

Fig 3. Two channels receiver of "SYRIUS-A".

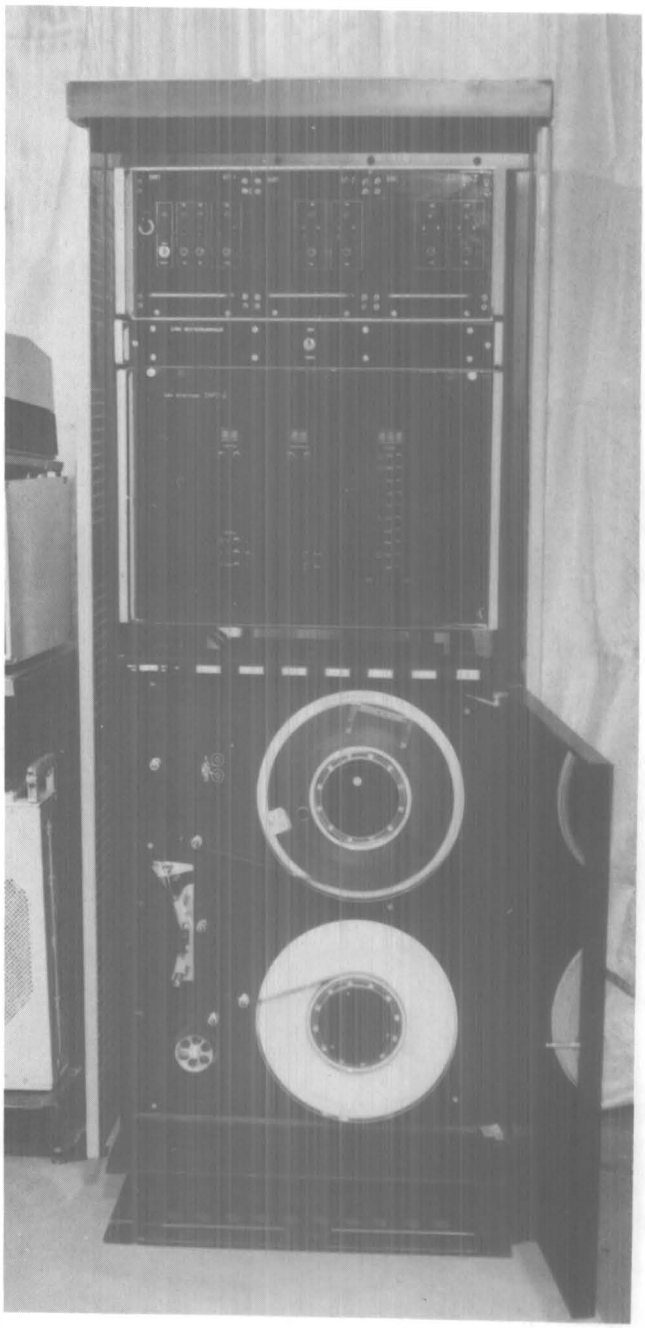

Fig 4. Data recorder of "SYRIUS-A".

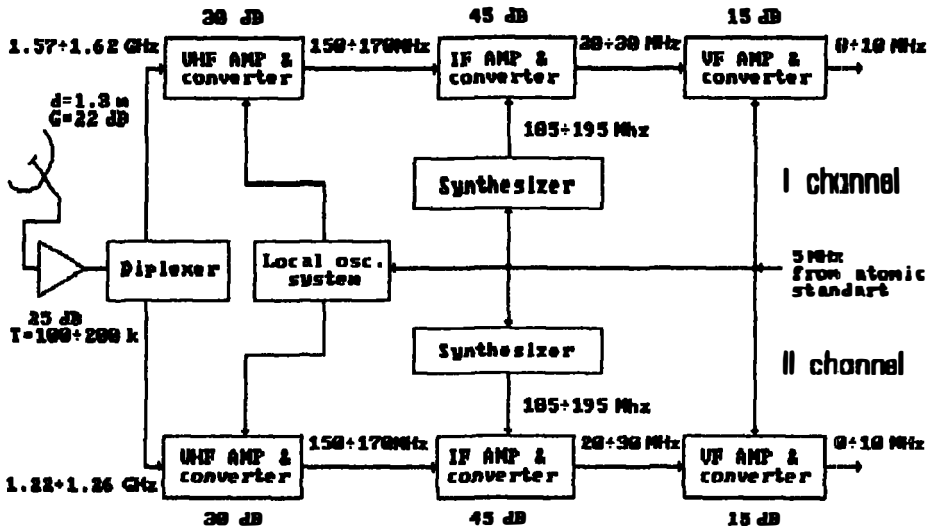

Fig 5. Block diagram of receiver of "SYRIUS-A".

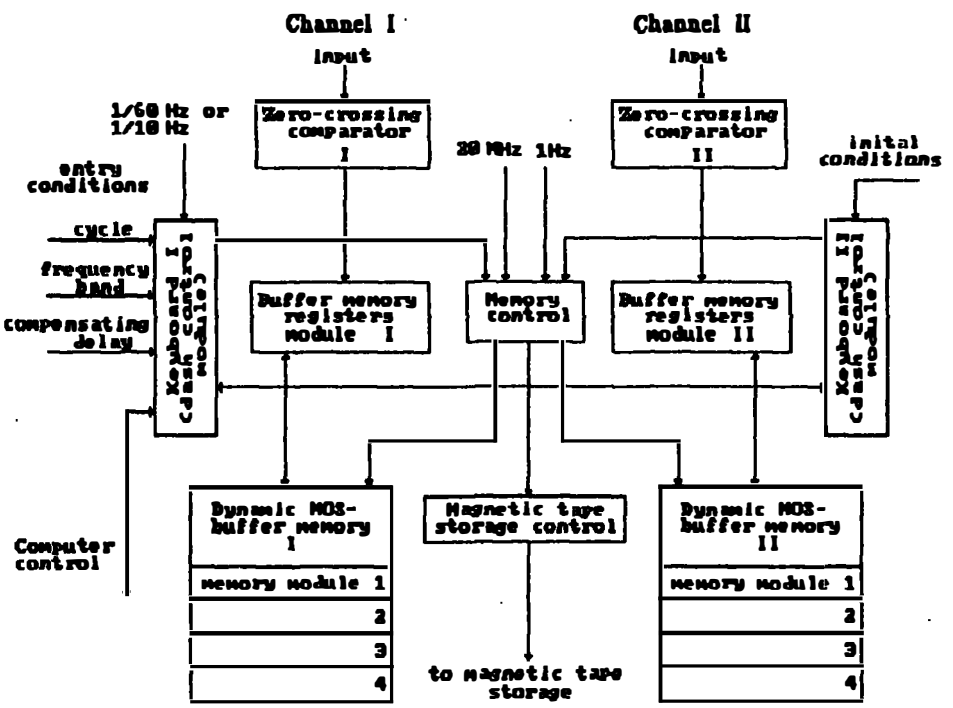

Fig 6. Block diagram of data recorder of "SYRIUS-A".

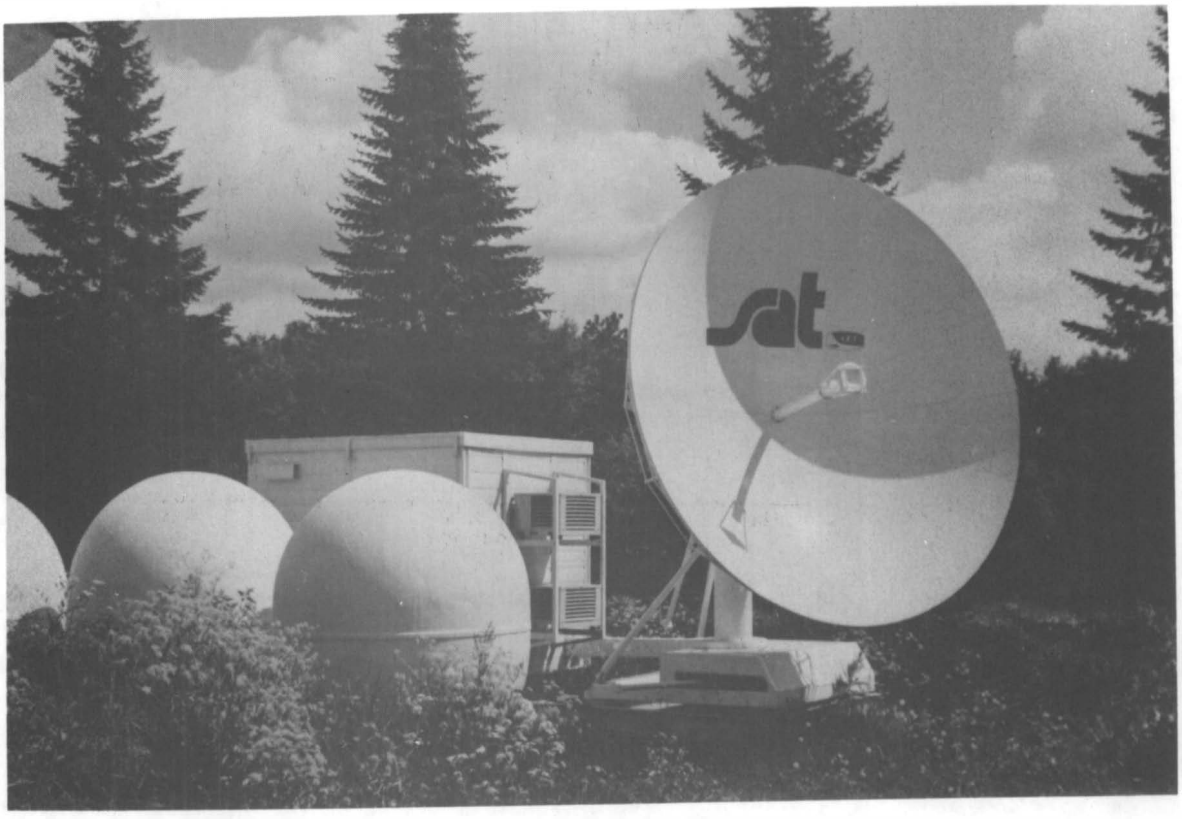

Fig 7. Antenna of "SYRIUS-A" (left) and satellite station "Tesla" (right).

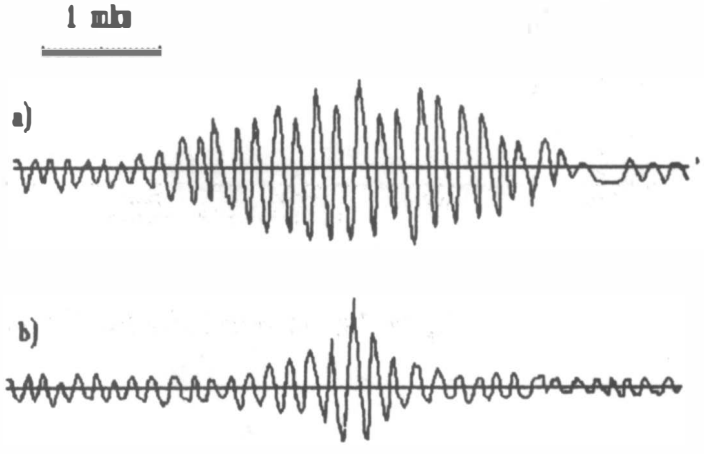

Fig 8. Functions of correlation of satellite: a) "GLONASS", b) "NAVSTAR".

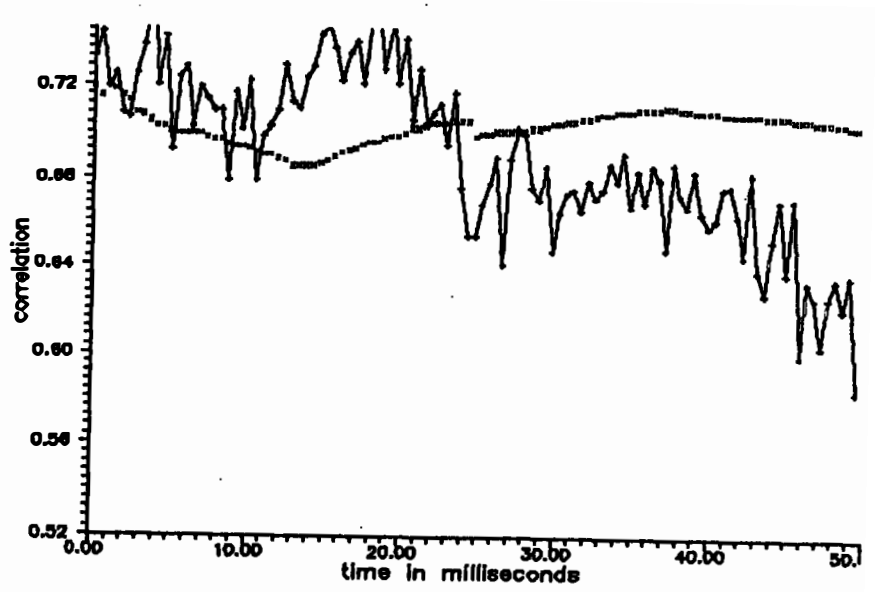

Fig 9. Loss of correlation for L1 band.

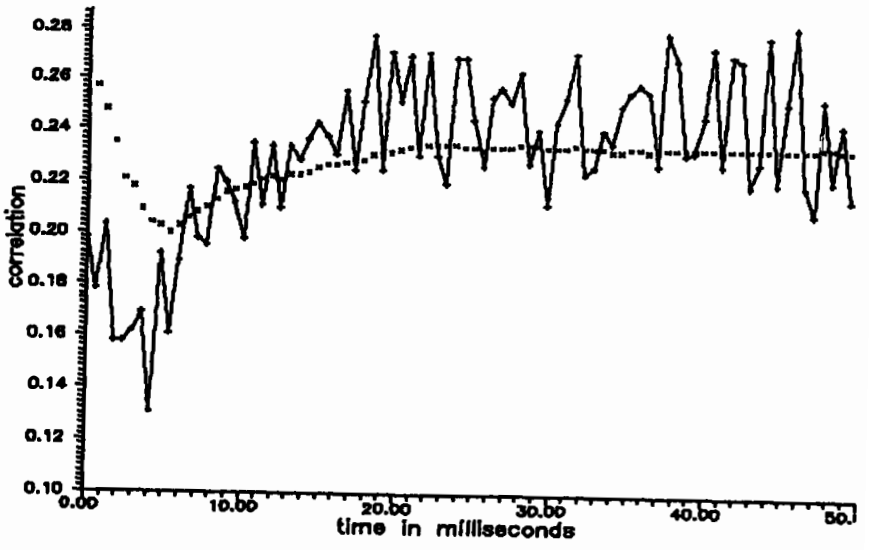

Fig 10. Loss of correlation for L2 band.

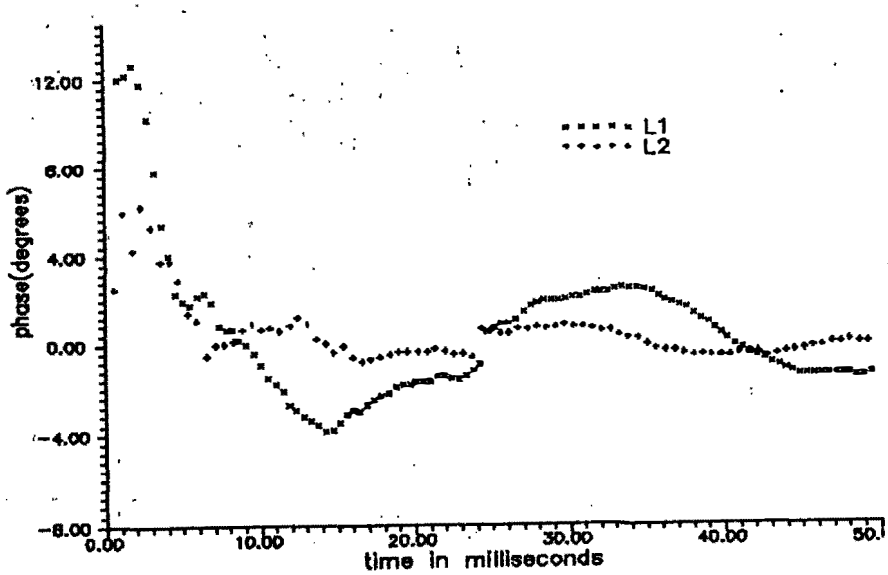

Fig 11. Short-time variations of fringe phases on baseline Svetloe-Firyuza. 26.01.91. Satellite SV14 (19982).

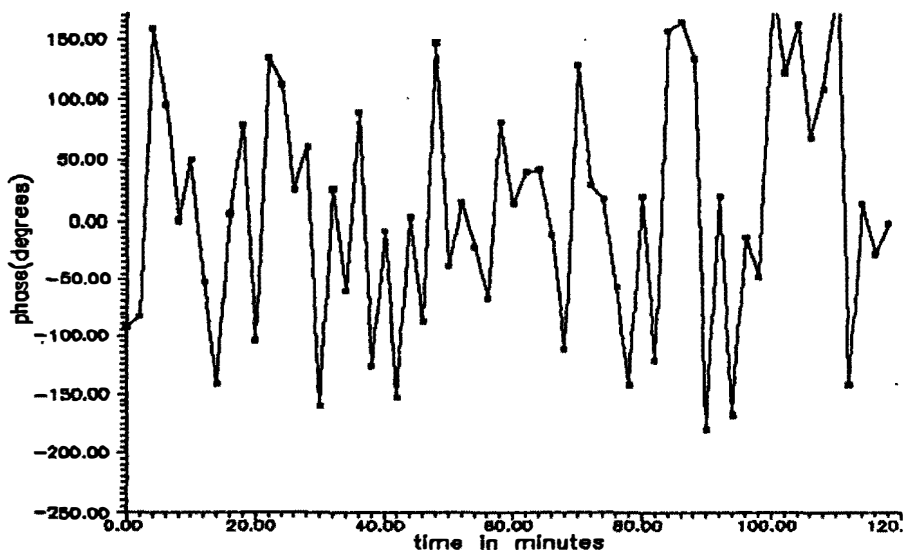

Fig 12. Long time behavior of fringe phases for L2 band on baseline Svetloe-Firyuza. 26.01.91. Satellite SV14 (19982).

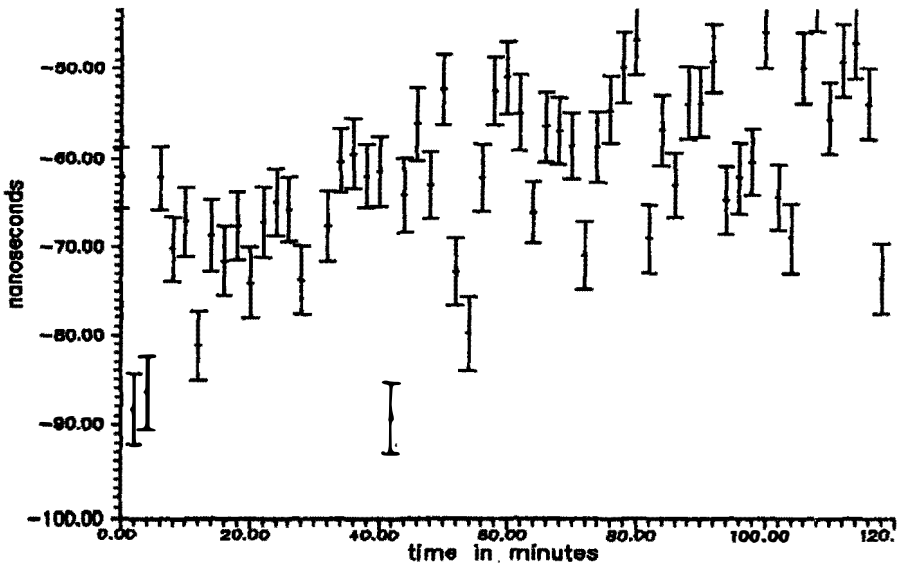

Fig 13. Time delay: ionospheric effects (observed) on baseline Svetloe-Firyuza. 26.01.91. Satellite SV14 (19982).

A High-Performance Transportable VLBI Correlator

N Kawaguchi and T Miyaji (Nobeyama Radio Observatory/NAO, Minamimaki, Minamisaku, Nagano, 384-13 JAPAN, 81-267-63-4384)
T Sasao, T Hara, S Kuji, K-H Sato, Y Tamura, K Asari, O Kameya, K Iwadate and S Abe (Mizusawa Astrogeodynamics Observatory/NAO, Hoshigaoka, Mizusawa, Iwate, 023 JAPAN, 81-197-24-7111)
S Yasuda (Tohoku University, Aza Aoba, Aramaki, Sendai, Miyagi, 980 JAPAN, 81-222-22-1800)
K Matsumoto (Denkitsushin University, Chofugaoka, Chofu, Tokyo, 182 JAPAN, 81-424-83-2161)

Abstract

A new XF VLBI correlator is under development at National Astronomical Observatory, Japan. It is optimized to process records of the new K-4 type 1 terminal, which facilitates a single-channel burst sampling mode. Therefore the correlator has a simple single-unit architecture similar to that of Mark II correlator. Yet the processing speed of 128 Mbps, supported by custom designed LSI's and powerful byte-serial circuitry, is high enough to handle virtually all existing multichannel records, including MK-3 and VLBA, by means of cyclic operations of the single unit. The correlator has 512 complex lags sufficient for processing 2 GHz-wide burst sampled data. Its usefulness in spectroscopy is guaranteed by the large number of lags and an astonishingly simple new correlation algorithm for 2-bit quantized data. The fringe search windows both in delay and rate are expandable up to 16 times. The basic configuration consists of two interfaces for K-4 recorders, one Mark III format converter and one correlation unit for single baseline processing. Expansion up to 5-station 10-baseline model is readily achievable. Its smallness (56 cm-wide and 80 cm-high) and transportability (less than 50 kg) will make it a user-friendly 'field instrument'.

1. Introduction

An appearance of compact, easy-to-use, inexpensive and transportable high-quality correlators will change the whole VLBI world. Such correlators will be widely distributed over many observatories on different continents, and people will get possibilities to quickly look

for fringes, to process their own data whenever they wish, to check receiving systems by looking at correlator outputs in-situ, to confirm fringes in real time with limited amount of data transmitted through a telecommunication line, to make a multi-station processor by just combining brought-in single-baseline correlators, and so on. In other words, such a correlator will become a handy 'field instrument' for VLBI community.

Although what is stated above would obviously imply a break-down of the monopoly of big correlation centers in the VLBI data processing, the small correlators will make significant contributions to the center works, too. In fact, then the correlation centers will be largely freed from the tedious fringe searches and processing of single-baseline records. They will be able to confine themselves mainly to process large-scale multi-baseline data only and will regularly receive well-checked records and accurate enough search-parameters from those observatories where the small correlators are in operation. Therefore, the turn-around times of the VLBI data processing as a whole will be greatly reduced. Moreover, the user-friendly correlators will expand the VLBI community, and eventually increase users of the big centers.

We will briefly describe a design of a new VLBI correlator which is under development at National Astronomical Observatory, Japan. The correlator aims at

- high-precision geodesy and astrometry with K-4 type 1 super-wideband burst-sampling recording system, which is also developed at NAO,
- high-resolution VLBI spectroscopy,
- easy fringe search,
- compatibility with existing VLBI systems,
- multi-baseline processing, and
- compactness and transportability.

2. Basic Specifications of New Correlator

Major specifications of the correlator are the followings.

1) 128 Mbit per second processing speed.
2) 512 complex lags.
3) 4 MHz maximum fringe frequency.
4) Correlation of 2-bit quantized data.
5) Expansion of fringe search windows up to 16 times.
6) Expandable up to 5-station 10-baseline processor.
7) Processing of K-4 type 0, K-4 type 1 and Mark III data.
8) Pulsar gating.
9) Compact: 56 cm (D), 80 cm (H) and 45.5 cm (D).
10) Transportable : lighter than 50 kg.

128 Mbit per second processing speed corresponds to the current

state of the art of the hardware circuitry. The speed is a half of the maximum recording speed of the K-4 recorder and twice as large as the standard recording speed of the K-4 type 0 terminal.

512 complex lags are required for fringe searches with 2 GHz super-wideband burst sampled records and convenient for high-resolution VLBI spectroscopy of maser line sources.

4 MHz maximum fringe frequency is needed for mm- or submm-wave VLBI.

The correlation of 2-bit quantized data is required for increasing sensitivity of VLBI observations, especially in line-spectrum researches.

The 16-time expansion of the fringe search windows facilitates quick and easy operations in the most time-consuming part of the VLBI data processing.

The expansion capability up to 5-station 10-baseline processor will enable us to form a multi-baseline system with brought-in correlators.

The compatibility with existing VLBI systems is essential for wide application of the correlator.

As a whole, the correlator could be labeled as 'C-4', since it will be Compact, Convenient and Cheap Correlator.

3. Configuration of Single-Baseline System

Figure 1 shows a configuration of the basic model for the single-baseline processing, which is composed of 2 correlator-interface units, a correlation unit and a Mark III format conversion (playback adapter) unit. Figure 2 is a schematic view of the system.

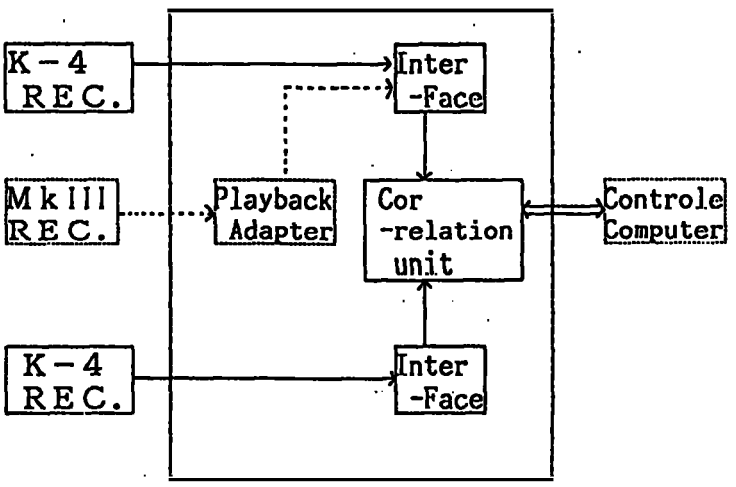

Figure 1 Basic configuration of single-baseline system

Data formats of Mark III and all other non-K-4 records are first converted to K-4 format. Then the format-converted data streams are fed

into the correlator-interface unit. This is done by respective format conversion units (currently the only Mark III format conversion unit is developed).

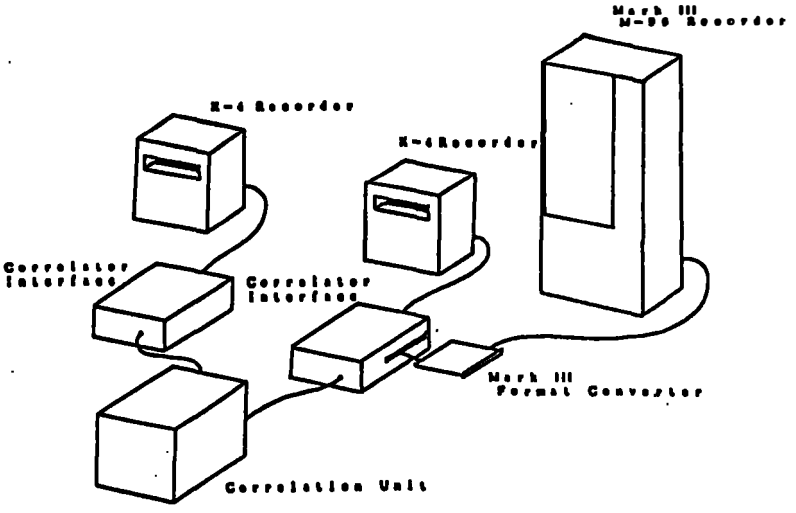

Figure 2 Schematic view of single-baseline correlator

4. Correlator-Interface Unit

The correlator-interface unit is designed as a 'station-based' device. Therefore one interface unit corresponds to one playback unit. The interface unit consists of 3 sub-units (Figure 3).

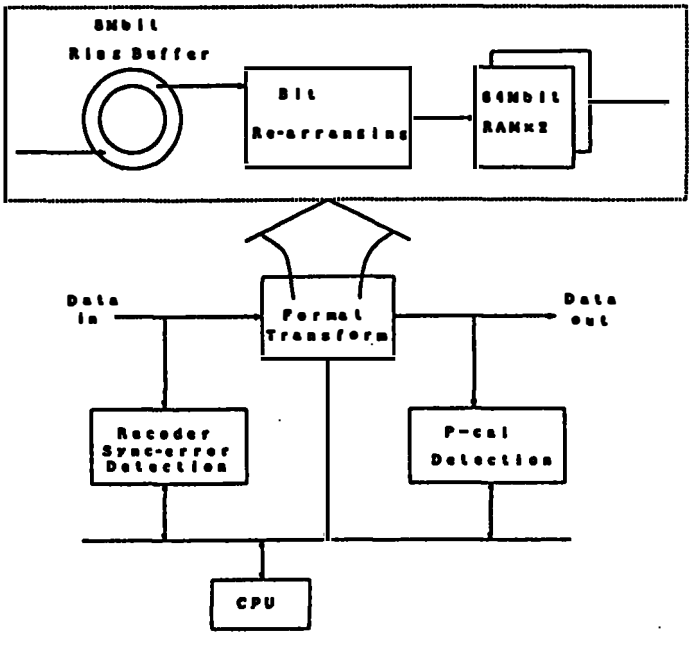

Figure 3 Correlator-interface unit

First, the recorder sync-error detection sub-unit detects errors in the synchronization of two played-back data for further operations to

synchronize bit-streams. Second, the format transform sub-unit converts multi-channel (or channel-parallel) data formats to those suited to processing in the correlation unit. Also the sub-unit virtually reduces the observation site to the Earth center by absorbing geometrical delay between the two with the aid of the 8 Mbit ring buffer, so that records from different observatories are roughly alined. Third, the p-cal detection sub-unit picks up phase-calibration tone-signals superposed on the data records.

The format transformation capability is the most distinctive feature of the correlator. The correlation unit itself has a simple single-unit (or single-module) architecture similar to that of Mark II correlator. Such a design was adopted because the correlator is optimized to process the K-4 type 1 burst sampled data. K-4 type 1 data format assumes 1-, 2- and 4-channel modes, of which the most important will be the 1-channel burst sampling mode. In the burst sampling mode, up to 2 GHz-wideband data will be digitized and stored in high-speed toggle memories intermittently, and read and recorded with reduced speed, corresponding to the maximum recorder speed. So, we need first of all a high-speed single-unit correlator to process the burst sampled data. Yet the 128 Mbit per second processor speed is high enough to handle almost all existing multi-channel records including K-4 type 0, Mark III and VLBA (optional), by means of cyclic operations of the single unit. For that purpose, channel-parallel records of every accumulation (or parameter) period must first be rearranged to channel-serial records. This is done by programmable logic devices and 64 Mbit × 2 double buffer of the format transform sub-unit. In our correlator, an accumulation period always corresponds to a fixed amount of data bits - 64Mbits. Therefore, actual 'hardware integration time' varies with recording speed and data format.

The same logics are used to repeatedly process a small segment of data streams, changing search parameters and shifting one data stream relative to the another, in order to expand search windows up to 16 times in both delay and delay rate.

5. Correlation Unit

The correlation unit is a single-module XF cross-correlation processor (Figure 4). Both delay tracking and fringe stopping are performed by respective sub-units of 'baseline-based' design. The high processing speed is supported by the custom designed cross-correlation LSI's and powerful 8-bit-parallel (or byte-serial) processing circuitly. The 128 Mbit per second speed is achieved by the byte-serial processing with 16 MHz byte clock. The parallel processing is composed of byte delay tracking, byte fringe stopping, byte integration

suppression (pulsar gating) and byte cross-correlation.

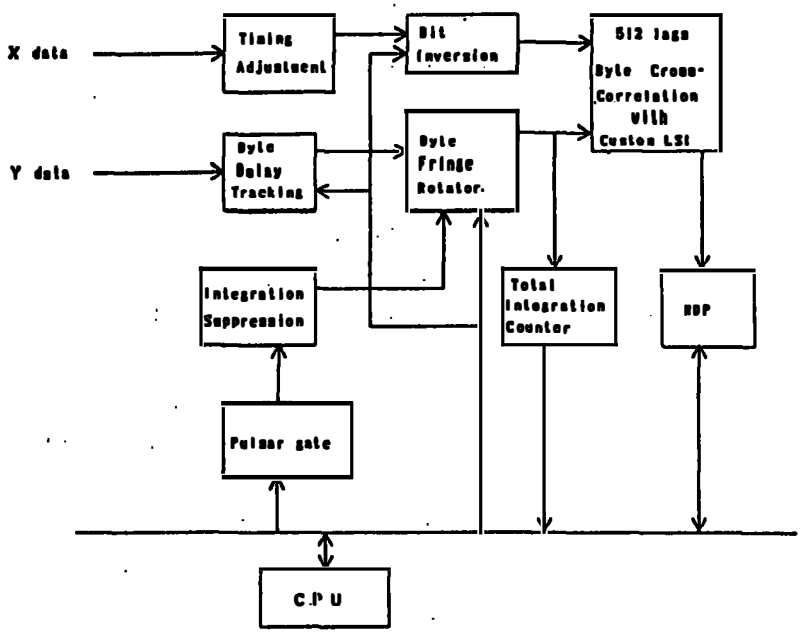

Figure 4 Correlation unit

As an example, the byte delay tracking scheme is shown in Figure 5. The parallel algorithm is realized by a combination of byte-shift and

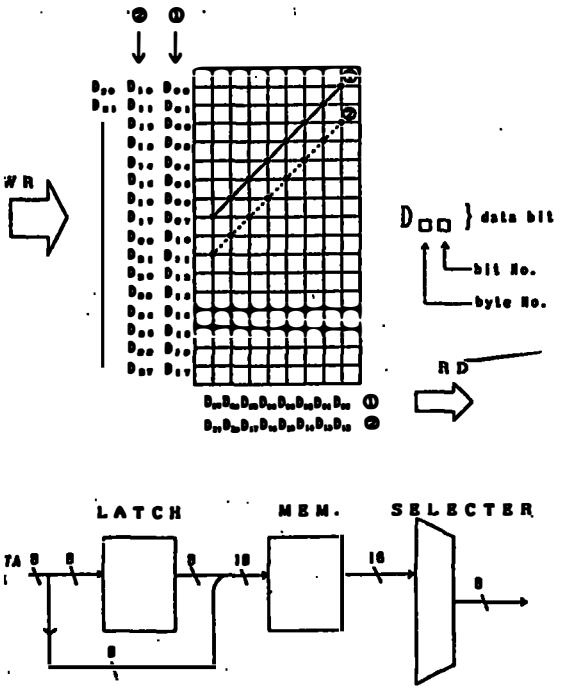

Figure 5 Byte delay tracking

bit-shift operations. The bit-shift is performed by a 16-bit selector acting on a 16-bit data formed by 2 successive data-bytes, while the byte shift is done by suitable addressing of a buffer memory when the accumulated shift-increment exceeds 8 bits.

Of course, all bit-shifts and jumps of the fringe rotator phase can occur only at byte boundaries in the byte-serial algorithm. In general, the timings are not optimally located for the operations. This gives rise to a certain amount of coherence loss. It is shown, however, that losses due to the effect are negligibly small.

6. Correlation of 2-bit Quantized Data

A simple and powerful algorithm was devised by N. Kawaguchi to process the 2-bit quantized data.

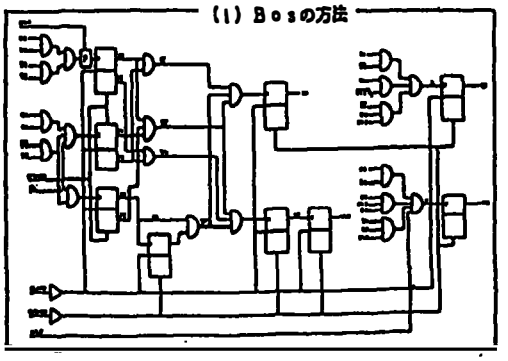

Kawaguchi

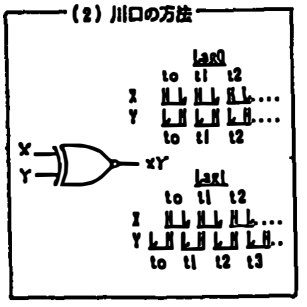

	00	01	10	11
00	4	2	-2	-4
01	2	0	0	-2
10	-2	0	0	2
11	-4	-2	2	4

Figure 6 Kawaguchi's correlation algorithm (middle) for 2-bit quantized data as compared with Bos's (top), and multiplication table (bottom)

An exclusive-nor logic, which is exactly the same with the usual one for the 1-bit quantized data, turns out to be capable of providing

proper 2-bit correlation results according to a multiplication table with lower-level products deleted shown in Figure 6 (Cooper, 1970). The proper results are obtained if we reverse higher- and lower bits in one of the two 2-bit quantized data-streams, apply the exclusive-nor logic to the modified data-streams and make suitable combinations of odd-lag-number and even-lag-number correlation results. The 2-bit processing algorithm is built in the cross-correlation LSI's, which are used to process both 1-bit and 2-bit quantized data. Switchings from one mode to another are realized by CPU commands. The algorithm is in fact astonishingly simple, much simpler than Bos's (1989), and yet improves the signal-to-noise ratios of spectral line observations by as much as 20 %.

The correlator is now in a final stage of the development and will be operational in the later half of 1991.

References

Bos, A., The N.F.R.A. Correlator Chip, Internal Technical Report of Netherlands Foundation for Radio Astronomy, April, 1989.

Cooper, B.F.C., Correlators with Two-Bit Quantization, Aust. J. Phys., 23, 521-527, 1970.

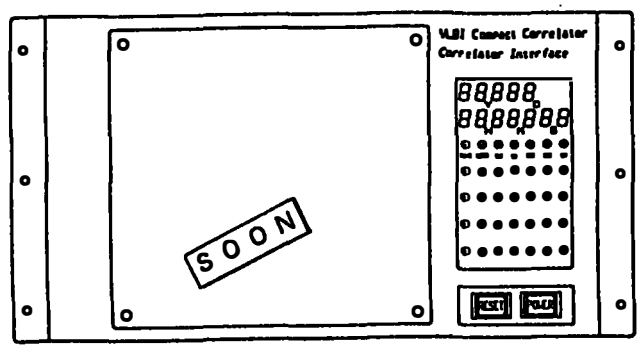

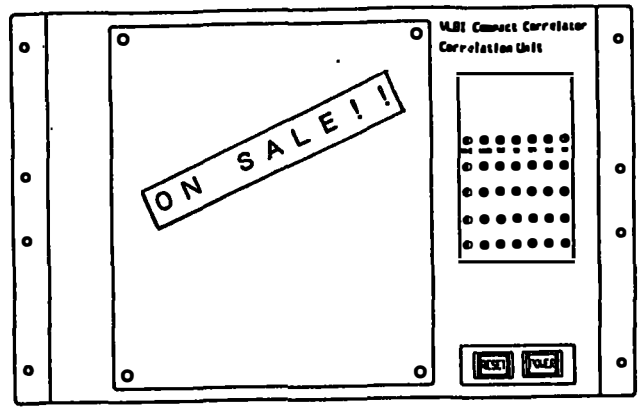

THE CANADIAN GEOPHYSICAL LONG BASELINE INTERFEROMETRY SYSTEM DESIGN

W T Petrachenko and P Mathieu (Geophysics Div, Geological Survey of Canada, Ottawa, Ont, Canada; 613-995-8720)
J Popelar (Geodetic Survey of Canada, Canada Centre for Surveying, Ottawa, Ont, Canada; 613-992-2725)
W H Cannon (Institute for Space and Terrestrial Science, York University, Toronto, Ont, Canada; 416-665-5459)
J L Yen (Dept of Electrical Engineering, University of Toronto, Toronto, Ont, Canada; 416-978-8756)

The Canadian Geophysical Long Baseline Interferometry system (CGLBI) is being developed to meet the following national objectives: the establishment of geodetic reference standards, the observation of crustal strain and its relation to seismic activity, and a quantitative assessment of global change.

The three major features which determine the performance of a modern geophysical VLBI system are its record rate, spanned bandwidth, and phase stability. The CGLBI system will have a maximum record rate of 128 Mb/s using the stacked VHS data recorders being developed for the RadioAstron project at the Institute for Space and Terrestrial Science (ISTS). A wide spanned bandwidth will be achieved by rapidly sequencing the frequency of the local oscillator of a single VLBA-compatible baseband converter. The latter will be able to switch rapidly amongst up to four IF inputs, each in the 100-1000 MHz range. The phase delay of the electronics will be monitored using at least two phase detectors each capable of processing a calibration tone with frequency anywhere within the baseband channel. Compensation for the geometrical delay and phase of the interferometer will be applied within the acquisition system prior to recording the data.

The above features of the CGLBI system have been carefully selected to achieve the design goals of flexibility, economy, operational efficiency and performance in geophysical applications.

I. Background

The principal objectives of the Canadian Geophysical Long Baseline Interferometry (*CGLBI*) program are: the observation of crustal strain and its relation to seismic activity, a quantitative assessment of global change, and the

establishment of Canadian geodetic reference standards.

The plan needed to achieve these objectives has recently been formalized with the definition of the Canadian Crustal Motion Network (see Figure 1). The network has four observational components: VLBI, GPS, absolute gravimetry and cryogenic gravimetry.

The 13 existing and proposed VLBI sites in the network are represented in the figure by square symbols. They are distributed roughly uniformly throughout the country at spacings of about 1000 km. In each case the VLBI sites are colocated with GPS sites. Established sites and those planned for the future are represented respectively by filled-in and open symbols. Up to the present time, 5 VLBI sites have been established. These have been occupied at varying levels of regularity as part of the NASA Crustal Dynamics Project. Although these international observations will continue to be given high priority, it is considered important that **all** VLBI sites in the network be reoccupied on a **regular** rotating basis at intervals not exceeding three years. The CGLBI S2 system is being developed as part of the effort to achieve this goal. Since most of the VLBI sites are in remote, inaccessible areas, transportability is an important feature of a VLBI system for use in Canada.

Central to the establishment of the VLBI component of the Canadian Crustal Motion Network is the use of the 46-meter fully steerable parabolic antenna located in Algonquin Park. The large collecting area of this dish makes possible the use of a small (approximately 3-meter) transportable dish at remote sites. It is intended that permanent antenna piers be established at each VLBI site and that only the dish, positioner and electronics be transported between locations. Each site will be occupied for a period of about 3 months on a rotating schedule. These relatively long occupations will allow the site position to be refined through repeated measurements and will minimize transportation costs.

Although Canada represents the second largest landmass in the world its population is comparatively small. The nation's large size and small population have been determinant in defining the following design goals of the CGLBI system:

1. low cost
2. operational efficiency
3. transportability
4. an ability to achieve the sensitivity, delay resolution and phase stability required by modern geophysical applications given the other constraints.

Unique features have been included in the CGLBI S2 system to achieve these goals. VHS cassette recorders are used to store the large amount of astronomical data required by VLBI. A single baseband converter along with a frequency agile local oscillator are used to synthesize a wide effective bandwidth thereby minimizing the required number both of baseband converters and correlator channels. The geometric delay and doppler corrections are applied within the

acquisition system prior to recording the data thus simplifying the correlator design. Finally, at least two flexible phase detectors are included within the acquisition system.

II. The CGLBI S2 Recording Terminal

The CGLBI S2 recording terminals are being developed at the Institute for Space and Terrestrial Science (ISTS) in Toronto as part of Canada's contribution to the orbital VLBI project *RadioAstron*. These terminals are physically configured as a stack of 8 S-VHS recorders. S-VHS transports have been chosen because they represent a mature technology. These transports and their tapes are inexpensive, robust and readily available and data density on tape is still high although no longer state of the art. Each transport achieves a record rate of 16 Mb/s for a system total of 128 Mb/s. In long play mode the raw bit error rate is 2.5e-5 and tape duration is 3.75 hours. Each record terminal includes one playback channel so that the integrity of the entire record path can be checked in the field. The terminals have a sophisticated operator interface and included extensive self diagnosis and powerful syncing and slewing features. At the present time one prototype recording terminal has been completed and the design of the playback terminal is underway. A Mark III reformatter has been included in the user interface and is currently being tested with a Mark III decoder. The estimated costs respectively of a recording and playback terminal are $50k and $60k.

A transportable version of the system is available. It comes in three 19 inch rack mountable components. The 8 VCRs are split equally between two identical modules. Each contains 4 VCRs, measures 19 inches by 15 inches and weighs about 60 lbs. The last module is smaller and lighter and contains the system's VME controller.

III. The CGLBI S2 Data Acquisition System

A prototype version of the CGLBI data acquisition terminal (DAT), having neither bandwidth synthesis nor phase calibration capabilities, has been built and successfully tested. The work required to include these features is in the planning and early design stage. A list of specifications (Table 1) and a detailed block diagram (Fig. 2) have been completed although these are subject to change due to the ongoing design efforts.

Four selectable I.F. inputs, each in the 100-1000 MHz range are included in the CGLBI data acquisition terminal specifications. These frequencies were chosen to achieve compatibility with standard Mark III, RF bandwidth upgraded Mark III and VLBA at the I.F. input level.

Only one baseband converter is included in the specifications and the standard

CGLBI observing mode will use both USB and LSB signals each with a bandwidth of 16 Mhz. There will be 4-level sampling at 32 Ms/s. The maximum sampled bit rate with these parameters will be 128 Mb/s which matches the total record rate of the S2 recorders. Since the baseband converter will be based in large part on the one used in the VLBA, all VLBA baseband channelizations will be available.

The LO settling time has been specified as less than 1 ms. The combination of the use of 4 selectable I.F. inputs, a single baseband converter and an LO with a short settling time make frequency agile bandwidth synthesis possible.

Compensation for the interferometer delay and doppler shift will be applied in the acquisition system prior to recording the data. Resolution in delay tracking will be better than 1/8 of a sample interval and resolution in phase tracking will be better than 1/32 of a cycle.

Phase tracking is achieved by offsetting the frequency of the baseband LO. As a result, the frequencies of the phase calibration tones are continuously changing. In order to detect these tones it is necessary to precisely control the phase of the tone detectors. In the CGLBI system phase cal detectors will be placed in the acquisition system thus providing a powerful real time diagnosis of system problems. They will further track phase at any frequency within the baseband channel.

As shown in figure 2, the CGLBI S2 DAT is composed of three assemblies, those being the intermediate frequency/baseband converter (IF/BBC) assembly, the local oscillator/sampler (LO/Sampler) assembly and the controller assembly.

In the IF/BBC assembly, four IF signals are input to a computer controlled SP4T switch. This allows both S and X band channels to be handled by the same baseband converter. A computer controlled attenuator and total power detector are included to maintain the signal levels well above the noise floor and well below saturation. The frequency of the input signals will be translated from the 100-1000 Mhz band to the 1050-1950 Mhz band using a local oscillator at 950 Mhz. It will be possible to control the phase of this LO so that the resulting frequency will be offset sufficiently to compensate for doppler shift of the input. The final baseband conversion will be accomplished using a local oscillator whose frequency can be set in 1 MHz increments within the 1050-1950 MHz range. The settling time for this synthesizer has been specified to be less than 1 ms. which will result in less than 1% loss of SNR if the frequency switching rate is less than 20 Hz and correlation is inhibited for a full millisecond after each channel hop. The 32 Mhz clock used by the sampler is offset to compensate for the interferometer geometry.

The controller is a VME based system including custom boards and a 68020 CPU with a 68881 co-processor. It interfaces to the control computer, the S2 recorder, and the IF/BBC and the LO/Sampler assembly. The two flexible tone detectors reside on the data quality analysis board and the direct digital

synthesizers (DDS's) used to control phase and delay tracking are included on the timing functions board.

IV. Future Plans

What is the future of this design philosophy? The most effective area of expansion is in the direction of greater data and record rates. Currently the S2 recording system achieves a data rate of 128 Mb/s. Engineering tests indicate that the system will perform well at double the scan rate which would support a data rate of 256 Mb/s. The professional digital video industry must mature before greater rates can be achieved at reasonable cost. Both the D2 and DX machines achieve raw record rates of about 150 Mb/s. A stack of 8 of these could record at a rate in excess of 1 Gb/s.

I.F. Inputs	4 selectable 100-1000 MHz
# of Baseband Converters	1
Baseband Channelization	16 MHz USB 16 MHz LSB
Samplers	4-level 32 Ms/s USB 4-level 32 Ms/s LSB
LO Settling Time	< 1 ms
Delay Tracking Resolution	< 1/8 sample interval
Phase Tracking Resolution	< 1/32 cycle
Phase Calibration	2 flexible phase detectors
Total Record Rate	128 Mb/s

Table 1 - CGLBI D.A.T. Specifications

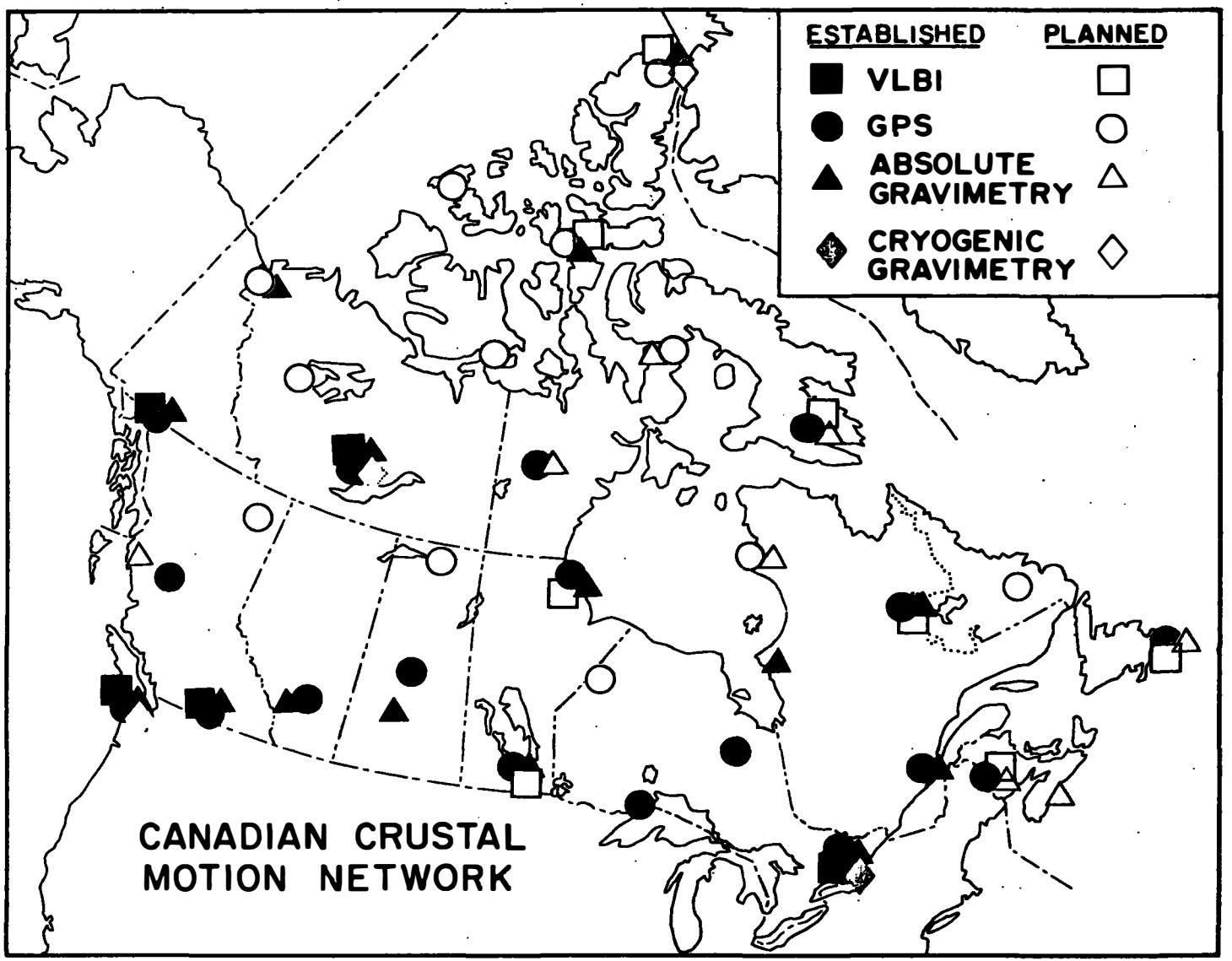

FIG 1: Canadian Crustal Motion Network

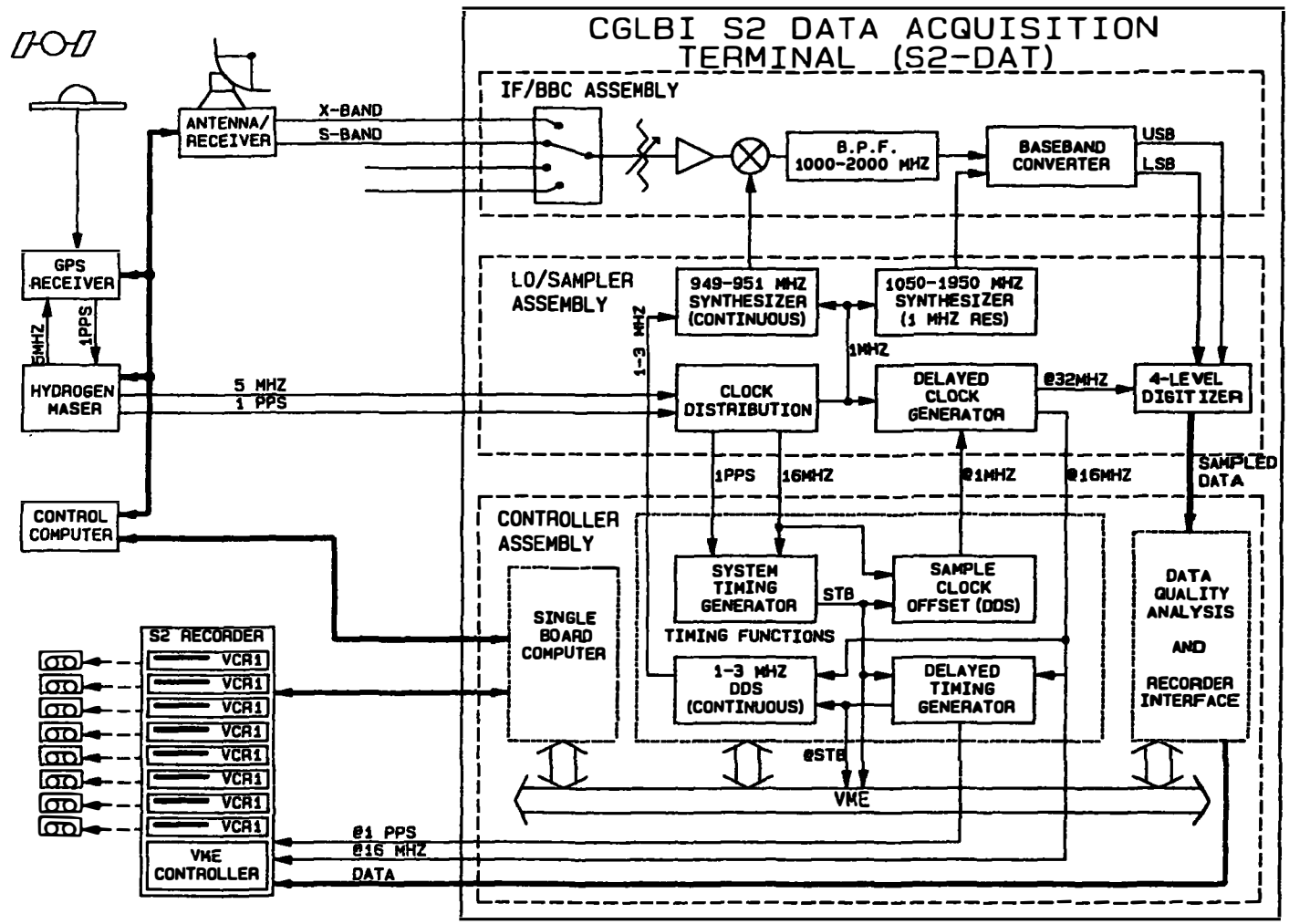

FIG 2: BLOCK DIAGRAM OF THE CGLBI S2 DATA ACQUISITION TERMINAL

Progress to Millimeter Accuracy VLBI: Synergism of Many Factors

T A Clark (Code 929.9, NASA/GSFC, Greenbelt, MD 20771, clark@tomcat.gsfc.nasa.gov)

Since the inception of geodetic VLBI in the late 1960's, its system accuracy has progressed at a rate of about on order-of-magnitude per decade. This progress has been achieved through parallel developments in a number of areas; this paper discusses the current state-of-the-art in geodetic VLBI as the synergistic interplay of all these factors:

- Improvements in instrumental sensitivity and stability;
- Improvements in calibration of instrumental biases;
- Improvements in the performance and reliability of high-stability frequency standards and time/frequency distribution hardware;
- Improvements in system reliability and station automation;
- Development of dedicated geodetic VLBI telescope facilities, correlators and operational networks;
- Improvements in theoretical models for the earth, its motion in space and relativistic effects;
- Development of new observing strategies designed to optimize recovery of both geodetic and "nuisance" parameters;
- Expansion and refinement of catalogs of "good" VLBI radio sources in both hemispheres;
- Development of stochastic parameter estimation techniques;
- Development of improved techniques for the calibration and estimation of atmospheric effects;
- Development of techniques for large "global" solutions encompassing many years of data;
- Intercomparisons between high accuracy geodetic techniques (VLBI, SLR, GPS) and intra-technique "friendly competition."

This paper illustrates the interdependence of these factors using more than 500,000 individual data points collected over the past decade by the NASA Crustal Dynamics Project (CDP) and the operational earth orientation networks. The current "best" VLBI performance is illustrated with data from the CDP's "R&D" experiments, which show repeatability of 1-2 mm horizontal, and 5-6 mm vertical. Finally, we prognosticate about the extension and improvement of performance (especially in the vertical) over the next few years to support measurements of post-glacial rebound, sea-level change, volcanology, earth orientation and plate tectonics.

NASA Crustal Dynamics Project Results: Sensitivity of Geodetic Results to Clock and Atmosphere Estimation Models

James W. Ryan and Chopo Ma
NASA/Goddard Space Flight Center

W.E. Himwich
Interferometrics Inc./NASA

ABSTRACT

Our VLBI analysis group has implemented a new, highly parametrized method to estimate residual clock and tropospheric refraction errors in geodetic VLBI data analysis. This method has replaced the sparsely parametrized polynomial method of the past and has many of the attributes of Kalman filters. We defined an objective measure of estimation performance and then carried out a comprehensive study to test the effectiveness of the new method compared to a method designed to mimic polynomial parametrization. We found no compelling evidence that the new method is more effective than the earlier method. Nonetheless, there are good reasons to continue to use the new method.

1. Background

The limiting error source for geodetic VLBI is mismodeling of tropospheric refraction (NASA, 1988). The NASA/Crustal Dynamics Projects (CDP) has vigorously investigated various methods of *a priori* calibration of the troposphere. In the past, much of this work was in the development of water vapor radiometers (WVRs) to measure the water vapor distribution over the observing sites. While the original specification for measuring the wet zenith path delay (<30 ps) has been met (Janssen, Elgered *et al.*), the WVRs have not been sufficiently accurate to eliminate the need to estimate tropospheric parameters in the data analysis and have had no significant impact on the accuracy achieved with geodetic VLBI (Kuehn *et al.*). The CDP has also pursued better methods to estimate tropospheric refraction effects in the data analysis. These methods have evolved, and an investigation of these methods and similar methods for clock error estimation is the subject of this paper.

From the beginning of geodetic VLBI in the late 1960s until the mid-1980s the techniques for modeling clock and atmosphere errors changed little. Clock errors were modeled with low order polynomials that were reinitialized at discontinuous clock jumps. Beginning in 1980 diurnal sinusoids of arbitrary amplitude and phase were also used. An analyst determined the appropriate form of the clock functions used for a particular session from an inspection of the post-fit delay residuals. The technique was time consuming, subjective, and without physical basis.

Atmosphere errors were initially estimated with one constant zenith path delay per station per session. This evolved into the use of a few (typically four per day) zenith path delays with uniform time intervals for each station. Later rates of change of zenith path delay within the time intervals were added and it became possible to maintain continuity in the zenith estimate as a function of time. Since the atmosphere errors appear in the post-fit residuals with an elevation dependence the analyst could not simply inspect the residuals to gain insight into how to set the parametrization. The exact form of the atmosphere parametrization was a subjective decision based on whether the analyst thought the data were fit to the level of the inherent noise.

Clock and atmosphere modeling changed considerably in the mid-1980s with the implementation of a Kalman filter by T.A. Herring (1990). The Kalman filter models the zenith path delay and clock errors at a station as

constantly changing stochastic functions characterized by their statistical properties, *i.e.*, the power laws of their evolution as functions of time. This was a breakthrough for many reasons. It provided a sound theoretical basis for the estimation model, produced dramatically better fits to the delay observations, and in practice appeared to generate more consistent geodetic results than the earlier techniques.

Our group at the Goddard Space Flight Center has implemented estimation methods in our data analysis that are direct decendents of the earlier polynomial methods but with many of the attributes of the Kalman filter. Our methods appear to produce results that are comparable to and are sometimes better than those produced by the Kalman filer. (See companion paper by Himwich *et al.* in this volume.) We make use of continuous, piecewise linear functions and constraints.

In an observing session our atmosphere estimation model for a given site is a function consisting of linear segments that join continuously. The initial zenith atmosphere delay is estimated without a constraint while the rate of change in each segment is constrained. The length of the linear segments is uniform for a given observing session and can range from 20 minutes to the duration of the session; we now use one hour intervals in routine processing. The rate constraint determines how quickly the model can respond to changes in atmospheric conditions that affect the zenith path delay. Our nominal constraint is 50 ps/hour, which is loose and corresponds to very turbulent weather conditions.

Our clock estimation model for each station is the sum of two functions. The first is a second order polynomial with three unconstrained parameters (clock epoch offset, frequency offset, and frequency drift) that is fit to all the data of the observing session. The second function is identical in form to the function used for the atmosphere model except that it has a value of 0 ps at the time of the first observation. The level of the constraint controls how quickly the clock model can respond to apparent changes in the clock behavior. We usually set the size of the constraint to a small multiple of the nominal Allan variance for hydrogen maser frequency standards in the 20 min to 1 hr integration interval, typically, $5*10^{-14}$. Given a real clock epoch jump, *i.e.*, discontinuous clock behavior, both functions are reinitialized; this occurs in only a few percent of the sessions.

2. The Problem

In the late 1980s nearly all VLBI groups adopted highly parametrized estimation methods after only limited testing. (JPL is a notable exception). As our contribution to this Chapman Conference we set out to investigate in a systematic and comprehensive way whether our new estimation methods are substantially better than the old methods. We did not investigate the effectiveness of the Kalman filter compared to the old methods, but our companion paper (Himwich *et al.*) compares results from our new methods with filter results.

3. What Is Better?

The first problem is to define "better" in a precise and useful way. Some possible definitions are:

"Better means more accurate." This would be the best test but is unusable since we do not know the true values.

"Better means smaller formal errors of the geodetic parameters." With least-squares parameter estimation techniques it is nearly always possible to make the formal errors smaller without necessarily improving the true uncertainties. This has some value but not much.

"Better means fitting the observations with smaller residuals." Adding more estimated parameters will nearly always produce better fits. This may be a necessary condition for a better method but is not sufficient to prove it is better.

"Better means more repeatable results, particularly for baseline lengths." This is the classic test of improvement in geodetic VLBI. As VLBI equipment and analysis techniques have progressed since the early days the time series of baseline lengths have become smoother. It is not a perfect test since we do not know at what level the real Earth will introduce variations into uniform baseline change. Nonetheless, we will use this criterion and define the repeatability of a baseline as the weighted rms scatter of individual baseline measurements about the line that fits the measurements over the time.

4. Model for Scaling of Baseline Length Error

Figure 1 is a plot of baseline length repeatability as a function of baseline length taken from our most recent CDP VLBI Annual Report (Caprette *et al.*). It shows the weighted rms scatter about constant linear evolution for baselines lengths. Since the principal parameter affecting repeatability is baseline length, we define an error scaling model of the form:

$$\text{error} = \text{floor} + \text{scale}*\text{length}$$

The floor is required because of fundamental noise-like errors independent of baseline length arising from the noise of the observations and from the non-rigidity of the telescopes. We fit the parameters to the data in Figure 1 to produce a VLBI error scaling model. Because of the form of the model, a few baselines at the longest lengths can dominate the scale and produce an unrepresentative result. To prevent this we have generated three models with different ranges of baseline lengths. We believe the model for the shortest range, 0-6000 km, best represents the current VLBI state-of-the-art because it encompasses nearly 80% of the baselines and nearly all baselines of tectonic interest. (Baselines nearly spanning the Earth have very little information about tectonic plate motions.)

Figure 1
Baseline Length Repeatability Versus Baseline Length

Full Range	4.9 mm + 2.6 ppb * length(mm)
0 to 9000 km	5.0 mm + 2.0 ppb * length(mm)
0 to 6000 km	6.8 mm + 1.1 ppb * length(mm)

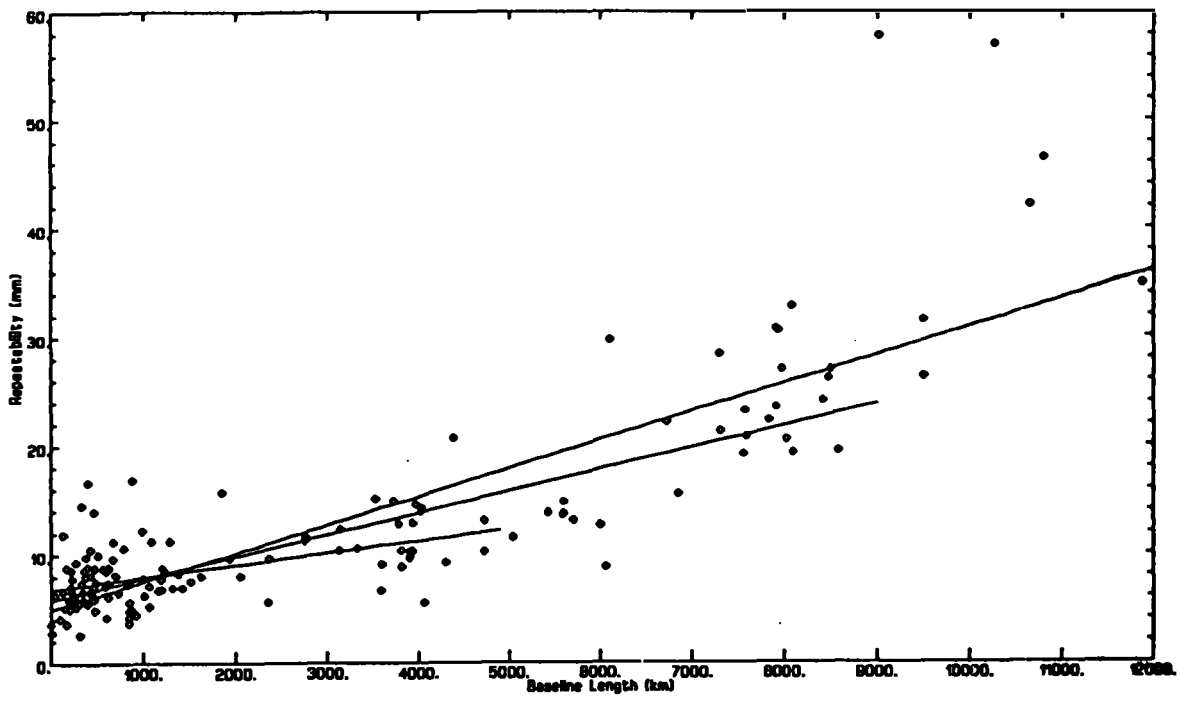

5. The Test Case

Testing of analysis methods in the past was largely anecdotal; only a small number and a limited class of observing sessions were analyzed. Our goal here was to produce a comprehensive test in which very many sessions of all types would be examined. We chose a data set including most of the Mark III geodetic data from 1979 to the end of 1989, the same set as that in our latest annual report (Caprette *et al.*). The set includes nearly all geodetic quality data acquired by NASA's CDP and the IRIS project. There are 1077 sessions with more than 485,000 observations and 402 baselines, of which 144 baselines had sufficient data to estimate baseline length repeatability. The types of sessions include IRIS earth rotation, mobile VLBI in the western US, Alaska, and Canada, and the full range of CDP fixed station networks. Because the set includes nearly all Mark III geodetic data it is perforce representative. (Since this data set is so large the most complicated test solutions discussed below required as much as two days of HP845 computer time to carry out.)

While our goal was to test the new parametrization methods against the polynomial parametrization methods of the past, this proved to be impossible to carry out in practice. The old clock method required that an analyst decide the exact form of the clock parametrization for each session, a practice that typically required a few hours per session. The analyst also specified the atmosphere parametrization. We abandoned this practice when we introduced the new methods. Consequently the most recent sessions could not be analyzed with the old methods without expending months of analyst time to determine the subjective parametrizations. We chose instead to compare highly parametrized solutions with solutions using the new methods but with only a few, very long intervals. We feel this mimics polynomial parametrization reasonably well. Except for the clock and atmosphere parameters being tested, all other aspects of these solutions were in our standard configuration as described in our most recent CDP annual report (Caprette *et al.*).

6. The Results for Atmospheric Parametrization

To test the effect of variation in the atmosphere interval we carried out a series of nine solutions. We uniformly parametrized the clocks with a 1-hour interval and set the clock and atmosphere constraints to their nominal values discussed above. The atmosphere intervals tested ranged from 20 minutes to one day. Table 1 shows the effect on the fit of the global solution, *i.e.*, the weighted rms post-fit delay residual for the nearly one-half million observations. The fit was 61 ps with a 1-day interval and decreased to 42 ps for a 20-min interval. The F-test, which compares the level of fit and the number of parameters estimated, showed that the introduction of new parameters was useful statistically until the transition from the 30-min to the 20-min interval. Based on post-fit residuals the highly parametrized estimates appear to be superior, but as discussed above this is not a very strong test.

The key test was to compare repeatability, *e.g.*, the baseline length error scaling plots, for the various solutions. We found that, except for the 1-day interval results, the plots were nearly indistinguishable. Table 2 shows the baseline error scaling laws from the set of solutions. To make the differences visible we also plot the differences between the repeatability values for the 20-min interval solution and the values from the other solutions in Figures 2.1 - 2.6. In each plot the horizontal scale is baseline length and the vertical scale is the repeatability difference for the 144 baselines used. Information that shows quantitatively which solution is better accompanies each plot. Consider Figure 2.6, which is a comparison of results from the 20-min and 1-day interval solutions. The 20-min solution had better length repeatability on 101 baselines while the 1-day solution was better for 40 baselines. For the remaining three baselines the repeatabilities were identical. The average repeatability was 8.9 mm for the 20-min solution and 10.1 mm for the 1-day solution. An inspection of the plot shows that for the short (<1000 km) baselines there is no trend, but beyond 1000 km the 20-min parametrization is clearly better. This is the only case where the new, highly parametrized solution is clearly better than the old, sparse parametrization. Consider Figure 2.5. The 6-hr solution actually had more baselines with better repeatability than the 20-min solution - 74 to 64. The average repeatability for 6 hours intervals was 9.0 mm, an insignificant difference from the 8.9 mm value for 20 minute intervals. In summary, while the highly parametrized solutions have much smaller post-fit delay residuals than the sparsely parametrized solutions, we have been unable to show

that the geodetic results are better. One zenith atmosphere delay and rate per station per day is clearly inferior, but that level of parametrization would not have been used even as recently as the mid-1980s.

Table 1
Global Weighted RMS Delay Fits
1100 Session SOLVE/GLOBL Solution

Atmosphere Interval (min)	Delay Fit (ps)	Reduced χ^2	Added Atm. Noise* (ps)
20	41.9	0.91	--
30	41.9	0.91	2.9
60	44.0	0.97	13.7
120	45.4	1.01	18.7
180	46.7	1.06	20.8
240	47.8	1.09	23.1
360	49.6	1.16	26.7
480	51.6	1.24	30.2
1440	61.0	1.70	44.4

*The added atm. noise value is computed based on the assumption that the '20-min interval' values reflect removing all atmospheric noise.

Table 2
Baseline Length Error Scaling Models
Atmosphere Interval Tests
0-6000 km Baselines

Atmosphere Interval (min.)	Floor (mm)	Scale (ppb)
20	7.0	1.0
30	7.1	1.0
60	7.0	1.1
120	7.0	1.0
180	6.9	1.0
240	6.9	1.0
360	6.7	1.1
480	6.8	1.2
1440	6.6	1.8

In an attempt to probe this unexpected result further we divided the baselines into two sets: mobile baselines (those involving at least one mobile VLBI site), and fixed baselines (those involving only fixed stations). We did this because the character of mobile data is quite different from that of fixed stations. Compared to fixed stations, mobile systems are less sensitive (produce observations of lower SNR), have very poor low elevation coverage, and are generally used to measure short baselines, where some common mode error rejection occurs. We used the 20-min and 6-hr solutions in this test. For the mobile baselines we found that the 6-hr parametrization produced better results in a ratio of 44 to 26, but the average repeatability was identical - 6.8 mm. For the fixed station baselines the comparison showed the 20-min parametrization produced better results in a ratio of 38 to 30. The average repeatability was 9.3 and 9.4 mm for 20 min and 6 hr, respectively. Thus, for baselines with relatively poor data, *i.e.*, the mobile baselines, the increased parametrization actually produced poorer results than the sparse. For baselines with strong data the increased parametrization produced marginally better results.

We also investigated halving the constraint value to 25 ps/hour and doubling it to 100 ps/hour. We found no difference in the average length repeatability at a level <1 mm, but the tighter constraint did produce better results when simply counting which parametrization produced the greatest number baselines with the best repeatability.

The primary goal of the CDP when it was established in 1980 was to measure contemporary plate motion rates. In terms of VLBI measurements the single most important type of information used to determine plate motion rates is baseline length rate. With this in mind we tabulated the effect of changing the atmosphere estimation interval on the baseline rates inferred from the time series of lengths. For all the intervals discussed above the rates agreed on average to better than one formal sigma, even when comparing the 20-min solution to the 1-day solution. When comparing parametrizations of 6 hours or less the agreement was on average 0.6 sigma or less. Since these sigmas are in general optimistic estimates of the true uncertainties the atmosphere parametrization interval has no significant effect on tectonic rates inferred from these data.

7. The Results for Clock Parametrization

To test the effect of varying the clock parametrization interval we made solutions with the clock interval set to 30, 60, 120 and 180 minutes while keeping a constant one hour atmosphere interval. We found that changing the clock parametrization interval had almost no effect on the baseline error scaling models. Table 3 shows the baseline length error scaling models for the 0-6000 km range. The average length repeatabilities were 8.9, 8.8, 8.7, and 8.8 mm for the 30, 60, 120, and 180-min interval solutions. These are insignificant differences. Compared to the 30-minute solution the other solutions all produced larger numbers of baselines with better repeatability, typically in a ratio of 80 baselines to 60. The 120-min solution was better than the 180-min solution by 65 to 62 baselines. In any case the results on average are quite insensitive to the clock interval in the range we tested.

We also tested varying the clock constraint. The standard clock constraint is $5*10^{-14}$ sec/sec. We ran solutions with the constraint set to $2.5*10^{-14}$ and $10*10^{-14}$ sec/sec. The three solutions produced the same length error scaling model in the 0-6000 km range and the identical average repeatability considering all baselines. Considering the three solutions and the full set of 144 baselines the repeatability differences were never greater than 1.0 mm and on average were less than 0.2 mm. The sensitivity to the clock constraint is very, very low.

Table 3
Baseline Length Error Scaling Models
Clock Interval Tests
0-6000 km Baselines

Clock Interval (min.)	Floor (mm)	Scale (ppb)
30	7.4	0.9
60	7.0	1.0
120	7.1	1.0
180	7.1	1.0

8. Summary

We set out to test whether our new, highly parametrized clock and atmosphere estimations methods were better than the old *ad hoc* methods. (In our own minds we set out to demonstrate the efficacy of these new methods.) Based on the criterion we chose, improved baseline length repeatability, the new methods did not consistently and significantly produce better results. There is evidence that for fixed stations the highly parametrized atmosphere estimations provide marginally better results than sparsely parametrized estimations. For mobile

baselines the result is just the opposite. For the clock parametrization, we found that there was very little sensitivity to the interval size within the range of intervals we tested. When we test varying clock and atmosphere constraints we found that the results were very insensitive to the level of constraints (within the range of reasonable constraints). In short we were unable to demonstrate that the new methods are conclusively better than the old.

These results should not be interpreted to mean that the new methods should be abandoned. There is much to be said for them: 1) They consistently produce post-fit delay residuals at or near the level of inherent random noise in the observations. (With the old methods the delay residuals were consistently dominated by short term systematic effects.) The residuals are then useful as a powerful diagnostic of station performance. 2) The polynomial parametrization method required that a large *ad hoc* variance be added to the observation variances so that the solution would have reduced χ^2 of 1. This size of the additional variance is greatly reduced with the new method. 3) The new method appears to produce more realistic formal errors. 4) A comparison of the estimated atmosphere values from the new method with results from water vapor radiometers consistently shows good agreement both in the overall level of the 'wet' delay and in its temporal behavior. 5) The new method eliminates the need for subjective parametrization by an analyst and typically saves one half to one day of analyst time per session.

When comparing the solutions with 20-min and 6-hr atmosphere parametrizations the fixed station baselines were marginally better with the higher parametrization and the mobile baselines were marginally better with the sparse parametrization. This seems to indicate that the highly parametrized solutions simply have too many degrees of freedom when the data quality is relatively poor (the mobile baselines). A goal for future research into parametrization methods is to understand how to tailor the number of degrees of freedom allowed in the estimation to the information content of the VLBI observations.

References:

Caprette, D.S., et. al., Crustal Dynamics Project data analysis--1990: VLBI geodetic results 1979-1989, NASA TM-100765, December 1990.

Elgered G., et. al., Geodesy by radio interferometry: water vapor radiometry for estimation of the wet delay, JGR, Vol. 96, No. B4, pp 6541-6555, April 10, 1991

Herring, T.A., et. al., Geodesy by radio interferometry: The applications of kalman filtering to the analysis of very long baseline interferometry, JGR Vol. 95, No.B8, pp 12561-12581, August 10, 1990.

Janssen, M.A., A new instrument for the determination of radio path delay due to atmospheric water vapor, IEEE Transactions on Geoscience and Remote Sensing, Vol. GE-23, No. 4, July, 1985.

Kuehn, C.E, W.E. Himwich, T.A. Clark, and C. Ma, An elvaluation of water vapor radiometer data for calibration of the wet path delay in VLBI experiments, Radio Science, in press 1991.

NASA, Geodynamics program summary report: 1979-1987, NASA Tech. Memo. 4065, Office of Space Science and Applications, Washington, D.C., 114 pp, 1988.

Consistency of Geodetic Information From Kalman Filtering and Batch Least-Squares

W. E. HIMWICH, D. S. MACMILLAN

Interferometrics Inc.

T. A. HERRING

Massachusetts Institute of Technology

C. MA, J. W. RYAN

Laboratory for Terrestrial Physics, NASA/GSFC

The analysis of geodetic VLBI data originally used a least-squares technique with only deterministic parameters. An implementation of this approach was developed in the SOLVE program at Goddard. In the 1980s, a Kalman filter analysis program, SOLVK, was developed at the Center for Astrophysics. Initially, filtering produced significantly better results than deterministic least-squares, as measured by baseline repeatability. This improvement was due primarily to the filter's ability to model short term clock and atmospheric variations. Subsequently, SOLVE was enhanced to include more sophisticated models. Although these models allow less variation than the stochastic processes used by the Kalman filter, they produce comparable results. The scaling law for the baseline repeatability for SOLVE is 4.7 mm + 2.3 ppb. For SOLVK the scaling law is 6.8 mm + 2.4 ppb. For the Westford-Ft.Davis baseline (3000 km), measured by more than 500 sessions, the overall repeatabilities relative to the smoothed length is 8.4±0.3 mm for both systems. However, for individual years of data there is less agreement in the repeatability. The baseline rates generally agree at the one sigma level. The differences in baseline repeatabilities and rates are probably due to differences in the data editing and different sensitivities to mismodeled and unmodeled effects. The availability of two independent estimation systems of comparable quality provides a valuable ability to cross check results. Exploring the remaining differences between the systems will improve our understanding of VLBI data analysis.

I. INTRODUCTION

The analysis of Mark III VLBI data has traditionally used least-squares estimation to determine geodetic and astrometric parameters of interest [*Clark et al.*, 1985]. This approach allows for the estimation and removal of nuisance effects, in particular, timing system and tropospheric delay variations. Historically, these effects were estimated using low-order polynomials to represent timing variations and a few zenith tropospheric delay parameters for each station in each experiment. This technique left a large amount of unmodeled systematic variation in the residuals. In an attempt to represent the effects of this unmodeled variation, a white noise component was added in quadrature to the *a priori* data weights to make the reduced χ^2 nearly unity. The SOLVE program developed at Goddard was an implementation of this approach.

In the 1980s, a Kalman filter, known as SOLVK, was developed for processing Mark III VLBI data [*Herring et al.*, 1990]. The filter approach uses stochastic processes to model the tropospheric and timing effects. Short term variations in these effects can be dynamically tracked by the filter because of the density of the VLBI observations and because the tropospheric delay has an elevation dependence that the timing variation does not. The results from SOLVK initially demonstrated a significant improvement in baseline repeatability over the traditional low-order polynomial approach used by SOLVE.

SOLVE was extended in the latter half of the 1980s to use a continuous model made of piecewise linear segments to represent the variations in the tropospheric delays and timing systems. Normally, segment lengths of about one hour are used. The adjustments of the piecewise segments are constrained by the application of pseudo-observations that reflect the approximate variation expected in the parameters. Using this approach the amount of white noise that must be added to make the reduced χ^2 close to unity is reduced significantly.

In the limiting case when the segment lengths are equal to the time between observations, this approach can be used to represent the simple stochastic processes used by SOLVK. Implementing a stochastic process in this way would be inappropriate because of the large amount of computation involved. However, for the typical segment lengths of one hour, the computational burden is much less than for SOLVK. The piecewise linear model approximates the true stochastic model and is sometimes referred to as a 'pseudo-stochastic' model.

The addition of pseudo-stochastic parameters to SOLVE addressed two of the major problems with polynomial parameterization: determining the "appropriate" order and boundaries for the polynomials and changing standards of what "appropriate" is [*Herring et al.*, 1990]. Using pseudo-stochastic clocks and atmospheres, the analyst makes relatively few subjective deci-

sions. The only boundaries that must be determined are for large clock breaks, which are fairly rare and unambiguous. Occasionally, the analyst may choose to loosen the model by weakening the constraint or shortening the parameterization interval because a clock or atmosphere is noisier than usual. Studies [*Ma et al.*, 1990 and *Ryan et al.*, 1991] indicate that variations of the adjustable features of this parameterization have relatively little effect on the results. In addition, the newer analysis scheme is more automated and allows the data to be reprocessed using a uniform treatment. Processing with SOLVE and SOLVK are now comparably objective.

The remainder of this paper discusses a comparison between the baseline repeatability from SOLVE and SOLVK.

II. Comparison Solutions

To assess the relative performance of SOLVE and SOLVK we compared the repeatability of the 139 most frequently measured Mark III baselines. The baseline lengths were estimated individually for each experiment. The set of lengths from all the experiments were fit to an offset and slope for each baseline. The weighted root-mean-square scatter of the residuals about the lines was calculated and compared. These solutions used the bulk of geodetic Mark III VLBI data available at the time, including 1159 observing sessions of IRIS, CDP fixed, CDP mobile, and NAVNET data, with about 600,000 Mark III VLBI observations.

The SOLVE solution used the standard SOLVE set-up. The vast majority of the atmosphere and clock models used one-hour linear segments. The atmosphere constraint level was typically set to 50 picoseconds/hour. The clock constraint level was set to five parts in 10^{14}. A few of the atmosphere and clock models used a shorter parameterization interval or weaker constraints. The baseline lengths were estimated from the group delays only.

The SOLVK solution used the standard SOLVK processing. The phase delay rates were used to estimate the power spectral density (PSD) of a white noise process driving an atmospheric random walk process for each station in each experiment. Typically, the PSD estimates were less than 0.75 ps^2/sec. These PSD estimates were used in the random walk model for the atmospheric variation in the group delay solution. Timing system variations were modeled using a combination of random walk and integrated walk models to give a variation of about one part in 10^{14} at 50 minutes. The baseline lengths were estimated from the group delays.

Both the SOLVE and SOLVK systems used the Chao wet mapping function to estimate the wet troposphere delay. This capability was recently added to SOLVE [*Kuehn et al.*, 1991].

The constraints used by SOLVE are heuristically related to those used by SOLVK. For the atmosphere model, the PSD of 0.75 ps^2/sec for a white noise process driving a random walk integrates to a sigma of about 50 ps at one hour, which is the value used by SOLVE. Since the PSD used by SOLVK is generally less than 0.75 ps^2/sec, the constraint used by SOLVE corresponds to a relatively loose constraint in SOLVK. For the clock model, SOLVE uses of 5 parts in 10^{14} at one hour which is also comparatively looser than SOLVK's 1 part in 10^{14} at 50 minutes.

Although the constraints levels used by the two programs are related, they cannot be directly compared. SOLVE specifies the constraint as a linear rate over a period of time. SOLVK specifies the constraint in terms of a random walk and integrated random walk. The spectral content of the two systems is different, particularly on time scales shorter than the segments lengths used by SOLVE.

A study of SOLVK [*Herring et al.*, 1990] and the previously cited studies of SOLVE [*Ma et al.*, 1990 and *Ryan et al.*, 1991] show that the results for both approaches are fairly insensitive to the actual levels of the constraints used. This is consistent with a calculation of the constraint 'share' in SOLVE using [*Theil*, 1963]. This calculation indicates that the constraints typically contribute less than a third of the final precision of the clock and atmosphere parameters. In SOLVE the primary role of the constraints is to prevent the solution from being indeterminate because of data gaps. For SOLVE the results are also fairly insensitive to the atmosphere and clock parameterization intervals [*Ryan et al.*, 1991].

III. Results

The results of the comparison are presented in Figure 1. The weighted root-mean-square (RMS) length repeatability averaged over all the baselines is 11.6 mm for SOLVE and 12.0 mm for SOLVK. SOLVE produced better repeatability for 112 baselines. SOLVK produced better repeatability for 25 baselines. For two baselines the repeatabilities were identical between the two systems.

The results show that SOLVE produced more repeatable results for most baselines. For SOLVE, an overall scaling law for the repeatabilities as a function of baseline length is 4.7 mm + 2.3 ppb. For SOLVK, the scaling law is 6.8 mm + 2.4 ppb. The difference in the repeatabilities is a small fraction of the repeatability itself. For example, from the scaling law for SOLVE, the repeatability for a baseline of 5000 km is 16.2 mm; for SOLVK the corresponding repeatability is 18.8 mm. The difference is about 15%.

The Ft. Davis-Westford baseline was examined in more detail. This baseline (3000 km) is one of the most frequently measured. Approximately 70 measurements a year, mostly by the IRIS program, have been made since 1984. Our solutions included over 500 determinations of the length. The lengths were smoothed with a 30 day box-car and the residuals to the smooth lengths were calculated. For both SOLVE and SOLVK, the overall repeatability (weighted RMS residual) was 8.4±0.3 mm. Table 1 gives the repeatabilities by year for the two systems calculated with a 50 day box-car. For the more recent data, 1987-1989, the repeatabilities are comparable, differing by only a few tenths of a millimeter. For the earliest data, 1981-1983, SOLVE produces better repeatability, For the intervening years, 1984-1986, SOLVK produces better repeatability.

A histogram of the baseline rate differences for the 139 baselines binned by one-half of the sigma of the determination is shown in Figure 2. Typically, the rates differ by one sigma or less. There is a slight bias in the results such that the rates from SOLVK are slightly more positive.

IV. Discussion

The difference in the repeatability between SOLVE and SOLVK can probably be attributed to three causes: differences in data editing, differences in the modeling of the atmospheric and clock

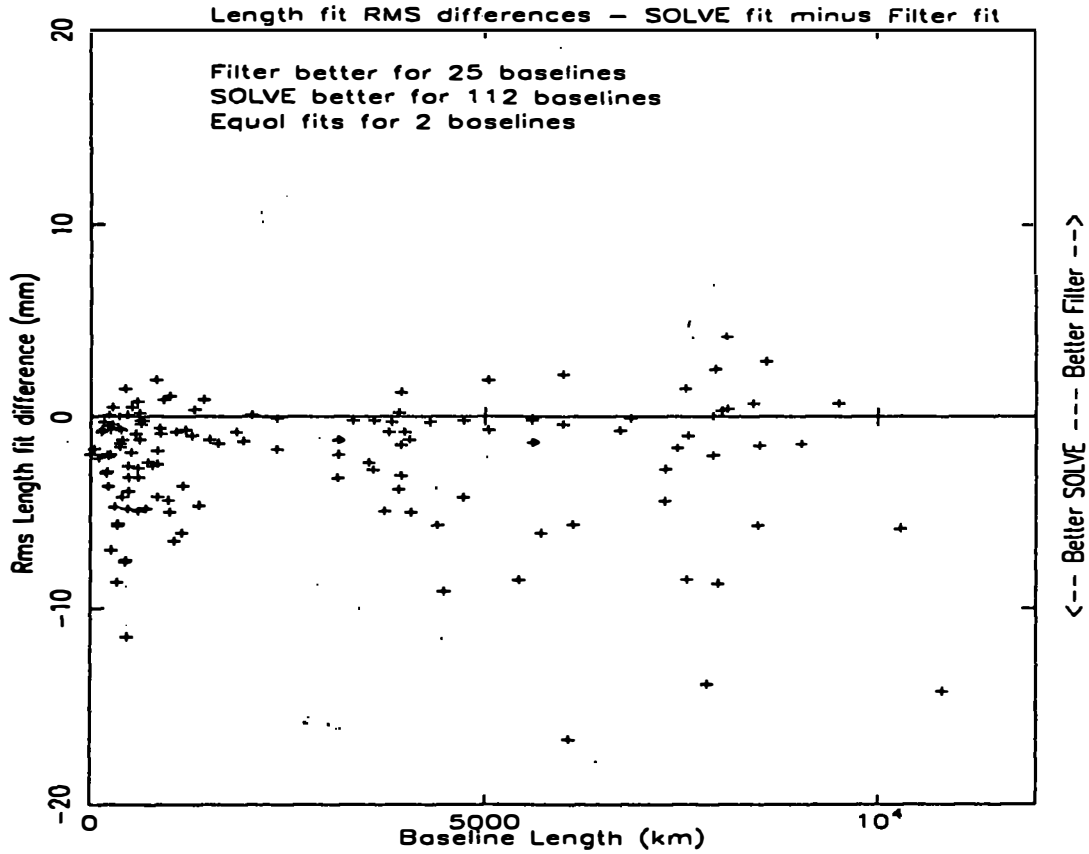

Figure 1. Plot of the baseline length repeatability differences, SOLVE minus SOLVK (Filter), by baseline length.

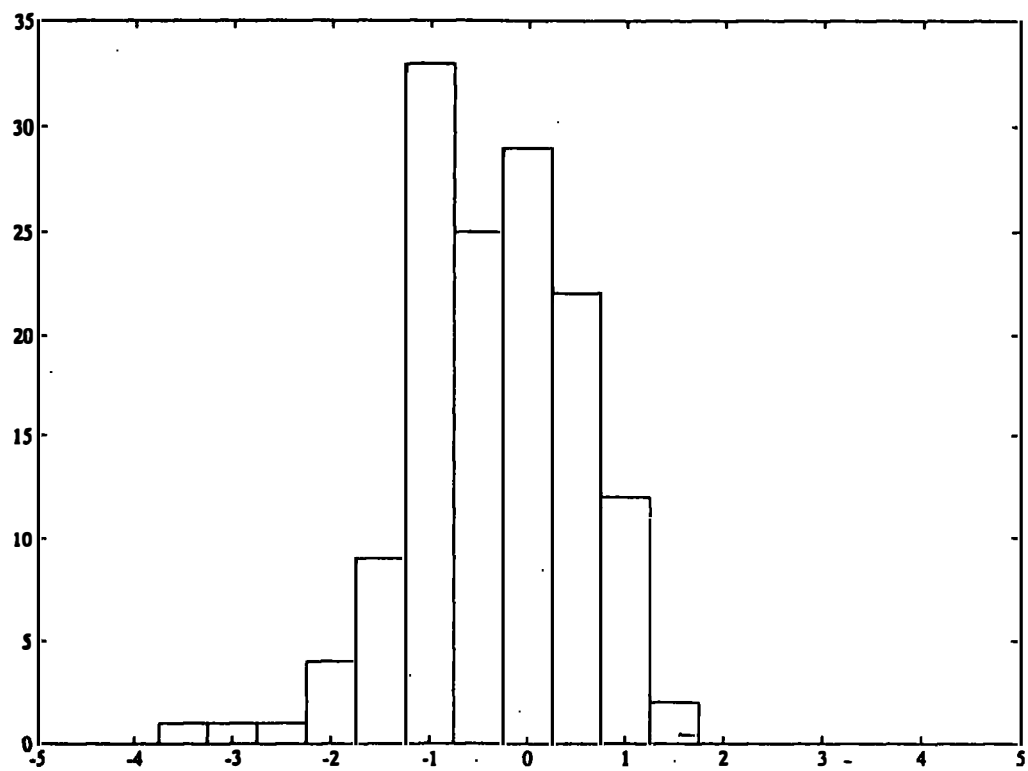

Figure 2. Histogram of baseline rate differences, SOLVE minus SOLVK. The rate differences are normalized by the sigma of the rate determination. One-half sigma bins are used.

Table 1. Ft. Davis-Westford Baseline Repeatability. The weighted root-mean-square of the residuals binned by year relative to a smoothed mean calculated with a 50 day boxcar.

Year	SOLVE	SOLVK
1981	16.8	17.9
1982	16.6	18.1
1983	9.9	11.2
1984	13.0	11.3
1985	9.6	8.8
1986	10.8	8.7
1987	9.8	9.4
1988	6.5	6.3
1989	4.8	5.1

effects, and differing sensitivities to other unmodeled effects. The relative importance of these effects is unclear at this time. It seems likely that data editing may play the most significant role.

Data editing is handled differently by the two systems. Use of data in SOLVE at Goddard always includes some human examination. Some outliers are removed manually and clock breaks epochs must be set. As a result, all data placed into large solutions at Goddard are looked at in some detail to see if they are reasonable. Typically, the data are edited to three times the fit scatter. The level of data editing depends on the particular analyst.

Data used by SOLVK may not be examined in detail. SOLVK includes a capability to automatically edit to some multiple of the data sigma, typically four times. Normally clock breaks are determined automatically. If the fit of an experiment indicates a problem may be present, it is examined in more detail for clock break and editing problems.

Both systems use statistically inappropriate editing criteria. A better criteria would take into account the effects of the estimated parameters on the distribution of the residuals. Neither SOLVE nor SOLVK account for this, although it may significantly effect the expected scattered of the residuals. This is true especially for low elevation observations which tend to contribute a disproportionately greater share of the information to the solution. Additionally, SOLVE does not take into account the individual data weights in the editing process. However, this error is ameliorated to some extent by the use of the white noise components, which tend to make the effective data weights more uniform for SOLVE.

The problem of data editing directly affected the development of the comparison data set. The editing of SOLVE is not sufficient for use in SOLVK, nor is SOLVK's editing sufficient for use in SOLVE. The primary problem is that depending on the details of the estimated parameters and the data distribution, both systems, generally in different situations, have enough freedom to absorb outliers. A point that is not an outlier for SOLVE may be one for SOLVK and vice-versa.

The effects of the data distribution and model geometry on the residual distribution can be calculated [for example, see equation 12.38 in *Vanicek and Krakiwsky*, 1986]. Using the residual distribution to determine whether data are true outliers may lead to more consistent data editing. Using the residual distribution may also make it possible to identify whether some points violate the model assumptions significantly. This may be useful for identifying and investigating modeling problems, such as mapping function errors at low elevations.

Besides data editing problems, mismodeling due to errors in the clock and atmosphere models may contribute to the differences in repeatability between SOLVE and SOLVK. The models used for the atmospheres and clocks by the two systems are different in their details. Both systems allow systematic behavior on time scales of an hour or more to be modeled. However, SOLVE has no provision to model variations on time periods shorter than the model segment lengths. These variations show up as colored noise. SOLVK on the other hand can model shorter term variations.

A second difference in the models is the variation allowed in the models. SOLVE effectively enforces a linear change in each model segment. SOLVK make no such requirement. Instead, SOLVK recovers, to some accuracy, a variation with the spectral content specified by the model. The model used by SOLVK is probably a more accurate representation of the physics, particularly on short times scales, than SOLVE's. However, even the model used by SOLVK is not perfect. The errors in the models used by both system contribute some error to the results. However, considering the insensitivity of the results to variations in the model parameters, it is probably a fairly small effect.

SOLVK's model is theoretically more elegant than SOLVE's. SOLVE permits rate changes only at the points where the linear segments meet. As already mentioned, SOLVK potentially represents the statistics of the clock and atmosphere variations more realistically than SOLVE. However, as shown by the slightly better repeatability of baselines from SOLVE, this theoretical superiority would appear not to be a significant advantage compared to other considerations.

Unmodeled effects may also contribute to the difference in the repeatabilities. The stochastic models used by SOLVK tend to distribute unmodeled effects differently than the more deterministic model used by SOLVE. As an example, antenna deformation, which is not explicitly modeled at this time, is likely to have different consequences for the two systems.

The differences in the repeatabilities by year for the Ft. Davis-Westford baseline are intriguing. It is interesting that the repeatabilities agree well in the latter years, 1987-1989, when the data are better and include more low elevation observations. The earlier years, 1981-1983, when SOLVE has better repeatability, are dominated by the single baseline POLARIS experiments. The period from 1984-1986 where SOLVK has better repeatability corresponds to the years when the 'Ft. Davis anomaly' went through its largest excursion and are also the initial years of the multi-baseline IRIS program. These differences are only intriguing now, although understanding them, if they are significant, may lead to a better understanding of the differences between SOLVE and SOLVK and perhaps the Ft. Davis anomaly as well.

The slight apparent bias in the baseline rates that appear in Figure 2 suggests that there is a small difference in the models used by the two systems, most likely in the atmosphere models. In particular, it is known that the baseline rates are sensitive to errors in the mapping function because of changes in the elevation coverage of the data [*Kuehn et al.*, 1991]. There may be some remaining discrepancy in the models used by SOLVE and SOLVK.

V. Conclusions

We have compared the baseline repeatabilities and rates derived from SOLVE and SOLVK solutions for many Mark III VLBI baselines. SOLVK uses stochastic parameters to model clock and atmosphere variations. SOLVE uses a more deterministic model that includes a pseudo-stochastic model for these variations. The baseline repeatabilities for the two techniques are very comparable, although generally SOLVE performs slightly better than SOLVK. The primary cause of the differences in the repeatabilities is most likely to be due to the data editing. To a lesser extent, mismodeling of the atmosphere and clocks and other unmodeled effects probably contribute. Since both systems provide good results they provide a valuable cross check for each other. The low level at which the two systems disagree shows that the differences in approach have relatively small consequences. Further work will be necessary to improve the consistency of the editing. Investigating the remaining differences in the baseline repeatabilities will improve our understanding of VLBI data.

References

Clark, T.A., Corey, B.E., Davis, J.L., Elgered, G., Herring, T.A., Hinteregger, H.F., Knight, C.A., Levine, J.I., Lundqvist, G.L., Ma, C., Nesman, E.F., Phillips, R.B., Rogers, A.E.E., Ronnang, B.O., Ryan, J.W., Schupler, B.R., Shaffer, D.B., Shapiro, I.I., Vandenberg, N.R., Webber, J.C., Whitney, A.R., Precision Geodesy Using the Mark-III Very-Long-Baseline Interferometer System, *IEEE Trans. Geosc. Remote Sensing, GE-23,* 438, 1985.

Herring, T.A., Davis, J.L., Shapiro, I.I, Geodesy by Radio Interferometry: The Application of Kalman Filtering to the Analysis of Very Long Baseline Interferometry Data, *J. Geophys. Res.*, 95(B8), 12561-12582, 1990

Kuehn, C.E., MacMillan, D.S., Ray, J.R., Sensitivity of Geodetic Parameter Estimates to the Assumed Distribution of the "Wet" Troposphere, *this volume, 1991.*

Ma, C., Sauber, J., Bell, L., Clark, T., Gordon, D., Himwich, W., Ryan, J., Measurement of Horizontal Motions in Alaska Using Very Long Baseline Interferometry, *J. Geophys. Res.*, 95(B13), 21991-22011, 1990

Ryan, J.W., Ma, C., Himwich, W.E., NASA Crustal Dynamics Project VLBI Results: Sensitivity of Geodetic Information to Clock and Atmosphere Estimation Models, *this volume*, 1991.

Theil, H. On the use of Incomplete Prior Information in Regression Analysis, *Amer. Stat. Ass. J.*, 58(302), 401-414, 1963.

Vanicek and Krakiwsky, Geodesy: The Concepts, North-Holland, Amsterdam, 1986

W. E. Himwich and D. S. MacMillan, Interferometrics Inc., Suite 1400, 8150 Leesburg Pike, Vienna, VA 22182.

T. A. Herring, Massachusetts Institute of Technology, 54-618, Cambridge, MA 02139.

C. Ma and J. W. Ryan, Laboratory for Terrestrial Physics, Code 926.9, NASA/Goddard Space Flight Center, Greenbelt, MD 20771.

Atmospheric Loading Effect on VLBI Observations

Seiji Manabe, Tadahiro Sato, Satoshi Sakai and Koichi Yokoyama

Division of Earth Rotation
National Astronomical Observatory
Hoshigaoka-cho, Mizusawa-shi, Iwate-ken 023 Japan

Abstract

We compute vertical displacements at most of the fixed VLBI stations by convolving the atmospheric surface pressure given by the Japanese Meteorological Agency Global Objective Analysis data and the load love numbers all over the earth. The vertical displacements even under the inverted barometer model are as large as 40mm at continental stations in extreme meteorological conditions. Analytic approximate formulae specific to individual stations are derived. The post-fit residuals are smaller than 1mm in the inverted barometer case and about 1.6mm in the non-inverted barometer case. The vertical displacements are compared with those determined with VLBI. It is found that the atmospheric loading is not a major source of variations of the observed vertical displacements.

I. Introduction

The earth's atmosphere loads the surfaces of the solid earth and oceans and depresses the solid earth vertically. It also produces a horizontal displacement because of the lateral inhomogeneity of the surface pressure distribution of the loading atmosphere although it is expected to be much smaller than the vertical displacement. This loading effect is not negligibly small if we require centimeter accuracy to a geodetic position measurement. In fact, the vertical position difference between the high and low extremities is as large as a few centimeters at continental stations.

Another important loading source is the tidal change of the sea level. It has computationally similar characteristics as those of the atmospheric load. Both of them depend on location of a point where the loading displacement is computed and need global integration of the loading effect over the whole earth's surface. The loading distribution is given by a global meteorological data such as the GANL(Global objective Analysis) data provided by the Japanese Meteorological Agency(JMA) in the case of the atmospheric loading, while tidal maps such as Schwiderski's(1980) are used in the case of the ocean tide. However, there is an important difference between the two loading problems. The tidal loading is purely periodic and needs to compute only amplitudes and phases of some major tidal constituents. On the other hand the atmospheric loading is not purely periodic but has wide continuous spectra. It is necessary to perform integration at each epoch when we want to know the displacement. This may be the major reason that there have been only few attempts to compute the displacement due to the atmospheric loading. Van Dam and Wahr(1987)

computed the atmospheric loading displacements at Westford and Onsala in one year by using a global meteorological data and found good correlations between the computed displacements and the baseline length changes.

An important aspect of the correction of the atmospheric loading displacement is that we often need an approximate formula analytically expressed in terms of local surface pressure at an observing site. Presently most of data analysts do not have a convenient access to global meteorological data and cannot perform the global integration. More important reason is that the present time resolution of the global meteorological data is only 12 hours despite the atmospheric pressure changes more rapidly.

In this paper we compute the vertical displacements due to the atmospheric loading at 31 VLBI stations for the period from 1984 to 1990 and derive analytic approximations that have the accuracy of 1mm.

II. Global meteorological data and method of computation

The basic method of computation is similar to that used for computing displacements due to the ocean tides. We adopt the same integration method developed by Sato and Hanada(1984) and use the GANL data provided by the JMA as basic global meteorological data. Characteristics of the GANL data are summarized in table 1.

Table 1. Characteristics of the GANL data.

Period	Mesh size (degrees)	Pressure level (mb)	interval (hours)
- 1987/6	2.5×2.5	1000,850,700,500,400,300,250,...	24
1987/7 - 1988/2	2.5×2.5	850,700,500,400,300,250,...	12
1988/3 -	1.875×1.875	1000,850,700,500,400,300,250,...	12

We first compute surface pressure at the mesh points on the land by taking into account the surface topography of the earth. The topography data originally given at 30'×30' mesh points are interpolated at the mesh points of the GANL. We compute pressure on the GANL mesh points by interpolating the heights of the pressure level surfaces. Since the GANL mesh is not fine enough to compute precisely the loading pressure near an observing site, we interpolate the GANL data at the topography mesh points to compute the loading in the region within 18.°75 from the observing site. The distribution of the surface pressure strongly reflects topography variation. It almost looks like a world topography map.

The surface pressure at the mesh points on the oceans is computed with the inverted barometer model. In this model the surface pressure at the individual mesh points over the oceans is replaced by common pressure averaged all over the oceans.

In order to compute the vertical displacement the surface pressure is converted to loading surface mass density with the relation:

$$m = \frac{p}{g}, \tag{1}$$

where g is the surface gravity. The convolution of surface mass density with the load love number K all over the earth's surface gives the vertical displacement u as:

$$u(\phi,\lambda) = \int_0^{2\pi}\int_{-\pi/2}^{\pi/2} m(\phi',\lambda')K(\theta)d\lambda' d\phi' , \tag{2}$$

where (λ,ϕ) and (λ',ϕ') are longitudes and latitudes of an observing site and a loading point, and θ is angular distance between these two points. We use Farrell's(1972) load love numbers as K. Detailed procedure to perform the above integration is given in Sato and Hanada(1984).

II. Accuracy of the GANL data

Before performing the integration given by equation (2) we have to examine how closely the interpolated surface pressure follows the actual pressure variation observed during VLBI observations. Figure 1 shows the pressure variation at Richmond in February, 1990. During this period an intensive burst observation campaign was conducted and almost continuous data spanning 11 days were obtained. The general trend of the GANL pressure closely follows the observed pressure. This means that the GANL data is usable at least for computing inter-day variation of the vertical positions.

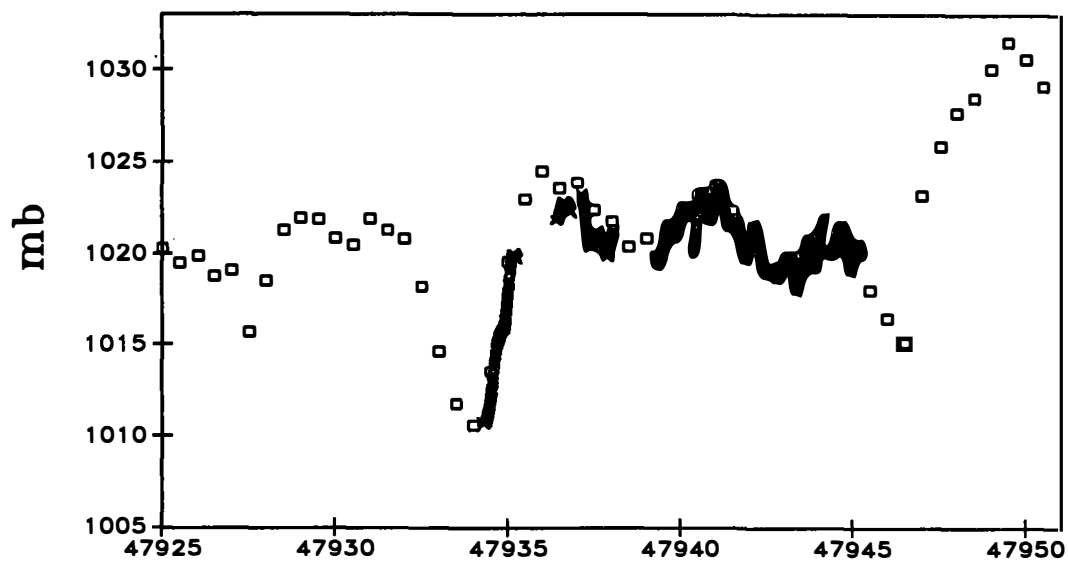

Figure 1. Variation of the surface pressure at Richmond. The squares are the spatially interpolated values from the GANL data at every 12 hours. The thick lines are the observed pressure. The abscissa is Julian day - 2400000.

Figure 2 shows differences of the observed pressure from the interpolated GANL

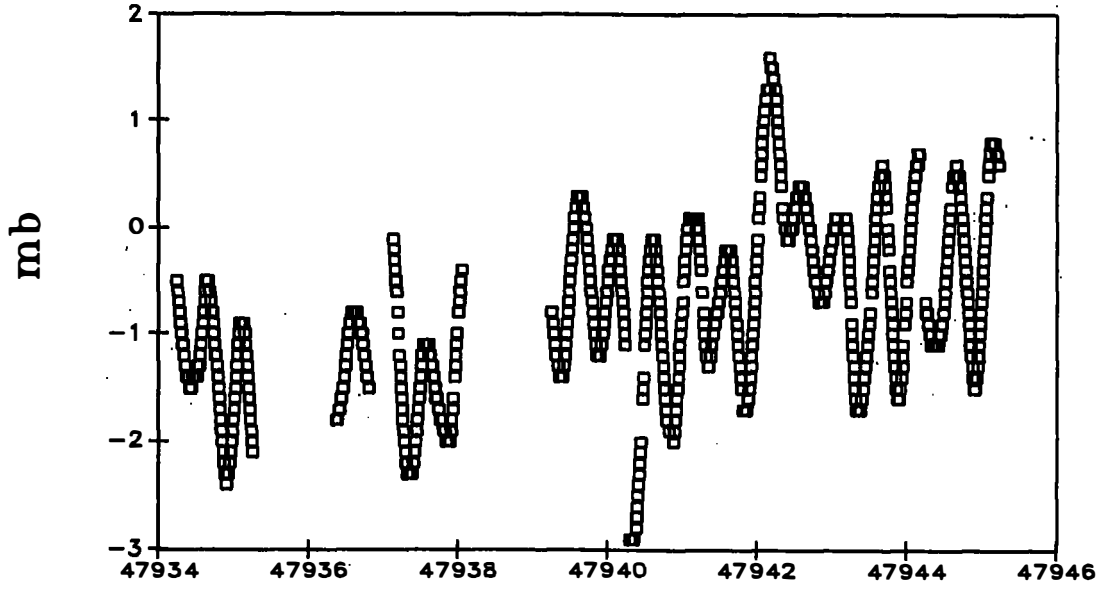

Figure 2: Differences of the observed pressure from the interpolated GANL pressure at Richmond. The abscissa is Julian day - 2400000.

values at the observation epochs. There is a mean offset of about 1mb. This magnitude of the offset is quite likely because the offset depends on, for example, the ground height of a barometer. More important feature is the existence of daily variations. The GANL data cannot follow such high frequency variations because its temporal resolution is only 12 hours. The amplitude of the daily variation is about 1mb. At the epochs when the GANL data is given the variation of the differences is much smaller than 1mb. Therefore, we can conclude the GANL data has accuracy better than 1mb at the GANL data epochs if we neglect a constant offset. The accuracy of the pressure interpolated between the GANL data epochs depends upon amplitudes of shorter period variations. The overall errors of the interpolated GANL values are about ±1mb in the present example.

III. Results of direct integration

In this section we show results of the direct integration given by equation (2) for Wettzell and Kauai for the period from March 1, 1988 to December 31, 1990. These stations are selected as typical continental and ocean stations. The GANL data is considered to be most accurate in this period(see table 1).

Figure 3 shows variations of u at Wettzell. The range of u between the high and low extremities is almost 40mm which is large enough to be detected, while usual u varies by only 15mm. The extremely high u correspond to extremely low pressure. The surface pressure variations in the same period is shown in Figure 4. By comparing the two figures we find very good correspondence between the peaks of u and p: low p corresponds to high u.

Figure 5 is a correlation diagram between u and p. The points are concentrated around a straight line. This means that the correspondence is not only in the epoch but also in the magnitude. This is a typical characteristic of u at continental stations when the inverted barometer model is adopted.

The correspondence between u and p is less clear at oceanic stations. Figures 6 and

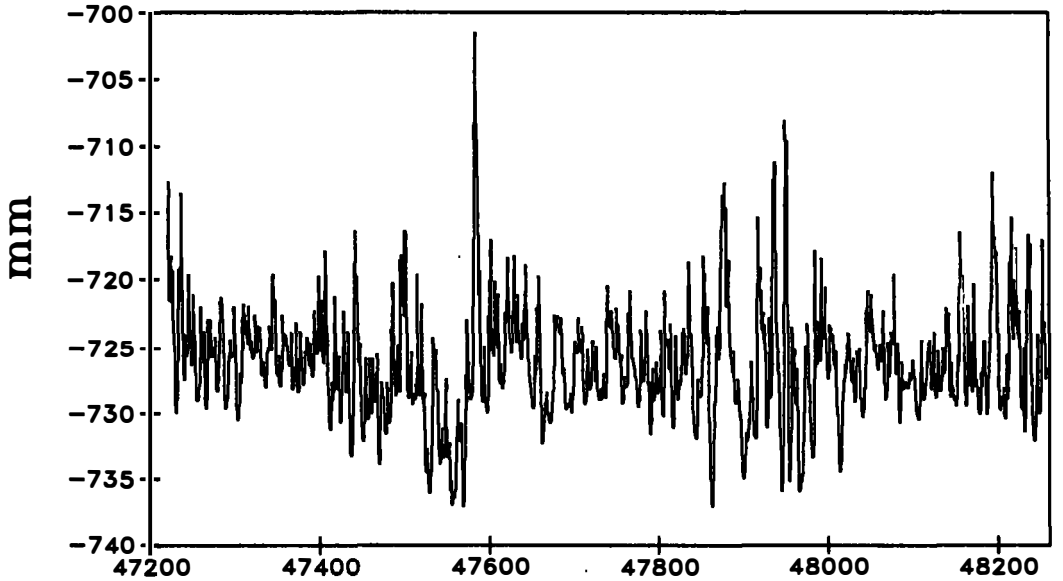

Figure 3. Variation of the vertical displacement u at Wettzell at every 12 hours from March 1, 1988 to December 31, 1990. The abscissa is Julian day-2400000. The unit of the ordinate is mm.

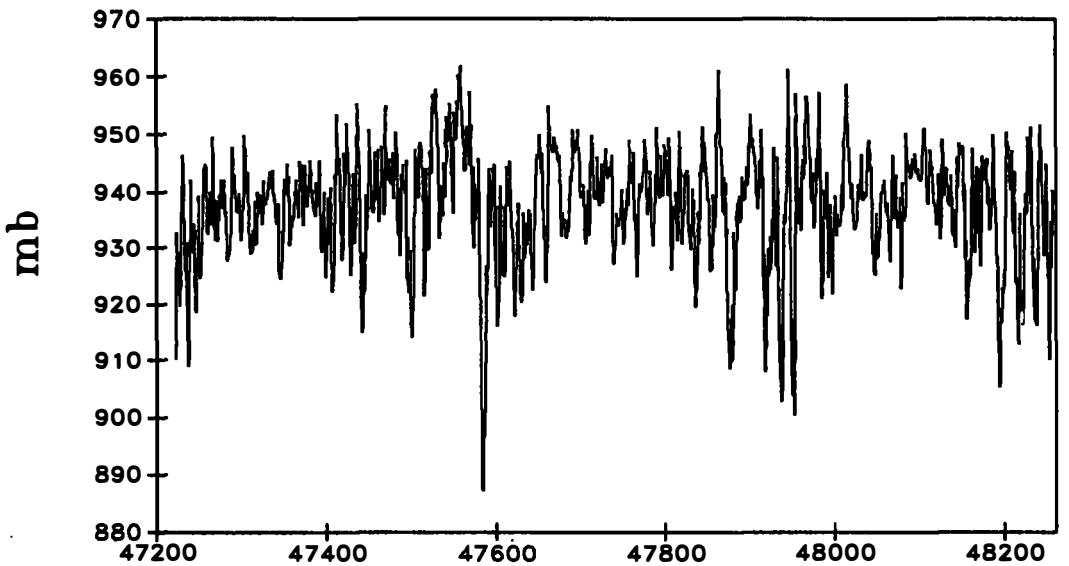

Figure 4. Variation of the surface pressure p at Wettzell at every 12 hours from March 1, 1988 to December 31, 1990. The abscissa is Julian day-2400000. The unit of the ordinate is mb.

7 show u and p at Kauai. The correspondence between u and p is good. However, u does not have extreme spikes which p has. As is seen in a correlation diagram given by figure 7, although u varies basically in proportion to p, the distribution of the points is more dispersed than that at Wettzell. This is the implication of the inverted barometer model. If the inverted barometer model is not adopted, the correspondence is the same as that at continental stations. The range of u, which is only 4mm, is much smaller than that at Wettzell because the surface pressure typically varies only 15mb and the inverted barometer model is adopted. Another noticeable characteristic of u at Kauai is that u has a clear annual signature. Since u at Kauai

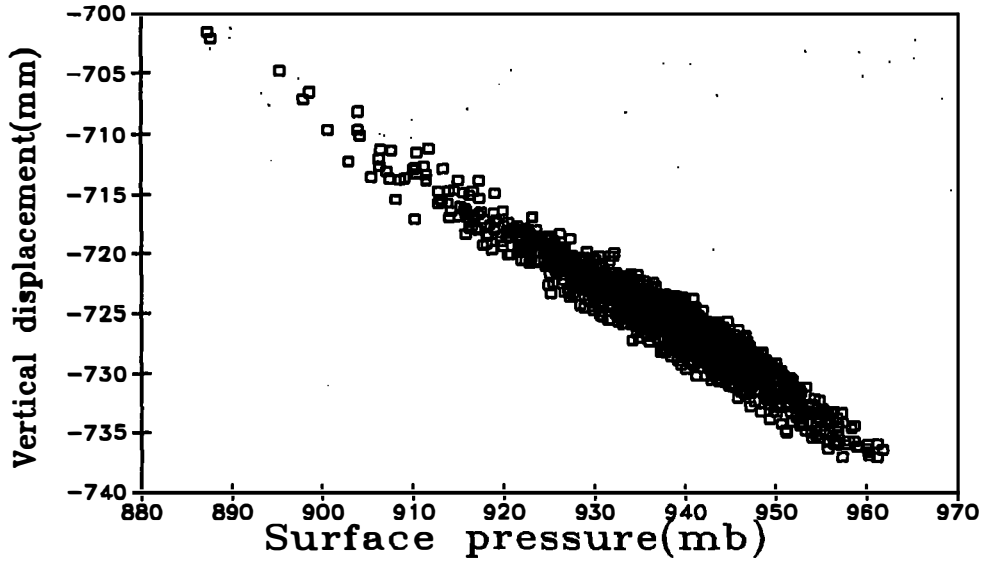

Figure 5. Correlation between the surface pressure p and the vertical displacement u at Wettzell. Each point corresponds to p and u at every 12 hours.

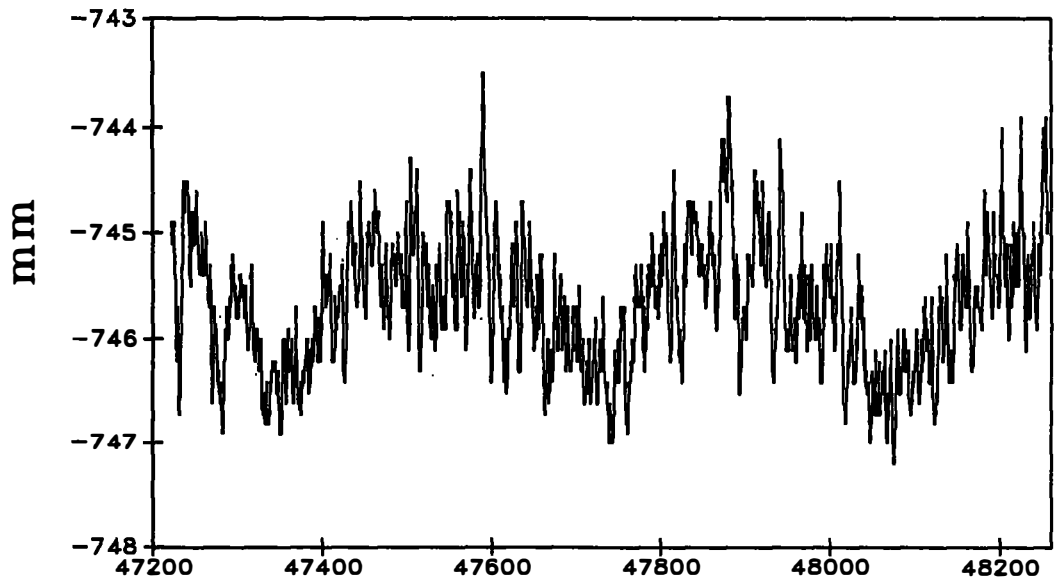

Figure 6. Variation of the vertical displacement at Kauai at every 12 hours from March 1, 1988 to December 31, 1990. The abscissa is Julian day-2400000. The unit of the ordinate is mm.

is considered to be due to the worldwide change of the surface atmospheric pressure under the inverted barometer hypothesis, it is suggested that an annual variation of u independent of the local surface pressure variation exists.

IV. Analytic approximation

Since the correspondence between u and p is fairly good, proportionality of u to p given by

is an appropriate approximation. Here u_m and p_m are means of u and p over the period

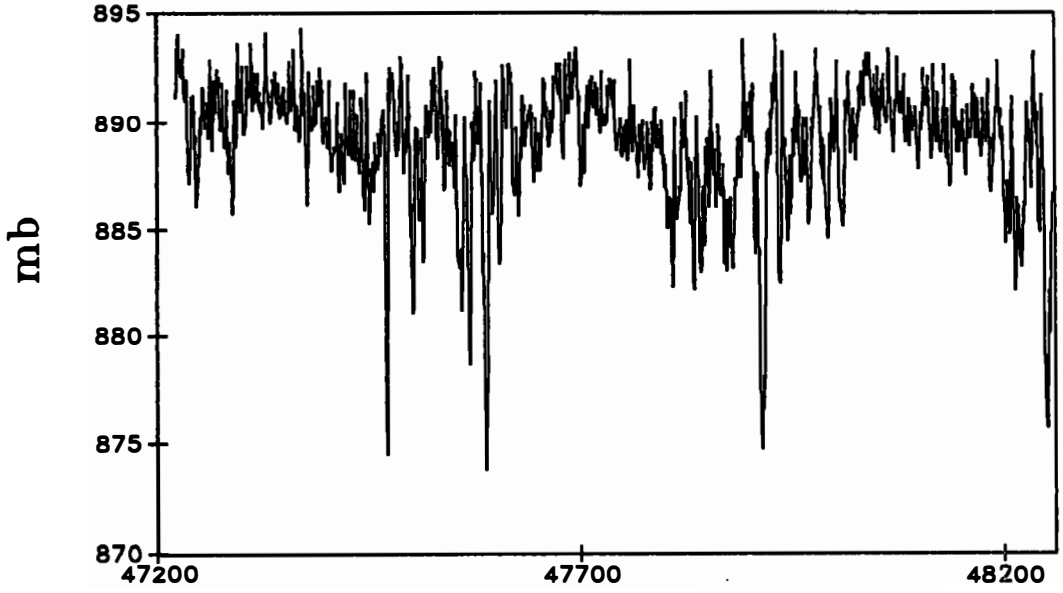

Figure 7. Variation of the surface pressure at Kauai at every 12 hours from March 1, 1988 to December 31, 1990. The abscissa is Julian day-2400000. The unit of the ordinate is mb.

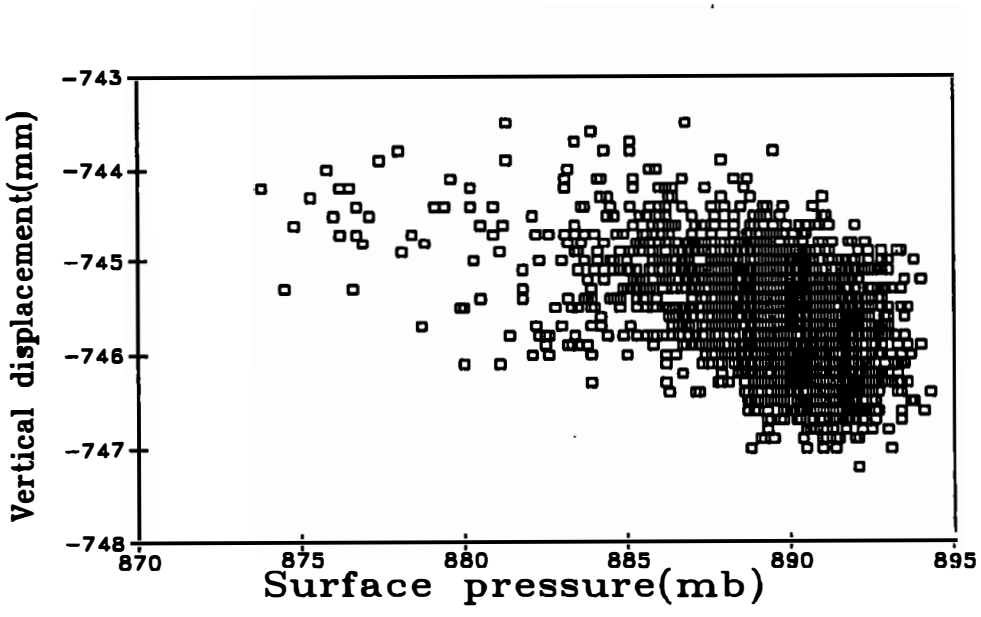

Figure 8. Correlation diagram between the surface pressure and the vertical displacement at Kauai. Note that the concentration around a strict proportionality is poorer than that for Wettzell.

$$u = u_m + c(p - p_m) \tag{3}$$

concerned. If we adopt equation (3), standard deviations of post-fit residuals are around 1.5mm. This value is much smaller than the range of u itself. However, it is not satisfactorily small if we require mm-accuracy. In addition there remain systematic variations in the post-fit residuals.

Figure 9 shows the post-fit residuals of u at Kauai with equation (3) as an approximate

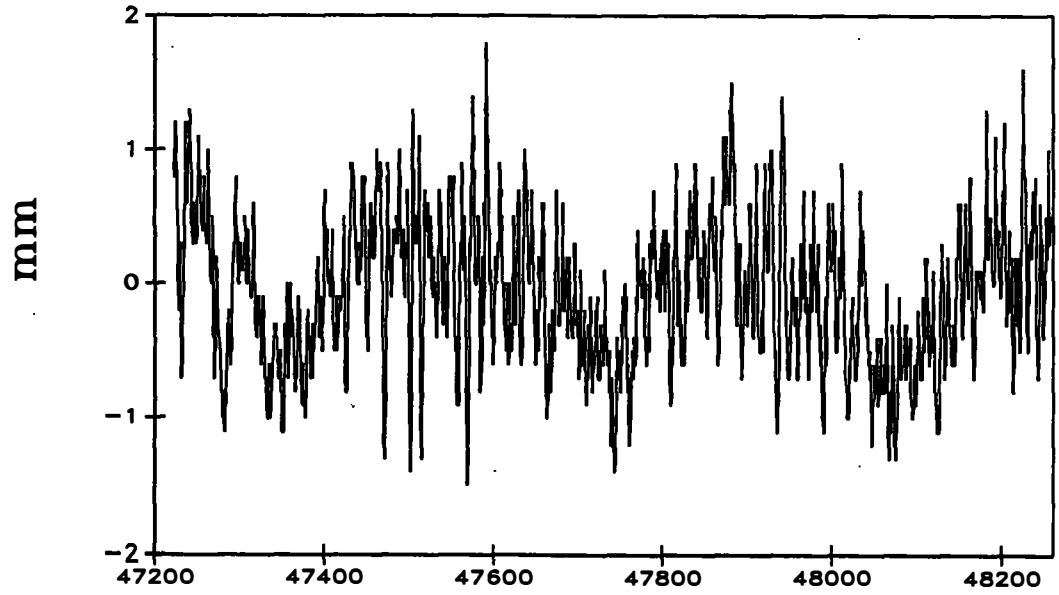

Figure 9. Residuals of u at Kauai after fitting $u=u_m+c(p-p_m)$. The abscissa is Julian day-2400000.

expression. The residuals have a clear annual signature. This example demonstrates necessity of introduction of annual terms to equation (3) as:

$$u = u_m + a\sin 2\pi t + b\sin 2\pi t + c(p-p_m) \tag{4}$$

If we adopt equation (4) as an analytic approximation, the annual signature disappears and the post-fit residuals are much reduced. Table 2 lists the estimated parameters at VLBI stations. The standard deviations of the post-fit residuals given in the column σ are smaller than 1mm for most of the stations. Therefore, it is concluded that equation (4) with table 2 has enough accuracy for geodetic vertical position determination with mm-accuracy. The response coefficient c of the vertical displacement to the local pressure change ranges from -0.054mm/mb at KWAJAL26 in mid-Pacific ocean to -0.542mm/mb at HARTRAO in South Africa.

If we do not adopt the inverted barometer model, in other words, we take into account the variation of the surface pressure on the oceans, there is no distinction between continental and oceanic stations. This is demonstrated in table 3 which gives the same parameters as table 2 in the non-inverted barometer case. Comparing the two tables we find that the response coefficients c of the oceanic stations increases very much. For example, c at KWAJAL26 is more than 20 times larger in the non-inverted barometer case. In contrast c's at the continental stations increases only as much as 30%. The standard deviations of the post-fit residuals also increase because the range of u variation increases.

V. Correspondence between computed and observed vertical displacements

The most straightforward way to see if the atmospheric loading effect is explainable observationally determined vertical displacements is the direct comparison. This is also the only way we can take, since we have not computed horizontal displacements and it is not possible to compare baseline length changes without knowing 3-dimensional displacements.

Wettzell is the most appropriate station to make the comparison, since it is a

Table 2. Parameters of the analytic approximation under the inverted barometer hypothesis. λ and ϕ are longitude and latitude of a station.

Station	p_m mb	u_m mm	a mm	b mm	c mm/mb	σ mm	λ deg	ϕ deg
ALGOPARK	989.25	-718.80	0.83	0.11	-0.435	1.01	281.93	45.96
DSS45	940.72	-729.08	0.76	-0.00	-0.423	0.56	148.98	-35.40
EFLSBERG	970.47	-736.87	0.23	-0.13	-0.413	1.04	6.88	50.52
FORTORDS	987.70	-709.40	0.74	0.30	-0.201	0.81	238.23	36.59
GILCREEK	972.67	-710.15	1.72	-0.05	-0.432	0.98	212.50	64.98
HARTRAO	862.68	-685.18	0.53	0.14	-0.540	0.44	27.69	-25.89
HATCREEK	903.05	-682.11	0.81	0.19	-0.387	0.94	238.53	40.82
HAYSTACK	1002.97	-727.46	1.14	0.06	-0.369	0.86	288.51	42.62
HRAS 085	841.41	-665.64	-0.36	-0.21	-0.532	0.72	256.05	30.64
KASHIMA	1005.92	-732.05	-0.30	0.10	-0.167	0.59	140.66	35.95
KAUAI	889.49	-745.61	0.47	0.05	-0.053	0.45	200.33	22.13
KWAJAL26	1006.41	-752.14	0.72	0.09	-0.031	0.51	167.48	9.40
MARPOINT	1017.62	-726.11	0.89	0.13	-0.406	0.85	282.77	38.37
MEDICINA	1010.55	-730.88	0.68	0.04	-0.431	0.79	11.65	44.52
MOJAVE12	912.82	-682.27	0.53	0.24	-0.457	0.84	243.11	35.33
NOBEY 6M	859.37	-716.74	-1.26	-0.37	-0.276	0.61	138.47	35.94
NOTO	1000.22	-738.13	-0.08	0.04	-0.210	0.70	14.99	36.88
NRAO85 3	926.90	-713.83	-0.41	-0.28	-0.479	0.91	280.16	38.43
NRAO 140	924.70	-713.77	-0.43	-0.29	-0.481	0.93	280.16	38.44
ONSALA60	1004.94	-739.67	0.48	-0.07	-0.254	0.92	11.93	57.40
OVRO 130	882.46	-665.29	0.61	0.32	-0.444	0.99	241.72	37.23
PLATTVIL	848.22	-640.33	0.48	0.13	-0.495	0.94	255.27	40.18
PRESIDIO	1010.85	-708.99	0.08	0.13	-0.092	1.17	237.54	37.81
PT REYES	1010.85	-710.49	0.15	0.13	-0.112	1.11	237.06	38.10
PVERDES	1008.69	-705.30	0.24	0.34	-0.159	0.98	241.60	33.74
RICHMOND	1017.73	-734.08	0.36	0.19	-0.175	0.58	279.62	25.61
SANPAULA	994.78	-701.80	0.68	0.41	-0.278	0.87	241.00	34.39
SESHAN25	1013.93	-711.30	-0.12	0.34	-0.379	0.56	121.20	31.10
VNDNBERG	1016.78	-711.01	0.41	0.32	-0.129	0.87	239.38	34.56
WESTFORD	1006.60	-727.49	1.20	0.09	-0.366	0.87	288.51	42.61
WETTZELL	938.96	-725.99	-0.67	-0.17	-0.442	1.00	12.88	49.15

continental station and is one of the stations producing a large number of observations. Figure 10 shows the variation of the vertical position at Wettzell determined with VLBI(Caprette *et. al*, 1990). The smooth curve in the figure is the smoothed variation that is optimal in the sense of the minimum ABIC(Akaike 1981). The residuals from this curve is considered to be random in a statistical sense. If there were a significant periodic component, the optimally smoothed variation must have had such a component. It is evident that the observed u does not have a significant annual component, while the annual component is most significant in the atmospheric u.

In order to see if rapid variations of VLBI u can be interpreted as being due to atmospheric u, atmospheric u is plotted against VLBI u in figure 11. VLBI u's plotted there

Table 3. Parameters of the analytic approximation under the non-inverted barometer hypothesis. λ and ϕ are longitude and latitude of a station.

Station	p_m mb	u_m mm	a mm	b mm	c mm/mb	σ mm	λ deg	ϕ deg
ALGOPARK	989.24	-726.87	0.78	-0.37	-0.453	1.52	281.93	45.96
DSS45	940.73	-738.68	0.86	-0.68	-0.620	1.68	148.98	-35.40
EFLSBERG	970.47	-735.55	0.67	-0.46	-0.557	1.75	6.88	50.52
FORTORDS	987.70	-734.94	0.50	-0.07	-0.501	1.39	238.23	36.59
GILCREEK	972.67	-716.13	1.95	-0.39	-0.536	1.79	212.50	64.98
HARTRAO	862.68	-689.11	0.55	0.49	-0.644	1.10	27.69	-25.89
HATCREEK	903.05	-700.80	0.51	-0.24	-0.517	1.48	238.53	40.82
HAYSTACK	1002.96	-723.98	1.09	-0.47	-0.458	1.58	288.51	42.62
HRAS 085	841.40	-669.52	-0.99	-0.50	-0.547	1.16	256.05	30.64
KASHIMA	1005.91	-754.93	-1.27	-0.10	-0.485	1.31	140.66	35.95
KAUAI	889.49	-747.99	0.19	-0.24	-0.638	1.07	200.33	22.13
KWAJAL26	1006.41	-765.72	0.72	0.44	-0.599	0.85	167.48	9.40
MARPOINT	1017.61	-724.47	0.63	-0.37	-0.460	1.47	282.77	38.37
MEDICINA	1010.56	-741.81	0.79	-0.19	-0.563	1.55	11.65	44.52
MOJAVE12	912.82	-688.31	-0.01	-0.16	-0.542	1.24	243.11	35.33
NOBEY 6M	859.37	-715.51	-3.31	-1.23	-0.539	1.37	138.47	35.94
NOTO	1000.22	-730.78	-0.70	-0.16	-0.571	1.32	14.99	36.88
NRAO85 3	926.90	-722.15	-0.84	-0.82	-0.528	1.36	280.16	38.43
NRAO 140	924.69	-721.97	-0.86	-0.83	-0.531	1.37	280.16	38.44
ONSALA60	1004.97	-743.29	0.84	-0.22	-0.517	1.68	11.93	57.40
OVRO 130	882.46	-666.63	0.10	-0.09	-0.517	1.32	241.72	37.23
PLATTVIL	848.22	-653.36	0.11	-0.17	-0.503	1.27	255.27	40.18
PRESIDIO	1018.38	-716.97	0.23	0.07	-0.429	1.32	237.54	37.81
PT REYES	1018.07	-724.77	0.48	0.12	-0.458	1.36	237.06	38.10
PVERDES	1008.69	-706.56	-0.42	0.10	-0.469	1.39	241.60	33.74
RICHMOND	1017.73	-754.39	-0.26	-0.09	-0.604	1.08	279.62	25.61
SANPAULA	994.78	-711.79	0.37	0.10	-0.498	1.22	241.00	34.39
SESHAN25	1013.93	-714.97	-0.97	0.27	-0.477	1.14	121.20	31.10
VNDNBERG	1016.78	-718.01	0.02	0.14	-0.458	1.29	239.38	34.56
WESTFORD	1006.59	-724.09	1.16	-0.44	-0.454	1.60	288.51	42.61
WETTZELL	938.97	-719.61	-0.57	-0.43	-0.523	1.39	12.88	49.15

are residuals from the smoothed variation shown in figure 10. The dispersion of VLBI u is larger than that of atmospheric u by one order of magnitude. There is no correlation between the two u's even if VLBI u's with large absolute values are excluded. The dispersion of VLBI u considerably decreased in and after 1988. However, there is no correlation between VLBI u and atmospheric u. Moreover, even optimally smoothed VLBI u has no correlation in this period. Therefore, we can conclude that the atmospheric loading is not a major source of the variation of the vertical displacements observed with VLBI. It should be noted that this does not mean that the atmospheric u is not necessary to be corrected for.

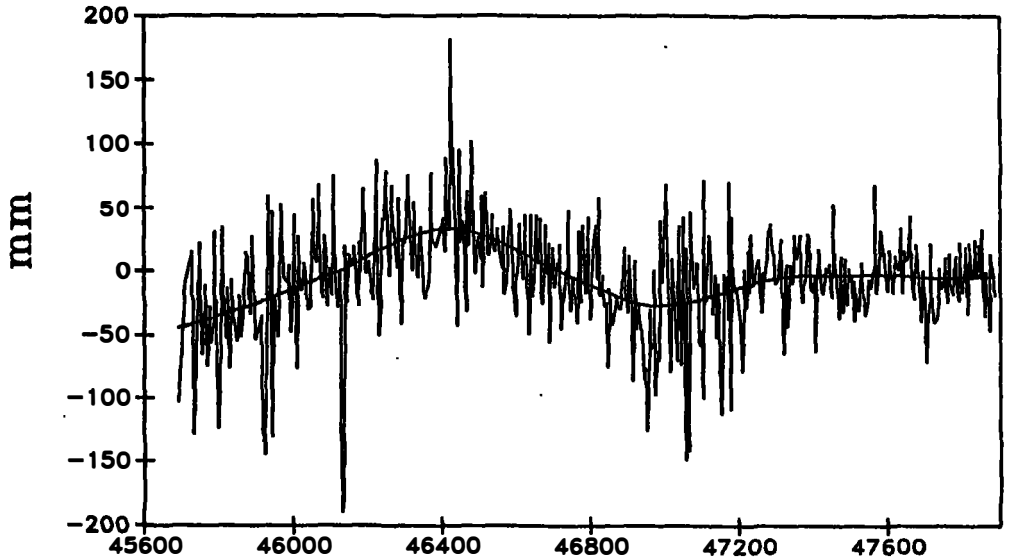

Figure 10. Variations of the vertical positions observed with VLBI at Wettzell from 1984 to 1989. The variations are expressed as differences from the mean. The optimally smoothed variation giving minimum ABIC is also shown.

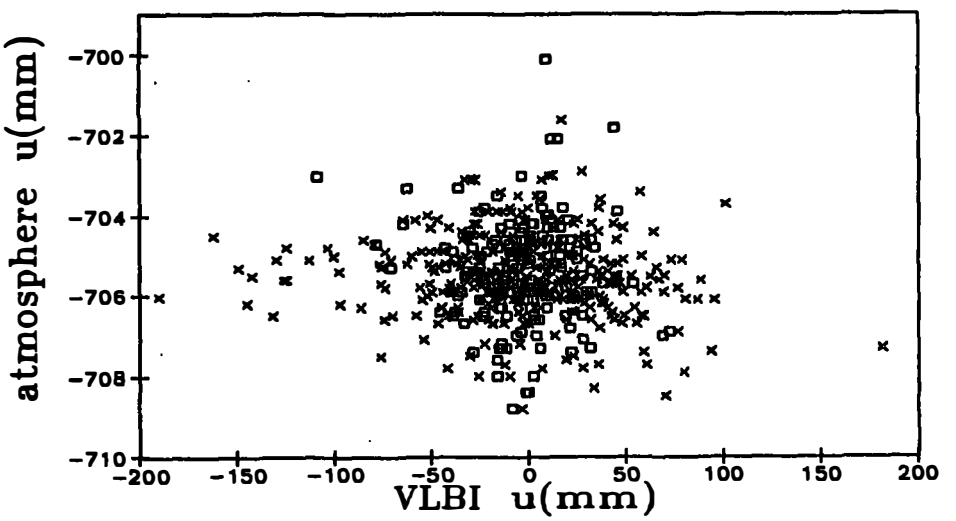

Figure 11. Correlation of atmospheric u against VLBI u at Wettzell. The crosses and squares show u's from 1984 to 1987 and 1988 to 1989, respectively. The units of the both axes are mm.

VI. Conclusion

The atmospheric loading causes vertical displacements in the rate about -0.4mm/mb or more at continental stations under the inverted barometer hypothesis. The rate is much smaller at oceanic stations. There exists annual variations independent of the local surface pressure. We can approximate the vertical displacements by using the expression given by equation (4) with the accuracy of 1mm. In the non-inverted barometer case the accuracy of the analytic approximation is 1.6mm.

The observationally determined vertical displacements is not explainable as being caused by the atmospheric loading, since the dispersion of the observed vertical displacements is too large. However, this does not deny necessity of correcting for the atmospheric loading effect. In fact, the loading displacement ranges by about 1cm during the actual VLBI observations.

References

Akaike, H., Likelihood and Bayes procedure, in *Bayesian Statistics*, Bernardo, J. M., De Groot, M. H., Lindley D. U. and Smith, A. F. M., eds. University Press, Valencia, Spain, 1980.

Farrell, W. E., Deformation of the Earth by surface loads, *Rev. Geophys.*, **10**, 761-97, 1972.

Caprette, D. S., Ma, C. and Ryan, J. W., Crustal Dynamics Project Data Analysis--1990, VLBI Geodetic Results 1979-1989, *NASA Tech. Mem.* **100765**, 1990.

Sato, T. and Hanada, H., Computer Program 'GOTIC' for the Computations of Oceanic Tidal Loading Effects, *Publ. Intern. Latit. Obs. Mizusawa*, **XVIII**, 29-47, 1984.

Schwiderski, E. W., On charting global ocean tides, *Rev. Geophys.*, **18**, 234-268, 1980.

Van Dam, T. M. and Wahr, J. M., Displacements of Earth's Surface Due to Atmospheric Loading: Effects on Gravity and Baseline Measurements, *J. Geophys. Res.*, **92**, 1281-1286, 1987.

Current Precision of VLBI Multi-Band Delay Observables

JIM R. RAY

Interferometrics Inc./Goddard Space Flight Center, Greenbelt, Maryland

BRIAN E. COREY

Haystack Observatory, Westford, Massachusetts

The precision of VLBI multi-band group delay observables collected with the Mark III system is assessed to determine whether the formal uncertainty, which depends only on the observation signal-to-noise ratio (SNR) and the rms spanned bandwidth, is a valid representation of the actual data quality. Two approaches are used: analysis of residual phases which result from the group delay fit across frequency, and comparison of group and phase delays. The phase residual analysis shows that the statistical properties of actual data deviate from the theoretical model. We model the observed phase variance as the sum of two components: the theoretical, SNR-dependent contribution modified by a scale factor plus a phase "noise floor." The scale factor is found to be $(1.1)^2$ for the standard X-band frequency sequence using 360 MHz spanned bandwidth and $(1.3)^2$ for the R&D doubled bandwidth data; the phase noise floor is $(1.7°)^2$ and $(2.2°)^2$, respectively. These phase noise values imply group delay precisions no better than 12 ps and 8 ps for standard and R&D X-band sequences. Analysis of group and phase delay differences has found a higher value for the R&D group delay noise floor, about 11-12 ps. Spurious signals, which corrupt the phase calibration phases, are observed at levels up to about -25 dB for several stations. These effects probably contribute most of the observed scatter in the phase residuals and the delay differences. The larger value for the group delay noise floor derived from the delay difference analysis probably reflects the fact that the spurious signals are generally strongest in the outer frequency channels thereby exerting a greater influence on group delay estimates. We are unable to explain the existence of SNR-dependent scale errors. It appears that the theoretical benefits of doubling the X-band spanned bandwidth, an enhancement tested in the NASA R&D program, have been largely realized as measured by phase stability (about two-thirds of the full potential) and somewhat less so as measured by group delay variations. The X-band phase stability of the Pie Town VLBA station is found to be poorer than the Mark III stations, for reasons not yet identified.

INTRODUCTION

Under most circumstances, VLBI geodetic determinations are probably limited by errors in calibrating for external delay contributions, especially those due to atmospheric propagation [*Clark et al.*, 1989; *Herring et al.*, 1991], and not by instrumental errors or by the precision of the observables *per se*. The precision of the VLBI observables is nevertheless important. While the noise-like effect of the nuisance atmospheric parameters normally included in VLBI data analysis depends primarily on the observing geometry (which determines the cross-correlations with the geodetic parameters), the magnitude of potential unmodelled errors may be influenced in subtle ways by the precision of the observables. More importantly, in certain state-of-the-art VLBI experiment series the observed geodetic repeatability is only slightly greater than that expected from the formal errors [*Davis et al.*, 1991; *MacMillan and Ray*, 1991], a strong indication that unmodelled errors can be controlled. As ongoing improvements are made, particularly in modelling atmospheric effects, the sensitivity of geodetic results to observation precision will likely increase. For these reasons, an assessment of the intrinsic precision of VLBI multi-band group delay observables is appropriate. Our emphasis here is on X-band observables obtained with the enhanced Mark IIIA data acquisition system developed by the NASA Crustal Dynamics Project (CDP) and demonstrated in the Extended R&D Experiment (ERDE) during October 1989 [*Corey and Clark*, 1991]. Results using this system with doubled X-band spanned bandwidth are compared with comparable data obtained with the standard configuration. Thus, this study also serves to assess the effectiveness of the hardware modifications made to implement the observational enhancements.

Group Delay Precision

The Mark III data acquisition system was a key development in applying VLBI to high-precision geodesy by increasing the system sensitivity and enabling the bandwidth synthesis technique to be used simultaneously for two wide frequency bands [*Clark et al.*, 1985]. In bandwidth synthesis, a signal is sampled in several discrete, relatively narrow channels spanning a broad frequency range [*Rogers*, 1970; *Hinteregger et al.*, 1972] to produce fringe phase estimates at a series of frequencies. Group delay is the change in fringe phase with respect to frequency and thus the group delay uncertainty varies inversely with the spanned bandwidth. Bandwidth synthesis thereby permits much more precise group delay observables than if the same recorded bandwidth were confined to a single channel. Importantly, Mark III allows group delay observations (made simultaneously at S-band and X-band to remove the dispersive effect of ionospheric propagation) precise enough for geophysically significant geodetic determinations without relying on the more precise but ambiguous (and therefore difficult to utilize) phase

delays that had conventionally been used in interferometry.

The theoretical standard deviation in the estimate of the group delay derived from VLBI bandwidth synthesis depends inversely only on the interferometer signal-to-noise ratio (SNR) and on the effective (rms) spanned bandwidth [*Clark et al.*, 1985]. (This ignores integer ambiguities, related to the minimum spacing between frequency channels, which are usually readily resolvable, and noise peaks falsely interpreted as signal, which are reliably avoided by requiring SNR $\geq$ 7.) The theoretical formulation assumes that a common system noise affects all frequency channels independently and equally, and that no other effects are important. There are, however, a variety of other instrumental effects that can introduce phase noise preferentially in one or more frequency channels, thereby affecting the group delay value [*Rogers*, 1991]. Spurious contributions to the phase calibration tones, used to align the phases of the independent frequency channels with respect to one another, are a particular concern. In addition, the finite capability of the correlator to extract a unique signal phase acts much like an additional system noise component [*Rogers*, 1991]. To allow for such effects, we can generalize the theoretical expression for the phase variance of an individual frequency channel to

$$\sigma_\phi^2 = \alpha^2 \cdot \sigma_{th}^2 + \sigma_o^2$$

where

$$\sigma_{th} = (360° \cdot \sqrt{N_{ch}}) / (2\pi \cdot \mathrm{SNR})$$

is the theoretical standard deviation of the phase in a single channel (in degrees). The signal-to-noise ratio SNR is the usual value for the coherent sum across N_{ch} frequency channels. Two empirical parameters have been introduced: α represents a possible scaling error while σ_o is the average phase noise (in degrees) per channel due to effects unaccounted for by SNR. From this, it follows that the generalized uncertainty expression for a group delay measurement (in time units) is

$$\sigma_\tau^2 = [\, \alpha / (2\pi \cdot \mathrm{SNR} \cdot B_{rms}) \,]^2 + [\, \sigma_o / (360° \cdot \sqrt{N_{ch}} \cdot B_{rms}) \,]^2$$

where B_{rms} is the rms spanned bandwidth. In circumstances where extraneous phase errors are large for only a few frequency channels, this formulation may be a poor representation of the actual quality of the group delays. Likewise, random delay-like variations within the Mark III system, which will contribute to the group delay scatter but not to the phase scatter across the frequency band, are neglected by this formalism. Note that as SNR grows large, the theoretical noise contribution vanishes leaving the empirical contribution as a "noise floor" for group delay data.

The purpose of this study is to examine VLBI performance changes with varying SNR to estimate a value for σ_o and hence to measure the group delay noise floor, as well as to determine whether a proportionality error α applies to the theoretical uncertainty. We are particularly interested in whether σ_o , the limiting phase noise per channel, changed when the X-band bandwidth was doubled for the enhanced Mark III system. If σ_o remains unchanged (or decreases) for the wider bandwidth, then the full factor two potential improvement in group delay precision will have been realized. Error sources which cause constant or nearly constant bias contributions to the group delay are not considered here.

METHODOLOGY

The basic methodology to assess group delay precision has been presented and applied by *Herring* [1983] who found that the apparent noise of VLBI observables did not have the statistical properties expected based purely on SNR due to large instrumental dispersions in the early Mark III system. For X-band data, a proportional error of 1.1-1.2 scaled the theoretical group delay standard deviation and a threshold noise floor of about 15 ps was observed. Two approaches were described by *Herring* to evaluate the quality of group delay observables: analysis of the residual phases by frequency channel which result from the fitting of the group delay in the data processing; comparison of group and phase delays under the assumption that errors in the phase delay observables are much smaller. To some extent, these approaches are complementary. Study of phase residuals is more basic in the sense that the phase scatter sets a lower bound on the group delay performance. On the other hand, comparison of differenced delays is more comprehensive, being sensitive to all instrumental effects that are not identical for both data types, including random delay variations that do not influence the phase residuals. These methods are explained below.

Analysis of Phase Residuals

Qualitatively, the processing of the raw VLBI data streams from each pair of stations can be thought of as producing fringe phase estimates for each frequency channel which, after applying calibration offsets, are used to fit a group delay, the derivative of phase with respect to frequency. In practice, the multi-band group delay is fit in a multi-dimensional Fourier search that also estimates simultaneously the single-band delay, the delay rate, and the visibility phase; refer to *Clark et al.* [1985]. The difference between the phase of each frequency channel and the phase computed from the observation-averaged group delay, delay rate, and the visibility phase is referred to as the residual phase. Ideally, the residual phases should be zero mean, Gaussian random quantities with a standard deviation which depends only on SNR. It is well established that this expectation is not realized for the reasons mentioned above and probably for others.

To characterize the departures from ideal behavior, we have computed standard deviations for the residual phases for every observation in a set of one-day VLBI observing sessions. In doing so, we first remove a weighted mean phase offset for each frequency channel calculated

separately for each one-day session, using the (unmodified) theoretical uncertainty as weights. Thus, our analysis is not sensitive to error sources which vary slowly compared to a day. The phase scatter across the frequency band for each observation is then computed weighting each phase residual by the number of data bits (accumulation periods) and the square of the fringe amplitude for that channel. The standard deviation computation assumes that the number of degrees of freedom is given by the number of frequency channels less two (for the removal of the observation-averaged visibility phase and the group delay, essentially an offset and a slope). In performing this analysis, only those observations that are nominally "good" with SNR values greater than 10 have been used.

The product of the above procedure was about 2000 determinations of the observed (σ_ϕ) and the theoretical (σ_{th}) phase scatters for each ERDE experiment day. Lines were fit to the squares of these quantities, or the observed and theoretical phase variances, to derive estimates for α, the proportionality error, and σ_o, the limiting phase noise per channel, for each day. Owing to the high data redundancy, the line-fitting was done in two steps. First, the data were binned in intervals of σ_{th} (equal numbers of points per bin) and within each bin the corresponding values for σ_ϕ^2 were averaged. The averaged values of σ_ϕ^2 versus σ_{th}^2 were then fit linearly. The number of bins used was 25 when all the data were analyzed and 20 for subsets of data.

Analysis of Group/Phase Differences

The VLBI group delay (τ) and phase (ϕ) observables can be decomposed into the following contributions

$$\tau = \tau^{geo} + \tau^{atm} + \tau^{clock} + \tau^{ion} + \tau^{source} + \tau^{inst}$$

$$\phi = \omega \cdot (\tau^{geo} + \tau^{atm} + \tau^{clock} - \tau^{ion}) + (\phi^{source} + \phi^{inst} + \phi^{feed} + 2\pi N)$$

where τ^{geo} is the geometric delay, τ^{atm} is the differential propagation delay due to the neutral atmosphere, τ^{clock} is the delay due to clock and cable differences, τ^{ion} is the differential ionospheric delay, τ^{source} and ϕ^{source} are the delay and phase offsets due to source structure, τ^{inst} and ϕ^{inst} are instrumental delay and phase offsets, ϕ^{feed} is the phase contribution due to the feed, ω is the angular observing frequency, and N is an integer number of cycles (ambiguities). The largest delay components are common to both observables so the delay difference is

$$\Delta = \tau - (\phi/\omega) = 2\tau^{ion} + \tau^{source} + \tau^{inst} - (\phi^{source} + \phi^{inst} + \phi^{feed} + 2\pi N)/\omega$$

There are two equivalent approaches for minimizing further the effects of non-instrumental error sources, both of which rely on having two VLBI stations near to one another. For a single, very short baseline, the non-instrumental effects will be minor and the ambiguities should be readily resolvable to a common value. The behavior of the scatter in Δ over time is then a direct measure of the instrumental differences. Moreover, under most normal conditions, the instrumental effects will be substantially larger for the group delays than for the phase delays, by roughly the ratio of the observing frequency divided by the rms bandwidth. This method has been applied by *Herring* [1983, 1991] to the 1.2-km baseline between Haystack and Westford in Massachusetts.

Alternatively, the delay differences for a pair of baselines from two nearby stations to a third arbitrary station can be differenced a second time. Thus, if i and j denote the nearby pair of stations and x denotes a third station, then the doubly differenced delay is

$$\Delta_{ij}^2 = \Delta_{ix} - \Delta_{jx} \approx 2\tau_{ij}^{ion} + (\tau_{ix}^{inst} - \tau_{jx}^{inst}) - (\phi_{ix}^{inst} - \phi_{jx}^{inst})/\omega - (2\pi M/\omega)$$

where M is an integer number of ambiguities and where the source contributions from the two long baselines ix and jx, being nearly equal, difference out. (We assume that the two nearby stations have the same type of antenna mount, so that ϕ^{feed} is nearly identical for the two baselines.) For baselines much shorter than the scale of the ionosphere (about 100 km), the ionospheric contribution can normally be neglected. Generally, two classes of error sources will contribute to the instrumental offsets: (1) station-based (*e.g.*, spurious signals that corrupt the measured phase calibration phases), and (2) baseline-dependent (*e.g.*, cross-polarized feeds at both ends of a baseline or mismatched baseband filters). For station-based errors, the differenced delay depends only on the performance of the two nearby stations, but not on that of the third. However, the performance of the third station is important for baseline-dependent errors. Note that this procedure cannot be applied when the instrumental variations are a substantial fraction of a cycle of phase as this renders the resolution of integer ambiguities unreliable.

For our study, the second approach, using doubly differenced delays, has been employed. As applied to the Extended R&D Experiment (ERDE) data set, which includes the nearby pair of stations at Westford and Haystack as well as three others, this provides significantly more observational data than using the Westford-Haystack baseline alone. Double differences were formed for all data using Fairbanks and Pie Town as third stations. Being considerably less sensitive, the Mojave baselines were not used for this analysis. Only those observations with group delay errors less than 15 ps (SNR greater than about 40) were selected to minimize difficulties with ambiguity resolution. The resulting data sets for Fairbanks and Pie Town contain about 1000 delays each. The standard error of each differenced delay is the root-sum-squared of the individual group delay standard errors, which dominate over the phase delay errors. The ambiguity resolution was performed independently for each ERDE session in a procedure which minimized the variance of the doubly differenced delays about their mean value. Having done this, an additive variance was found for each set of double differences for each ERDE session such that when added

to the average variance expected from the formal errors, the sum equals the average variance of the doubly differenced delays. Ideally, we would prefer to estimate a scale parameter for the formal errors, as well as the additive noise. However, the limited range of formal errors did not permit a reliable estimate for a scale error. Therefore, the scale error determined from the analysis of phase residuals was assumed to apply to the double differences.

DATA SETS

For this investigation, we have examined data from two specially designed VLBI experiment series conducted by the CDP. The ATD (for Advanced Technique Development) series ran monthly in 1987 and bimonthly in 1988 using the stations at Westford (MA), Mojave (CA), Ft. Davis (TX), and Fairbanks (AK). The primary objective was to test the effectiveness of an observing strategy with scans as frequent as possible (nominally, about 800-900 per day) spread uniformly over elevation and azimuth down to the lowest possible elevation angles (*viz.*, 4.5° at Westford). The data acquisition hardware was standard, however. We have used the six ATD sessions in 1988 as a measure of the performance of the Mark III system in its standard geodetic configuration [*Clark et al.*, 1985]. Two of these sessions used modified networks: the Goldstone (CA) antenna DSS-13 substituted for Ft. Davis in the July session; the VLBA antenna at Pie Town (NM) substituted for Fairbanks in the Sept. session. In the latter case, Pie Town used VLBA data acquisition hardware with a five-frequency subset of the standard geodetic eight-frequency X-band sequence (see Table 1).

TABLE 1. VLBI X-band Frequency Sequences (all units MHz)

	standard		R&D	
frequency channels (USB):	8210.99		8212.99	
	8220.99	*	8252.99	
	8250.99		8352.99	
	8310.99		8512.99	*
	8420.99	*	8732.99	
	8500.99	*	8852.99	*
	8550.99		8912.99	
	8570.99		8932.99	
spanned bandwidth	360.		720.	
rms spanned bandwidth	140.22		280.43	
channel bandwidth	2.		4.	

* These frequencies were not used at Pie Town.

The data set of prime interest is from the ERDE (for Extended R&D Experiment) campaign which ran for 12 sessions over a 17-day period in Oct. 1989. The design and network for ERDE was an evolutionary extension of the ATD series. The Ft. Davis antenna was replaced by the faster slewing, more sensitive Pie Town antenna, and Haystack (MA), 1.2 km from Westford, was added for redundancy. The basic observing strategy was similar to the ATDs except that even lower elevation angles were possible at Haystack and Pie Town (down to about 2.5°). The most significant changes concern the data acquisition configuration. Hardware modifications [*Corey and Clark*, 1991] allowed both the total span and the bandwidth of each channel to be doubled at X-band (see Table 1). (Similar enhancements were also made at S-band except that the span was increased by only 50%.) The increased spanned bandwidth should ideally improve the X-band group delay precision, for fixed SNR, by a factor of two; the increased data sampling rate (or channel bandwidth) allowed a fixed SNR to be achieved in an integration time shorter by $\sqrt{2}$. More than 2000 observations, among 10 baselines, were scheduled per ERDE session. Also important was the design and deployment of a new phase calibrator unit with improved stability. In preparation for the ERDE campaign, considerable effort was made to verify the proper performance of each system and to attenuate such undesirable elements as spurious signal contributions to the phase calibration tones.

Pie Town differs from the other ERDE stations in using VLBA acquisition hardware and control software rather than the Mark III system. It was also new, having been used for VLBI for the first time in 1988. Because the VLBA system uses only eight simultaneous frequency channels, rather than the 14 standard for Mark III (eight for X-band and six for S-band), special procedures were necessary for compatibility. The Pie Town channels were split evenly between X-band and S-band, and time multiplexing among frequency settings ("frequency switching") was used to extend the coverage to six frequencies in each band. This was done holding the two outer frequencies of each band fixed for each full integration while switching two other channels between four inner frequencies every 15 seconds. Two of the X-band R&D frequencies were not sampled at all at Pie Town (see Table 1).

RESULTS OF PHASE RESIDUALS ANALYSIS

The phase residual analysis procedure described above was applied to all 12 days of the Oct. 1989 ERDE campaign, treating each day separately. To compare the performance of the enhanced Mark III capabilities used in ERDE (primarily, doubled X-band spanned bandwidth and doubled data sampling rates) with the standard system, the same analysis was also applied to the six ATD sessions from 1988. The results for determinations of the proportionality error α and the limiting phase noise per channel σ_o are listed in Tables 2 and 3, respectively. Because the analysis of the ERDE data showed a larger phase scatter for the Pie Town baselines than for the others, the results have been tabulated separately for Pie Town and for non-Pie Town baselines. The difference in data quality is illustrated in Figure 1 which shows an example of the observed versus theoretical phase scatter, for the ERDE day 17 Oct.

One of the ATD sessions (08 Sept., see Table 3) happened to use the Pie Town station in a test mode. In

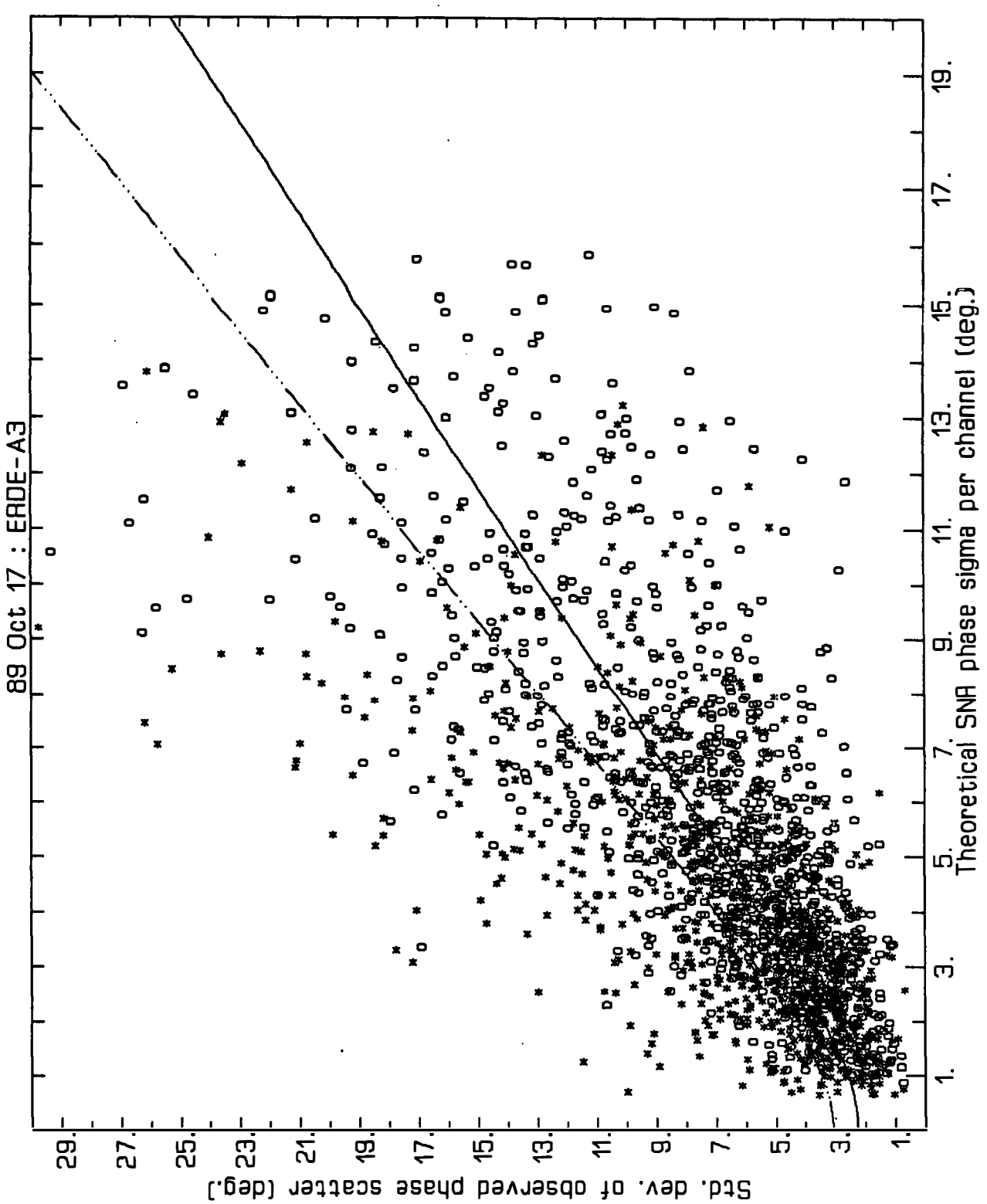

Fig. 1. Observed standard deviation of the residual phase variation across the X-band span for each observation in the ERDE session of 17 Oct. 1989 plotted against the theoretical phase uncertainty based on SNR. Observations involving the VLBA antenna at Pie Town are distinguished (*) from the others (o). The fit (linear in the variances) to the Pie Town subset is shown with a dashed-dot line while the fit for the remaining baselines is shown with a solid line.

this case, the only instance where Pie Town used a subset of the standard X-band frequency sequence, its phase stability was better than the Mark III stations, in stark contrast to the situation for the ERDE sessions.

TABLE 2. Phase Scatter Results for R&D X-band

ERDE sessions (1989)	non-Pie Town baselines		Pie Town baselines	
	α	σ_α	α	σ_α
15 Oct	1.29	2.63°	1.54	3.14°
16 Oct	1.24	2.13°	1.54	3.00°
17 Oct	1.26	2.26°	1.57	3.09°
18 Oct	1.30	2.04°	1.58	2.95°
22 Oct	1.27	2.61°	1.49	3.55°
23 Oct	1.33	1.62°	1.48	2.99°
25 Oct	1.26	2.12°	1.61	4.05°
26 Oct	1.24	2.36°	1.39	3.83°
27 Oct	1.29	1.87°	1.59	3.05°
28 Oct	1.22	1.92°	1.43	3.30°
30 Oct	1.28	2.37°	1.64	3.24°
31 Oct	1.26	2.33°	1.63	2.81°
averages	1.27	2.19°	1.54	3.25°
std. dev.	0.03	0.30°	0.08	0.38°

TABLE 3. Phase Scatter Results for Standard X-band

ATD sessions (1988)	non-Pie Town baselines		Pie Town baselines	
	α	σ_α	α	σ_α
27 Jan	1.10	2.12°	--	--
17 Mar	1.18	1.59°	--	--
16 May	1.15	1.40°	--	--
08 Jul	1.07	1.95°	--	--
08 Sep	1.16	1.39°	1.23	0.63°
29 Nov	1.14	1.47°	--	--
averages	1.13	1.65°	1.23	0.63°
std. dev.	0.04	0.31°	--	--

Effect of Ionospheric Dispersion

Our primary interest in this study is the assessment of instrumental noise levels. A non-instrumental effect that could contribute significantly to the phase scatter results described above is ionospheric dispersion. Since the phase change due to ionospheric propagation varies inversely with the frequency, the group delay fit, which is linear in frequency, will not entirely absorb the ionospheric effect, especially for large bandwidth spans. To evaluate the magnitude of the phase scatter that could result from ionospheric dispersion, let us consider the passage of a radio wavefront through an ionized medium. Neglecting second order effects, the change in phase (in radians) is

$$\phi^{ion} = -\left(e^2 n_e / 2m_e c\varepsilon_o\omega \right)$$

where e is the charge of an electron, n_e is the column number density of free electrons, m_e is the electron mass, c is the speed of light, and ε_o is the permittivity of free space. Then

$$\tau^{ion} = \partial\phi^{ion}/\partial\omega = -\phi^{ion}/\omega$$

is the corresponding group delay effect. Given an independent determination of the electron number density we could compute directly the phase variation with frequency due to the ionosphere and remove this effect from the VLBI observation phase residuals before calculating the phase scatter. Unfortunately, direct line-of-sight values for n_e are not routinely available. On the other hand, for geodetic observations, two separate frequency bands are recorded simultaneously to determine the ionospheric delay. Thus, we have

$$\tau_X = \tau^{geo} + \tau_X^{ion}$$

and

$$\tau_S = \tau^{geo} + (f_X/f_S)^2 \tau_X^{ion} + O$$

for the X- and S-band observables, where τ^{geo} represents all delay contributions that are independent of frequency in addition to the geometric delay, f_X and f_S are the effective frequencies of the two bands, and O is a constant instrumental offset between the bands. Solving for the X-band propagation delay in terms of the observables gives

$$\tau_X^{ion} = \mu(\tau_X - \tau_S) + \mu O$$

where

$$\mu \equiv f_S^2 / (f_S^2 - f_X^2)$$

which implies the following relationship between the ionospheric phase change at frequency f and the dual-band group delay observables τ_X and τ_S

$$\phi^{ion}(f) = -(2\pi f_X^2 \mu/f) \cdot (\tau_X - \tau_S + O)$$

We see that, while the dual-band group observables provide a direct estimate of the ionospheric phase change, the result is biased by an unknown instrumental offset O. Ordinarily, this offset is absorbed into the differential clock parameters which must be included in the geodetic data analysis. However, while the absolute magnitude of the ionospheric effect remains unknown, the time variance of the ionospheric phase depends only on the time variance of the dual-band delay difference $(\tau_X - \tau_S)$ if the instrumental offset is constant. To estimate the ionospheric variance contribution to the phase residuals of an individual frequency channel, consider a linear fit to the ionospheric phase variation $\phi^{ion}(f)$. If f_1 and f_2 represent the two frequencies where the line fit and the ionospheric curve are equal, then the misfit of the line at the frequency f_0 halfway between f_1 and f_2 is

$$\Delta\phi^{ion}(f_0) = \phi^{ion}(f_0) - [(\phi^{ion}(f_1) + \phi^{ion}(f_2))/2]$$

$$= \phi^{ion}(f_0) - \phi^{ion}(f_0)[(f_0/f_1 + f_0/f_2)/2]$$

$$= -\phi^{ion}(f_0)\,[\delta f^2/(f_0^2 - \delta f^2)]$$

where $\delta f = f_0 - f_1 = f_2 - f_0$. Using the previous relation for $\phi^{ion}(f)$ in terms of the dual-band observables and considering only the time variance of the quantities, we then have

$$\mathrm{var}(\Delta\phi^{ion}(f_0)) = (2\pi f_X^2\, \mu/f_0)^2\, [\delta f^2/(f_0^2 - \delta f^2)]^2\, \mathrm{var}(\tau_X - \tau_S)$$

for the time variance of the phase residual due to ionospheric curvature, at the center frequency f_0 of the X-band span. The variance at other frequency channels relative to f_0 can be determined by empirical line fitting to the form $\phi^{ion}(f)$. Table 4 lists the rms phase variations for the R&D and standard X-band frequency sequences relative to the band center.

This approach still does not enable calibration of the phase residuals for the effect of ionospheric propagation, but it does permit a direct estimate of the time variance of the effect using the group delay observables τ_X and τ_S. The ionospheric variances so determined can then be compared with the time variation of the observed phase residuals to determine the significance of the ionospheric effect. We have performed such comparisons for all the VLBI sessions analyzed and found typical rms phase variations due to the ionosphere of about 2°-3° for the long ERDE baselines at 8512.99 MHz (the channel with the largest effect). This compares with roughly 5° of total phase scatter (about mean values) at the same frequency. We conclude that the effect of the ionosphere is not insignificant, but, on the other hand, neglect of the effect does not seriously degrade the R&D results given in Table 2. For the ATD series (Table 3), using the narrower standard X-band frequency sequence, ionospheric phase scatters are even smaller, less than about 1° in all channels.

TABLE 4. Relative Ionospheric RMS Phase Variations

frequency channel	rms residual w.r.t. band center * standard	R&D
1	0.54	0.70
2	0.42	0.33
3	0.06	0.37
4	0.65	0.93
5	0.89	0.68
6	0.36	0.03
7	0.30	0.40
8	0.65	0.57

* f_0 = 8390.99 MHz, δf = 143 MHz for standard X-band; f_0 = 8572.99 MHz, δf = 285 MHz for R&D X-band.

Summary of Phase Residual Results

Using the average values listed in Tables 2 and 3, and neglecting possible minor ionospheric contamination, our results from the phase residual analysis can be summarized by

for R&D Mark III X-band (8 channels):

$$\sigma_\phi^2 = (1.27)^2\, \sigma_{th}^2 + (2.2°)^2 \;\Rightarrow\; \sigma_\tau\,(\mathrm{SNR}\to\infty) = 8\ \mathrm{ps}$$

for standard Mark III X-band (8 channels):

$$\sigma_\phi^2 = (1.13)^2\, \sigma_{th}^2 + (1.7°)^2 \;\Rightarrow\; \sigma_\tau\,(\mathrm{SNR}\to\infty) = 12\ \mathrm{ps}$$

For Pie Town baselines, for which VLBA acquisition hardware was used at one station and where only six of the eight R&D frequency channels were observed, the phase residual analysis gives

$$\sigma_\phi^2 = (1.54)^2\, \sigma_{th}^2 + (3.3°)^2 \;\Rightarrow\; \sigma_\tau\,(\mathrm{SNR}\to\infty) = 13\ \mathrm{ps}$$

Results of Differenced Delay Analysis

Doubly differenced delays were computed for each ERDE session using pairs of observations from Westford and Haystack to either Pie Town or Fairbanks. The details of the analysis procedure are discussed in an earlier section. Figure 2 illustrates the results for the ERDE day 25 Oct. for the Westford and Haystack baseline pairs to Pie Town. It is apparent that the overall scatter about a mean is greater than the formal errors would indicate and that there are distinct systematic trends in the double differences. The amounts of added "noise" needed to fit the observed scatter in the double differences are tabulated in Table 5 for each ERDE session, separately using Pie Town or Fairbanks as the distant third station. In determining these values, it has been assumed that the theoretical uncertainties should be rescaled by a factor of 1.27, as found from the phase residual analysis. Estimation of an independent scale parameter from the double differences, in addition to the additive noise floor, was not feasible due to the limited range of theoretical uncertainties that was obtained. The additive noise values given in Table 5 are expressed as degrees of phase at the reference frequency 8212.99 MHz. To convert to units of time delay, the values should be divided by 2.96° per ps.

The results are consistent in implying an additive noise component of about 11-12 ps, with a scatter in the determination of about 4 ps. We interpret this as an observational "floor" for the group delay uncertainty. A corresponding analysis has not been done for the ATD data set, which used the standard X-band frequency sequence, because those experiments did not include a short baseline.

Inspection of the double differences versus time shows that a significant portion of the observed scatter has a systematic character. Likely candidates for such behavior are instrumental error sources that corrupt the phase calibration phases, such as spurious signals, receiver intermodulation, and receiver images [*Rogers*, 1991]. The differential ionospheric delay between Haystack and Westford could conceivably introduce slow variations into the double differences. However, analysis of the S- and X-band phase delays on the Haystack-Westford baseline during ERDE has shown that the rms ionospheric delay on this baseline is less than 1 ps, with peak fluctuations less than 3 ps [*Herring*, 1991], which is negligible. Cross polarization, which is the largest instrumental error source

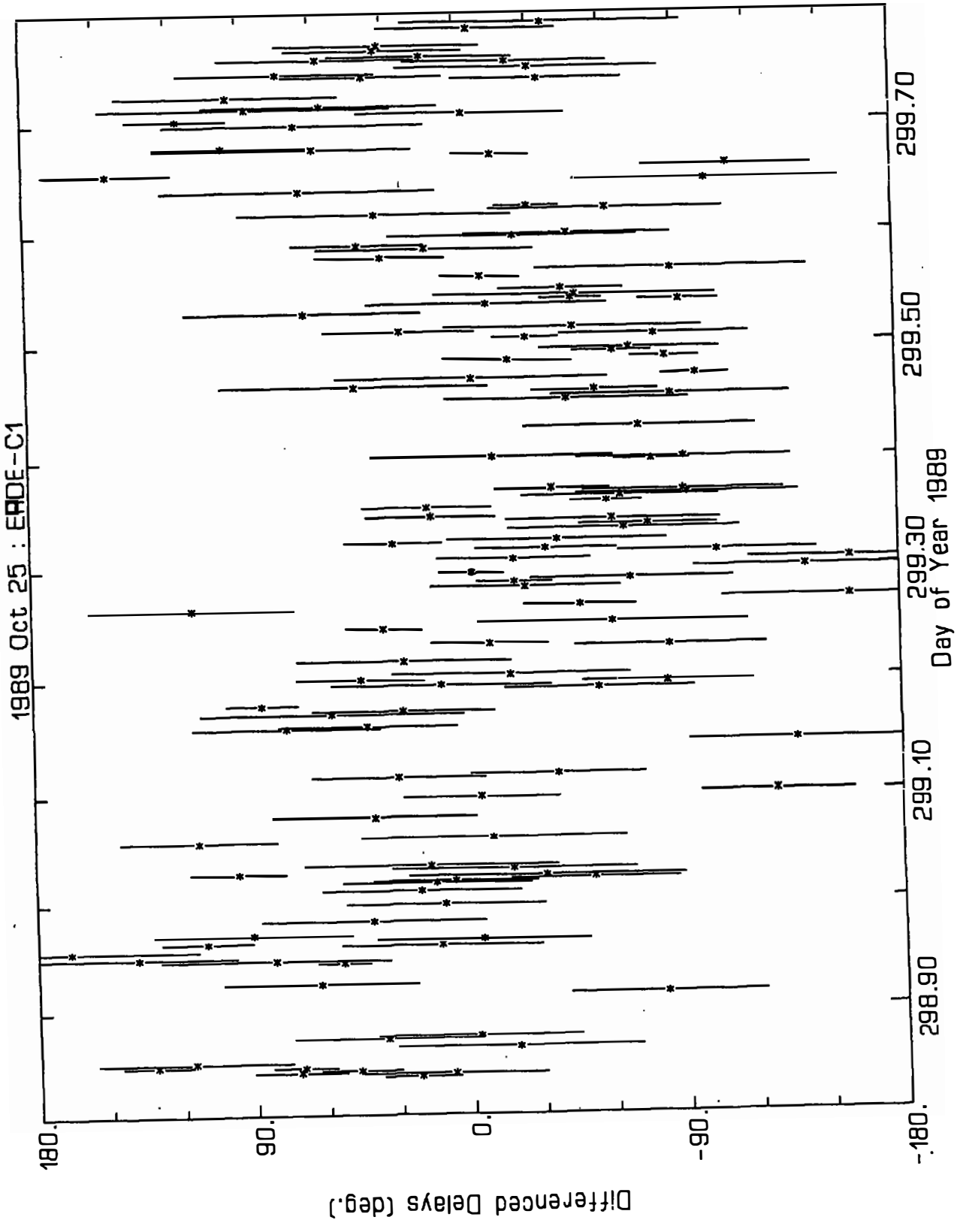

Fig. 2. Doubly differenced delays (expressed in terms of degrees of phase at the reference frequency 8212.99 MHz) for the ERDE baselines Westford-Pie Town and Haystack-Pie Town on 25 Oct. 1989. The error bars are the one-sigma theoretical uncertainties based on SNR.

given by *Rogers*, would be expected to produce delay variations on the time scale of minutes, as the antennas move from one radio source to the next. Such variations should repeat from day to day, however, since the same observing schedule was followed during each ERDE session.

TABLE 5. Added Noise from Double Differences *

ERDE sessions (1989)	Westford, Haystack baselines to: Pie Town	Fairbanks
15 Oct	57.9°	41.0°
16 Oct	–	23.4
17 Oct	27.3	33.2
18 Oct	9.5	33.2
22 Oct	24.4	30.8
23 Oct	30.0	27.5
25 Oct	32.2	35.4
26 Oct	22.4	34.6
27 Oct	34.1	34.9
28 Oct	33.3	35.9
30 Oct	35.9	32.4
31 Oct	35.7	49.6
averages	31.2°	34.3°
	10.5 ps	11.6 ps
std. dev.	11.7°	6.5°
	4.0 ps	2.2 ps

* Empirical uncertainty per baseline observation which, when added in quadrature to 1.27 times the rms standard error, gives the rms scatter of the double differences (see text). Units are degrees of phase at the frequency 8212.99 MHz; 2.96° equals 1 ps. The additive variance determined for the 16 Oct. ERDE session using Pie Town was negative.

In order to investigate the nature of the observed added noise, we used the double differences to construct triply differenced delays of two sorts: (1) 3-station triple differences, each of which is the difference between two double differences from successive days, for the same triplet of stations and the same source at the same hour angle; and (2) 4-station triple differences, each of which is the difference between the Pie Town/Haystack/Westford and Fairbanks/Haystack/Westford double differences for the same scan on the same day. Delay errors that repeat from day to day will be cancelled in the 3-station differences, and station-based instrumental delays (originating at Haystack and Westford) will be cancelled in the 4-station differences. Table 6 lists the noise floors computed from the triple differences for the complete set of ERDE data.

It must be noted that the observational uncertainty is compounded by such successive differencing, which may limit the usefulness of this technique. Typical standard errors for the double and triple differences lie in the range 10°-60° and 20°-80°, respectively. Proper resolution of the phase delay ambiguities is problematical at the upper ends of these ranges. In order to test the sensitivity of our results to the range of standard errors, we repeated the noise floor analyses with an upper bound of 40° on the standard error for each differenced delay. The new data sets contained between one-third and two-thirds as many delays as the original. The results with the truncated data sets are given in Table 6. For all five differenced delay types, the new noise floor is higher, as expected if some of the differenced delays in the complete data sets had their phase delay ambiguities improperly resolved. The noise floor is also increased in all cases if the scale factor for the standard errors is set to unity instead of 1.27; the increase is only 15-20% for the full sets of double differences, but the 4-station triple difference noise floor rises threefold to 20.6° (7.0 ps).

TABLE 6. Added Noise from Differenced Delays *

difference type	all ERDE data		Only diff. delays with $\sigma < 40°$	
PT double diffs.	30.6°	10.3 ps	33.9°	11.5 ps
Fb double diffs.	35.2	11.9	36.5	12.3
PT 3-sta. triple diffs.	21.0	7.1	29.6	10.0
Fb 3-sta. triple diffs.	23.2	7.8	27.1	9.2
4-sta. triple diffs.	6.9	2.3	13.8	4.7

* Empirical uncertainty per baseline observation which must be added in quadrature to 1.27 times the rms standard error to account for the observed scatter in the differenced delays of various types. Units are degrees of phase at the frequency 8212.99 MHz; 2.96° equals 1 ps. PT = Pie Town; Fb = Fairbanks. See text for a description of differenced delay types.

Discussion

Comparison of Results

Our analysis of X-band phase residuals from the group delay fits for doubled bandwidth data implies a delay "noise floor" of about 8 ps. This is a substantial reduction from the corresponding value of 12 ps for the standard X-band frequency sequence although slightly greater than the 6 ps expected theoretically if the performance of all system elements remained unchanged using the wider spanned bandwidth. In fact, the phase stability is somewhat poorer over the broader span, increasing from 1.7° (360 MHz span) to 2.2° (720 MHz span) for the limiting noise figure, accompanied by an increase from 1.13 to 1.27 for the factor which scales the SNR-dependent theoretical uncertainty. Fortunately, the poorer phase stability only partially offsets the improvement obtained by doubling the frequency span so that the observed gain is about two-thirds of the potential benefit. Results from the analysis of group and phase delay differences imply group delay uncertainties no better than about 11-12 ps for the ERDE data set, somewhat larger than the 8 ps floor set by the phase residuals. It is likely that the discrepancy is largely explained by the presence of delay variations within the Mark III data acquisition system that affect the group delays without introducing scatter in the phase residuals. All the error sources listed by *Rogers* [1991] are potential contributors of such delay variations.

Herring [1991] has performed an analysis of the Westford-Haystack data from the ERDE campaign, as well

as from earlier VLBI sessions, which is similar to our differenced delay analysis. He has explicitly resolved the phase cycle ambiguities to determine the geodetic parameters for the 1.2-km baseline. Differences between the group and phase delays have been fit as a function of SNR to give

$$\sigma_\tau^2 = (1.27)^2\, \sigma_{th}^2 + (17\ \text{ps})^2 \quad \text{for R\&D X-band}$$

$$\sigma_\tau^2 = (1.13)^2\, \sigma_{th}^2 + (22\ \text{ps})^2 \quad \text{for standard X-band}$$

Interestingly, the proportionality factors to scale the theoretical uncertainty which are determined by *Herring* agree precisely with the corresponding values found here from the phase residual analysis. We interpret this to mean that the underlying cause of this defect in the group delay theoretical uncertainty is related to excess phase scatter and not to sources of delay variation. On the other hand, *Herring's* floor on the ERDE group delay uncertainty, 17 ps, which is probably dominated by delay-only variations, is larger than our determination from doubly differenced delays, 11-12 ps. The difference may not be significant, however, given the observed scatter of about 4 ps in our result. If we use an intermediate value of 15 ps as the X-band group delay noise floor for the R&D frequency sequence and compare this with the 8 ps value implied by the phase residual scatter, we then infer the existence of about 13 ps of delay-like "noise" (averaged over one-day periods) in excess of that expected from the phase residual scatter.

Two facets of the differenced delay results point to station-based errors (*e.g.*, spurious signals), and not baseline-dependent errors (*e.g.*, polarization impurities), as being the dominant source of excess scatter. First, the noise floors estimated from the Pie Town and Fairbanks double differences are consistent with each other (see Table 5). Because the polarization purity of the VLBA Pie Town antenna feed is superior to that of the feeds used at Fairbanks, Westford, and probably Haystack, and because the differential feed rotation angle between Pie Town and Haystack/Westford varies over only a small range (about 90°) during each ERDE session, a large cross-polarization contribution to the Fairbanks double differences would be expected to make them much larger than the Pie Town double differences, which is contrary to what is observed. Second, of all of the additive noise estimates, the lowest is found for the 4-station triple differences (see Table 6), which are sensitive to baseline-dependent errors. The fact that the additive noise values for the 3-station triple differences are somewhat lower than the double difference values could point to significant cross-polarization effects (which repeat daily), but it may just as well indicate that some portion of the station-based errors also repeats.

Sources of Excess Phase Scatter

Analysis of the phase residuals for the standard X-band frequency sequence indicates a limiting phase stability of about 1.7° per channel. (This result applies to a baseline observation involving a pair of stations so the corresponding phase uncertainty at a single station would be about 1.2° per channel, on average.) In doubling the X-band span, the limiting phase scatter increases to about 2.2° which indicates that the sources of phase variation worsen over the broader span. This is not surprising given that the performance of certain elements of the data acquisition system is known to be poorer over the new frequency range above 8.6 GHz [*Corey and Clark*, 1991]. In particular, fringe amplitudes in this range are generally lower and spurious contributions at the phase calibration frequencies tend to be higher, although there is considerable variation among the stations.

We believe the dominant instrumental error source is spurious signals. *Rogers* [1991] estimates this source to be of moderate importance compared to other contributors, assuming that the spurious signals are no more than -40 dB relative to the phase calibration tones. Our own inspection of the phase calibration phase and amplitude behavior extracted from the ERDE data indicates spurious signal levels much higher than -40 dB. At a minimum, we estimate the spurious signals to be as large as -23.5 dB in the three highest frequency channels at Haystack, -30 to -26 dB in the lowest frequency at Fairbanks, and -35 to -30 dB in the highest frequency at Mojave. The levels at Pie Town cannot be reliably estimated due to the very limited range of variation of the system phase at that station. Only Westford shows no evidence for spurious signals. The spurious signal level at Haystack could cause variations up to ±4° in the measured phases of the affected channels. Some portion of the variation will be absorbed into the group delay estimates, especially when the outer frequency channels are most seriously affected, with group delay errors up to ±15 ps. The problem of spurious signals is tractable and appropriate measures can be taken to identify and attenuate the offending signal sources.

The proportionality error in the theoretical phase uncertainty, denoted as α above, is well determined from the phase residual analysis: 1.13 for the standard X-band frequency sequence and 1.27 for the R&D sequence. Confidence in these values is bolstered by *Herring's* finding of the same results from his comparison of group and phase delays for the Westford-Haystack baseline. We are unable to identify a probable source for this proportionality error. The possibility of an error in the calculation of SNR of the necessary size seems very unlikely, and the different results for standard and R&D frequency sequences would not be explained by such a defect. A scale error in the value of the effective bandwidth span, such as could be imagined due to uneven amplitude distributions across the observing band, might account for the proportionality error for the group delay scatter but cannot explain the phase residual results for which the fringe amplitudes were used as data weights.

Sources of Excess Delay Scatter

Comparison of our differenced delay results with the phase residual analysis implies an excess delay-like

variation of roughly 13 ps (see previous discussion). Our triple difference results and a check for spurious signals indicate that the sources are predominantly station-based and not baseline-dependent. Spurious contributions to the phase calibration signals are clearly important. It appears that they contribute more group delay scatter than expected from the phase residual scatter because the outer frequency channels are preferentially affected. Thus, more of the induced phase variation is absorbed into the group delay estimates than would occur if the spurious signals affected all channels equally or preferentially the interior channels.

Special Considerations for Pie Town VLBA Station

The phase stability of the Pie Town data in ERDE is significantly poorer than for the other stations. Analysis of the Pie Town baselines found a limiting phase noise value of 3.3° per channel compared with 2.2° for the Mark III-only baselines. Converting from baseline results to equivalent station-dependent noise figures, Pie Town contributes about 2.9° of phase noise per channel while the other stations cause only about 1.6°. Several features distinguish Pie Town from the remaining network. The VLBA data acquisition system, which is installed at Pie Town, has not been as thoroughly tested and exercised as the Mark III system which has been in widespread use for more than a decade. The possibility exists for subtle instrumental instabilities that have otherwise gone undetected.

In addition, the frequency switching technique, used at Pie Town to enable fewer instrumental channels to sample a broader bandwidth range, may introduce excess phase scatter at the interior frequencies, which are observed to have greater instability. This explanation is consistent with the much better performance observed at Pie Town during the single ATD session where a subset of the standard X-band sequence was used without frequency switching. On the other hand, however, in an examination of simultaneous ERDE S-band data from Pie Town, where frequency switching was also used, the residual phase scatter was somewhat less than for the Mark III stations. This observation would seem to eliminate frequency switching *per se* as the primary cause of the poorer stability.

Based in part on our results for the Mark III stations, we speculate that spurious signals may be responsible for the Pie Town phase residual results. The phase calibration phase and amplitude values extracted from the ERDE data, however, cannot be used to test this hypothesis because the range of instrumental phase variation is too small to clearly distinguish the effects of spurious signals.

Effectiveness of Wider X-band Span

Based on the phase residual analysis, implementation of expanded bandwidth coverage at X-band has been largely effective in accomplishing the desired reduction in measurement uncertainty. The inferred group delay noise floor due to phase scatter drops from about 12 ps for the standard frequency sequence to about 8 ps with the doubled span. The observed group delay scatters have a higher floor, about 11-12 ps based on our analysis of group-phase delay differences for doubled X-band bandwidth; *Herring* [1991] finds a somewhat higher floor of 17 ps for the R&D frequency sequence. In any event, this floor, like that inferred from the phase scatter, is also improved over the standard frequency sequence, according to *Herring*, who reports a limiting group delay scatter of about 22 ps for this case. We conclude, therefore, that the wider bandwidth span demonstrated in the ERDE campaign has been substantially effective. However, spurious signals at the phase calibration frequencies are widespread and often much stronger than the -40 dB specification. These are probably the primary component of the observed phase and group delay "noise" floors.

Acknowledgements. Tom Herring kindly provided his phase connection results for the Westford-Haystack baseline in advance of their publication and has offered numerous helpful suggestions, for which we are indebted. This work benefitted greatly from our many discussions with Tom Clark and Alan Rogers, who pointed out the possible significance of ionospheric contributions to the phase residuals of the widened X-band. Bob Potash, Dan MacMillan, and Dave Shaffer provided helpful critiques. The Pie Town data were made possible by the VLBA and the National Radio Astronomy Observatory, which is operated by Associated Universities, Inc. under cooperative agreement with the National Science Foundation.

References

Clark, T.A., *et al.*, Precision geodesy using the Mark-III very-long-baseline interferometer system, *IEEE Trans. Geosci. Remote Sens.*, *GE-23*, 438-449, 1985.

Clark, T.A., W.G. Melbourne, Ch. Reigber, L.E. Young, and T.P. Yunck, Instrumentation: Microwave techniques, in *Proceedings of an International Workshop held at Erice, The Interdisciplinary Role of Space Geodesy, Lecture Notes in Earth Sciences* (I.I. Mueller and S. Zerbini, eds.), vol. 22, Springer-Verlag, Berlin, 148-162, 1989.

Corey, B.E., and T.A. Clark, The RF bandwidth upgrade: Doubling the X-band spanned bandwidth of geodetic VLBI receiving systems, this volume, 1991.

Davis, J.L., T.A. Herring, and I.I. Shapiro, Effects of atmospheric modeling errors on determinations of baseline vectors from very long baseline interferometry, *J. Geophys. Res.*, *96*(B1), 643-650, 1991.

Herring, T.A., Precision and accuracy of intercontinental distance determinations using radio interferometry, Ph.D. thesis, Massachusetts Institute of Technology, Cambridge, 1983.

Herring, T.A., Submillimeter horizontal position determination using very long baseline interferometry, submitted to *J. Geophys. Res.*, 1991.

Herring, T.A., T.A. Clark, and A.E.E. Rogers, Very long baseline interferometry, in *Solid Earth Sciences in the 1990s. Vol. III Measurement Techniques and Technology Panel Report*, NASA, Greenbelt, MD, 56-66, 1991 (in press).

Hinteregger, H.F., *et al.*, Precision geodesy via radio interferometry, *Science*, *178*, 396-398, 1972.

MacMillan, D.S., and J.R. Ray, Current precision of VLBI vertical determinations, this volume, 1991.

Rogers, A.E.E., Very-long-baseline interferometry with large bandwidth for phase-delay measurements, *Radio Sci.*, *5*, 1239-1248, 1970.

Rogers, A.E.E., Instrumental improvements to achieve millimeter accuracy, this volume, 1991.

J.R. Ray, Interferometrics Inc., GSFC/NASA, Code 926.9, Greenbelt, MD 20771 (jrr@bootes.gsfc.nasa.gov).

B.E. Corey, Haystack Observatory, Westford, MA 01886 (bec@wells.haystack.edu).

Sensitivity of Geodetic Parameter Estimates to the Assumed Distribution of the "Wet" Troposphere

C.E. Kuehn and D.S. MacMillan

The analysis discussed in this paper grew out of a sensitivity analysis performed in January 1991. In that sensitivity analysis we compared the effects of systematic errors in wet and dry mapping functions in VLBI atmosphere models on baseline length measurements.

In VLBI analyses the total atmosphere propagation delay, $L(\epsilon)$, at elevation, ϵ, at each station is represented as the sum of two terms:

$$[1] \qquad L(\epsilon) = Z_{dry} \cdot m_{dry}(\epsilon) + Z_{wet} \cdot m_{wet}(\epsilon)$$

In this equation, Z is the zenith delay, m is the mapping function, and the subscripts indicate the "dry" (hydrostatic) and "wet" components of the delay. Typically, the dry zenith delay is calculated from the ground pressure [Saastamoinen, 1972] and the wet zenith delay is parameterized (either stochastically or with a simple deterministic function) and estimated using the VLBI group delay data. A typical hydrostatic mapping function used in VLBI analysis is CfA2.2 [Davis et al., 1985]. Two common functions that have been used for the wet mapping function are the Chao wet and Chao dry mapping functions [Chao, 1974]. In figure 1, we have plotted these two mapping functions (in units of airmass) as a function of elevation. Although different models of the elevation dependence of propagation corrections for the wet and dry atmosphere constituents have been available for many years, it has often been assumed that the form of the wet mapping function, $m_{wet}(\epsilon)$, did not matter to VLBI analyses because: (1) the zenith dry delay is an order of magnitude larger than the zenith wet delay, and (2) the zenith wet delay is dynamically estimated in the VLBI analysis procedure.

The sensitivity analysis demonstrated that for R&D 90 VLBI schedules, a 2 cm dry zenith path delay error (i.e. either a barometer pressure offset of about 10 mbar or an approximately 75 m error in the vertical position offset between the VLBI reference point and the barometer) would induce a systematic error of 3 mm in the length of 4000 km baselines assuming the atmosphere model of equation 1. If the wet mapping function, $m_{wet}(\epsilon)$, were replaced with $m_{dry}(\epsilon)$ in equation 1, this systematic error would not occur. In that case, however, a 1-2 cm systematic error would be induced on 4000 km baselines assuming a nominal 10 cm zenith wet delay.

From the sensitivity analysis, it is clear that systematic errors in baseline lengths at the 1-2 cm level (5-10 mm for IRIS 88 schedules) could arise from using an incorrect form of the wet mapping function. In figure 1, we compare two forms of the wet mapping function. Also plotted, for comparison, is the "mapping function" arising from a homogeneous spherical shell of height h about the earth (radius R):

$$[2] \quad m_{sphere}(\epsilon) = -(R/h) \cdot \sin\epsilon + [(R/h)^2 \cdot \sin^2\epsilon + 2 \cdot (R/h) + 1]^{1/2}$$

The Chao dry mapping function is close to equation 2, with h=12 km; the Chao wet mapping function is close to equation 2, with h=3 km.

We analyzed the complete set of VLBI experiments (1374 sessions between 8/79 and 12/90) using the Chao dry mapping function and the Chao wet mapping function for $m_{wet}(\epsilon)$ in equation 1. CfA2.2 was used for $m_{dry}(\epsilon)$ in equation 1; only observations above 5° elevation were included in the analysis. Baseline lengths measured with the Chao wet mapping function are longer than those determined using the Chao dry mapping function (see figure 2). The sense of the scale error of 1.7 ppb is to yield better agreement between SLR and VLBI results when the Chao wet mapping

function is used.

In figure 3, we have plotted the difference in the repeatability of baseline length measurements from the two analyses (Chao wet and Chao dry for the wet mapping function, $m_{wet}(\epsilon)$, in equation 1) as a function of baseline length. We define repeatability as the weighted rms scatter of the residuals of baseline length measurements fit to an offset and a rate. We have plotted results for those baselines measured at least 20 times during the period 8/79 through 12/90. We see that the repeatability is clearly better (smaller rms scatter) when the Chao wet form of the wet mapping function is used.

We now examine in more detail the results from the two solutions for a single, well-measured IRIS baseline, Westford-Wettzell. In figure 4, we have plotted the difference in the Westford-Wettzell baseline length measurements for the two solutions as a function of time. We see a strong seasonal signal in this figure. Clearly the two solutions are much more alike during the winter. In the summer the Westford-Wettzell baseline length obtained using the Chao wet mapping function is longer than that determined using the Chao dry mapping function. The difference between the two solutions is more pronounced after 1988, when lower elevation observations were added to the IRIS schedule. In figure 5, we again plot the baseline length difference, but in this case we have restricted the analysis, for the entire set of 1374 VLBI sessions, to observations above 10° elevation. In this case there is no enhancement of the seasonal trend after 1988.

Returning to figure 4, we note that the baseline length evolution of the two solutions is 14.7 ± 0.3 mm/yr (Chao dry) and 16.3 ± 0.3 mm/yr (Chao wet). The evolution of the difference between the two solutions, 1.6 mm/yr, is shown as the dashed line in figure 4 and arises from the inclusion of low elevation observations in IRIS schedules after 1988.

The repeatability of the Westford-Wettzell baseline length in the two solutions is 12.2 mm (Chao dry) and 11.7 mm (Chao wet). The Chao dry solution has 3.5 mm more scatter (in the rss sense) than the Chao wet solution. The solid line in figure 4 is the weighted mean of the differenced baseline length measurements within a 60-day window (nominally 13 measurements). The wrms scatter of the differenced, smoothed (60-day mean) baseline length measurements about the dashed line is 3.4 mm. This leads us to conclude that the repeatability difference between the Chao dry and Chao wet solutions is due to a seasonal systematic in the baseline length measurements determined in the former (Chao dry) solution.

Systematic errors in atmosphere models can also be investigated through solutions that discard data below some minimum elevation angle. This approach capitalizes on the idea that elevation dependent systematic errors in atmosphere models will have a stronger effect on solutions that include data at lower elevations. In figure 6, we have plotted the difference in repeatability as a function of baseline length for two solutions: one with a 5° low elevation limit (the Chao wet solution of figures 2 through 5) and one with a 10° low elevation limit. Both solutions used the Chao wet form of the wet mapping function, $m_{wet}(\epsilon)$, in equation 1. In general, the repeatabiltiy is better (smaller scatter) when the low elevation observations are included in the analysis. This leads us to conclude that the atmosphere model used in these solutions, CfA2.2 (dry) and Chao wet (wet), is no worse at 5° elevation than at 10° elevation.

In figure 7, we compare the results of elevation cut-off tests on the Westford-Wettzell baseline for solutions using Chao wet and Chao dry for the wet mapping function, $m_{wet}(\epsilon)$. The solid line is the difference in the Westford-Wettzell baseline lengths from the 5° and 10° elevation limited solutions of figure 6, both of which were analyzed with the Chao wet form of the wet mapping function. The baseline length differences are plotted as a function of time. The dashed line is again the baseline length difference between 5° and 10° elevation limited solutions, but for solutions analyzed with the Chao dry form of the wet mapping function. It is clear from figure 7 that the elevation cut-off tests reveal seasonal trends in the Westford-Wettzell baseline length measurements. It is also clear that these seasonal effects are reduced by using the Chao wet instead of the Chao dry form of the wet mapping function in the VLBI analysis. The solid line (Chao wet solutions) of

figure 7 is replotted with a smaller vertical scale in figure 8. In general, the 5° elevation limit solution baseline lengths are shorter than the 10° elevation limit solution baseline lengths in the summer and longer in the winter.

In figure 9, once more we have plotted the solid line of figure 7 (Chao wet solutions), together with the baseline length difference from another elevation cut-off test. In the new solutions (dashed line) we have used the same Chao wet form of the wet mapping function, but have modified the CfA2.2 dry mapping function, $m_{dry}(\epsilon)$. In the default CfA2.2 dry mapping function, the tropopause height and lapse rate are 10 km and -5.6 K/km; the modified values are 12 km and -7 K/km. Typical values for Westford in the summer are 12 km and -6 K/km, and in the winter 10 km and -5 K/km. Figure 9 suggests that the seasonal variation in the elevation cut-off tests may be further reduced by using parameters in the CfA2.2 dry mapping function that are "tuned" for the appropriate season, together with the Chao wet form of the wet mapping function.

In conclusion, we have found that (1) better baseline length repeatabilities are obtained with lower (Chao wet, h = 3 km, eqn 2) rather than higher wet mapping function scale heights (Chao dry, h = 12 km, eqn 2). For 4000 km baselines, wrms scatter in geodetic parameters is reduced by 2.5 mm (length) and 5.2 mm (inferred vertical). We have also found that (2) changing the scale height of the wet mapping function induces seasonal variations in baseline lengths that are strongly elevation dependent. Such elevation dependent effects will affect VLBI baseline rate determinations because low elevation coverage in VLBI schedules has changed over the years. Lowering the wet scale height (moving from Chao dry to Chao wet for the wet mapping function) brings VLBI Atlantic baseline rates into closer agreement with the NUVEL model. Finally, (3) baseline lengths are sensitive to the choice of wet mapping function. Lowering the wet scale height increases the scale of the VLBI reference frame, reducing the VLBI/SLR discrepancy by about 2 ppb.

References

Chao, C.C., The Tropospheric Calibration Model for Mariner Mars 1971, *JPL Technical Report 32-1587*, 1974.

Davis, J.L., et al., Geodesy by radio interferometry: Effects of atmospheric modeling errors on estimates of baseline length, *Radio Science, 20(6)*, 1593-1607, 1985.

Saastamoinen, J., Atmospheric Correction for the troposphere and stratosphere in radio ranging of satellites, in *The Use of Artificial Satellites for Geodesy, Geophys. Monogr. Ser.*, vol. 15, ed. by S.W. Henriksen et al., 247-251, AGU, Washington, D.C., 1972.

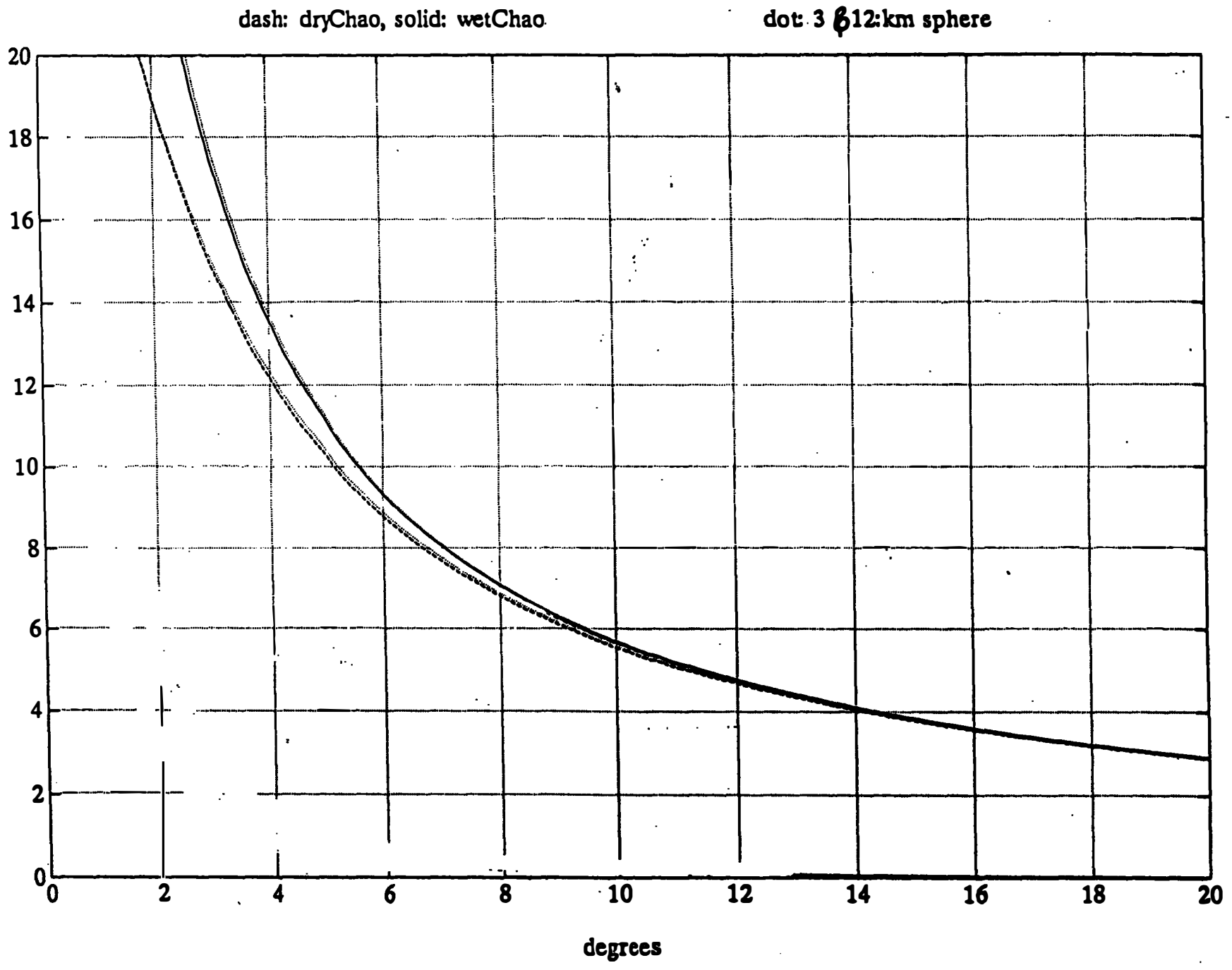

Figure 1

mapping function in airmass

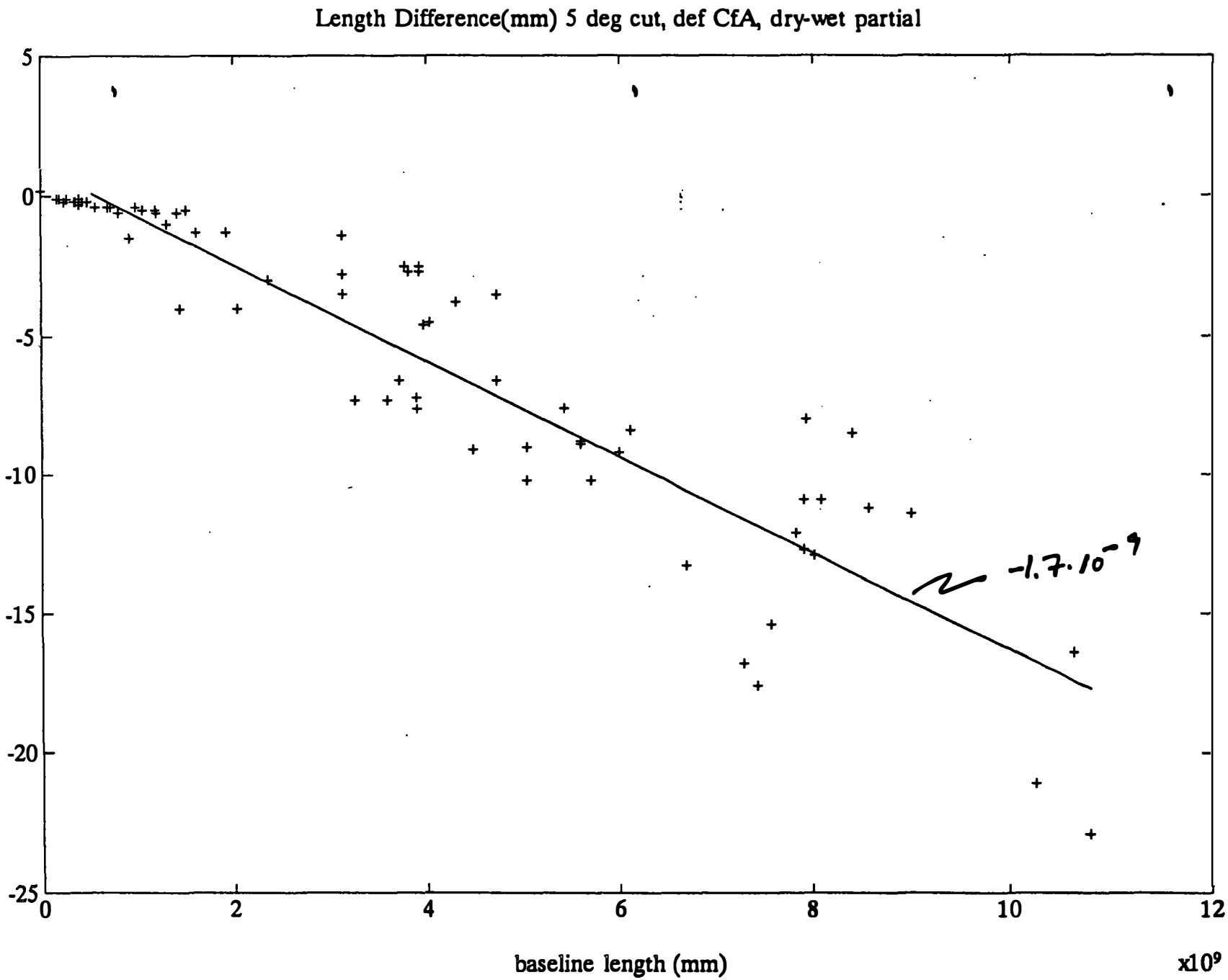

Length Difference (mm); wet partial means longer baselines

Figure 2

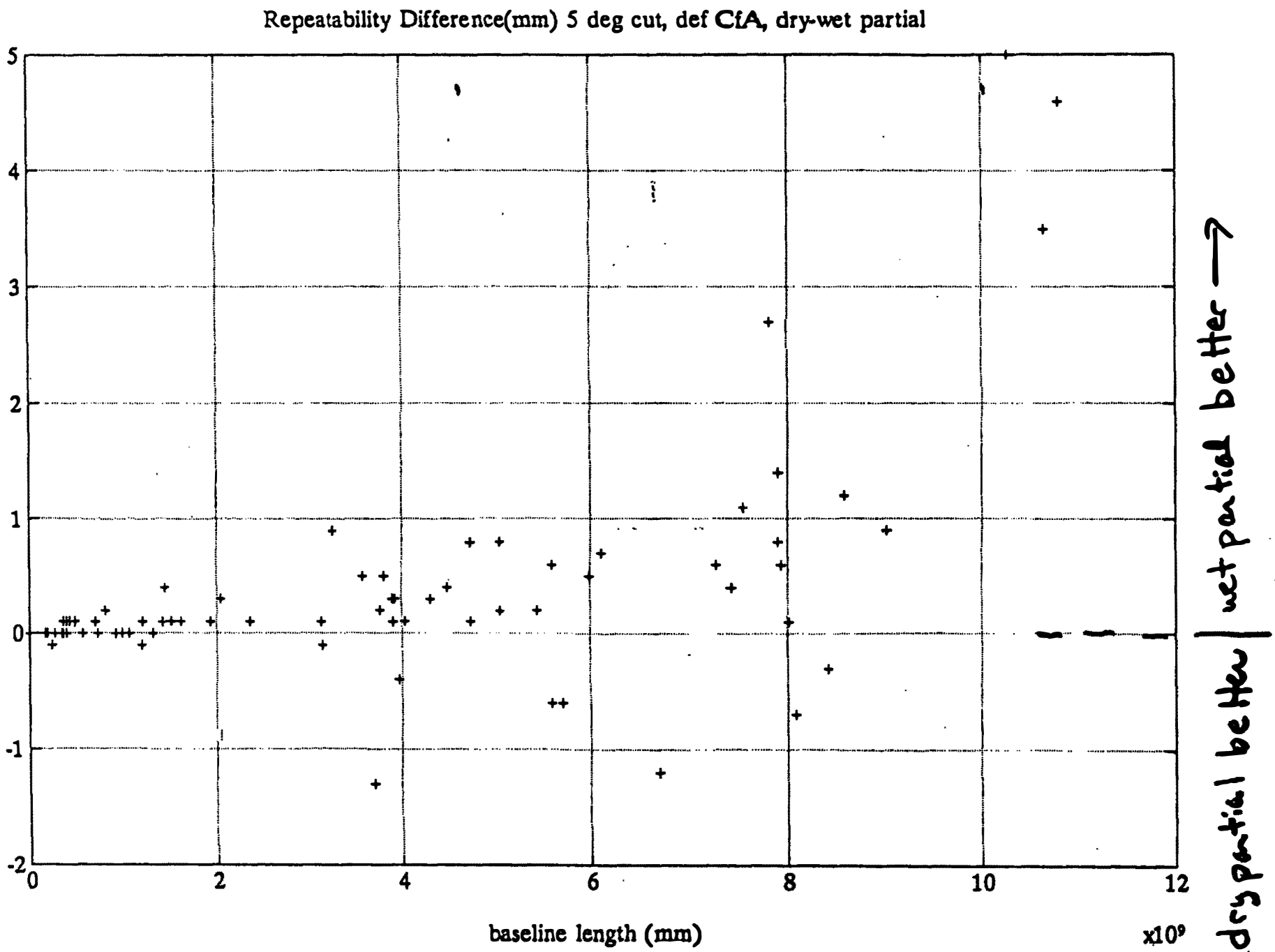
Repeatability Difference(mm) 5 deg cut, def CfA, dry-wet partial
5
4
3
2
1
0
-1
-2
0
2
4
6
8
10
12
baseline length (mm)
x10⁹
wrms(dry partial)-wrms(wet partial)
← dry partial better
wet partial better →

Figure 3

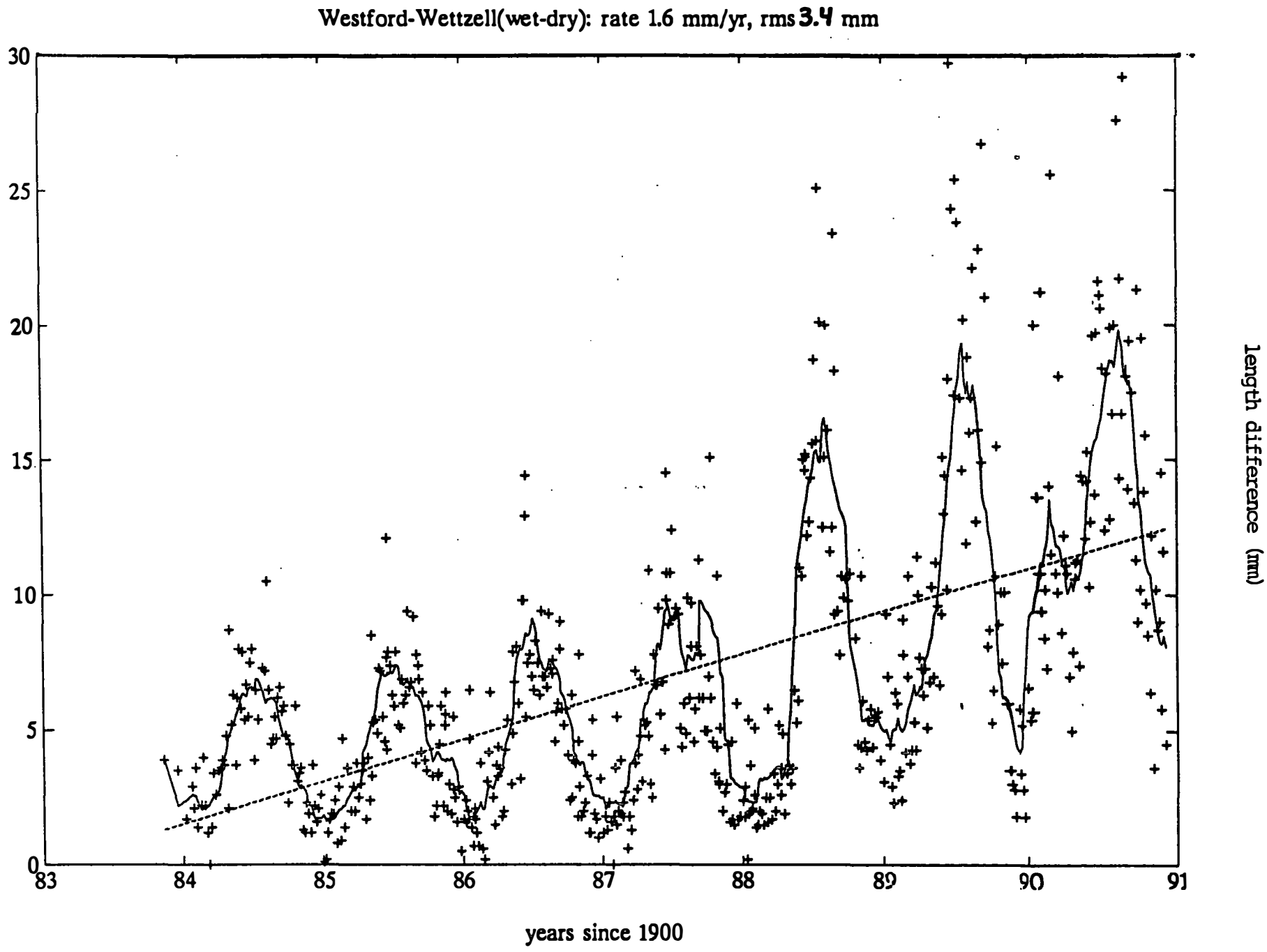
Westford-Wettzell(wet-dry): rate 1.6 mm/yr, rms 3.4 mm
length difference (mm)
years since 1900
0
5
10
15
20
25
30
83
84
85
86
87
88
89
90
91

Figure 4

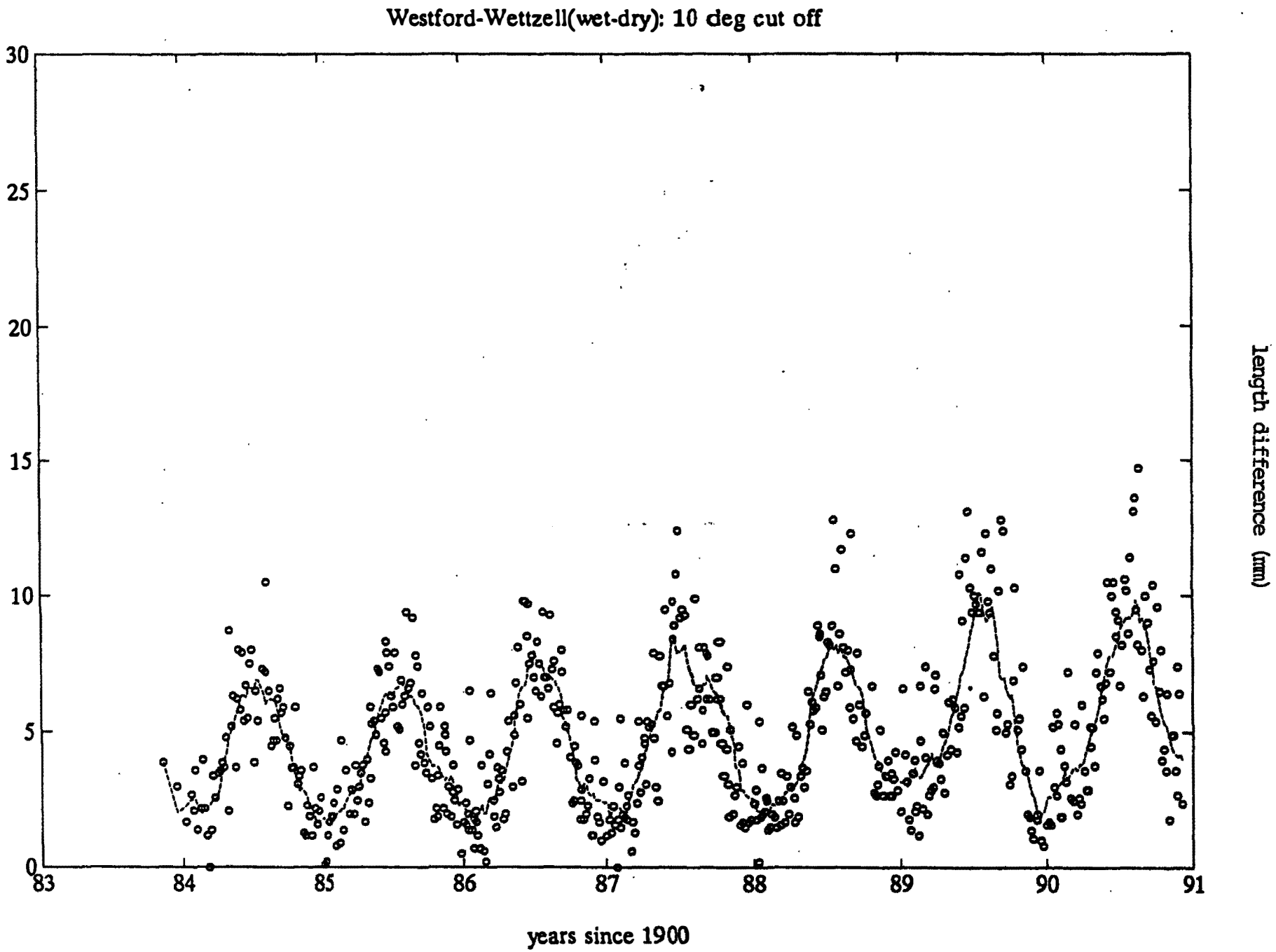
Westford-Wettzell(wet-dry): 10 deg cut off
length difference (mm)
years since 1900
0
5
10
15
20
25
30
83
84
85
86
87
88
89
90
91

Figure 5

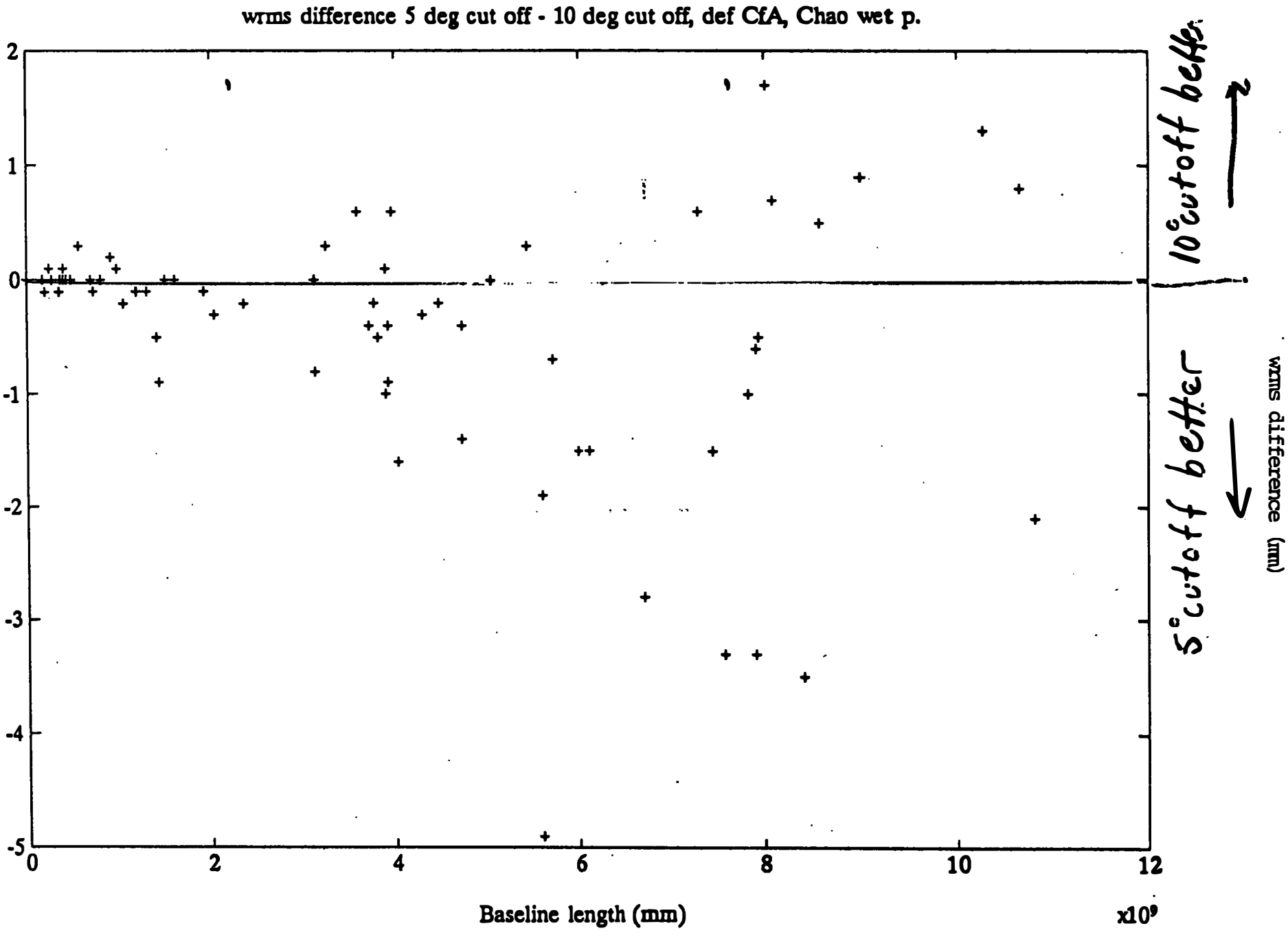
wrms difference 5 deg cut off - 10 deg cut off, def CfA, Chao wet p.
2
1
0
-1
-2
-3
-4
-5
0
2
4
6
8
10
12
Baseline length (mm)
x10⁹
wrms difference (mm)
10° cutoff better
5° cutoff better

Figure 6

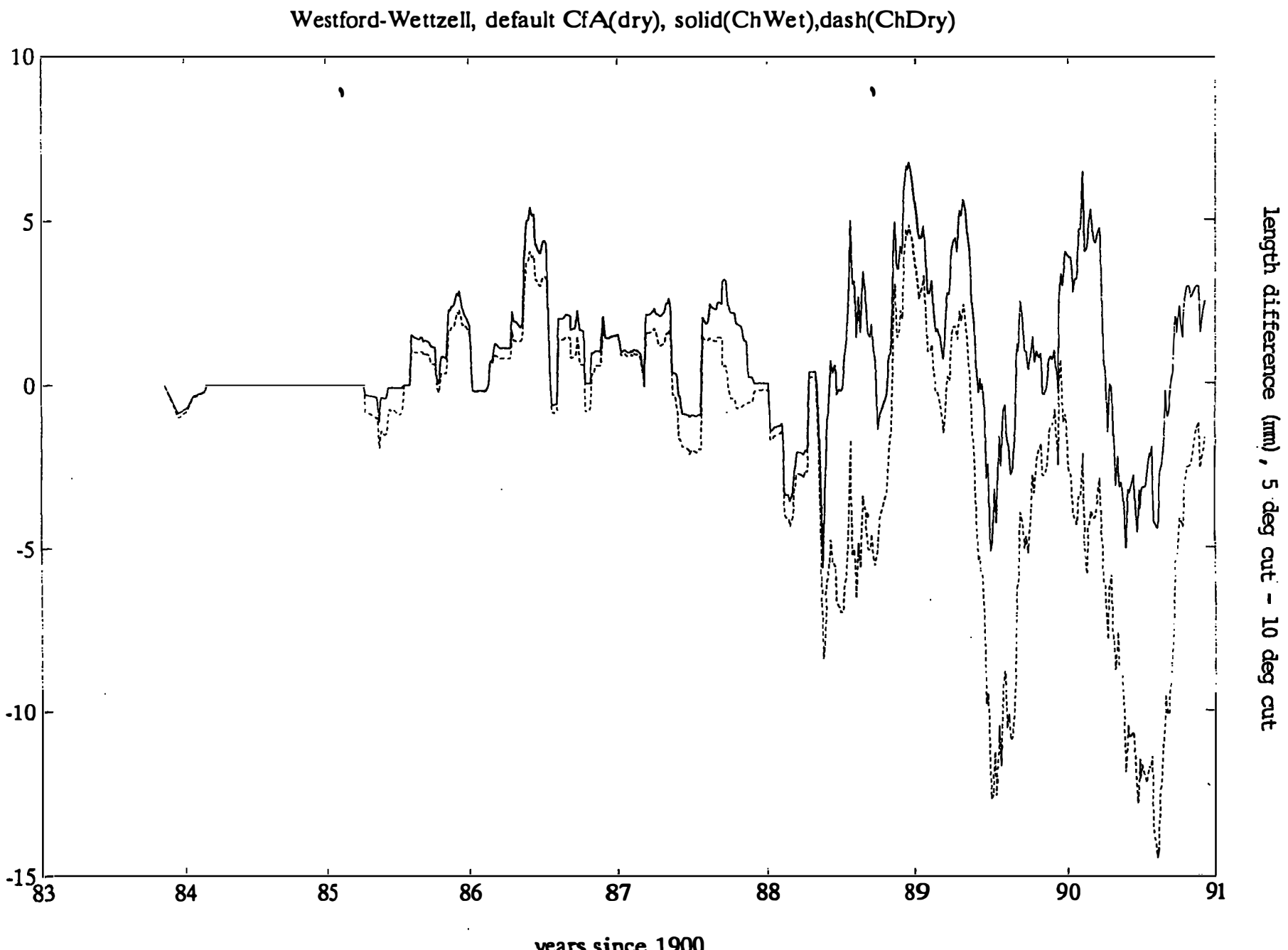
Westford-Wettzell, default CfA(dry), solid(ChWet),dash(ChDry)
10
5
0
-5
-10
-15
83
84
85
86
87
88
89
90
91
years since 1900
length difference (mm), 5 deg cut - 10 deg cut

Figure 7

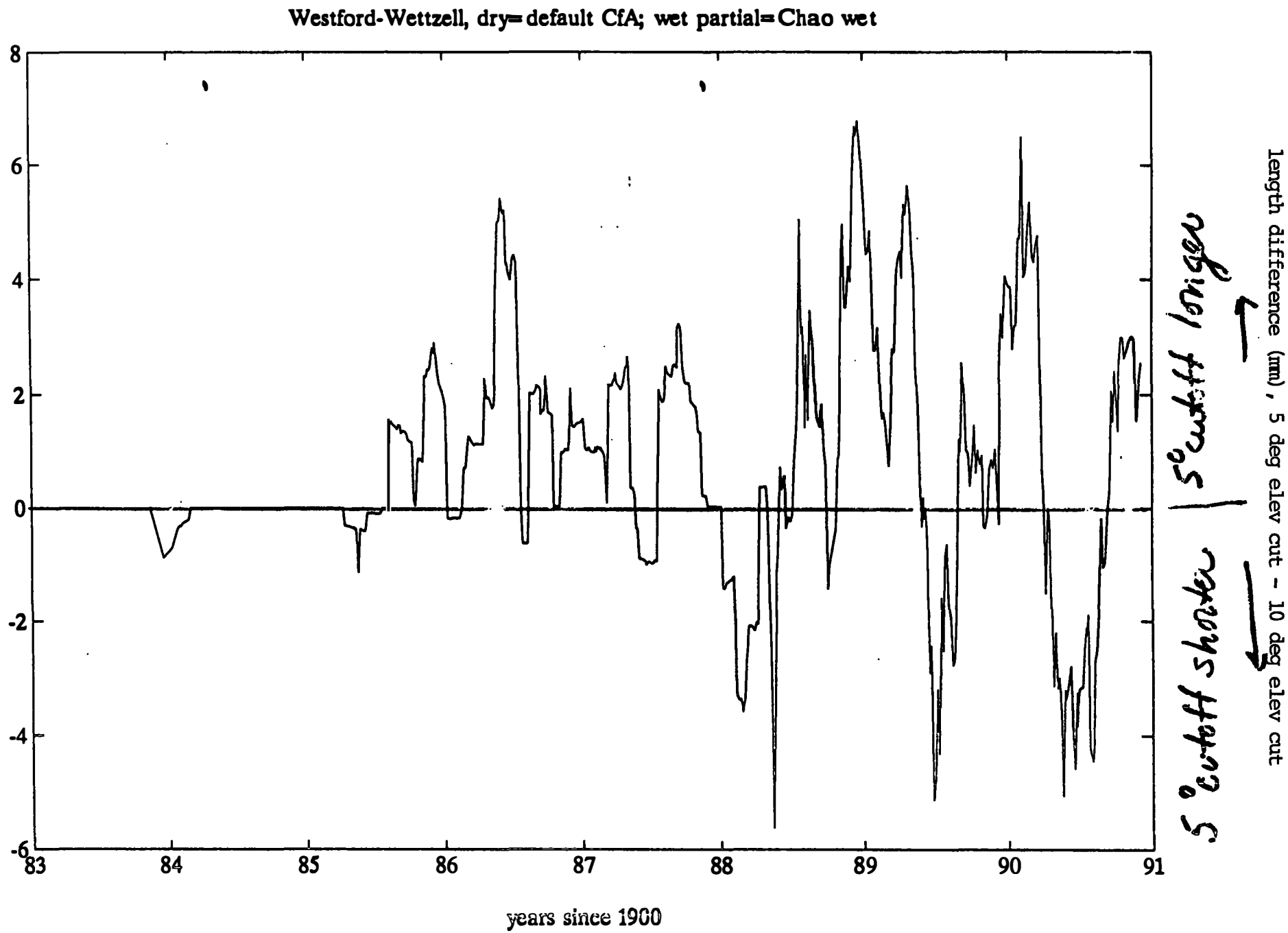
Westford-Wettzell, dry=default CfA; wet partial=Chao wet
length difference (mm), 5 deg elev cut - 10 deg elev cut
8
6
4
2
0
-2
-4
-6
83
84
85
86
87
88
89
90
91
years since 1900
negative length
5° elev cutoff
positive length
10° elev cutoff

Figure 8

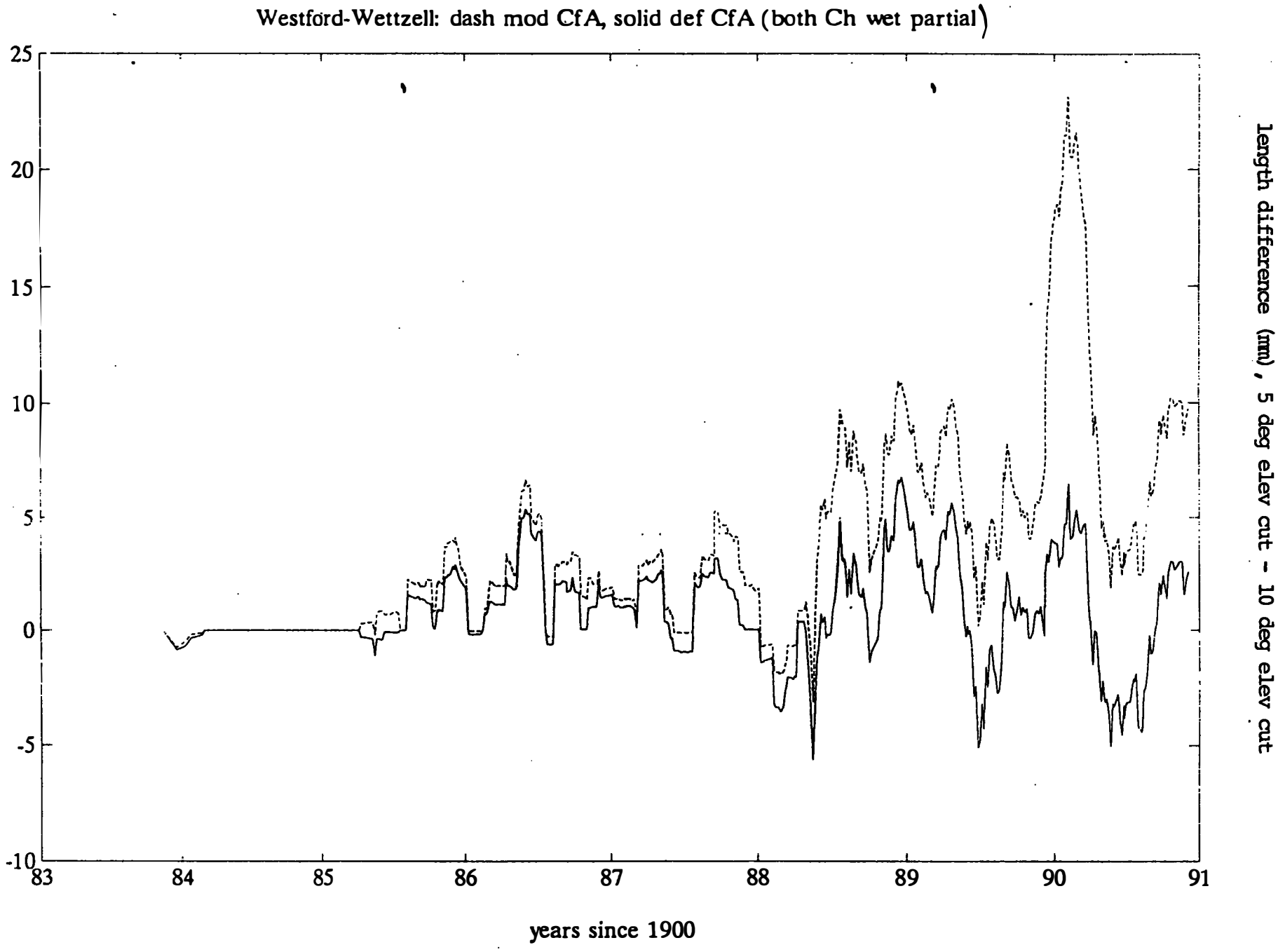
Westford-Wettzell: dash mod CfA, solid def CfA (both Ch wet partial)
25
20
15
10
5
0
-5
-10
83
84
85
86
87
88
89
90
91
years since 1900
length difference (mm), 5 deg elev cut - 10 deg elev cut

Figure 9

Vertical Change and Atmosphere Correction in VLBI

A.E.Niell
Haystack Observatory, MIT
Westford, MA 01886

For a series of eighteen geodetic VLBI experiments spanning 1987 and 1988 correction for the dry atmosphere propagation delay was made two ways: 1) an analytic mapping function and 2) raytracing of radiosonde data. The use of raytracing to calculate 'priori' dry delays reduced the annual variation of length on baseline to Alaska by reducing vertical change, compared to using the CfA2.2 dry mapping function. Simple simulations are used to calculate sensitivities to errors in mapping function: approximately half of the error of the estimated atmospheric path delay at the lowest elevation goes into the vertical. The presence of horizontal gradients in the atmosphere can produce errors in either the horizontal or vertical or both, depending on the symmetry in azimuth of the observations. These considerations influenced the design of the geodetic R&D network and schedule for 1991.

1. INTRODUCTION

The theoretical *precision* of the estimate of the local vertical coordinate of a geodetic VLBI station improves as the minimum observed elevation angle at that station decreases. Unfortunately, errors in the atmosphere model increase so the repeatability may be degraded (Davis et al. 1985, Herring 1986).

In order to take advantage of the better precision to be obtained from lower elevation observations, Lanyi (1984) and Davis et al. (1985) developed improved mapping functions for the dry component of the atmosphere. Lanyi's approach offers a potentially superior performance since it allows for an isothermal layer characterizing the temperature profile. If no isothermal layer is specified, the results agree well with the mapping function of Davis *et al.* (1985), designated CfA2.2. Both require assumptions or additional information about the lapse rate and tropopause height, but otherwise depend only on surface meteorology. For certain climates, assumed average values of the additional parameter of Lanyi may, without additional knowledge, provide better average performance than CfA2.2. Because the majority of the data of the NASA Crustal Dynamics Project has been analyzed with CfA2.2, it will be studied in this paper. The conclusions should apply to Lanyi, used in a default mode, also.

From elevation cut-off tests performed on the series of Low-El observations analyzed with CfA2.2 Davis et al. (1991) estimated that remaining vertical errors due to unmodeled atmosphere (mapping function errors) were less than 19 mm rms. Furthermore, the combination of this mapping function with a stochastic estimation of the atmosphere wet zenith delay was shown to give good agreement with short-term variations in water vapor delay as measured by a Water Vapor Radiometer, at a level of less than 10 mm (Herring *et al.* 1990 (HDS), Elgered *et al.* 1991).

Since the time those tests were performed, the precision of the VLBI measurements has improved considerably and observing techniques have matured. As a consequence the accuracy and usage of an analytic mapping function needs to be re-examined. Davis *et al.* (1985) indicated areas in which CfA2.2, which is used for correction of the dry (or hydrostatic) component, could be improved, and both the dry and wet mapping functions as currently implemented suffer shortcomings. 1) In practice, although dictated primarily by software limitations, the lapse rate and troposphere height of the dry mapping function are assumed to be site-independent, or, if site-dependent, to be constant in time. 2) The wet mapping function normally used, Chao "wet" (1972), is independent of any external information, such as local, seasonal, or site-specific meteorological conditions. The primary effects of these problems are 1) to introduce a station dependent bias in the estimation of the local vertical station position and 2) to produce a seasonal variation in station height. The latter arises primarily from departures of the surface temperature from that expected by extrapolating downward from altitudes greater than a few kilometers. These effects can be demonstrated by comparing the results obtained using an analytic mapping function to results obtained with atmosphere corrections made using radiosonde data. In this paper I will 1) describe a simulation that indicates the sensitivities of station position estimation to errors in mapping functions in the absence of horizontal gradients, 2) present the difference between radiosonde raytrace correction and CfA2.2 mapping function for the dry atmosphere using data from the eighteen Analysis and Technique Development (ATD) experiments of the NASA Crustal Dynamics Project which were carried out in 1987-1988, and 3) describe a simulation that demonstrates the effect of a horizontal gradient of refractivity on station position estimation if the gradient is not taken into account.

2. SENSITIVITY TO DRY MAPPING FUNCTION ERROR

What is the sensitivity of the estimate of the local vertical at a VLBI station to an error in the mapping function? Does the sensitivity depend on the minimum observed elevation angle at a station?

To investigate these questions I constructed a simple one-station group delay model for which I estimated the three local components of position, a three parameter clock model (offset, rate, and acceleration), and the zenith atmospheric path delay. I approximated the properties of an observing schedule of a current R&D program by assuming that sixteen scans could be made in one hour, and that these observations are well distributed in azimuth and elevation. Four observations were made at each azimuth of 45°, 135°, 225°, and 315° at elevations of 80°, 40°, 12°, and either 10°, 8°, or 5°. Nominal surface meteorology parameters were assumed, and CfA2.2 was used to calculate the partial derivatives for the estimation of the zenith path delay. No wet component was introduced. To simulate a difference between the true atmosphere and an imperfect model, "observed" residual delays were calculated by introducing an error of -10°C in the surface temperature used by the mapping function. All observations were given an uncertainty of 1 mm. If no errors were introduced by the imperfect model, the estimated correction to the input parameters (position, clocks, and atmosphere) would be zero. In this test the horizontal station position corrections were much less than one mm, but the departures from zero of the estimated vertical positions were quite large. The results are summarized in the first three numerical rows of Table 1.

Table 1. Elevation dependence of vertical error due to atmospheric model error.

Minimum elevation (degrees)	Excess atmospheric path at the minimum elevation (mm)	Vertical error introduced [1] (mm)	Uncertainty in vertical estimate (mm)
10.0	15	9	2.6
8.0	27	16	2.4
5.0	79	48	1.4
5.0/30.0	79	39[2]	1.7

[1] East and north coordinates estimated to be less than one mm except as noted.
[2] East coordinate estimated to be +6 mm.

As the minimum observed elevation is reduced from 10° to 5°, the uncertainty in the estimate of the station vertical decreases by almost 50%. However, the estimate of the vertical position error increases from 9 mm for a minimum elevation of 10° to 48 mm for a minimum elevation of 5°. In all of the cases the vertical position error is about 60% of the path length error at each of the lowest observed elevations. Thus, if this sensitivity were applicable to complete analysis of real data, the rule of thumb would be that approximately half of the path length error at the lowest observed elevation would appear as a height error.

For baseline greater than a few hundred kilometers in length the minimum observed elevation may not be the same for all azimuths (depending on the location of other stations in the VLBI network). This will introduce an error in the station position estimate in a different direction than that for an incorrect mapping function. I have mimicked the observing pattern for the Westford antenna for a VLBI array which includes other stations to the west, allowing a minimum elevation of only 30° to the east while maintaining the distribution down to 5° in the west. For observed elevations of 80°, 50°, 40°, and 30° at azimuths 45° and 135° the results of the simulation are given in the fourth row of Table 1 and labeled '5.0/30.0'. While reducing the sensitivity for the vertical error (39 mm instead of 48 mm for the same excess path of 79 mm), an error of 6 mm is introduced into the estimate of the east coordinate. Thus, even though both the model atmosphere and the mapping function are independent of azimuth, the asymmetry of the observing sequence combined with the error in mapping function introduces both a vertical and a horizontal error in the estimated position. It is important to note that this error depends strongly on the lowest observed elevations and not some average around the horizon.

Unfortunately, most VLBI networks do result in an azimuthally asymmetric distribution of minimum elevations for most stations, due either to the lack of surrounding stations, or, as in the case of HRAS_085 and other similar antennas, due to the equatorial mount and limited hour angle coverage. The impact, however, depends on the actual geometry and on the magnitude of the mapping function error. The effect on the ATD experiments will be described in the next two sections.

3. THE ATD EXPERIMENTS

Monthly in 1987 and bi-monthly in 1988, geodetic VLBI measurements were made using antennas of the NASA Crustal Dynamics Project at Westford, Massachusetts; Ft. Davis, Texas (HRAS_085); Mojave, California; and Gilmore Creek, Alaska (Gilcreek). An observing schedule was written using extensive sub-netting to allow each antenna maximum sky coverage, rather than restricting observations to the union of sky visible to all antennas. In addition several successive scans were made at the lowest elevations possible in order to provide redundancy for the most significant observations and to increase the sensitivity of the vertical estimation. This latter practice followed that established by the LO_EL observations using Westford and Mojave (Davis, *et al.* 1990) to which the ATD program was a follow-on. Several improvements resulted from the addition of the antennas in Texas and Alaska. 1) The sky coverages at Westford and Mojave were improved; 2) the average delay precision of all observations was improved and more scans were obtained during the twenty-six hours of each experiment due to the much better sensitivity of the added larger antennas.

Of the eighteen experiments Westford and Mojave obtained data in all, Gilcreek missed one, and Ft. Davis missed four, leaving thirteen with data from all four stations. Typical delay precision was twenty picoseconds, with a range from less than ten to almost 200 picoseconds. Phase delay rates were used only to establish the atmosphere statistics used for the Kalman filter analysis (HDS). The typical formal uncertainty of the north and east components of station location was 1 - 2 millimeters for all stations, while the vertical uncertainties ranged from ~5 mm for Gilcreek to ~9 mm for HRAS_085.

4. USING RADIOSONDE DATA FOR ATMOSPHERE CORRECTION

In order to provide a better estimate of the effect of the troposphere on the delay which might result from using more realistic atmospheric conditions at the time of each experiment, radiosonde data were obtained from sites as near as possible to each of the VLBI stations. The distance to the radiosonde launch site ranged from 25 km at Gilcreek to several hundred km at Mojave. The atmosphere was assumed to depend on height only, and a raytrace program was used to calculate the *a priori* dry and wet delays for each site, scan, and experiment. As mentioned above the zenith path at each station was assumed to behave as a random walk in time with the statistics for each station estimated from the phase delay rate data (HDS).

In order to study the effect of changing only the dry atmosphere correction a standard solution was made for which all stations used the same dry and wet atmosphere model. For this 'standard' solution the zenith dry delay was calculated using Saastamoinen's formula (Saastamoinen 1972) and this zenith delay was mapped to the observed elevation using the CfA2.2 mapping function with lapse rate of -5.6 K/km and height of tropopause of 10 km, the nominal values used for the analysis of all CDP data. The *a priori* wet delay was zero and the wet Chao mapping function was used (Chao 1972). To provide the comparison four more solutions were run, substituting each time the raytrace calculation of the dry atmosphere delay at one station for that used in the standard solution. In all solutions the positions of all stations were estimated with a five meter *a priori* uncertainty. For each of the eighteen experiments, on replacing the Saas/CfA calculation with the raytrace correction, the horizontal and vertical

positions of those stations which used the standard atmosphere treatment, and the horizontal position of the station for which the atmosphere correction was altered, changed by less than a millimeter. The differences in local vertical obtained for this station are shown in Figure 1a through 1d.

The annual variation in local vertical is clearly seen in all stations, except possibly Westford. Assuming the raytrace of the radiosonde data provides a more accurate correction to the dry atmosphere, this seasonal height difference is to be interpreted as a spurious signal introduced by the use of a time-invariant mapping function. The maximum range of variation is 35 mm for the Alaska site (figure 1a), which is probably due to the very large temperature inversions which exist in the winter. Temperature inversions also affect Westford. For Ft. Davis and Mojave the variation is probably due to the combined effects of large errors in the lapse rate and tropopause height and of changes in surface temperature inversion with season.

The evidence that this seasonal difference in vertical is an artifact of the CfA2.2 mapping function is the reduction, from 5.6 mm to 3.9 mm, of the weighted rms deviation of all seventeen **length** measurements of the Mojave-Gilcreek baseline about a constant rate when using the raytrace correction. This corresponds to a removal of 4.0 mm of additional "noise" from the Saas/CfA solutions, and is consistent with the 35 mm annual variation of the Gilcreek vertical. For the Westford baseline the evaluation is not simple since the rms scatter of baseline lengths is dominated by two very large outliers (1987 August and 1988 March); small changes in these two points dominate the significance of any improvement (or degradation) of the majority of points.

How does the sensitivity of vertical change for the ATD data (due to the two different methods of correction) compare with the results of the simulation described above? The dependence of vertical change on excess path at 12 hours UT at 6 degrees elevation for Gilcreek is shown in figure 2. The slope is ~ 0.3, or about half that found in the simulation.

Thus there are two differences between the simulation and the analysis of real data: the sensitivity of vertical change to path length error is less for the real analysis, and there is no apparent horizontal displacement, even though the observing schedules are far from symmetric.

The most obvious difference between the simulation and the real data is the inclusion of stochastic variation of both clock and atmosphere in the ATD analysis. To check that this is related to the differences, the stochastic variation was turned off, leaving a clock offset and rate and a zenith atmosphere offset to be estimated, and a solution for the ATD data on only the Westford to Gilcreek baseline was made. The radiosonde data were substituted for CfA at Gilcreek only. For half of the experiments the horizontal dosplacements were greater than 10% of the vertical error and were within 20° of the azimuth direction of Westford. This confirms that the stochastic estimation does, indeed, absorb some of the residuals that do not fit the (mis)modeled atmosphere correction. This effect will also make it more difficult to estimate horizontal gradients from the data (see next section).

There is a second difference between the simulation and the analysis of the real data. For the simulation the estimation partial derivatives are perfect for the "true atmosphere", while for the

real data the Chao mapping function for the wet is not correct for either CfA2.2 or for the raytrace correction. However, the vertical difference should depend primarily on the CfA-raytrace difference.

Thus, the comparison of analysis of the ATD data using a mapping function which depends only on surface meteorology with that using atmosphere corrections which utilizes contemporary three dimensional atmospheric data demonstrates that seasonal variations of up to 35 millimeters are being introduced into the estimated vertical coordinates.

5. HORIZONTAL GRADIENT OF REFRACTIVITY

Intuitively, horizontal gradients in the atmosphere would be expected to "move" a site in the direction of the gradient, since the delay would be too large in one direction and too small in the opposite. Gradients will exist in the dry troposphere due to large scale weather systems, which change significantly in direction and magnitude over twenty-four hours, and in the wet troposphere due to fluctuations in water vapor density which give zenith path variations of greater than a few millimeters in half an hour (Treuhaft and Lanyi 1987).

The effect of a time-invariant horizontal gradient of refractivity due to the atmosphere can be studied using the simulation model described above. The horizontal gradient in the atmospheric vertical path is modeled as an azimuth dependent elevation angle offset of the form

$$\text{elev_offset} = \text{delta_el} * \cos(\text{azimuth} - \Theta)$$

where Θ is the azimuth direction of increasing zenith path length. This offset is added to the elevation angle for which the observed delay (path length) is calculated.

I have used a "tilt" of the atmosphere (delta_el in the equation above) of one arc minute to the west. The magnitude is not unusual for gradients in refractivity calculated from horizontal variations in temperature and pressure observed on weather maps. The azimuth of the gradient is such that observations to the west appear to pass through a lower part of the atmosphere than those taken at the same physical elevation angle to the east. Two cases were examined having the same azimuths and elevations of observation as for the previous simulations. In this test, however, no error was introduced into the mapping function in the form of incorrect temperature or other parameter. The error was in assuming azimuthal symmetry in the path delay, when, in fact, there was a variation with azimuth.

As might be expected intuitively, for the symmetric observing sequence (observing the same elevations at the four equally spaced azimuths), the estimated displacement of the station was only in the horizontal direction and was due west. The extra path due to the gradient was +48 mm to the southwest and northwest and -48 mm to the southeast and northeast at 5° elevation. The estimated position was 35 mm west, so ~1/3 of the differential path for the observed directions (southwest-northeast) was converted to a horizontal position change.

The observing sequence which went down only to 30 degrees at azimuths 45° and 135° produced a different result. For an excess path of 48 mm at 5° elevation in azimuths 225° and 315°, the

position error was entirely in the vertical with a displacement of +18 mm upward. Thus, ~1/3 of the error at 5°, which was not matched by observations 180° away in azimuth, went into the vertical.

6. IMPACT ON NETWORK DESIGN

Following the ATD series of observations a research program was begun in which the VLBA antenna at Pie Town, New Mexico replaced the Ft. Davis antenna. Instrumental improvements were made in the CDP receiver systems (Corey and Clark 1991) and a new schedule was written to take advantage of the improved sensitivity resulting from the hardware changes and from the addition of Pie Town. A significant advantage to the addition of the VLBA antenna was the improvement in sky coverage: the VLBA antennas can obtain observations down to an elevation of three degrees at all azimuths. With this coverage and the location of Pie Town relative to the other antennas, full sky coverage could be achieved at Mojave down to its elevation limit of ten degrees, at Pie Town down to three degrees, and the coverage at Westford was improved to the southwest. These observations, known as ERDE, continued from 1989 October through the end of 1990.

In order to extend the full sky coverage the 1991 R&D program was expanded to include the antennas at Kauai, Hawaii and Wettzell, Germany. This now provides rather uniform azimuth and elevation coverage for Westford and Gilcreek as well as for Mojave and for the VLBA antenna in New Mexico. Only the last added antennas suffer the limited azimuth coverage, and this can be solved only with a global array.

7. SUMMARY

Simulations point out the variety of situations that exist with respect to weather patterns, observing sequences, and mapping function errors. Errors in azimuthally symmetric mapping functions may produce apparent displacements in both the vertical and horizontal, though primarily in the vertical, while unmodeled horizontal gradients in the troposphere may produce apparent displacements in either the vertical, horizontal, or both.

Seasonal variations in estimates of vertical site position are introduced by analytic mapping functions which do not take into account time variations in the three-dimensional structure of the troposphere. The use of radiosonde data to correct for the dry troposphere for eighteen VLBI experiments spanning two years has reduced the effect by up to 35 millimeters for the Gilcreek, Alaska site. After the removal of a constant rate the weighted rms deviation of the length of the 3800 km baseline from Mojave, California to Gilcreek, Alaska is reduced from 5.6 to 3.9 mm, indicating a long-term precision of 1 ppb.

Analysis of the ATD data showed that only about half of the errors predicted by the simulations actually materialized, due to the absorption of the larger residuals as stochastic variations in the clock and atmosphere. A similar problem may also occur when attempting to estimate the effects of horizontal gradients. This redistribution of the residuals may be allowed, however, only because the values assumed for the Markov properties of the clocks and atmospheres are too large, thus diluting the true potential accuracy of the geodetic data. The problem of ascertaining

the statistical properties of the clocks and atmospheres remains coupled to the correct modeling of the spatial variation of the troposphere.

Acknowledgements. I thank Jim Davis and Tom Herring for many discussions, for generating the first version of raytrace program, and for creating the SOLVK package with which the analysis in this paper was done. I rediscovered many of the tests they had made and relations they had established much earlier. Also, my thanks to Clara Kuehn and Dan MacMillan for obtaining much of the radiosonde data, and to Jim Ray for valuable contributions in many areas.

REFERENCES

Chao, C.C. "A model for tropospheric calibration from daily surface and radiosonde balloon measurements", *Tech. Memo, Calif. Inst. Tech., Jet Propulsion Lab., 391-350*, 17 pp., 1972.

Corey, B.E., and T.A. Clark, "The RF bandwidth upgrade: Doubling the X-band spanned bandwidth of geodetic VLBI receiving systems", this volume, 1991.

Davis, J.L., T.A.Herring, and I.I.Shapiro, A.E.E.Rogers, and G.Elgered, "Geodesy by radio interferometry: Effects of atmospheric modeling errors on estimates of baseline length," *Radio Science*, **20**, 1593-1607, 1985.

Davis, J.L., T.A.Herring, and I.I.Shapiro, "Effects of atmospheric modeling errors on determinations of baseline vectors from very long baseline interferometry", *J. Geophys. Res*, **96**, 643-650, 1991.

Elgered, G., J.L.Davis, T.A.Herring, and I.I.Shapiro, "Geodesy by Radio Interferometry: Water Vapor Radiometry for Estimation of Wet Delay", *J. Geophys. Res*, **96**, 6541-6555, 1991.

Herring, T.A., "Precision of Vertical Estimates from Very Long Baseline Interferometry", *J. Geophys, Res.*, **91**, 9177-9182, 1986.

Herring, T.A., J.L.Davis, and I.I.Shapiro, "Geodesy by radio interferometry: The application of Kalman filtering to the analysis of very long baseline interferometry data", *J. Geophys. Res.*, **95**, 12,561-12,581, 1990 (HDS).

Lanyi, G.E., "Tropospheric calibration in radio interfereometry", in *Proceedings of the International Symposium on Space Techniques for Geodynamics*, J. Somogyi and C. Reigber, eds., IAG/COSPAR, pp. 184-195, Sopron, Hungary, 1984.

Saastamoinen, J., "Atmospheric correction for the troposphere and stratosphere in radio ranging of satellites" in *The Use of Artificial Satellites for Geodesy, Geophys. Monogr. Ser.*, vol 15, S.W. Henriksen *et al.*, eds, pp. 247-251, AGU, Washington, D.C., 1972.

Treuhaft, R.N., and G.E.Lanyi, "The effect of the dynamic wet troposphere on radio interferometric measurements", *Radio Science*, **22**, 251-265, 1987.

Figure captions

Figure 1. Difference in local vertical for each station of the ATD experiments when the Saastamoinen zenith delay and CfA2.2 mapping function are substituted for the dry atmospheric path delay calculated using radiosonde data from the vicinity of each station. 1a) Gilcreek, Alaska. 1b) Westford, Massachusetts. 1c) Mojave, California. 1d) Ft. Davis, Texas.

Figure 2. Dependence of change in vertical station position on excess atmospheric path length at 6 degree elevation for Gilcreek.

(August 2, 1991)

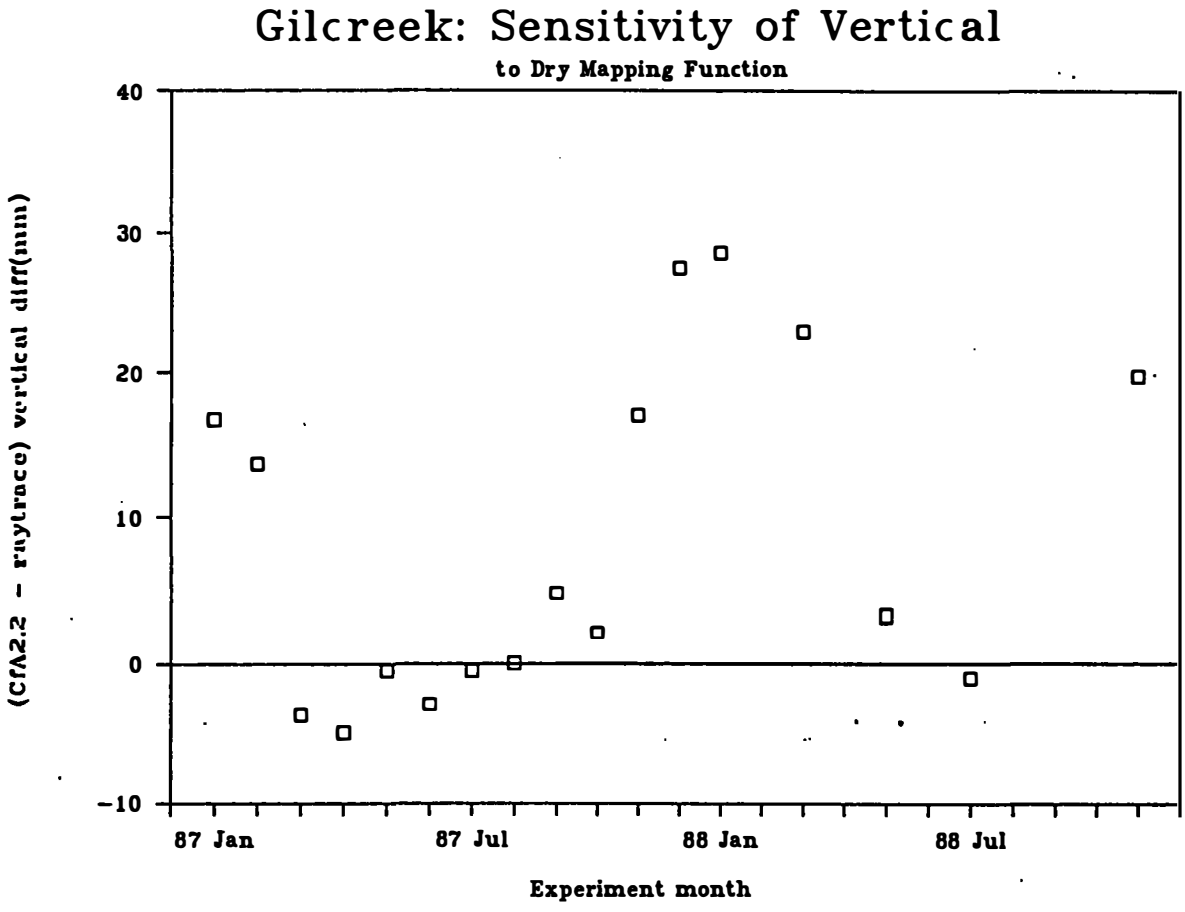

Figure 1a.

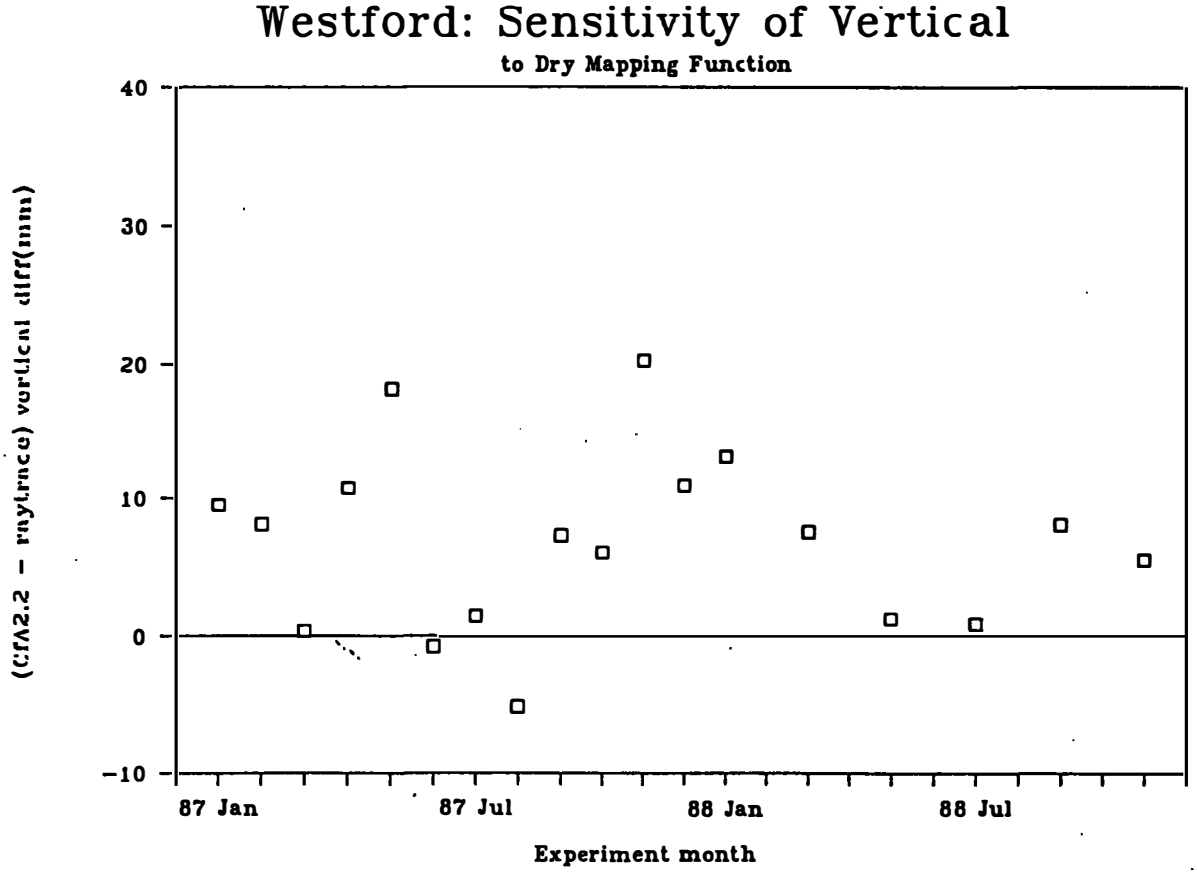

Figure 1b.

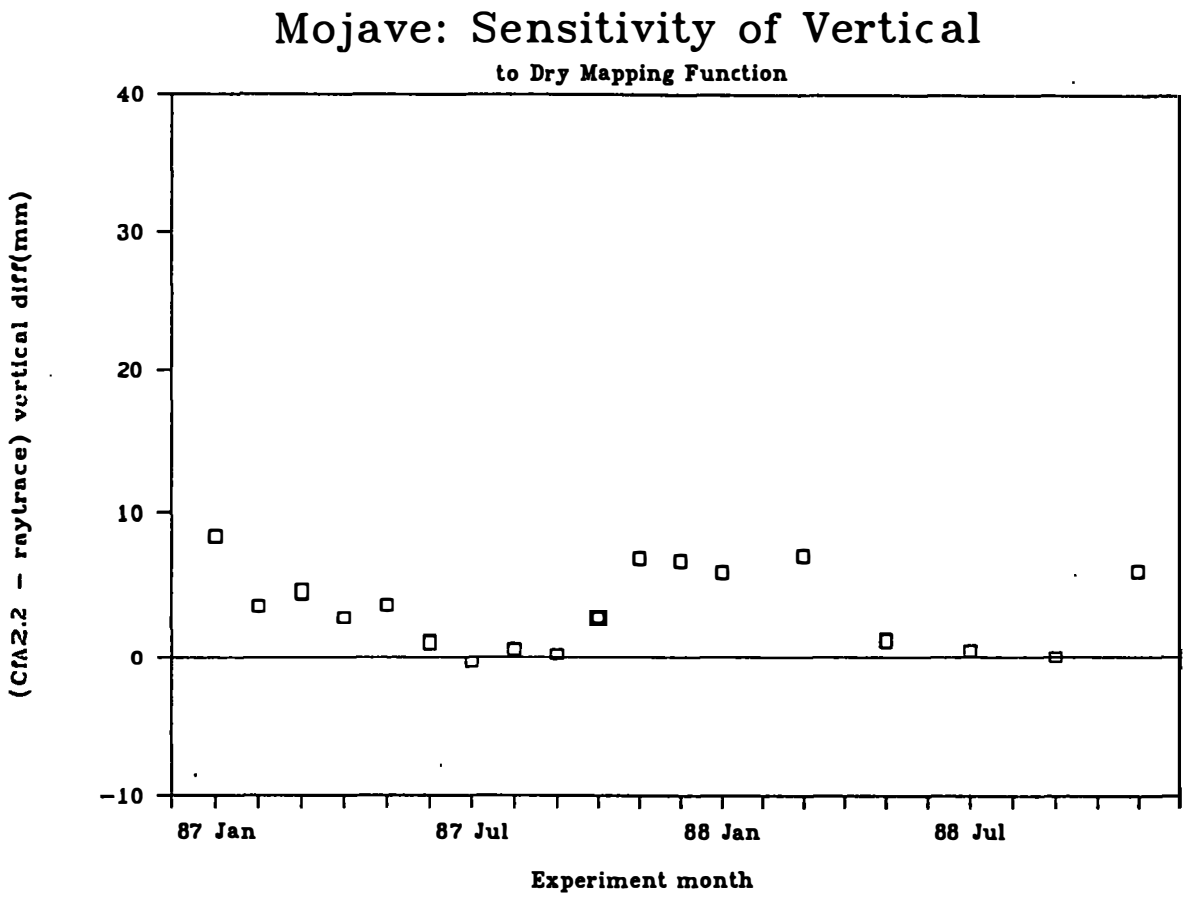

Figure 1c.

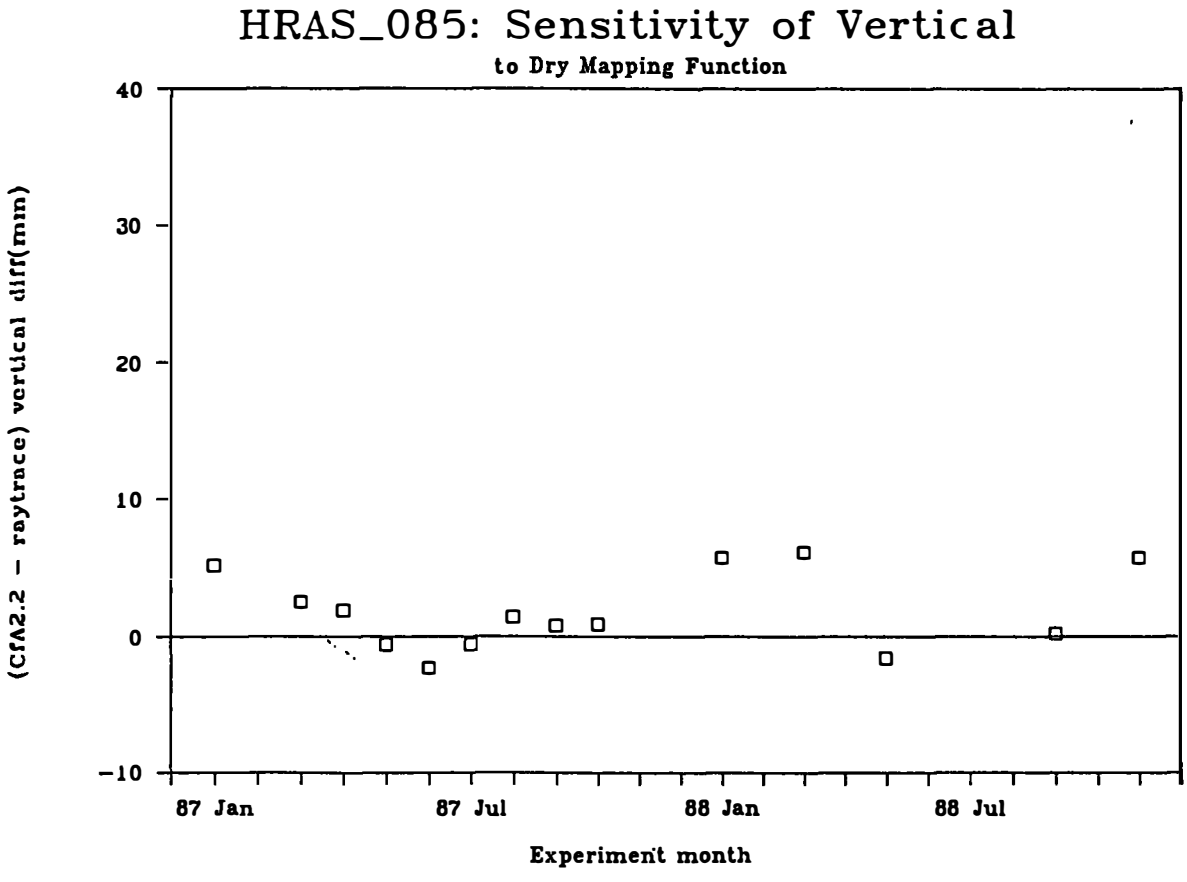

Figure 1d.

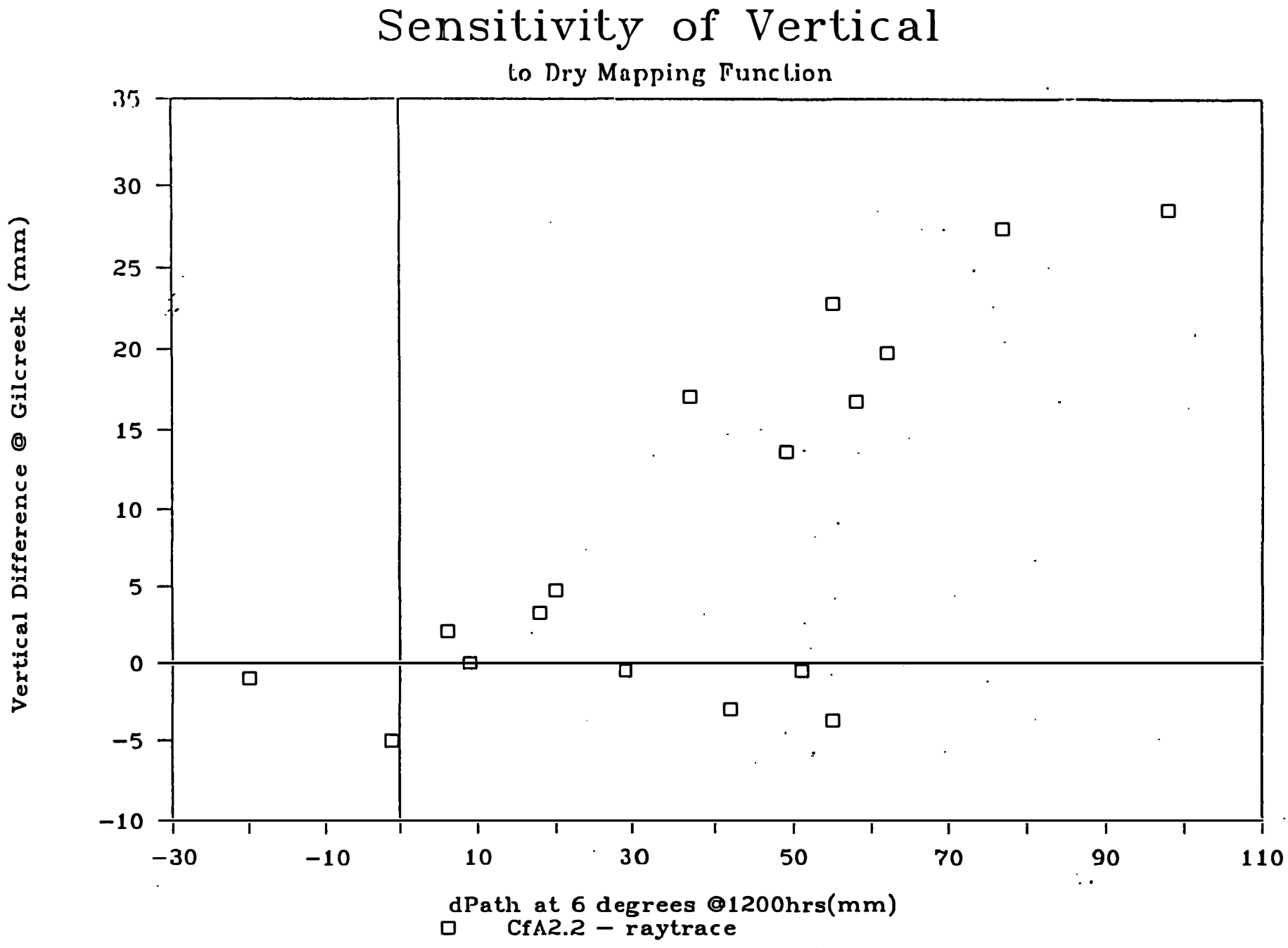
Sensitivity of Vertical
to Dry Mapping Function
Vertical Difference @ Gilcreek (mm)
35
30
25
20
15
10
5
0
-5
-10
-30
-10
10
30
50
70
90
110
dPath at 6 degrees @1200hrs(mm)
CfA2.2 — raytrace

Figure 2.

Modeling Antenna Effects for Millimeter-Level VLBI

C S Jacobs (Jet Propulsion Laboratory, California Institute of Technology, Pasadena, CA 91109; 818-354-7490)

As part of an effort to improve VLBI delay models to the mm level, VLBI phase delay measurements using pairs of antennas separated by 0.2 to 20 km have been made. While formal delay precisions are approx 0.2 mm, the accuracy of the measurements has been limited by systematic errors in the delay model that are one or two orders of magnitude larger than the precision. Because short baselines greatly reduce sensitivity to geophysical effects, these experiments are particularly sensitive to antenna and instrumental systematic effects. In an effort to reduce these systematic errors, we have refined the model of VLBI antennas in two ways. First, we have modeled the effect of gravity deformation on the signal delay through the antenna. This effect ranges from 10 to 80 mm and is a function of antenna, subreflector configuration, and elevation. Second, for antennas with non-intersecting axes, we have modeled the effect of axis offsets on the tropospheric delay. This effect can be as large as 10 mm and is a function of antenna mount type, axis offset distance, and antenna orientation. Our investigations show that these model refinements change baseline parameter estimates by amounts comparable to the size of the refinement.

Comparison of Two Different Scheduling Philosophies for Earth Orientation Measurements Using Very Long Baseline Interferometry

T M Eubanks, D N Matsakis, D D McCarthy, and B A Archinal (All at: the U.S. Naval Observatory, Washington, DC 20392-5100)

Although Very Long Baseline Interferometry (VLBI) is perhaps the most powerful method of global geodetic positioning yet devised, obtaining the highest accuracy from VLBI observations requires that careful attention be given to observation scheduling. While covariance analysis is a useful tool for examining different VLBI schedules, it is only as accurate as the models used, and it is still desirable to test different schedules using real data. The U.S. Naval Observatory (USNO) operates the Navy VLBI Network (NAVNET) program to monitor changes in the rotation of the Earth on a regular basis. As part of its participation in the National Earth Orientation Service, a test of scheduling philosophies was performed during 1990. Two different sets of schedules were generated for the Navy network and during parts of calendar year 1990 these schedules were run on alternating observing sessions. This paper will describe results from this schedule comparison.

The NavNet program measures the Earth rotation primarily with weekly 24-hour-duration VLBI experiments using telescopes in Alaska, Hawaii, Florida, and West Virginia. Two sets of schedules were prepared, one by the USNO and the other by the National Geodetic Survey (NGS). The NGS schedules used shorter scan lengths together with a lower nominal SNR to obtain ~30% more observations in a 24-hour period. The USNO schedules used roughly twice the number of sources and concentrated on maximizing the return from the transverse baseline orientation component. The NGS schedules required, on average, 31% longer to correlate. The results from the two schedules were roughly equal in accuracy. Both schedules suffered from a seasonal variation in delay residual scatter. When that variation was taken into account, the USNO schedules tended to have slightly smaller UT1 and polar motion formal errors. The NGS schedules were better able to determine the local vertical component of station position (not directly of concern in Earth orientation), with formal errors and residual scatters roughly half of those from the USNO schedules. Conversely, the Earth orientation results from USNO schedules were 20% to 50% less sensitive to unmodeled errors in the station local vertical.

Applications of Sub-Milliarcsecond Astrometric Techniques to Geodetic Measurements

Stephen T. Lowe and Robert N. Treuhaft
Jet Propulsion Laboratory
4800 Oak Grove Drive, Pasadena CA 91109
MS 238-700, (818/354-1042)

This paper presents a geodetic differential VLBI technique which can result in part-per-billion differential baseline measurements using only a few hours of data. The technique is very similar to a sub-nanoradian astrometric technique[1] used to make the first measurement of planetary relativistic deflection[2] As an example of this differential geodetic technique, the data used in the referenced deflection experiment (which were not optimized for geodetic work) were reanalyzed to obtain differential baseline components.

The data set for this experiment consisted of two four-hour sessions; one taken on 21 March 1988 and the other on 2 April 1988. Both sessions observed the same sidereal schedule using the DSN California-Australia baseline between DSS 15 and DSS 43 (DSS 13 was also used in the experiment; the DSS 13–DSS 43 baseline could be added to this analysis in the future). S and X-band data, spanning approximately 40 and 100 MHz respectively, were taken with the Mark III data acquisition system in mode A. These data were correlated using the JPL/CIT Block II correlator[3] and fringe fit[4] to extract the BWS delay and phase delay rate observables for each scan.

The dominant BWS delay and phase delay rate errors, white system noise and correlated tropospheric noise, were modeled. The white system noise was calculated from the correlated amplitude and number of data samples, and was typically 10–20 picoseconds for the delay and 1.5–3.0 femtoseconds/second for the rate. The tropospheric delay and rate covariance was calculated using the Treuhaft-Lanyi model[5] An overall normalization to this model was calculated using the delay rate data alone because they are assumed to be dominated by troposphere noise. The normalization constants for the geodetic example presented here were taken from the referenced deflection measurement where they were adjusted until a rate-data fit resulted in a reduced χ^2 equal to one. The white system noise was added to the resulting troposphere covariance matrix to give the final observation covariance matrix.

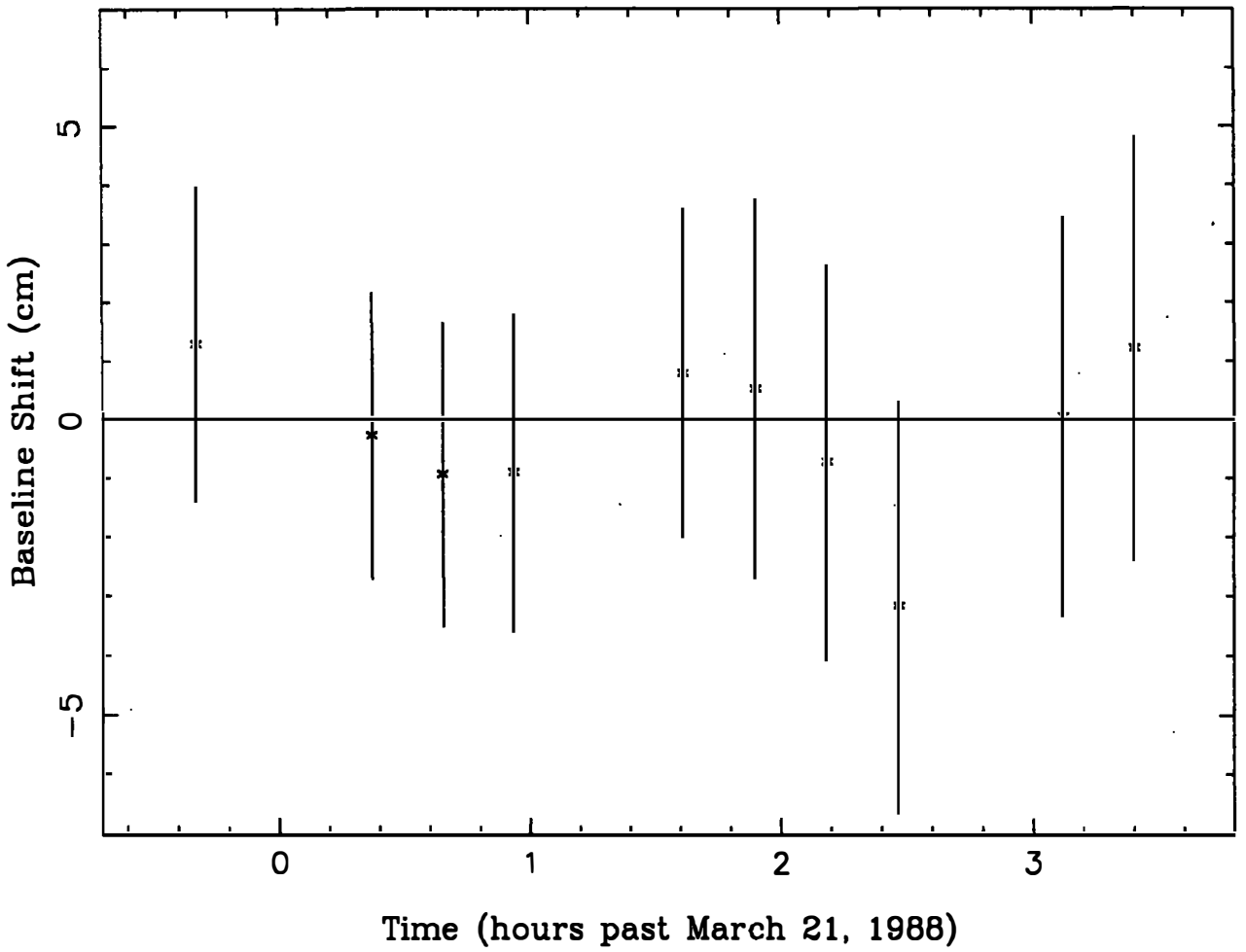

Fig. 1. Differential baseline shift as a function of time.

A linear least-squares fit was used to extract the x, y and z baseline components at 10 times throughout the session; these ten partitions of the data were identical to those used for the referenced relativistic deflection measurement. Four additional parameters were extracted: two describing the difference in clock and clock rate between the two stations and two describing the static zenith troposphere at each site. Each of the ten baseline solutions was constrained so the change in baseline components pointed along a single direction in the sky. This was done because, for a single observation, the delay is only sensitive to the baseline shift in the direction of the source. The direction chosen pointed approximately to center of the set of observed sources, but was not optimized on the final result (this could be done to find the direction to which this experiment is most sensitive). Since each of the ten baseline solutions was constrained to point along

a common space-fixed vector, the baseline solutions in the earth-fixed frame rotated over the four hour experiment duration as the earth rotated.

After fitting, the ten baseline shifts from the a priori positions for each of the two sessions were typically between 0 and 6 cm. The differences in baseline shifts between the two sessions are shown in Figure 1. The weighted average of these differential baseline shifts is −6.9 mm with a 6.6 mm standard deviation; although the meaning of such an average is complicated in the earth-fixed frame (due to each point measuring the shift along the same space-fixed direction), the combined measurement error shows the potential accuracy of this technique. The RMS about zero is 12.8 mm which indicates the accuracy per point. The reduced χ^2 is 0.45; this may indicate a problem in the normalization of the troposphere covariance matrix which could be due to non-tropospheric contributions to the rate residuals.

References

1. Treuhaft, R. N., "Deep Space Tracking in Local Reference Frames," Jet Propulsion Laboratory TDA Progress Report 42-94, p. 1-15, August 1988.
2. Treuhaft, R. N. and Lowe, S. T.,"A Measurement of Planetary Relativistic Deflection," accepted for publication in Astronomical Journal, tentatively scheduled for October 1991 issue. Preprints available on request.
3. Thomas, J. B., "Interferometry Theory for the Block II Processor," JPL Pub. 87-29, 1987.
4. Lowe, S. T., "Theory of Post-Block II VLBI Observable Extraction", JPL Report in press.
5. Treuhaft, R. N. and Lanyi, G. E. "The Effect of the Dynamic Wet Troposphere on Radio Interferometric Measurements," Radio Sci. 22, 251, 1987.

RELATIVISTIC EFFECTS ON VLBI OBSERVABLES AND DATA PROCESSING ALGORITHMS

Ronald W. Hellings and Bahman Shahid-Saless
Jet Propulsion Laboratory
301-150
California Institute of Technology
Pasadena, CA 91109

Neil Ashby
Department of Physics, Campus Box 390
University of Colorado, Boulder, CO 80309

I. INTRODUCTION

Einstein's General Theory of Relativity predicts that the presence of matter in the solar system will curve spacetime. Fig. 1 depicts a two-dimensional analog of such a curvature. This fact of nature creates a problem for those doing space and time measurements in the solar system. In Euclidian geometry, there is a simple relationship between cartesian coordinates of two points and the distance between the points:

$$l^2 = \sum_{i=1}^{3} ({x_2}^i - {x_1}^i)^2, \tag{1}$$

where i labels the coordinate and the subscript labels the point. However, in curved space, no set of coordinates exists for which Eq. (1) is everywhere valid. The best one can do is to cover the space with an arbitrary coordinate system and then relate physical distances to coordinate differences by the integral

$$l = \int_1^2 \sqrt{g_{ij} dx^i dx^j}, \tag{2}$$

where g_{ij} is the metric tensor. Thus, in the solar system, any coordinate system one could use would have only indirect relationship to the results of a physical measurement, with the form of the metric tensor being a necessary ingredient along with the coordinates of the two events.

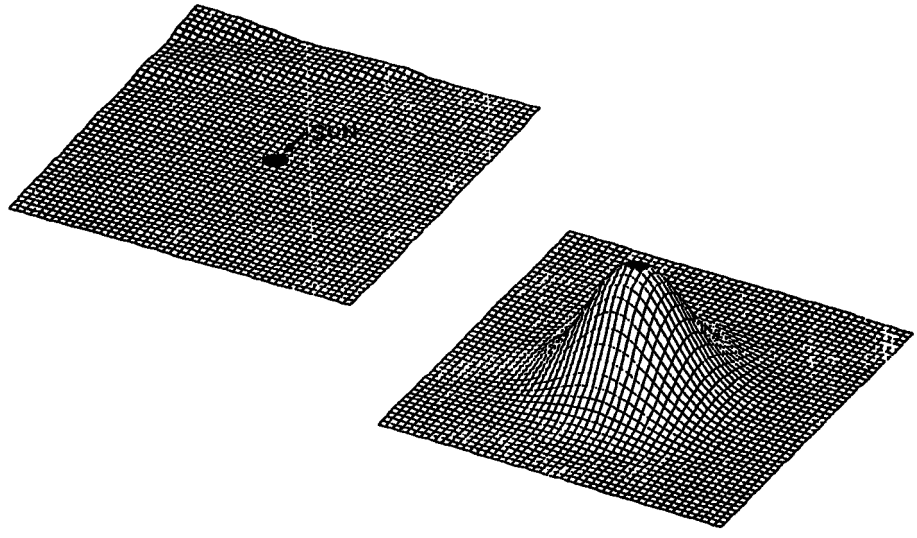

Figure 1. Two-dimensional analog of the curving of spacetime by the mass of the sun.

An example of the type of coordinate system that is regularly used is shown in Fig. (2). Each point of the curved space may be identified with its projection into the underlying flat space beneath it, but the physical distance between points in the curved space is not given by Eq. (1). The underlying coordinate system shown is analogous to the asympotically-flat post-Newtonian coordinate system that is used for relativistic solar system dynamics.

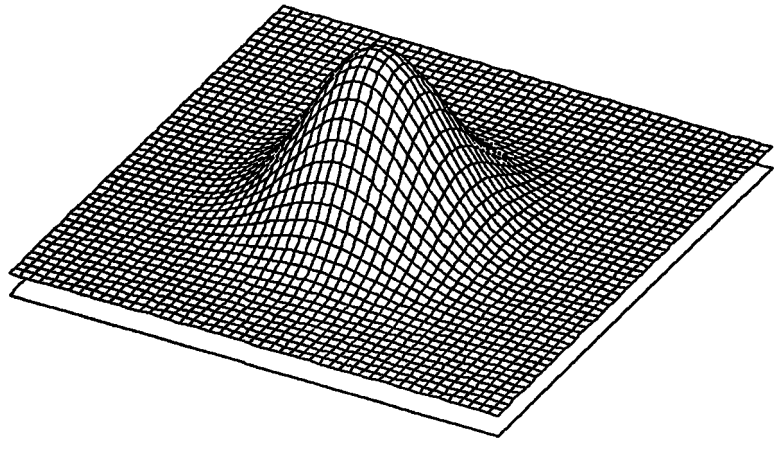

Figure 2. Example of a coordinate system that covers the curved space.

In a small region of the curved space, a local patch of flat space could be attached. Physical distance-type coordinates could be used in this small patch, but this coordinate system woyld not be the same as the underlying coordinate system because of the way the curved space slants up relative to the underlying plane. Similarly, in a small region of spacetime around the sun, a coordinate system can be found in which the spatial coordinates represent physical distances and the time coordinate represents time kept by physical clocks. These coordinates will then have a scale difference relative to the post-Newtonian coordinates of the solar system, due to the curvature produced by the gravitational field of the sun.

The sun is not the only body in the solar system, however, and the curvature of spacetime in the solar system is more complicated than indicated by Fig. 2. In particular, the earth's gravitational field produces a local perturbation in the overall solar system curvature, as depicted in Fig. 3. This complication creates no problem in principle. The same solar system coordinates can be used, but the metric tensor needed to relate coordinates to physical measurements will simply be more complicated than it would be if the earth were not there. Similarly, if one wants to find a local patch of spacetime near the earth to cover with locally-flat coordinates, then the patch cannot be as large as it would be without the earth present, since the presence of the earth changes the curvature on a much smaller scale.

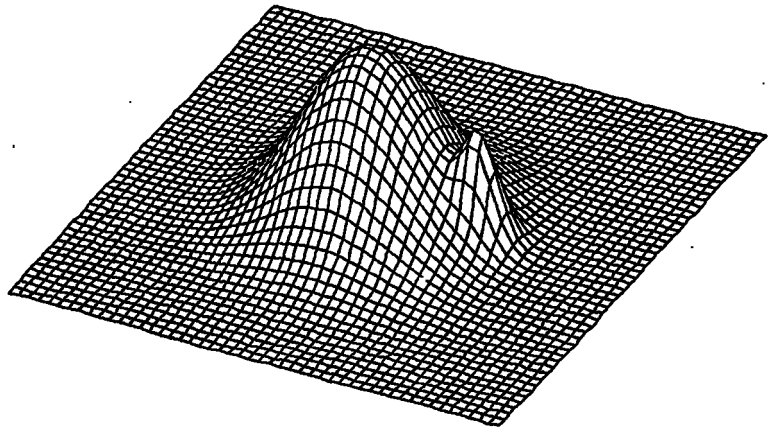

Figure 3. The local curvature produced by the earth.

Now the problem in VLBI is that the local space and time measurements one would like to make cover a spatial region as large as the entire earth. At the level of accuracy where the earth's gravitational field is not negligible, it is not possible to find a single coordinate system that will represent physical measurements. The local curvature must be taken into account in the algorithm and the space time coordinates will not be the same as physical

baselines and atomic time delays between arrival times at the two VLBI stations. What we will end up chosing as our VLBI coordinate system is the analog for the local region around the earth of the underlying post-Newtonian coordinate system for the solar system. This choice, which we will call *terrestrial coordinates*, is depicted in Fig. 4. We emphasize that the relationship between the VLBI time coordinate and a difference in atomic times of arrival of phase at two antennas should involve a correction for the gravitational potential of the earth and that the VLBI coordinate baseline will differ from the physical, surveyed, distance between antennas by a term of the same origin. The only exception to this statement arises when, as we discuss in Section III, the VLBI time coordinate is deliberately rescaled so as to agree with the atomic time kept at the stations. This choice simplifies the time part of the model at the expense of complicating the spatial part.

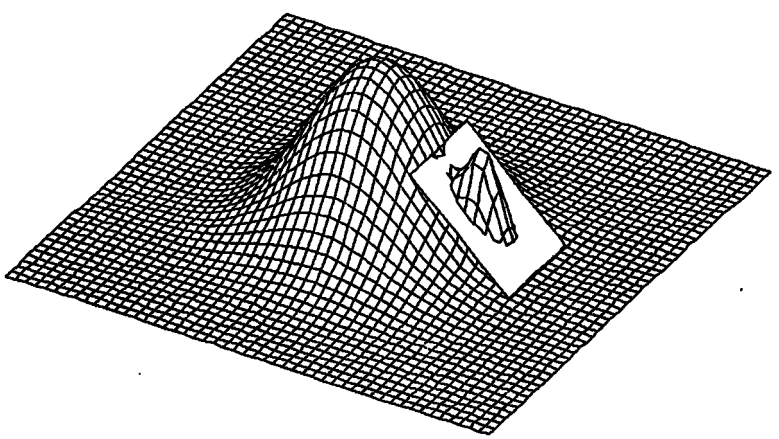

Figure 4. Analog of VLBI coordinates in the field of the earth.

It is our goal in this paper to derive a relativistic model of the VLBI observable, to picosecond accuracy, thus extending the original work of Hellings[1] as in Shahid-Saless *et al.*[2]. The outline of the paper is as follows. In Section II, we discuss the transformation from solar system barycentric coordinates, in which the equations of motion for photons are simplest, to terrestrial coordinates, which are most closely related to the physical measurements that are made. In Section III, we derive the picosecond-accuracy relativistic equation relating the observable (difference in atomic times of arrival of photons at two VLBI stations) to the parameters of the model (solar system barycentric coordinates of the earth and the geocentric coordinates of the stations). We use the standard fully conservative Parameterized Post-Newtonian (PPN) framework as described in Ref. (6).

II. THE LOCAL INERTIAL FRAME OF REFERENCE

In VLBI, signals from distant sources pass through the solar system and are received at stations on the surface of the earth. Signal propagation is most easily described in a PPN coordinate system with origin at the solar system barycenter. However barycentric coordinate time does not coincide with the local geocentric time measured by Earth observers. Signal phase measurements made by atomic clocks located in a laboratory on the geoid must be related to the solar system coordinates in such a way as to yield physically meaningful results. The problem in VLBI, as mentioned in section I, is that the local laboratory must extend across the entire earth. At the picosecond level of accuracy one may not ignore the curvature of spacetime produced by the mass of the earth, so a transformation to Minkowski coordinates is not possible over a large enough region of spacetime. This problem is similar to the one faced in the relativistic analysis of earth-orbiting satellite data. The solution which has been found[3,4] is to transform to an intermediate reference frame in which the earth is the source of local gravitational physics in a terrestrial "laboratory." This choice of coordinate frame is also to be preferred for VLBI. Not only will it produce a simply interpretable expression for the observable phase delays between two antennas, but it will also have the advantage that the baselines derived from the VLBI model and station locations derived from satellite laser ranging will have the same interpretation.

The local reference frame we have chosen is an extension of Fermi normal coordinates to include contributions from local sources, thus approximating as closely as possible a geocentric Newtonian reference frame. When the local terrestrial gravitational physics is worked out in this frame, the metric will contain certain non-linear terms in the Sun's potential and other Earth-Sun interactions which are negligibly small for our purposes. The main contributions to the local metric are composed of terms arising from the Earth's potential and terms representing tidal forces due to distant sources. Given this metric, the local coordinates can be related to the physical space and time measurements via the standard techniques in relativity.

Construction of the local inertial reference frame has been worked out for simple cases previously.[4,5] We take a model of the solar system to be composed of point masses moving along their respective geodesics. We then attach a set of four mutually orthonormal basis vectors (a tetrad) to the center-of-mass of the Earth. These vectors will be parallel-transported along the Earth's geodesic as defined by the gravitational field of other external sources in the solar system. The tetrad will then serve as a basis to expand the barycentric coordinates of an event in terms of the local inertial coordinates—the Fermi normal coordinates. This expansion in local coordinates will provide the transformation between the two coordinate systems.

The metric $G_{\mu\nu}$ representing the geometry of the solar system can be written in terms of PPN potentials. Given this PPN metric one can use the geodesic equations to find the geodesic path along which the center of the Earth moves. Next we consider an event P, in the neighborhood of the Earth, given by the coordinates (T, X^i) in the barycentric frame and (t, x^i) in the geocentric frame. Since the Fermi spatial coordinates are by definition time-orthogonal in the local frame, one can find an event P_0 with local coordinates $(t, x^i = 0)$ and barycentric coordinates (T_0, X_E^k) which is an event at the origin of the local frame and is simultaneous with P as seen in the local frame. However, as seen by barycentric observers,

the two events P and P_0 are not simultaneous. One must account for this lack of simultaneity in calculating barycentric distances. This will be discussed in Section III in more detail.

Following the construction of the transformations given in Ref. (4) one can write the barycentric coordinates (T, X^i) of P in terms of the local inertial geocentric coordinates of P and the barycentric coordinates of P_0. We present the transformations to quadratic order in Fermi coordinates for completeness. The transformations are

$$\begin{aligned} cT =& cT_0 + \mathbf{V}_E \cdot \mathbf{x}/c[1 + (2+\gamma)U + \frac{1}{2}V_E^2/c^2 + \mathbf{A}_E \cdot \mathbf{x}/c^2] \\ &+ G_{0k}x^k + \Omega^{kl}V_E^m x^n \delta_{km}\delta_{ln}/c + \frac{1}{2}G_{0k,l}x^k x^l - \frac{1}{2}\gamma r^2 U_{,0}, \end{aligned} \tag{3a}$$

$$\begin{aligned} X^k =& X_E^k(T_0) + x^k(1 - \gamma U - \gamma \mathbf{A}_E \cdot \mathbf{x}/c^2) + \frac{1}{2}V_E^k \mathbf{V}_E \cdot \mathbf{x}/c^2 \\ &+ \Omega^{kl}x^m \delta_{lm} + \frac{1}{2}\gamma r^2 A_E{}^k/c^2, \end{aligned} \tag{3b}$$

where T_0 is the barycentric time coordinate of the event P_0 and is related to the local time of that event by

$$T_0 = \int (1 + U + \frac{1}{2}V_E^2/c^2)dt.$$

X_E^k, V_E^k and A_E^k are the barycentric position, velocity, and acceleration of the Earth's center of mass, respectively, and U is the negative of the gravitational potential due to other bodies in the Solar System, divided by c^2 and evaluated at the center of the Earth. G_{0k} represents gravitomagnetic components of the metric. The antisymmetric matrix Ω^{kl} arises in the construction of the tetrad and represents the net rotation due to geodetic and gravitomagnetic precession of the local frame axes relative to the solar system barycentric coordinate grid.

III. VLBI MEASUREMENTS WITH PICOSECOND ACCURACY

Having the transformations at hand, we are ready to relate measurements made in the two frames by considering the arrival of signals from a distant source at two Earth based antennas at their respective local coordinate times. At the picosecond level of accuracy the transformation equations (3a) and (3b) simplify somewhat. A rough estimate of the sizes of the contributions are $V_E/c \approx 1 \times 10^{-4}$, $x^k \approx 6 \times 10^6$ m, $U \approx 1 \times 10^{-8}$, $(\mathbf{V}_E \cdot \mathbf{x})/c^2 \approx 2 \times 10^{-6}$ sec and $A_E^k/c^2 \approx 3 \times 10^{-20}\mathrm{m}^{-1}$. Thus the terms involving $\mathbf{V}_E \cdot \mathbf{x}$ multiplying U, V_E^2 and $\mathbf{A}_E \cdot \mathbf{x}$ in Eq. (3a) are all of order 10^{-19} sec or less and may be dropped. Furthermore, G_{0k} is approximately $4UV_S/c^3$, where V_S is the velocity of the Sun around the barycenter, and is of order 10^{-17} sec. The term $G_{0k,l}$ is 10^4 times smaller still, and the $U_{,0}r^2$ term is of order 10^{-16} sec. The quadratic terms in Eq. (3b) are less than 10^{-6}m and are negligible. With these simplifications the transformations are just

$$T = T_0 + \mathbf{V}_E \cdot \mathbf{x}/c^2 + \Omega^{kl}V_E^m x^n \delta_{km}\delta_{ln}/c^2, \tag{3c}$$

$$X^k = X_E^k(T_0) + x^k(1-\gamma U) + \frac{1}{2}V_E^k \mathbf{V}_E \cdot \mathbf{x}/c^2 + \Omega^{kl} x^m \delta_{lm}. \tag{3d}$$

We consider antennas #1 and #2, located at two different sites on the geoid, receiving signals at local times t_1 and t_2 respectively. Using the spatial transformations, the barycentric coordinate distance between the two ground stations can be written as

$$\begin{aligned} X_2^k(T_2) - X_1^k(T_1) = X_E^k(T_{0_2}) - X_E^k(T_{0_1}) + [x_2^k(t_2) - x_1^k(t_1)](1-\gamma U) \\ + \frac{1}{2c^2} V_E^k [\mathbf{V}_E \cdot (\mathbf{x}_2(t_2) - \mathbf{x}_1(t_1))] + \Omega^{kl}\delta_{ml}[x_2^m(t_2) - x_1^m(t_1)]. \end{aligned} \tag{4}$$

In the interval $T_{0_2} - T_{0_1}$ the center of the Earth will have traversed a coordinate distance given by

$$X_E^k(T_{0_2}) - X_E^k(T_{0_1}) = V_E^k(T_{0_2} - T_{0_1}),$$

and the antennas located on the geoid will undergo a rotation such that

$$x_2^k(t_2) - x_1^k(t_1) = x_2^k(t_1) - x_1^k(t_1) + (t_2 - t_1) w_2^k, \tag{5a}$$

where $\mathbf{w}_2$ is the velocity of the antenna #2 due to Earth's rotation relative to local inertial axes. We define the terrestrial baseline $\mathbf{b}$ as the distance between the two antennas, measured simultaneously with respect to observers in the local frame at the instant t_1. Thus Eq. (5a) may be rewritten as

$$\mathbf{x}_2(t_2) - \mathbf{x}_1(t_1) = \mathbf{b} + (t_2 - t_1)\mathbf{w}_2. \tag{5b}$$

With this, Eq. (4) gives

$$\begin{aligned} X_2^k - X_1^k =& V_E^k(T_{0_2} - T_{0_1}) + [b^k + w_2^k(t_2 - t_1)](1-\gamma U) \\ &+ \frac{1}{2c^2} V_E^k [\mathbf{V}_E \cdot (\mathbf{b} + \mathbf{w}_2(t_2 - t_1))] + \Omega^{kl}\delta_{lm}[b^m + w_2^m(t_2 - t_1)]. \end{aligned} \tag{6}$$

However, as noted earlier, the barycentric time of the event of reception T is not simultaneous with barycentric coordinate clocks at the origin of the local frame T_0. This is evident in Eq. (3c):

$$\begin{aligned} T_1 &= T_{0_1} + \mathbf{V}_E \cdot \mathbf{x}_1/c^2 + \ldots.. \\ T_2 &= T_{0_2} + \mathbf{V}_E \cdot \mathbf{x}_2/c^2 + \ldots.. \end{aligned}$$

Substituting this correction into Eq. (6) gives

$$\begin{aligned} X_2^k - X_1^k =& V_E^k(T_2 - T_1) + [b^k + w_2^k(t_2 - t_1)](1-\gamma U) \\ &- \frac{1}{2c^2} V_E^k [\mathbf{V}_E \cdot (\mathbf{b} + \mathbf{w}_2(t_2 - t_1))] + \Omega^{kl}\delta_{lm}[b^m + w_2^m(t_2 - t_1)]. \end{aligned} \tag{7}$$

The above equation now includes the effects arising from relativity of simultaneity.

In the barycentric frame, electromagnetic signals undergo a relativistic time delay due to the field of the Sun, the Earth, and the other planets in the solar system. Denoting $\mathbf{k}$ to be the unit vector in the initial direction of propagation of photons, far from the solar system, one can show that the time interval between reception at the two antennas can be written as

$$T_2 - T_1 = \frac{1}{c}\mathbf{k}\cdot(\mathbf{X}_2 - \mathbf{X}_1) + \Delta T_g, \tag{8}$$

where ΔT_g represents the total gravitational time delay due to the potentials of the solar system bodies. Multiplying Eq. (7) by $\mathbf{k}$ and substituting the result into Eq. (8) gives

$$\begin{aligned} cT_2 - cT_1 = \mathbf{k}\cdot\mathbf{V}_E(T_2 - T_1) + k^i[\delta_{ij} + \Omega_{ij}][b^j(1-\gamma U) + W_2^j(t_2 - t_1)] \\ - \frac{1}{2c^2}V_E^i k_i V_E^j[b_j + w_{2j}(t_2 - t_1)] + \Delta T_g. \end{aligned} \tag{9}$$

Over the interval between the VLBI events, the earth's velocity and the external solar system potential are essentially constant. Thus, the time transformation, Eq. (3c), can be written, with the help of Eq (5b), as

$$c(T_2 - T_1) = (1 + U + \frac{1}{2}V_E^2/c^2)c(t_2 - t_1) + \frac{V_e^i}{c^2}[\delta_{ij} + \Omega_{ij}][b^j + w_2^j(t_2 - t_1)]. \tag{10}$$

Solving Eqs. (9) and (10) for the local time interval we get

$$\begin{aligned} c(t_2 - t_1)[(1 - \mathbf{k}\cdot\mathbf{V}_E/c)(1 + U + \frac{1}{2}\frac{v^2}{c^2}) - (k^i - \frac{V_E^i}{c})(\delta_{ij} + \Omega_{ij})\frac{w_2^j}{c}] = \\ k^i(\delta_{ij} + \Omega_{ij})b^j(1-\gamma U) - (1 - \mathbf{k}\cdot\mathbf{V}_E)\frac{V^i}{c}(\delta_{ij} + \Omega_{ij})b^j \\ - \frac{1}{2c^2}V_E^i k_i V_E^j b_j + \Delta T_g. \end{aligned} \tag{11}$$

The above equation represents the local geocentric time interval between reception of signals from a distant source at the two antennas on the geoid. This includes corrections arising from lack of simultaneity, Lorentz contraction, local gravitational curvature, and geodetic precession.

The antisymmetric matrix Ω_{ij} in Eq. (11) always appears in the combination $\delta_{ij} + \Omega_{ij}$. To first order, it represents the rotation between the barycentric frame, which is asymptotically fixed with respect to points at infinity, and the local inertial frame, which is by definition freely falling and therefore undergoing geodetic precession. In the case of the Earth, geodetic precession causes a secular rotation of the inertial frame axes with respect to distant stars with a magnitude of about 19 milliarcseconds per year. However, tidal and other effects, some of which are yet ill-determined in terms of fundamental physics, cause much larger precessions of the pole. These effects are routinely measured and used in transforming from

an equatorial reference frame of date to a solar system inertial reference frame. Thus the rotation matrix used in such transformations has implicitly corrected for geodetic precession as well. If we choose our geocentric coordinates to be directionally fixed with respect to the solar system axes, then the rotation terms should be dropped, leaving the simpler expression:

$$\begin{aligned} c(t_2 - t_1) = (1 - \mathbf{k}\cdot\mathbf{V}_E/c - \mathbf{k}\cdot\mathbf{w}_2/c)^{-1} \\ \left\{\mathbf{k}\cdot\mathbf{b}\left[1 - (1+\gamma)U - \frac{1}{2}V_E^2/c^2 - \mathbf{V}_E\cdot\mathbf{w}_2/c^2\right]\right. \\ \left. - \mathbf{V}_E\cdot\mathbf{b}/c + \frac{1}{2}\mathbf{k}\cdot\mathbf{V}_E\mathbf{b}\cdot\mathbf{V}_E/c^2 + \Delta T_g\right\}. \end{aligned} \tag{12}$$

Finally it is important to note that the expression calculated in Eq. (12) gives the post-Newtonian terrestrial time difference as measured by observers at the origin of the local frame. The time coordinate used in geocentric gravitational dynamics of local Earth satellites is Terrestrial Dynamical Time (TDT) which is essentially the time kept by atomic clocks on the Earth's geoid (TAI). The proper time τ kept by a clock on the geoid is related to the geocentric PPN coordinate time t by

$$\tau = (1 - \phi_0)t, \tag{13a}$$

where ϕ_0 is the negative of Earth's potential, modified by the rotational contributions and evaluated at the geoid,[7]

$$\phi_0 = \frac{GM_E}{c^2 a}\left(1 + \frac{1}{2}J_2\right) + \frac{1}{2c^2}(\Omega_E a)^2 = 6.9694 \times 10^{-10},$$

with a as the Earth's equatorial radius, Ω_E as the angular velocity of the Earth's rotation, and J_2 as the Earth's quadrupole moment coefficient.

Use of Eq. (13a) in the expression for the VLBI observable gives a term linear in ϕ_0 in the final formula. However, there is good reason to want to rescale the spatial coordinates. This is that most dynamical analysis programs use TDT as time coordinate without modifying the geodesic equations of light propagation. They are therefore implicitly rescaling the spatial coordinates by the same amount:

$$\chi^i = (1 - \phi_0)x^i. \tag{13b}$$

Therefore, if one desires VLBI-determined baselines to agree with Satellite Laser Ranging baselines, then one should insert both transformations into Eq. (12), resulting in a rescaling of both sides of Eq. (12). The final equation relating the VLBI observable to the parameters of the model is thus simply

$$
\begin{aligned}
c(\tau_2 - \tau_1) = (1 - \mathbf{k}\cdot\mathbf{V}_E/c - \mathbf{k}\cdot\mathbf{w}_2/c)^{-1} \\
\left\{\mathbf{k}\cdot\mathbf{b}\left[1 - (1+\gamma)U - \frac{1}{2}V_E^2/c^2 - \mathbf{V}_E\cdot\mathbf{w}_2/c^2\right]\right. \\
\left. - \mathbf{V}_E\cdot\mathbf{b}/c + \frac{1}{2}\mathbf{k}\cdot\mathbf{V}_E\mathbf{b}\cdot\mathbf{V}_E/c^2 + \Delta T_g\right\}.
\end{aligned} \tag{14}
$$

In this final expression, $\tau_2 - \tau_1$ is the TAI (or UTC) time difference between the two reception events at the two VLBI antennas. $\mathbf{k}$ is a unit vector in the asymptotic incoming signal direction. It is thus the negative of a constant barycentric unit vector pointing toward the right ascension and declination of the source. $\mathbf{b}$ is the rescaled instantaneous geocentric coordinate baseline from point of reception to point of reception, including the constant antenna-to-antenna baseline *and* including antenna mechanical zenith angle corrections, tidal corrections, etc. U is the total solar system potential at the center-of-mass of the earth, excluding the earth's potential, and $\mathbf{V}_E$ is the barycentric coordinate velocity of the earth. Both U and $\mathbf{V}_E$ need to be evaluated via a planetary ephemeris at the time of reception (whether at t_2 or t_1 does not matter). At the required level of accuracy, a constant rotation rate model for the earth suffices for $\mathbf{w}_2$. ΔT_g should be calculated using the logarithmic version of the formulas for gravitational time delay, as given by the usual time delay formula,

$$
\Delta T_g = \delta t_2 - \delta t_1 = (\gamma + 1)\sum_p \frac{GM_p}{c^3}\ln\left[\frac{|\mathbf{R}_{p1}| + \mathbf{e}_p\cdot\mathbf{R}_{p1}}{|\mathbf{R}_{p2}| + \mathbf{e}_p\cdot\mathbf{R}_{p2}}\right], \tag{15}
$$

in order to maintain picosecond accuracy for rays that pass near the solar limb. It must also include the contribution from the earth's potential.

To understand the meaning of the local coordinate system, we display the local metric after the conformal transformations given by Eqs. (13). To order v^2/c^2, it is

$$
\begin{aligned}
ds^2 = &\left\{1 - 2\frac{GM_E}{c^2 r}\left[1 + \frac{1}{2}J_2\frac{a^2}{r^2}(1 - 3cos^2\theta)\right] + 2\phi_0\right\}c^2 d\tau^2 \\
&- \left\{1 + 2\gamma\frac{GM_E}{c^2 r}\left[1 + \frac{1}{2}J_2\frac{a^2}{r^2}(1 - 3cos^2\theta)\right] + 2\phi_0\right\}d\chi^i d\chi^j \delta_{ij} + 2\chi^j\frac{d\Omega^{ji}}{d\tau}d\chi^i d\tau,
\end{aligned} \tag{16}
$$

where θ refers to the standard azimuthal angle measured from the axis of rotation. If other applications, such as satellite laser ranging (SLR), are to use VLBI coordinates, or if the SLR baselines are to be compared with VLBI baselines, then Eq. (16) is the metric that these applications must use. The price that must be paid for the various choices made in arriving at VLBI coordinates is apparent from Eq. (16). The off-diagonal components of the metric (the terms containing Ω_{ij}) appear as a result of choosing a non-inertial frame that has its axes point in fixed directions with respect to solar system axes. This will then complicate the local dynamics.[8] The ϕ_0 arises in the $d\tau^2$ term because of the choice of TDT as a time coordinate, and in the $d\chi^i d\chi^j$ term because of the need for a coordinate speed of light that is equal to c, rather than $(1+\phi_0)c$. The time coordinate is the same as the proper time read by clocks on the geoid. However, the spatial coordinates are not proper distances (as would be

measured, for example, in geophysical surveys). There is no problem in this choice of spatial coordinates. Both VLBI and SLR algorithms have made this choice, and will thus agree on their baseline measurements but will not agree with survey results unless the survey results are related to the coordinates via the metric of Eq. 16.

REFERENCES

1. R. W. Hellings, Astro. J. **91**, 650 (1986)
2. B. Shahid-Saless, R.W. Hellings, and N. Ashby, Geophys. Res. Lett., **18**, 1139 (1991).
3. N. Ashby and B. Bertotti, Phys. Rev. Lett. **52**, 485 (1984).
4. N. Ashby and B. Bertotti, Phys. Rev. D**34**,2246 (1986).
5. B. Shahid-Saless and N. Ashby, Phys. Rev. D**38**, 1645 (1988).
6. C. M. Will, *Theory and Experiment in Gravitational Physics*, Cambridge University Press, Cambridge (1981).
7. N. Ashby and D. W. Allen, Phys. Rev. Lett. **53**, 1858 (1984).
8. N. Ashby and B. Shahid-Saless, Phys. Rev. D**42**, 1118 (1990).

RELATIVITY and VLBI

Irwin I. Shapiro

Harvard-Smithsonian Center for Astrophysics
60 Garden Street, Cambridge MA 02138

SECTION I: INTRODUCTION

Rather than give a quantitative enumeration of the various general relativistic corrections to a Newtonian formulation of the VLBI observables, I provide a qualitative overview of the relevant issues. The point is solely to broaden the perspective of those VLBI practitioners who have not formally studied general relativity.

What is wrong with Newton's theory? The main reasons Einstein was troubled by Newton's theory of gravity were:

(1) The theory incorporates "action at a distance." For example, if Planet X moves, the force experienced by Planet Y changes instantaneously, according to Newton's theory, no matter what the distance between X and Y; and

(2) Newton's theory is set in a space-time framework of three spatial coordinates and one temporal coordinate that remain separate and immutable. This separation of space and time is inconsistent with Einstein's theory of special relativity as is the action-at-a-distance aspect, which violates the proposition that no "signals" propagate faster than the speed of light.

To replace Newton's theory of gravity, Einstein devised a new one that was consistent with special relativity. He considered space-time to be a four-dimensional continuum described by a metric. This metric, by definition, describes the "distance" between neighboring points in the (four-dimensional) space ($ds^2 = \ldots$). How is this metric to be determined? Einstein's brilliant idea was to have the metric determined by the distribution of mass and energy in the system through a set of (non-linear) differential equations. The left sides of these (tensor) equations depend only on the metric and are limited to derivatives of no higher order than the second; the right sides of the equations depend solely on the mass and energy of the system. These so-called field equations are both elegant and deceptively simple. Also, being non-linear, the field equations can and here do imply the equations of motion. That is, the equations of motion, say of particles in the system, can be deduced from the field equations alone. This situation is in sharp contrast to Newton's theory; in the latter, Poisson's equation is the analog of the equations for the metric tensor in general relativity -- the field equations -- and determines the gravitational potential from a mass

distribution. But Newton's theory requires supplementary equations of motion that cannot be deduced from Poisson's equation.

What is the connection between Newton's theory of gravity and general relativity? The fundamental bases for these theories are very different, yet one can show that for a system in which the gravitational field is "weak" and the velocities of particles are "small" compared to the velocity of light, Newton's equations of motion form a good approximation. Under general conditions, Einstein's equations are extraordinarily difficult to deal with and substantial progress has been made in solving them only in very special cases or by use of sophisticated numerical techniques. Luckily, in the solar system, we are in the weak field-low velocity limit which can be handled satisfactorily by a "v/c" expansion of the solutions to the relevant equations. At present, the first terms after the Newtonian ones in this expansion -- the so-called post-Newtonian limit -- provide sufficient accuracy for analysis of VLBI data.

SECTION II: OBSERVABLES

In VLBI, time is the one and only observable: We use clocks to measure epochs at which light signals arrive at specific locations (space-time "events"). With one minor exception (see below), there is no need to introduce or to consider concepts such as "physical lengths," *i.e.* meter sticks. These are irrelevant. Indeed, discussions of the physical length between two widely separated places on Earth is virtually impossible to define operationally and, in any event, would be "time-dependent" due to changes in a variety of effects that would occur while the measurements were being made. (How would one know how to place the meter sticks end-to-end to measure the distance between an antenna on one continent and another antenna on a different continent? And how long would it take to make such a measurement?) Thus, it is best to banish this concept from core, at least for the purposes of VLBI. The only exception would be the measurement of very short distances to allow "ties" between neighboring (spatial) reference points that serve to mark space-time events corresponding to different systems, for example side-by-side locations of satellite-laser-ranging and VLBI systems.

SECTION III: COORDINATE SYSTEMS

The main problem we face in developing a model for VLBI measurements is the construction of appropriate expressions for clock readings at epochs of arrival there of light signals. These expressions are written in terms of specific coordinates. What coordinate frame should we use? The two obvious candidates are a solar-system barycentric and a geocentric (or topocentric) frame. It is reasonable to use the solar-system barycenter for describing the motion of solar-system bodies and of light rays emitted by extragalactic objects. But, for descriptions of sites on the surface of the rotating Earth, clearly solar-system barycentric coordinates are not the obvious choice. We can profit by using both of these frames. We can choose coordinates in each to express the trajectories of clocks and of light rays with the "intersections" of these giving us our events. The choice of coordinates in each frame is arbitrary and has *no* operational significance: the results for observables, *i.e.* clock readings, must be the same, independent of what coordinates we choose for carrying out our calculations. Confusion, however, often reigns because the same symbols are used to represent distinct sets of coordinates. The reason for this seeming absurdity is based on the fact that in Euclidian space we conventionally use a particular set of symbols to describe a particular type of coordinate system (such as Cartesian or spherical). However, in general relativity, there are

an infinite number of coordinate systems that one can lay down, with all of them having the same asymptotic meaning, *i.e.*, far from all masses the coordinates correspond to a particular Euclidian system, or, more properly, to a Minkowskian (special relativity) system.

Let us examine briefly the solar-system barycentric and geocentric frames. The former is freely falling in our galaxy, which, in turn, is freely falling in the Universe. It is relatively easy to show that as far as the position of the Earth with respect to the solar-system barycenter is concerned, tidal effects due to other masses in our galaxy and in the more distant parts of the Universe are quite negligible compared to achievable measurement accuracies. The Earth, for its part, is freely falling in the solar system. But tidal effects here, due to the other masses in the solar system, primarily the Sun, are *not* negligible. Moreover, the Earth is rotating, which, of course, affects the trajectories of the clocks. Thus, in the post-Newtonian limit of general relativity, we must consider a number of effects of spin-orbit coupling and spatial curvature, such as geodetic precession.

How can we connect, or transform between, coordinates in one of our two "natural" coordinate frames and those in the other? That is, how do we transform between two sets of coordinates, one each for representing solar-system bodies and for representing points on the surface of the Earth? This transformation can be carried out in the post-Newtonian limit using any one of a number of different approaches. The details are mostly straightforward, but some are subtle, making this transformation the most difficult part of the whole enterprise. Overall, transforming from the solar-system barycentric to the geocentric frame is, in effect, transforming to a local Lorentz frame (were the Earth's mass zero). In keeping with our qualitative broad-brush approach, we will not discuss the nuances of this transformation and the modifications necessary to account for topocentric effects.

SECTION IV: CLOCKS AND BASELINES

How do clocks behave? It is always assumed, in tune with our best experimental understanding, that clock rates are *un*affected by acceleration. This assumption is critical because, with rare exceptions, our clocks are not in free fall; they are firmly placed on the Earth's surface and "feel" the ground pushing up on them. How do we describe their behavior within the theory of general relativity? General relativity includes a quantity called "proper time" which is identified with the time kept by an "ideal" (atomic) clock moving along a trajectory in space-time. Readings of such an ideal clock can be expressed as a function of the coordinates chosen for use in calculations, a stark contrast to Newtonian theory where time is time is time is .... However, even Einstein found no universal imperative for defining any specific event as the "origin" of time or for defining how many oscillations of an atomic system ought to be identified with the unit of time. Choices of origin and rate of proper time in relation, say, to those for our terrestrial atomic clocks, are therefore arbitrary. We may make the best use we can of this freedom! How? What do we wish to accomplish? Because it is a nice property, we try to keep atomic time and our coordinate time from diverging. Whereas the proper time for an atomic clock on the geoid is proportional to geocentric coordinate time, when the latter is "reasonably" defined, this proper time is *not* simply proportional to barycentric coordinate time when the latter is "reasonably" chosen. Because of this fact, we use our rate freedom to limit "runaway" (the freedom of choice of time origin, by contrast, presents no particular issue). We choose a rate constant to average out as well as possible the differences between atomic and coordinate time. But these differences depend on planetary motions whose orbital periods are not commensurate; furthermore, the planetary orbits themselves

change in time due to the mutual interactions between the planets. One practical solution to this problem, which we incorporated some dozen years ago, is to choose an averaging time equal to approximately five orbital periods of Jupiter which also nearly coincides with two orbital periods of Saturn.

What about other effects on our observable, such as the propagation medium through which the signals travel, the nonspherically symmetric parts of the Earth's gravitational potential, the elastic properties of the Earth, etc.? The standard approach here is to "graft" Newtonian theory on to general relativity. We calculate the effects on the observable of all these other properties of the system, using Newtonian theory, and simply add them to the corresponding general relativistic representation of the observable. This procedure is adequate for VLBI at the picosecond level of clock measurements, but, of course, is not acceptable in principle for arbitrary accuracy.

In general, a clock reading will be a function of the position and motion of the clock and of the trajectory of the light signal whose intersection with the clock defines our "events." What about baselines? We can define a baseline in a "natural" way in this description, in terms, for example, of differences of the geocentric coordinates of pairs of events: a light signal's arrivals at two antennas. Here, too, however, there are some subtleties and "arbitrariness" which we will not pursue in this qualitative presentation.

SECTION V: PARAMETER ESTIMATION

The analysis of the clock readings, the observables, involves in broad terms the comparison of the observed epochs with expressions for these epochs which depend on parameters that describe the positions of the antenna sites, the tidal breathing of the Earth, the directions to the sources, the properties of the propagation medium, the imperfections in the atomic clocks used, etc. Standard filtering techniques are then used to make estimates of these parameters from this comparison. This part of the process is independent of nuances of general relativity and is well known to VLBI practitioners. We thus end our overview here.

CONSISTENT RELATIVISTIC VLBI THEORY WITH PICOSECOND ACCURACY†

M. SOFFEL[1], J. MÜLLER[2], X. WU[1], C. XU[1]

[1] *Theoretical Astrophysics*
Uni. Tübingen Auf der Morgenstelle 10
7400 Tübingen, FRG

[2] *Technical Uni. Munich*
Institut f. Astron. u. Physikal. Geodäsie
Arcisstr. 21
8000 Munich 2, FRG

1. Introduction

All astrometric, celestial mechanical and geodetic problems, where the planetary system plays a role, require the use of both *barycentric* and *geocentric* coordinates. This is in fact the major problem for the relativistic formulation of VLBI. The barycentric system is usually employed to describe the motion of the planetary system; in VLBI it is necessary to describe the (radio) signal propagation from distant radio sources to the antennas. On the other hand a geocentric system is needed in oder to define meaningful baselines and to study geophysical effects in a relatively "simple" manner. Not each geocentric coordinate system will equally well be suited for these purposes and one faces the problem how to define "good local, geocentric" coordinates. Note, that in barycentric (or "bad" geocentric) coordinates relativistic effects are of the order $(v_\oplus/c)^2 \sim 10^{-8}$ leading to effects of the order of 1 m for the Earth-Moon distance or about 10 cm for the LAGEOS orbit. In "good" geocentric coordinates, however, relativistic effects are one order of magnitude smaller (the Earth's gravitational potential devided by c^2 is $\sim 10^{-9}$) and effects from all other bodies (Moon, Sun, etc.) are small and of tidal nature.

Let us give an example concerning the solar time delay in satellite laser ranging (SLR). In barycentric coordinates $(t, \mathbf{x})$ the coordinate time difference between

† Paper presented at the Chapman Conference on Geodetic VLBI: Monitoring Global Change, April 22-26, 1991, Washington, D.C. Work supported by the Deutsche Forschungsgemeinschaft (DFG) and the Volkswagen Stiftung; M.S. kindly acknowledges the receipt of a Heisenberg fellowship.

emission and absorption of a light pulse in SLR is given by

$$c(t_a - t_e) = (r_{er} + r_{ra}) + \Delta_\odot + \Delta_\oplus,$$

where

$$r_{er} = |\mathbf{x}_S(t_r) - \mathbf{x}_T(t_e)|$$

(S refers to the satellite, T refers to the tracking station). Here, the Δ-terms describe the gravitational time delay (the Shapiro effect) caused by the Sun and the Earth. We have

$$\Delta_\odot/2 = \frac{2GM_\odot}{c^2} \ln\left[\frac{r_T + r_S + b}{r_T + r_S - b}\right] \sim \frac{2U_\odot}{c^2} b,$$

where $\mathbf{b}$ denotes the barycentric baseline vector:

$$\mathbf{b} = \mathbf{x}_S(t_r) - \mathbf{x}_T(t_r)$$

If now geocentric (proper) time T and a geocentric "baseline" vector $\mathbf{B}$ are introduced with

$$\frac{dT}{dt} \simeq \left[1 - \frac{U_\odot}{c^2} - \frac{1}{2}\left(\frac{\mathbf{v}_\oplus}{c}\right)^2\right]$$

and

$$\mathbf{b} \simeq \left(1 - \frac{U_\odot}{c^2} - \frac{1}{2}\frac{\mathbf{v}_\oplus \otimes \mathbf{v}_\oplus}{c^2}\right) \mathbf{B}$$

then at this level of approximation the time delay caused by the Sun is just canceled and we are left with

$$c(T_a - T_e) \simeq 2\mathbf{B} + \Delta_\oplus.$$

Because of the equivalence principle all external bodies only lead to (small) tidal effects. This example nicely demonstrates the meaning of "good" local geocentric coordinates: effects from external bodies become strongly effaced and the local metric at the center of the Earth agrees with the Minkowski metric from special relativity. To construct a "good" GRS effects from special and general relativity should be taken into account. We can formulate some requirements for "good" geocentric coordinates $(T, \boldsymbol{X})$:

- $T \propto$ TDT (proper time)
- metric = $(\text{metric})_\oplus$ + (tidal terms)
- $(\text{metric})_\oplus$ can directly be expressed in terms of multipole moments of the Earth
- the relation $(t, \mathbf{x}) \leftrightarrow (T, \boldsymbol{X})$ should be "simple".

From these requirements one can show that the relation between global and local coordinates has to be of the form

$$x^\mu = z^\mu_\oplus(T) + e^\mu_a(T)X^a + \xi^\mu(T, X^a)$$

instead of the "bad" relation

$$t = T$$

$$x^i = z^i_{\oplus}(T) + X^i$$

from Newtonian physics. Here, ξ^μ contains all terms which are at least quadratic in the local space coordinate X^a.

Now, our problem of coordinates is contained in the *basic problem* of a consistent PN celestial mechanics of an N-body system, a problem which comprises at least the following three parts

- the external problem (global dynamics, center of mass motion etc.),
- the internal problem (local gravitational structure)
- and the way they fit together (relativistic theory of reference systems).

The new Damour–Soffel–Xu scheme (1990, 91a,b) solves theses problems consistently in a new and elegant manner at the level of the first post-Newtonian approximation to Einstein's theory of gravity. Using this DSX-formalism it is not difficult to derive expressions for the VLBI variables (Soffel et al., 1991), as will be described below.

2. Post-Newtonian VLBI Theory For The Group Delay

We consider some radio signal being emitted from some remote source at barycentric coordinate time t_0 and position $\mathbf{x}_0$. We consider two "light-rays", contained in the signal, which arrive at two VLBI antennas (called 1 and 2) at coordinate time t_1 and t_2. This barycentric coordinate time t is also called TCB. Let us denote the "Euclidean unit vector" from the source to the barycenter by $\boldsymbol{k}$ ($k^i k^i = 1$). Then the barycentric coordinate arrival time difference $t_2 - t_1$ to first post-Newtonian order is given by

$$\Delta t \equiv t_2 - t_1 = -\frac{1}{c}\left[\mathbf{x}_1(t_1) - \mathbf{x}_2(t_2)\right] \cdot \boldsymbol{k} + (\Delta t)_{\mathrm{grav}}, \tag{1}$$

where $\mathbf{x}_i(t_i)$ denotes the barycentric coordinate position of antenna i at coordinate time t_i. $(\Delta t)_{\mathrm{grav}}$ is the gravitational time delay, resulting from solving the equation for null geodesics (light rays) in some background metric describing the gravitational influence of the Sun and the planets. To sufficient accuracy $(\Delta t)_{\mathrm{grav}}$ can be written as a sum over the contributions of the various massive bodies in the solar system.

Now, for picosecond accuracy it is sufficient to consider the spherical part of the gravitational potential in $(\Delta t)_{\mathrm{grav}}$ only. Taking earlier results from Richter and

Matzner (1983) we estimate the contribution from the quadrupole moment of the Sun to the time delay to be much less than a picosecond ($\sim 10^{-18}$ s). The effect from the angular momentum of the Sun (a gravitomagnetic effect of 1.5 post-Newtonian order) is of the same order, while the dominant post-post Newtonian terms are expected to be less than about 1 picosecond. † For the solar contribution we can neglect the motion of the Sun about the barycenter and the usual "light-time equation" for the spherical field can be written in the form (e.g. Soffel, 1989)

$$(\Delta t)^{\odot}_{\rm grav} \simeq \frac{2m_{\odot}}{c} \ln\left(\frac{|\mathbf{x}_1| - \mathbf{x}_1 \cdot \boldsymbol{k}}{|\mathbf{x}_2| - \mathbf{x}_2 \cdot \boldsymbol{k}}\right), \tag{2}$$

where $\mathbf{x}_i$ refers to t_i and $m_{\odot} \equiv GM_{\odot}/c^2 = 1.48\,\mathrm{km}$. The time difference Δt can be neglected in the ln-term and writing

$$\mathbf{x}_i = \mathbf{x}_{\oplus} + \Delta \boldsymbol{r}_i$$

we obtain (Finkelstein et al., 1983; Zeller et al., 1986):

$$(\Delta t)^{\odot}_{\rm grav} \simeq \frac{2m_{\odot}}{\mathrm{c}} \ln\left[\frac{r_{\oplus}(1 - \boldsymbol{e}_{\oplus} \cdot \boldsymbol{k}) + \Delta \boldsymbol{r}_1 \cdot (\boldsymbol{e}_{\oplus} - \boldsymbol{k}) + (\Delta \boldsymbol{r}_1)^2/2r_{\oplus} - (\boldsymbol{e}_{\oplus} \cdot \Delta \boldsymbol{r}_1)^2/2r_{\oplus}}{r_{\oplus}(1 - \boldsymbol{e}_{\oplus} \cdot \boldsymbol{k}) + \Delta \boldsymbol{r}_2 \cdot (\boldsymbol{e}_{\oplus} - \boldsymbol{k}) + (\Delta \boldsymbol{r}_2)^2/2r_{\oplus} - (\boldsymbol{e}_{\oplus} \cdot \Delta \boldsymbol{r}_2)^2/2r_{\oplus}}\right] \tag{3}$$

with

$$\boldsymbol{e}_{\oplus} \equiv \mathbf{x}_{\oplus}/r_{\oplus}; \quad r_{\oplus} = |\mathbf{x}_{\oplus}| = (x^i_{\oplus} x^i_{\oplus})^{1/2}.$$

For baselines of $\sim 6000\,\mathrm{km}$, the $(\Delta \boldsymbol{r}_i)^2$-terms are of order 3×10^{-14} sec and can be neglected for picosec-accuracy.

For the gravitational time delay due to the Earth one finds ($m_{\oplus} = GM_{\oplus}/\mathrm{c}^2 = 0.44\,\mathrm{cm}$)

$$(\Delta t)^{\oplus}_{\rm grav} \simeq \frac{2m_{\oplus}}{c} \ln\left[\frac{|\Delta \boldsymbol{r}_1| - \Delta \boldsymbol{r}_1 \cdot \boldsymbol{k}}{|\Delta \boldsymbol{r}_2| - \Delta \boldsymbol{r}_2 \cdot \boldsymbol{k}}\right], \tag{4}$$

if the motion of the Earth during signal propagation is neglected. Similarly, for any other planet A, if its motion is neglected, one obtains

$$(\Delta t)^{A}_{\rm grav} \simeq \frac{2m_A}{c} \ln\left[\frac{|\mathbf{x}_{A1}| - \mathbf{x}_{A1} \cdot \boldsymbol{k}}{|\mathbf{x}_{A2}| - \mathbf{x}_{A2} \cdot \boldsymbol{k}}\right], \tag{5}$$

where $\mathbf{x}_{Ai} = \mathbf{x}_i - \mathbf{x}_A$. Note that the maximal gravitational time delays due to Jupiter, Saturn, Uranus and Neptune are of order 1.6(Jup), .6(Sat), .2(U) and .2(N) nanosec

† S. Klioner and V. Brumberg (see this volume) claim that the post-post Newtonian contribution from the spherical field of the Sun can be as large as a few hundred picoseconds at the limb and falls off rapidly with angular separation; this effect is subject to further investigations.

resprectively, but these values decrease rapidly with increasing angular distance from the limb of the planet. E.g. 10 arcmin from the center of the planet the gravitational time delay amounts only to about 60 picosec for Jupiter, 9 picosec for Saturn and about one picosec for Uranus. To consider the barycentric motion of the planet during signal propagation the position of the planet might be taken at the time of closest approach (e.g. Hellings, 1986); this point has been investigated by Klioner (this volume) in more detail.

Let us define baselines at signal arriving time t_1 at antenna 1. Let the barycentric baseline b be defined as

$$\mathbf{b}(t_1) \equiv \mathbf{x}_1(t_1) - \mathbf{x}_2(t_1), \tag{6}$$

then a Taylor expansion of $\mathbf{x}_2(t_2)$ about t_1 yields ($O(n) \equiv O(c^{-n})$)

$$\begin{aligned}\Delta t = & -\frac{1}{c}(\mathbf{b}\cdot\boldsymbol{k})\left[1+\frac{1}{c}(\dot{\mathbf{x}}_2\cdot\boldsymbol{k})+\frac{1}{c^2}(\dot{\mathbf{x}}_2\cdot\boldsymbol{k})^2-\frac{1}{2c^2}(\mathbf{b}\cdot\boldsymbol{k})(\ddot{\mathbf{x}}_2\cdot\boldsymbol{k})\right] \\ & + (\Delta t)_{\mathrm{grav}} + O(4),\end{aligned} \tag{7}$$

all quantities now referring to barycentric coordinate time t_1. We call this relation the "VLBI-delay equation", describing the barycentric coordinate time delay Δt entirely by quantities defined in the global system.

We will now relate the various barycentric quantities with corresponding geocentric ones apart from the propagation vector $\boldsymbol{k}$. This will remind us that the process of signal propagation from the source to the antennas cannot be formulated in the local, accelerated, geocentric system. We now write the time transformation in the form (Damour et al., 1990, 91a,b)

$$\begin{aligned} ct &= z^0_\oplus(T) + e^0_a(T)X^a + O(3) \\ &= \int_{T_0}^{T} ce^0_0\, dT' + e^0_a(T)X^a + O(3) \\ &= c(T-T_0) + \frac{1}{c}\int_{T_0}^{T}\left(\overline{U}(z_\oplus)+\frac{1}{2}\mathbf{v}^2_\oplus\right)dT' + \frac{1}{c}R^i_a(T)v^i_\oplus(T)X^a + O(3).\end{aligned}$$

Here, T = TCG is the geocentric coordinate time and X^a the geocentric spatial coordinate. $\overline{U}$ is the *external* gravitational potential which does *not* include the contribution from the Earth. Replacing T' by t' in the integral and considering that R^i_a is a slowly time dependent matrix we can relate $\Delta t = t_2 - t_1$ with the corresponding local time interval $\Delta T = \Delta\mathrm{TCG} = T_2 - T_1$:

$$\begin{aligned}\Delta t = \Delta T &+ \frac{1}{c^2}\int_{t_1}^{t_2}\left(\overline{U}(z_\oplus)+\frac{1}{2}\mathbf{v}^2_\oplus\right)dt' \\ &+ \frac{1}{c^2}R^i_a v^i_\oplus(T_2)X^a_2(T_2) - \frac{1}{c^2}R^i_a v^i_\oplus(T_1)X^a_1(T_1) + O(4).\end{aligned}$$

With

$$v^i_\oplus(T_2)X^a_2(T_2) \simeq v^i_\oplus X^a_2 - v^i_\oplus V^a_2\left(\frac{\mathbf{b}\cdot\boldsymbol{k}}{c}\right) - a^i_\oplus X^a_2\left(\frac{\mathbf{b}\cdot\boldsymbol{k}}{c}\right) + O(2),$$

where quantities on the right hand side now refer to T_1, we formally get the relation

$$\Delta t = \Delta T + \frac{1}{c^2}\left[-\mathbf{v}_\oplus\cdot\mathbf{B} + \int_{t_1}^{t_2}\left(\overline{U}(\boldsymbol{z}_\oplus) + \frac{1}{2}\mathbf{v}^2_\oplus\right)dt'\right]$$
$$- \frac{1}{c^3}\left[(\mathbf{v}_\oplus\cdot\mathbf{v}_2)(\mathbf{b}\cdot\boldsymbol{k}) + (\boldsymbol{a}_\oplus\cdot\Delta\boldsymbol{r}_2)(\mathbf{b}\cdot\boldsymbol{k})\right] + O(4), \tag{8}$$

where

$$\mathbf{B}(T_1) \equiv \boldsymbol{X}_1(T_1) - \boldsymbol{X}_2(T_1)$$

and

$$B^i \equiv R^i_a B^a$$
$$v^i_2 \equiv R^i_a V^a_2$$
$$\Delta r^i_2 \equiv R^i_a X^a_2.$$

$\mathbf{v}_2$ is the geocentric velocity of antenna 2. Next, we will relate the barycentric baseline vector $\mathbf{b}(t_1)$ appearing in the VLBI-delay equation (7), with the corresponding geocentric one $\mathbf{B}(T_1)$. Using the notation of Damour et al. (1990, 91a,b) we find

$$x^i_1(t_1) - x^i_2(t_2) = z^i_\oplus(t_1) - z^i_\oplus(t_2) + R^i_a\left(X^a_1(T_1) - X^a_2(T_2)\right)$$
$$- \frac{1}{c^2}\left(\frac{1}{2}v^i_\oplus v^k_\oplus + \overline{U}(\boldsymbol{z}_\oplus)\delta_{ik}\right)B^k + \xi^i(T_1, X^a_1) - \xi^i(T_2, X^a_2) \tag{9}$$

with

$$\xi^i = \frac{1}{c^2}e^i_a(T)\left[\frac{1}{2}A^a_\oplus \boldsymbol{X}^2 - X^a(\boldsymbol{A}_\oplus\cdot\boldsymbol{X})\right] + O(4) \tag{10}$$

and

$$A^a_\oplus(T) \equiv e^i_a(T)\frac{d^2 z^i_\oplus}{dT^2}.$$

With

$$z^i_\oplus(t_1) - z^i_\oplus(t_2) \simeq -v^i_\oplus\Delta t - \frac{1}{2}a^i_\oplus(\Delta t)^2,$$

$$x^i_1(t_1) - x^i_2(t_2) \simeq b^i(t_1) - (\Delta t)\dot{x}^i_2(t_1) - \frac{1}{2}(\Delta t)^2\ddot{x}^i_2(t_1)$$

and

$$X^a_1(T_1) - X^a_2(T_2) \simeq B^a(T_1) - \left(\frac{d}{dT}X^a_2\right)\Delta T - \frac{1}{2}\left(\frac{d^2}{dT^2}X^a_2\right)(\Delta T)^2,$$

where

$$\Delta T = \Delta t + \frac{1}{c^2}\mathbf{v}_\oplus \cdot \mathbf{B} + O(3),$$

(the integral in (8) is practically of order c^{-3}) the desired relation between barycentric and geocentric baselines reads

$$b^i = B^i - \frac{1}{c^2}(\mathbf{v}_\oplus \cdot \mathbf{B})v_2^i - \frac{1}{c^2}\left(\frac{1}{2}v_\oplus^i v_\oplus^k + \overline{U}(z_\oplus)\delta_{ik}\right)B^k + \Delta\xi^i + O(3) \qquad (11)$$

with

$$\Delta\xi^i \equiv \xi^i(T_1, X_1^a) - \xi^i(T_2, X_2^a).$$

Using equation (8), the VLBI-delay equation (7) for (Δt) and the relation (11) for the baselines we obtain the formal expression ($\mathbf{B} \cdot \boldsymbol{k} = B^i k^i$ etc.):

$$\begin{aligned}
\Delta T = & \\
& -\frac{1}{c}(\mathbf{B}\cdot\boldsymbol{k}) - \frac{1}{c^2}(\mathbf{B}\cdot\boldsymbol{k})\boldsymbol{k}\cdot(\mathbf{v}_\oplus + \mathbf{v}_2) + \frac{1}{c^2}(\mathbf{v}_\oplus\cdot\mathbf{B}) \\
& + \frac{1}{c^3}(\mathbf{v}_\oplus\cdot\mathbf{v}_2)(\mathbf{B}\cdot\boldsymbol{k}) - \frac{1}{c^3}(\mathbf{B}\cdot\boldsymbol{k})[\boldsymbol{k}\cdot(\mathbf{v}_\oplus+\mathbf{v}_2)]^2 + \frac{1}{c^3}(\mathbf{B}\cdot\boldsymbol{k})\overline{U}(z_\oplus) \\
& + \frac{1}{2c^3}(\mathbf{v}_\oplus\cdot\boldsymbol{k})(\mathbf{v}_\oplus\cdot\mathbf{B}) + \frac{1}{c^3}(\mathbf{v}_\oplus\cdot\mathbf{B})(\mathbf{v}_2\cdot\boldsymbol{k}) - \frac{1}{c^2}\int_{t_1}^{t_2}\left(\overline{U}(z_\oplus) + \frac{1}{2}\mathbf{v}_\oplus^2\right)dt' \\
& - \frac{1}{c}k^i\Delta\xi^i + \frac{1}{2c^3}(\mathbf{B}\cdot\boldsymbol{k})^2\boldsymbol{k}(\boldsymbol{a}_\oplus + \dot{\mathbf{v}}_2) + \frac{1}{c^3}(\mathbf{B}\cdot\boldsymbol{k})(\boldsymbol{a}_\oplus\cdot\Delta\boldsymbol{r}_2) \\
& + (\Delta t)_{\mathrm{grav}} + O(4). \qquad (12)
\end{aligned}$$

Keeping only terms with amplitudes greater than 1 picosec for baselines of the order of 6000 km, we approximately find:

$$\begin{aligned}
\Delta T = & \\
& -\frac{1}{c}(\mathbf{B}\cdot\boldsymbol{k}) - \frac{1}{c^2}(\mathbf{B}\cdot\boldsymbol{k})\boldsymbol{k}\cdot(\mathbf{v}_\oplus + \mathbf{v}_2) + \frac{1}{c^2}(\mathbf{v}_\oplus\cdot\mathbf{B}) \\
& + \frac{1}{c^3}(\mathbf{v}_\oplus\cdot\mathbf{v}_2)(\mathbf{B}\cdot\boldsymbol{k}) - \frac{1}{c^3}(\mathbf{B}\cdot\boldsymbol{k})[\boldsymbol{k}\cdot(\mathbf{v}_\oplus+\mathbf{v}_2)]^2 + \frac{1}{c^3}(\mathbf{B}\cdot\boldsymbol{k})\left(2\overline{U}(z_\oplus) + \frac{1}{2}\mathbf{v}_\oplus^2\right) \\
& + \frac{1}{2c^3}(\mathbf{v}_\oplus\cdot\boldsymbol{k})(\mathbf{v}_\oplus\cdot\mathbf{B}) + \frac{1}{c^3}(\mathbf{v}_\oplus\cdot\mathbf{B})(\mathbf{v}_2\cdot\boldsymbol{k}) + (\Delta t)_{\mathrm{grav}}. \qquad (13)
\end{aligned}$$

Finally, the geocentric coordinate time T can be related with proper time τ as indicated by some (atomic) clock located at some VLBI station. Neglecting all tidal effects on local clock rates for clocks at rest at the Earth's surface we find

$$\frac{d\tau}{dT} \simeq 1 - \frac{1}{c^2}\left(U_\oplus(\boldsymbol{X}) + \frac{1}{2}(\boldsymbol{\Omega}\times\boldsymbol{X})^2\right) = 1 - \frac{1}{c^2}U_{\mathrm{geo}}(\boldsymbol{X}), \qquad (14)$$

where $U_\oplus$ is the gravitational potential of the Earth and $\mathbf{\Omega}$ is the angular velocity of the Earth's rotation. This can be written in the form

$$d\tau \simeq \left[1 - \frac{1}{c^2}U^0_{\rm geo} + \frac{1}{c^2}g(\psi)h\right] dT, \tag{15}$$

where $U^0_{\rm geo}$ is the geopotential at the geoid, $g(\psi) = (9.78027 + 0.05192\sin^2\psi) \times 10^2\,{\rm cm/s^2}$ is the latitude dependent gravity acceleration and h is the height above the geoid. Instead of using this formula for the $T \leftrightarrow \tau$ relation, we split it into two parts, defining $\tau^* = {\rm TT}$ as proper time on the geoid:

$$d\tau^* = d({\rm TT}) \equiv \left(1 - \frac{1}{c^2}U^0_{\rm geo}\right) dT \equiv \kappa_0\, dT = \kappa_0\, d({\rm TCG}) \tag{16a}$$

$$d\tau = \left(1 + \frac{1}{c^2}g(\psi)h\right) d\tau^*. \tag{16b}$$

The constant κ_0 relating τ^* with the geocentric coordinate time T has the numerical value

$$\kappa_0 \simeq 1 - 6.9 \times 10^{-10}.$$

Finally we would like to adress the question of the orientation of spatial coordinates of the local geocentric system. This orientation is determined by the matrix R^i_a (remember that in eqs.(12) and (13) $\mathbf{B}\cdot\boldsymbol{k} = B^i k^i$ with $B^i = R^i_a B^a$). There are two preferred choices for R^i_a leading to geocentric coordinates which are either

- fixed star oriented (kinematically non-rotating)
- or locally inertial (dynamically non-rotating).

In the first case of kinematically non-rotating coordinates we can take $R^i_a = \delta^i_a$. Then the geodesic precession will be in the precession-nutation matrices as well as in the dynamical equations (e.g. for satellies orbiting the Earth); it will not appear in the group delay equations (12) or (13). On the other hand if dynamically non-rotating geocentric coordinates are chosen then the geodesic precession (secular and annual term) has to be included in the R^i_a matrix. In this case the precession-nutation matrices (and dynamical equations) do not contain the geodesic precession.

References

Brumberg, V.A., 1990, "Essential Relativistic Celestial Mechanics", Hilger, Bristol

Brumberg, V.A., Kopejkin, S.M., 1988, in: "Reference Systems", J.Kovalevsky, I.I. Mueller and B.Kolaczek (eds.), Reidel, Dordrecht

Brumberg, V.A., Kopejkin, S.M., 1989, Nuovo Cim. B103, 63

Blanchet,L., Damour,T., 1989, Ann. Inst. Henri Poincaré, **50**, 377

Damour,T., Soffel,M., Xu,C., 1990a, in: "Les Journées 1990", Systemes de Reference Spatio-Temporels, N.Capitaine (ed.), Observatoire de Paris

Damour,T., Soffel,M., Xu,C., 1991a, "General Relativistic Celestial Mechanics I. Method and Definition of Reference Systems", Phys.Rev. D, in press

Damour,T., Soffel,M., Xu,C., 1991b, "Relativistic Celestial Mechanics and Reference Frames", Proc. of the IAU Colloqium 127, Virginia Beach, Oct., 14-20, 1990

Finkelstein,A.M., Kreinovich,V.J., Pandey,S.N., 1983, Astrophys. Space Sci. **94**, 233

Hellings, R.W., 1986, Astron. J. **91**, 650

Herring, T., 1989, Memo to Jim Ryan, dated January, 30, 1989 based upon previous notes by I.I.Shapiro

Misner,C., Thorne,K.S., Wheeler,J.A., 1973, "Gravitation", Freeman, San Francisco

Richter, G.W., Matzner, R.A., 1983, Phys. Rev. 28, 3007

Soffel,M., Ruder,H., Schneider,M., Campbell,J., Schuh,H., 1986, in: "Relativistic effects in Celestial Mechanics and Geodesy", J.Kovalevsky and V.Brumberg (eds.), Reidel, Dordrecht

Soffel,M., 1989, "Relativity in Astrometry, Celestial Mechanics and Geodesy", Springer, Heidelberg, Berlin, New York

Soffel, M., Müller, J., Wu, X., Xu, C., 1991, Astron. J., in press

Will,C., 1981, "Theory and Experiment in Gravitational Physics", Cambridge University Press, Cambridge

Zeller,G., Soffel,M., Ruder,H., Schneider,M., 1986, Veröff. der Bayr. Komm. f.d. Intern. Erdmessung, Astronomisch-Geodätische Arbeiten, Heft Nr.48, pp. 218-236

GENERAL RELATIVISTIC MODEL OF VLBI OBSERVABLES

SERGEI A. KLIONER
Institute of Applied Astronomy,
197042, 8, Zhdanovskaya st.,
Leningrad, USSR

Abstract. A consistent general relativistic model of VLBI observations of quasars, pulsars, interplanetary stations and Earth satellites is described. The present model is accurate at the level of 1 ps of time delay and 1 fs/s of delay rate.

Our treatment is based on a relativistic hierarchy of reference systems (RS). A barycentric RS is used to study the light propagation from distant celestial objects as well as the motion of the bodies inside the Solar system. All quantities defined in the neighborhood of the Earth such as positions and velocities of earth-based antennas and Earth satellites are described in a local inertial geocentric RS.

Particular attention is given to gravitational effects. We consider the influence of spherically symmetric fields in post-Newtonian and post-post-Newtonian approximations as well as the effects of the quadrupole gravitational fields of the Solar system bodies and their translational and rotational motion.

1. Introduction

The present accuracy of VLBI observations makes us to use a model of VLBI observables, which is accurate at the level of 1 ps of time delay and 1 fs/s of delay rate. There are many papers devoted to relativistic models of VLBI observables [Brumberg, 1981; Finkelstein et al., 1983; Murray, 1983; Gubanov et al., 1983; Pavlov, 1985; Brumberg, 1986; Hellings, 1986; Murray, 1986; Cannon et al., 1986; Soffel et al., 1986; Zeller et al., 1986; Cannon, Lisewski, 1987; Zhu, Groten, 1988; Soffel et al., 1990; Hellings, Shahid-Saless, 1990; Kopejkin, 1990; Aleksandrov et al., 1990]. Although not all results of these papers coincide with each other, the papers published in last two or three years are in agreement. Nevertheless, some points of VLBI modeling have not been discussed till now.

First, the formula, describing the delay rate with acceptable accuracy, has not been published. The delay rate is often modeled by numerical differentiation of time delay. The operation of numerical differentiation is numerically unstable. That is why the construction of a separate analytical model of this observable seems to be useful.

Second, gravitational effects should be considered with more details. At the level of 1 ps we cannot confine ourselves to the post-Newtonian effects in spherically symmetric gravitational field. A number of second-order contributions has to be analyzed as well.

Third, at the present time there is no adequate relativistic model of VLBI observations of Earth satellites and near-Earth spacecrafts.

2. Basic Concepts

The basic problem of VLBI is shown on Fig.1. Let we have a source whose position relative to some reference system (RS) is $\underline{x}_s$. At the moment t_0 of the coordinate time of this RS the source emits a signal, which arrives at two stations at the moments t_1 and t_2. The coordinates of the stations at the moments of reception are $\underline{x}_1$ and $\underline{x}_2$ respectively. Each station has its own atomic clock, which measures proper time of the station. The moments of reception correspond to the clocks' reading τ_1 and τ_2. Our aim is to calculate the observed quantities, that is time delay $\Delta\tau = \tau_2 - \tau_1$ and its derivative with respect to the proper time of one of the stations, on the basis of trajectories of the observers and the source, and some other additional information.

Some care must be taken in choosing RS to be used. According to the basic principle of General Relativity, an analysis of any process may be performed in any RS. The choice of RS is governed mostly by the considerations of convenience. At the present time it is widely accepted that in order to analyze properly VLBI observations of remote sources one need at least two relativistic reference systems (RS) [Kopejkin, 1990; Hellings, Shahid-Saless, 1990; Soffel at al.,1990]. A barycentric RS (BRS) turns out to be convenient for the analysis of the light propagation from distant celestial objects as well as the motion of bodies inside the Solar system. A local inertial geocentric RS (GRS) is adequate for the analysis of processes occurring in the neighborhood of the Earth, that is the motion of an Earth satellite, the light propagation between a satellite and an earth-based observer, and the rotation of the Earth.

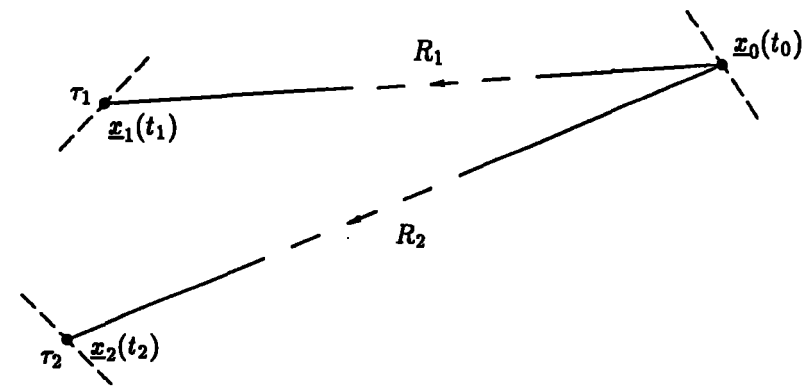

Fig.1. VLBI observations.

In the construction of both BRS and GRS there is a marked degree of arbitrariness. Different approaches to the construction of the reference systems in question have been developed by a number of authors [Ashby, Bertotti, 1986; Brumberg, Kopejkin, 1989; Voinov, 1990; Damour et al., 1990; Brumberg, 1991]. The model presented in this paper is based on the hierarchy of relativistic reference systems developed in [Brumberg, Kopejkin, 1989; Brumberg, 1991]. We denote barycentric coordinate time and spatial coordinates by (t, x^i), and geocentric ones by (u, w^i). The details of the construction of BRS and GRS as well as the explicit formulas describing their metric tensors can be found in [Kopejkin, 1988; Brumberg, Kopejkin, 1989; Brumberg, 1991; Klioner, 1991].

The coordinate transformation between the BRS and GRS coordinates has the form

$$u = t - \frac{1}{c^2}(A(t) + \underline{v}_E \underline{r}_E) + O(c^{-4}), \tag{2.1}$$

$$\begin{aligned} w^i = r^i_E + \frac{1}{c^2}\Big\{ & \frac{1}{2} v^i_E (\underline{v}_E \underline{r}_E) + q F^{ij} r^j_E + r^i_E \overline{U}(t, \underline{x}_E(t)) \\ & + r^i_E (\underline{a}_E \underline{r}_E) - \frac{1}{2} a^i_E r^2_E \Big\} + O(c^{-4}), \end{aligned} \tag{2.2}$$

$$\frac{dA}{dt} = \frac{1}{2} v^2_E + \overline{U}(t, \underline{x}_E(t)), \tag{2.3}$$

$$\frac{dF^{ij}}{dt} = 3 v^{[i}_E \overline{U}_{,k]}(t, \underline{x}_E(t)) - 4 \overline{U}^{[i}{}_{,k]}(t, \underline{x}_E(t)) + \ldots, \tag{2.4}$$

$$\overline{U}(t, \underline{x}) = \sum_{A \neq E} \left\{ \frac{G M_A}{r_A} + \frac{3}{2} \frac{G I^A_{ij} N^i_A N^j_A}{r^3_A} + \ldots \right\}, \tag{2.5a}$$

$$\overline{U}^i(t, \underline{x}) = \sum_{A \neq E} \left\{ \frac{G M_A}{r_A} v^i_A + \frac{1}{2} G \epsilon^i{}_{jk} S^j_E \frac{N^k_E}{r^2_E} + \ldots \right\}, \tag{2.5b}$$

where $\underline{r}_A = \underline{x} - \underline{x}_A$; $\underline{N}_A = \underline{r}_A/r_A$; $\epsilon^i{}_{jk}$ is fully antisymmetric Levi-Civita symbol; $\underline{x}_A, \underline{v}_A, \underline{a}_A$ are barycentric coordinates, velocity and acceleration of the body A respectively; S^i_A is the angular momentum (spin) of that body; I^A_{ij} is its trace-free quadrupole moment; and q is a numerical parameter. Value $q = 1$ corresponds to dynamically non-rotating GRS, while value $q = 1$ leads to kinematically non-rotating one [Brumberg, 1991].

All possible sources can be divided into three groups. The first group contains remote sources: quasars and pulsars. When we deal with such sources, we can either neglect parallax and proper motion at all or confine ourselves to few leading terms describing these effects. Interplanetary spacecrafts belong to the second group. Here we must account for parallax and proper motion to the full degree. The position of the source must be represented herewith by its rectangular coordinates directly rather than by the direction to the source. Finally, the third group contains the sources which are extremely near to the Earth, that is Earth satellites.

As far as observers are concerned, two situations may be considered: (1) the observers are situated anywhere in the Solar system; (2) the observers are situated on the Earth's surface or on an Earth satellite. In this paper we will consider the situation when both observers are situated in the neighborhood of the Earth.

Let us outline the principal steps needed to construct the model.

1. We have to choose RS(s) to be used in each particular case. If the motions of both source and observers can be described adequately in BRS, we can use only this RS. If both source and observers are situated in the neighborhood of the Earth, we can use GRS only. If we have a distant source (quasar, pulsar or interplanetary station) while the observers are situated near the Earth, we must use both BRS and GRS.
2. In the chosen RS using the laws of the light propagation we have to find the formula for the difference of coordinate moments of reception of the signal at two stations. Here we take into account the influence of the motion of a source and observers as well as the effect of gravitational fields on the light propagation.
3. In the case when we have a distant source while observers are situated near the Earth, we use BRS to describe the light propagation and the motion of the source, and GRS to describe the motion of the observers. In this case we must calculate barycentric coordinates of the observers on the basis of their geocentric coordinates.
4. We have to convert coordinate time difference $t_2 - t_1$ into observable time delay $\tau_2 - \tau_1$ and perform corresponding procedure for delay rate.

Thus, to analyze VLBI observations we must know: (1) how the light propagates in BRS and GRS, and (2) how proper time of an observer relates to the coordinate time of GRS.

The proper time τ_a of an observer moving along the trajectory $\underline{w}_a(u)$ is defined by [Brumberg,1991; Klioner, 1991]:

$$\begin{aligned}\frac{d}{du}\tau_a = 1 - \frac{1}{c^2}\Big\{&\frac{1}{2}\underline{w}_a^2(u) + U_E(u, \underline{w}_a(u)) \\ &+ GM_L\left(|\underline{w}_a(u) + \underline{r}_{EL}|^{-1} - r_{EL}^{-1} + r_{EL}^{-3}\,\underline{w}_a(u)\underline{r}_{EL}\right) \\ &+ \frac{1}{2}GM_S\frac{w_a^2(u)}{r_{ES}^3}(3\cos^2\alpha_S(u) - 1) + \dots\Big\},\end{aligned} \tag{2.6}$$

$$\cos\alpha_S = \frac{\underline{w}_a\underline{r}_{ES}}{w_a r_{ES}}, \quad \underline{r}_{EA} = \underline{x}_E - \underline{x}_A,$$

U_E being the gravitational potential of the Earth. The third and fourth terms in (2.6) describe the tidal influence of the Moon and Sun respectively. It should be noted that the tidal potential of external bodies results in the additional difference between the GRS

coordinate time u and the proper time τ_a of an observer rigidly connected to the Earth's surface. This additional difference consists of the secular drift (about $2 \cdot 10^{-17}$) and a number of periodic terms. The two largest periodic terms – diurnal and semi-diurnal – have the amplitudes 0.3 ps and 0.2 ps respectively. The influence of these periodic terms on the observable time delay could in principle amount to ~ 1 ps, but apparently is compensated by the usual piecewise-quadratic clock model.

3. Propagation of the light

At the level of accuracy of 1 ps we have to consider not only post-Newtonian effects in the light propagation, but several smaller effects as well. The first effect that we investigate is the influence of the translational motion of gravitating bodies. It is widely accepted that the coordinates of a gravitating body should be evaluated at the moment of closest approach of the received signal to that body. But at the present time there is no theoretical proof of this statement. We have some considerations on this point.

The equations of the light propagation have the form

$$\begin{aligned}\ddot{\underline{x}} = -\sum_A \frac{GM_A}{r_A^3}\underline{r}_A \Bigg\{ & \left(1 + \frac{\dot{\underline{x}}\dot{\underline{x}} - 4\dot{\underline{x}}_A\dot{\underline{x}}}{c^2}\right) \\ & + \frac{1}{c^2}\dot{\underline{x}}\left(3\underline{r}_A\dot{\underline{x}}_A - 4\underline{r}_A\dot{\underline{x}} + \frac{1}{c^2}\left(4(\underline{r}_A\dot{\underline{x}})(\dot{\underline{x}}_A\dot{\underline{x}}) - (\dot{\underline{x}}\dot{\underline{x}})(\underline{r}_A\dot{\underline{x}}_A)\right)\right) \\ & + \frac{4}{c^2}\dot{\underline{x}}_A(\underline{r}_A\dot{\underline{x}})\Bigg\}.\end{aligned} \tag{3.1}$$

Here we suppose that gravitating bodies are point masses, which move along arbitrary trajectories. The right-hand side of (3.1) contains the usual post-Newtonian terms as well as the terms which are proportional to the velocities $\dot{\underline{x}}_A$ of gravitating bodies. Post-post-Newtonian terms are neglected. The right-hand side of the equations depends on the positions and velocities of gravitating bodies which are complicated functions of time. To integrate the equations of motion analytically we must use an approximation of the functions $\underline{x}_A$ and $\dot{\underline{x}}_A$. Usually the positions of the bodies are supposed to be constant. We make next step and suppose that the positions of bodies are linear functions of time, that is we expand the function $\underline{x}_A$ in Taylor series around some unknown moment t_A and limit ourselves to the first two terms

$$\underline{x}_A = \underline{x}_A(t_A) + \underline{v}_A(t_A)(t - t_A) + O\left(a_A(t_A)(t - t_A)^2\right). \tag{3.2}$$

Substituting this linear function into the equation (3.1) and using usual initial values

$$\underline{x}(t_0) = \underline{x}_0, \quad \dot{\underline{x}}(-\infty) = c\underline{\sigma}, \quad \underline{\sigma}\underline{\sigma} = 1 \tag{3.3}$$

we can integrate the equation (3.1) [Klioner, 1989a]:

$$\begin{aligned}&\underline{x}(t) = \underline{x}_0 + c\underline{\sigma}(t - t_0) + \Delta\underline{x}, \\ &\Delta\underline{x} = -\sum_A \frac{2GM_A}{c^2}\left\{\underline{\sigma} \times (\underline{r}_{A0} \times \underline{g}_A)[A(t) - A(t_0)] + \underline{g}_A[B(t) - B(t_0)]\right\}, \\ &A = (g_A r_A - \underline{g}_A\underline{r}_A)^{-1}, \quad B = \ln(g_A r_A + \underline{g}_A\underline{r}_A), \quad \underline{g}_A = \underline{\sigma} - \underline{v}_A(t_A)/c, \quad \underline{r}_{A0} = \underline{r}_A(t_0).\end{aligned} \tag{3.4}$$

The question around what moment we must perform the expansion (3.2) still remains. Our aim is to find moment t_A which gives minimal inaccuracy of the equation of motion of a

photon. Substitution of (3.2) into (3.1) enables one to see that the remainder term of (3.2) gives the error in the right-hand side of (3.1), which can be estimated as [Klioner, Kopejkin, 1991]

$$
\begin{aligned}
|\delta\ddot{\underline{x}}| &\lesssim \left|\frac{\partial F^i}{\partial x_A^j} a_A^j (t-t_A)^2 + \frac{\partial F^i}{\partial v_A^j} a_A^j (t-t_A)\right| \\
&\lesssim \sum_A \frac{GM_A}{r_A} a_A \left\{ 4\frac{(t-t_A)^2}{r_A^2} + \frac{9}{c}\frac{|t-t_A|}{r_A} \right\} \\
&\leq \frac{1}{c^2} \sum_A \frac{GM_A}{r_A} a_A \left\{ 4\frac{l_A^2}{d_A^2} + 9\frac{l_A}{d_A} \right\}.
\end{aligned}
\tag{3.5}
$$

Here $l_A = |\underline{x}(t_A) - \underline{x}_A(t_A)|$ is the distance between the body A and the photon at the moment t_A, and d_A is the same distance at the moment of their closest approach; $\underline{d}_A = \underline{\sigma} \times (\underline{r}_{A0} \times \underline{\sigma})$. It is obvious that to minimize the error of the photon's acceleration $|\delta\ddot{\underline{x}}|$ we must choose t_A equal to the moment of closest approach. In this case the error is estimated as $|\delta\ddot{\underline{x}}| \lesssim 13c^{-2}\sum_A GM_A a_A r_A^{-1}$, and we can be sure that the error is of higher order of magnitude than the effects we account for explicitly. Indeed, the error $|\delta\ddot{\underline{x}}|$ in this case results in post-post-Newtonian effects. Thus we have proven that the coordinates (and velocity) of the gravitating body A have to be evaluated at the moment of closest approach of the photon to that body.

In the case of the initial-value problem (3.3) the moment t_A can be calculated as

$$
\begin{aligned}
&t_A = \min(t_0, t_*), \\
&t_* = t_0 - c^{-1}\underline{\sigma}\,\underline{r}_{A0} - c^{-2}\left(2(\underline{\sigma}\,\underline{r}_{A0})(\underline{\sigma}\,\underline{v}_A) - \underline{v}_A \underline{r}_{A0}\right), \quad \underline{v}_A = \underline{v}_A(t_0).
\end{aligned}
\tag{3.6}
$$

Besides the effect just discussed we have considered some other second-order effects in the light propagation. For constructing a model of VLBI observation the formula which describes the coordinate time for a photon to propagate from one fixed point to another one is essential. Let us consider a boundary-value problem

$$
\underline{x}(t_0) = \underline{x}_0, \quad \underline{x}(t) = \underline{x}, \quad \underline{R}(t, t_0) = \underline{x} - \underline{x}_0, \quad t \geq t_0. \tag{3.7}
$$

Using the results of the papers [Brumberg, 1987; Klioner, 1989b] one gets

$$
c(t - t_0) = R + \Delta R_{pN} + \Delta R_Q + \Delta R_M + \Delta R_R + \Delta R_{ppN}, \tag{3.8}
$$

$$
\Delta R_{pN} + \Delta R_M = \sum_A \frac{2GM_A}{c^2}\left(1 - \frac{1}{c}\underline{\sigma}\,\underline{v}_A\right) \ln \frac{r_A + r_{A0} + g_A R}{r_A + r_{A0} - g_A R}, \tag{3.9}
$$

$$
\begin{aligned}
&\Delta R_Q = \sum_A \frac{G}{c^2} I_{pq}^A \{\mathcal{T}_A^{pq}(t) - \mathcal{T}_A^{pq}(t_0)\}, \\
&\quad \mathcal{T}_A^{pq}(t) = \sigma^p \sigma^q \left[\underline{\sigma}\,\underline{N}_A (d_A^{-2} - r_A^{-2})\right] - 2\sigma^p d_A^q r_A^{-3} + h_A^p h_A^q \left[\underline{\sigma}\,\underline{N}_A (2d_A^{-2} + r_A^{-2})\right],
\end{aligned}
\tag{3.10}
$$

$$
\Delta R_R = \sum_A \frac{2G}{c^3} \frac{\underline{S}_A(\underline{\sigma} \times \underline{h}_A)}{d_A} (\underline{\sigma}\,\underline{N}_A - \underline{\sigma}\,\underline{N}_{A0}), \tag{3.11}
$$

$$
\begin{aligned}
\Delta R_{ppN} = \frac{G^2 M_S^2}{c^4} \Bigg\{ &\frac{15}{4d_S} \arccos \underline{N}_S \underline{N}_{S0} - \frac{4R}{r_S r_{S0} + \underline{r}_S \underline{r}_{S0}} \\
&+ \frac{1}{8R}\left(\frac{r_{S0}^2 - r_S^2 - R^2}{r_S^2} + \frac{r_S^2 - r_{S0}^2 - R^2}{r_{S0}^2}\right)\Bigg\},
\end{aligned}
\tag{3.12}
$$

$$
\underline{h}_A = \underline{d}_A / d_A, \quad \underline{N}_A = \underline{r}_A / r_A, \quad \underline{N}_{A0} = \underline{N}_A(t_0).
$$

Here ΔR_{pN} and ΔR_{ppN} are the effects of the spherically symmetric gravitational fields in post- and post-post-Newtonian approximations, ΔR_Q, ΔR_M and ΔR_R are the terms induced by the quadrupole gravitational field of the Solar system bodies and their translational and rotational motions respectively.

In the case of the boundary-value problem (3.7) the moment of closest approach can be written as

$$t_A = \min(t, \max(t_0, t_*)), \tag{3.13}$$

t_* being defined by (3.6).

The equations of the light propagation in GRS are quite simple because the gravitational fields of all the bodies except the Earth manifest themselves only in the form of tidal terms. With the accuracy sufficient for the purposes of this paper the interval of GRS coordinate time $u-u_0$ for a photon to propagate from one fixed point $\underline{w}_0$ to another one $\underline{w}$ can be written as [Voinov, 1990; Klioner, 1991]

$$c(u-u_0) = |\underline{w}-\underline{w}_0| + \frac{2GM_E}{c^2}\ln\frac{w+w_0+|\underline{w}-\underline{w}_0|}{w+w_0-|\underline{w}-\underline{w}_0|}. \tag{3.14}$$

4. Remote sources

4.1. VLBI IN THE SOLAR SYSTEM: GENERAL FORMULAS

In the following calculations we assume that the distance between a source and the Solar system is not greater than 50 pc (this is the distance to the nearest known pulsar PSR1929+10). The proper motion is supposed to be less than 10″/yr. In the notations of Fig.1 we can write two equations relating the moments t_1 and t_2 to the moment of emission of the signal t_0

$$\begin{aligned} c(t_i - t_0) &= R_i + \Delta R_i, \\ \underline{R}_i &= \underline{x}_i(t_i) - \underline{x}_s(t_0), \end{aligned} \tag{4.1}$$

where ΔR_i are the gravitational retardations of the light propagating from $\underline{x}_s(t_0)$ to $\underline{x}_i(t_i)$. Subtracting the equation corresponding to $i=2$ and that corresponding to $i=1$, using the formula $\underline{x}_2(t_2) = \underline{x}_2(t_1) + \dot{\underline{x}}_2(t_1)(t_2-t_1) + \frac{1}{2}\ddot{\underline{x}}_2(t_1)(t_2-t_1)^2$, and considering $x_s = |\underline{x}_s(t_0)| \to \infty$, one can easily obtain

$$\begin{aligned} c\Delta t = c(t_2-t_1) = -\underline{k}\,\underline{b}\Big(&1 - c^{-1}\underline{k}\,\dot{\underline{x}}_2(t_1) + c^{-2}(\underline{k}\,\dot{\underline{x}}_2(t_1))^2 \\ &- c^{-3}(\underline{k}\,\dot{\underline{x}}_2(t_1))^3 + c^{-1}\frac{\underline{x}_2(t_1)(\underline{k}\times\dot{\underline{x}}_2(t_1)\times\underline{k}))}{x_s}\Big) \\ &+ \Big(\frac{|\underline{k}\times\underline{b}|^2 + 2\underline{x}_1(t_1)(\underline{k}\times(\underline{b}\times\underline{k}))}{2x_s} + c\Delta t_{gr}\Big)\times \\ &\times\left(1 - c^{-1}\underline{k}\,\dot{\underline{x}}_2(t_1)\right) - \frac{1}{2}c^{-2}(\underline{k}\,\ddot{\underline{x}}_2(t_1))(\underline{k}\,\underline{b})^2, \end{aligned} \tag{4.2}$$

where $\underline{k} = \underline{x}_s(t_0)/x_s(t_0)$, $\Delta t_{gr} = c^{-1}(\Delta R_2 - \Delta R_1)$ is gravitational time delay, $\underline{b} = \underline{b}(t_1) = \underline{x}_2(t_1) - \underline{x}_1(t_1)$ is the barycentric baseline vector. When calculating Δt_{gr} we can believe that $\underline{x}_2(t_2) = \underline{x}_2(t_1 - c^{-1}\underline{k}\,\underline{b})$. We neglect herewith terms, which are $\lesssim$ 0.03 ps.

Given sufficiently long row of observations one could measure the proper motion of the source. Let the coordinates of the latter be

$$\underline{x}_s(T) = \underline{x}_s(T^*) + \underline{V}(T - T^*) + \frac{1}{2}\underline{A}(T - T^*)^2. \tag{4.3}$$

It is easy to see that

$$\underline{k}(t) = \underline{k}_0 + \underline{\mu}\Delta T + \frac{1}{2}\dot{\underline{\mu}}\Delta T^2 + \ldots, \tag{4.4}$$

where $\underline{k}_0 = \underline{k}(t^*) = \underline{x}_s(T^*)/x_s(T^*)$, t^* is the moment of observation of the signal emitted by the source at the moment T^* (we suppose that t^* is the moment at which we start to observe the source), t is the moment at which we observe the signal emitted at the moment T,

$$\Delta T = T - T^* = (1 + c^{-1}\underline{k}_0\underline{V})^{-1}\left(t - t^* + c^{-1}\underline{k}_0(\underline{x}_1(t) - \underline{x}_1(t^*))\right), \tag{4.5}$$

$$\begin{aligned} \underline{\mu} &= x_s^{-1}\underline{k}_0 \times (\underline{V} \times \underline{k}_0), \\ \dot{\underline{\mu}} &= x_s^{-1}\underline{k}_0 \times (\underline{A} \times \underline{k}_0) - x_s^{-2}(\underline{k}_0|\underline{k}_0 \times \underline{V}|^2 + 2(\underline{k}_0\underline{V})(\underline{k}_0 \times (\underline{k}_0 \times \underline{V}))) \end{aligned} \tag{4.6}$$

To calculate the observed delay rate the formula describing dt_2/dt_1 is needed. By differentiating (4.2) as an implicit function $\Phi(t_1, t_2) \equiv 0$, one gets

$$\begin{aligned} \frac{dt_2}{dt_1} &= 1 + c^{-1}\underline{k}(\dot{\underline{x}}_1 - \dot{\underline{x}}_2) + c^{-2}\underline{k}\,\dot{\underline{x}}_2(\underline{k}\,\dot{\underline{x}}_2 - \underline{k}\,\dot{\underline{x}}_1) \\ &+ c^{-3}(\underline{k}\,\dot{\underline{x}}_2)^2(\underline{k}\,\dot{\underline{x}}_1 - \underline{k}\,\dot{\underline{x}}_2) - 2c^{-1}(\underline{x}_2 - \underline{x}_1)\frac{\underline{\mu}}{1 + c^{-1}\underline{k}\,\underline{V}} \\ &+ c^{-1}\frac{\underline{x}_1(\underline{k} \times ((\dot{\underline{x}}_2 - \dot{\underline{x}}_1) \times \underline{k})) + (\underline{x}_2 - \underline{x}_1)(\underline{k} \times (\dot{\underline{x}}_2 \times \underline{k}))}{x_s} \\ &+ \frac{\partial}{\partial t_1}\Delta t_{gr} + \frac{\partial}{\partial t_2}\Delta t_{gr} + c^{-1}\underline{k}\,\dot{\underline{x}}_1\frac{\partial}{\partial t_2}\Delta t_{gr} \\ &- c^{-1}\underline{k}\,\dot{\underline{x}}_2\left(2\frac{\partial}{\partial t_2}\Delta t_{gr} + \frac{\partial}{\partial t_1}\Delta t_{gr}\right), \quad \underline{x}_i = \underline{x}_i(t_i),\ \dot{\underline{x}}_i = \dot{\underline{x}}_i(t_i). \end{aligned} \tag{4.7}$$

In (4.7) we suppose that t_2 has been already calculated using (4.2)–(4.6).

4.2. GRAVITATIONAL EFFECTS

According to the definition $\Delta t_{gr} = c^{-1}(\Delta R_2 - \Delta R_1)$. On the analogy of (3.8) we can write

$$\Delta t_{gr} = \Delta t_{pN} + \Delta t_M + \Delta t_R + \Delta t_Q + \Delta t_{ppN}. \tag{4.8}$$

Let us analyze each term separately.

1. <u>The post-Newtonian effects in the fields of moving bodies</u>.

On the basis of (3.9) one gets

$$\begin{aligned} \Delta t_{pN} + \Delta t_M &= \sum_A \frac{2GM_A}{c^2}\left(1 + \frac{1}{c}\underline{k}\,\underline{v}_A(t_{A1})\right)\ln\frac{r_{A1} + \underline{k}\,\underline{r}_{A1}}{r_{A2} + \underline{k}\,\underline{r}_{A2}}, \\ \underline{r}_{Ai} &= \underline{x}_i(t_i) - \underline{x}_A(t_{Ai}), \end{aligned} \tag{4.9}$$

where the moments t_{Ai} are defined by (3.13). The coordinates of a gravitating body have to be evaluated at the moment of closest approach of the photon to that body. This is essential for correct modeling. For example, the evaluation of the Jupiter's coordinates at the moment of reception of a signal on the Earth results in the error ~ 0.5 ns for the baseline $b = 6000$ km. One can neglect herewith the difference between t_{A2} and t_{A1} (the maximal error resulting from this difference for baseline $b = 50000$ km is caused by Jupiter and $\lesssim$ 0.4 ps).

The influence of the non-stationary gravitational field induced by the translational motion of the masses is described by the factor $(1+c^{-1}\underline{k}\,\underline{v}_A(t_{A1}))$ in (3.9). It is easy to see that if $b \leq 50000$ km, its magnitude is less than 0.5 ps (see Table 2).

The magnitudes of Δt_{gr} for several bodies are given in Table 1. In each case two values are shown. The upper value corresponds to $b = 6000$ km, while the lower one corresponds to $b = 50000$ km. If the ratio of b and d_A is sufficiently small, the magnitude of Δt_{gr} is proportional to b and decreases with the angular distance ϕ_A between the body's center of mass and the source as $\cot\phi/2$.

Table 1

Body	Angular distance from the body's center				
	grazing ray	1°	30°	90°	175°
Sun	169 ns 1410 ns	45 ns 369 ns	1.5 ns 12 ns	0.4 ns 3.3 ps	17 ns 0.14 ns
Jupiter	1.5 ns 10 ns	11 ps 92 ps	0.4 ps 3 ps	0.1 ps 0.8 ps	—
Saturn	0.5 ns 3.4 ns	2 ps 13 ps	0.05 ps 0.4 ps	—	—
Uran	0.18 ns 0.94 ns	0.1 ps 1 ps	—	—	—
Neptune	0.23 ns 1.1 ns	0.1 ps 1 ps	—	—	—
Mercury	4 ps 10 ps	0.04 ps 0.12 ps	—	—	—
Venus	33 ps 107 ps	0.4 ps 3.6 ps	0.02 ps 0.1 ps	—	—
Mars	6.5 ps 17.5 ps	0.04 ps 0.33 ps	—	—	—
Moon	1.1 ps 2.5 ps	0.47 ps 1.6 ps	0.02 ps 0.2 ps	—	—
Earth	both observers on the Earth: 21 ps one observer on a satellite: 100 ps				

2. The influence of quadrupole fields.

Using (3.10) one can obtain

$$\Delta t_Q = \sum_A c^{-3} G (f^{pq}_{A2} - f^{pq}_{A1}) I^A_{pq},$$
$$f^{pq}_{Ai} = \left(1 - (\underline{k}\,\underline{N}_{Ai})^3\right) \frac{k^p k^q}{d^2_{Ai}} + \frac{2k^p d^q_{Ai}}{r^3_{Ai}} + \left(2 - 3\underline{k}\,\underline{N}_{Ai} + (\underline{k}\,\underline{N}_{Ai})^3\right) \frac{d^p_{Ai} d^q_{Ai}}{d^4_{Ai}}. \tag{4.10}$$

For an axisymmetric body $\Delta t_Q = 2c^{-3} G M_A J^A_2 (1 - P^2_A (P_A + b)^{-2})$, P_A being the radius of the body A and J^A_2 being the coefficient of the second zonal harmonic of its gravitational field (see Table 2). The magnitude of Δt_Q decreases with ϕ_A very rapidly — as $\cot^3\phi_A$.

3. The influence of the rotation of the bodies.

Using (3.11) one gets

$$\Delta t_R = \sum_A 2c^{-4} G \underline{k} \times \underline{S}_A (\mathcal{F}_{A2} - \mathcal{F}_{A1}), \quad \mathcal{F}_{Ai} = \frac{\underline{N}_{Ai}}{r_{Ai} + \underline{k}\,\underline{r}_{Ai}}. \tag{4.11}$$

A single body gives $|\Delta t_R| \leq 4c^{-4} P_A^{-1} G S_A b/(P_A + b)$ (see Table 2). The magnitude of Δt_R decreases with ϕ_A as $\cot^2\phi_A$. The effect of the Sun's rotation given in Table 2 corresponds to the case of rigid rotation. Accounting for the fact that the Sun's core rotates faster than its surface [Hill et al., 1986] results in seven-fold increasing of the given magnitude.

Table 2

Body	Δt_R	Δt_Q	Δt_M
Sun	0.06 ps 0.5 ps	0.2 ps 1.3 ps	0.01 ps 0.09 ps
Jupiter	0.02 ps 0.1 ps	21 ps 91 ps	0.07 ps 0.46 ps
Saturn	—	8 ps 32 ps	0.02 ps 0.12 ps
Uran	—	2 ps 5 ps	—
Neptune	—	0.7 ps 2 ps	—

4. The post-post-Newtonian effects.

The equation (3.12) gives

$$\Delta t_{ppN} = \sum_A \frac{G^2 M_A^2}{c^5} \left\{ -\frac{4}{r_{A2} + \underline{k}\,\underline{r}_{A2}} + \frac{4}{r_{A1} + \underline{k}\,\underline{r}_{A1}} + \frac{\underline{k}\,\underline{N}_{A2}}{4r_{A2}} - \frac{\underline{k}\,\underline{N}_{A1}}{4r_{A1}} \right.$$
$$\left. + \frac{15}{4|\underline{k} \times \underline{r}_{A2}|} \arccos \underline{k}\,\underline{N}_{A2} - \frac{15}{4|\underline{k} \times \underline{r}_{A1}|} \arccos \underline{k}\,\underline{N}_{A1} \right\}. \tag{4.12}$$

The first two terms in the braces are most important in the cases which are interesting for practice. Their magnitude can be estimated as $16c^{-5}G^2M_A^2 l_A b P_A^{-3}$, $l_A \gg b$ being the distance between the body A and the observers. The magnitude of Δt_{ppN} decreases as $\cot^3 \phi_A$. The numerical estimates are given in Table 3.

Table 3

Body	Angular distance from the body's center				
	grazing ray	1′	10′	1°	10°
Sun	307 ps 2339 ps	—	—	6 ps 47 ps	0.05 ps 0.4 ps
Jupiter	1.5 ps 6.6 ps	0.03 ps 0.2 ps	0.1 fs 1 fs	—	—
Saturn	0.4 ps 1.5 ps	1 fs 10 fs	—	—	—
Uran	0.1 ps 0.5 ps	0.01 fs	—	—	—
Neptune	0.3 ps 1.1 ps	0.01 fs	—	—	—

The influence of gravitational effects on the delay rate observable results from the partial derivatives of Δt_{gr} containing in (4.7). Let us show the explicit formulas for the derivatives of Δt_{pN}:

$$\frac{\partial}{\partial t_i} \Delta t_{pN} = (-1)^{i+1} \sum_A \frac{2GM_A}{c^3} \frac{\underline{N}_{Ai} + \underline{k}}{r_{Ai} + \underline{k}\,\underline{r}_{Ai}} (\dot{\underline{x}}_i(t_i) - \dot{\underline{x}}_A(t_{A1})), \quad i = 1, 2. \tag{4.13}$$

When observing a source which is close to superior conjunction with the Sun or giant planets, the significant effect may result from Δt_Q and Δt_{ppN}, which change rapidly with the angular distance. The necessary formulas can be obtained using (4.10), (4.12). The effects of Δt_M and Δt_R are negligibly small (< 0.1 fs/s).

4.3. VLBI ON THE EARTH AND IN NEAR-EARTH SPACE

All the quantities we have dealt with till now are BRS coordinate quantities. To use the formulas of the two previous Sections we must have barycentric coordinates $\underline{x}_i$, velocities $\dot{\underline{x}}_i$ and accelerations $\ddot{\underline{x}}_i$ of both observers. However, it is convenient to describe earth-based observers and Earth satellites in GRS. Thus, we must calculate barycentric coordinates, velocities and acceleration on the basis of geocentric ones $\underline{w}_i$, $\dot{\underline{w}}_i$ and $\ddot{\underline{w}}_i$.

First of all, we have to derive an expression relating the barycentric baseline vector $\underline{b} = \underline{b}(t_1) = \underline{x}(t_1) - \underline{x}(t_1)$ and geocentric one $\underline{B} = \underline{B}(u_1) = \underline{w}(u_1) - \underline{w}(u_1)$. We suppose that the events which have coordinates $(t_i, \underline{x}_i(t_i))$ in BRS and the events whose GRS coordinates are $(u_i, \underline{w}_i(u_i))$ coincide. That is the GRS coordinate moments of reception of the signal at i-th station are u_i, and the geocentric coordinates of the stations at these moments are $\underline{w}_i(u_i)$. Further, the event $(t_1, \underline{x}_2(t_1))$ in BRS corresponds to the event $(u', \underline{w}_2(u'))$ in GRS. The moment u' is not necessarily equal to u_1. Here, we account for the fact that two events, which are simultaneous in one RS, are not necessarily simultaneous in another one. This phenomenon as applied to the definitions of the baseline vectors in BRS and GRS results in an additional relativistic effect [Kopejkin, 1990; Soffel et al., 1990]. It is easy to see from (2.1) that

$$u' - u = -c^2 \underline{v}_E(t_1)\underline{b} + O(c^{-4}). \tag{4.14}$$

Using (2.2) and (4.14) one gets

$$\begin{aligned} b^i = B^i - c^{-2}\Big\{ & \frac{1}{2}(\underline{B}\,\underline{v}_E)v_E^i + (\underline{B}\,\underline{v}_E)\dot{w}_2^i + qF^{ij}B^j + \overline{U}(t_1, \underline{x}_E)B^i \\ & + \underline{w_2^i(\underline{a}_E\underline{w}_2) - w_1^i(\underline{a}_E\underline{w}_1) - \frac{1}{2}(\underline{B}\,(\underline{w}_1 + \underline{w}_2))a_E^i}\Big\}, \end{aligned} \tag{4.15}$$

a dot over $\underline{w}$ denoting differentiation with respect to the GRS coordinate time u. All barycentric quantities – $\underline{b}, \underline{x}_E, \underline{v}_E, \underline{a}_E, F^{ij}$ – are evaluated at the moment t_1, while the geocentric quantities – $\underline{B}, \underline{w}_i, \dot{\underline{w}}_i$ – at the moment u_1. Hereafter the <u>underlined</u> terms is essential only in the case of a space-born observations. In the analysis of terrestrial observations these terms can be neglected.

The transformation between $\underline{x}_i$ and $\underline{w}_i$ is described by (2.2). The relation of $\dot{\underline{x}}_i$ and $\dot{\underline{w}}_i$ is

$$\begin{aligned} \dot{x}^i = v_E^i + \dot{w}^i - c^{-2}\Big\{ & \Big(\frac{1}{2}v_E^2 + 2\overline{U}(t, \underline{x}_E) + \underline{2\underline{a}_E\underline{w} + \underline{v}_E\dot{\underline{w}}}\Big)\dot{w}^i \\ & + \frac{1}{2}v_E^i(\underline{v}_E\dot{\underline{w}}) + q(\underline{\dot{F}^{ij}w^j} + F^{ij}\dot{w}^j) + \underline{w^i(\underline{a}_E\dot{\underline{w}})} \\ & + \underline{\frac{1}{2}a_E^i(\underline{v}_E\underline{w}) + \frac{1}{2}v_E^i(\underline{a}_E\underline{w}) - a_E^i(\underline{w}\dot{\underline{w}})}\Big\}. \end{aligned} \tag{4.16}$$

The difference of the geocentric velocity $\dot{\underline{w}}$ and its Newtonian value $\dot{\underline{x}} - \underline{v}_E$ is about $3 \cdot 10^{-4}$ m/s in the case of an Earth satellite situated at the distance $|\underline{w}| \leq 50000$ km from the Earth, and $\sim 2 \cdot 10^{-5}$ m/s for an earth-based observer. The accuracy of (4.16) is $\sim 10^{-7}$ m/s. Such an accuracy is needed only for the model of delay rate. In the model of time delay barycentric velocities and accelerations can be calculated using their Newtonian expressions

$$\begin{aligned} \dot{\underline{x}}_i(t_1) &= \underline{v}_E(t_1) + \dot{\underline{w}}_i(u_1), \\ \ddot{\underline{x}}_2(t_1) &= \underline{a}_E(t_1) + \ddot{\underline{w}}_2(u_1). \end{aligned} \tag{4.17}$$

The final step towards the complete relativistic model of time delay is the conversion of the BRS coordinate time interval $\Delta t = t_2 - t_1$ into observable time delay. It is convenient to

perform this conversion in two stages. First, we convert Δt into $\Delta u = u_2 - u_1$, and then we find an expression relating Δu to immediately observable quantity.

Considering two events – receptions of the signal at the first and second stations – and using (2.1)–(2.2), we get

$$\begin{aligned}\Delta u = \Delta t &- c^{-2}\underline{v}_E(t_1)\underline{B} + c^{-3}\underline{k}\,\underline{B}\Big(\frac{1}{2}v_E^2(t_1) + \underline{v}_E(t_1)\dot{\underline{w}}_2(u_1)\\ &+ \overline{U}(t_1, \underline{x}_E(t_1)) + \underline{a}_E(t_1)\underline{w}_2(u_1)\Big)\\ &- c^{-4}\Big(\underline{2\underline{v}_E(t_1)\underline{B}\;\overline{U}(t_1, \underline{x}_E(t_1))} + \underline{\frac{1}{2}(\underline{k}\,\underline{B})^2(2\underline{v}_E(t_1)\ddot{\underline{w}}_2(u_1))}\Big).\end{aligned} \tag{4.18}$$

The observable time delay is the difference of the readings of atomic clocks situated at the stations. Let us suppose that at certain moment u^* the clocks were synchronized with respect to the GRS coordinate time. Thus, we can consider that at the moment u^* the readings of the clocks coincide: $\tau_1(u^*, \underline{w}_1(u^*)) = \tau_2(u^*, \underline{w}_2(u^*)) = \tau^*$. The equation (2.6) enables us to write

$$\begin{aligned}\Delta\tau &= \tau_2(u_2, \underline{w}_2(u_2)) - \tau_1(u_1, \underline{w}_1(u_1))\\ &= \Delta u - \frac{1}{c^2}\left\{\frac{1}{2}\dot{\underline{w}}_2^2(u_1) + U_E(u_1, \underline{w}_2(u_1))\right\}\Delta u\\ &+ \int_{u^*}^{u_1}(\dot{\tau}_2(u, \underline{w}_2(u)) - \dot{\tau}_1(u, \underline{w}_1(u))\,du.\end{aligned} \tag{4.19}$$

For earth-based observers the coefficient of Δu in the second term is practically constant and equal to $-6.969290 \cdot 10^{-10}$. The third, integral term is due to clocks' desynchronization at the moment u_1. This term can be expressed as

$$\Delta\tau_{syn} = \int_{u^*}^{u_1}(\dot{\tau}_2 - \dot{\tau}_1)\,dt \approx c^{-2}g(h_2 - h_1)(u_1 - u^*), \tag{4.20}$$

where h_i is the height of the i-th observer relative to the geoid, g is the gravitational acceleration at the geoid. We neglect herewith periodic terms induced by the tidal influence of the Sun and Moon. The amplitude of these terms is $\lesssim$ 1 ps. Thus, the term $\Delta\tau_{syn}$ is linear with respect to u_1. In practice this term is not distinguishable from technical difference of the clocks' rates, and can be accounted for by the piecewise-linear clock model.

In the case when the second observer is situated on an Earth satellite both second and third terms in (4.19) must be calculated explicitly.

The second term in (4.19) results from the difference of the mean rates of the coordinate time u and the proper time of the second station τ_2. If we use coordinate time scale $\tilde{u} = ku$, where k is the constant factor chosen in such a manner that the mean rates of $\tilde{u}$ and the proper time of an observer situated on the geoid be equal, then the term under consideration becomes equal to $c^{-2}gh_2\Delta\tilde{u}$. This value is much less than 1 ps and can be neglected. Our conclusion concerning this question totally coincides with that of the paper [Hellings, Shahid-Saless, 1990].

The observed delay rate can be written as

$$\Delta\dot{\tau} \equiv \frac{d(\tau_2 - \tau_1)}{d\tau_1} = \frac{d\tau_2}{d\tau_1} - 1 = \frac{d\tau_2}{du_2}\left(\frac{d\tau_1}{du_1}\right)^{-1}\left(\frac{dt_2}{du_2}\right)^{-1}\frac{dt_1}{du_1}\frac{dt_2}{dt_1} - 1. \tag{4.21}$$

The quantities $d\tau_i/du_i = d\tau_i/du|_{u=u_i}$ are defined by the equation (2.6). If both observers are situated on the Earth's surface, the influence of these two factors is negligible, because they result in nearly constant term $c^{-2}g(h_2 - h_1)$, which is naturally accounted for by the clock

model. The quantities dt_i/du_i are the derivatives of the BRS coordinate time with respect the GRS one, evaluated along the world line of i-th observer at the moment u_i:

$$\frac{dt_i}{du_i} = 1 + c^{-2}\left\{\frac{1}{2}v_E^2(t_i) + \overline{U}(t_i, \underline{x}_E(t_i)) + \underline{a}_E(t_i)\underline{w}_i(u_i) + \underline{v}_E(t_i)\dot{\underline{w}}_i(u_i)\right\}. \tag{4.22}$$

The derivative dt_2/dt_1 is defined by (4.7) and (4.13).

Thus, we have the complete set of formulas enabling one to model VLBI observations of remote sources. In order to obtain the explicit expression for time delay one must substitute (4.18), (4.2), (4.15), (4.17) and (4.9)–(4.12) into (4.19). The formula for delay rate might be obtained by substituting (4.22), (4.7), (4.13) and (4.16) into (4.21). In our opinion, it is convenient to perform these substitutions numerically.

It should be noted that the expression for the non-gravitational part of time delay for an infinitely distant source as observed by an earth-based instrument coincides with the analogous results of the papers [Kopejkin, 1990; Soffel et al., 1990] at the level of accuracy of 1 ps.

5. VLBI observations of interplanetary spacecrafts

Let coordinates of a spacecraft moving somewhere in the Solar system be $\underline{x}_s(t)$. In this Section we follow the notations of Fig.1. The equations (4.1) remain to be valid, and with the accuracy of 1 ps time delay can be written as

$$\begin{aligned}\Delta t \equiv t_2 - t_1 = \Delta t_0 &\left(1 - c^{-1}\underline{n}\,\dot{\underline{x}}_2(t_1) + c^{-2}(\underline{n}\,\dot{\underline{x}}_2(t_1))^2\right)\\ &+ \Delta t_{gr}\left(1 - c^{-1}\underline{n}\,\dot{\underline{x}}_2(t_1)\right) + \frac{1}{2}L_2^{-1}|\underline{n}\times\dot{\underline{x}}_2(t_1)|^2(\Delta t_0)^2,\end{aligned} \tag{5.1}$$

where

$$\Delta t_0 = c^{-1}(L_2 - L_1), \quad \underline{L}_i = \underline{x}_s(t_0) - \underline{x}_i(t_1), \quad \underline{n} = \underline{L}_2/L_2. \tag{5.2}$$

The difference $L_2 - L_1$ can be either written as [Krivova, 1991]

$$L_2 - L_1 = -(\underline{L}_1 - \underline{L}_2)\frac{\underline{L}_2 + \underline{L}_1}{L_2 + L_1}, \quad \underline{L}_1 - \underline{L}_2 = \underline{x}_2(t_1) - \underline{x}_1(t_1) = \underline{b}(t_1) = \underline{b} \tag{5.3}$$

or expanded in powers of the parallax b/L

$$L_2 - L_1 = -\underline{n}\,\underline{b} - \frac{1}{2}L_2^{-1}|\underline{n}\times\underline{b}|^2 + \frac{1}{2}L_2^{-2}(\underline{n}\,\underline{b})|\underline{n}\times\underline{b}|^2 + O(b^4/L_2^3). \tag{5.4}$$

The moment of emission t_0 is calculated on the basis of a preliminary theory of the motion of the spacecraft, observers and gravitating bodies of the Solar system.

When calculating Δt_{gr} it is sufficient to consider that $t_2 = t_1 + \Delta t_0$. It should be noted that because of finite distance between observers and spacecrafts we can not calculate Δt_{gr} using the formulas of Section 4.2. The original definition $\Delta t_{gr} = c^{-1}(\Delta R_2 - \Delta R_1)$ together with (3.8)–(3.12) should be used instead. For example, if we observe a source at the angular distance 30° from the Sun and at the distance 3 A.U. from the Earth, the value of Δt_{gr} is not 1.5 ns as indicated in Table 1, but 1.05 ns.

The conversion of the barycentric coordinate time interval Δt into the observed time delay $\Delta\tau$ is to be performed following the scheme described in Section 4.3.

The observed delay rate is defined by (4.21). In the case under consideration the last factor in (4.19) can be written as

$$\frac{dt_2}{dt_1} = \frac{dt_2}{dt_0}\left(\frac{dt_1}{dt_0}\right)^{-1}. \tag{5.5}$$

The derivatives dt_i/dt_0 are calculated from the equations (4.1) considered as implicit functions $\Phi_i(t_i, t_0) = -c(t_i - t_0) + R_i + \Delta R_i \equiv 0$:

$$\frac{dt_i}{dt_0} = -\frac{\frac{\partial}{\partial t_0}\Phi_i}{\frac{\partial}{\partial t_i}\Phi_i} = \frac{1 - c^{-1}\underline{R}_i/R_i\ \dot{\underline{x}}_s(t_0) + 2c^{-1}\frac{\partial}{\partial t_0}\Delta R_i}{1 - c^{-1}\underline{R}_i/R_i\ \dot{\underline{x}}_i(t_i) - 2c^{-1}\frac{\partial}{\partial t_i}\Delta R_i}. \tag{5.6}$$

Using the equations of Section 3 one can derive the partial derivatives of ΔR_i. Let us show the explicit expressions for the spherically symmetric post-Newtonian components of the gravitational field:

$$\begin{aligned}
&\frac{\partial}{\partial t_\alpha}\Delta R_i = \sum_A \frac{4GM_A}{c^2}\ \frac{K_\alpha}{(r_{Ai} + r_{As})^2 - R_i^2}, \quad \alpha = 0, i, \\
&K_0 = -(r_{Ai} + r_{As})\frac{\underline{R}_i}{R_i}\ \dot{\underline{x}}_s(t_0) - R_i\ \frac{\underline{r}_{As}}{r_{As}}\ \dot{\underline{x}}_s(t_0), \\
&K_i = (r_{Ai} + r_{As})\frac{\underline{R}_i}{R_i}\ \dot{\underline{x}}_i(t_i) - R_i\ \frac{\underline{r}_{Ai}}{r_{Ai}}\ \dot{\underline{x}}_i(t_i), \\
&\underline{r}_{As} = \underline{x}_s(t_0) - \underline{x}_A(t_A).
\end{aligned} \tag{5.7}$$

6. VLBI observations of Earth satellites

Let us proceed to the observations of near-Earth sources — Earth satellites. This kind of observations implies that both observers and a source are situated in the neighborhood of the Earth. This circumstance enables one to describe all the processes involved by means of GRS. The following formulas and estimates are valid for any source whose distance from the Earth is less than 10^6 km. As before, we follow the notations of Fig.1, but all coordinate quantities are those defined in GRS, that is we use the GRS coordinate time u instead of t, and the GRS spatial coordinates w^i instead of x^i.

The coordinate time delay $\Delta u = u_2 - u_1$ is defined by

$$\begin{aligned}
&\Delta u = u_2 - u_1 = \Delta u_0\left(1 - c^{-1}\underline{n}\,\dot{\underline{w}}_2(u_1)\right) + \Delta u_{gr}, \\
&\Delta u_0 = c^{-1}(L_2 - L_1), \quad \underline{L}_i = \underline{w}_s(u_0) - \underline{w}_i(u_1), \quad \underline{n} = \underline{L}_2/L_2,
\end{aligned} \tag{6.1}$$

$$\begin{aligned}
&\Delta u_{gr} = \frac{2GM_E}{c^3}\ln\frac{(w_2 + w_s + |\underline{w}_2 - \underline{w}_s|)\,(w_1 + w_s - |\underline{w}_1 - \underline{w}_s|)}{(w_2 + w_s - |\underline{w}_2 - \underline{w}_s|)\,(w_1 + w_s + |\underline{w}_1 - \underline{w}_s|)}, \\
&\underline{w}_2 = \underline{w}_2(u_2), \quad \underline{w}_1 = \underline{w}_1(u_1), \quad \underline{w}_s = \underline{w}_s(u_0),
\end{aligned} \tag{6.2}$$

the absolute value of Δu_{gr} being less than 21 ps. The value of Δu_0 is to be calculated using the formulas which are similar to (5.3)–(5.4). The second term in (6.1) describes the retardation of the baseline and may amount to 33 ns.

The conversion of Δu into the observed time delay can be performed on the basis of the equations (4.19)–(4.20). In this Section we suppose that both observers are situated on the Earth's surface. Accounting for this circumstance the observed time delay is written as

$$\begin{aligned}
\Delta u = u_2 - u_1 = \Delta u_0\left(1 - c^{-1}\underline{n}\,\dot{\underline{w}}_2(u_1)\right) + \Delta u_{gr} \\
- \frac{1}{c^2}\left\{\frac{1}{2}\dot{w}_2^2(u_1) + U_E(u_1, \underline{w}_2(u_1))\right\}\Delta u_0.
\end{aligned} \tag{6.3}$$

If the accuracy of observations is 0.1 ns, one can neglect the second and third terms in (6.3). In the case when observed sources are Earth satellites it is sufficient to calculate the moment of the emission of the signal u_0 according to the formula

$$u_0 = u_1 - c^{-1}\,|\underline{w}_s(u_1) - \underline{w}_1(u_1)| - c^{-2}\,(\underline{w}_s(u_1) - \underline{w}_1(u_1))\,\underline{\dot{w}}_s(u_1). \tag{6.4}$$

The error which results from this approximate value of u_0 is less than 0.1 ps in time delay and 0.1 fs/s in delay rate.

The observed delay rate can be written as

$$\Delta\dot{\tau} \equiv \frac{d(\tau_2 - \tau_1)}{d\tau_1} = \frac{d\tau_2}{d\tau_1} - 1 = \frac{d\tau_2}{du_2}\left(\frac{d\tau_1}{du_1}\right)^{-1}\frac{du_2}{du_0}\left(\frac{du_1}{du_0}\right)^{-1} - 1. \tag{6.5}$$

The derivatives $d\tau_i/du_i$ are defined by (2.6). The moments u_i and u_0 are connected by the equation of the light propagation in GRS (3.14). The derivatives du_i/du_0 can be calculated by the formulas which are quite similar to (5.6). With the accuracy of 1 fs/s one gets

$$\begin{aligned}\Delta\dot{\tau} = {} & c^{-2}g(h_2 - h_1) + c^{-1}\Big((\underline{m}_2 - \underline{m}_1)\,\underline{\dot{w}}_s + \underline{m}_1\,\underline{\dot{w}}_1 - \underline{m}_2\,\underline{\dot{w}}_2\Big) \\ & - c^{-2}\Big((\underline{m}_2 - \underline{m}_1)\,\underline{\dot{w}}_s\,[\underline{m}_1\,\underline{\dot{w}}_s - \underline{m}_1\,\underline{\dot{w}}_1 + \underline{m}_2\,\underline{\dot{w}}_2] - \underline{m}_2\,\underline{\dot{w}}_2(\underline{m}_2\,\underline{\dot{w}}_2 - \underline{m}_1\,\underline{\dot{w}}_1)\Big) \\ & + c^{-3}\Big((\underline{m}_2 - \underline{m}_1)\,\underline{\dot{w}}_s\,[\underline{m}_1\,\underline{\dot{w}}_s - \underline{m}_1\,\underline{\dot{w}}_1 + \underline{m}_2\,\underline{\dot{w}}_2](\underline{m}_1\,\underline{\dot{w}}_s)\Big) + \Delta\dot{\tau}_{gr},\end{aligned} \tag{6.6}$$

$$\begin{aligned}\Delta\dot{\tau}_{gr} = \frac{4GM_E}{c^3}(S_2 - S_1), \quad S_i = \frac{\underline{m}_i(\underline{\dot{w}}_s - \underline{\dot{w}}_i)(w_s + w_i) - (\underline{k}_i\underline{\dot{w}}_i + \underline{k}_s\underline{\dot{w}}_s)R_i}{(w_s + w_i)^2 - R_i^2}. \\ \underline{R}_i = \underline{w}_s - \underline{w}_i,\ \underline{m}_i = \underline{R}_i/R_i,\ \underline{k}_i = \underline{w}_i/w_i,\ \underline{k}_s = \underline{w}_s/w_s,\ \underline{w}_i = \underline{w}_i(u_i),\ \underline{w}_s = \underline{w}_s(u_0).\end{aligned} \tag{6.7}$$

The first term in (6.6) is nearly constant and compensated by the clock model. The value of $\Delta\dot{\tau}_{gr}$ for near-Earth satellites may amount to 50 fs/s.

In the conclusion let us notice that VLBI observations of Earth satellites can be modeled in BRS as well. In this case the algorithm coincides with that for interplanetary spacecrafts. However, the use of GRS leads to physically more adequate model, which at the same time turns out to be significantly simpler.

References

Aleksandrov, A.N., Zhdanov, V.I., Parnovskij, S.L.: 1990. The relativistic reference frame near the Earth and radiointerferometric observations. *Kinematica i Fizika Neb. Tel*, **6**(2), 3–7. (in Russian).

Ashby, N., Bertotti, B.: 1986. "Relativistic effects in local inertial frames." *Phys. Rev.*, **D34**(8), 2246–2259.

Brumberg, V.A.: 1981. "Relativistic effects in radar, optical and radiointerferometric measurements." Astron.Zh., **58**(1), 181–193.

Brumberg,V.A.: 1986. "Relativistic reductions of astronomical observations." In: H.K. Eichorn, R.J. Leacock (eds.), *Astrometric Techniques*, Reidel, Dordrecht, 19–42.

Brumberg, V.A.: 1987. "Post-post-Newtonian propagation of light in the Schwarzschild field." *Kinematica i Fizika Neb. Tel*, **3**(1), 8–13. (in Russian).

Brumberg, V.A.: 1991. "Relativistic hierarchy of reference systems and time scales." In:*Proc. IAU Colloquium No.127*, in press.

Brumberg, V.A., Kopejkin, S.M.: 1989. "Relativistic theory of celestial reference frames." In: J. Kovalevsky,I.I. Muller, B. Kolaczek (eds.), *Reference Systems* Kluwer, Dordrecht, 115.

Cannon, W.H., Lisewski, D.: 1987. "VLBI in deep space: relativistic formulation of the time delay equation." IUGG 19th General Assembly, Vancouver, Proc. of IAG symposia, **1**, 51–66.

Cannon, W.H., Lisewski, D., Finkelstein, A.M., Kreinovich, V.Ya.: 1986. "Relativistic effects in Earth based and cosmic long baseline interferometry." In: J. Kovalevsky, V.A. Brumberg (eds.), *Relativity in Celestial mechanics and Astrometry*, Reidel, Dordrecht, 255–268.

Damour, T., Soffel, M., Xu, C., 1990. "General Relativistic Celestial Mechanics I. Method and Definition of Reference Systems." In: N. Capitaine (ed.), *Les Journées 1990*, Observatoire de Paris.
Finkelstein, A.M., Kreinovich, V.J., Pandey, S.N.: 1983. "Relativistic reductions for radiointerferometrical observables." *Astrophys. and Space Sci.*, **94**, 233–247.
Gubanov, V.S., Finkelstein, A.M., Fridman, P.A., 1983. *Introduction to radio astrometry*, Nauka, Moscow. (in Russian).
Hellings, R.W.: 1986. "Relativistic effects in astronomical timing measurements." *Astron. J.*, **91**(3), 650–659; **92** (6), 1446.
Hellings, R.W., Shahid-Saless, B.: 1990. "A picosecond relativistic VLBI model." JPL Relativity Technical Memo, October 22.
Hill, H.A., Rabaey, G.R., Rosenwald, R.D.: 1986. "The Sun's gravitational quadrupole moment inferred from the fine structure of the acoustic and gravity normal mode spectra of the Sun." In: J. Kovalevsky, V.A. Brumberg (eds), *Relativity in Celestial mechanics and Astrometry*, Reidel, Dordrecht, 345–353.
Klioner, S.A.: 1989a. "Propagation of the Light in the Barycentric Reference System considering the Motion of the Gravitating Masses" *Preprint of the Institute of Applied Astronomy No 6*, Leningrad. (in Russian).
Klioner, S.A.: 1989b. "Influence of the Quadrupole Field and Rotation of the Bodies on the Light Propagation in the Barycentric Reference System" *Preprint of the Institute of Applied Astronomy No 12*, Leningrad. (in Russian).
Klioner, S.A.:1991. "Relativistic reduction of astronomical observations." *Ph.D. Thesis*, Institute of Applied Astronomy, Leningrad. (in Russian).
Klioner, S.A., Kopejkin, S.M., 1991. "Microarcsecond astrometry in space: relativistic effects and reduction of observations." (submitted to *Astronomical Journal*).
Krivova, N.V., 1991. Private communication.
Kopejkin, S.M.: 1988. "Celestial Coordinate Reference Systems in Curved Space-Time." *Celestial Mechanics*, **44**, 87–115. (in Russian).
Kopejkin, S.M.: 1990. "Theory of general relativity in radioastromonical observations." *Astron.Zh.*, **67**(1), 10–20.
Murray, C.A.: 1983. *Vectorial Astrometry*. Adam Hilder Ltd, Bristol.
Murray, C.A.: 1986. "Relativity in astrometry." In: J. Kovalevsky, V.A. Brumberg (eds.), *Relativity in Celestial mechanics and Astrometry*, Reidel, Dordrecht, 169–175.
Pavlov, N.B.: 1985. "On the relativistic theory of astrometric observations. III. Radio interferometry of remote sources." *Soviet Astronomy*, **29**, 98–102
Soffel, M., Müller, J., Wu, X., Xu, C.: 1990. Consistent relativistic VLBI theory with picosecond accuracy. (unpublished)
Soffel, M., Ruder, H., Schneider, M., Campbell, J., Schuh, H.: 1986. "Relativistic effects in geodetic VLBI measurements." In: J. Kovalevsky, V.A. Brumberg (eds.), *Relativity in Celestial mechanics and Astrometry*, Reidel, Dordrecht, 277–282.
Voinov, A.V.: 1990. "Relativistic equations of motion of an Earth satellite." *Manuscripta Geodaetica*, **15**, 65–73.
Zeller, G., Soffel, M., Ruder, H., Schneider, M.: 1986. "Relativistische Effekte bei der Laufzeitdifferenz der VLBI", *Astronomisch-Geodätische Arbeiten*, Heft Nr.**48**, Bayerischen Akademie der Wissenschaften, München, 218–236.
Zhu, S.Y., Groten, E.: 1988. "Relativistic effects in VLBI time delay measurements." *Manuscripta Geodaetica*, **13**(1), 33–39.

A New Measurement of Solar Gravitational Deflection of Radio Signals using VLBI

D.S. Robertson, W.E. Carter and W.H. Dillinger

Laboratory for Geosciences, Office of Ocean and Earth Sciences, NOAA,
Rockville, Maryland 20852

Abstract:

Modern very-long-baseline interferometry (VLBI) observations can measure the deflection of electromagnetic radiation in the solar gravity field with an accuracy exceeding 1 milli-arc-second (*mas*). A generalized formulation of the deflection is given by Misner *et al.* [1973, p. 1103] as:

$$\delta\alpha = \frac{(1 + \gamma)\, M_s}{r_E} \left(\frac{1 + \cos\alpha}{1 - \cos\alpha}\right)^{1/2}$$

where α is the angle between the Sun and the observed object, M_s is the mass of the Sun in geometrized units (1.477×10^5 cm) [See Misner *et al.*, 1973, p. 36], r_E is the Earth-Sun distance in cm, and γ is a parameter whose value ranges from 1 in general relativity to -1 (no deflection). For $\gamma = 1$ the deflection is 1750 *mas* at the solar limb, 4 *mas* at $\alpha = 90°$, and 0 at $\alpha = 180°$. Our analysis of ten years of VLBI data, reported in Robertson et al., [1991], yielded an estimate of γ of 1.0002, with a formal standard error of 0.00096 and an estimated standard error of 0.002. This determination is comparable in accuracy and in good agreement with the determination from Mars-Viking time delay measurements [Reasenberg *et al.*, 1979]. Here we will show in more detail how the observations were distributed, both in time and in Sun angle, and explore what can be done to improve the determination of γ through the next 11-year period of the solar cycle.

In the late 1960's Shapiro [1967, 1970] recognized that VLBI measurements of the relativistic deflection of signals from extragalactic radio sources by the gravity field of the Sun could potentially yield an accurate estimate of γ. The National Oceanic and Atmospheric Administration's POLARIS and IRIS projects [Carter *et al.*, 1985] and the National Aeronautic and Space Administration's Crustal Dynamics Project (CDP) [Coates *et al.*, 1985] produce large sets of VLBI observations having the requisite angular resolution and broad distribution of Sun angles required to estimate γ. These data were analyzed by Robertson *et al.* [1991], and found to yield an estimate of γ of 1.0002, with a formal standard error of 0.00096 and an estimated standard error of 0.002. The estimated standard error was derived from a series of numerical experiments that tested the estimate of γ for sensitivity to errors in atmospheric refraction, nutation, Earth orientation, source structure, Earth tides, tectonic displacement, ocean and barometric loading, and antenna deformation modeling errors.

There are many ways in which this determination of γ could be improved in the future. Some of the expected improvements in the VLBI observations can be cataloged as follows:

- Double spanned bandwidth observations (720 MHz instead of the 360 MHz used in most of the observations reported here) have been tested. This roughly doubles the accuracy of each individual delay measurement (T.A. Clark, NASA, private communication).
- Planned order-of-magnitude increases in the bit recording rates will improve the SNR, allowing measurements closer to the Sun (A.R. Whitney, Haystack Observatory, private communication).
- Improvements in atmosphere modeling using increased coverage of low-elevation observations should improve the overall accuracy of the determinations [Davis *et al.*, 1985; 1988].
- Improved instrumental stability, including such things as improved delay and phase calibration equipment, could lead to significant improvements in the VLBI measurements (A.E.E. Rogers, Haystack Observatory, private communication).
- Two southern hemisphere radio sources that are not currently included in our routine observing programs (2128-123 and 1958-179), which are strong enough to produce good data at small Sun angles, are being added to the IRIS observing program.

- New observing stations, especially in the southern hemisphere, will increase the number of measurements and improve their distribution in the sky. Also, the very long north-south baselines that will become available with the implementation of the southern hemisphere sites will improve the sensitivity of the networks in declination. This is important because, for sources that are not actually occulted by the Sun, the maximum gravitational deflection occurs more nearly in the direction of declination than right ascension.

- The next sunspot minimum in a few years should be accompanied by reduced solar corona activity, allowing observations closer to the solar limb.

- Improvements in our knowledge of the fundamental physical behavior of the Earth, particularly its nutations, but also its tectonic and tidal deformations and response to barometric loading, could reduce the need to estimate those parameters, and thereby improve the estimate of γ even with data extant today.

A study of the distribution of observations as a function of Sun angle reveals that, although a wide variety of Sun angles was observed during the decade 1980-1990, many observations at low Sun angles were missed. Figure 1 shows the observations that had deflections greater than about 40 milliseconds, plotted against a single calendar year, *i.e.*, the ten years are "stacked" as though the observations were taken in a single year, to highlight the coverage of individual sources through the calendar (approximately solar) year.

A large fraction of the data close to the Sun was taken on OJ287 (the spike in early August) but there are some curious gaps in the OJ287 coverage that will be examined below. 0229+131 (early May), which passes close enough to the Sun to produce deflections as large as 300 milliseconds, was not observed for deflections much larger than 140 milliseconds, largely due to the weakness of this source at S-Band, which is more strongly corrupted by the solar corona than X-band. 1958-179 and 2128-123 (January and February), which are in the southern hemisphere, have only recently been added to the IRIS observing schedules, and their observations are still sparse.

The gaps in the OJ287 coverage result from the 5-day spacing of the IRIS-A 24-hour observing schedules. Figure 2 shows the coverage of OJ287 for the IRIS 5-day observing sessions closest to occultation for the period 1984-1990. The relation of the observing sessions to the time of the conjunction changes from year to year because a solar year is 0.25 days longer than a multiple of

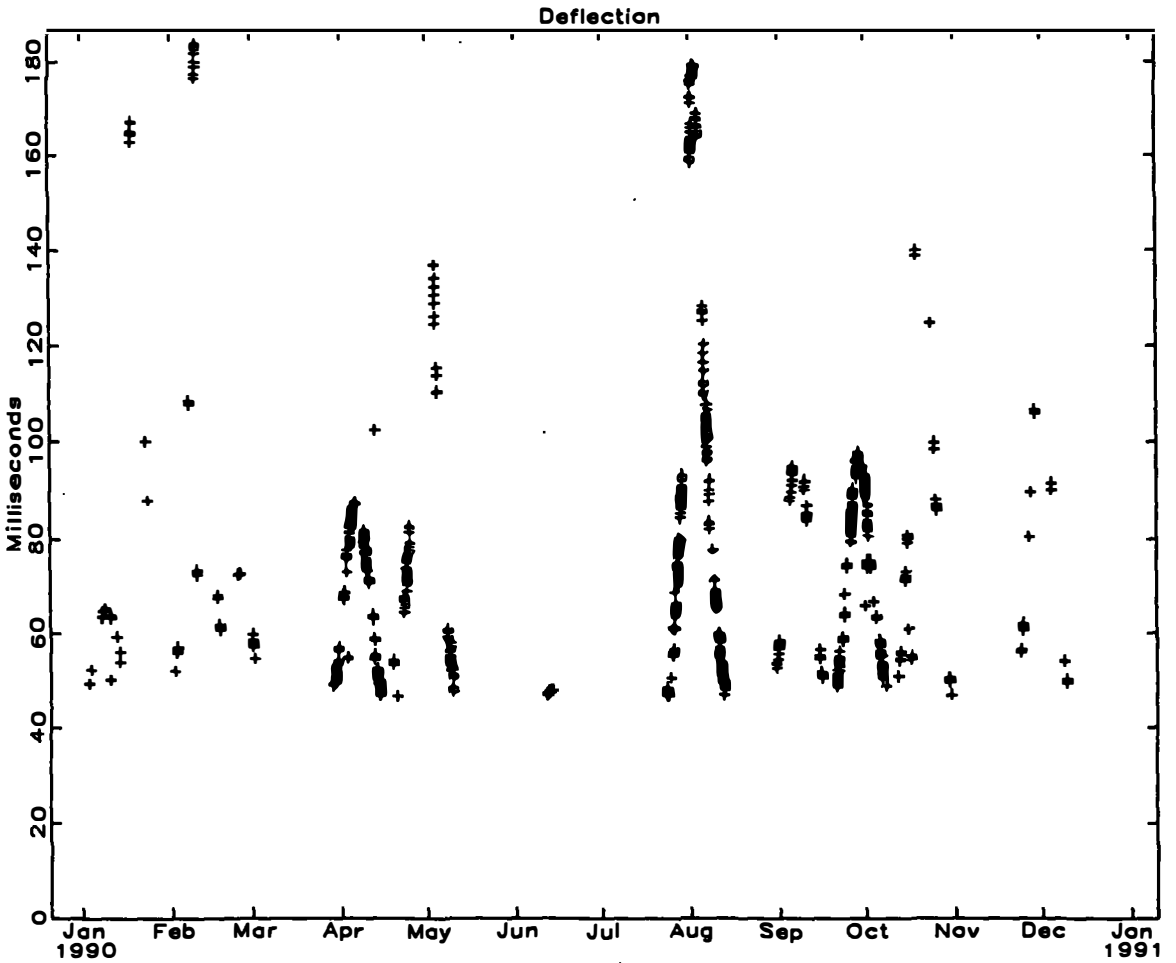

Figure 1. Relativistic deflection of the observed sources for the observations within 10° of the Sun.

5 days. The "spike" in the deflection curve is only about 10 days wide, too narrow to completely sample with a 5-day window. We were fortunate in that the observing sessions happened to coincide closely with the maximum deflection times during the interval 1984-1988 when the solar activity was comparatively light.

Figure 3 shows the same data as figure 1, but plotted against the actual observing time (that is, not folded into a single calendar year). It is clear that most of the large deflection observations were taken during the period from roughly 1984-1988, when the solar activity was at its minimum. Figure 4 shows the solar activity, as measured by the 10.7 cm microwave flux intensity. This solar

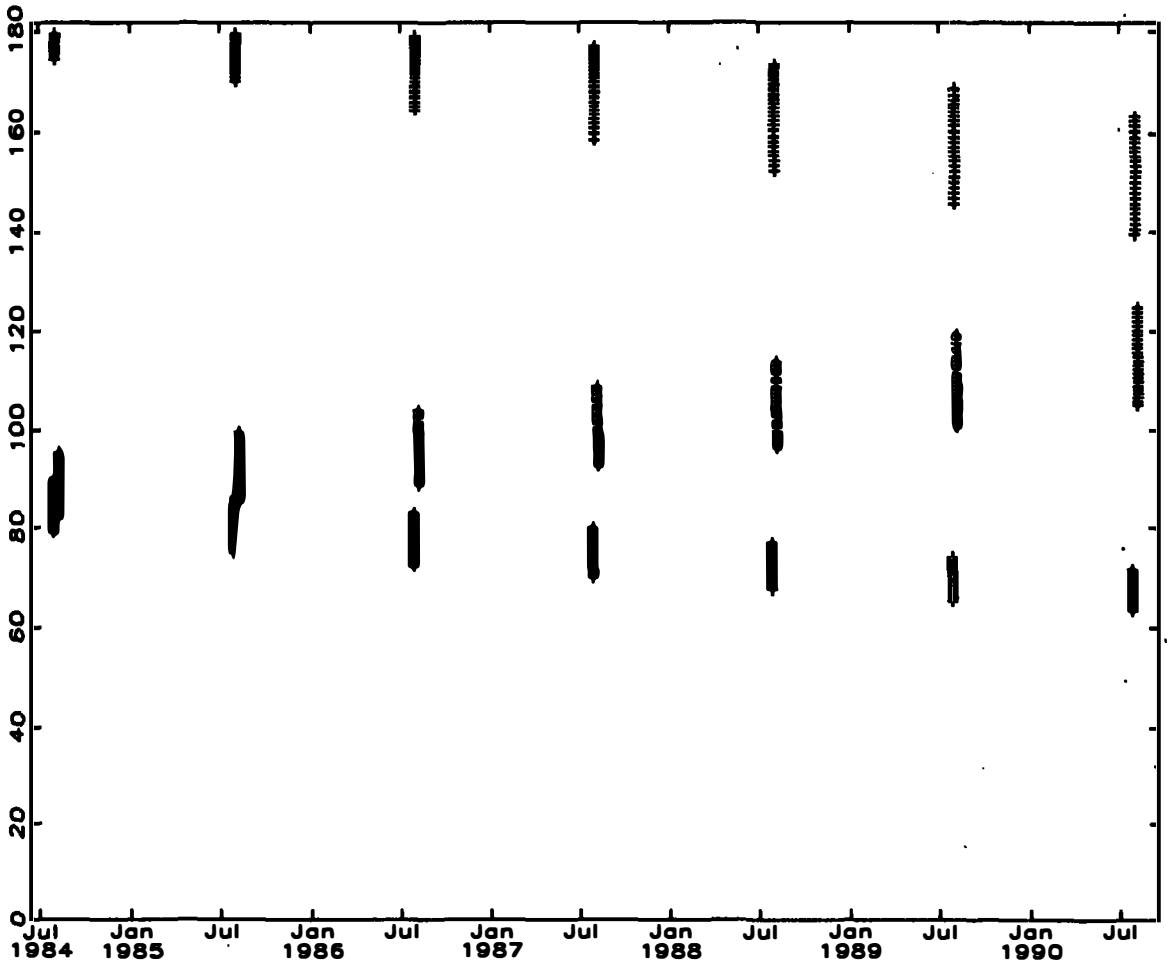

Figure 2. Theoretical relativistic deflection of the radio source OJ287, plotted on dates of the IRIS 5-day observing sessions close to the conjunction with the sun.

microwave emission correlates strongly with other measures of solar activity, such as sunspot counts. It is clear from figure 3 that although a fair number of observations were obtained with deflections as large as 180 milliseconds, that considerably more could have been made with a little more attention to the observing schedules.

Thus, in addition to the hardware upgrades and new stations that are anticipated during the next decade, certain actions should be taken particularly during the next interval of solar quiescence. Figure 6 shows a plot prepared by NASA in support of manned spacecraft activities that shows a prediction of the next solar activity cycle. The optimal period for Sun-grazing VLBI observations

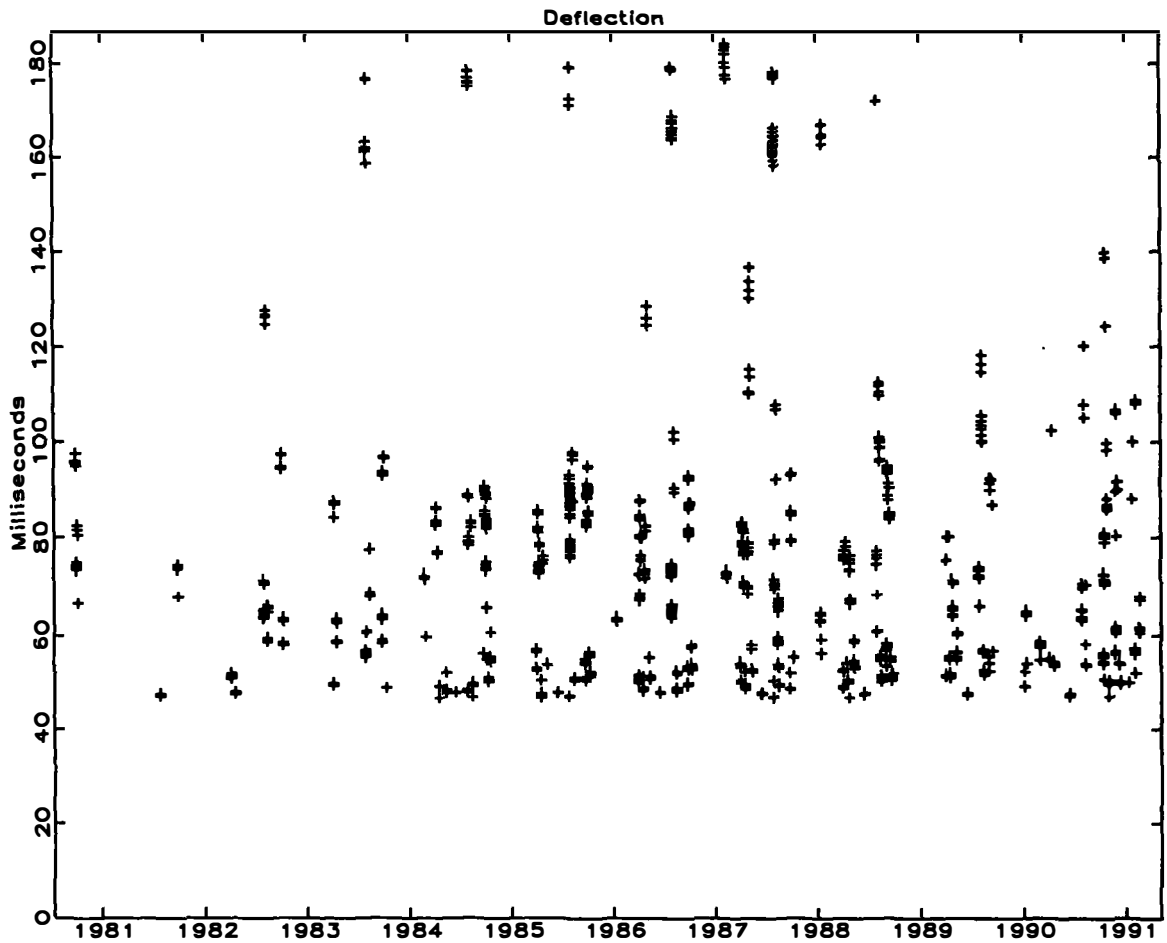

Figure 3. Same data as figure 1, but plotted against the actual observing data, rather than folded into a single year.

should commence sometime in 1993-94 and continue through about 1999. Some of the actions that should be taken during this period include:

1. Optimize the epochs of observing sessions to observe maximum deflection--for observing programs that are not tied to a specific observing schedule.
2. Increase the observation durations for the Sun-grazing sources when they are close to the Sun.
3. Find new sources close to the ecliptic--this is unlikely unless a time-variable source "turns on."
4. Upgrade the VLBI station hardware as noted above.
5. Outfit a southern hemisphere network.

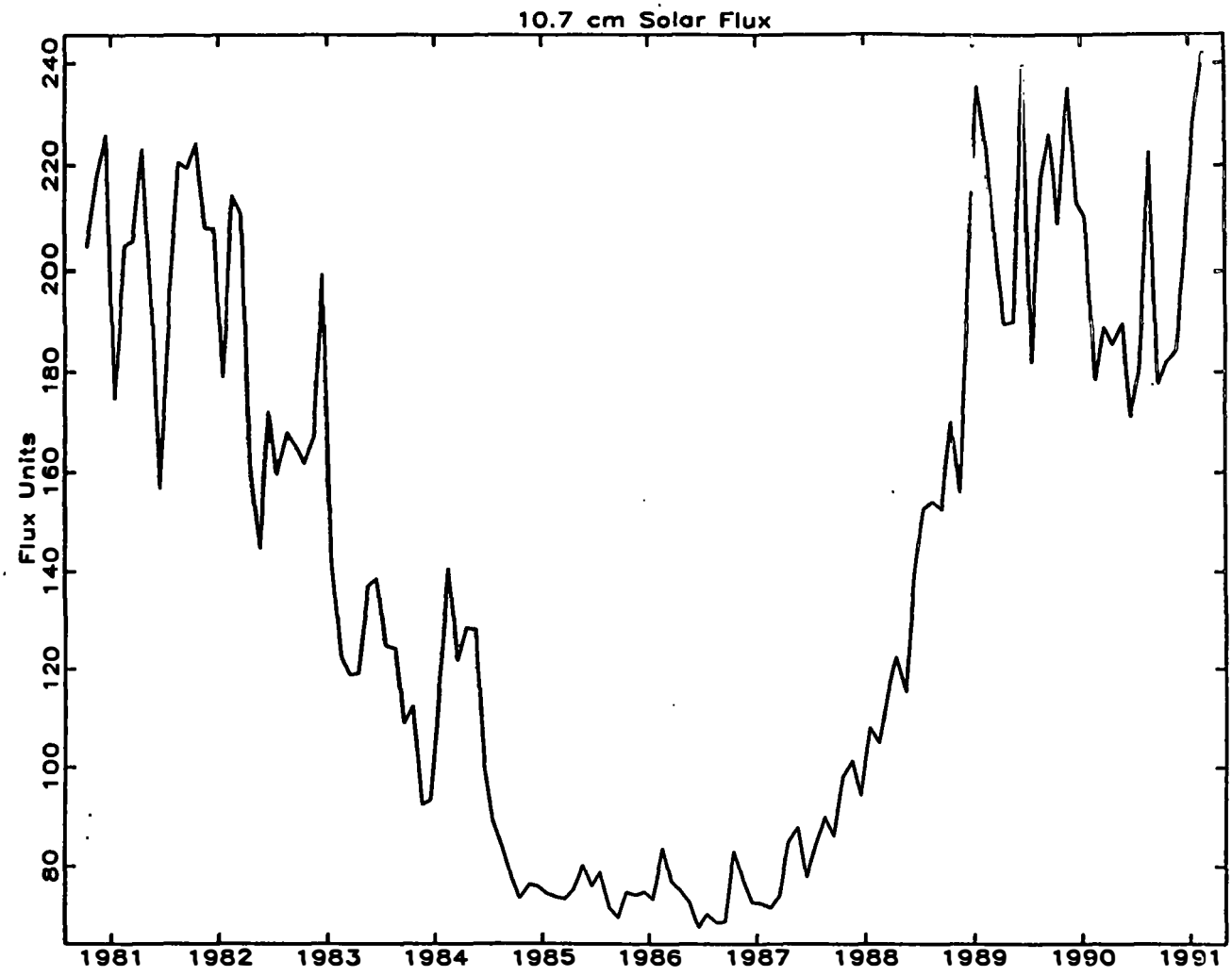

Figure 4. Solar activity for the period 1980-1990, as measured by the 10.7 cm microwave emission from the sun.

6. Increase the time-density of routine Earth rotation measurements.

7. Organize special relativity observing sessions.

8. Make use of the VLBA.

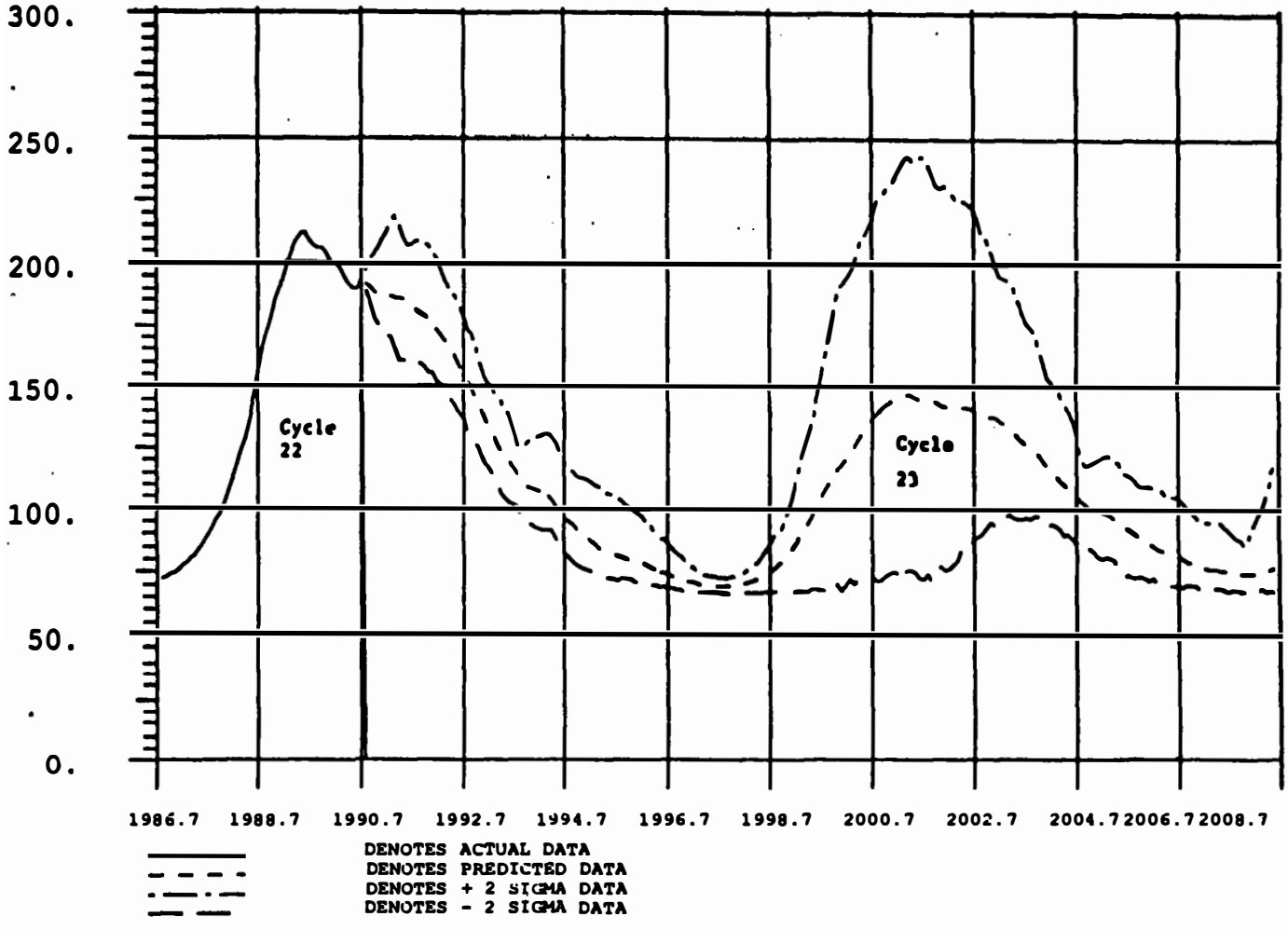

Figure 5. Projection of probable solar activity for the period from 1990 to 2008.

How much can we expect to improve the determination of γ with these changes? There are many imponderables that preclude giving a precise estimate at the present time: what will be the level of solar activity, what stations will be observing, what hardware upgrades will be implemented, and basically, what data will we be able to obtain? We cannot determine, for example, whether we might be on the brink of another "Maunder Minimum" of solar activity. Of course at some point

systematic errors may begin to dominate the problem, and at that point taking further data may fail to improve the estimates of γ significantly. It is not perfectly clear where this cutoff will occur. The only thing that is fairly clear is that we should be able to do substantially better in estimating γ in the next decade than we did in the last.

References:

Carter, W.E., D.S. Robertson, and J.R. MacKay, 1985, Geodetic Radio Interferometric Surveying: Applications and Results, *J. Geophys. Res.*, **90**, 4577-4587.

Coates, R.J., H. Frey, J. Bosworth, and G. Mead, 1985, Space-Age Geodesy: the NASA Crustal Dynamics Project, *IEEE Transactions on Geoscience and Remote Sensing*, **GE-23**, 358-368, 1985.

Davis, J.L., T.A. Herring, I.I. Shapiro, A.E.E. Rogers, and G. Elgered, 1985, Geodesy by Radio Interferometry: Effects of Atmospheric Modeling Errors on Estimates of Baseline Length, *Radio Science*, **20**, 1593-1607.

Davis, J.L., T.A. Herring, and I.I. Shapiro, 1988, Geodesy by Radio Interferometry: 1-2 Part-per-billion Precision for Transcontinental Baselines, in *Proceedings of IAU Symposium No. 129: The Impact of VLBI on Astrophysics and Geophysics*, M. Reid and J.M. Moran (eds.), Kluwer Academic Publishers, Dordrecht, Holland, 367-368.

Misner, C.W., K.S. Thorne and J.A. Wheeler, *Gravitation*, (W.H. Freeman, San Francisco, 1973).

Reasenberg, R.D., I.I. Shapiro, P.E. MacNeil, R.B. Goldstein, J.C. Breidenthal J.P Brenkle, D.L. Cain, T.M. Kaufman, T.A. Komarek, and A.I. Zygielbaum, 1979, *Viking* Relativity Experiment: Verification of Signal Retardation by Solar Gravity, *Astrophys J. Lett.*, **234**, L219-L221.

Robertson, D.S., W.E. Carter and W.H. Dillinger, 1991, A New Measurement of Solar Gravitational Deflection of Radio Signals Using VLBI, *Nature*, **349**, 768-770.

Shapiro, I.I., 1967, New Method for the Detection of Light Deflection by Solar Gravity, *Science*, **157**, 806-808.

Shapiro, I.I. and C.A. Knight, 1970, Geophysical Applications of Long-Baseline Radio Interferometry, in *Earthquake Displacement Fields and the Rotation of the Earth*, L. Mansinha, D.E. Smylie and A.E. Beck, eds., 285-301, (D. Reidel, Dordrecht, Holland)

STUDIES OF THE EARTH-ATMOSPHERE-OCEAN MOMENTUM EXCHANGE: STATUS AND PROSPECTS

Richard D. Rosen - Atmospheric and Environmental Research, Inc.
840 Memorial Drive, Cambridge, MA 02139

I. STATUS

The past decade has seen remarkable advances in the study of the Earth's variable rate of rotation and the role of the Earth's fluid envelope in exciting this variability. This progress was achieved because of independent breakthroughs in the geodetic and atmospheric measurements of the relevant geophysical parameters. It is now accepted that changes in the atmosphere's angular momentum explain most, if not all, of the nontidal changes in the length-of-day over a broad range of time scales up to the decadal, at which point core-mantle coupling assumes dominance. The pursuit of this result has encompassed a broad spectrum of research, including studies of tropospheric and stratospheric wind fields, the El Niño/Southern Oscillation, and tropical 40-50 day wind oscillations. Although these topics were reviewed at some length during my lecture, only a brief outline of them will be offered here.

The breakthrough in atmospheric measurements alluded to above is one of the enduring legacies of the Global Weather Experiment of 1978-79, during which an unprecedented array of observing systems was used to monitor the atmosphere. In preparation for this Experiment, the operational weather centers in a number of countries began to develop new data analysis systems that could assimilate observations not only from the traditional network of rawinsonde stations but also from satellites, aircraft, and other platforms. With the promise of more global coverage made by these newer observing systems, the analysis systems could also be designed to encompass the entire horizontal extent of the atmosphere. Thus, in September 1974 the first operational global data analysis system was introduced by the U.S. National Meteorological Center (NMC), thereby enabling atmospheric angular momentum (AAM) to be evaluated not only with global data but also on a twice-daily basis, the frequency of these analyses. Twice-daily values of the zonal wind, needed to evaluate relative AAM, were archived by NMC in a convenient form beginning January 1, 1976. From that date onward, it no longer became necessary, as in the past, to rely on monthly mean station-based statistics to study the relationship between relative AAM and Δl.o.d., thus reducing worries about temporal aliasing or lack of resolution in such studies.

Today, a number of meteorological centers are making values of relative AAM available on a routine basis, along with the pressure-related component of total AAM and other relevant parameters (Salstein and Kann, 1991). Comparisons of AAM from these different centers provide a basis (albeit not a perfect one) for assessing the accuracy of this quantity. An example is shown in Fig. 1, in which values of the relative angular momentum of the atmosphere between 1000 and 50 mb from NMC and from the European Centre for Medium Range Weather Forecasts (EC) have been differenced for each calendar year since 1981. Although initially quite large, the mean difference between the two centers has diminished considerably in recent years. Perhaps more significant, however, is the evolution of the standard deviation of the NMC-EC relative AAM difference series, since this provides a measure of the random error in the atmospheric analyses. The figure reveals, encouragingly, that this statistic has become smaller with time, currently leveling off at a value near 2×10^{24} kg m^2 s^{-1}, or about 0.034 ms in Δl.o.d. units. Because of certain assumptions about interpreting this statistic, however, this value should probably be regarded as a lower limit on the random error in relative AAM values. A number of improvements in data analysis techniques are expected to be implemented at the meteorological centers over the next 3-5 years (Kalnay et al., 1991), which hopefully will lead to still further reductions in AAM errors.

The emphasis of studies relating changes in AAM to those in l.o.d. has thus far been largely phenomenological. The AAM time series is characterized by a rich variety of temporal variability (Rosen et al., 1991), and it is convenient to separate studies of AAM fluctuations and attendant signals in Δl.o.d. into three categories corresponding to interannual, seasonal, and intra-annual time scales:

(a) On interannual time scales, the peak in AAM and Δl.o.d. during early 1983 was so marked that it drew early attention (Carter et al., 1984) and was quickly related to the strong El Niño/Southern Oscillation (ENSO) event over the Pacific Ocean that reached its mature stage at that time (Rosen et al., 1984). Upon examining data for 1972-86, Chao (1988) later concludes that most of the interannual variation in l.o.d. is caused by ENSO-related changes in AAM. Salstein and Rosen (1986) had demonstrated a long-term connection between El Niño events and Δl.o.d. using a historical record of fluctuations in l.o.d. dating back to 1860, suggesting the possibility that such historical Earth rotation series might serve as a proxy for other interannual atmospheric signals. Chao (1989) provides evidence that the equatorial stratosphere's quasi-biennial oscillation imparts a detectable interannual signal to the l.o.d. series. Finally, expanding on an analysis approach used by Rosen et al. (1984), Dickey et al. (1991) discover that interannual variations in extratropical relative

AAM values appear to be coherently linked to antecedent tropical anomalies on these time scales, thereby yielding potentially new insights into tropical-extratropical coupling.

(b) On seasonal time scales, it is possible, in principle, for a variety of geophysical processes to make contributions to the global momentum budget, which has added a multidisciplinary appeal to studying behavior at these periods. In addition, data constraints limited early studies of the momentum budget to seasonal and longer time scales, hence providing a historical basis for continuing to analyze seasonal budgets. More fundamentally, though, seasonal changes in l.o.d. represent the largest signal in this quantity on less than decadal periods and are, therefore, of intrinsic importance. Rosen and Salstein (1985) show that imbalances previously thought to exist in the solid Earth-atmosphere momentum budget at annual and semiannual periods may be largely eliminated by incorporating wind data through as much of the height of the atmosphere, including the stratosphere, as possible. Naito and Kikuchi (1990) reach a somewhat different conclusion, but Rosen and Salstein (1991) reassert their view that if geophysical processes other than atmospheric winds are contributing to seasonal changes in l.o.d., then they must be doing so at levels smaller than the error in the wind data. As these errors decrease in the future with improved meteorological analyses, it will be very worthwhile to visit this subject anew.

(c) It is on intra-annual time scales that the modern atmospheric and geodetic data sets have been especially important in yielding new breakthroughs. An early success involved linking 40-50 day variations in l.o.d. to tropical wind field oscillations found by Madden and Julian (1971) with this period (Langley et al., 1981; Anderson and Rosen, 1983). The discovery of these 40-50 day fluctuations in l.o.d. and AAM helped spur renewed interest in the Madden-Julian oscillation, and a large body of literature on this subject has emerged during the last several years. At still higher frequencies, Rosen et al. (1990) demonstrate that changes in l.o.d. as short as a fortnight can be attributed almost entirely to atmospheric forcing. Figure 2 updates the analysis of Rosen et al. (1990), showing that coherence between total AAM and l.o.d. begins to falter at around a fortnight but remains significant for periods down to about 10 days. The loss of coherence at very high frequencies may be due to errors in the atmospheric and geodetic measurements or to the emergence of a third body, such as the oceans, in affecting the momentum budget at rapid time scales. (Shortcomings in solid body tidal models may also be a factor.) The first possibility is supported by the observation that the coherence between NMC and EC series of relative AAM also begin to lose coherence at high frequencies, although not so severely as do AAM and l.o.d. in Fig. 2. The second explanation is supported by Ponte's (1990) demonstration

that barotropic ocean waves are capable of transferring momentum between the atmosphere and solid Earth within a few days, so that changes in Earth rotation, at high frequencies at least, ought to be diagnosed within the framework of a coupled solid Earth-atmosphere-ocean system instead of the simpler two-body solid Earth-atmosphere system that is the foundation for Fig. 2.

The above synopsis has, of necessity, been cursory and regrettably has omitted reference to many important contributions to this subject area (see the review by Hide and Dickey, 1990, for example, for further perspectives on the status of Earth rotation research). Hopefully, though, it is sufficient to set the stage for some brief concluding comments about prospects for future efforts in this field.

II. PROSPECTS

One of the important challenges remaining in the subject is to explain the discrepancies that still exist in the global momentum budget, at all frequencies. The discrepancies between Δl.o.d. and AAM at high frequencies illustrated in Fig. 2 mark a frontier in our skill at determining these quantities and in understanding their behavior. Efforts have already begun to obtain improved, high density observations of Earth rotation (Clark et al., 1990; Herring, 1990), and plans for additional measurement campaigns are being formulated (Dickey, 1991). As noted earlier, improvements in atmospheric data sets are also anticipated in the forseeable future, which, in combination with expected further insights into the role of the ocean, ought to allow progress to be made on resolving the differences between AAM and l.o.d. series displayed in Fig. 2.

Another challenge that is likely to receive meaningful attention in the near future concerns the manner in which the various components of the Earth-atmosphere-ocean system are dynamically coupled on different time scales. Although a number of studies have already addressed this issue, at least for certain portions of the temporal domain, the relative importance of the two torques (mountain and surface friction) coupling the solid Earth and atmosphere as a function of frequency remains poorly quantified. The schematic in Fig. 3 provides a sketch of my current understanding of this issue, but major uncertainties still exist about the real shape of the two curves depicted in the figure. New data sets are becoming available (White, 1991) that can address this problem, however, and new sensors, such as scatterometers, will be flown aboard satellites this decade that also promise to contribute importantly to its solution. Hence, it appears that we are entering a new era in the study of Earth-atmosphere-ocean momentum exchanges in which the focus will turn

more and more to understanding the processes responsible for linking these components of the global system together.

ACKNOWLEDGMENTS

This material was prepared with support provided by NOAA's Climate and Global Change Program under grant NA89AA-D-AC202 and NASA's Crustal Dynamics Project under contract NAS5-28195.

REFERENCES

Anderson, J. R., and R. D. Rosen, The latitude-height structure of 40-50 day variations in atmospheric angular momentum, *J. Atmos. Sci., 40*, 1584-1591, 1983.

Boer, G. J., Earth-atmosphere exchange of angular momentum simulated in a general circulation model and implications for the length of day, *J. Geophys. Res., 94*, 5511-5531, 1990.

Carter, W. E., D. S. Robertson, J. E. Pettey, B. D. Tapley, B. E. Schutz, R. J. Eanes, and M. Lufeng, Variations in the rotation of the Earth, *Science, 224*, 957-961, 1984.

Chao, B. F., Correlation of interannual length-of-day variation with El Niño/Southern Oscillation, 1972-1986, *J. Geophys. Res., 93*, 7709-7715, 1988.

Chao, B. F., Length-of-day variations caused by El Niño-Southern Oscillation and quasi-biennial oscillation, *Science, 243*, 923-925, 1989.

Clark, T. A., J. W. Ryan, and K. D. Baver, ERDE: High resolution observations of Earth orientation parameters by Very Long Baseline Interferometry, *EOS, 71*, 1271, 1990.

Dickey, J. O., High-time resolution measurements of Earth rotation, *this volume*, 1991.

Dickey, J. O., S. L. Marcus, and R. Hide, manuscript in preparation, 1991.

Gutzler, D. S., and R. M. Ponte, Exchange of momentum among atmosphere, ocean, and solid Earth associated with the Madden-Julian Oscillation, *J. Geophys. Res., 95*, 18,679-18,686, 1990.

Herring, T. A., Geodetic results from the October 1989 Extended R&D VLBI experiment, *EOS, 71*, 1271, 1990.

Hide, R., and J. O. Dickey, Earth's variable rotation, JPL Geodesy and Geophysics Preprint No. 205, 36 pp., 1990.

Kalnay, E., R. Petersen, M. Kanamitsu, and W. E. Baker, U.S. operational numerical weather prediction, *Rev. Geophys., Supplement*, 104-114, 1991.

Langley, R. B., R. W. King, I. I. Shapiro, R. D. Rosen, and D. A. Salstein, Atmospheric angular momentum and the length of day: A common fluctuation with a period near 50 days, *Nature, 294*, 730-732, 1981.

Madden, R. A., Relationships between changes in the length of day and the 40- to 50-day oscillation in the tropics, *J. Geophys. Res.*, *92*, 8391-8399, 1987.

Madden, R. A., Large intraseasonal variations in wind stress over the tropical Pacific, *J. Geophys. Res.*, *93*, 5333-5340, 1988.

Madden, R. A., and P. R. Julian, Detection of a 40-50 day oscillation in the zonal wind in the tropical Pacific, *J. Atmos. Sci.*, *28*, 702-708, 1971.

Naito, I., and N. Kikuchi, A seasonal budget of the Earth's axial angular momentum, *Geophys. Res. Lett.*, *17*, 631-634, 1990.

Newton, C. W., Mountain torques in the global angular momentum balance, *J. Atmos. Sci.*, *28*, 623-628, 1971.

Ponte, R. M., Barotropic motions and the exchange of angular momentum between the oceans and solid earth, *J. Geophys. Res.*, *95*, 11,369-11,374, 1990.

Rosen, R. D., and D. A. Salstein, Contribution of stratospheric winds to annual and semiannual fluctuations in atmospheric angular momentum and the length of day, *J. Geophys. Res.*, *90*, 8033-8041, 1985.

Rosen, R. D., and D. A. Salstein, Comment on "A seasonal budget of the Earth's axial angular momentum" by Naito and Kikuchi, *Geophys. Res. Lett.*, *submitted*, 1991.

Rosen, R. D., D. A. Salstein, T. M. Eubanks, J. O. Dickey, and J. A. Steppe, An El Niño signal in atmospheric angular momentum and Earth rotation, *Science*, *225*, 411-414, 1984.

Rosen, R. D., D. A. Salstein, and T. M. Wood, Discrepancies in the Earth-atmosphere angular momentum budget, *J. Geophys. Res.*, *95*, 265-279, 1990.

Rosen, R. D., D. A. Salstein, and T. M. Wood, Zonal contributions to global momentum variations on intraseasonal through interannual time scales, *J. Geophys. Res.*, *96*, 5145-5151, 1991.

Salstein, D. A., and D. M. Kann, Developments at the Sub-bureau for Atmospheric Angular Momentum of the IERS, *this volume*, 1991.

Salstein, D. A., and R. D. Rosen, Earth rotation as a proxy for interannual variability in atmospheric circulation, 1860-present, *J. Clim. Appl. Meteorol.*, *25*, 1870-1877, 1986.

Swinbank, R., The global atmospheric angular momentum balance inferred from analyses made during the FGGE, *Quart. J. R. Met. Soc.*, *111*, 977-992, 1985.

White, G. H., Mountain and surface stress torques in NMC analyses, *this volume*, 1991.

Wolf, W. L., and R. B. Smith, Length-of-day changes and mountain torque during El Niño, *J. Atmos. Sci.*, *44*, 3656-3660, 1987.

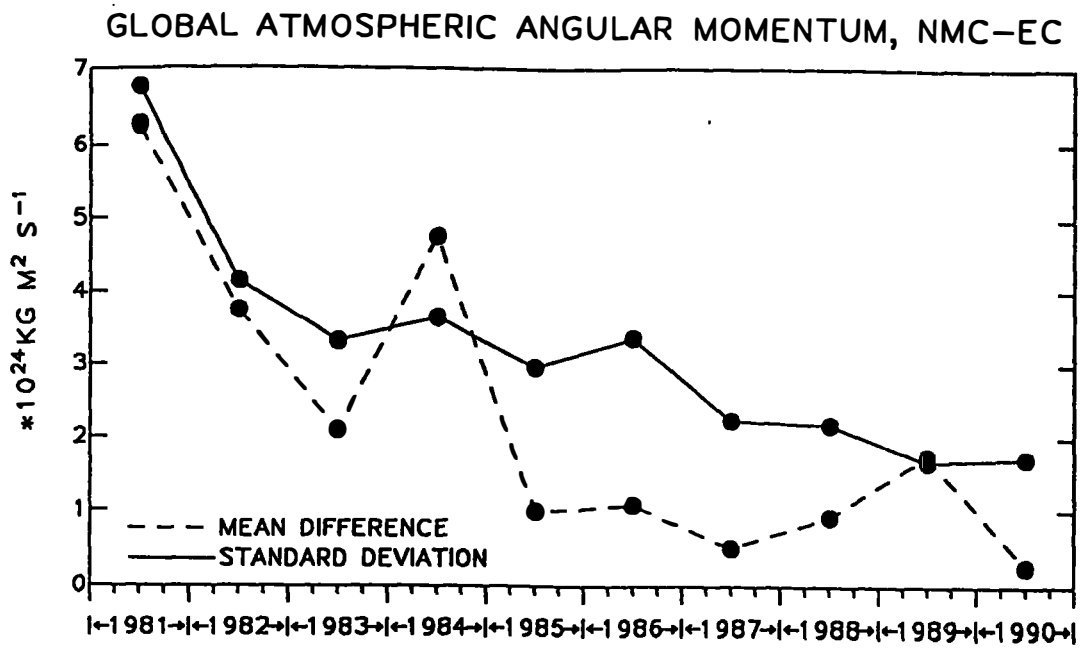

Fig. 1. Annual values of the mean and standard deviation of the difference series between NMC and EC daily estimates of the relative angular momentum of the atmosphere (the so-called wind term) between 1000 and 50 mb.

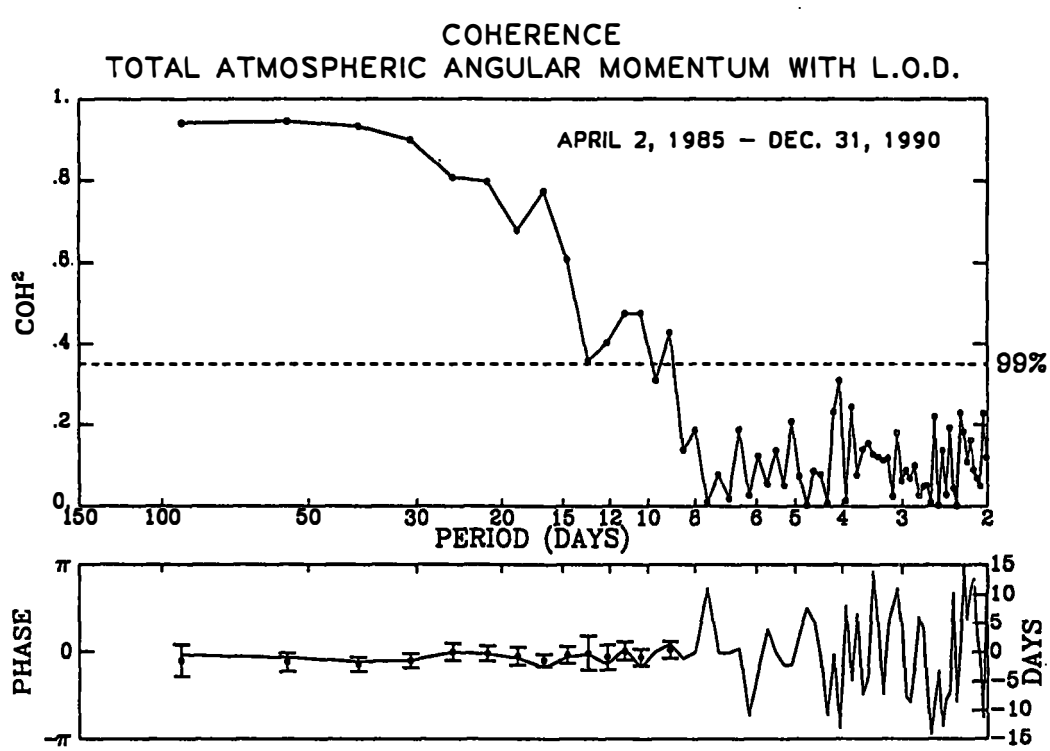

Fig. 2. Coherence-squared between once-daily values of Δl.o.d. and total atmospheric angular momentum (the sum of the pressure and wind terms) determined from NMC wind field analyses between 1000 and 50 mb and surface pressure analyses for the period April 2, 1985, to December 31, 1990.

An estimate of the 99% statistical level of confidence is included on the plot. The abscissa is logarithmic in frequency but is marked in terms of period (in units of days). At the bottom, the phase (in units of radians along the left ordinate) by which total atmospheric angular momentum leads Δl.o.d. as a function of period. For each period that the coherence squared exceeds the 99% level, the phase relationship is also indicated in units of days (right ordinate) with vertical bars indicating the limits of confidence at the 99% level.

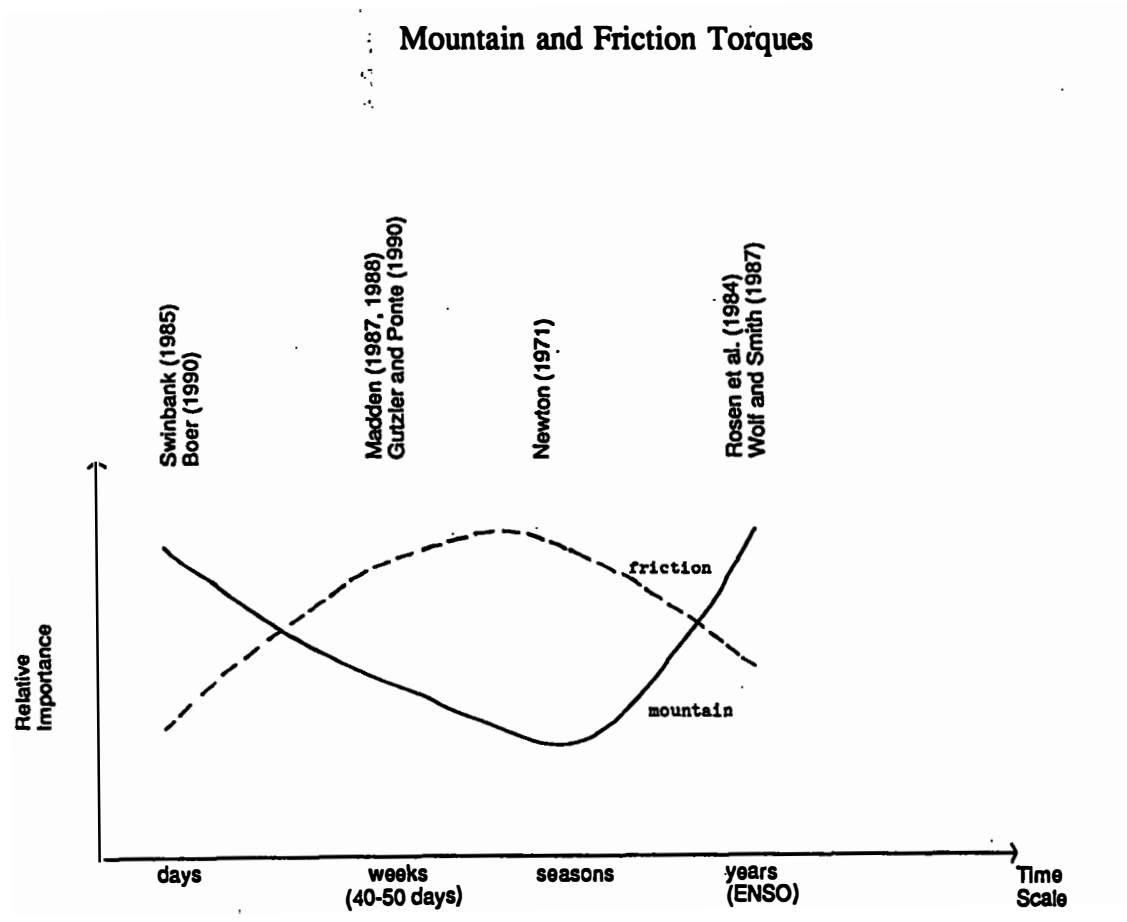

Fig. 3. Schematic representation of the relative importance of the mountain and friction torques in effecting momentum exchanges between the atmosphere and solid Earth, as a function of time scale. Some relevant references for the time scales indicated are cited along the top of the plot.

The NMC Global Analysis and Forecast System: Where are we going?

Eugenia Kalnay
National Meteorological Center
Washington DC 20233

1. Introduction

As reviewed in this conference, the atmospheric angular momentum determined from global operational analyses and forecasts, has been found to be usefully associated with the lengh-of-day. Unfortunately, it is also affected by deficiencies in the analysis systems, and improvements made operationally are therefore reflected as perceived changes in the angular momentum.

In this paper we give an overview of current research and near term plans for the development of the global model and data assimilation system at the National Meteorological Center (NMC). Of particular relevance because of their impact on the determination of atmospheric angular momentum are the new analysis system denoted Spectral Statistical Interpolation (Section 2.3), and the plans for long term homogeneous re-analyses (Section 5).

2. Global analysis and modeling

2.1 Evolution of skill

The development of the global system until late 1990 was reviewed in Kalnay et al. (1990), which also contains several statistical estimates of skill, indicating that the forecast skill has improved considerably at short and medium range. Some of the highlights are that the current three-day forecast is now as accurate as the one-day forecast was ten to 15 years ago, that the well known "skill gap" that existed between the NMC forecasts and those of the European Center for Medium Range Weather Forecasts has now been very substantially reduced, and that the forecast skill in the Southern Hemisphere is comparable to the level attained in the Northern Hemisphere only 3-5 years ago.

In the rest of the paper we concentrate on recent research and and plans. Many of the papers referred to are presented in the Proceedings of the American Meteorological Society Ninth Conference on Numerical Weather Prediction, Denver CO, 14-18 October 1991.

2.2 Global spectral model

NMC has been using a global spectral model since 1981 (Sela, 1988) for aviation and medium range forecasting. The model has undergone many changes, based on the idea that for global forecasting, especially beyond the first few days, it is important to simulate as realistically as possible all physical processes that take place in the atmosphere. For that reason, there has been not only an

increase in the model resolution, but also considerable improvements in the parameterization of sub-grid scale physical processes (Kanamitsu, 1989, Kalnay et al., 1990, Campana et al., 1991, White and Campana, 1991). The result of these changes has been a model which, when integrated for long periods, simulates very realistically the observed climatology (Kanamitsu et al, 1990, Mo et al., 1990, Mo and Kalnay, 1991). Nevertheless, some problems, also generic to other advanced general circulation models, still remain. A new detailed diagnostic budget study (Kanamitsu and Saha, 1991) promises to give guidance for further improvement of systematic errors.

On March 6, 1991, the model horizontal resolution was increased from triangular truncation T80 to T126, equivalent to a grid resolution change from 160 km to 105 km. Several other changes were also implemented, and have resulted in finer scale and more realistic precipitation forecasts (Iredell et al, 1991). The vertical resolution will be increased from the current 19 levels to about 28 in the fall of this year.

Continued increased resolution may require the use of a semi-Lagrangian scheme for the hydrodynamics, and in this area we expect to test the new method of Bates et al. (1991). In the next few years we also plan to intensify the development of coupled global systems. We are undergoing tests coupling the atmospheric model to an ocean model (A. Leetmaa, pers. comm.), a Simple Biosphere Model (E. Schneider, pers. comm.), and an ocean mixed layer model (S. Brenner, pers. comm.). Plans to couple the model with a sea ice model and to include condensed water are also underway.

2.3 Spectral Statistical Interpolation, 4-D Variational Analysis and the model adjoint.

An important advance in global analysis is the new variational Spectral Statistical Interpolation scheme (Parrish and Derber, 1991, Derber et al, 1991a), which replaced the operational OI on June 25 1991. The SSI, which performs global analysis directly on the model variables, and uses all data at once, has been found to have a number of important advantages over the conventional OI analysis: The forecasts are on the average more skillful, the data are generally better fit, there is much less spin-up (Saha and Kanamitsu, 1991), there is no need to perform normal mode initialization, and the fact that it is based on a variational formulation makes handling of non-standard data much easier. It should be emphasized that the SSI, although already clearly superior to OI, still has substantial potential for development and further improvements.

Steve Cohn (1991, pers. comm.) has made theoretical advances that should make feasible, within a few years, the operational use of Kalman filtering in conjunction with the SSI. Briefly, he has shown that by taking advantage of the hyperbolic nature of the equations of motion, it is possible to produce forecast equations for the model error covariances which are of the same dimension as

the model, rather than of dimension N times the model, where N is the number of degrees of freedom. Although these equations still require the development of appropriate closure assumptions, very promising work is underway in this area, in collaboration with NASA/GLA.

An alternative approach equally promising is the 4-D variational analysis method, which is under development at several centers (France, ECMWF, NMC and GLA). In order to explore this method, a linear and adjoint versions of the NMC model hydrodynamics were developed in collaboration with FSU (Zou et al., 1991). The adjoint of the physical parameterizations will be developed also within this collaboration.

We plan to use the adiabatic version of the adjoint model in 4-D variational tests since for the very short range forecasts used in the assimilation cycle, and for the computation of increments with respect to the first guess, it is likely that diabatic effects are small (Derber, pers. comm.). The adjoint of the model has many other powerful potential applications, and one of them, the optimal estimation of the model systematic errors, is presented in Derber et al., (1991b).

3. Complex quality control

The improvement of the operational quality control system at NMC has been a major effort in the last few years. This development was guided by the principle of complex quality control (CQC) developed by Gandin (1988), which is to make the decision to accept, reject, or even correct data that may contain rough errors, only after several independent QC checks have been completed. These checks can include hydrostatic checks, increment checks (difference of observation from first guess), and horizontal interpolation and vertical interpolation statistical checks. A Decision Making Algorithm (DMA) is executed only after all of the checks have been made, using all of the available information.

Two major developments have taken place in this area. One is involved mainly with the QC of rawinsondes, which are still the most important and highest quality source of information for the NH, and which can be used to check other data. An advanced hydrostatic CQC of rawinsondes has been in operations for two years, and its results are discussed In Gandin (1991) and Morone (1991). This CQC of heights and temperatures has been recently extended to involve several additional statistical interpolation checks (Collins, 1991). The result of this very advanced expert system is that the confidence of the decisions, and the percentage of observations corrected has increased by more than 50%.

A second effort, which is a complex QC within the OI framework which does not attempt to correct the data, has been operational since December 1990, replacing the previous "gross" and "buddy" checks (Woollen 1991, Ballish, 1991). It quality controls all

observations available, including satellite data. The advantages of performing separate cheks versus a single OI QC check has been shown (Woollen, 1991). Additions planned to this system include checks of the static stability of the soundings within the CQC approach.

A near term goal for NMC is to limit human intervention in the QC to monitoring the decisions of the CQC, and to make decisions only in those cases where a confident decision cannot be made by the CQC.

4. New observing systems

A new "interactive" analysis/forecast/retrieval system developed jointly by NESDIS and NMC will include the use of the 6 h model forecast as a first guess for the inversion of satellite radiances to obtain temperature and humidity soundings. Satellite sensors do not have high vertical resolution, and the current use of a climatology-based library search for first guess (Fleming et al., 1986, 1988) implies that the unresolved vertical scales are derived from climatological statistics. The use of the model first guess, on the other hand, will ensure that for the scales unresolved by satellite data, the model short range forecast, which is generally quite accurate, will not be changed. Preliminary results are very encouraging, and indicate that for cloudy retrievals the errors should be reduced near the surface by more than 1 K (Baker, 1991).

The satellite products mentioned above will be combined with additional satellite data derived from other sensors: The Special Sensor Microwave Imager (SSM/I) provides accurate estimates of total precipitable water over ocean, as well as oceanic surface wind speed and snow and ice cover. The forthcoming European Research Satellite (ERS-1) will provide surface wind and wave heights over the oceans. More accurate methods to retrieve cloud-track winds should increase their accuracy considerably. These new types of data will not only be used to improve model parameterizations, but will also be utilized during the analysis cycle. For example, a method of physical initialization (Mathur et al., 1991) is being tested for the assimilation of satellite estimates of tropical precipitation.

5. Reanalysis and climate data assimilation

Although the use of operational analyses produced by analysis/forecast systems has become an important tool for climate research, the frequent changes and improvements of the NWP systems have produced large spurious apparent climate changes. NMC is involved in two complementary projects (CDAS and Reanalysis, see Fig. 1) that address the need for long analysis records with a frozen system (Kistler et al, 1991, Kalnay and Jenne, 1991).

CDAS and Reanalysis

Basic concept:

```
                                                Execution(xxx)

     |1958                |1979                1992|          2000|
     |                    |                        |              |
     |                    |                        |xxxxxxxxxxxx> |
     |                    |                        |     CDAS     |
     |                    |                        |              |
     |=========================================>                  |
     |    35 year "pocket" reanalysis             |xxxx          |
     |                    |                        |              |
     |                    |                        |              |
     |                    |=======================>    xxxxxxx   |
     |                    | "full" (CDAS) reanalysis              |
     |                    |                        |              |
```

and then start again with the CDAS 2000!

Fig. 1: Schematic of the proposed strategy for CDAS and Reanalysis.

The Climate Data Assimilation System (CDAS), due to become operational in 1993, will be a a high resolution T126-28 levels "post-analysis", performed a week after real time, coupled with an ocean data assimilation system (Leetmaa and Ji, 1989), and with the use of delayed data, and a time interpolation component of the complex quality control.

The CDAS, developed in collaboration with GFDL, will provide a frozen analysis for climate use starting in 1993. A Reanalysis Project, in collaboration with NCAR, will provide a longer climate record. Two reanalyses are planned: one performed with a fast T62 system, starting in 1958, will produce 35 years of reanalysis, and will be executed between 1993 and 1995 if the computer and other resources are available. The second reanalysis, performed with a system identical to the CDAS, will perform a reanalysis from 1979 to the beginning of the operational CDAS. This reanalysis/CDAS will be executed during 1996-1999, and will provide a coupled ocean-atmosphere frozen analysis for almost 20 years.

6. Conclusions

The use of global atmospheric analyses to estimate variations of angular momentum, and hence the length of the day, has had remarkably successful results, as discussed in this conference. However, the quality of the estimation has been impaired to some extent by deficiencies in the global analysis and forecast systems. Especially important is the fact that improvements in

the models and methods of analysis have resulted in perceived changes of the angular momentum as well as other parameters. In addition, the problem of spin-up affects quite seriously the operational analyses, since the model is constantly making 6-hour forecasts.

Two programs of the National Meteorological Center should make major contributions to solving these problems: a) the implementation of a variational analysis (Spectral Statistical Interpolation, SSI) has improved the tropical analysis, eliminated the need for normal mode initialization, and reduced substantially the spin-up. b) The NMC Reanalysis/CDAS project, which includes a very long (35 years) homogeneous reanalysis with a state-of-the-art system, should provide a substantial solution to the problem of spurious perceived changes.

REFERENCES:

Baker, Wayman, 1991: Joint NESDIS/NASA/NMC effort to develop an advanced satellite retrieval system. Proc. of the 9th Amer. Meteor. Soc. Conference on Numerical Weather Prediction. Denver, CO, Oct. 1991.

Campana, K. A., K. E. Mitchell, S. K. Yang, Y. Hou and L. L. Stowe, 1991: Validation and improvement of cloud parameterization at the National Meteorological Center. Proc. of the 9th Amer. Meteor. Soc. Conference on Numerical Weather Prediction. Denver, CO, Oct. 1991.

Collins, William G., 1991: Complex quality control of rawinsonde heights and temperatures at the NMC. Proc. of the 9th Amer. Meteor. Soc. Conference on Numerical Weather Prediction. Denver, CO, Oct. 1991.

Derber, John and Joseph Sela, 1991: The estimation of systematic model error using variational techniques. Proc. of the 9th Amer. Meteor. Soc. Conference on Numerical Weather Prediction. Denver, CO, Oct. 1991.

Gandin, L. S., 1988: Complex quality control of meteorological observations. Mon. Wea. Rev., 116, 1137-1156.

Gandin, L. S., 1991: Two years of operational comprehensive hydrostatic quality control at the NMC. Proc. of the 9th Amer. Meteor. Soc. Conference on Numerical Weather Prediction. Denver, CO, Oct. 1991.

Iredell, M., J. Alpert, K. Campana, P. Caplan, D. Deaven, M. Kanamitsu, B. Katz, H.-L. Pan, J. Sela and G. White, 1991: Implementation of the T126 spectral model at NMC. Proc. of the 9th Amer. Meteor. Soc. Conference on Numerical Weather Prediction. Denver, CO, Oct. 1991.

Kalnay, E., R. Petersen, M. Kanamitsu, and W. E. Baker, 1991: U. S. operational numerical weather prediction. Reviews of Geophysics. IUGG. In press.

Kalnay, E., and R. Jenne, 1991: Summary of the NMC/NCAR reanalysis workshop of April 25-26 1991. Submitted to the Bull. Am. Met. Soc.

Kanamitsu, M., 1989: Description of the NMC flobal data assimilation and forecast system. Weather and Forecasting, 335-342.

Kanamitsu, M., K. C. Mo and E. Kalnay, 1991: Annual cycle integration of the NMC MRF model: Control experiment and the effect of resolution. Am. Met. Soc., 118, 2543-2567.

Kanamitsu, M. and S. Saha, 1991: Budget analysis of the systematic error of the National Meteorological Center medium range forecast model. Proc. of the 9th Amer. Meteor. Soc. Conference on Numerical Weather Prediction. Denver, CO, Oct. 1991.

Kistler, R., K. C. Mo and E. Kalnay, 1991: Reanalysis, climate data assimilation and the impact of model resolution. Proc. of the 9th Amer. Meteor. Soc. Conference on Numerical Weather Prediction. Denver, CO, Oct. 1991.

Leetmaa, A. and Ming Ji, 1989: Operational hindcasting of the tropical Pacific. Dyn. Atmos. Oceans, 13, 465-490.

Mathur, M. B., H. S. Bedi, T. N. Krishnamurti, M. Kanamitsu and J. S. Woollen, 1991: Assimilation of satellite-derived rainfall for improving tropical forecasts. Proc. of the 9th Amer. Meteor. Soc. Conference on Numerical Weather Prediction. Denver, CO, Oct. 1991.

Mo, K. C., J. Zimmerman, E. Kalnay and M. Kanamitsu, 1991: A GCM study of the 1988 United States drought. Mon. Wea. Rev., May issue.

Mo, K. C. and E., 1991: Impact of Sea Surface temperature anomalies on the skill of monthly forecasts. In press, Monthly Weather Review.

Pan, Hua-Lu, 1991: Soil moisture initialization for medium and short range forecast models. Proc. of the 9th Amer. Meteor. Soc. Conference on Numerical Weather Prediction. Denver, CO, Oct. 1991.

Parrish, D. F. and J. C. Derber, 1991: The NMC's spectral statistical interpolation analysis system. Submitted to Mon. Wea. Rev.

Parrish, D. F. and J. C. Derber, 1991: The NMC global

variational analysis system. Proc. of the 9th Amer. Meteor. Soc. Conference on Numerical Weather Prediction. Denver, CO, Oct. 1991.

Saha, S. and M. Kanamitsu, 1991: A study of the spin-up characteristics of the NMC operational and experimental analysis and forecast systems. Proc. of the 9th Amer. Meteor. Soc. Conference on Numerical Weather Prediction. Denver, CO, Oct. 1991.

Sela, J., 1988: The new T80 NMC operational spectral model. Preprints 8th Conference on Numerical Weather Prediction, Baltimore, Maryland, Boston: Am. Met. Soc. pp. 312-313.

Woollen, J. S., 1991: New NMC Operational OI Quality Control. Proc. of the 9th Amer. Meteor. Soc. Conference on Numerical Weather Prediction. Denver, CO, Oct. 1991.

Zou, X., I. M. Navon, J. Derber, D. Parrish and J. Sela, 1991: Variational data assimilation with the direct and adjoint primitive equations and the implicit normal mode initialization. Proc. of the 9th Amer. Meteor. Soc. Conference on Numerical Weather Prediction. Denver, CO, Oct. 1991.

(This page intentionally left blank)

DEVELOPMENTS AT THE SUB-BUREAU FOR ATMOSPHERIC ANGULAR MOMENTUM OF THE IERS

David A. Salstein - Atmospheric and Environmental Research, Inc.
840 Memorial Drive, Cambridge, MA 02139

Deirdre M. Kann - Climate Analysis Center, National Meteorological Center, Washington, DC 20233

I. INTRODUCTION

It is widely accepted that the atmosphere plays a vital role in exciting small but measurable changes in the earth's rotation because of exchanges of angular momentum within the earth-atmosphere system. Variations in the earth orientation vector are detected by VLBI and other techniques, and are reckoned as changes in the length of day (its axial component) and in the wobble, or motions of the pole (its equatorial components). Given the importance of the changes in length of day and polar motion to understanding earth dynamics and precise deep-space and terrestrial navigation, the geodesy community needs to monitor series of atmospheric angular momentum values and their forecasts. Because such data are routinely available only from the large meteorological centers, the International Earth Rotation Service (IERS) invited the U.S. National Meteorological Center (NMC) to organize a Sub-bureau for Atmospheric Angular Momentum (SBAAM). The SBAAM has been formally operating under the direction of A. J. Miller of NOAA/National Meteorological Center/Climate Analysis Center since October 1989. The organizational structure of the SBAAM within the IERS, and operations of the Sub-bureau are highlighted in Figs. 1 and 2.

The functions of the SBAAM are to collect, distribute, archive, and analyze earth orientation-related atmospheric data from a number of weather centers. Participating meteorological centers besides NMC are the United Kingdom Meteorological Office (UKMO), the European Centre for Medium-Range Weather Forecasts (ECMWF), and the Japan Meteorological Agency (JMA). The SBAAM has designed a system for retrieving data in as near real time as possible to permit their use for purposes requiring rapid access. The NMC data are produced on site, and are available quickly, and the UKMO data are rapidly transmitted to the SBAAM on the Global Telecommunications System (GTS). For the ECMWF and the JMA, the centers that are not yet contributing data to the SBAAM by rapid access, we are in the process of arranging that transmittal on the GTS.

Routine access to Sub-bureau files through a dial-up system at NMC is available to the scientific community. A set of user notes to support this service is available from the Sub-bureau.

Several research areas are underway at the SBAAM as related to the time series of earth orientation-related quantities. First, we actively compare the analysis quantities from the several weather centers, and note disagreements, discontinuities, and other problems. Secondly, we are assessing the skill of forecasts of the atmospheric excitation parameters. Also, we are comparing different definitions of the world ocean for the purpose of defining the oceanic response to atmospheric pressure loading, often known as the inverted barometer (IB) response.

In the next section, we discuss the parameters that are archived by the Sub-bureau. Comparisons and forecast assessments are presented in section III.

II. SBAAM PARAMETERS

Effective atmospheric angular momentum (EAAM) functions are described by Barnes et al. (1983), who related atmospheric motions and mass distribution to earth rotation and polar motion. (Fig. 3) The first two functions, χ_1 and χ_2, the equatorial components, are associated with the excitation of polar motion. The axial component, χ_3, is involved with changes in the length of day. The functions can be further partitioned into contributions by wind (W) and pressure (P). The calculation of wind contributions involves the computation of integrals over the depth of the atmosphere, which varies in the global models. Therefore, wind contributions to a set pressure, the 100 millibar level, as well as to the top of each meteorological model, were desired so that values from the various centers could be compared more accurately. Changes in the mass distribution, and hence the moment of inertia, of the atmosphere, are closely related to its two-dimensional surface pressure field. The pressure-related components from the centers can be compared without regard to the vertical construction of the model. A key issue is the extent to which an equilibrium response of the ocean modifies the changes in the pressure distribution felt by the solid earth. At certain time scales, this IB response acts to reduce the equivalent angular momentum fluctuations of the atmosphere. Because the IB exists to at least a certain extent, calculations with this IB correction are performed in parallel to the regular pressure terms.

Other meteorological parameters are included in the Sub-bureau files. Zonal mean zonal wind, from which the χ_3 term can be calculated, and zonal mean temperatures, whose gradients are related to overall zonal winds, are SBAAM analysis fields. Routine specification of the mass

distribution of the atmosphere, expressed in a low-order spherical harmonic expansion, is important in the study of various problems in geodynamics and geodesy, including the effects of mass redistribution on satellite orbits. Therefore, these coefficients are also SBAAM fields.

Two files, an analysis file and a forecast file, were specified by the Sub-bureau for archiving. A complete list of Sub-bureau files is given in Fig. 4. The analysis file is calculated twice daily (00 hr and 12 hr UTC). Additional files are being prepared at the Sub-bureau for research purposes. Forecasts of zonal mean zonal winds out to the longest lead times forms one such file. Analyses using several definitions of the world ocean for the purpose of calculating the IB correction forms two other files.

III. Research results from the SBAAM

Fig. 5 shows the analysis values of EAAM components for the period since October 1989 from NMC and JMA, the two meteorological centers that supply the full set of SBAAM quantities. We note some salient features here. The wind terms are integrated to the top model level of each center; therefore, they can be somewhat different. This difference can be noticed in the strength of the seasonal cycle in some components, especially the χ_3-wind term. Despite these differences, general agreement exists among the values from the centers. Such agreement can be analyzed by an empirical orthogonal function analysis (e.g., Salstein et al., 1983), which picks out the common variability present in a number of series. Also the mean values in some pressure-related terms vary with center due to the different orography models used by each center. A jump in the NMC pressure terms in March 1991 due to model changes is clearly evident, and should be removed when using these results.

An example of forecast errors computed from the ECMWF system for 3- 5- and 10-day lead times is shown in Fig. 6. Comparisons with a persistence based forecast are also depicted. For the χ_3-wind term, a notable bias in the earlier part of the period exists. This is apparently related to excessive forecasts of tropical easterly zonal winds within the ECMWF model, whose errors were reduced with the introduction of evaporative terms in May 1990. Similar results with the NMC system showed a negative bias as well (Rosen et al, 1991). Assessment of forecast skills (Rosen et al., 1987) is given in Fig. 7 for selected terms for the three centers that provide forecasts. The measure of skill, S, which can range from any negative value to a relatively perfect 100%, involves a comparison of the mean-square errors from both the forecast model and persistence-based forecasts. The presence of the bias in the χ_3-wind term, was accounted for by its removal. The skills are positive out to ten days (with one minor exception) for all three centers.

At present, we have compared some versions of the inverted barometer formulation. The issue we are testing is what difference the definition of the world ocean makes on the magnitude of the IB response. As one motivation for the study, Ponte et al. (1991) have demonstrated that parts of the ocean farthest from the center of the open ocean obey the IB response the least. Therefore, parallel runs to create the Sub-bureau parameters were performed for an ocean without the Arctic, and without the Arctic and the inland seas. Results for the χ_1 and χ_2 parameters are given in Fig. 8. There is some some difference among the IB versions, but of lesser magnitude than the difference between any IB formulation and the non-IB model. This is an ongoing effort, and the optimal representation of the ocean for the IB formulation in an operational setting has not yet been resolved.

ACKNOWLEDGMENTS

Work at AER was sponsored by the NOAA Climate and Global Change Program under grant NA89AA-D-AC202 and by EOS Project of NASA through Contract NAS5-33010.

REFERENCES

Barnes, R.T.H., R. Hide, A.A. White, and C.A. Wilson, 1983: Atmospheric angular momentum fluctuations, length-of-day changes and polar motion. *Proc. Roy. Soc. Lond. A, 387*, 31-73.

Ponte, R.M., D.A. Salstein, and R.D. Rosen, 1991: Sea level response to pressure forcing in a barotropic numerical model, *J. Phys. Oceanog.*, *21*, 1043-1057.

Rosen, R.D., D.A. Salstein, T. Nehrkorn, M.R.P. McCalla, A.J. Miller, J.O. Dickey, T.M. Eubanks, and J.A. Steppe, 1987: Medium-range numerical forecasts of atmospheric angular momentum. *Mon. Wea. Rev.*, *115*, 2170-2175.

Rosen, R.D., D.A. Salstein, and T. Nehrkorn, 1991: Predictions of zonal wind and angular momentum by the NMC medium-range forecast model during 1985-1989, *Mon. Wea. Rev.*, *119*, 208-217.

Salstein, D.A., R.D. Rosen, and J.P. Peixoto, 1983: Modes of variability in annual hemispheric water vapor and transport fields, *J. Atmos. Sci.*, *40*, 788-803.

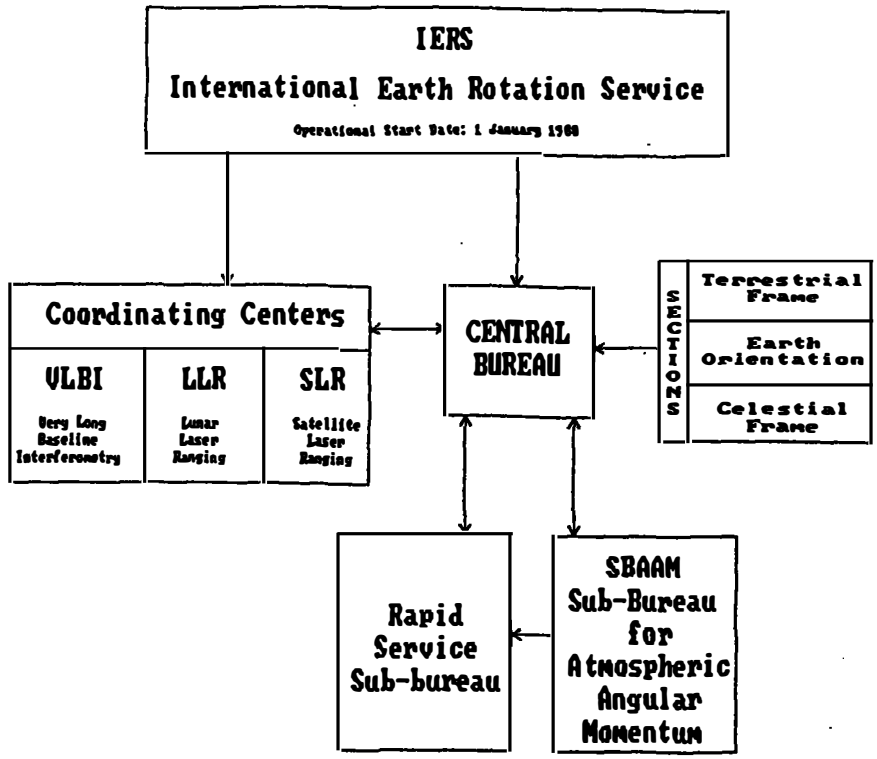

Fig. 1. ORGANIZATION OF THE IERS. The International Earth Rotation Service, whose Central Bureau is housed at the Observatory of Paris, is concerned with the earth's orientation and reference frames. It combines and analyzes earth rotation data from coordinating centers which develop data from VLBI and other advanced techniques. The Rapid Service Sub-bureau provides some of these data to users who need it quickly. The Sub-bureau for Atmospheric Angular Momentum (SBAAM), housed at NMC, collects and supplies relevant atmospheric data to the Central Bureau.

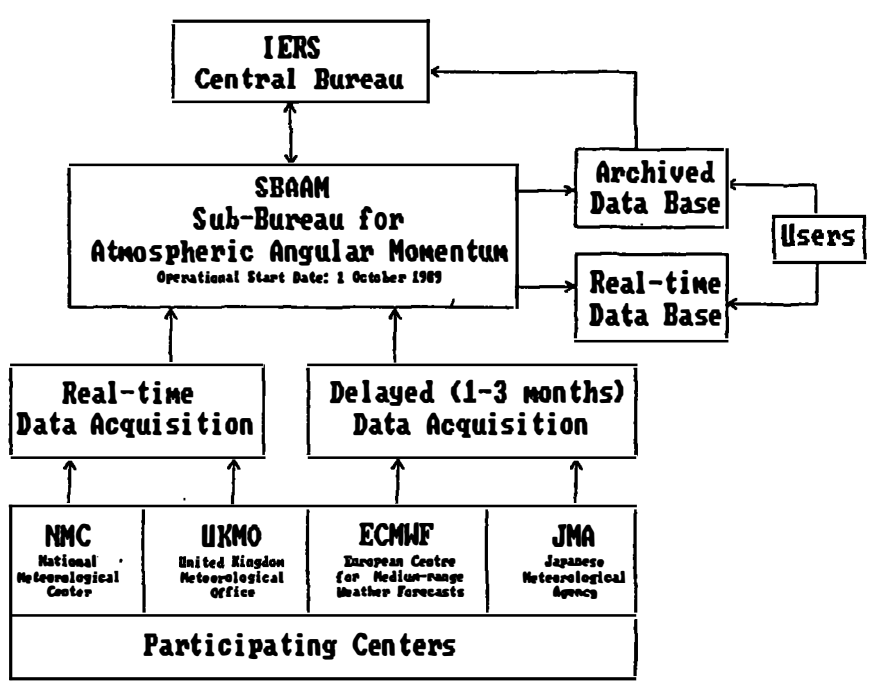

Fig. 2. OPERATIONS OF THE SBAAM. The SBAAM receives data in either real-time or delayed mode from participating meteorological centers and supplies it to interested users. Additional analyses and evaluations of the Sub-bureau data are taking place at Atmospheric and Environmental Research, Inc., (AER) in Cambridge, Massachusetts.

$$\chi_1^P = \frac{-1.00R^4}{(C-A)g} \int\int p_s \sin\phi \cos^2\phi \cos\lambda \, d\lambda \, d\phi$$

$$\chi_1^W = \frac{-1.43R^3}{\Omega(C-A)g} \int\int\int (u \sin\phi \cos\phi \cos\lambda - v \cos\phi \sin\lambda) \, d\lambda \, d\phi \, dp$$

$$\chi_2^P = \frac{-1.00R^4}{(C-A)g} \int\int p_s \sin\phi \cos^2\phi \sin\lambda \, d\lambda \, d\phi$$

$$\chi_2^W = \frac{-1.43R^3}{\Omega(C-A)g} \int\int\int (u \sin\phi \cos\phi \sin\lambda + v \cos\phi \cos\lambda) \, d\lambda \, d\phi \, dp$$

$$\chi_3^P = \frac{0.70R^4}{Cg} \int\int p_s \cos^3\phi \, d\lambda \, d\phi$$

$$\chi_3^W = \frac{R^3}{C\Omega g} \int\int\int u \cos^2\phi \, d\lambda \, d\phi \, dp$$

R = radius of earth	g = acceleration of gravity	p = pressure
C = axial moment of inertia of earth	u = zonal wind	ϕ = latitude
A = equatorial moment of inertia of earth	v = meridional wind	λ = longitude
Ω = mean rotation rate of earth	p_s = surface pressure	

Fig. 3. Formulas for the χ_1, χ_2, and χ_3 components according to Barnes et al. (1983). The χ_1 and χ_2 terms are dependent on wavenumber-1 harmonics of winds and pressures, whereas χ_3 depends on their zonal means.

SBAAM Parameters

Analysis Parameters	Specification
AAM Equatorial χ_1, χ_2 AAM Axial χ_3	Hemispheric values for wind, pressure & pressure + i.b.
Zonal Mean Zonal Winds Zonal Mean Temperatures	5° latitude intervals, 12 mandatory pressure levels
Mean Surface Pressure	global average
Surface Pressure Coefficients	triangular truncation to wave 4 zonals only to wave 20
Forecast Parameters	**Specification**
AAM Equatorial χ_1, χ_2 AAM Axial χ_3	Global forecast values at 12-h intervals to 10 days for wind, pressure, pressure + i.b.

Fig. 4. Parameters that are collected, archived, and distributed by the Sub-bureau. The three components of atmospheric angular momentum are related to winds and surface pressure. The pressure terms may be modified by the oceanic inverted barometer (IB) effect, and so two forms are independently computed. Both analysis and forecast quantities are collected. Related parameters include the zonal mean winds and temperatures, and mean values and spectral coefficients of the surface pressure field.

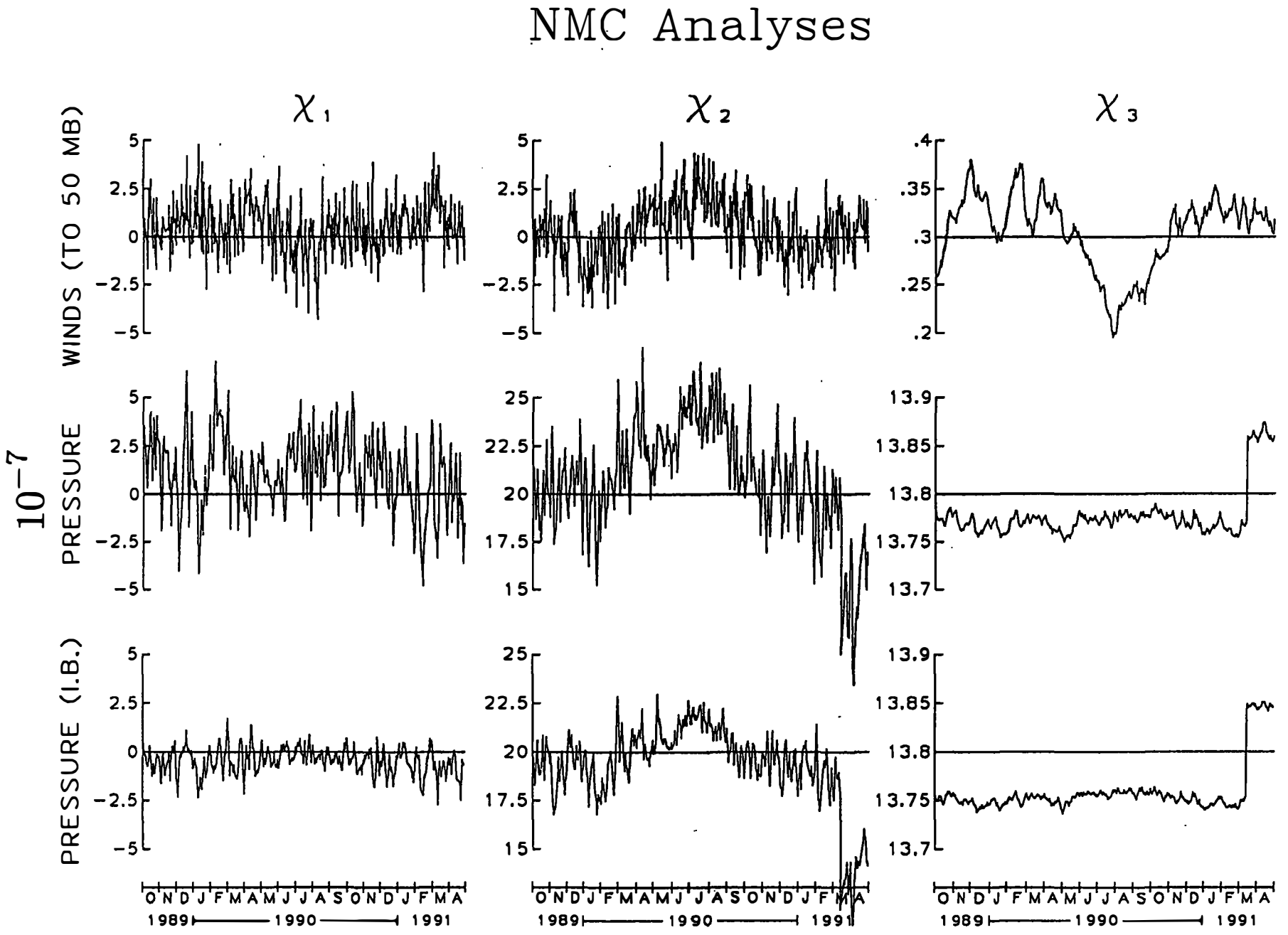

Fig. 5a. Values of the global effective atmospheric angular momentum functions χ_1, χ_2, and χ_3 for wind, pressure, and pressure (IB) from the NMC analysis system since the start of SBAAM operations. Units are non dimensional, multiplied by 10^{-7}.

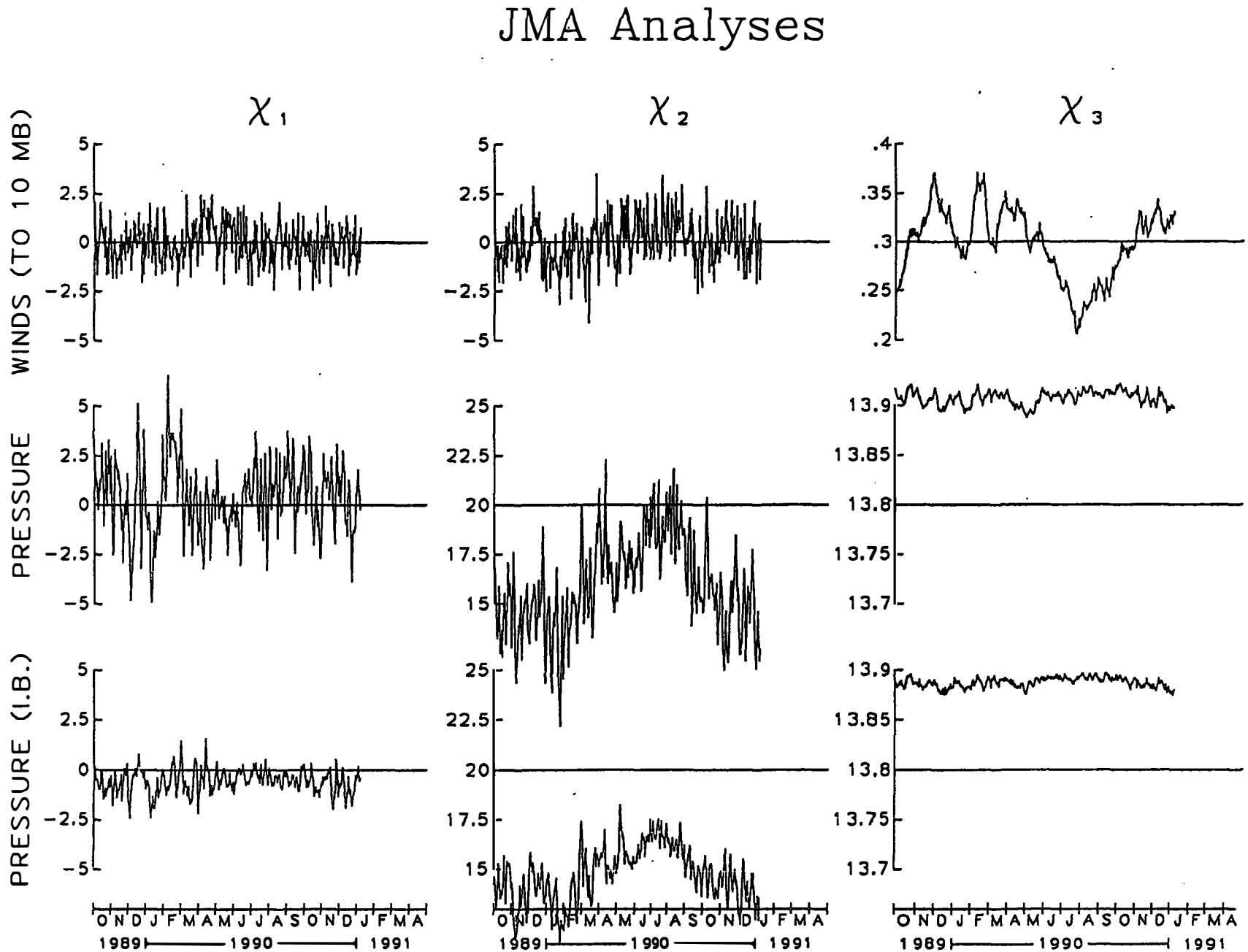

Fig. 5b. Same as 1a, but from the JMA system.

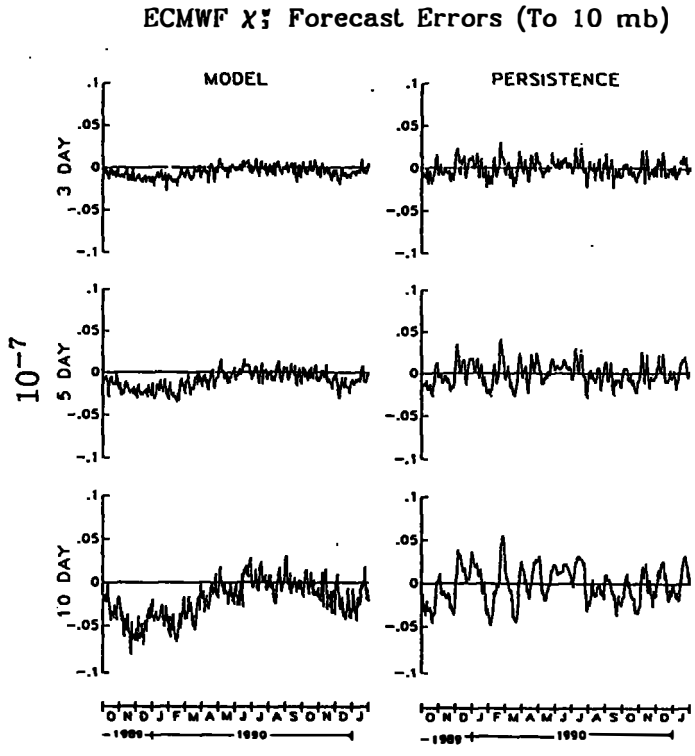

Fig. 6. Forecast errors of χ_3^W at 3, 5, and 10 days in non-dimensional units for model- and persistence-based forecasts from ECMWF.

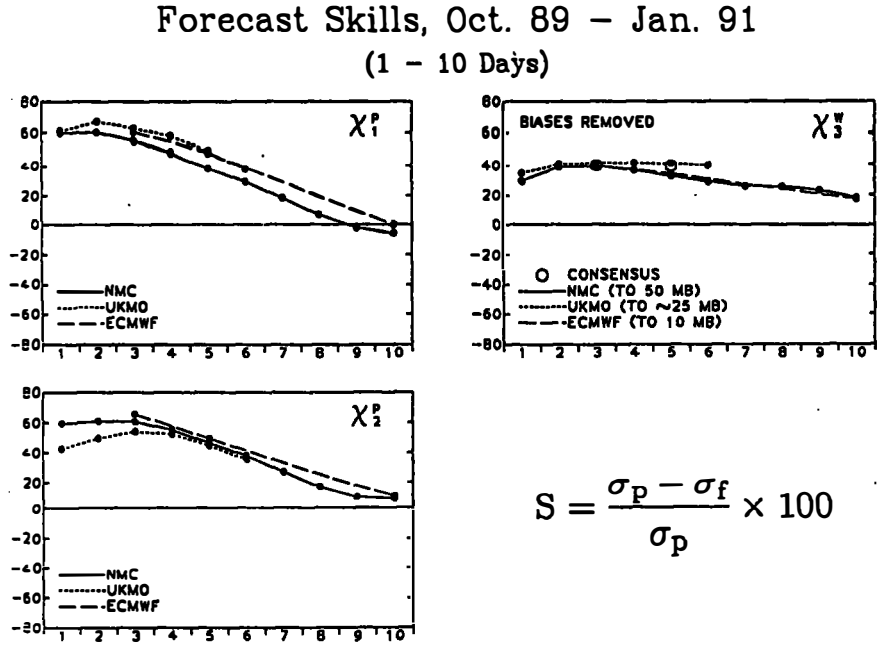

$$S = \frac{\sigma_p - \sigma_f}{\sigma_p} \times 100$$

Fig. 7. A comparison of skills from model-based forecasts, out to 10 days, for χ_1^P, χ_2^P and χ_3^W, the terms most responsible for their respective component's earth rotation excitation, from NMC, UKMO, and ECMWF. The skill, S of these pressure and wind terms, is defined by the formula above where σ_p and σ_f are the rms errors of the persistence and model forecasts respectively. Biases have been removed from the χ_3^W terms in the lower right hand panel. Skill of a consensus forecast, defined as the mean of the centers' forecasts, is given for the χ_3^W term.

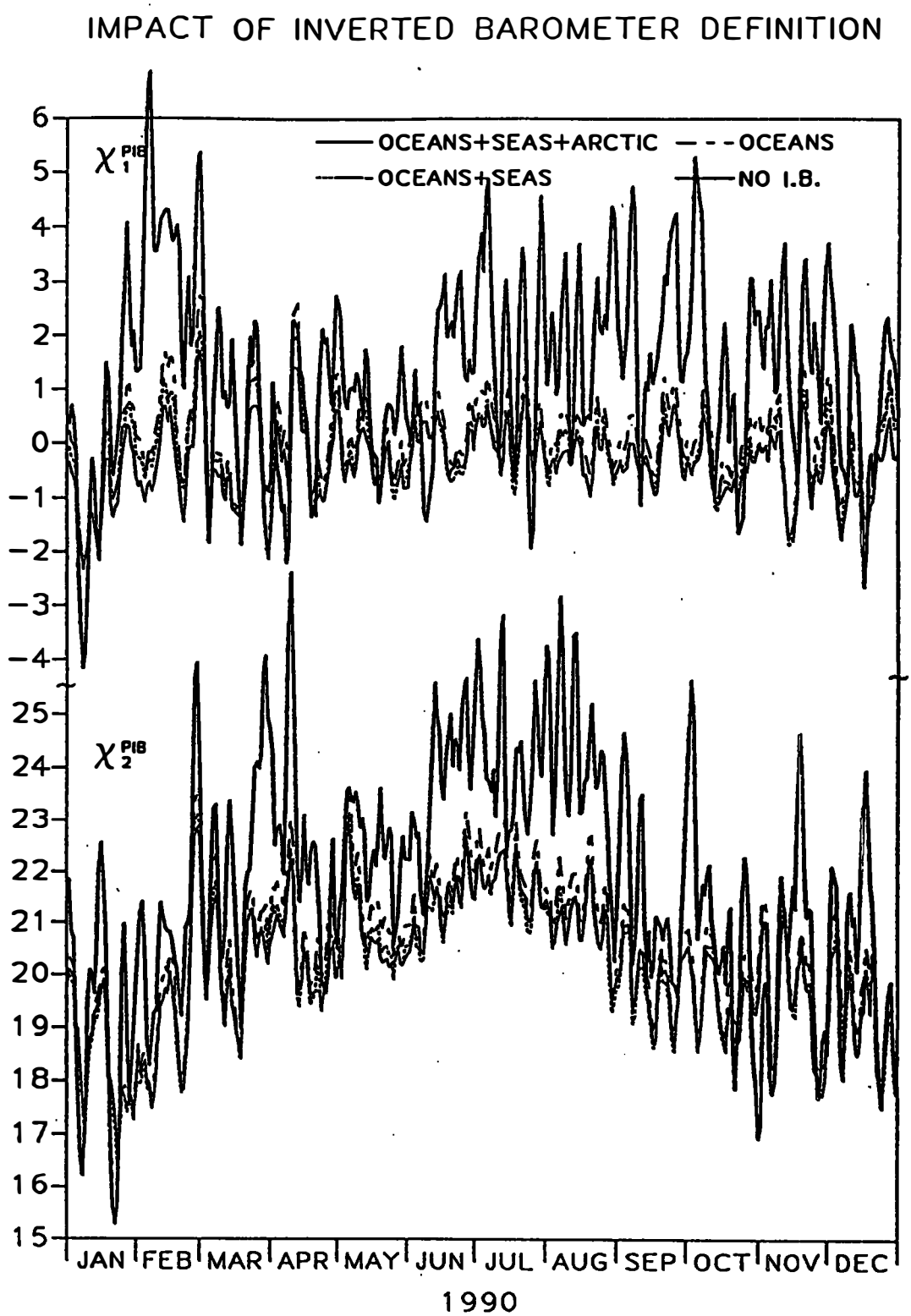

Fig. 8. Values of the global χ_1 and χ_2 pressure terms resulting from three world ocean definitions, as described in text, for the inverted barometer (IB), and for the pressure terms without the inverted barometer model, for 1990. Units are non-dimensional, multiplied by 10^{-7}.

THE RUNNING RMS DIFFERENCE BETWEEN LENGTH-OF-DAY AND VARIOUS MEASURES OF ATMOSPHERIC ANGULAR MOMENTUM

R. S. Gross, J. A. Steppe, and J. O. Dickey
Jet Propulsion Laboratory
California Institute of Technology
4800 Oak Grove Drive
Pasadena, CA 91109-8099
USA

ABSTRACT. The axial component of the Earth's atmospheric angular momentum (AAM) has been shown, in general, to be highly correlated with changes in the length-of-day (lod). Estimates of the atmosphere's angular momentum are currently produced by the National Meteorological Center (NMC) in the United States, the European Centre for Medium-Range Weather Forecasts (ECMWF) in the United Kingdom, the United Kingdom Meteorological Office (UKMO), and the Japanese Meteorological Agency (JMA). Even though each center has access to the same raw meteorological data, the subsequent data selection, processing and assimilation procedures followed by each center are different. Furthermore, each center produces a number of estimates of the AAM under different procedures and assumptions (such as with and without the inverted barometer correction). Thus, there are a variety of measures of the AAM available, not only from different centers, but also from each center. This study individually compares the available AAM series to the lod as a means of determining which series most closely represents (in an rms sense) the lod at any given time.

The length-of-day data set used in this study is one produced at JPL resulting from a Kalman filter-based approach to combining and analyzing independent observations of UT1. The AAM and lod data sets are first pre-processed, removing (when necessary) step-like offsets from the AAM data sets caused by model changes, and removing a two year running average from the lod data set as a means of removing the long-term, decadal, lod variations of (presumably) non-atmospheric origin. The root-mean-square (rms) difference between the lod and some AAM data set is then computed within a sliding window having fixed length of 365 days. These results indicate that the rms difference between the lod and any of the measures of the AAM (no matter how the data sets are processed) is time variable, and that the particular AAM series that is closest to the lod at any given time changes with time. But, in general, the JMA "analysis" and ECMWF "zero hour forecast" results are closer to the lod than similarly determined results from the other centers. This finding may result from the fact that the JMA "analysis" and ECMWF "zero hour forecast" results are computed by integrating the atmospheric wind term to a greater height than is done for the other results.

1. Introduction

On time scales of less than a few years, fluctuations in the axial component of the atmosphere's angular momentum have been shown to be highly correlated with variations in the Earth's length-of-day [e.g., *Barnes et al.*, 1983; *Rosen and Salstein*, 1983, 1985; *Rosen et al.*, 1984; *Eubanks et al.*, 1985; *Morgan et al.*, 1985; *Hide and Dickey*, 1991]. Estimates of the atmosphere's angular momentum are produced from the output of atmospheric general circulation models operated for weather prediction purposes [*Hide*, 1989b; *Arpe*, 1990; *Kann and Salstein*, 1990; *Naito et al.*, 1990]. Since the atmospheric angular momentum (AAM) is so highly correlated with the length-

of-day (lod), we are presented with the opportunity of using the lod as a reference series against which the various AAM series currently available can be compared. This is undertaken here as a means of evaluating the available AAM series in order to determine which is closest (in an rms sense) to the lod. This is done by computing the square root of the mean of the squares (rms) of the difference between an individual AAM series and the length-of-day within a sliding window of length 365 days. The questions to which answers are sought in a study such as this are: 1) Which center is producing AAM values closest to the lod? 2) Are AAM values valid at midnight closer to midnight lod values, or are noon AAM values closer to noon lod values? 3) Are AAM "analysis" or "zero hour forecast" values closer to the lod? 4) Does including the pressure term in the AAM computation yield values closer to the lod than just including the wind term? If so, does making the inverted barometer approximation yield values closer to the lod than not making this assumption?

2. Data Sets and Pre-Processing

The length-of-day data set used in this study is that produced at the Jet Propulsion Laboratory from a Kalman filter-based combination, smoothing, and interpolation of independent observations of the Earth's orientation [*Eubanks*, 1988; *Morabito et al.*, 1988; *Gross and Steppe*, 1991a, 1991b]. In order to be able to compare midnight and noon AAM series to the length-of-day without needing to interpolate the AAM values, two lod series were generated, one containing daily values (without gaps) at midnight spanning June 21.0, 1976 to January 18.0, 1991, and the other containing daily values (without gaps) at noon spanning June 20.5, 1976 to January 17.5, 1991. Using the tidal model of *Yoder et al.* [1981], both long and short period tidal influences were removed from the UT1 observations prior to Kalman filtering, thereby removing these tidal effects from the resulting lod series. The length-of-day exhibits fluctuations on decadal time scales that are thought to be caused by interactions between the Earth's core and mantle [e.g., *Munk and MacDonald*, 1960; *Lambeck*, 1980]. Since these long-period lod variations are not thought to be caused by the atmosphere, they were removed from the lod series by forming, and then removing, a two-year moving average of the lod series.

The atmospheric angular momentum data sets used in this study are listed in Tables 1 and 2. Table 1 gives some information about the "analysis" AAM data sets derived from the weather prediction models of the Japanese Meteorological Agency (JMA), the National Meteorological Center (NMC), the European Centre for Medium-Range Weather Forecasts (ECMWF), and the United Kingdom Meteorological Office (UKMO). Table 2 gives the same information for the "zero hour forecast" data sets derived from the NMC, ECMWF, and UKMO models (AAM forecasts are not currently available from the JMA model). In computing the atmospheric angular momentum, two integrals must be evaluated [e.g., *Barnes et al.*, 1983]: 1) a wind term involving an integral of the atmospheric winds to some cutoff height, and 2) a pressure term involving an integral of the surface pressure field. In computing the pressure term, an assumption needs to be made as to the response of the oceans to changes in atmospheric pressure. The assumptions usually made are: 1) that the oceans respond as an inverted barometer wherein the height of the ocean varies with the atmospheric pressure such that the pressure on the crust at the bottom of the ocean is constant, and 2) that the oceans respond as a rigid body fully transmitting the atmospheric pressure variations to the oceanic crust. The entries in the column labelled "inverted barometer" in Tables 1 and 2 indicate whether the pressure term is computed assuming the inverted barometer approximation, assuming rigid oceans, or under both assumptions. The entries in the column labelled "wind cutoff height" in Tables 1 and 2 give the height (expressed as an atmospheric pressure level) to which the wind term is integrated for each data set.

Prior to comparing these AAM data sets to the length-of-day, they were pre-processed in order to place them in a uniform format having the same units. The ECMWF "analysis" data sets valid at 9 UT were linearly interpolated to noon (12 UT) and the JMA "analysis" data sets valid at 6 UT were linearly interpolated to both midnight (0 UT) and noon. Gaps in the AAM data sets were neither filled nor interpolated across. A scale factor of 9.80/9.81 was applied to the JMA values in

TABLE 1. "ANALYSIS" AAM DATA SETS

ANALYSIS CENTER	DATA SPAN	DATA EPOCH	WIND CUTOFF HEIGHT	INVERTED BAROMETER
JMA	28SEP83–04DEC83	0 & 12 UT	10 mb	with & without
JMA	12DEC83–30JUN86	6 UT	10 mb	with & without
JMA	01JUL86–30JUN90	0 & 12 UT	10 mb	with & without
NMC	01JUL76–29AUG83	0 UT	50 mb	with & without
NMC	30AUG83–28FEB91	0 & 12 UT	50 mb	with & without
ECMWF	01DEC79–30NOV80	12 UT	50 mb	without
ECMWF	01DEC80–15MAR82	0 UT	50 mb	without
ECMWF	16MAR82–29FEB84	12 UT	50 mb	without
ECMWF	01MAR84–15MAR84	0 UT	50 mb	without
ECMWF	16MAR84–31MAY87	12 UT	50 mb	without
ECMWF	01JUN87–31JAN88	9 UT	50 mb	without
UKMO	01MAY83–01NOV86	0 UT	30 mb	without

TABLE 2. "ZERO HOUR FORECAST" AAM DATA SETS

ANALYSIS CENTER	DATA SPAN	DATA EPOCH	WIND CUTOFF HEIGHT	INVERTED BAROMETER
JMA	------	------	------	------
NMC	10NOV85–01APR91	0 UT	100 mb	wind only
NMC	02OCT89–01APR91	0 UT	50 mb	with & without
ECMWF	01JAN86–31DEC87	12 UT	near 10 mb	without
ECMWF	01JAN88–31JAN91	0 & 12 UT	near 10 mb	without
UKMO	27NOV86–07FEB91	0 & 12 UT	near 25 mb	without

order to change the value of the gravitational acceleration used in determining the JMA AAM values to be the same as that used in computing the AAM values from the other weather prediction models [*Naito et al.*, 1987]. Finally, obvious model-induced step-like changes in the AAM series were removed.

Atmospheric models are developed at the JMA, NMC, ECMWF, and UKMO for the purposes of weather prediction. Modifications are being continually made to these models in order

to improve their weather prediction ability. Some of these improvements may affect the resulting AAM values, introducing step-like changes in the AAM series at the time the model modification is implemented. These step-like changes in the AAM series need to be removed prior to comparing the AAM series to the lod. Step-like changes were found by differencing an individual AAM series with a simple average of all other, similarly computed AAM series, thereby forming a residual series. If no other AAM series was available (such as prior to 1979), then the residual series was formed by differencing the AAM series with the lod. In this manner, obvious step-like changes were found in the ECMWF "analysis" series at March 31.5, 1981, April 21.0, 1983, February 1.0, 1984, and May 1.0, 1985, and in the NMC "analysis" series at May 28.25, 1986 and August 12.25, 1987. These dates correspond to dates of known changes to the models at these centers [*Salstein*, 1988; *Hide*, 1989a]. The step-like offsets were removed from the AAM series by fitting separate smoothing splines [*Reinsch*, 1967, 1971] to the AAM residual on either side of the step. The offset of the smoothing splines at the time of the model change yields the estimate of the step amplitude which was then added to the AAM values prior to the time of the step. For the purposes of the spline fit, the AAM uncertainty was assumed to be 0.03 ms and the splines were fit to the AAM residual values such that the reduced chi-square of the fit was one.

3. Approach

Each available AAM data set is compared, individually, to the length-of-day. Midnight AAM data sets are compared to the midnight lod series, and noon AAM data sets are compared to the noon lod series. The comparison is done in the time domain by forming the root-mean-square (rms) of the difference of the AAM and lod data sets within a window of length 365 days. The rms is computed only if the total number of missing data points within the window is less than 10% of the window's length. A window length of 365 days was chosen as a compromise between forming a localized estimate (i.e., having a small window length) and producing a reasonably smooth result (i.e., having a large window length). The resulting rms value is time-tagged at the mid-point of the window. By sliding the window down the time series one day at a time, repeating the rms computation at each window position, a time history is obtained of the rms difference between the AAM series and the length-of-day.

The mean of the differenced series within the window was removed prior to forming the rms, so that the standard deviation of the AAM-lod difference is actually being calculated. The window was demeaned in order to localize the effects on the rms calculation of step-like changes in the AAM series induced by changes to the weather prediction models used to produce the AAM estimates. Visibly obvious step-like changes in the AAM series were detected and removed as described above. However, there may be additional step-like changes which escaped detection and were therefore not removed from the AAM series. This possibility was accounted for here by demeaning the differenced series within the window at each window position. In this manner, the effect of any step-like changes in the AAM values is localized to the windows within which that step-like change occurs, and does not affect the rms computation at previous or subsequent times. Note that only the mean has been removed from within each window. No seasonal terms have been removed, either from within each individual window, or from the series as a whole.

4. Results, Discussion and Conclusions

Figures 1–6 show plots of the resulting running rms difference between the atmospheric angular momentum and the length-of-day. Figures 1, 2, 3, and 4 show the results for the UKMO, ECMWF, NMC, and JMA "analysis" AAM values, respectively, and Figures 5 and 6 show the results for the UKMO and ECMWF "zero hour forecast" AAM values, respectively. There are no UKMO "analysis" AAM values at noon (Table 2) and the overlap of the filtered lod series (long period terms removed) with the NMC "zero hour forecast" AAM series computed by including the pressure term is less than the window length of 365 days (results for the 100 mb wind only term

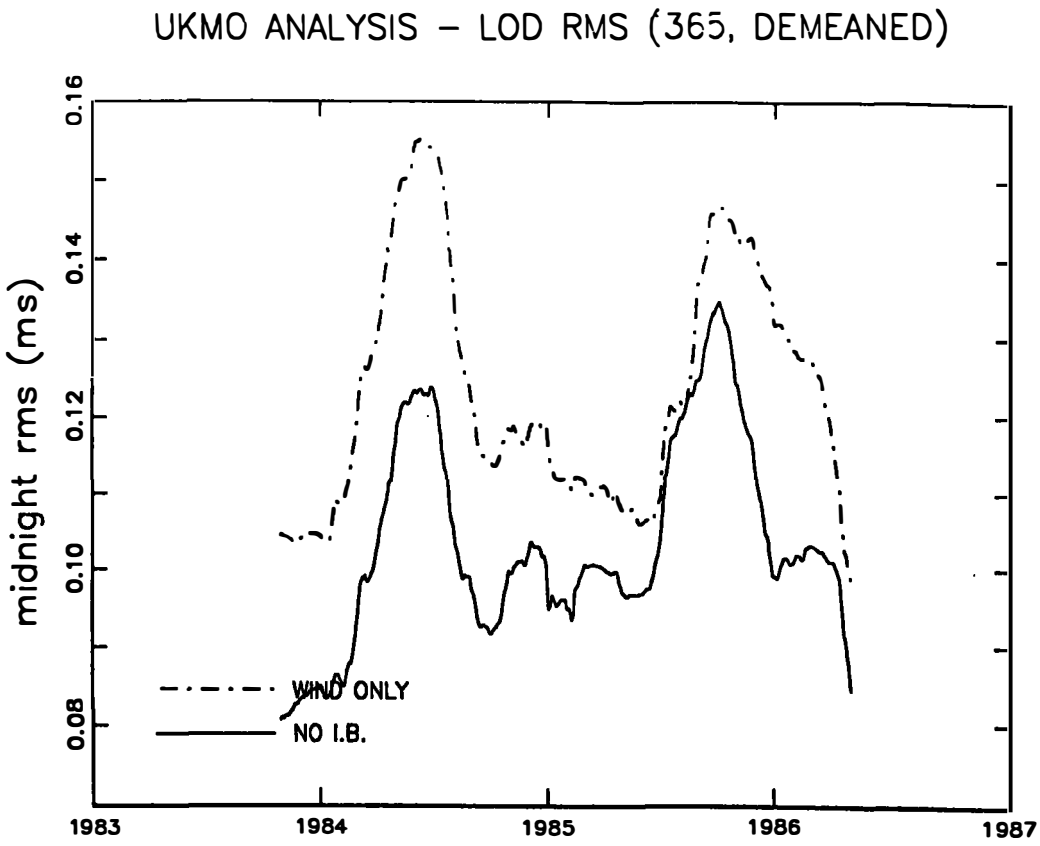

Fig. 1. Running rms of the difference between the length-of-day and AAM "analysis" results from the United Kingdom Meteorological Office.

are shown in Figure 10). Each figure shows results for the running rms of the AAM-lod difference in which, where available, the AAM has been computed under different assumptions (wind term only, wind term plus pressure term computed without the inverted barometer approximation, wind term plus pressure term computed with the inverted barometer approximation).

For the UKMO AAM "analysis" results (Figure 1), it is clear that computing the AAM by including the pressure term without the inverted barometer approximation results in an AAM series that is closer to the length-of-day (in an rms sense) than by computing it from the wind term only. For most of the time, this is also true for the ECMWF "analysis" results (Figure 2). But there are periods of time (e.g., mid-1986) wherein computing the ECMWF "analysis" AAM from only the wind term results in AAM values closer to the length-of-day. The situation is less clear for the NMC and JMA "analysis" results (Figures 3 and 4, respectively). For a good part of the time it appears that computing the AAM from only the wind term yields values furthest from the lod, but there are periods of time (e.g., mid-1988 for the NMC, Figure 3; mid-1985 for the JMA, Figure 4) where this is not true. As for the question about whether or not computing the pressure term with the inverted barometer approximation yields AAM values closer to the lod, this appears to be true for only part of the time for the NMC (Figure 3) and JMA (Figure 4) "analysis" results. Finally, for the most part, the midnight and noon "analysis" results are identical (Figures 3 and 4). There is virtually no difference between the midnight and noon wind only results for both the NMC and JMA, but there appear to be some differences between the midnight and noon results in which the AAM is calculated by including the pressure term (whether or not the inverted barometer

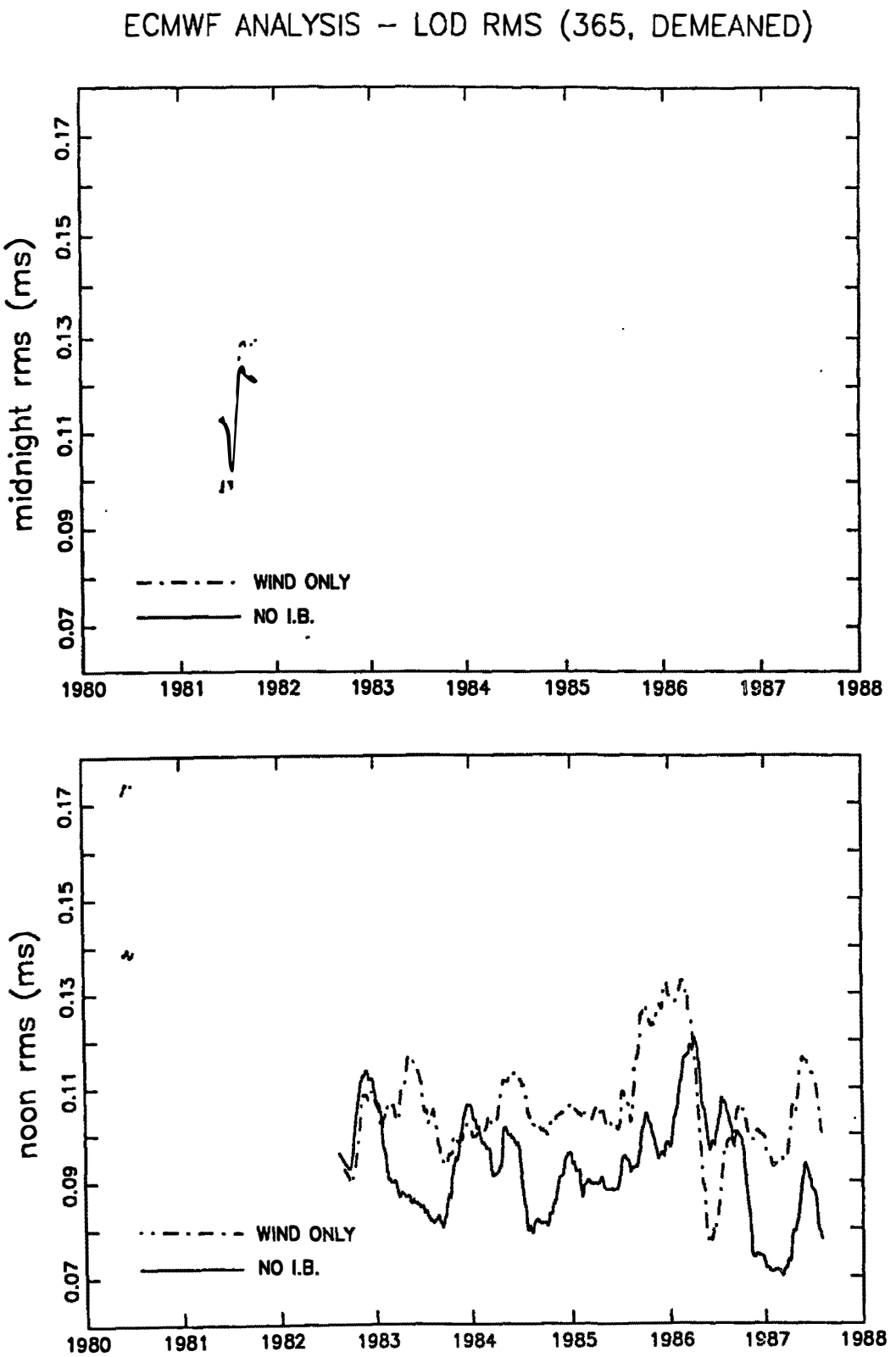

Fig. 2. Running rms of the difference between the length-of-day and AAM "analysis" results from the European Centre for Medium-Range Weather Forecasts.

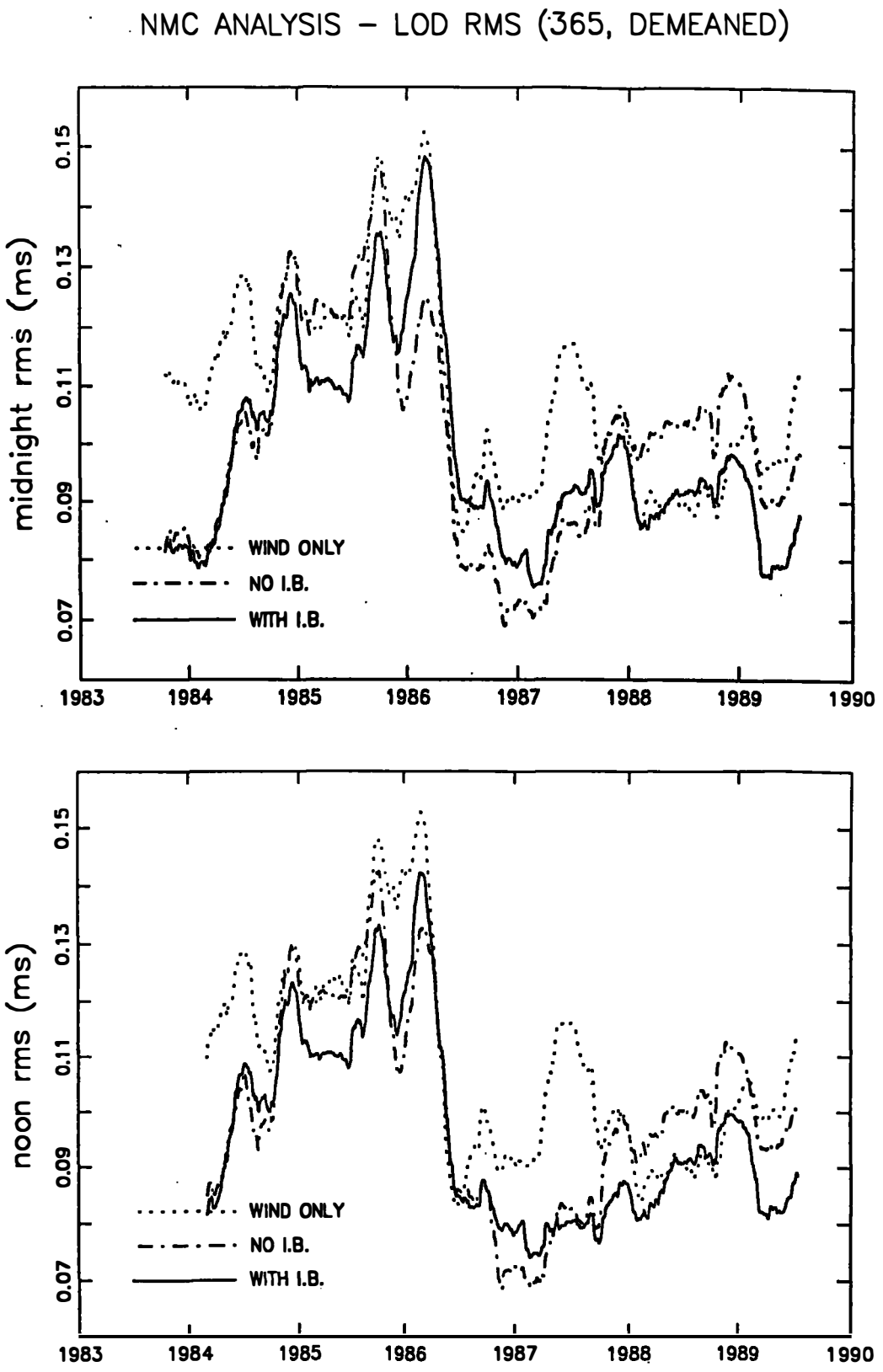

Fig. 3. Running rms of the difference between the length-of-day and AAM "analysis" results from the National Meteorological Center.

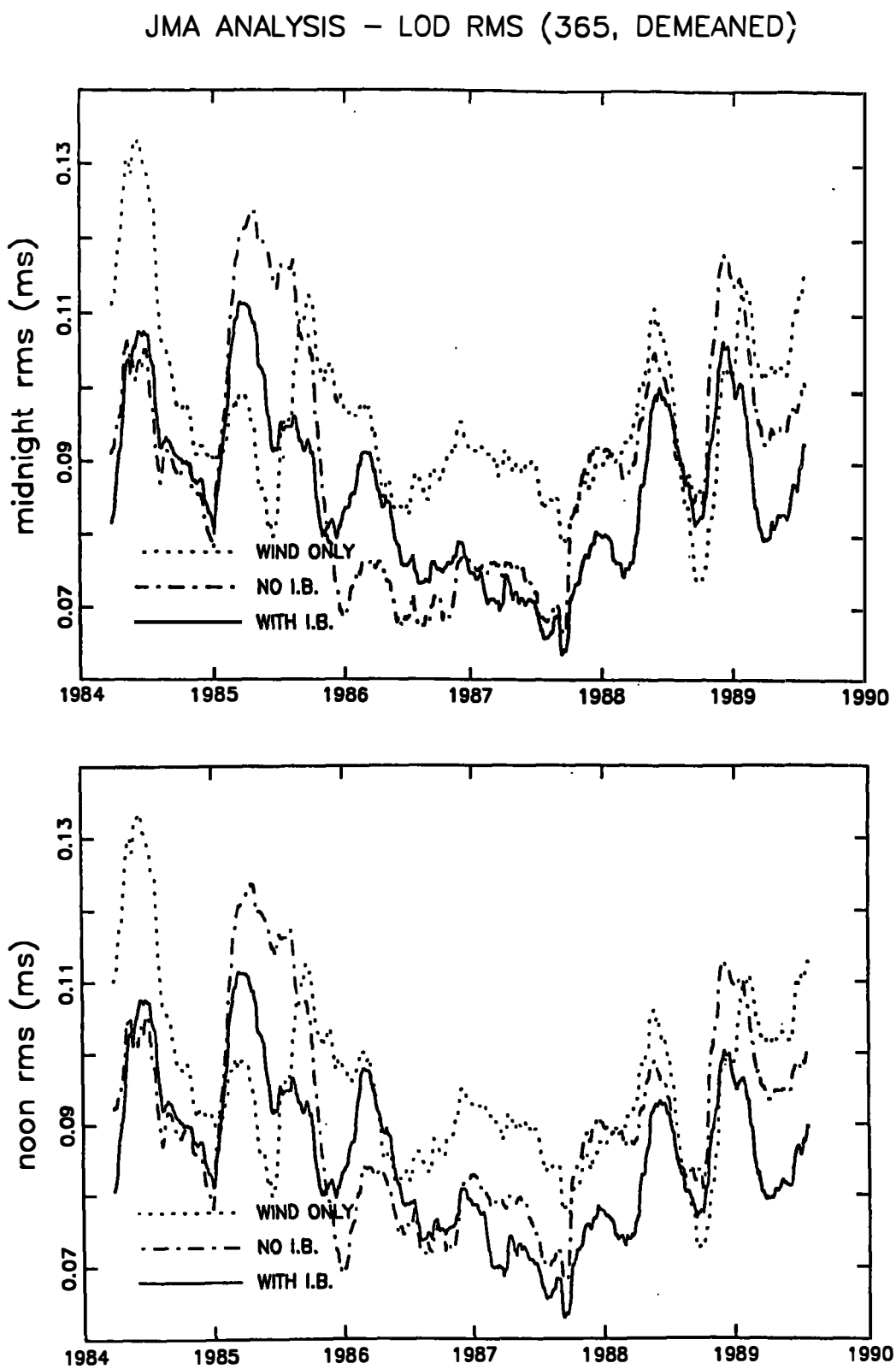

Fig. 4. Running rms of the difference between the length-of-day and AAM "analysis" results from the Japanese Meteorological Agency.

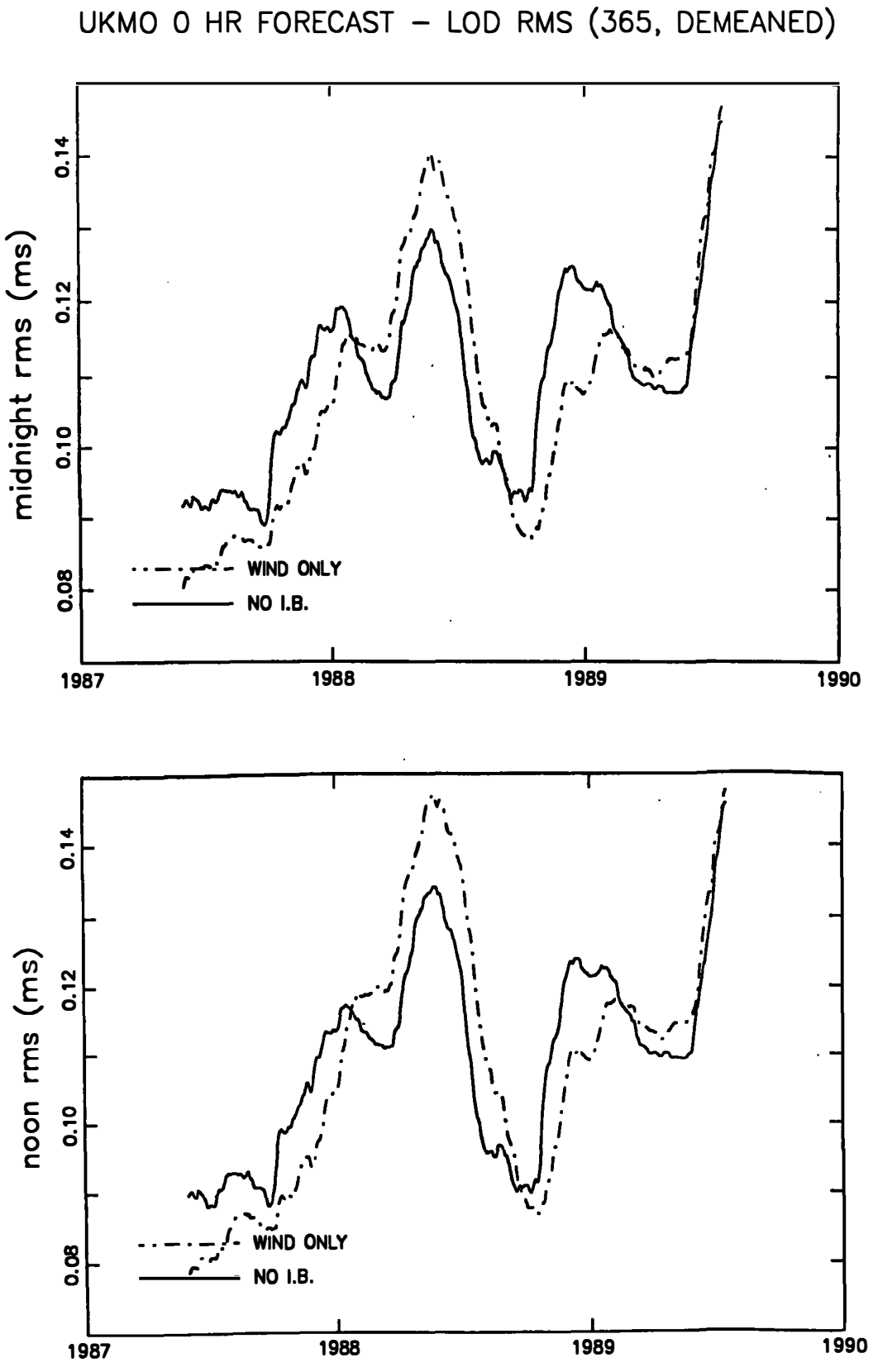

Fig. 5. Running rms of the difference between the length-of-day and AAM "zero hour forecast" results from the United Kingdom Meteorological Office.

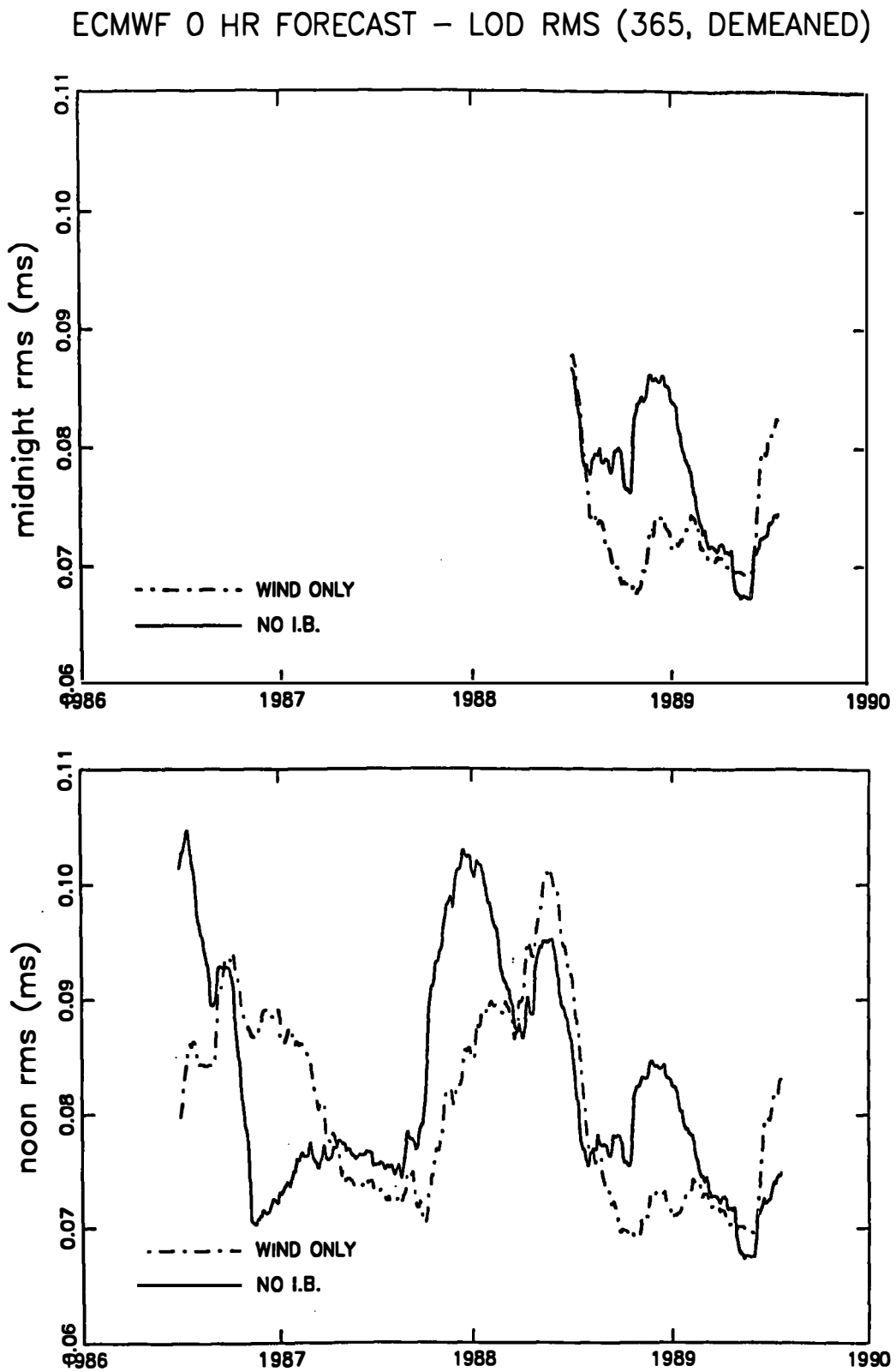

Fig. 6. Running rms of the difference between the length-of-day and AAM "zero hour forecast" results from the European Centre for Medium-Range Weather Forecasts.

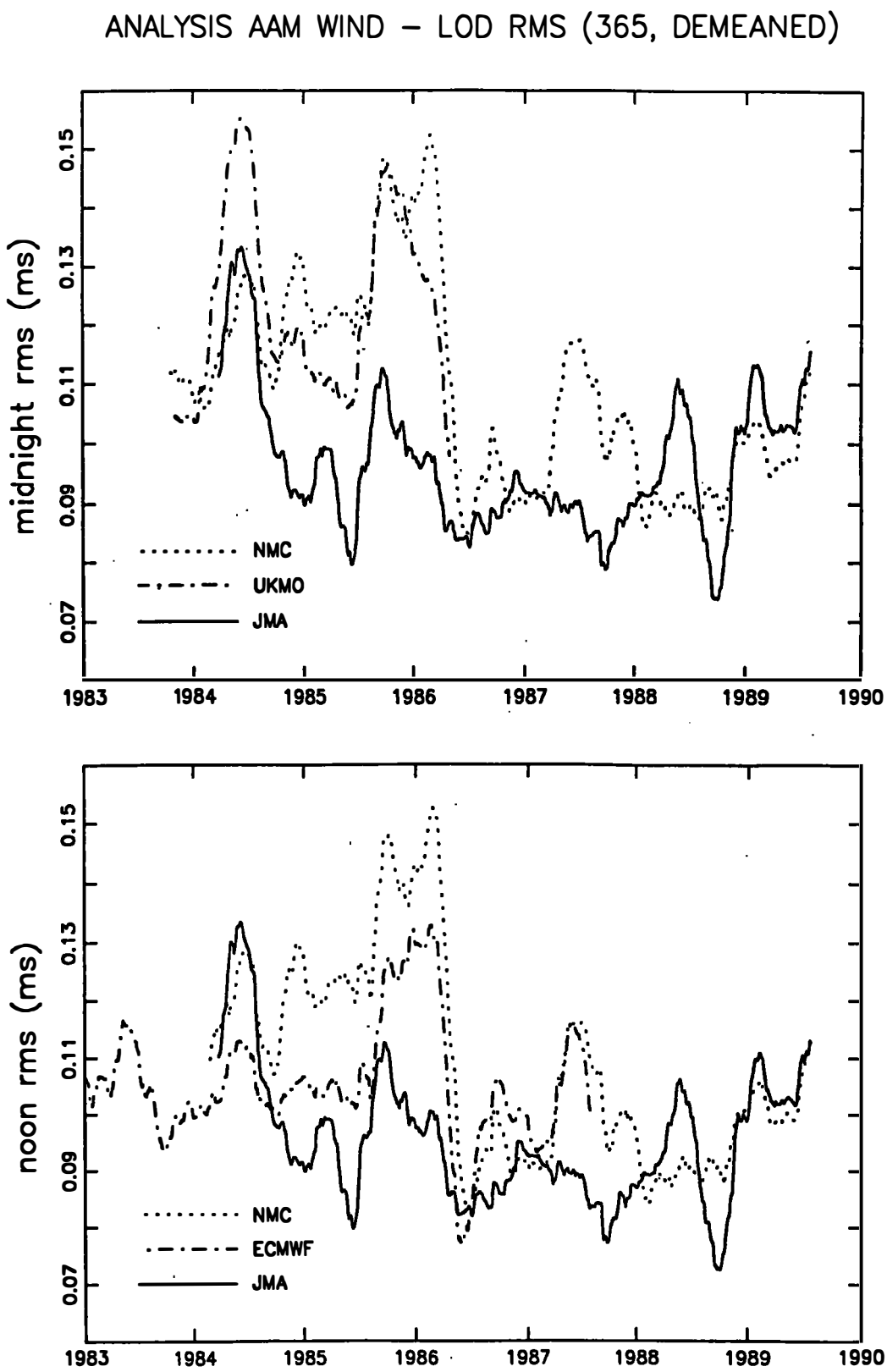

Fig. 7. Running rms of the difference between the length-of-day and AAM "analysis" results computed by including only the wind term.

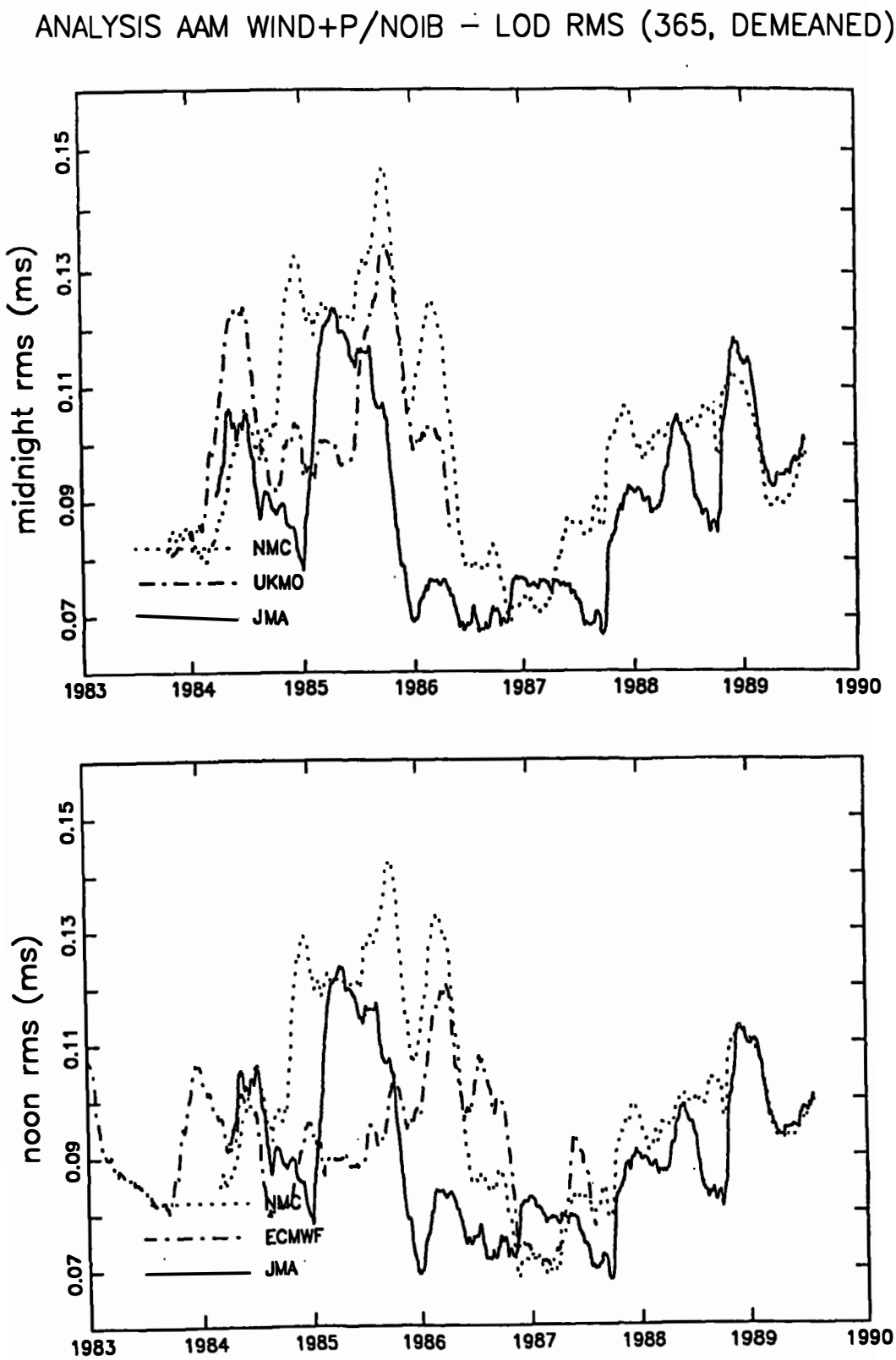

Fig. 8. Running rms of the difference between the length-of-day and AAM "analysis" results computed by including the wind and pressure (without the inverted barometer approximation) terms.

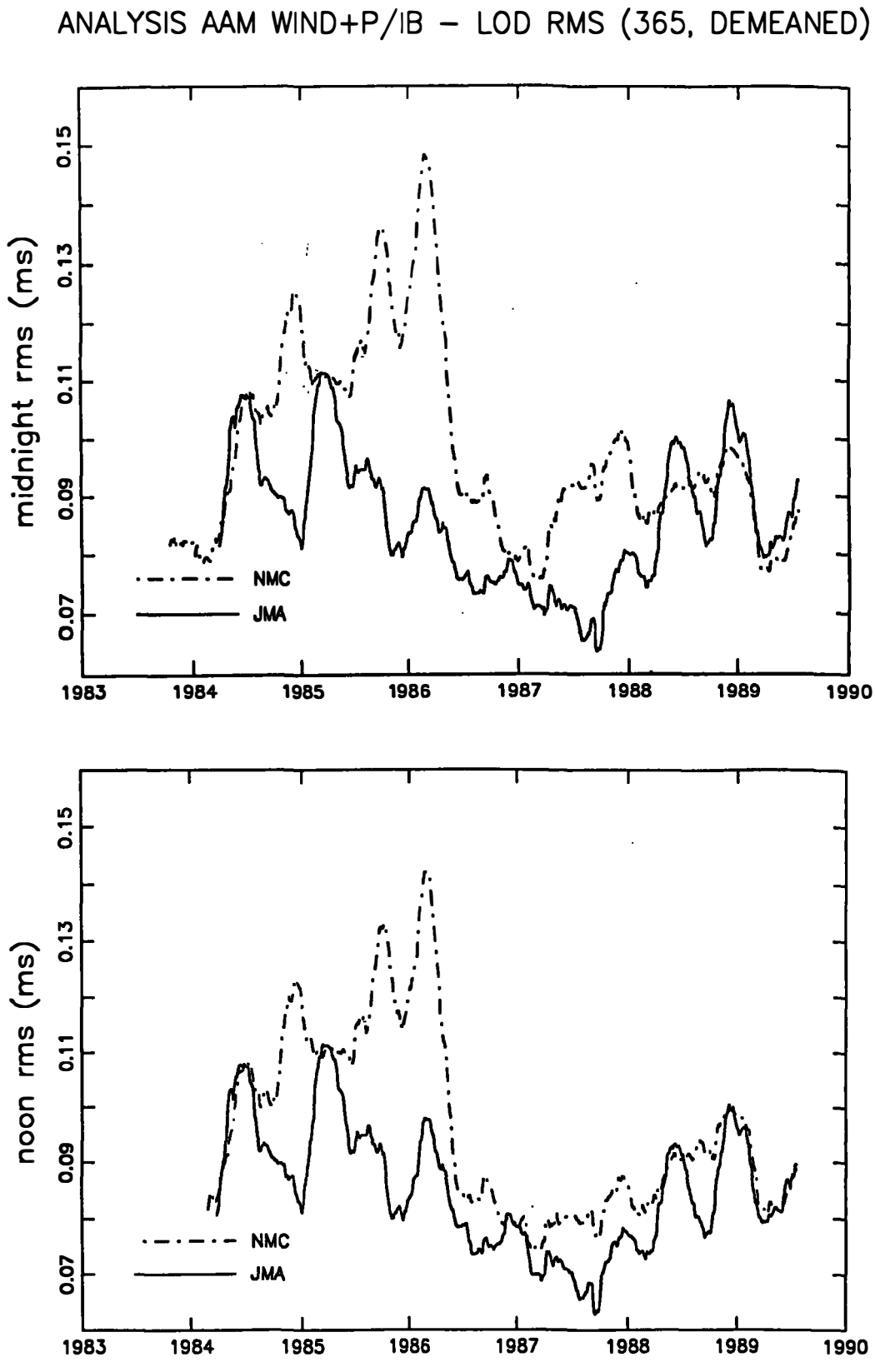

Fig. 9. Running rms of the difference between the length-of-day and AAM "analysis" results computed by including the wind and pressure (with the inverted barometer approximation) terms.

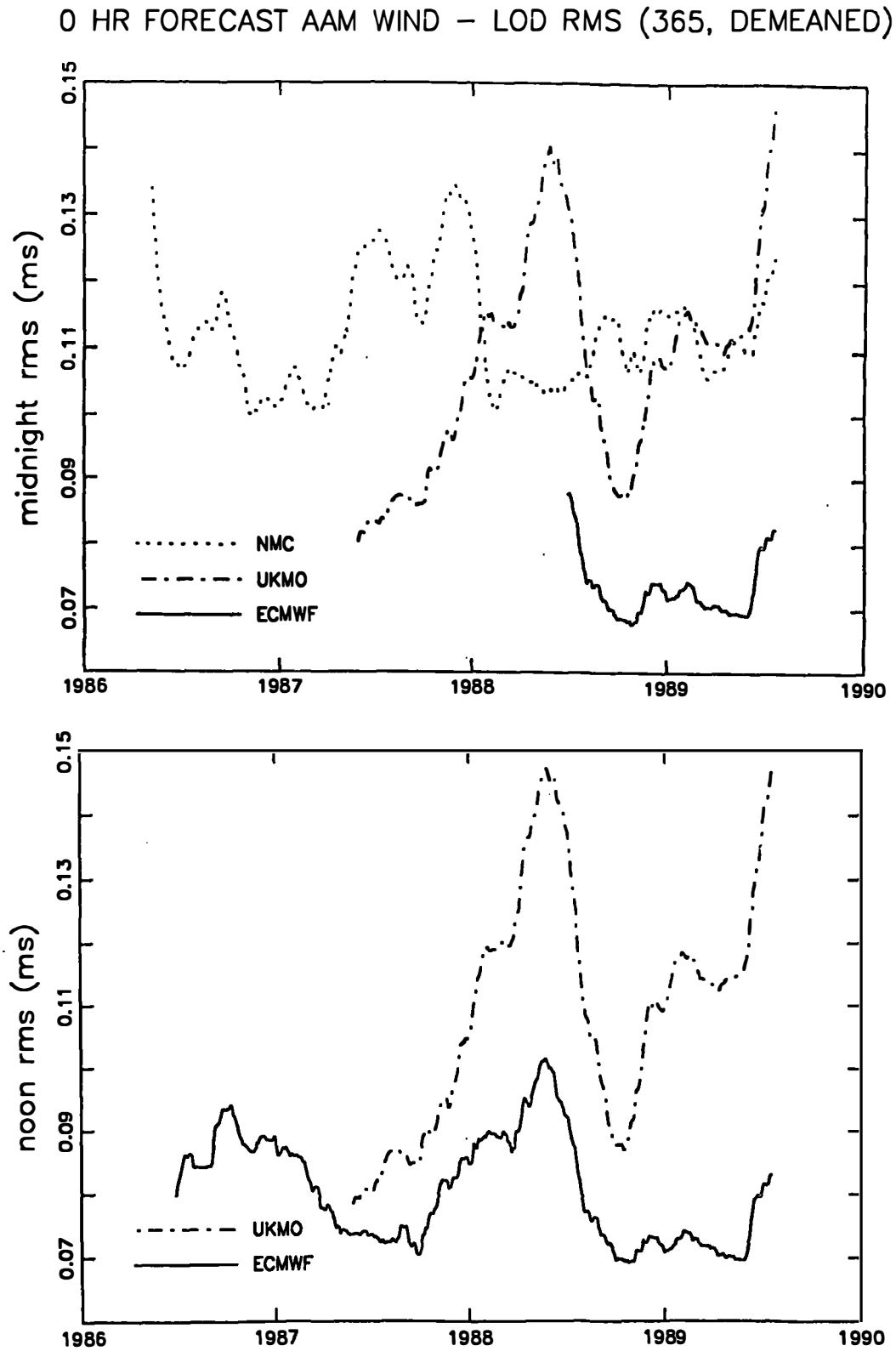

Fig. 10. Running rms of the difference between the length-of-day and AAM "zero hour forecast" results computed by including only the wind term.

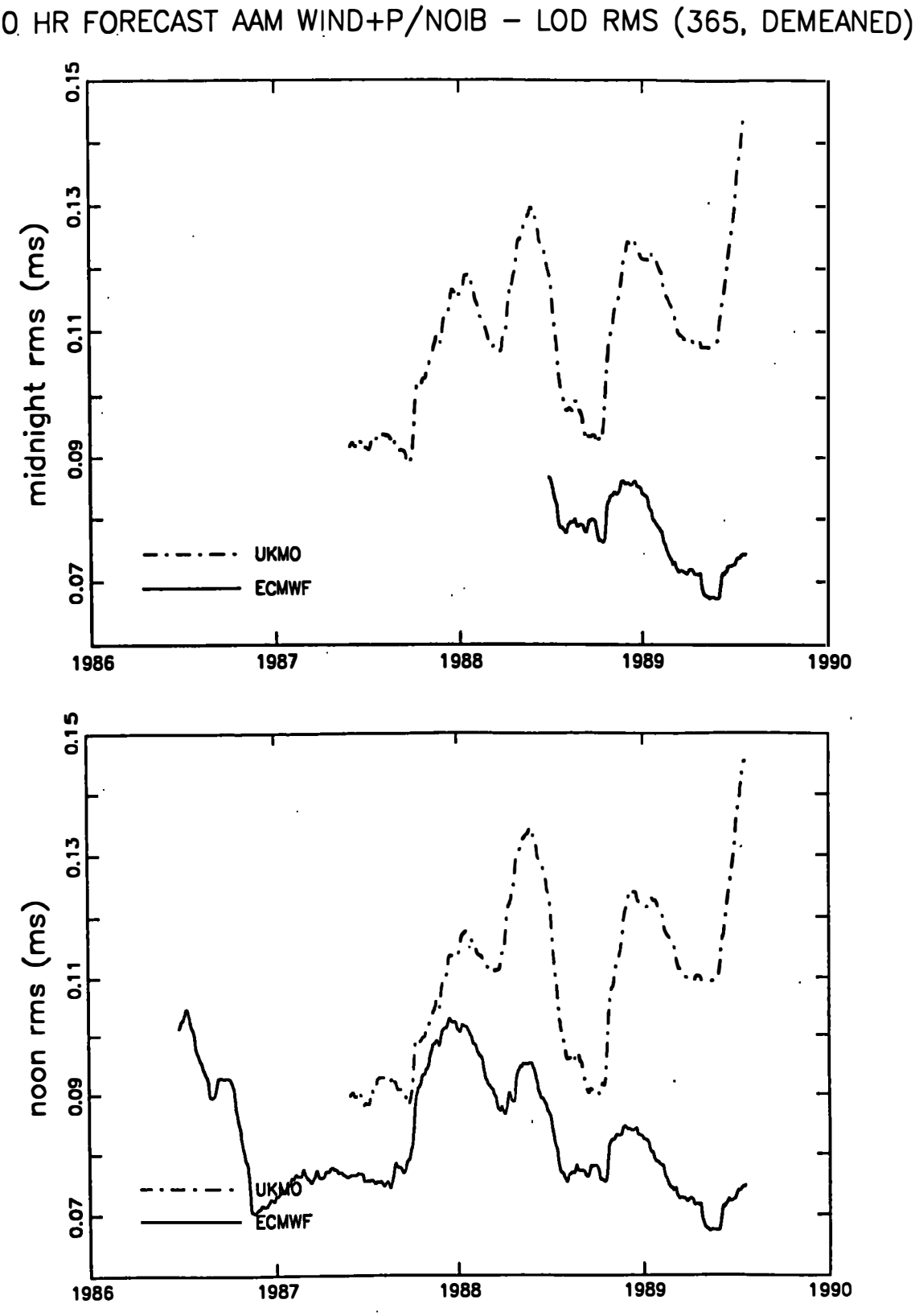

Fig. 11. Running rms of the difference between the length-of-day and AAM "zero hour forecast" results computed by including the wind and pressure (without the inverted barometer approximation) terms.

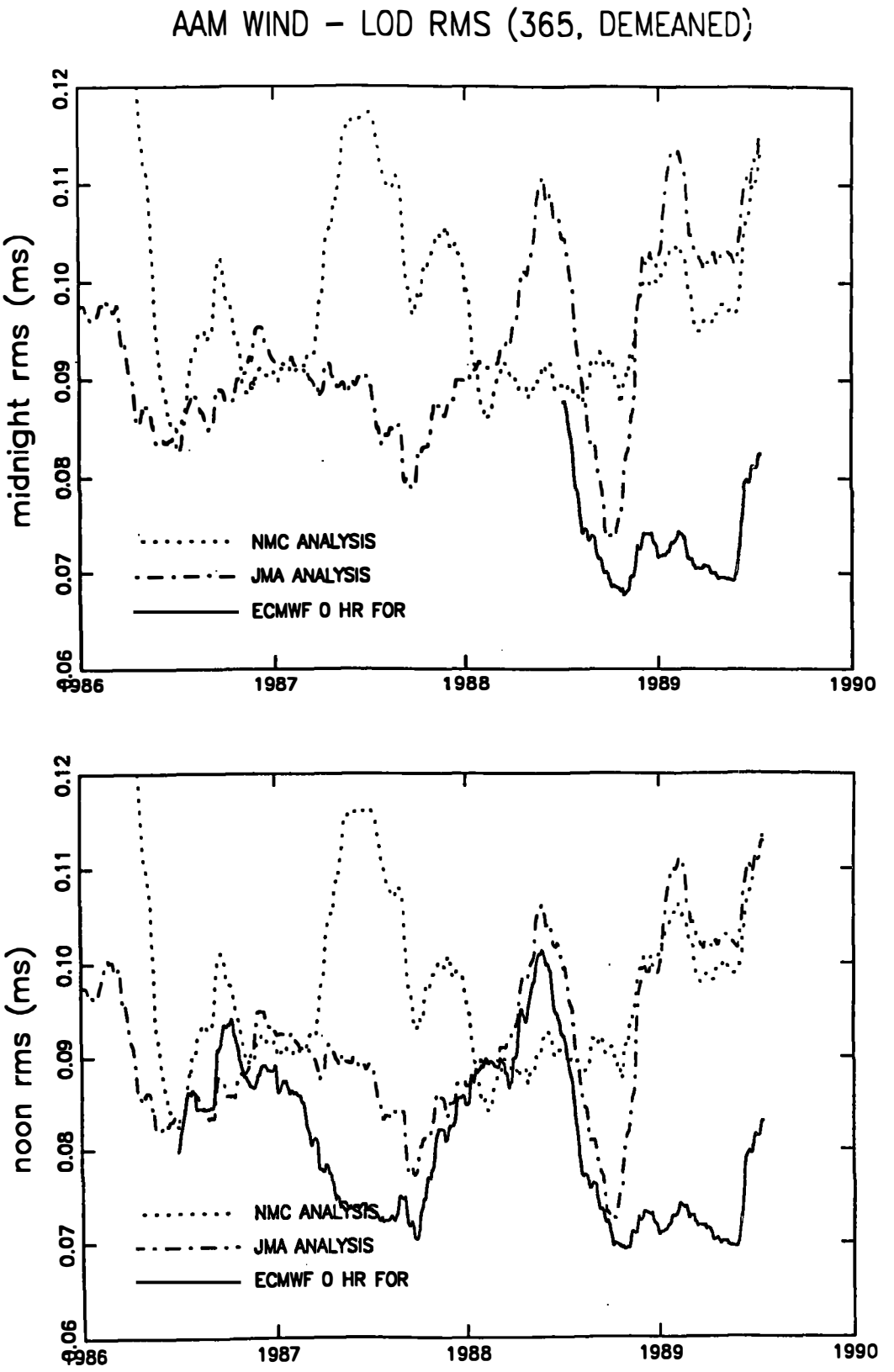

Fig. 12. Running rms of the difference between the length-of-day and selected AAM "analysis" and "zero hour forecast" results computed by including only the wind term.

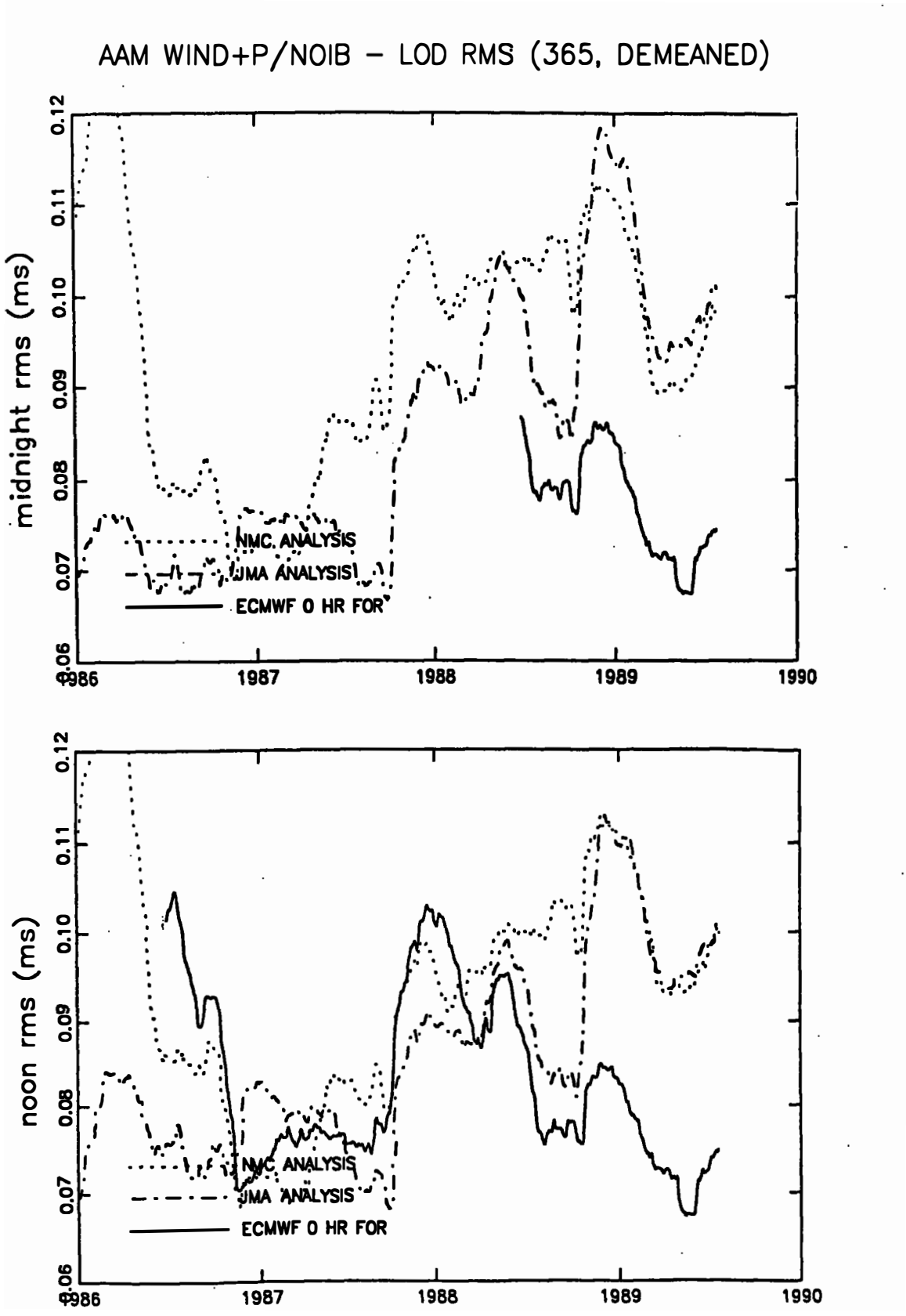

Fig. 13. Running rms of the difference between the length-of-day and selected AAM "analysis" and "zero hour forecast" results computed by including the wind and pressure (without the inverted barometer approximation) terms.

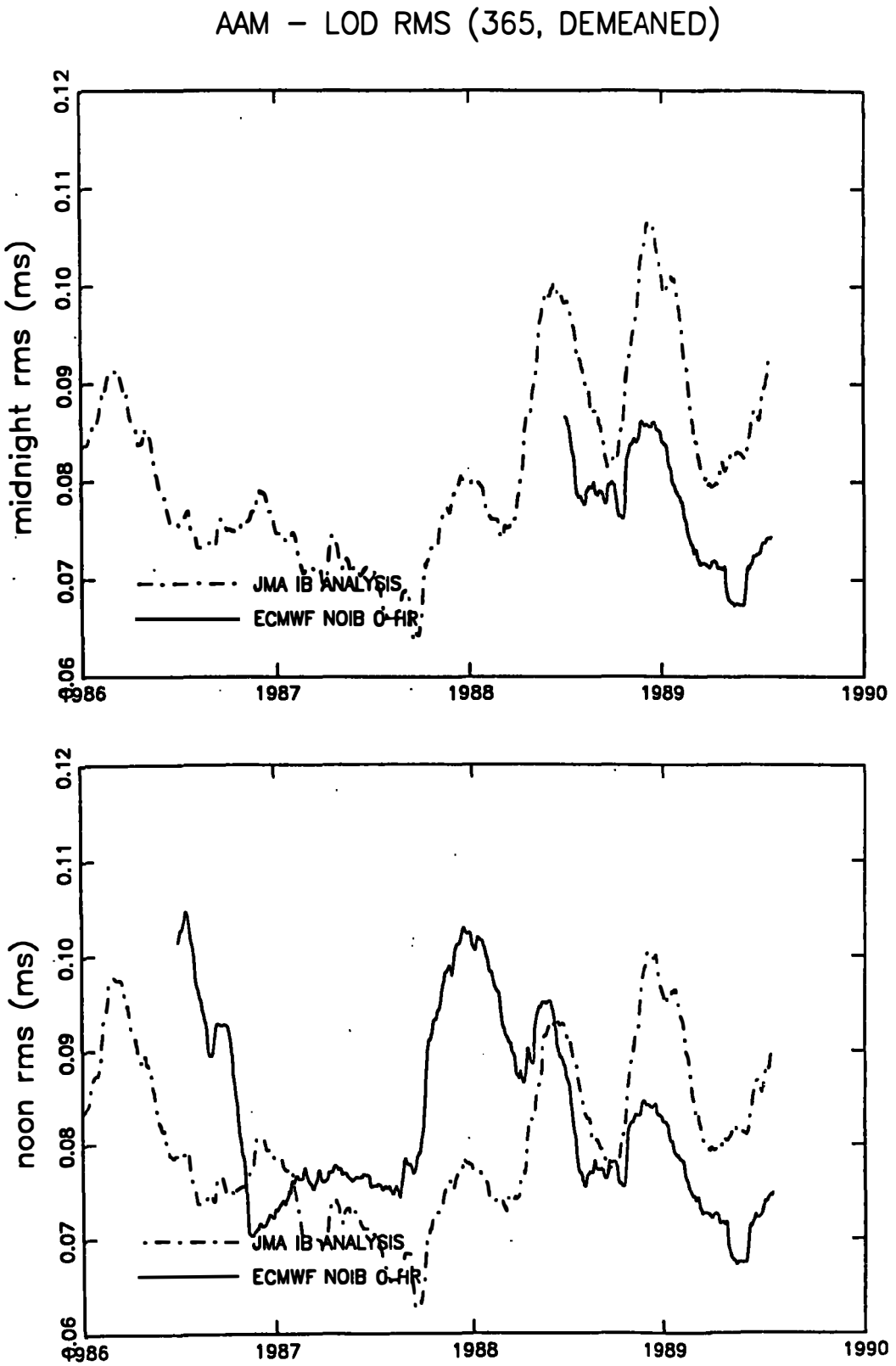

Fig. 14. Running rms of the difference between the length-of-day and selected AAM "analysis" and "zero hour forecast" results.

approximation is made; e.g., during 1987 for the NMC, Figure 3; during 1987 for the JMA, Figure 4). For the most recent time period (post-1989) for both the NMC and JMA "analysis" results, computing the AAM by including the pressure term with the inverted barometer approximation yields values closer to the lod than computing it by including the pressure term without the inverted barometer approximation, which is in turn closer than computing it from only the wind term.

For the UKMO "zero hour forecast" results (Figure 5), the midnight and noon results are virtually identical, and no conclusion can be reached about whether or not including the pressure term in the AAM calculation results in values closer to the length-of-day. For about half of the time this seems to be the case, but not for the rest of the time. The situation with the ECMWF "zero hour forecast" results (Figure 6) is very similar to that of the UKMO "zero hour forecast" results.

The rest of the figures show the same results, but in different combinations in order to facilitate their intercomparison for purposes of determining which AAM series is closest to the lod. Figures 7-11 show plots of the running rms of the AAM-lod difference in which the AAM is computed from only the wind term (Figure 7 for "analysis" results, Figure 10 for "zero hour forecast" results), the wind term plus the pressure term without the inverted barometer approximation (Figure 8 for "analysis" results, Figure 11 for "zero hour forecast" results), and the wind term plus the pressure term with the inverted barometer approximation (Figure 9 for "analysis" results). In general, for the "analysis" results (Figures 7-9), it appears that the JMA results are closer to the lod than the others (although there are periods of time when results from other weather prediction centers are closer), and for the "zero hour forecast" results (Figures 10-11) it is clear that the ECMWF values are closest to the lod.

In Figures 12 and 13, the ECMWF "zero hour forecast" results are compared to similarly computed "analysis" results. Figure 12 compares the results when the AAM is computed from only the wind term, and it is seen that for most of the time the ECMWF "zero hour forecast" results are closer to the lod than are the JMA or NMC "analysis" results. Figure 13 compares the results when the AAM is computed by also including the pressure term without the inverted barometer approximation, and it is seen that in the later time period (post-mid-1988), the ECMWF "zero hour forecast" results are again closest to the lod, although before this the JMA "analysis" results seem to be (in general) closest to the lod.

From Figures 7-9 it appears to be generally true that the JMA "analysis" results are closer to the lod than similarly computed "analysis" results from the other weather prediction centers, and from Figure 9 this is clearly seen to be the case when the AAM values are computed by including the pressure term with the inverted barometer approximation. From Figure 4, since 1987 it is clear that the JMA "analysis" results computed by including the pressure term with the inverted barometer approximation yields results closer to the length-of-day than by computing it with only the wind term, or without the inverted barometer approximation. From Figures 10 and 11 it is clear that the ECMWF "zero hour forecast" results are closer to the lod than similarly computed "zero hour forecast" results from the other weather prediction centers [from Figure 6 it is not clear whether including the pressure term (without the inverted barometer approximation) yields ECMWF "zero hour forecast" results that are closer to the lod than not including it]. As an attempt to compare the "best" "analysis" results with the "best" "zero hour forecast" results, Figure 14 plots the running rms of the AAM-lod difference for the JMA "analysis" results computed by including the pressure term with the inverted barometer approximation, along with the ECMWF "zero hour forecast" results computed by including the pressure term without the inverted barometer approximation (note that for this purpose the ECMWF "zero hour forecast" wind only results could just as well have been plotted instead). As can be seen, during the later time period (post-mid-1988), the ECMWF results are closest to the lod, but the JMA results are closer at earlier time periods.

In summary, these results indicate that the AAM "analysis" series closest to the length-of-day (in an rms sense) are the JMA results, and the AAM "zero hour forecast" series closest to the lod are the ECMWF results. From Tables 1 and 2 it is seen that these two AAM results are computed by integrating the atmospheric wind term to a greater height than is done for the other

results. Thus, it is likely that these two results are the closest to the lod since they are computed by including more of the atmospheric winds than are included in the other results.

ACKNOWLEDGMENTS. The work described in this paper was performed at the Jet Propulsion Laboratory, California Institute of Technology, under contract with the National Aeronautics and Space Administration.

References

Arpe, K., Effective atmospheric angular momentum functions computed at the European Centre for Medium-Range Weather Forecasts, in *IERS Technical Note 5: Earth Orientation and Reference Frame Determinations, Atmospheric Excitation Functions, up to 1989 (Annex to the IERS Annual Report for 1989)*, p. 87, Observatoire de Paris, Paris, France, 1990.

Barnes, R. T. H., R. Hide, A. A. White, and C. A. Wilson, Atmospheric angular momentum fluctuations, length-of-day changes and polar motion, *Proc. R. Soc. London*, **A387**, 31-73, 1983.

Eubanks, T. M., Combined Earth orientation series smoothed by a Kalman filter, in *Bureau International de l'Heure Annual Report for 1987*, pp. D85-D86, Observatoire de Paris, Paris, France, 1988.

Eubanks, T. M., J. A. Steppe, J. O. Dickey, and P. S. Callahan, A spectral analysis of the Earth's angular momentum budget, *J. Geophys. Res.*, **90**, 5385-5404, 1985.

Gross, R. S., and J. A. Steppe, A combination of Earth orientation data: SPACE90 (submitted), *IERS Annual Report for 1990*, Observatoire de Paris, Paris, France, 1991a.

Gross, R. S., and J. A. Steppe, The stability of the terrestrial reference frame inferred from Earth orientation series, paper presented at AGU Chapman Conference on Geodetic VLBI: Monitoring Global Change (this volume), Amer. Geophys. Union, Washington D. C., April 22-26, 1991b.

Hide, R., Effective atmospheric angular momentum functions computed by the U.K. Meteorological Office using data processed at the European Centre for Medium-Range Weather Forecasting, in *IERS Technical Note 2: Earth Orientation and Reference Frame Determinations, Atmospheric Excitation Functions, up to 1988 (Annex to the IERS Annual Report for 1988)*, pp. 85-86, Observatorie de Paris, Paris, France, 1989a.

Hide, R., Effective atmospheric angular momentum functions computed by the U.K. Meteorological Office using data processed at the U.K. Meteorological Office, in *IERS Technical Note 2: Earth Orientation and Reference Frame Determinations, Atmospheric Excitation Functions, up to 1988 (Annex to the IERS Annual Report for 1988)*, pp. 87-88, Observatorie de Paris, Paris, France, 1989b.

Hide, R., and J. O. Dickey, Earth's variable rotation, *Science*, in press, 1991.

Kann, D. M., and D. A. Salstein, Effective atmospheric angular momentum functions and related parameters computed at the U.S. National Meteorological Center, in *IERS Technical Note 5: Earth Orientation and Reference Frame Determinations, Atmospheric Excitation Functions, up to 1989 (Annex to the IERS Annual Report for 1989)*, pp. 83-85, Observatoire de Paris, Paris, France, 1990.

Lambeck, K., *The Earth's Variable Rotation: Geophysical Causes and Consequences*, 449 pp., Cambridge University Press, New York, 1980.

Morabito, D. D., T. M. Eubanks, and J. A. Steppe, Kalman filtering of Earth orientation changes, in *The Earth's Rotation and Reference Frames for Geodesy and Geodynamics*, edited by A. K. Babcock and G. A. Wilkins, pp. 257-267, D. Reidel, Dordrecht, Holland, 1988.

Morgan, P. J., R. W. King, and I. I. Shapiro, Length of day and atmospheric angular momentum: A comparison for 1981-1983, *J. Geophys. Res.*, **90**, 12645-12652, 1985.

Munk, W. H., and G. J. F. MacDonald, *The Rotation of the Earth: A Geophysical Discussion*, 323 pp., Cambridge University Press, New York, 1960.

Naito, I., and N. Kikuchi, Effective atmospheric angular momentum functions computed from the JMA data, in *Bureau International de l'Heure Annual Report for 1986*, pp. D55-D56, Observatoire de Paris, Paris, France, 1987.

Naito, I., Y. Goto, and N. Kikuchi, Effective atmospheric angular momentum functions computed from the Japanese Meteorological Agency data, in *IERS Technical Note 5: Earth Orientation and Reference Frame Determinations, Atmospheric Excitation Functions, up to 1989 (Annex to the IERS Annual Report for 1989)*, pp. 89-90, Observatoire de Paris, Paris, France, 1990.

Reinsch, C. H., Smoothing by spline functions, *Numer. Math.*, **10**, 177-183, 1967.

Reinsch, C. H., Smoothing by spline functions II, *Numer. Math.*, **16**, 451-454, 1971.

Rosen, R. D., and D. A. Salstein, Variations in atmospheric angular momentum on global and regional scales and the length of day, *J. Geophys. Res.*, **88**, 5451-5470, 1983.

Rosen, R. D., and D. A. Salstein, Contribution of stratospheric winds to annual and semi-annual fluctuations in atmospheric angular momentum and the length of day, *J. Geophys. Res.*, **90**, 8033-8041, 1985.

Rosen, R. D., D. A. Salstein, T. M. Eubanks, J. O. Dickey, and J. A. Steppe, An El Niño signal in atmospheric angular momentum and Earth rotation, *Science*, **225**, 411-414, 1984.

Salstein, D. A., Effective angular momentum functions for Earth rotation and polar motion from the United States NMC analysis, in *Bureau International de l'Heure Annual Report for 1987*, pp. D87-D88, Observatoire de Paris, Paris, France, 1988.

Yoder, C. F., J. G. Williams, and M. E. Parke, Tidal variations of Earth rotation, *J. Geophys. Res.*, **86**, 881-891, 1981.

High Time Resolution Measurements of Earth Rotation

J. O. Dickey

Jet Propulsion Laboratory
California Institute of Technology
Pasadena, CA 91109-8099 USA

ABSTRACT

High time resolution measurements of Earth rotation and atmospheric angular momentum (AAM) and their interpretation have been proposed as a major research thrust for the 1990s. A campaign is planned to obtain these measurements utilizing all space geodetic techniques and to collect the best available complementary geophysical, oceanographic and atmospheric data. This paper highlights its motivation and scientific benefits and briefly discusses its plans.

INTRODUCTION

High time resolution measurements of Earth rotation and atmospheric angular momentum (AAM) and their interpretation has been proposed as a major research area for the 1990s, both by the workshop held at Erice in 1988 on the "Interdisciplinary Role of Space Geodesy" *(Mueller and Zerbini,* 1989) and by the NASA Workshop on Geodynamics and Geology held in July 1989 to plan NASA Solid Earth Science Programs for the coming decade *(Dickey et al.,* 1991). The NASA Crustal Dynamics Project VLBI group at Goddard Space Flight Center conducted a first Extended Research and Development Experiment (ERDE) in October, 1989 designed to obtain high-time resolution measurements of the Earth's orientation by the VLBI technique and to test improvements in the VLBI measurement system *(Clark et al.,* 1990). These special sessions were coordinated with the normal IRIS-A measurements. A campaign has been proposed to involve all space geodetic techniques and obtain the best available complementary geophysical, oceanographic and atmospheric data. The coordination will be effected through the International Earth Rotation Service.

MOTIVATION AND SCIENTIFIC BENEFITS

The scientific benefits to be obtained from this campaign include increased understanding of the properties and origin of short-period fluctuations in the Earth's orientation, improvements to the tidal model at sub-monthly periods, and improved ability to predict changes in the Earth's rotation up to a month in advance. A goal here is to observe and understand the interactions of the atmosphere and ocean with the rotational dynamics of the Earth, and their contributions to the excitation of Earth rotation variations over time scales of hours to months. At these frequencies, a number of geophysical processes are thought to be capable of affecting the Earth's rotation, including atmospheric wind and pressure changes, oceanic current and sea level changes, oceanic and solid Earth tidal motions, and seismic motions. High-frequency measurements, and complementary analyses, can be expected to lead to delineation of short-period tidal, atmospheric, oceanic, and seismic effects on length-of-day (LOD) and polar motion. These in turn will improve our understanding of broad-band wobble excitation processes, fluid-core resonance

characteristics, and mechanisms of oceanic/atmospheric coupling to the solid Earth.

In particular, the Earth's angular momentum budget (both axial and non-axial) can be examined at high frequencies. Recent studies have found significant coherence between modern estimates of LOD and AAM down to about 14 days *(Dickey et al., 1989; Rosen et al.*, 1990). The high-frequency limit of the relationship between LOD and AAM is an area of current active research and is central to our understanding of the Earth's angular momentum budget. No significant lags or leads at the few day level have been established, indicating little or no non-tidal contribution from the oceans. However, the ocean via the mechanism of barotropic waves could contribute on time scales of a few days to the Earth's angular momentum budget *(Ponte,* 1990). Hence, a comparison of AAM and LOD at these high frequencies could uncover the ocean's role and further elucidate our understanding of the interaction between the solid Earth and the atmosphere. This would allow the role of atmosphere and oceans in the Earth orientation variations at high frequencies to be quantified. The appropriateness of the inverted barometer approximation at high frequencies could be investigated, and the respective roles of mountain torque and wind stress in solid Earth-atmosphere interaction could be examined.

In addition, the International Earth Rotation Service (IERS) is interested in evaluating the ability of the Global Positioning System (GPS) to recover Earth rotation parameters. Since the GPS technique is thought to be able to recover accurate Earth rotation parameters at sub-daily sampling intervals, this campaign should focus on high-time resolution measurements of Earth orientation. In order to facilitate intercomparisons of results obtained by the GPS technique and the other space-geodetic techniques it is important for the Very Long Baseline Interferometry (VLBI) and satellite/lunar laser ranging (SLR and LLR) systems to be major participants in this campaign and that measurements be coordinated.

PLANS

Two types of campaigns are proposed: two short duration campaigns in 1991 and a main campaign in 1992. The first short campaign coincides with the large GPS experiment, known variously as CASA DOS or GIG '91, which was conducted from January 22, 1991 through February 13, 1991. A global network of over 140 GPS receivers was deployed, many of which were collocated at VLBI and SLR sites. The second short campaign takes place in May or June, 1991. This would allow for observing sessions in both Northern Hemisphere Winter and Summer, analogous to those of FGGE [First GARP (Global Atmospheric Research Program) Global Experiment]. During these short campaigns in 1991, no special measurements were requested of the space-geodetic techniques, but the meteorological centers have been requested to produce their AAM results at intervals of six hours and, in addition, to provide estimates of the surface torques. It should be noted that a high density of Earth rotation measurements are already planned through the existing NAVNET and IRIS/POLARIS scheduling. After the analysis of results from these short campaigns of 1991, measurement needs for the major campaign will be assessed as well.

The main campaign should be held in 1992; coordination will be sought with the GPS experiment planned for Summer 1992 by the IERS and the proposed IGS (International GPS Service) as well as with the international laser tracking network. During the main campaign both the UARS (Upper Atmosphere Research Satellite) and the ERS-1 should be providing complementary atmospheric information; sea-surface stresses should be available from the ERS- 1 scatterometer.

ACKNOWLEDGEMENTS.

We acknowledge interesting discussions with T. M. Eubanks, A. P. Freedman, R. S. Gross, R. Hide, S. L. Marcus, R. D. Rosen, D. A. Salstein, and J. A. Steppe. The work of this author was carried out at the Jet Propulsion Laboratory, California Institute of Technology, under contract with the National Aeronautics and Space Administration.

REFERENCES

Clark, T. A., Ryan, J. W. and Baver, K. D., ERDE: High Resolution Observations of Earth Orientation Parameters by Very Long Baseline Interferometry, *EOS, Trans. Amer. Geophys. Union,* **71**,1271, 1990.

Dickey, J. O., B. E. Schutz, S. R. Dickman, T. M. Eubanks, M. Feissel, T. A. Herring, I. I. Mueller, R. D. Rosen, J. M. Wahr, and C. R. Wilson, Earth Rotation/Reference Frames Science Panel Position Paper, *Solid Earth Science for the 1990s, NASA* Technical Memorandum, 4256, Vol. 2, VII--VII-23, 1991.

Dickey, J. O., S. L. Marcus, J. A. Steppe, and R. Hide, An Investigation of the Earth's Angular Momentum Budget at High Frequencies, *EOS Trans. AGU,* **70**, 1058, 1989.

Mueller, I. I. and S. Zerbini, *The Interdisciplinary Role of Space Geodesy,* Proceedings of an International Workshop held at Ettore Majorana Center for Scientific Culture, International School of Geodesy, Erice, Sicily, Italy (July 23-29, 1988), Lecture Notes in Earth Sciences, Springer-Verlag, New York, 1989.

Ponte, R. M., Barotropic Motions and the Exchange of Angular Momentum between the Oceans and the Solid Earth, *J. Geophys. Res.*, **95**, 11369-11374, 1990.

Rosen, R. D., D. A. Salstein, and T. M. Wood, Discrepancies in the Earth-atmosphere angular momentum budget, J. *Geophys. Res.*, **95**, 265-279, 1990.

MOUNTAIN AND SURFACE STRESS TORQUES IN NMC ANALYSES

Glenn H. White
Development Division
National Meteorological Center
National Weather Service/NOAA
Washington, D.C. 20233

This study examines the exchange of angular momentum between the atmosphere and the earth's surface. Torques exerted on the atmosphere by pressure differences across mountains and by friction with the earth's surface are calculated from global atmospheric analyses produced 4 times a day at NMC as initial states for numerical weather forecasts. The approach here follows that of Swinbank (1985) and Boer (1990).

Atmospheric angular momentum, m, can be written as:

$$m = \Omega a^2 \cos^2\phi + u a \cos\phi \qquad (1)$$

where Ω is the earth's rotation rate, u is zonal wind, a is the radius of the earth, ϕ latitude and λ longitude. The rate of change of angular momentum is given by:

$$\frac{Dm}{Dt} = -\frac{\partial \Phi}{\partial \lambda} - g \frac{\partial \tau}{\partial p} a \cos\phi \qquad (2)$$

where Φ is geopotential, p pressure, g the acceleration of gravity and τ the zonal component of shearing stress. Vertically integrating and zonally averaging (2) yields:

$$\frac{\partial}{\partial t}\left[\int_0^{p_*} m \frac{dp}{g}\right] + \frac{1}{a\cos\phi}\frac{\partial}{\partial\phi}\left(\left[\int_0^{p_*} m v \frac{dp}{g}\right]\cos\phi\right)$$
$$= -\left[\int_0^{p_*} \frac{\partial z}{\partial \lambda} dp\right] - a\cos\phi\left[\tau_*\right] \qquad (3)$$
$$= -\left[p_* \frac{\partial z_*}{\partial \lambda}\right] - a\cos\phi\left[\tau_*\right]$$

where Z is geopotential height, p_* is surface pressure, Z_* surface height, v meridional wind and τ_* the zonal component of surface friction.

Mountain torque for a given latitude belt $\Delta\phi$ is calculated as:

$$Q_M = \frac{a^2}{g}\cos\phi\,\Delta\phi \sum_i p_* \frac{\partial \Phi_*}{\partial \lambda}\Delta\lambda \qquad (4a)$$

$$= \frac{a^2}{g}\cos\phi\,\Delta\phi \sum_i p_* \sum_k \left(\frac{\partial \Phi_k}{\partial \lambda} + RT_k \frac{\partial \ln p_*}{\partial \lambda}\right)\Delta\sigma_k \Delta\lambda \qquad (4b)$$

where the sum in (4a) is over longitude and the second sum in (4b) is over the model's vertical layers. The NMC model uses a sigma ($\sigma = p\backslash p_*$) vertical coordinate. T_k is the temperature of the kth sigma layer. The total global mountain torque is:

$$4\pi a^2 \left\langle p_* \frac{\partial Z_*}{\partial \lambda} \right\rangle \qquad (5)$$

where $\langle\rangle$ indicates a global average value. A positive torque indicates a loss of westerly angular momentum by the atmosphere to the earth.

Surface stress torque for a latitude belt $\Delta\phi$ is:

$$Q_F = a^3 \cos^2\phi\,\Delta\phi \sum_i \tau_* \Delta\lambda \qquad (6)$$

The total torque on the atmosphere by surface stress is:

$$4\pi a^2 \langle a\cos\phi\,\tau_* \rangle \qquad (7)$$

The NMC global spectral model had triangular truncation to wavenumber 80 in Jan. 1991 (MRF89); this increased to 126 in early March (MRF91). The model has parameterizations of gravity wave drag, deep and shallow convection, long and short wave radiation, and model diagnosed clouds. The model is more fully described in Kanamitsu (1989). The MRF89 used enhanced mountains in Jan. 1991; MRF91 forecasts have mean mountains.

Mountain torques were calculated from initialized sigma analyses. The zonal derivative is taken in spectral space; the product of surface pressure and the derivative is calculated on the Gaussian grid appropriate for the spectral resolution (243 x 122 for T80, 384 x 190 for T126) and then transformed to a regular grid of the same dimensions where the zonal and global means were calculated. Calculation of mountain torque in the exact formulation of the model was found to be essential.

Equations (4a) and (4b) give two different methods of calculating mountain torque. Previous studies have found substantial differences in mountain torque calculated by the

two methods. Fig. 1 compares the latitudinal distribution of mountain torque calculated by the two methods from 000 GMT analyses for Jan. 1-20. The first method (left) uses orography and is given by (4a); the second (right) uses heights and temperatures from each sigma layer and is given by (4b). The two methods give nearly identical results, indicating a high degree of precision in the procedure and analyses used here. Results below are from the method in equation (4a).

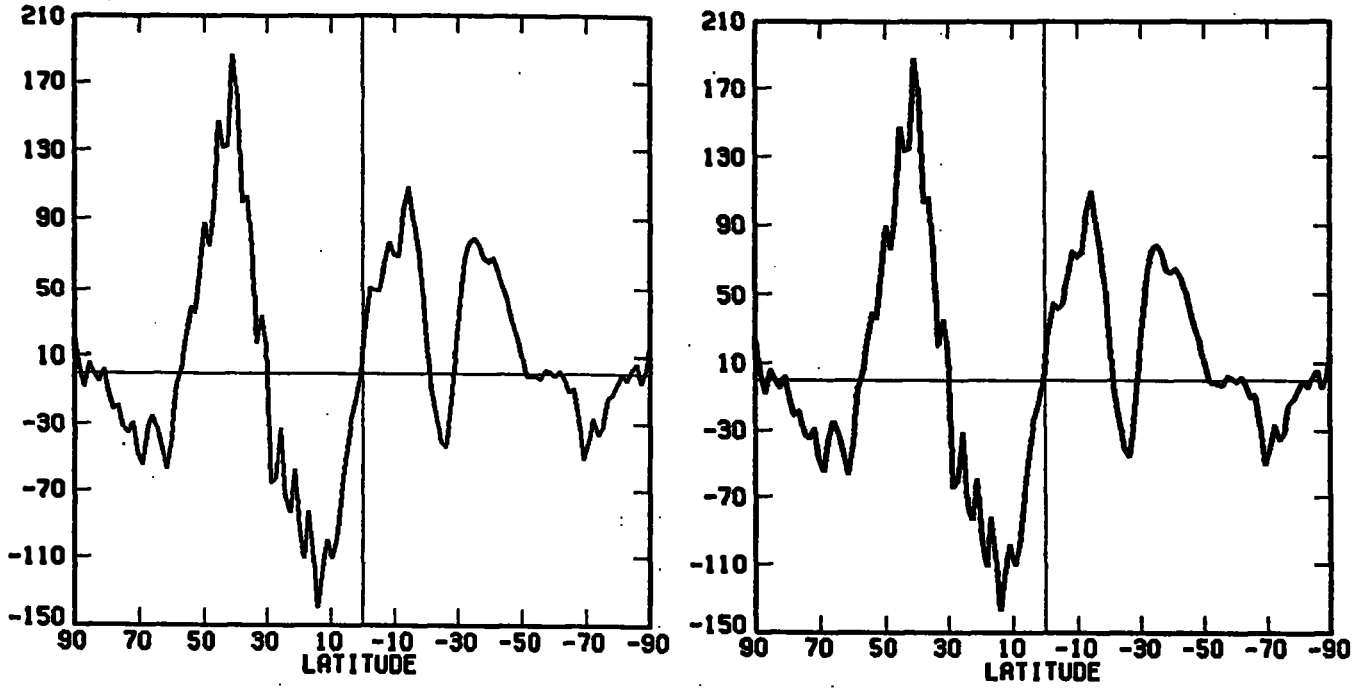

Fig. 1 Latitudinal distribution of mountain torque in .01 Hadleys (10^{18} Newton-meters) /1.5° latitude from 000 GMT analyses for Jan. 1-20, 1991 calculated from (left) surface height and (right) geopotential heights on sigma levels.

NMC analyses contain realistic diurnal and semidiurnal tides. Fig. 2 contrasts the zonal distribution of mountain torque for Jan. 1991 as calculated from analyses for 000 GMT (dotted) and 1200 GMT (solid). The two are equivalent in the Northern Hemisphere, but are quite different in the Southern Hemisphere where considerably more torque occurs at 000 GMT. This could reflect a diurnal fluctuation in surface pressure over South America east of the Andes during the Southern Hemisphere summer. As a result most of the figures below are calculated from analyses every 6 hours.

The effect of the March model change on mountain torque is shown in Fig. 3 where mountain torque for Jan. 20-29, 1991 was calculated from 000 GMT analyses by the T80 MRF89 with enhanced mountains (solid) and from 000 GMT analyses by the T126 MRF91 with mean mountains (dashed). The replacement of enhanced mountains by mean mountains lowered surface heights by as much as 400 m in the Andes and substantially reduced mountain torque. The patterns of torque are similar. The model change had much less effect on surface stress, as can be seen in Fig. 4.

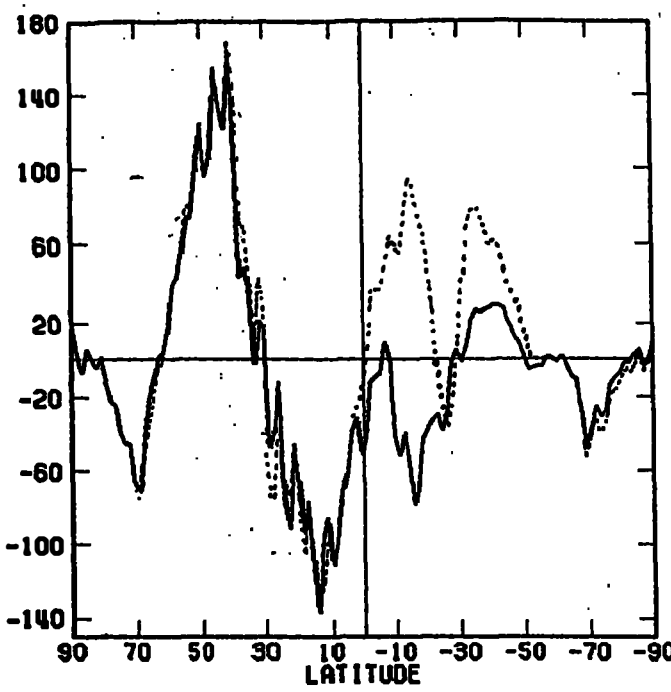

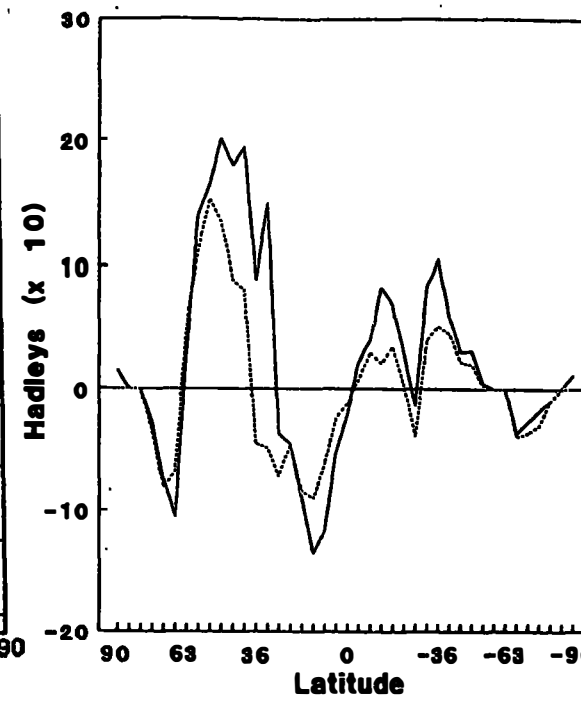

(left) Fig. 2 Mountain torque in .01 Hadleys/1.5° latitude from 00 GMT(dotted) and 1200 GMT analyses for Jan. 1991.
(right) Fig.3 Mountain torque in .1 Hadleys/1.5° latitude in 000 GMT analyses for Jan. 20-29, 1991 from the T80 model with enhanced orography (solid) and from the T126 model with mean orography (dotted).

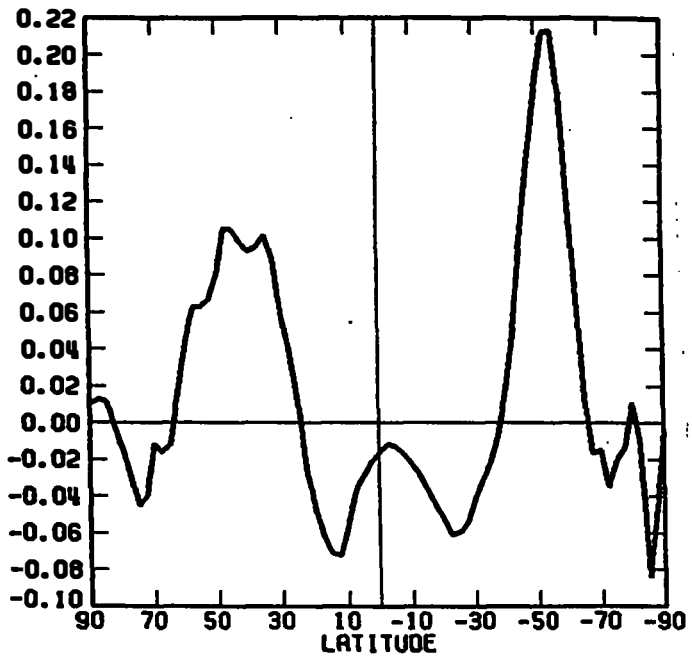

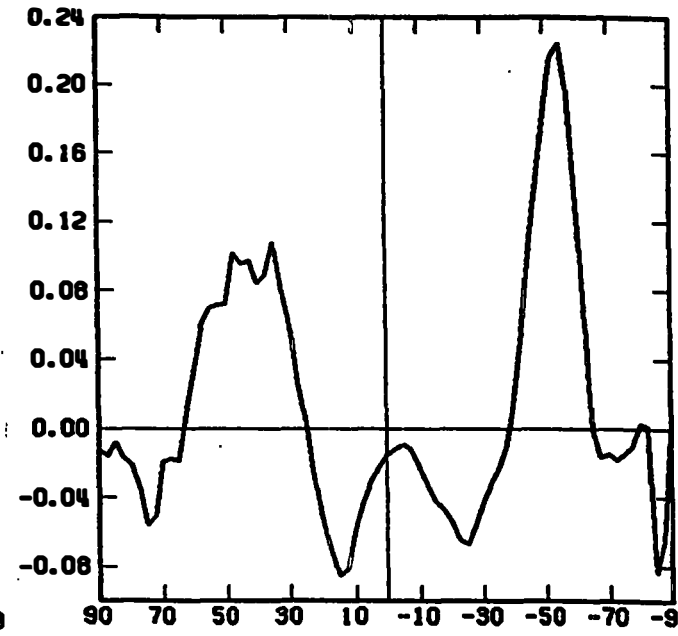

Fig. 4 Surface stress in Newton/m² in 0-24 hr forecasts for March 2-6, 1991 with (left) the MRF89 T80 model and (right) the MRF91 T126 model.

The surface stresses used here were calculated during the last half of a six-hour forecast used to generate a "first guess" which is then merged with observed data to form an analysis. Surface stress in the NMC model generally resembles the climatology of Hellerman and Rosenstein (1983) over the oceans, although stresses associated with the tropical tradewinds may be slightly weak. Surface stress near 50S exceed climatological estimates in a region where the lack of data reduces confidence in both analyses and climatologies. Over land the effect of gravity wave drag is included in surface stress.

Fig. 5 displays the latitudinal distribution of mountain and surface stress torques during Jan. 1-15, Apr. 6-19, and June 14-24, 1991. Values for January are from T80 analyses and correspond to approximately 1.5 degree latitude belts; values for April and June from T126 analyses cover 1 degree latitude belts. This difference alone makes values in Fig. 5 for April and June one-third less than values for January. Fig. 5 is generally similar to earlier results by Swinbank (1985), Boer (1990), Wahr and Oort (1984), and Newton (1971).

Strong positive mountain torques appear in the Northern Hemisphere midlatitudes in January and April, but are substantially weaker in June, when the Northern Hemisphere midlatitude winds are weaker. A substantial negative torque appears between 30N and the equator in January; it is much weaker in April and is replaced by a positive torque in June. During June low-level westerlies appear in the eastern hemisphere north of the equator, in association with the summertime south Asian monsoon. In the Southern Hemisphere the Andes appear to make a substantial contribution to mountain torque, producing a positive torque nearly everywhere in January and negative torques in low latitudes in April and June. The midlatitude Andes force a positive torque in all 3 months; during June their torque is as strong as Northern Hemisphere values.

Peak values of the torque due to surface stress exceed peak values of mountain torque in all 3 periods; however, cosiderable cancellation occurs between low and high latitudes. The Southern Hemisphere exhibits much less seasonal change than the Northern Hemisphere, where strong positive stress torques in midlatitudes during winter are much weaker in summer and quite strong negative stress torques in the northern tropics in winter are replaced by weak positive torques in summer.

Fig. 6 shows daily global torques for Jan. 1991 and March 27-June 24, 1991. Global values of mountain torques vary strongly from day to day, reflecting the passage of individual strong synoptic systems across mountain ranges, and tends to dominate day to day variations in the total torque. Surface stress torque is dominated by lower frequency variability, but can be as strong as mountain torque.

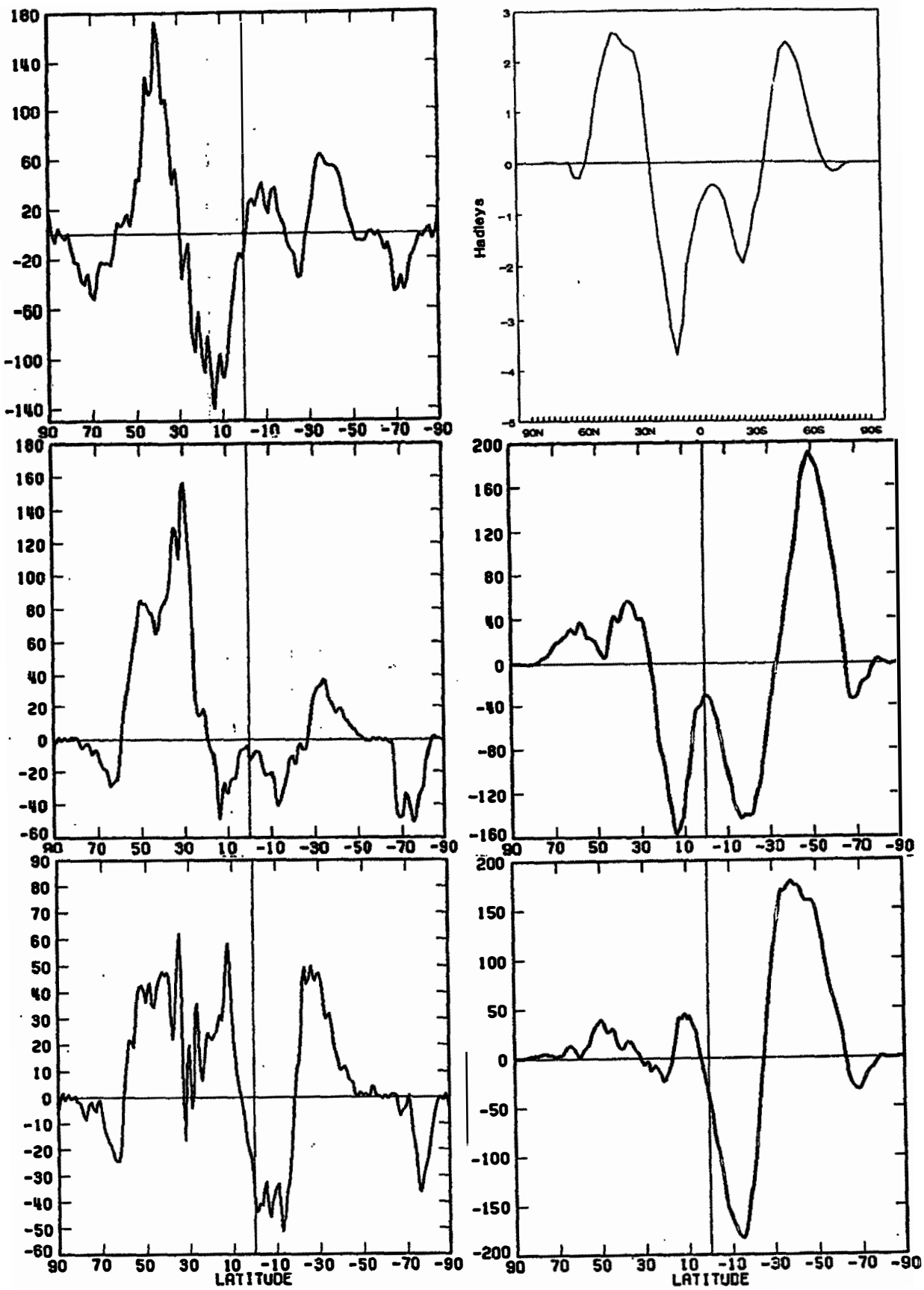

Fig. 5 Latitudinal distribution of mountain torque (left) and surface stress torque (right) from 4 analyses/day for (top) Jan. 1-15, 1991, (middle) Apr. 6-19, 1991, and (bottom) June 14-24, 1991. Torques are in (top left) .01 Hadleys/1.5° latitude, (top right) Hadleys/1.5° latitude, (middle and bottom) .01 Hadleys/1° latitude.

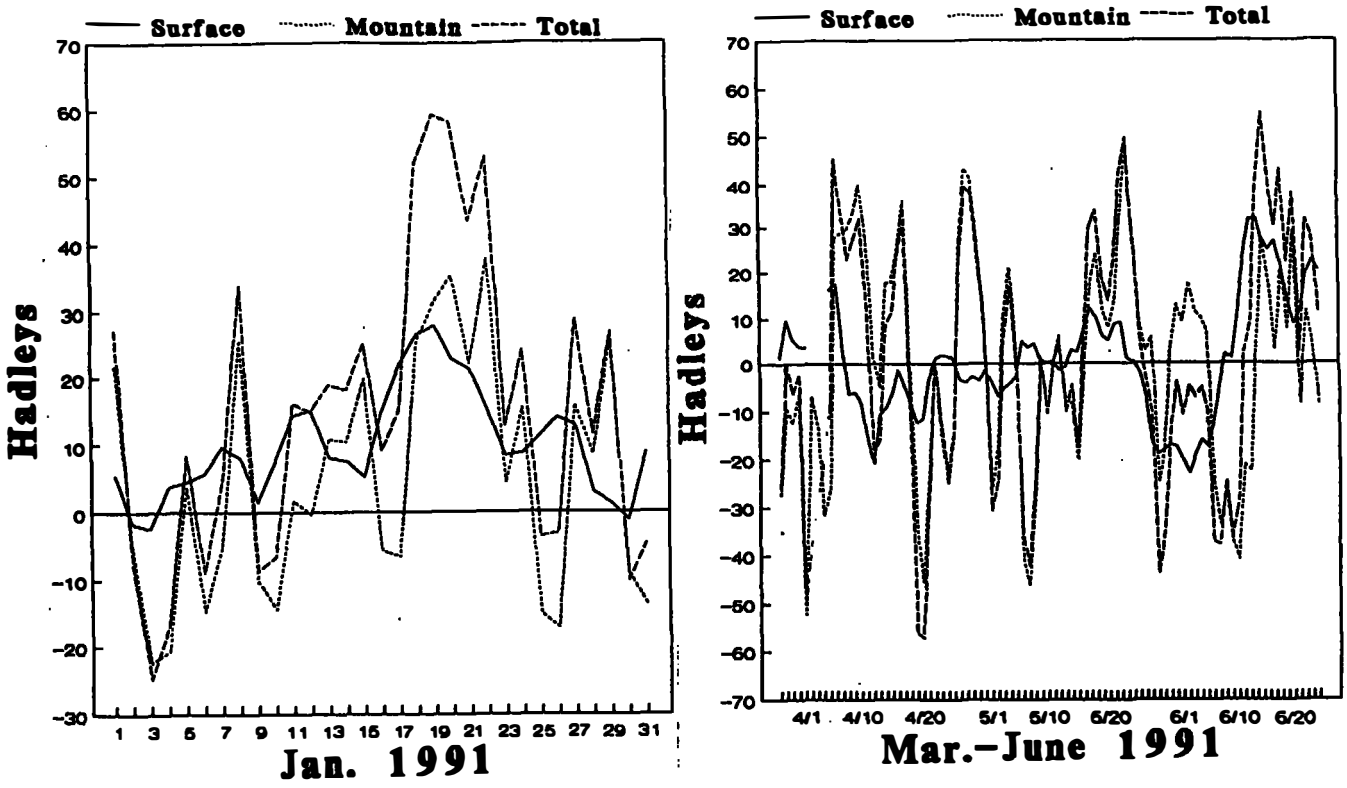

Fig. 6 Daily values of global surface stress (solid), mountain (short dashes), and total torques (long dashes) for Jan. 1991 and Mar. 27-June 24, 1991.

CONCLUSIONS

Calculation of mountain torque from NMC analyses appears to give very precise results; however, the calculation needs to be done as consistently as possible with the NMC model's formulation and should use analyses every 6 hours. The results suggest that calculating the entire angular momentum balance in the exact framework of the NMC model may produce a more accurate angular momentum balance. However, the torques shown here need to be checked by comparison with changes in angular momentum. NMC sigma analyses and surface stresses are now being archived at the National Center for Atmospheric Research.

Mountain torque varies substantially from day to day and tends to dominate variations in total torque. Surface stress torque varies more slowly, but can contribute substantially to total torque.

ACKNOWLEDGMENTS I would like to thank M. Kanamitsu, R. Rosen and D. Salstein for their encouragement and M. Iredell, M. Kanamitsu, R. Kistler and H.-L. Pan for their help.

REFERENCES

Boer, G.J., 1990: Atmospheric exchange of angular momentum simulated in a general circulation model and implications for the length of day. J.Geophys.Res., 95, 5511-5531.

Hellerman, S., and M. Rosenstein, 1983: Normal monthly wind

stress. J.Phys.Ocean., 13, 1093-1104.

Kanamitsu, M., 1989: Description of the NMC global data assimilation and forecast system. Wea.Fcst.,4,335-342.

Newton, C.W., 1971: Mountain torques in the global angular momentum balance. J.Atmos.Sci., 28, 623-628.

Swinbank, R., 1985: The global atmospheric angular momentum balance inferred from analyses made during the FGGE. Quart.J.Roy.Meteor.Soc., 111, 977-992.

Wahr, J.M., and A.H. Oort, 1984: Friction- and mountain-torque estimates from global atmospheric data. J.Atmos. Sci., 41, 190-204.

Angular momentum in the ocean and mechanisms of exchange with the atmosphere and solid Earth

Rui M. Ponte
Atmospheric and Environmental Research, Inc.
840 Memorial Dr., Cambridge, MA 02139

1. Introduction

The role of the ocean in contributing to variations in the earth's rotation about its polar axis is explored. We review the nature of the various torques acting on the ocean and their relative importance in inducing variability in oceanic angular momentum M. The wind stress torque at the ocean surface is important for angular momentum transfers with the atmosphere, while pressure torques at continental boundaries are the main mechanism for angular momentum exchanges between the ocean and the solid earth. Numerical results from a constant density ocean model suggest a balance between the wind and pressure torques, resulting in a small net torque on the ocean and consequently small fluctuations in M. Very small sea level differences across continental boundaries are sufficient to balance applied wind torques. The implications of this finding are discussed in relation to the observed large zonal (i.e. longitudinal) tilts in sea level across oceanic basins.

In the case where a nonzero net torque acts on the ocean, variations in oceanic angular momentum and hence residuals in the solid Earth-atmosphere angular momentum budget are expected. In this regard, contributions of El Niño oceanic signals to the global momentum budget at interannual time scales have been suggested recently. The plausibility of this hypothesis is briefly examined to illustrate the relative roles of zonal currents and mass redistribution (in latitude) in causing fluctuations in M. The importance of accounting for subsurface effects when interpreting sea level and surface current variability is addressed.

2. The angular momentum equation

The time rate of change of oceanic angular momentum about the polar axis (M) is governed by the following general equation

$$\frac{\mathrm{d}}{\mathrm{d}t}\int_V \rho m dV = \int_V \left\{-\frac{\partial p}{\partial \lambda} + \rho a \cos\phi \mathcal{V}_\lambda\right\} dV \tag{1}$$

where

$$m = a\cos\phi u + \Omega a^2 \cos^2\phi \tag{2}$$

is the angular momentum per unit mass, λ and ϕ denote longitude and latitude, V is the volume of the global ocean, u, ρ and p denote zonal velocity, density and pressure, Ω is the Earth's angular velocity taken to be constant, a is the mean radius of the Earth, and $\mathcal{V}_\lambda$ represent viscous forces.

Fluctuations in $M(=\int_V \rho m dV)$ can be caused by variability in either the zonal velocity field, the density structure (ρ), which contributes mainly to changes in the oceanic moment of inertia, and sea level (η). Fluctuations in sea level only affect the moment of inertia if they are associated with redistribution of mass in latitude.

The quantities on the right hand side of (1) represent the external torques acting on the ocean. The first term which involves the pressure field p can be expressed using integration by parts as

$$\int_S -p(-H)\frac{\partial H}{\partial \lambda} dS \tag{3}$$

where H is the ocean depth and the integral is over the bottom surface S. This term represents exchanges of momentum between the ocean and solid earth through pressure torques acting on the solid boundaries. The other term associated with viscous forces represents exchanges with both the atmosphere (through surface wind stresses) and the solid Earth (through normal and tangential stresses at the boundaries).

Evaluation of (1) in its most general form is complicated and involves in principle solving for the global ocean circulation using a primitive equation numerical model forced

by momentum, heat and mass fluxes at the ocean-atmosphere interface. However, a number of simplifications can be applied to make the problem more tractable. Simple scale analysis using typical values of wind stress, oceanic boundary layer widths, and viscosity coefficients suggests that, to a first approximation, pressure and wind torques are the largest torques acting on the ocean. One can thus neglect viscous stresses acting at the bottom and at side walls. Similarly, the most important topographic features capable of sustaining large-scale zonal pressure torques are the continental walls. Thus, a flat-bottom ocean with vertical side walls can be used to study the pressure torque.

A further simplification in the dynamics is discussed by Ponte (1990). For linear, inviscid motions on a horizontally homogeneous, flat-bottom ocean, the vertically independent (barotropic) and dependent (baroclinic) regimes of circulation decouple in general. As explained in detail by Ponte, the barotropic regime is the most relevant for purposes of angular momentum calculations, since the baroclinic component contributes little to the vertically integrated quantities involved in the momentum budget, and can be studied by letting the density $\rho =$ constant.

3. Angular momentum in a barotropic ocean

Given the simplifications just discussed, we will consider the angular momentum balance in an ocean with constant density and constant depth, bounded by straight coasts at longitudes λ_1, λ_2 and latitudes ϕ_1, ϕ_2, and forced at the surface by a zonal wind stress τ. The only other frictional process included is a simple linear bottom drag with coefficient b. These assumptions lead to the simplified angular momentum equation (Ponte 1990)

$$\frac{\mathrm{d}M}{\mathrm{d}t} = T_c + T_w + T_b \tag{4}$$

where

$$T_c = -g\rho H \int_{\phi_1}^{\phi_2} [\eta(\lambda_2) - \eta(\lambda_1)] a^2 \cos\phi d\phi \tag{5}$$

$$T_w = \int \tau a \cos\phi dS \tag{6}$$

$$T_b = -b\rho H \int u a \cos\phi dS \tag{7}$$

Here, variability in M is due to changes in zonal currents and sea level only. T_c denotes the continental torque (to use the terminology of Oort [1985]) and depends only on the difference in sea level η across the ocean basin. T_w and T_b represent the wind and bottom friction torques, respectively.

Given a wind stress field, the angular momentum balance in (4) can be studied by solving for the u and η oceanic fields using an appropriate numerical model of the ocean circulation. Such calculations have been done by Ponte (1990) and more recently by Ponte and Gutzler (1991) in the context of the 40-50 day variability in the tropical regions. Fig. 1 shows the results obtained by Ponte and Gutzler (1991) using an oscillatory wind stress (period of 45 days), which acts over an area confined to the middle of the model basin, and is turned on at $t = 0$. A balance between T_c and T_w is quickly established after less than half a day after the wind is switched on; this balance holds at all times, with $T_b << T_w, T_c$. Thus, the net torque on the ocean is much smaller than the applied wind torque and fluctuations in M are relatively small. The angular momentum exchanged between the ocean and atmosphere through T_w is rapidly conveyed to and exchanged with the solid Earth through T_c.

At a time of maximum eastward winds, the largest $\Delta\eta$ across the basin is roughly 0.4 cm. In general, very small signals in sea level can balance the wind torques. For example, to balance the wind torque provided by a zonal mean wind stress of amplitude $\tau = 0.1$ N m^{-2} (a typical value for mean stress over the ocean) acting over an ocean 5000 km wide and 5000 m deep, a $\Delta\eta \sim 1$ cm is sufficient. Now, observed values of $\Delta\eta$ across basins are an order of magnitude larger (see, e.g., Oort 1985). However, most of this sea level signal is related with baroclinic processes and does not provide a net pressure torque on the wall (e.g., Ponte 1990).

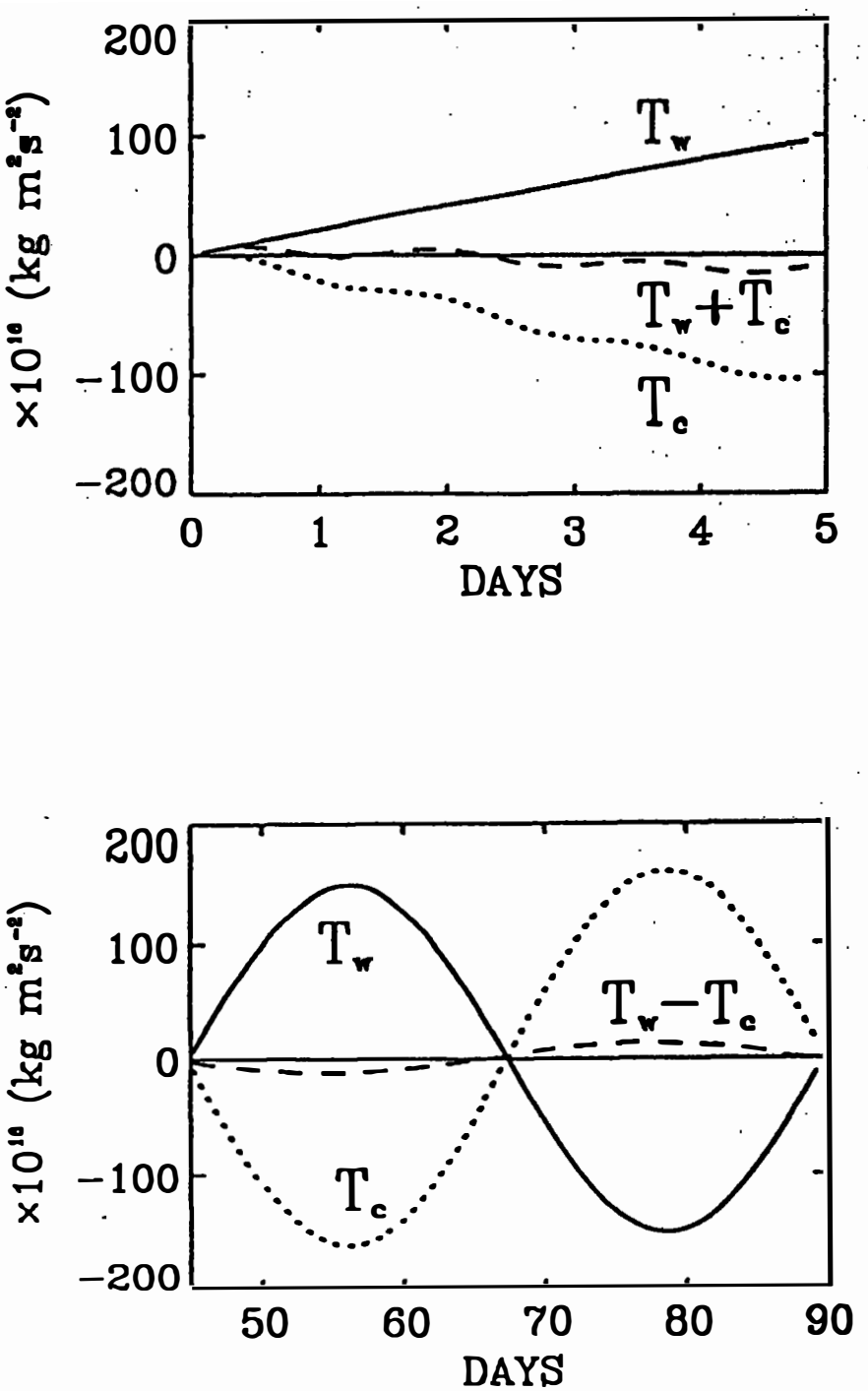

Fig. 1. Torques for days 0-5 (upper panel) and 45-90 (lower panel) of the numerical integration described in Ponte and Gutzler (1991) showing the rapid establishment of a dominant balance between the wind and continental torques, which holds throughout the integration.

For the purposes of understanding this effect, one can think of the pressure anomaly on the wall as composed of two modes depicted in Fig. 2. The barotropic anomaly has a relatively small amplitude (i.e. small η signal) but is constant with depth and does not involve any changes in the subsurface density levels. The baroclinic anomaly has a large surface amplitude (i.e., large η signal) but oscillates in sign with depth due to correlated changes in the depth of subsurface density levels. The vertical integral of the baroclinic pressure anomaly is generally much smaller than the barotropic component (e.g., Ponte 1990), and thus the large sea level signal related to baroclinic processes does not contribute much to the torque on the walls.

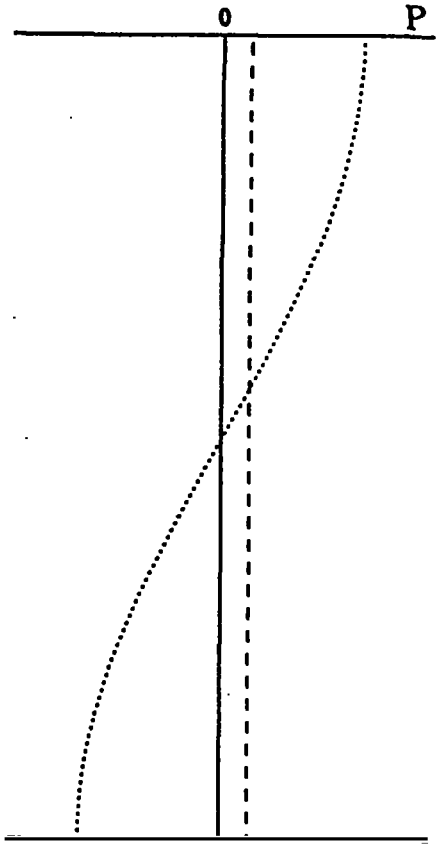

Fig. 2. Schematic representation of the vertical structure of barotropic (dashed line) and barotropic (dotted line) pressure anomalies. Units are arbitrary.

4. El Niño and oceanic angular momentum

When the sum of the torques acting on the ocean is not zero and changes in M are sufficiently large, discrepancies in the angular momentum budget of the atmosphere and solid Earth should occur. Such discrepancies have been documented by Rosen et al. (1990) for interannual time scales. Although a plausible explanation involves core-mantle interactions, the discrepancies seem to roughly coincide with El Niño events. Rosen et al. raise the question of whether changes in M during El Niño could account for the missing variability. The unexplained signal in the atmosphere-solid Earth momentum budget of order 0.1 ms implies a corresponding $\Delta M \sim 6 \times 10^{24}$ kg m s^{-2} using Rosen et al.'s (1990) conversion formula.

The discussion of this subject here is only qualitative, but serves to illustrate the need to account for baroclinic effects when interpreting sea level and surface current variability. For simplicity, the discussion focuses only on the magnitude (not the sign) of anomalies in M during El Niño.

a. Zonal velocity changes during El Niño

In general, zonal velocity anomalies in the ocean can be taken to represent fluctuations in M. An anomalous upper layer eastward flux of 40×10^6 m^3/s in the tropical Pacific has been reported by Wyrtki (1985) during El Niño. Given any reasonable zonal structure to this volume flux, the angular momentum anomalies implied are of the right order of magnitude to account for the Rosen et al. discrepancy. However, for our purposes, it is important to realize that there must be a westward return flow either in the deeper layers or in off-equatorial regions, otherwise the eastward flux of 40×10^6 m^3/s would imply unrealistic sea level changes in the eastern Pacific. For example, to accommodate 40×10^6 m^3/s of water flowing into a region 80° by 20° wide (roughly half the area of the equatorial Pacific) would require changes in sea level larger than 10 cm/day over the whole area.

The westward flux needs to be of the same order of magnitude as the upper layer, near-equatorial eastward flux, if one does not want to have unrealistic horizontal convergence of mass and associated sea level changes. The anomalies in oceanic angular momentum are thus much smaller than when calculations are based on Wyrtki's (1985) eastward flows. In fact, the sea level in the tropical Pacific is observed to be lower by about 10 cm after El Niño (Wyrtki 1985). These changes occur over many months and, even if all this water piled up in the eastern Pacific with no return flows westward, the implied zonal velocities and corresponding angular momentum anomalies would be negligible compared to the values needed to account for the unexplained variability in Rosen et al.'s records.

b. Changes in oceanic moment of inertia during El Niño

Large-scale mass redistributions are known to occur during El Niño in the Pacific ocean. Observations analyzed by Wyrtki (1985) indicate that after an El Niño event sea level over the equatorial Pacific is lower by roughly 10 cm, with compensating rises in the extra-equatorial regions. Such changes, if taken to represent real mass redistribution in latitude, could imply a change in oceanic momentum of inertia of sufficient magnitude to explain the Rosen et al.'s results. However, one has to account again for the changes in the subsurface mass field that accompany those in sea level.

To a reasonable approximation, one can think of the tropical ocean as a medium consisting of two layers of different constant densities (Wyrtki 1985). In this limit, a deeper (shallower) sea level implies a lower (higher) interface between the two layers in such a manner that the vertically integrated mass anomalies are essentially zero. Thus, in a stratified ocean, the vertically integrated mass anomalies are much smaller than expected from η measurements alone. For example, if the two-layer approximation is valid to within 20%, sea level changes of 10 cm during El Niño may correspond to mass redistribution equivalent to shifting 2 cm of water between the equator and higher latitudes. The corresponding

changes in M would be much smaller than what is needed to account for discrepancy in the atmosphere-solid Earth angular momentum budget (order of 0.1 ms).

The above qualitative discussion sheds some doubts on the hypothesis that El Niño signals in the ocean can explain discrepancies found by Rosen et al. (1990) in the atmosphere-solid Earth momentum budget at interannual time scales.

5. Summary

Some aspects of the oceanic angular momentum problem and the ocean's role in the planetary angular momentum budget were briefly discussed. We have suggested that pressure and wind torques are the most important external torques acting on the ocean, and that angular momentum exchanged between atmosphere and ocean through wind stresses can be quickly transported to the solid boundaries via barotropic processes and transferred to the solid Earth through pressure (or continental) torques. In addition, fairly small sea level differences across basins (order of 1 cm) are sufficient to balance observed wind stress torques. We have also illustrated the importance of including variability in subsurface oceanic fields when interpreting oceanic records with regard to fluctuations in angular momentum.

Acknowledgements. This material was prepared with support provided by NOAA's Climate and Global Change Program under grant NA89AA-D-AC202.

References

Oort, A. H., 1985. Balance conditions in the earth's climate system. *Advances in Geophysics, 28A*, Academic Press, 75-98.

Ponte, R. M., 1990. Barotropic motions and the exchange of angular momentum between the oceans and solid earth. *J. Geophys. Res., 95*, 11369-11374.

Ponte, R. M., and D. S. Gutzler, 1991. The Madden-Julian oscillation and the angular momentum balance in a barotropic ocean model. *J. Geophys. Res., 96*, 835-842.

Rosen, R. D., D. A. Salstein, and T. M. Wood, 1990. Discrepancies in the earth-atmosphere angular momentum budget. *J. Geophys. Res., 95*, 265-279.

Wyrtki, K., 1985. Water displacements in the Pacific and the genesis of El Niño cycles. *J. Geophys. Res., 90*, 7129-7132.

Intercomparison of AAM Analysis and Forecast Data in UT1 Estimation and Prediction

A. P. Freedman
J. O. Dickey

Jet Propulsion Laboratory
California Institute of Technology
Pasadena, CA 91109

Summary

To enable precise real-time tracking and navigation of interplanetary spacecraft, a JPL-developed Kalman Earth Orientation Filter (KEOF) is being used to estimate and predict polar motion and Universal Time (UT1). KEOF employs a diverse set of geodetic and atmospheric data to optimize its solutions. Geodetic observations of UT1 or its time derivative, length of day (LOD), are by themselves currently insufficient to guarantee the real-time UT1 accuracy required for spacecraft applications, due to the relatively long turnaround time required to process them. Hence KEOF utilizes a meteorological proxy for LOD: the axial atmospheric angular momentum (AAM) and AAM forecast data generated in a rapid-turnaround mode by the U.S. National Meteorological Center (NMC) as a byproduct of its operational weather forecasting models.

We have investigated the effect that AAM and AAM 5-day forecast data have on KEOF's ability to predict UT1 up to 10 days in the future. We demonstrate that AAM data as a whole are very useful, and, in fact, essential, for meeting the required goals for real-time UT1 estimation. AAM forecast data are beneficial in improving UT1 predictions beyond a few days. We show that, of the various geodetic data sets used operationally, the most critical for near-real-time estimation is that of TEMPO VLBI, produced by JPL using NASA's Deep Space Network.

We also examine the effects of using different AAM and AAM forecast data sets, and compare results obtained with AAM data from the NMC to those obtained with AAM data from the European Centre for Medium-Range Weather Forecasting (ECMWF) and the United Kingdom Meteorological Office (UKMO). We consider the effects of the wind and pressure terms, both with and without the inverted barometer approximation, and of integrating the winds to different heights in the atmosphere.

Introduction

Precise knowledge of real-time Earth orientation is required for accurate tracking and navigation of deep-space and interplanetary spacecraft. The most problematic component of Earth orientation is UT1, Earth's angle of rotation, as it is highly variable over time and rather unpredictable. Current geodetic measurements of UT1 are by themselves inadequate for navigational purposes, not due to their level of accuracy (which is excep-

tionally good), but rather to their extensive data reduction requirements which can delay the Earth orientation solutions by more than two weeks. Even the quickest typical turnaround times for current techniques (two or three days for TEMPO VLBI) are not sufficient during many periods when UT1 is varying particularly rapidly.

New geodetic techniques that can make measurements frequently and reduce them rapidly promise to ameliorate this problem in the future, but for the present, other solutions must be found. One involves the use of axial atmospheric angular momentum (AAM) as a proxy data set for the rate of rotation (i.e., the time derivative of UT1), also known as length of day (LOD). Numerous studies have shown that, at periods from a few years down to at least 10 day, LOD and AAM are highly correlated (see *Hide and Dickey* [1991] for a recent review of this literature). AAM estimates are available daily from a number of operational weather forecasting centers. In addition, three centers also generate forecasts of AAM, providing a prediction of LOD variability based on physical, rather than stochastic, models.

At the Jet Propulsion Laboratory, California Institute of Technology (JPL), our group has implemented a Kalman filter for assimilating, interpolating, smoothing, and extrapolating geodetic Earth orientation and AAM data [*Morabito et al.*, 1988; *Dickey et al.*,1988; *Freedman et al.*, 1991]. This filter, known as the Kalman Earth Orientation Filter (KEOF), combines geodetic data of diverse types to solve for both UT and polar motion, as well as their respective excitation functions [*Barnes et al.*, 1983]. It also has the ability to use AAM and AAM forecast data as modeled forms of LOD, hence, to use them to estimate up-to-the-minute values of UT1 as well as predictions of UT1 a number of days into the future.

The relationship between UT1 (U) and LOD (Λ) as modeled within the filter is:

$$\frac{dU}{dt} = -\Lambda$$

$$\frac{d\Lambda}{dt} = \omega_\Lambda$$

Λ corresponds to the excess length-of-day with all tidal terms from two weeks to 18 years removed, while U is UT1–UTC also corrected for tidal effects. ω_Λ represents a white-noise stochastic process; thus, LOD is modeled as a random walk (integrated white noise) while UT1 is modeled as an integrated random walk. The AAM (A) component is described by:

$$A = \Lambda + \mu_A$$

$$\frac{d\mu_A}{dt} = \omega_A$$

where AAM differs from LOD by a difference term, μ_A, that also behaves as a random walk (with a much smaller variance, however). AAM forecast values (F) are modeled by:

$$F = A + \mu_F + b$$

$$\frac{d\mu_F}{dt} = -\frac{\mu_F}{\tau_{\text{lead}}} + \omega_F$$

Hence, the AAM forecasts are treated as the sum of the true AAM, a constant bias term b, and an exponentially decaying term μ_F with long-term random walk behavior. The exponential time constant is τ_{lead}, the forecast lead time (see *Freedman et al.* [1991] for a justification of these models).

The goal of this study is to evaluate the effectiveness of utilizing AAM and AAM forecast data in the estimation and prediction of UT1. How does our ability to interpolate and extrapolate UT1 with geodetic data alone compare with that when geodetic data are combined with AAM and AAM forecast data? In addition, there are a variety of AAM options available, including AAM from three different forecast centers, AAM generated using different meteorological quantities, and AAM forecasts with different lead times; which AAM series is best for our purposes?

To answer these questions, we have constructed a version of KEOF that is automated to do numerous sequential case studies. We use these case-study results to generate statistical measures of the filtering accuracy. The automated filtering strategy is shown in Figure 1a. First, a reference UT1 time series is created by filtering all geodetic data without AAM. This filtering is done in an optimal smoothing mode [*Morabito et al.*, 1988] and requires a complete, long-term time series.

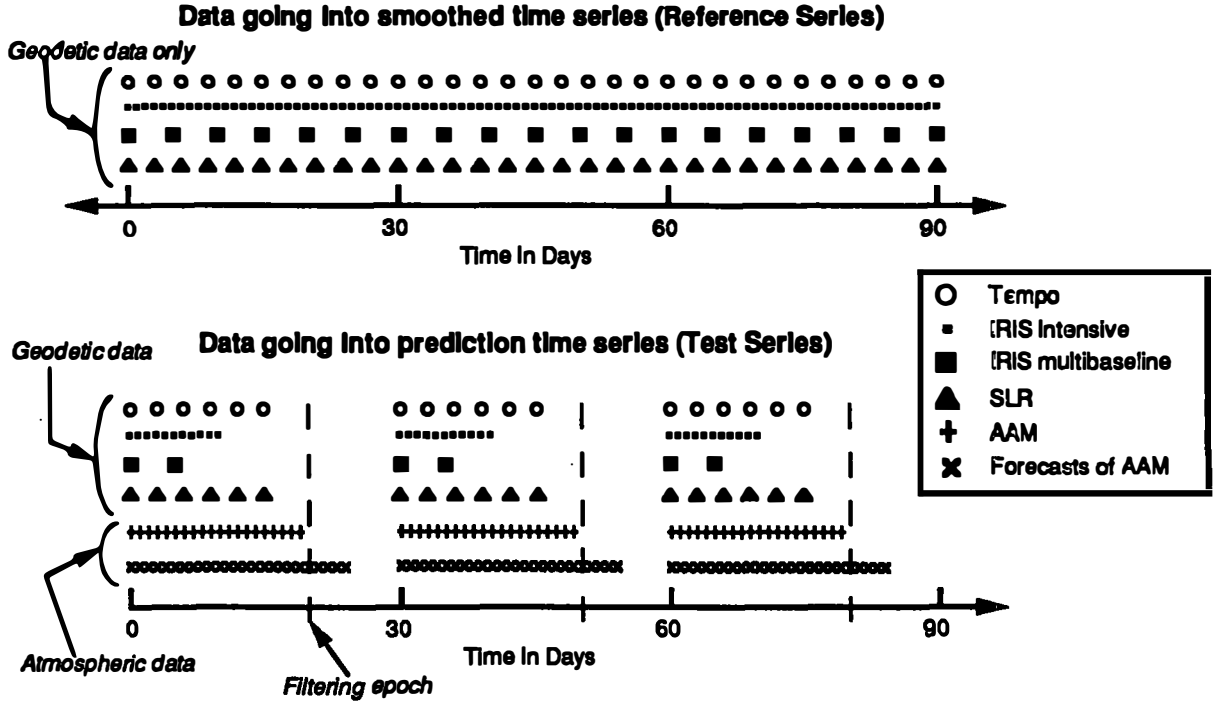

Figure 1a

Fig. 1 Schematic descriptions of the multiple sequential case-study filtering tool.
a) Filtering strategies for the Reference Series (above) and the Test Series (below).
b) Time series of errors in the filter estimates and predictions.
c) Definition of terms used in describing a filtering cycle (see text).

The automated portion of this multiple case-study filter is then run to generate a set of consecutive time series (the "test series") that closely correspond to the results of a series of operational filter runs. These differ from the reference run in that not all geodetic data are available up to the assumed filtering epoch, AAM and AAM forecast data are included along with the geodetic data, and UT1 is extrapolated beyond the filtering epoch. The test series are differenced with the reference series' smoothed values at each time point, and the resulting errors in the UT1 estimates and predictions are examined for overall behavior and trends (see Fig. 1b).

The test series consists of a number of consecutive simulations of operational KEOF runs. Each simulation is run over a specified time span, referred to as a cycle (see Fig. 1c). The filter initiates each cycle with the full state and covariance matrices generated by a normal KEOF run using all data prior to that point in time, equivalent to commencing the filter operation well before the beginning of the cycle. Within each cycle is a ref-

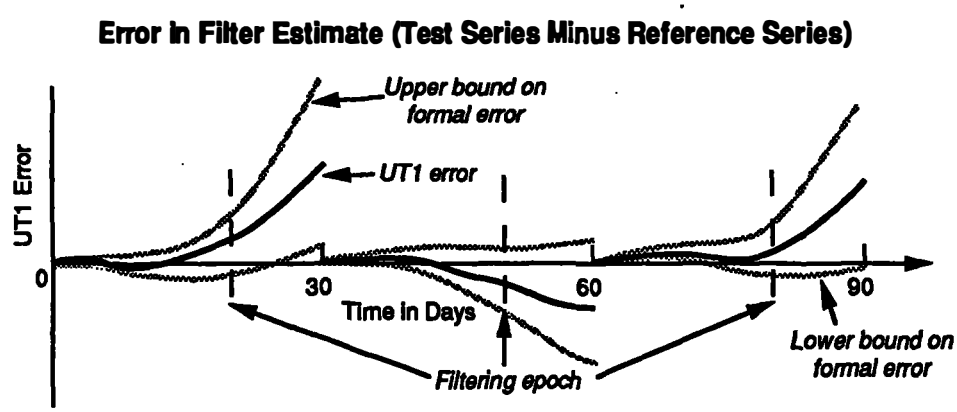

Figure 1b

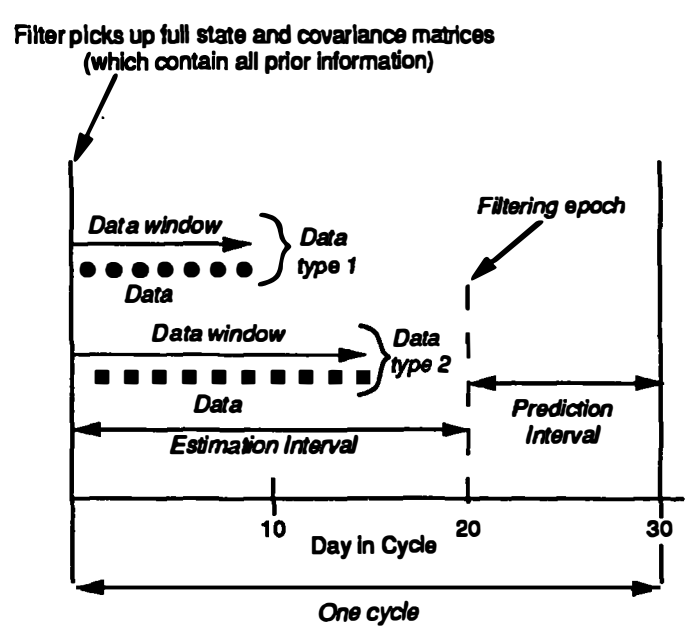

Figure 1c

erence time point corresponding to the simulated filtering epoch. Each data type is available within a cycle for a specified length of time known as the window for that data type. For example, in the 30 day cycles that follow, the reference epoch is at day 20 in the cycle, TEMPO VLBI data are available in a window extending from the beginning of the cycle to three days before the reference time (i.e., day 17 of the cycle), and AAM 5-day forecast data fill a window from day 0 to day 24 (i.e., the AAM data available at the filtering epoch on day 20 are the processed AAM zero-hour data up to day 19 and the 5-day AAM forecasts up to day 24).

A key indicator of filtering accuracy is the RMS error at each day in the cycle, obtained by summing over all the cycles. Thus the RMS error is

$$\varepsilon_{rms,\,i} = \left(\frac{1}{M} \sum_{j=1}^{M} \varepsilon_{j,i}^{2} \right)^{1/2}$$

where i is the day number of the cycle (i = 1, ..., N) for cycles of N days, j is the cycle number (j = 1, ..., M) with the test series consisting of M cycles, and $\varepsilon_{j,i}$ is the difference between the simulated operational (test) filter value and the reference filter value on day i of cycle j. These RMS errors will be illustrated in the following sections. Statistics are also available for the mean error, mean absolute error, standard deviation about the mean, etc., but these other statistical quantities all yield results consistent with those shown by the RMS error.

The Operational Data

A variety of data sets are used in operational KEOF processing. These data are summarized in Table 1. There are four sets of geodetic data, three obtained with very-long-baseline interferometry (VLBI) and one with satellite laser ranging (SLR). The TEMPO

Table 1. Operational data sets employed [a]

Name	Type	Parameters	Frequency [b]	Typical Delay	Rapid Turnaround
TEMPO [c]	VLBI	UT0 / var.-lat.[d]	twice / week	3 days	1 day
IRIS multibaseline	VLBI	PM, UT1	once / 5 days	14 days	10 days
IRIS intensive	VLBI	UT1	daily	10 days	7 days
U. Texas, CSR	SLR	PM	once / 3 days	5 days	3 days
NMC 0-hour	AAM	AAM Analysis	daily	1 day	1 day
NMC 5-day	AAMF	AAM Forecast	daily	1 day	1 day

[a] NAVNET, CDP VLBI, and LLR data are not included in this analysis, although NAVNET is now used operationally (with characteristics similar to those of IRIS multibaseline).
[b] All techniques experience data dropouts, so data are not strictly regular.
[c] TEMPO data are acquired on two baselines, each of which is measured once per week.
[d] TEMPO measurements are of UT0 and variation of latitude, linear combinations of polar motion (PM) and UT1.

VLBI data are the most timely, with data turnaround times of one to three days. SLR data, from the Center for Space Research (CSR), U. Texas at Austin, are also processed fairly rapidly–within three to five days. Note that only polar motion (PM) data from SLR are used, since the UT1 values from SLR are sometimes corrupted by long-period nodal errors [*IERS*, 1989]. VLBI measurements from the National Geodetic Survey provide the bulk of the geodetic data through the IRIS multiple-baseline (UT1 and PM) and IRIS intensive (UT1 only) programs. These are the most precise and accurate data, but they take the longest to process—sometimes two weeks or more. Recently, U.S. Naval Observatory NAVNET VLBI data have also been used operationally. These data have characteristics very similar to those of the IRIS multibaseline data.

Two AAM data sets are used operationally: zero-hour forecasts (also known as analysis values) and five-day forecasts. These data are obtained from the NMC daily, with one-to-two day turnaround. For historical continuity, a specific AAM quantity provided by the NMC, derived from atmospheric wind variations up to a level of 100 mbar in the atmosphere, is currently being used. This does not yield quite as accurate a picture of true atmospheric angular momentum variations as it would if the stratosphere and atmospheric pressure variations were also considered, but these quantities have only become available from the NMC relatively recently (see below).

The first issue we address is how beneficial AAM and AAM forecast data are in predicting UT1. Three prediction time series were generated in which (1) only geodetic data

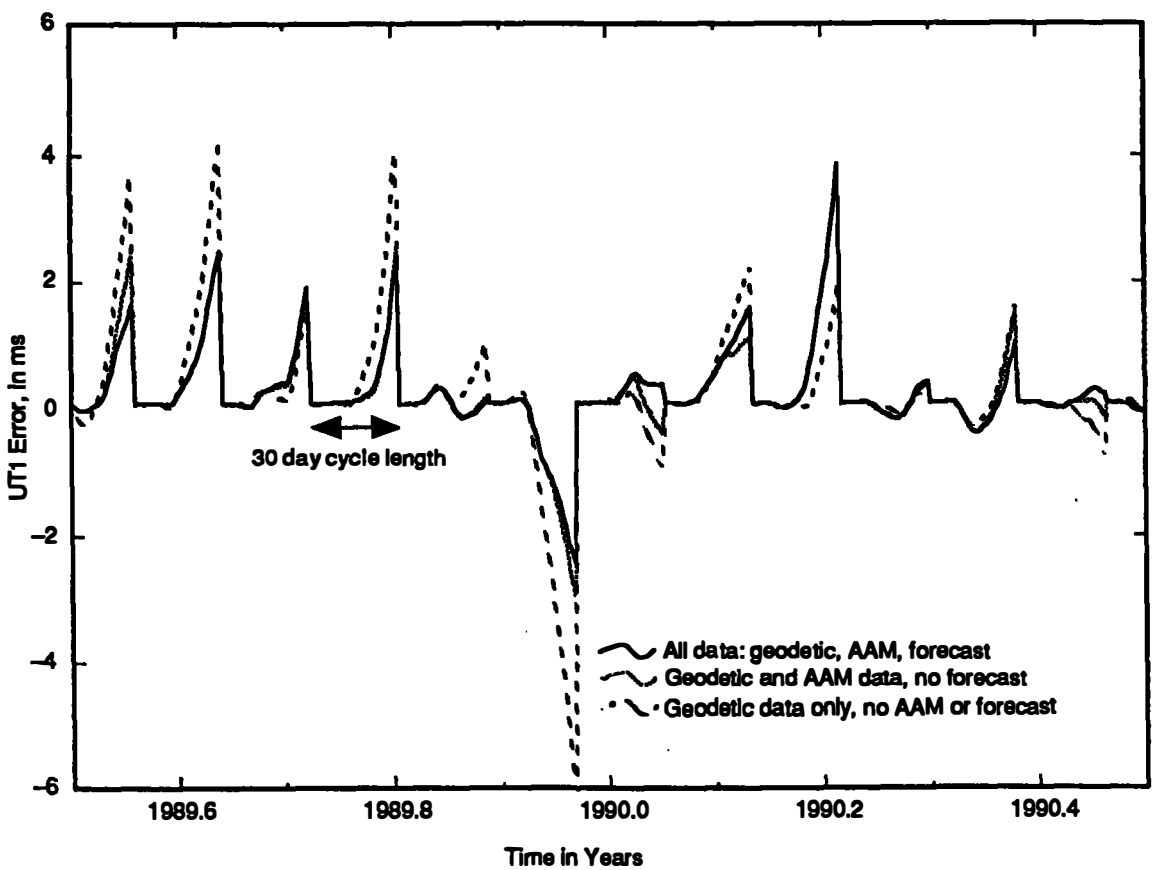

Fig. 2 Errors in the UT1 filter estimate for a one-year period. Three data series are shown.

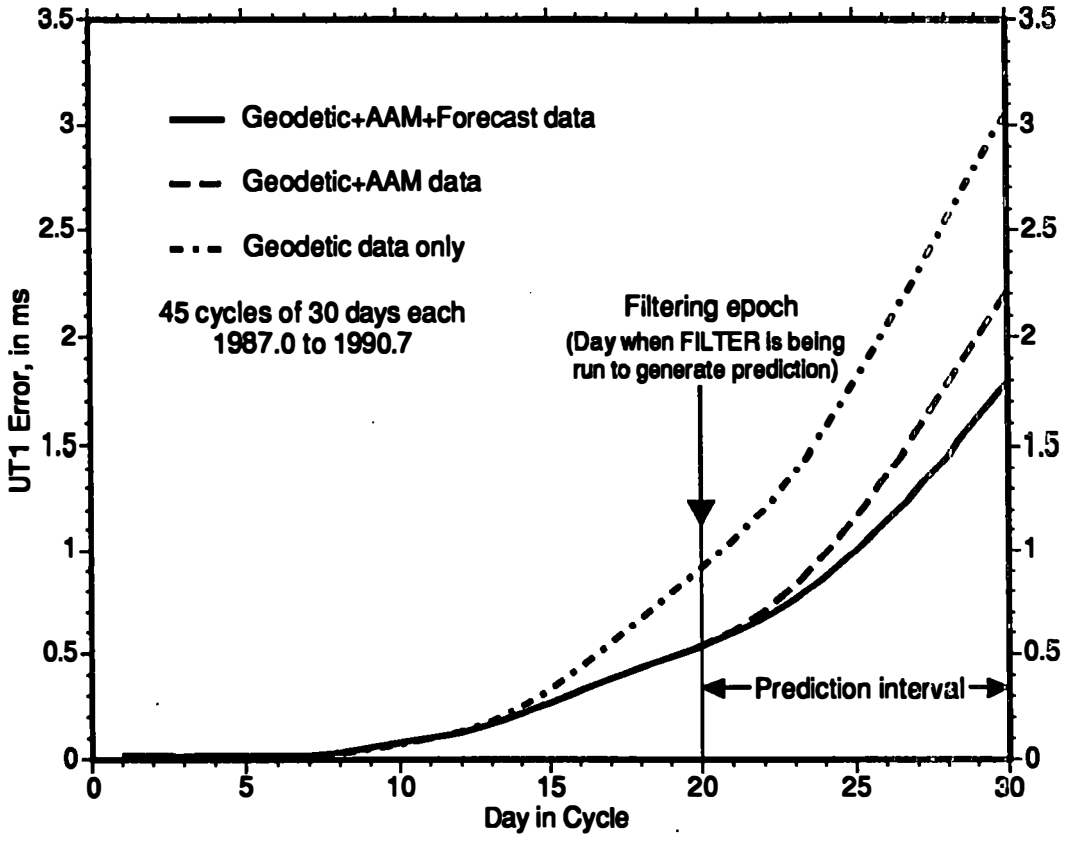

Fig. 3 RMS of filtered UT1 errors. Three data series are shown, illustrating the effects of adding AAM zero-hour and five-day forecast data to the geodetic data.

were used to predict UT1, (2) AAM analysis data were used along with the geodetic data to predict UT1, and (3) both AAM analysis and 5-day forecast data were used to augment the geodetic data. Approximately $3\frac{1}{2}$ years of data were used, sufficient to form 45 consecutive cycles each with a length of 30 days. Each series was differenced with a reference "true" UT1 series created by filtering and smoothing only the geodetic data shown in Table 1 in a non-real-time mode. Figure 2 shows a one-year section of the four-year time series. Note that the UT1 errors are highly time variable, and that no one series always possesses the smallest errors. However, it seems clear that geodetic data by themselves generally yield larger errors than the series incorporating atmospheric data.

These trends are quantified in Figure 3, which shows the RMS prediction error for these three time series. The geodetic-data-only series errors begin to grow well before all the geodetic data are exhausted, diverging from the geodetic-plus-AAM curves five or more days before the epoch when the filter is run. By the filtering epoch, the geodetic-plus-AAM series exhibits errors about 0.4 ms smaller than those of the geodetic-data-only series. The effect of including AAM forecast data is much less pronounced, and only becomes significant a few days after the filtering epoch.

Figure 4 illustrates the ability to predict LOD for the same three data sets. Here, the differences between the various curves are even more pronounced, and the behavior of the curves reveals more about the processes that influence the filtering. For example,

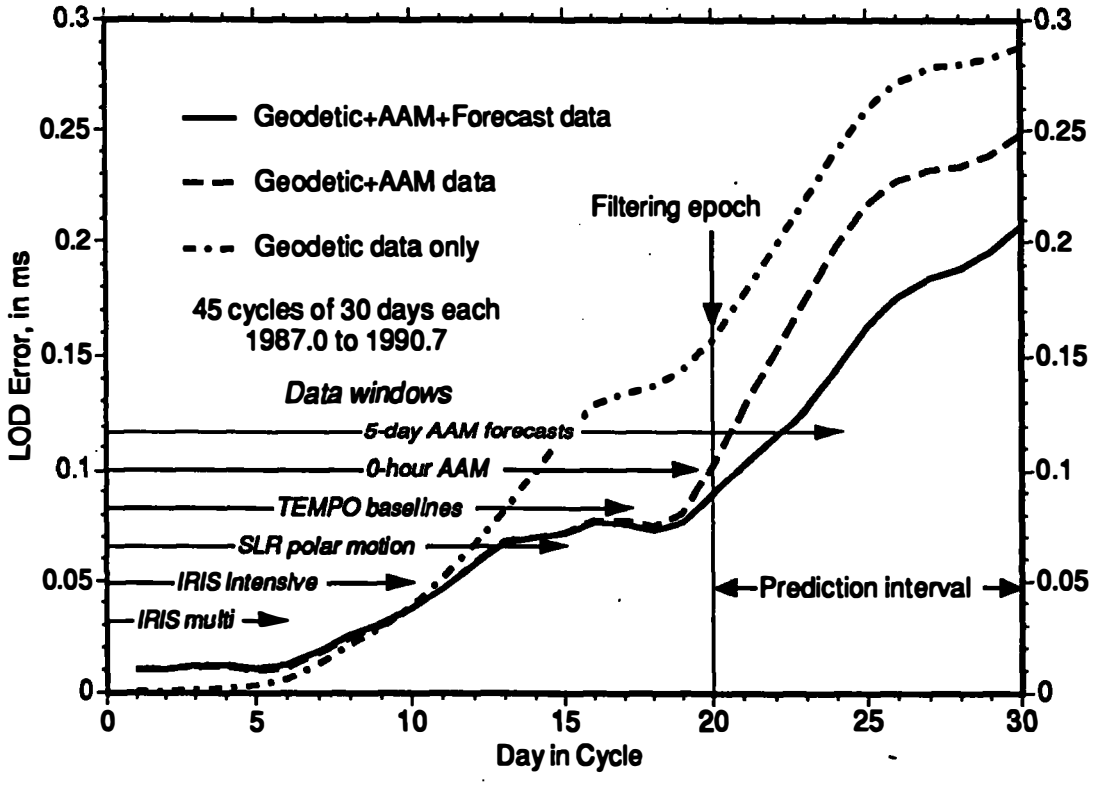

Fig. 4 RMS of filtered LOD errors for same three data series.

errors in all the curves begin to grow as the high-precision IRIS multibaseline data drop out of the picture (day 6 in cycle). After the daily IRIS intensive data drop out (day 10 in cycle), the effect of daily AAM data can be seen. The geodetic-data-only curve grows to a level governed by the ability of TEMPO data to monitor LOD. After the TEMPO data end (day 17 in cycle), the LOD errors continue to grow at a rate consistent with the random-walk model for LOD behavior. The curves incorporating AAM data show much smaller errors due to the constraints provided by daily AAM. As the geodetic-plus-AAM analysis data curve loses its data (at day 19 in cycle), its errors begin to grow in parallel with the geodetic-data-only error curve. In this case, including AAM forecast data significantly helps LOD prediction from the filtering epoch onwards.

The effect of neglecting various geodetic data types has also been studied and is illustrated in Figure 5. The most influential data types for UT1 prediction in our operational mode are the TEMPO VLBI data and the IRIS intensive data. In Fig. 5, these data sets have respectively been deleted (but all AAM data have been retained). Clearly, TEMPO data are important for estimating UT1 errors after the IRIS data become unavailable, whereas the IRIS intensive data are most critical for constraining the errors of the higher-precision UT1 estimates generated when all data types are available. This plot illustrates well the need for a rapid-turnaround TEMPO-like technique in real-time UT1 estimation.

The significance of turnaround time in processing the data is illustrated further in Figure 6. In Table 1, the shortest turnaround times that are sometimes achieved are listed

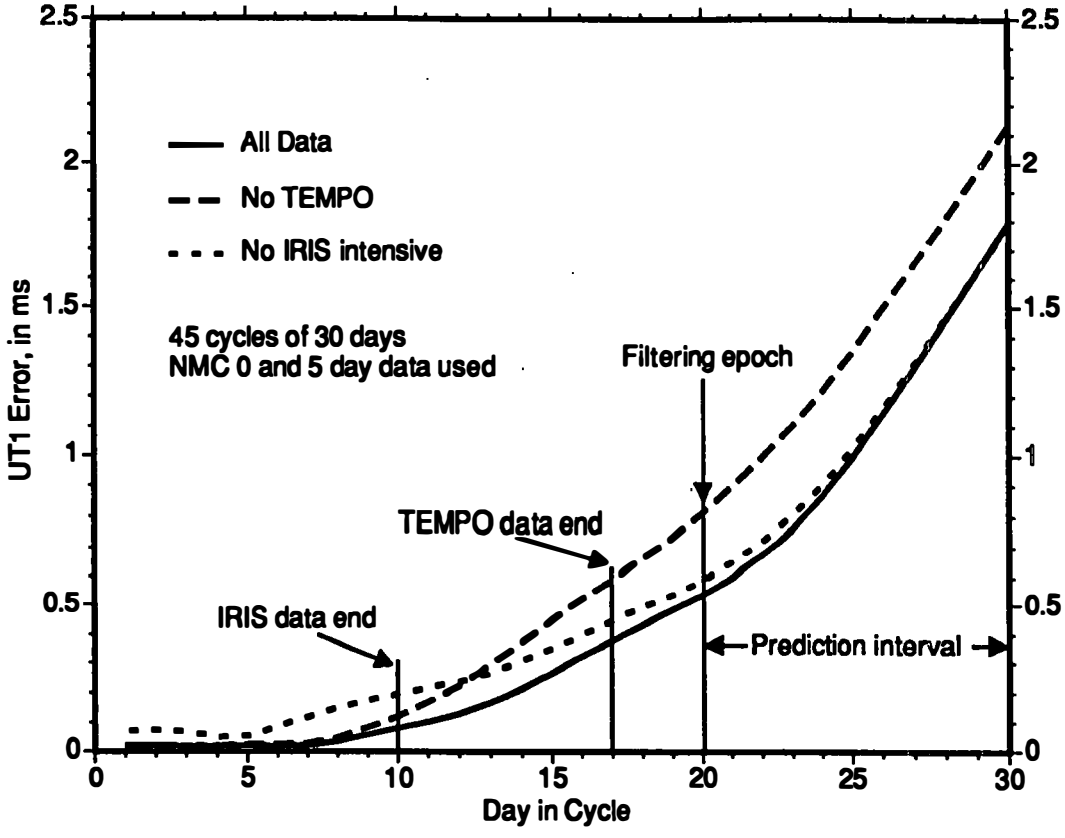

Fig. 5 RMS of filtered UT1 errors, comparing the effects of deleting various geodetic data sets.

next to the typical turnaround times for each series. The predicted UT1 errors achieved with these rapid-turnaround geodetic data are shown side-by-side with the errors resulting from typical data turnaround times in Fig. 6, both with and without AAM and AAM forecast data. Rapid geodetic data turnaround makes a substantial difference in UT1 prediction accuracy: in the absence of AAM data, the improvement is more than 0.3 ms from about day 17 onwards. With AAM analysis and forecast data, timely geodetic data again improve the UT1 estimates, but the level of improvement is a smaller 0.2 ms. Furthermore, from about day 19, the estimates with standard turnaround and AAM are superior to those with rapid turnaround but no AAM. Hence, the urgency of the need for the most timely geodetic data is somewhat alleviated by the use of AAM data.

One caveat should be mentioned regarding the multiple case-study tool and the interpretation of Figs. 3 to 6. The case-study tool assumes fixed epochs when running the filter to generate operational UT1 predictions, regardless of the data actually available at that epoch. In reality, the operator may choose to run KEOF only when a new TEMPO measurement has just become available. Thus, in our series of case studies, the last available TEMPO point usually lies between days 13 and 17 of the cycle, whereas in true filter operation, a TEMPO point usually lies in day 16 or 17 of the cycle. This may partially explain the apparent superiority of the AAM-but-no-TEMPO curve (Fig. 5) over the TEMPO-but-no-AAM curve of Fig. 3 around the filtering epoch (day 20). Note that the

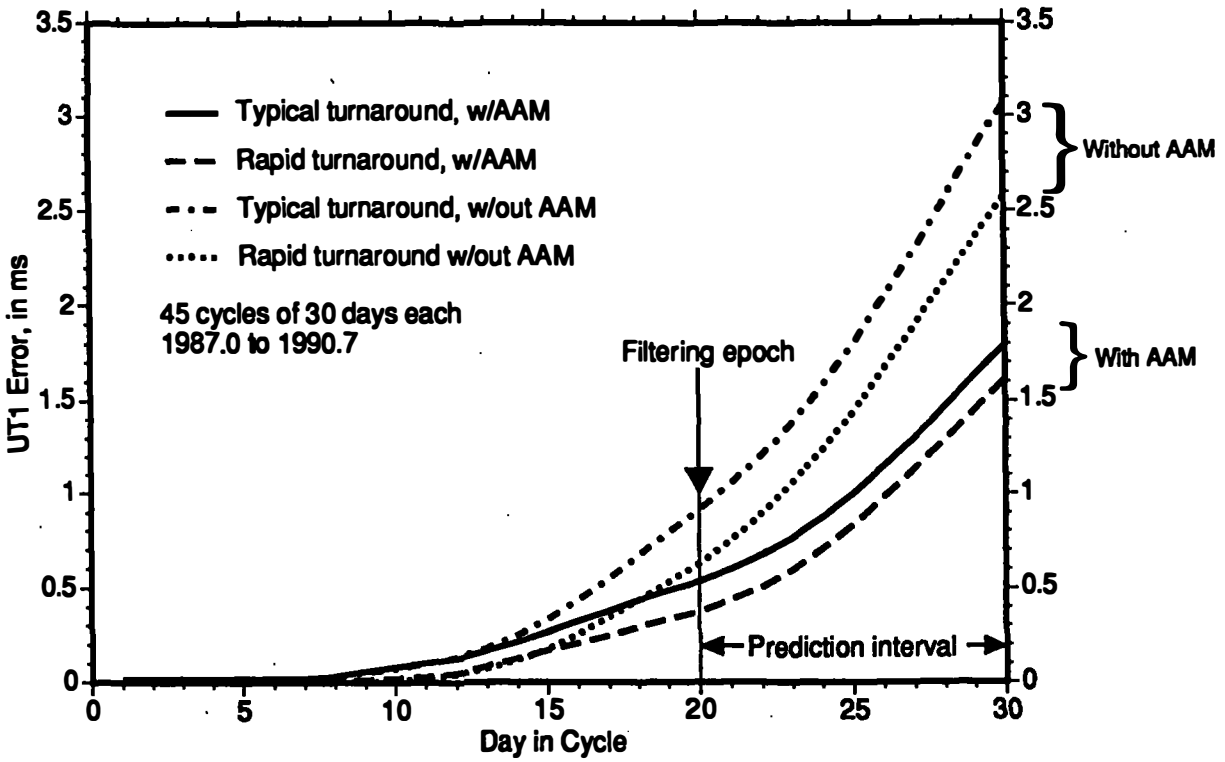

Fig. 6 RMS of filtered UT1 errors, comparing the effects of different data turnaround times.

rapid-turnaround TEMPO-but-no-AAM curve (Fig. 6) in fact does better near day 20 than the AAM-but-no-TEMPO curve.

AAM quantities are evaluated every 12 or 24 hours, depending on the service, hence they provide valuable information concerning the high-frequency component of Earth rotation. This is especially important after the daily IRIS intensive data are no longer available. These daily AAM measurements are a useful complement to the TEMPO geodetic data, which are available every three or four days. Furthermore, the TEMPO data do not directly reveal UT1, rather, they monitor UT0 and variation of latitude; hence they need to be combined with other information within the filter to yield UT1. For all these reasons, utilizing AAM data significantly improves estimates of UT1 both prior to and following the prediction epoch, even when TEMPO data with their rapid turnaround times are available.

Intercomparing AAM Data Sets

As discussed above, the AAM data sets currently in operational use are those produced by the NMC. They are zero-hour and five-day AAM forecast series that have been released daily for over five years. Since October 1989, the NMC has been releasing in real time AAM data sets that are more complete with regard to atmospheric components that affect AAM. In addition, other meteorological centers around the globe produce

routine estimates of AAM quantities. We have studied how these other AAM data sets affect the prediction of UT1, and have compared them to the series now in use.

These AAM data sets are summarized in Table 2. The NMC produces forecasts from 0 out to 10 days, while the United Kingdom Meteorological Office (UKMO) produces daily forecasts from 0 out to 6 days. The European Centre for Medium-Range Weather Forecasting (ECMWF) produces forecasts at 0, 3, 5, and 10 days. In the results shown below, only the 0-hour and 5-day forecasts, common to all three centers, are compared. The NMC and UKMO data are currently available in real time, with plans for the ECMWF data soon to be available also. Although they are not, or have not for very long, been available in real time, both the UKMO and the ECMWF data have, for a number of years, been provided on a quarterly basis; it is these longer time spans of data that are used in this study. All three centers generate estimates of AAM based on the zonally averaged zonal winds up to the tops of their model atmospheres (with these model tops varying as shown in Table 2). They also compute the effect on AAM of pressure variations in the atmosphere. In addition, the NMC computes the effect of pressure variations modified by the inverted barometer approximation [e.g., *Munk and Macdonald*, 1960], wherein the ocean is assumed to respond as a fluid to atmospheric pressure variations, resulting in no net pressure variation or torque on the ocean floor.

The NMC data set in operational use is the AAM term computed from atmospheric winds up to the 100 mbar level of the atmosphere. This quantity ignores winds in the stratosphere, known to play a significant role in the angular momentum budget of the Earth [*Rosen and Salstein*, 1985], and also ignores the effects of pressure variations. As a rule, however, pressure variations tend to produce small changes in AAM, hence they have a relatively minor effect on short-term AAM variability [*Barnes et al.*, 1983; *Rosen et al.*, 1990]. Ignoring the stratosphere has the effect of reducing the amplitude of variations in AAM, hence underestimating the variability of LOD somewhat.

An important fact to keep in mind when interpreting the results shown below compar-

Table 2. AAM data sets under study

Name	Forecasts used	Real-time?	Meteorological Quantities [a,b]	Time Span
NMC	0-hour 5-day	yes	W100, WT(50), P, IBP	W100 ~4 years WT, P, IBP ~1 yr [c]
UKMO	0-hour 5-day	yes	WT(25), P	~4 years
ECMWF	0-hour 5-day	no	WT(10), P	~4 years

[a] Meteorological quantities are: winds (W), pressure (P), and pressure assuming the inverted barometer approximation to be valid (IBP).

[b] Winds can be integrated through the top of the model (WT(10, 25, or 50 mbar), depending on center), or cut off at 100 mbar as the NMC does (W100). Height in the atmosphere is denoted by pressure level, where the surface is at ~1000 mbar and 100 mbar corresponds to the bottom of the stratosphere.

[c] Prior to late 1989, NMC only released forecasts of AAM based on winds to 100 mbar.

ing the presently used AAM time series with other AAM series, is that the analysis and modeling used to incorporate AAM into the Kalman filter was performed with the operational AAM data set. Since the filter model is optimized for this quantity, any other AAM quantity, whether including more of the stratosphere or the pressure term, or from another center, may not be utilized by the filter in an optimal fashion.

In Figure 7, we compare UT1 predictions incorporating the AAM series from the two other meteorological centers to predictions made using the current operational AAM series. Both the UKMO and the ECMWF data appear to do a somewhat better job than the current NMC AAM, with the ECMWF time series showing the best performance. This result is consistent with those from a number of other studies intercomparing the various AAM data sets [*Gross et al.*, 1991; *Bell et al.*, 1990; *Rosen et al.*, 1991], and may be attributable to the ECMWF's integration of the atmosphere up to the highest level of the services considered (see Table 2), thus including a considerable portion of the stratosphere in estimates of AAM. The performance of the UKMO data is intermediate between that of the other two services between day 15 and day 25 of the cycle, which is consistent with the fact that the UKMO integrates the atmosphere to an intermediate value of 25 mbar. The increase in error after day 25 may be a result of larger errors in the UKMO forecast data set prior to 1988 which *Rosen et al.* [1991] have noted.

Incorporating the pressure terms improves the performance of the AAM from about day 13 of the cycle to about day 23, after which point the pressure terms appear to have a

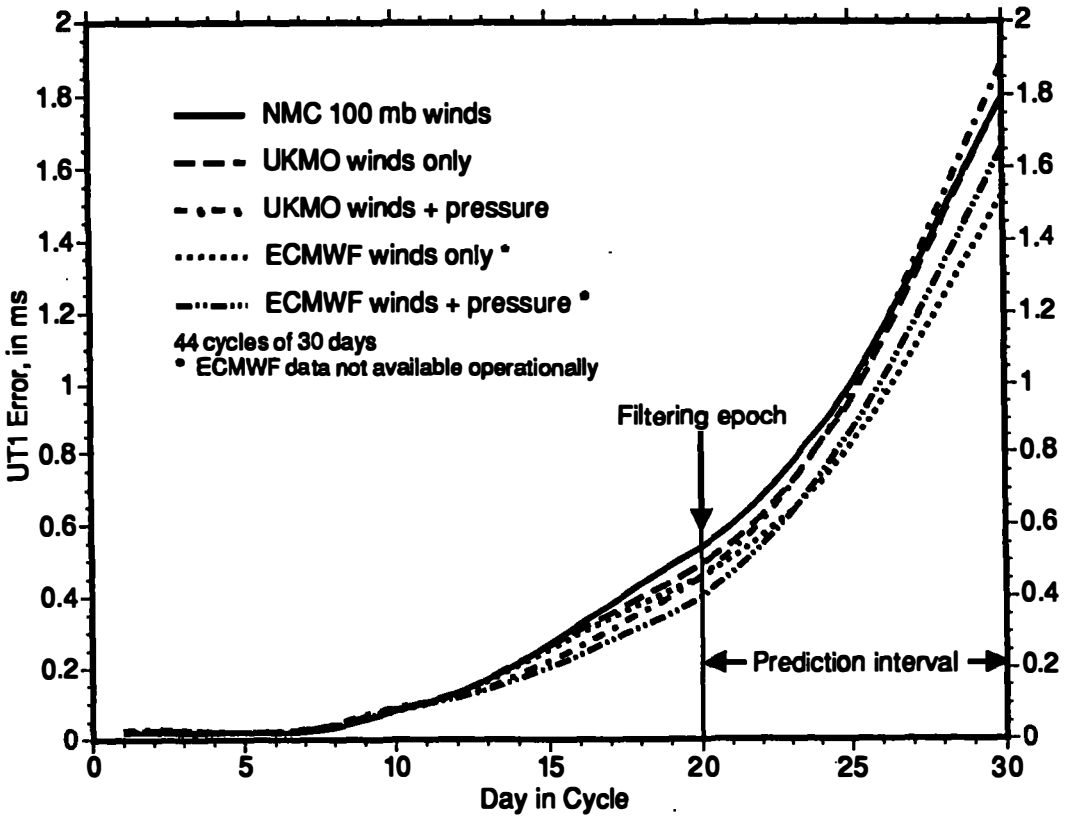

Fig. 7 RMS of filtered UT1 errors, comparing the AAM data provided by different centers.

detrimental effect on the UT1 predictions. Preliminary research, however, indicates that this behavior is time dependent, and that the pressure term has a uniformly beneficial effect on UT1 estimates and forecasts during the last year of the data time span, i.e., from the end of 1989 onwards.

The NMC now generates AAM forecast series based on winds up to 50 mbar, together with the pressure term with and without the inverted barometer approximation. Unfortunately, these have only been available since the end of 1989, so the long time series of predictions essential for an accurate statistical evaluation of these series' effectiveness do not exist. We have, however, taken a shorter time span of data, consisting of 11 cycles, to examine. Although these results are not as reliable as those obtained with a much longer time series, nevertheless they are valid over the time span considered and serve to illuminate the relative merits and disadvantages of the respective time series.

The UT1 predictions stemming from these AAM time series are shown in Figure 8. As expected, the inclusion of the atmosphere up to the 50 mbar level does improve predictions. In addition, incorporating the pressure term without the inverted barometer approximation shows a dramatically beneficial effect. Work is ongoing to ascertain whether this large improvement due to the pressure term is truly as robust as it appears. The substantial difference in the effect of adding the pressure term seen in Figs. 7 and 8 appears to be a result of the epoch under study, rather than a function of the meteorological center producing the pressure estimate. (Recall that Fig. 7 addresses the period from

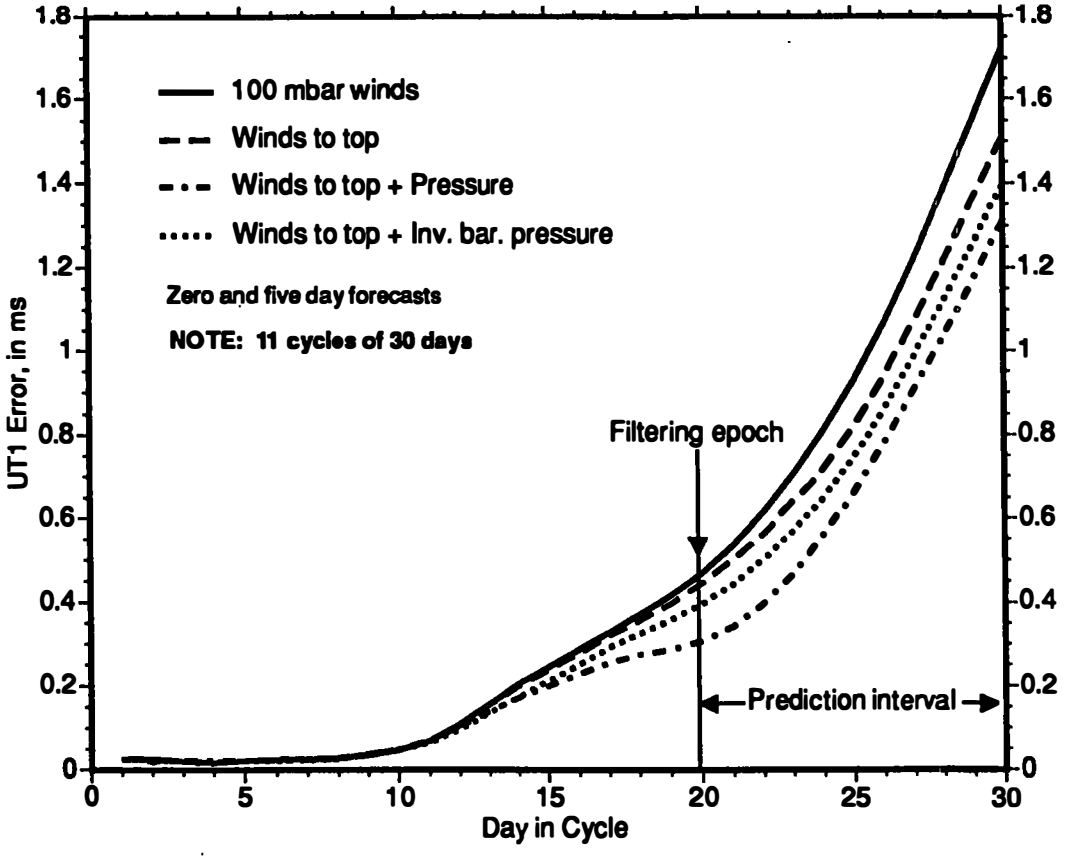

Fig. 8 RMS of filtered UT1 errors, comparing the different quantities provided by the NMC.

1987 through 1990, while Fig. 8 includes data only since the end of 1989).

Conclusions

For purposes of near-real-time estimation and short-term prediction of UT1 variations, meteorologically-determined atmospheric angular momentum information is an important adjunct to geodetic measurements of Earth orientation. Both zero-hour and five-day AAM forecasts have a significant impact on predicting UT1, with the zero-hour data showing great benefit after daily geodetic UT1 estimates become unavailable, and the five-day forecast data improving the prediction of UT1 beyond a few days in the future.

It is clear that TEMPO data are a critical geodetic data set for real-time knowledge of UT1 due to their rapid turnaround time. Also evident is the need to expedite the data processing of all techniques to achieve the shortest turnaround times possible. Even with rapid-turnaround geodetic data, however, AAM data are still of great benefit.

Our studies indicate that improvements can be made to the current operational KEOF procedures. Intercomparisons between the data from various centers indicate that the ECMWF data are the best to use as a proxy LOD data type. This is due, at least in part, to its integration of the atmosphere to the highest level (10 mbar) of any of the considered series. However, these data are not yet available in a rapid-turnaround mode. It is also not yet clear whether incorporating the AAM pressure term is the best procedure, but research is ongoing to clarify this issue. At least until the ECMWF data become available rapidly, the best data to use appear to be those from the NMC incorporating as much of the stratosphere as possible together with the AAM pressure term.

Acknowledgements

We wish to thank J. A. Steppe, R. S. Gross and L.-Y. Sung for helpful discussions, and S. Mulligan for software development. The work described in this paper was carried out by the Jet Propulsion Laboratory, California Institute of Technology, under contract with the National Aeronautics and Space Administration.

References

Barnes, R.T.H., Hide, R., White, A.A., and Wilson, C.A., "Atmospheric Angular Momentum Fluctuations, Length-of-Day Changes and Polar Motion," *Proc. R. Soc. London, Ser. A, 387*, 31-73, 1983.

Bell, M.J., Hide, R., and Sakellarides, G., "Atmospheric Angular Momentum Forecasts as Novel Tests of Global Numerical Weather Prediction Models," *Phil. Trans. Roy. Soc. Lond. A.*, in press, 1990.

Dickey, J.O., Freedman, A.P., Deutsch, K., Steppe, J.A., and Eubanks, T.M., "Short-Term Prediction of Length of Day Using Atmospheric Angular Momentum Data and the JPL Kalman Filter" (abstract), *EOS, Trans. A.G.U., 69*, 1153, 1988.

Eubanks, T.M., Steppe, J.A., Dickey, J.O., and Callahan, P.S., "A Spectral Analysis of the Earth's Angular Momentum Budget," *J. Geophys. Res. 90*, 5385–5404, 1985.

Freedman, A.P., Dickey, J.O., Steppe, J.A., Sung, L.-Y., and Eubanks, T.M., "The Short-Term Prediction of Universal Time and Length of Day Using Atmospheric Angular Momentum," in preparation, 1991.

Gross, R.S., Steppe, J.A., and Dickey, J.O., "The Running RMS Difference Between Length-of-Day and Various Measures of Atmospheric Angular Momentum," (paper presented at the A.G.U. Chapman

Conference on Geodetic VLBI: Monitoring Global Change,Washington, D.C., April 1991), this volume, 1991.

Hide, R. and Dickey, J.O., "Earth's Variable Rotation," *Science*, in the press, 1991.

IERS, *IERS Technical Note 2*, (Earth orientation and reference frame determinations, atmospheric excitation functions, up to 1988; Annex to the IERS Annual Report for 1988), Central Bureau of IERS—Observatoire de Paris, June, 1989.

Morabito, D.D., Eubanks, T.M., and Steppe, J.A., "Kalman Filtering of Earth Orientation Changes," in *The Earth's Rotation and Reference Frames for Geodesy and Geodynamics*, A.K. Babcock and G.A. Wilkins, eds, pp. 257–267, (Proceedings of the 128th Symposium of the International Astronomical Union, Coolfont, West Virginia, 20-24 October, 1986), Kluwer Acad. Publ., Dordrecht, Holland, 1988.

Munk, W.H., and Macdonald, G.J.F., *The Rotation of the Earth, A Geophysical Discussion*, Cambridge University Press, Cambridge, England, 1960.

Rosen, R.D., and Salstein, D.A., "Contribution of Stratospheric Winds to Annual and Semiannual Fluctuations in Atmospheric Angular Momentum and the Length of Day," *J. Geophys. Res.*, *90*, 8033-8041, 1985.

Rosen, R.D., Salstein, D.A., and Wood, T.M., "Discrepancies in the Earth-Atmosphere Angular Momentum Budget," *J. Geophys. Res.*, *95*, 265-279, 1990.

Rosen, R.D., Salstein, D.A., Nehrkorn, T., and Nelson, P.R., "Atmospheric Model Based Forecasts of Earth Rotation: Fourth Year Progress Report," internal report submitted to Jet Propulsion Laboratory, California Institute of Technology, January 31, 1991.

Atmospheric Excitation of the Earth's Annual Wobble: 1980-1988

B. Fong Chao

Geodynamics Branch, NASA Goddard Space Flight Center, Greenbelt, Maryland 20771

Andrew Y. Au

ST Systems Corp., 4400 Forbes Boulevard, Lanham, Maryland 20706

Global meteorological analyses from the European Centre for Medium Range Weather Forecasts (ECMWF) are employed to compute the atmospheric excitation χ of the polar motion for the nine year period of 1980-1988. Both the matter-component χ(matter) and the motion-component χ(motion) are computed; the former with and without the oceanic inverted barometer (IB) effect. It is found that χ(motion) contributes significantly to the total excitation χ overall and non-negligibly to the annual signal in χ, or the annual wobble excitation, in particular. Our results for the annual wobble excitation, in terms of the prograde component χ^+ and the retrograde component χ^- for January 1, are χ^+ = (16.8 mas, -93°) and χ^- = (15.6 mas, -98°) with IB, and χ^+ = (17.3 mas, -101°) and χ^- = (28.1 mas, -112°) without IB. These results are within the (rather large) range of previous estimates. The IB effect has a small impact on χ^+ whereas its impact on χ^- is considerable. The (better determined) prograde components χ^+ are then compared with the Kalman-filter combined solution from space geodetic observations: (17.3 mas, -61°). Although the amplitudes are nearly equal, large phase discrepancies exist between the atmospheric and the observed value. The resolution of this discrepancy awaits a better knowledge of the seasonal angular-momentum budget of the Earth's surface fluid elements.

1. Introduction

The rotation of the Earth varies with time. Its equatorial component in a geographic reference frame is known as the polar motion. Apart from a slow drift, the polar motion is observed to consist mainly of the Chandler wobble and an annual wobble. The Chandler wobble is a 14-month free oscillation of the Earth, continually excited by geophysical source(s) yet to be identified. The annual wobble, on the other hand, is a forced oscillation with a period of 12 months. It has long been recognized that changes in the atmospheric angular momentum (AAM), with power concentrated at seasonal periods, are a primary cause for the annual wobble [e.g., *Munk and MacDonald*, 1960]. Under the conservation of angular momentum, any AAM change is reflected in the (solid) Earth's rotation. Several authors in the past have calculated AAM time series, expressed in terms of the polar-motion excitation function χ, using meteorological data available at the time [*Munk and Hassan*, 1961; *Sidorenkov*, 1973; *Wilson and Haubrich*, 1976; *Daillet*, 1981; *Merriam*, 1982; *Wahr*, 1983]. The present paper is a revisit of the subject using modern meteorological data; the bulk of the results has been published in *Chao and Au* [1991a].

The main motivation is the following. Many of the previous estimates mentioned above for the atmospheric excitation of the annual wobble, when combined with *Van Hylckama*'s [1970] estimate of the contribution from the continental surface-water storage to χ, were found to account roughly

for the observed χ within (rather large) data uncertainties. This has led to the suggestion that the annual-wobble forcing mechanisms have been identified [e.g., *Wilson and Haubrich*, 1976; *Vondrdk and Pejović*, 1988].

However, two problems ought to be recognized:

(a) As summarized in Table 1 (symbols will be explained in Section 2), the previous estimates are in considerable discord. This is generally attributed to the large differences in the data sets that were analyzed. No post-1973 data have been used in these studies, and most of them relied heavily on data gathered during the first half of the century in the form of monthly means or seasonal differences. The inadequacy of these data has been repeatedly pointed out [*Wilson and Haubrich*, 1976; *Daillet*, 1981; *Merriam*, 1982; *Wahr*, 1983; *Gao and Sun*, 1987], and all authors agree in saying that more comprehensive data are necessary. In particular, lacking pertinent wind data at the time, most previous studies of the atmospheric excitation of the annual wobble only computed the "matter" term, χ(matter), while neglecting the "motion" term, χ(motion) (see below). Studies that did include χ(motion) did so by estimating an equivalent torque [e.g., *Wilson and Haubrich*, 1976; *Wahr*, 1982] and declared it to be small.

(b) In an analysis combining snow accumulation data from satellite remote sensing techniques and conventional data for rainfall, *Chao and O'Connor* [1988] have recently argued that *Van Hylckama*'s [1970] estimate is grossly inaccurate. The key consideration is the double-cancellation effect that is inherent in the continental surface-water excitation of the Earth's polar motion (a surface harmonic function of degree 2 and order 1) — namely, that between the Eastern- and Western-hemispheric components and that between the snow and rain components. As a result, a seemingly benign error in the hydrological data can be greatly magnified in χ. The fact that a data set appears reasonable in its seasonal and latitudinal dependence by no means guarantees a realistic χ estimate. *Chao and O'Connor* [1988] concluded from their computation that the continental surface-water storage plays only a rather minor role in the annual-wobble excitation. Recently, *Kuehne and Wilson* [1991] reached the same conclusion by way of a different approach and an independent hydrological data set.

This paper will use the meteorological data analyzed by the European Centre for Medium-Range Weather Forecasts (ECMWF) for the period of 1980–1988. The ECMWF and similar data sets have quickly found wide usage in geodynamics studies. For example, they have been used to link AAM fluctuations unequivocally with length-of-day variations on a wide range of time scales [e.g., *Rosen and Salstein*, 1983; *Eubanks et al.*, 1985; and many others]. They have explained some of the "rapid" polar motion [*Barnes et al.*, 1983; *Eubanks et al.*, 1988], which contributes to the excitation of the Chandler wobble. *Chao and Au* [1991b] have also used them to study variations in the Earth's gravitational field caused by the atmospheric mass redistribution.

2. Theory

The modern theory of polar motion excitation was developed by *Munk and MacDonald* [1960]. Subsequently, *Wahr* [1982] and *Barnes et al.* [1983] have given complete formulas for the excitation due to AAM. A review was given in *Chao and Au* [1991a].

The polar motion excitation is given in terms of the complex-valued, dimensionless excitation function $\chi \equiv \chi_x + i\chi_y$ in the geographical coordinates measured in radians, where the x, y, and z axes point to the Greenwich Meridian, 90°E Longitude, and the North Pole, respectively. The *observed* polar motion m is governed by:

$$\dot{m} = i\,\sigma\,(m - \chi) \tag{1}$$

where σ is the free Chandler frequency $2\pi/435$ day^{-1}. For convenience and to conform to geodetic convention, we will convert χ into milliarcseconds (mas): 1 mas = 4.847×10^{-9} radian,

corresponding to a distance of ~3 cm on the Earth's surface. Our analysis will consist of the following. We will solve for the "observed" χ from the observed m based on equation (1). This is a procedure of numerical deconvolution. The observed χ will next be compared with the atmospheric χ computed from global meteorological data. The importance of the AAM in the polar motion excitation can then be determined quantitatively, and the discrepancy can be assessed in terms of other possible geophysical causes.

For the atmospheric variations, χ consists of two physical terms: a "matter" term arising from the xz and yz products of inertia of the atmosphere, and a "motion" term from the relative angular momentum of the atmosphere [*Barnes et al.*, 1983]. Explicitly, in spherical coordinates,

$$\chi = \chi(\text{matter}) + \chi(\text{motion})$$

$$= \frac{1.00\,R^4}{g(C-A)} \int P \cos\theta \sin\theta\, e^{i\lambda}\, d\sigma + \frac{1.43\,R^3}{\Omega g(C-A)} \int (u\cos\theta + iv) e^{i\lambda}\, d\sigma\, dp \tag{2}$$

where R, g, and Ω are respectively the Earth's mean radius, mean surface gravity, and mean angular spin rate; C and A are the Earth's polar and equatorial moments of inertia; P is the surface air pressure; u and v are the eastward and northward components of the wind velocity. The integration for χ(matter) is over the unit sphere with surface element $d\sigma = \sin\theta\, d\theta\, d\lambda$ (θ and λ being the co-latitude and east longitude), while that for χ(motion) also includes the integration over vertical height in terms of the air pressure p. A hydrostatic profile for p has been assumed, and vertical motions are ignored. The factor 1.43 accounts for the Earth's rotational deformation, whereas the factor 1.00 allows additionally for the Earth's elastic yielding under surface loading [*Munk and MacDonald*, 1960].

Note that traditionally the polar motion excitation is given in term of the Ψ function [*Munk and MacDonald*, 1960]. Ψ differs from the χ function by terms involving the time derivatives of χ(matter) and χ(motion). *Gross* [1991] has shown that while Ψ is indeed with respect to the geographical reference frame, geodetic measurement of polar motion refers to χ. In other words, it is χ that is exciting the observed polar motion as expressed in equation (1). In the case of the atmosphere, the difference between Ψ and χ is rather small numerically, and its evaluation is susceptible to data noise. In fact, *Chao and Au* [1991a] neglected this difference, so that their Ψ function became identical to the χ function.

The response of the fluid ocean to the overlying atmospheric loading/unloading should be properly treated in evaluating (2). The measured P over the oceans applies directly only if the oceans were rigid. Otherwise it needs to be modified. In the extreme case where the ocean can react completely isostatically as an inverted barometer (IB), the effective P will be uniform over the ocean, varying only with time in accordance with the total mass change over the ocean. The implications of the IB hypothesis have been discussed at length by, e.g., *Merriam* [1982] and *Wahr* [1982]. Here, without sufficient knowledge about the behavior of the real oceans on the time scale of interest, we will do the computation both ways: with and without the IB effect.

3. Data and Computation

The ECMWF database that we use spans 9 years: 1980–1988. It consists of the geopotential height and wind velocity at seven sampling altitudes corresponding to pressure levels of 1000, 850, 700, 500, 300, 200, and 100 mb. The data are given twice daily at 00UT (Greenwich midnight) and 12UT (Greenwich noon) on a global grid of 2.5° latitude by 2.5° longitude. They have been pre-processed and interpolated onto a 2° latitude by 2.5° longitude grid [*Schubert et al.*, 1990]. Surface

pressure values have been derived at the mean elevation (0 m at the sea level) for each grid point, and the nominal wind velocity at altitudes lower than the mean elevation is set to zero.

The computation of χ(matter) only requires surface pressure data. That of χ(motion) involves an integration in altitude (see equation 2). The discretization of the altitude levels entails some numerical interpolation scheme, for which we simply choose a linear one (i.e., a trapezoidal integration). The integration is cut off at the altitude level of 100 mb as given, leaving out the stratospheric contribution (this will be discussed later). The horizontal integration over the

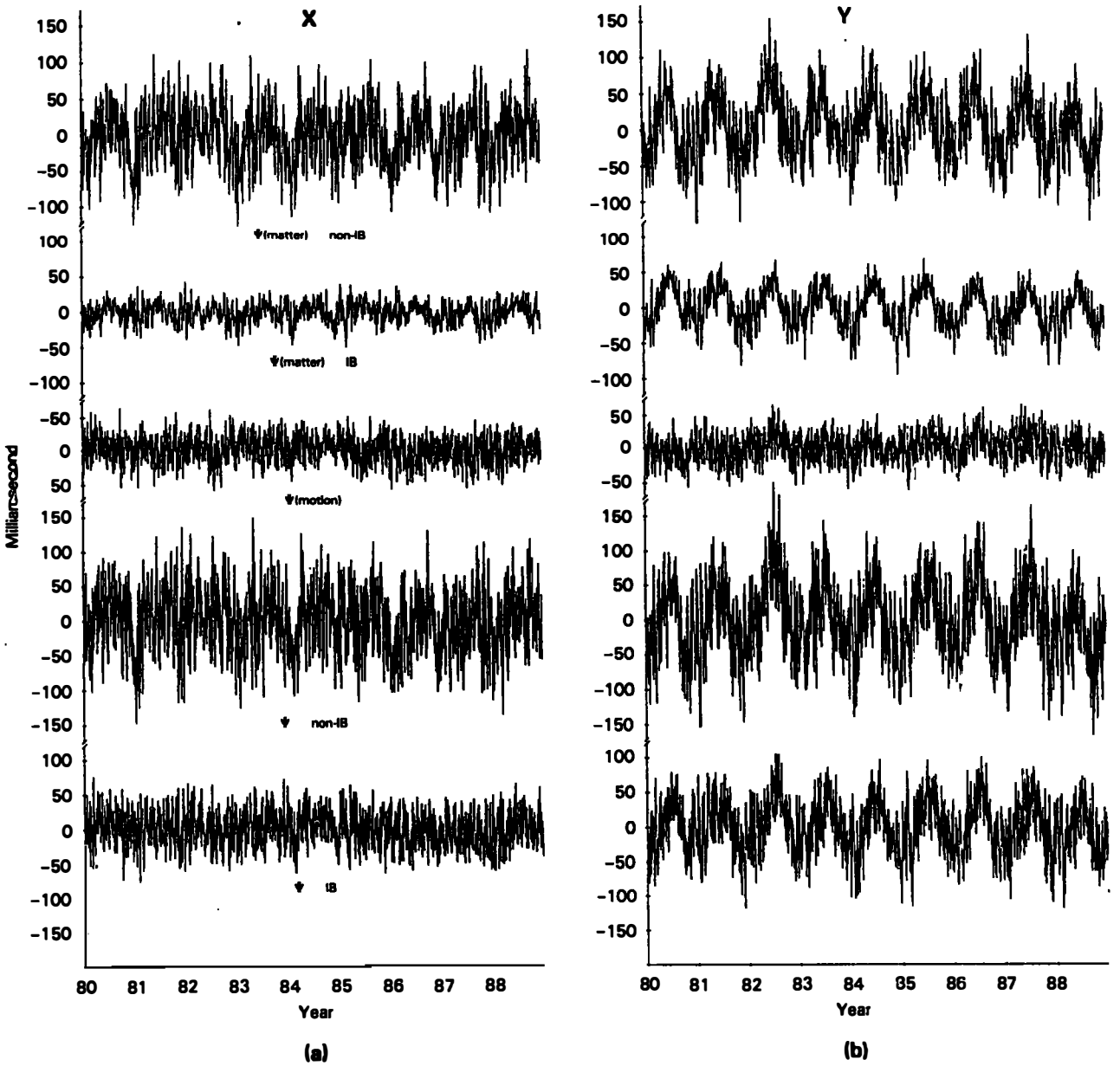

Fig. 1. (a) The x components of the atmospheric excitation of the polar motion for 1980–1988: χ(matter) (without and with the inverted barometer (IB) effect), χ(motion), and their sum χ (without and with IB effect). (b) Same as (a) but for the y components.

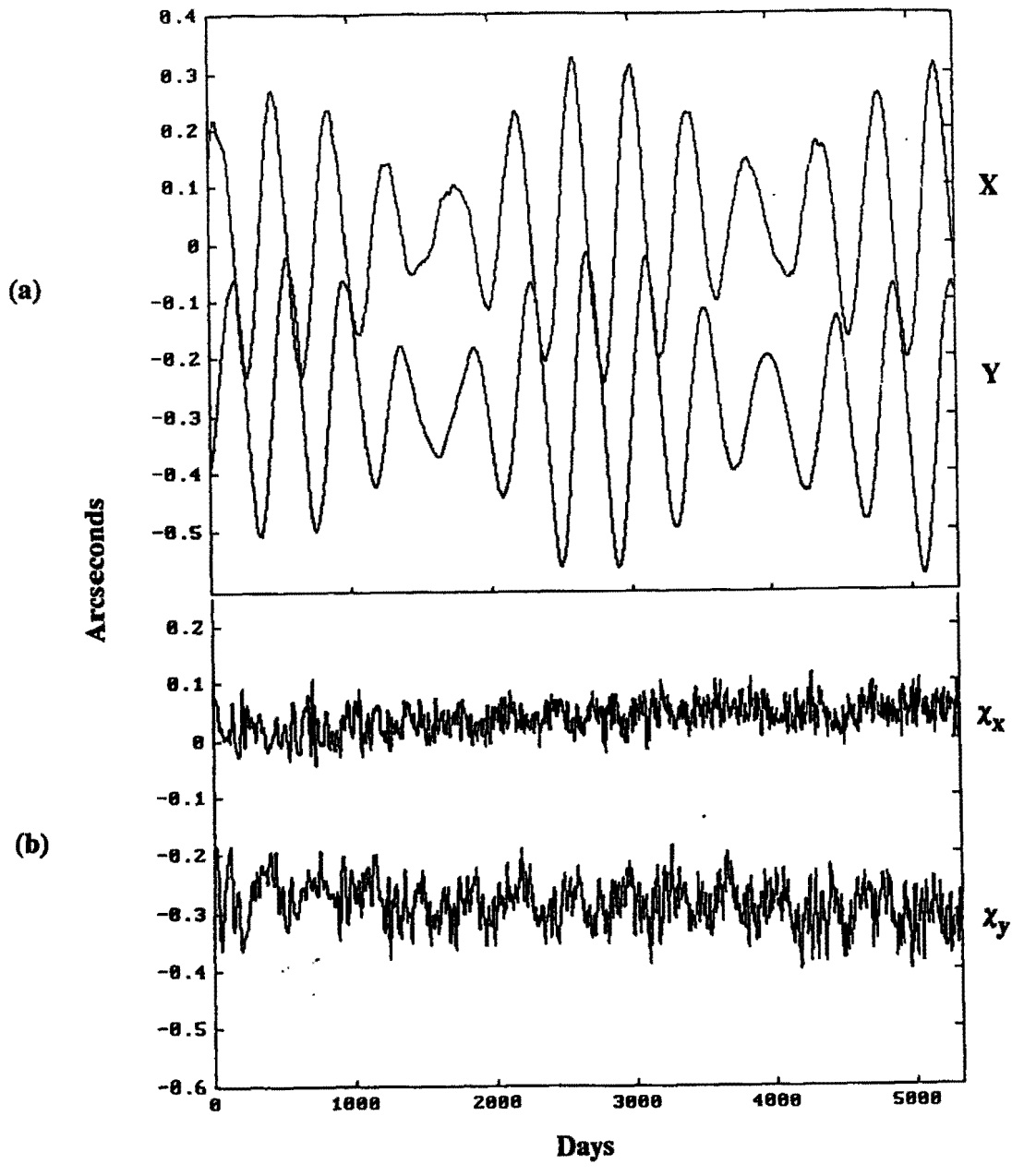

Figure 2. (a) Daily x and y values of the polar motion m (in arcseconds) obtained from a Kalman-filter combination of space geodetic observations, for the period of 1976/6/21.0 to 1991/1/18.0. (b) The excitation function χ obtained from (a) through numerical deconvolution.

geographical grid is also done with the trapezoidal rule.

Our results will be those computed for "mean daily" values obtained simply by averaging the 00UT and 12UT values. For χ(matter), the 00UT series and the 12UT series differ only slightly. There are, however, notable differences between the 00UT and the 12UT series for χ(motion): not only do the high-frequency fluctuations appear uncorrelated [as previously pointed out by, e.g., *Eubanks et al.*, 1988], the annual phases are found to be almost opposite in sign with the annual amplitude for 00UT larger than that for 12UT by only about 30 per cent. This leads to a much reduced mean-daily χ(motion) contribution to the annual-wobble excitation than either series individually. *Bell et al.* [1991] has given a lengthy discussion of this phenomenon and its probable

cause. How realistic our mean-daily series is with respect to the annual-wobble excitation depends on the amount of aliasing error in the twice-daily sampling. If the actual fluctuation is primarily diurnal, as appears to be the case [*Bell et al.*, 1991; see also *Vondrdk and Pejović*, 1988], then the error should not be serious. Given the present data, this is the best one can hope to achieve [see also *Brzeziński*, 1987].

Figure 1 shows our computed atmospheric excitation series for 1980–1988. The mean values have been removed. Several sets are shown in both x- and y-components: χ(matter)-non-IB (without the IB effect) and χ(matter)-IB (with the IB effect), χ(motion), and their sums χ-non-IB and χ-IB. Notice the significant contribution of χ(motion) to the total excitation χ overall (but subject to the above caveat in high-frequency χ(motion) estimate).

We have also computed the series for the individual Northern and Southern hemispheres (results not shown). In general the seasonal phases of the hemispheric components are rather different. The most notable hemispheric difference is in χ_y(matter): unlike the Northern Hemisphere, the Southern Hemisphere shows little seasonality and a much smaller amplitude (especially in the IB case), evidently because of the large area of the southern oceans.

The above computed χ series will be compared with those derived from observed polar motion. The polar motion has been observed by a variety of space geodetic techniques. Here we choose those obtained by lunar laser ranging, satellite laser ranging to Lageos, and Very-long-baseline interferometry (including IRIS, NAVNET and DSN). The measurements are combined by means of a Kalman filter into daily (averaged or interpolated) pole positions [courtesy of R. S. Gross]. The complete data set is displayed in Figures 2(a) and 3. The excitation series χ were obtained through a deconvolution of the polar motion data with a free (prograde) Chandler wobble having a natural period of 435 days and a Q value of 100. They are displayed in Figures 2(b) and 3. Note that the observations prior to about 1980 are much noisier and less dense. Figure 4 shows the power spectra, where the positive frequency gives the prograde component and the negative frequency gives the retrograde component.

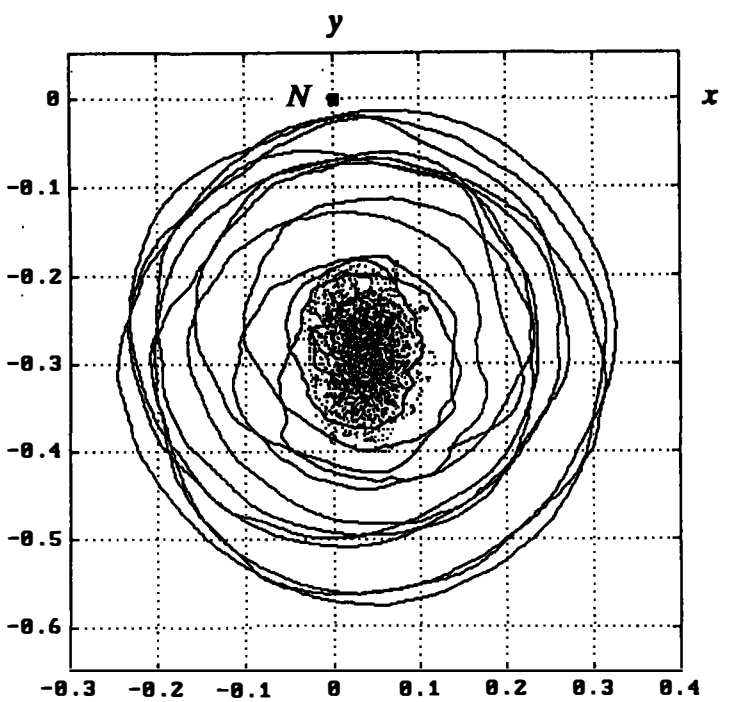

Figure 3. The solid curve shows polar motion m in units of arcsecond (same as Figure 2a but plotted as a 2-dimensional path). The cluster of points correspond to the excitation function χ given in Figure 2(b). N indicates the nominal North Pole, and x and y give the coordinate axes.

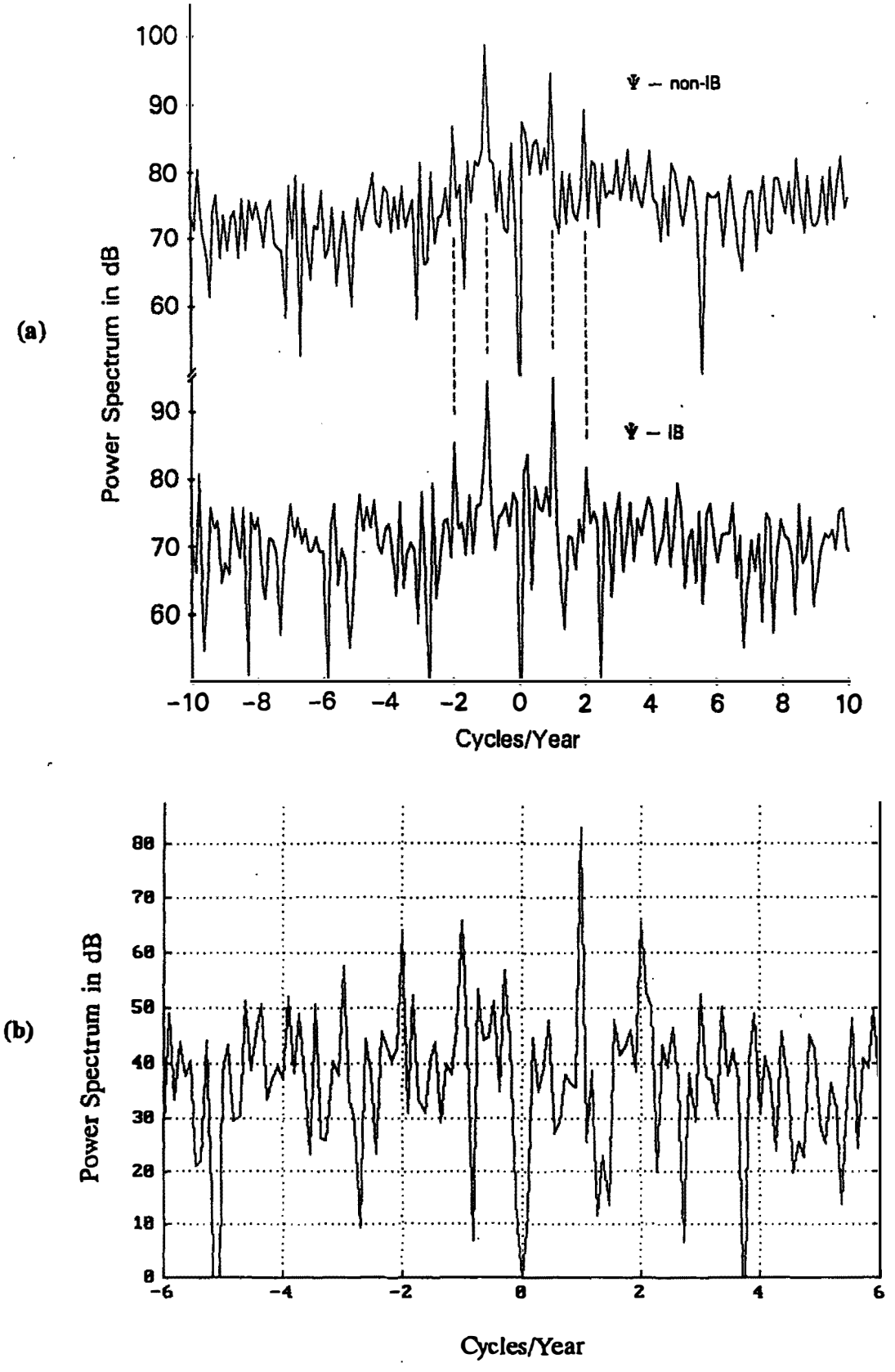

Figure 4. (a) Power spectrum of the atmospheric excitation of the polar motion, 1980–1988: without and with the inverted barometer (IB) effect (Figure 1). (b) Same as (a) but for the observed excitation function χ (Figure 2b).

4. Results and Discussion

This section concentrates on the strong seasonal signals, which are especially prominent in the y-components. Interannual variations are also evident, and a study of them with respect to El Niño episodes and the Chandler wobble excitation will be reported elsewhere.

Our task now is to extract the annual signals from the excitation series. Thus, for a given series, a composite "mean year" is first generated by a straight averaging of the nine years. Then a linear combination of an annual and a semi-annual sinusoid is fitted to the mean year series in a least-squares sense. The annual signals thus obtained are our results for the atmospheric excitation of the annual wobble. As is customary, they are converted from their x- and y-components into prograde and retrograde components, expressed in terms of their respective values χ^+ and χ^- for January 1 [*Munk and MacDonald*, 1960]. We do this for χ(matter) and χ(motion) individually as well.

Table 1 summarizes previous as well as our present estimates for the atmospheric χ^+ and χ^-. (Note that *Wahr*'s [1983] values have been reduced by a factor of 1.12 in order to be consistent with the others and so facilitate comparison. The factor 1.12 in *Wahr* was meant to account for the non-participation of the fluid core in the polar motion excitation). The estimates are given in the polar form: (Amplitude, Phase), where Amplitude is in units of milliarcseconds and Phase in degrees of east longitude for January 1.

Corresponding χ^+ and χ^- values from space geodetic observations (Figures 3 and 4) for the same period (1980-1988) are obtained following an identical procedure as above. The results are given at the bottom of Table 1 for comparison. For completeness, we also present our corresponding estimates with respect to the semi-annual terms in Table 2. However, it should be noted that only the prograde annual component, being close in frequency to the Chandler resonance, is well determined in the observations owing to its relatively high signal-to-noise ratio [*Wilson and Haubrich*, 1976]. The observed values for the retrograde annual term and the semi-annual terms may not be sufficiently accurate. Hence we shall focus here on χ^+ for comparisons.

The following facts from Table 1 are noted:

(a) Our present χ(matter) estimates, presumably the most reliable to date, fall within the (rather large) range of previous values despite large differences in the meteorological data sets that have been employed.

(b) Although smaller than χ(matter), the contribution of χ(motion) is not insignificant, particularly in χ^+. This provides the first quantitative qualification of the previous belief that χ(motion) only plays a minor role in the annual-wobble excitation.

(c) While its impact on the retrograde and the semi-annual components [for χ(matter)] is large, the IB effect has little impact on the prograde component χ^+. This fortuitous fact, presumably owing to the Earth's particular continent-ocean geography, makes comparisons of χ^+ practically free from our lack of knowledge about the true behavior of the oceans with respect to the IB response.

(d) Rather large discrepancies exist between the computed excitations and those observed. The discrepancy for χ^+, call it $\Delta\chi^+$, can be seen from Figure 5: it is somewhat larger than 10 mas with a phase angle (for January 1) of about 10°. Since the computed and observed amplitudes are nearly equal, $\Delta\chi^+$ arises solely from the large phase lead of the observed χ^+ of about 40° (corresponding to about 40 days in the annual cycle). Little of the latter can be attributed to uncertainties in the atmospheric phase estimates judging from the robustness (within a few degrees) evident in Table 1. Rather, it indicates the presence of other important, seasonal excitation sources at work.

The solar annual *Sa* tide, being zonal in its potential, does not have any appreciable impact on the polar motion: it gives rise to an excitation of no more than a fraction of 1 mas [e.g., *Lambeck*, 1988]. It does so through the oceanic tidal response; the solid Earth's response stays zonal and is orthogonal to, and hence has no effect on, the polar motion.

Table 1. A survey of previous along with our present estimates of the atmospheric excitation of the annual wobble, compared with those observed. Quantities are given in polar form: (Amplitude, Phase), where Amplitude refers to $|\chi^+|$ (for the prograde component) or $|\chi^-|$ (for the retrograde component) in units of milliarcseconds, and Phase is in degrees of east longitude for January 1.

Author	Type	χ^+	χ^-
	χ(matter) only		
Munk & Hassan [1961]	IB	(13.8, -102°)	(13.1, -94°)
Sidorenkov [1973]	IB	(19.2, -102°)	(19.2, -102°)
Wilson & Haubrich [1976]	IB	(11.4, -108°)	(11.2, -105°)
	non-IB	(17.3, -103°)	(27.4, -120°)
Daillet [1981]	IB	(14.1, -104°)	(15.5, -107°)
	non-IB	(18.4, -109°)	(23.9, -118°)
Merriam [1982]	IB	(11.5, -98°)	(11.5, -111°)
Wahr [1983]	IB	(19.9, -103°)	(18.6, -93°)
This study [1991]	IB	(13.3, -100°)	(14.4, -104°)
	non-IB	(14.0, -110°)	(27.2, -116°)
	χ(motion) only		
This study	—	(4.0, -70°)	(2.0, -51°)
	χ(matter) + χ(motion)		
This study	IB	(16.8, -93°)	(15.6, -98°)
	non-IB	(17.3, -101°)	(28.1, -112°)
This study	*Observed*	(17.3, -61°)	(7.1, -103°)

Table 2. Same as Table 1, but for our results with respect to the semi-annual components.

Type	χ^+	χ^-
χ(matter) only		
IB	(2.1, 54°)	(4.4, 96°)
non-IB	(7.7, 143°)	(5.1 135°)
χ(motion) only		
—	(1.8, 104°)	(2.2, 166°)
χ(matter) + χ(motion)		
IB	(3.6, 77°)	(5.6, 118°)
non-IB	(9.2, 136°)	(7.1, 144°)
Observed	(7.3, 93°)	(5.9, 123°)

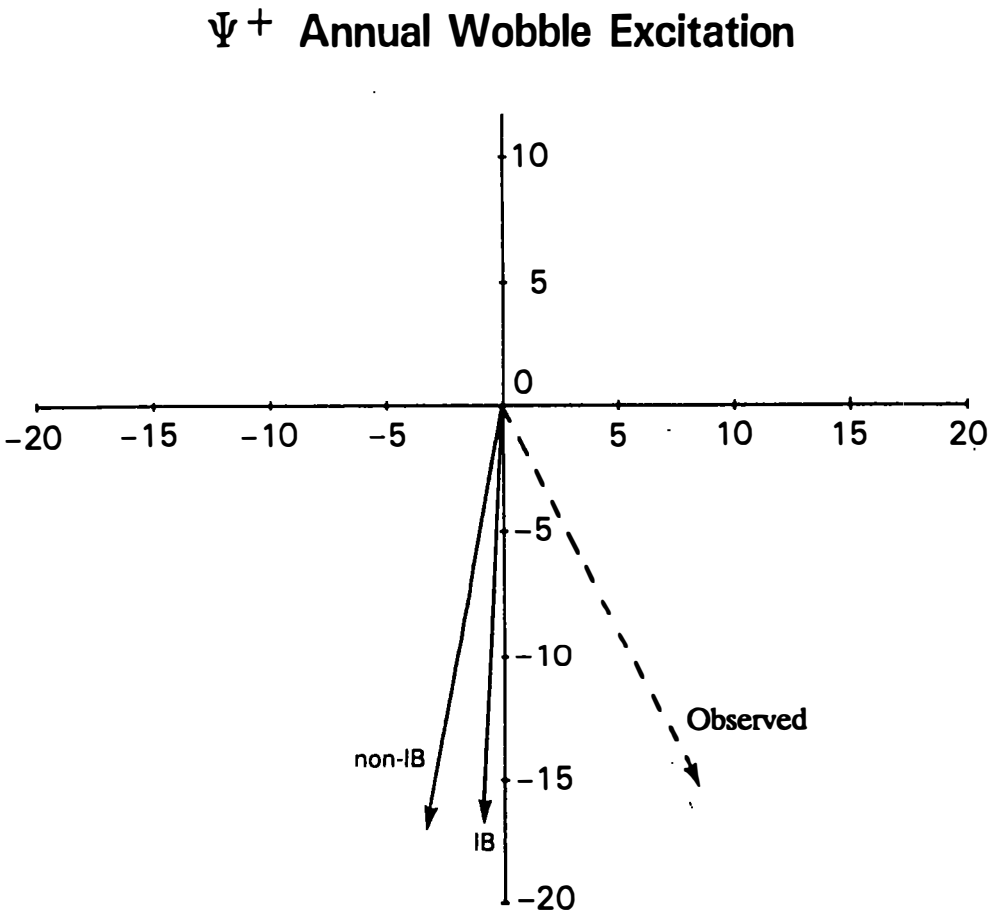

Fig. 5. The prograde component χ^+ of the atmospheric excitation of the annual wobble, 1980–1988, with and without the inverted barometer (IB) effect, compared with the observed. The vector pointing is for January 1 and the unit is milliarcsecond.

Among sources of meteorological origin that have been examined in the past, continental surface-water storage has been demonstrated to be insignificant (cf. Section 1): both *Chao and O'Connor* [1988] and *Kuehne and Wilson* [1991] obtained a χ^+ of less than 2 mas. The wind stressed sea-level excitation is on the same order of magnitude [*O'Connor*, 1980], whereas major lakes contribute even less [*Chao*, 1988]. These, by themselves, are all too small to account for $\Delta\chi^+$.

The result of *Chao and O'Connor* [1988] excluded Greenland and Antarctica, simply because their water balances are virtually unknown on either seasonal or secular time scales [cf. *Douglas et al.*, 1990]. Their contribution to the annual wobble, although potentially important as far as the total continental surface-water excitation is concerned, is probably insignificant with respect to $\Delta\chi^+$ judging from the polar location of Antarctica and the relatively small area of Greenland. The continental underground-water storage undoubtedly fluctuates seasonally but was also left out in the budget of the surface-water storage because of the lack of any global observations. This contribution, again, may not be significant for $\Delta\chi^+$, being a subset of the surface-water budget subject to the same cancellation effects (cf. Section 1).

As mentioned in Section 3, our result leaves out χ(motion) due to the stratosphere. The stratospheric winds have been shown to contribute significantly to the seasonal as well as interannual variations in LOD [*Taylor et al.*, 1985; *Rosen and Salstein*, 1985; *Chao*, 1989]. Their contribution to the annual wobble excitation is potentially significant although unlikely to be any larger than its tropospheric counterpart and therefore unlikely to account for $\Delta\chi^+$ in itself. This, however, remains to be determined [I. Naito, personal communication, 1990]. Finally, possible

contributions from seasonal variations in the ocean circulation have not been considered. Such global data are unavailable at the present time.

It may be that the combination of all the above can account for the observed $\Delta\chi^+$; but until future observations (on ground as well as from space) can provide the necessary data, the problem of the source of the annual-wobble excitation will remain only partially solved.

Acknowledgments. We are grateful to ECMWF for providing the meteorological data, and R. S. Gross for the polar motion data used in this analysis.

References

Barnes, R. T. H., R. Hide, A. A. White, and C. A. Wilson, Atmospheric angular momentum fluctuations, length-of-day changes and polar motion, *Proc. Roy. Soc. Lond., A 387,* 31-73, 1983.

Bell, M. J., R. Hide, and G. Sakellarides, Atmospheric angular momentum forecasts as novel tests of global numerical weather prediction models, in press, *Phil. Trans. Soc. Lond.,* 1991.

Brzeziński, A., Statistical investigations on atmospheric angular momentum functions and on their effects on polar motion, *Manuscripta Geodaetica, 12,* 268-281, 1987.

Chao, B. F., Excitation of the Earth's polar motion due to mass variation in major hydrological reservoirs, *J. Geophys. Res., 93,* 13811-13819, 1988.

Chao, B. F., Length-of-day variations caused by El Niño-Southern Oscillation and Quasi-Biennial Oscillation, *Science, 243,* 923-925, 1989.

Chao, B. F., and W. P. O'Connor, Global surface water-induced seasonal variations in the Earth's rotation and gravitational field, *Geophys. J., 94,* 263-270, 1988.

Chao, B. F., and A. Y. Au, Atmospheric excitation of the Earth's annual wobble: 1980-1988, *J. Geophys. Res., 96,* 6577-6582, 1991a.

Chao, B. F., and A. Y. Au, Temporal variation of the earth's low-degree zonal gravitational field caused by atmospheric mass redistribution, 1980-1988, *J. Geophys. Res., 96,* 6569-6575, 1991b.

Daillet, S., Atmospheric excitation of the annual wobble, *Geophys. J. Roy. Astron. Soc., 64,* 373-380, 1981.

Douglas, B. C., R. E. Cheney, L. Miller, R. W. Agreen, W. E. Carter, and D. S. Robertson, Greenland ice sheet: Is it growing or shrinking? Letter to *Science, 248,* 288, 1990.

Eubanks, T. M., J. A. Steppe, J. O. Dickey, and P. S. Callahan, A spectral analysis of the Earth's angular momentum budget, *J. Geophys. Res., 90,* 5385-5404, 1985.

Eubanks, T. M., J. A. Steppe, J. O. Dickey, R. D. Rosen, and D. A. Salstein, Causes of rapid motions of the Earth's pole, *Nature, 334,* 115-119, 1988.

Gao, B. X., and Y. X. Sun, The excitations of air mass distribution of 1970-1980 (in Chinese), *Acta Astron. Sinica, 28,* 46-51, 1987.

Gross, R. S., Correspondence between theory and observations of polar motion, *EOS, Trans. AGU, 72,* 94, 1991.

Kuehne, J. W., and C. R. Wilson, Terrestrial water storage and polar motion, submitted, *J. Geophys. Res.,* 1991.

Lambeck, K., *Geophysical Geodesy,* Oxford Univ. Press, 1988.

Merriam, J. B., Meteorological excitation of the annual polar motion, *Geophys. J. R. Astron. Soc., 70,* 41-56, 1982.

Munk, W. H., and G. J. F. MacDonald, *The Rotation of the Earth,* Cambridge Univ. Press, New York, 1960.

Munk, W. H., and E. M. Hassan, Atmospheric excitation of the Earth's wobble, *Geophys. J. Roy. Astron. Soc., 4,* 339-358, 1961.

O'Connor, W. P., Estimate of wind stressed sea level excitation of the Earth's annual wobble, *Geophys. J. Roy. Astron. Soc., 60,* 187-207, 1980.

Rosen, R. D., and D. A. Salstein, Variations in atmospheric angular momentum on global and regional scales and the length of day, *J. Geophys. Res., 88,* 5451-5470, 1983.

Rosen, R. D., and D. A. Salstein, Contribution of stratospheric winds to annual and semi-annual fluctuations in atmospheric angular momentum and the length of the day, *J. Geophys. Res., 90,* 8033-8041, 1985.

Schubert, S., C. K. Park, W. Higgins, S. Moorthi, and M. Suarez, An atlas of ECMWF analysis, *NASA/GSFC TM-100747,* 1990.

Sidorenkov, N., The inertia tensor of the atmosphere, the annual variation of its components, and the variations of the Earth's rotation, Izv. Acad. Sci. USSR: *Atmos. Oceanic Phys., 9,* 339-351, 1973.

Taylor, H. A., H. G. Mayr, and L. Kramer, Contributions of high-altitude winds and atmospheric moment of inertia to the atmospheric angular momentum-Earth rotation relationship, *J. Geophys. Res., 90,* 3889-3896, 1985.

Van Hylckama, T. E. A., Water balance and Earth unbalance, in International Assoc. Sci. Hydrology, *Proc. Read. Symp. World Water Balance, 92,* 434-444, 1970.

Vondrák, J., and N. Pejović, Atmospheric excitation of polar motion: Comparison of the polar motion spectrum with spectra of effective atmospheric angular momentum functions, *Bull. Astron. Inst. Czeck., 39,* 172-185, 1988.

Wahr, J. M., The effects of the atmosphere and oceans on the Earth's wobble - I: Theory, *Geophys. J. Roy. Astron. Soc., 70,* 349-372, 1982.

Wahr, J. M., The effects of the atmosphere and oceans on the Earth's wobble and on the seasonal variations in the length of day - II: Results, *Geophys. J. Roy. Astron. Soc., 74,* 451-487, 1983.

Wilson, C. R., and R. A. Haubrich, Meteorological excitation of the Earth's wobble, *Geophys. J. Roy. Astron. Soc., 46,* 707-743, 1976.

CURRENT AND FUTURE ACCURACY OF EARTH ROTATION MEASUREMENTS

Thomas A. Herring and Danan Dong
Massachusetts Institute of Technology, Cambridge, Massachusetts, 02139

ABSTRACT

The development of space-based geodetic techniques (very-long-baseline interferometry (VLBI), satellite laser ranging (SLR) and the global positioning system (GPS)) has allowed the complete rotational motion of the Earth to be measured with unprecedented accuracy and time resolution. With VLBI the full complement of orientation parameters of the Earth rotation i.e., the position of the rotation axis with respect to the crust and in inertial space, and changes in the rate of rotation can be measured with sub-milliarcsecond precision and with one-day (and at times less than one day) temporal resolution. We discuss the current state-of-the-art of these measurements and the likely improvements over the next 3 to 5 years. We will consider the effects of tidally-driven ocean currents on diurnal and semidiurnal Earth rotation changes; and the long-term definition and maintenance of a terrestrial reference frame in the presence on non-secular motions of the sites used to realize the frame. We also examine results from the recent International Earth Rotation Service (IERS) Global Positioning System (GPS) experiment to evaluate the possibility that GPS can provide a complementary system capable of monitoring Earth rotation (specifically polar motion) with accuracy and time resolution comparable to VLBI.

1. INTRODUCTION

During the last decade the introduction of space-based geodetic methods for the determination the rotation parameters of the Earth has lead to a dramatic improvement in both the accuracy and time resolution of these types of measurements over that offered by conventional astronomical measurements. Space geodetic methods are now sufficiently accurate that detailed geophysical studies can be carried with out these data (see, for review, *Wahr* [1988]). These data have been used to study the details of the angular momentum exchanges between the atmosphere and the solid Earth [*Eubanks et al.*, 1988; *Rosen et al.*, 1990], and to provide estimates of such geophysical quantities as the flattening of the core-mantle boundary [*Gwinn et al.*, 1986; *Herring et al.*, 1986]. Studies of the balance of angular momentum between the atmosphere and solid Earth have shown coherence between atmospheric angular momentum (AAM) changes and Earth rotation changes for periods between two weeks and two years with no detectable lag (< 3 days) between the time series. In order to better understand the nature of the coupling between the solid-Earth and the atmosphere, much higher temporal resolution is needed to determine if a lag exists or if some third component of the Earth system (such as the oceans) play a significant role in the angular momentum balance.

At the longer time scales appropriate for global change studies, stability of Earth rotation measurements becomes critical. For these studies, a well defined and stable coordinate system is needed for measuring the small signals expected to be generated by global warming, and measurable as changes in mean sea level and as crustal loading signals generated by water redistributions and changing ice-sheet loads.

Despite the current accuracy of Earth rotation measurements, there is a need for continued studies of alternative techniques for measuring Earth rotation and improvements to existing techniques. Some part of the loss of coherence between AAM and Earth rotation is due to the noise in the geodetic measurements. For long period studies, "noise" from local deformations of the sites in geodetic measurements will become the limiting error source. In the absence of detailed models for these local deformations, this latter class of problems can only be minimized by determining Earth rotations from a large number of stations distributed around the Earth.

In this paper we address some aspects of the issues raised above. In section 2, high frequency Earth rotation variations are discussed, and we examine the effects of ocean tidal currents which introduce diurnal and semidiurnal variations in the rotation of the Earth—a result predicted by *Yoder* [1981] and accurately computed for the M2 tide by *Baader et al.* [1983] and for the major diurnal and semidiurnal tides by *Broshe et al.* [1989]. High frequency variations in UT1 (after correction for ocean current effects) are also examined. In section 3, stability of Earth rotation measurements are examined firstly by considering the stability of radio telescopes themselves, and then by examining the stability of some specific baselines which have been measured numerous times over the last 10 years. In section 4, we consider new techniques for measurement Earth rotation by examining the data from the International Earth Rotation Service (IERS) intensive Global Positioning System (GPS) measurement program carried out in January and February, 1991 (GIG–91). We conclude by summarizing the current accuracy of Earth rotation measurements, and by speculating on future prospects for improvements.

2. HIGH FREQUENCY EARTH ROTATION MEASUREMENTS

Over recent years as studies of high frequency Earth rotation studies have been carried out it has become apparent that strong diurnal and semidiurnal signals exist in the sub-daily frequency range [*Dong and Herring*, 1990]. Analysis of these changes also indicates that these signals should be expected from the angular momentum associated with tidally induced ocean currents [*Baader et al.*, 1983; *Broshe et al.*, 1989]. The topics addressed here are discussed in more detail in *Herring and Dong* [1991], but we briefly outline the problem and show some the results from these studies.

In the presence of tidally driven variations, *UT1* can be written as

$$UT1 = \overline{UT1} + \sum_{i=1}^{n} (u_c^s)_i \cos(\theta_i - 2\gamma) + (u_s^s)_i \sin(\theta_i - 2\gamma) + \sum_{i=1}^{n} (u_c^d)_i \cos(\theta_i - \gamma) + (u_s^d)_i \sin(\theta_i - \gamma) \tag{1}$$

where $\overline{UT1}$ is the slowly varying part of *UT1* and the terms inside the summations are the semidiurnal and diurnal variations with γ denoting Greenwich Sidereal Time (*GST*) plus π (the π is added for consistency with Doodson's tidal arguments), θ_i is the slowly varying part of the tidal argument that depends on the lunar and solar orbits (here we choose to express θ_i as functions of Brown's fundamental arguments in the

same way as used for the nutation series), and the coefficients $(u_c^s)_i$, $(u_s^s)_i$, $(u_c^d)_i$, and $(u_s^d)_i$ are the cosine and sine terms (subscripts) of the semidiurnal and diurnal (superscripts) contributions to *UT1* from the *i*th term in the series. The summation extends of over terms in the periodic expansion of the Moon's and Sun's motions. In practice, it appears that only a small number of the terms are needed to account for all diurnal and semidiurnal variations with amplitudes greater than 1 μs.

The arguments θ_i are grouped such that for each θ_i with a positive time derivative there is also an argument with the oppositely signed derivative (see, for example, *Melchior* [1978]). By denoting such pairs of arguments by θ_j and θ_{-j}, equation (1) can be manipulated to the form

$$UT1 = \overline{UT1} + U_c^s \cos 2\gamma + U_s^s \sin 2\gamma + U_c^d \cos \gamma + U_s^d \sin \gamma \tag{2}$$

where the coefficients U_c^s, U_s^s, U_c^d, and U_s^d are given by

$$\begin{aligned}
U_c^s &= \sum_{j=1}^{n/2} [(u_c^s)_j + (u_c^s)_{-j}] \cos \theta_j + [(u_s^s)_j - (u_s^s)_{-j}] \sin \theta_j \\
U_s^s &= \sum_{j=1}^{n/2} [(u_c^s)_j - (u_c^s)_{-j}] \sin \theta_j - [(u_s^s)_j + (u_s^s)_{-j}] \cos \theta_j \\
U_c^d &= \sum_{j=1}^{n/2} [(u_c^d)_j + (u_c^d)_{-j}] \cos \theta_j + [(u_s^d)_j - (u_s^d)_{-j}] \sin \theta_j \\
U_s^d &= \sum_{j=1}^{n/2} [(u_c^d)_j - (u_c^d)_{-j}] \sin \theta_j - [(u_s^d)_j + (u_s^d)_{-j}] \cos \theta_j
\end{aligned} \tag{3}$$

These are the quantities determined when the amplitudes of UT1 signals with periods of one and two cycles per sidereal day (cpsd) are estimated from single 24-hour VLBI observing sessions. Figure 1 shows the estimates of the semidiurnal cosine and sine coefficients (U_c^s and U_s^s,) from the analysis of 6 years of VLBI data. Initially it appears that these signals are purely noise; however, this impression is an artifact of the spacing of the VLBI observing sessions (approximately once every 5-days) and the dominant signal being associated with the M_2 tide, which in this analysis scheme aliases to a period of 13.66 days. If instead of using 2 cpsd as the reference frequency for the estimating the quadrature components of the semidiurnal UT1 variations, we choose a frequency closer to that of the M2 tide, the period of the alias signal will be increased. (If the M_2 tidal frequency itself were used then the resultant coefficients would be constant. There would be still some time variation due to signals at non-M_2 tidal frequencies.) The result of such a "re-mixing" of the results shown in Figure 1 are shown in Figure 2. Now it is apparent that there is a strong signal present. (The remixing aliased 13.66 day period terms to approximately annual periods).

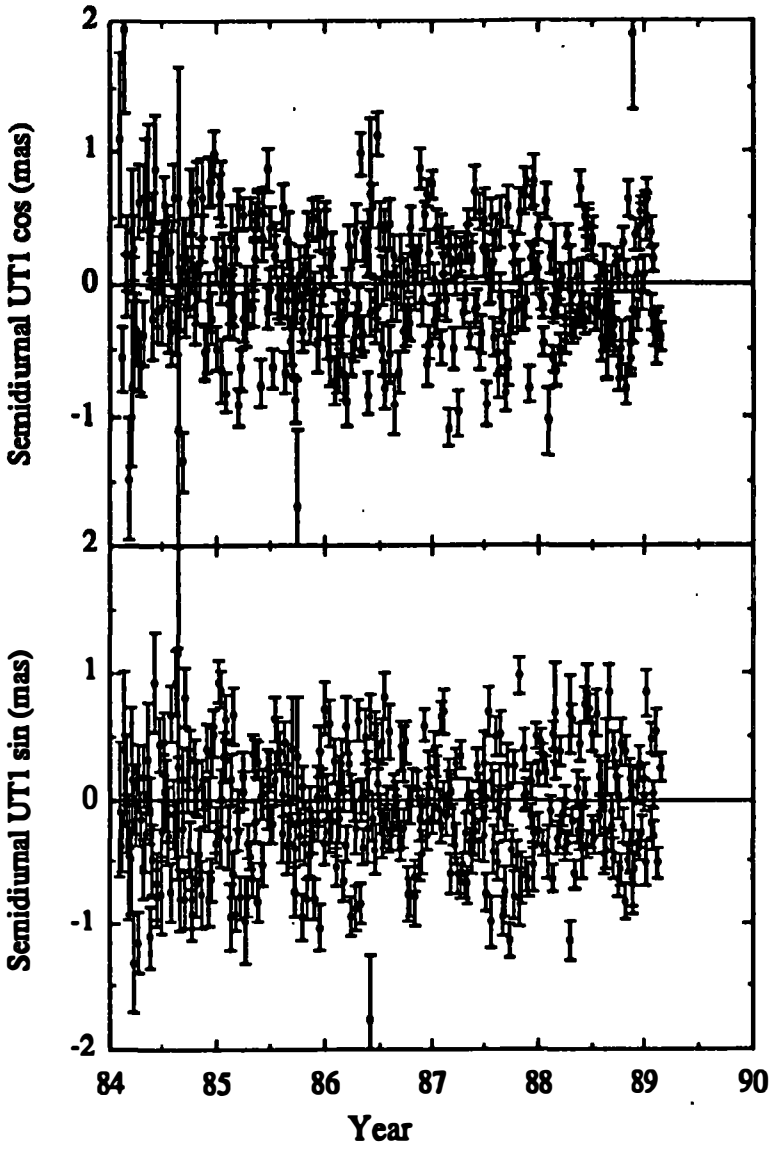

Figure 1. Observed values of the cosine and sine amplitudes of semidiurnal UT1 variations discussed in the text. These results were obtained from the analysis of 5 years of IRIS VLBI data.

Alternative approaches to assessing the nature of the signals imbedded in the time domain results are the computation of the power spectral density function (PSD) or the estimation of the quadrature components of the signals at the aliased frequencies associated with the major tides. The advantage of the PSD approach is that the presence of other signals in the tidal bands can be determined. As examples, Figures 3 and 4 show the PSDs of the semidiurnal and diurnal variations in UT1. Based on the 99.5% confidence intervals for these results, there are no significant signals at non-tidal frequencies indicating that estimation of coefficients at the tidal frequencies is consistent with the observed values. In Table 1, the amplitudes of the UT1 variations at the major tidal frequencies are given. (These results are based on the analysis of a larger data set than that used used to compute the PSDs in Figures 3 and 4, and therefore the uncertainty of these estimates is less than that implied by the PSDs.)

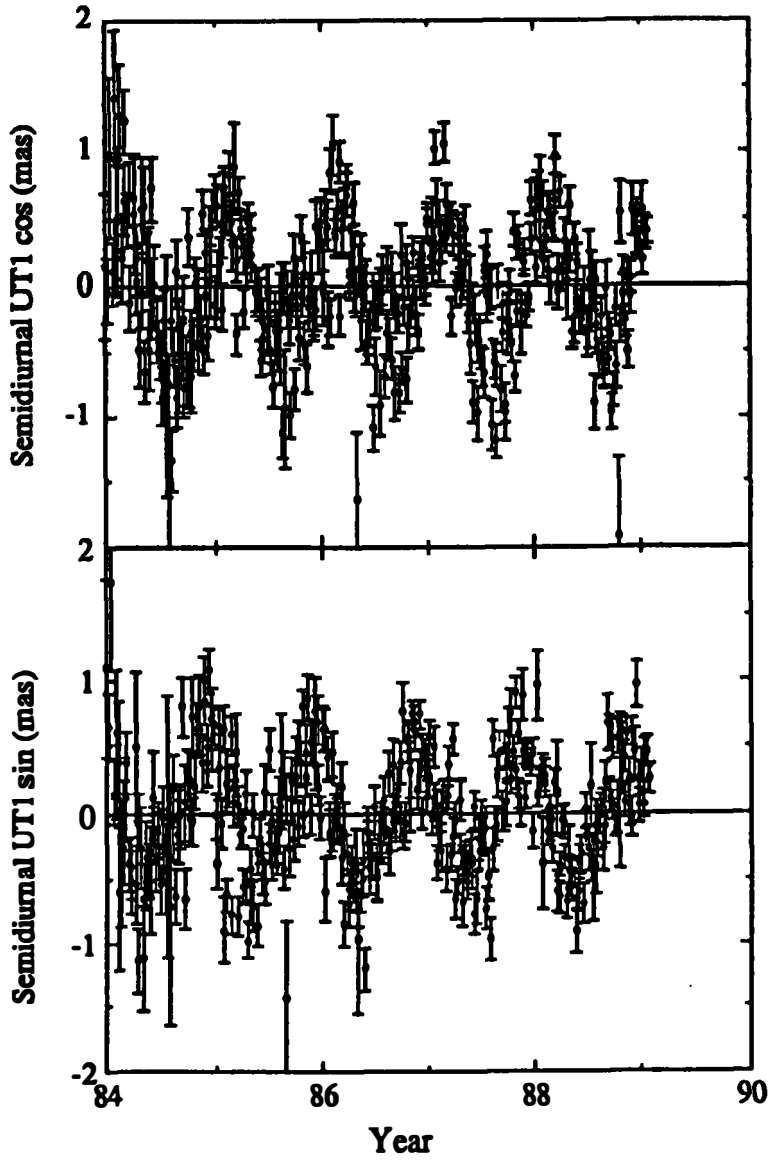

Figure 2. Esimates of the cosine and sine amplitudes of semidiurnal UT1 variations after remixing the signals so that the M2 tide would appear with approximately an annual signature. The remixed signals are given by $u_c = A(t)\cos(\phi(t)-2\pi\,\Delta f\,t)$ and $u_s = A(t)\sin(\phi(t)-2\pi\,\Delta f\,t)$, where $A(t)$ and $\phi(t)$ are the amplitude and phase of the signal shown in Figure 1 (one pair per experiment), t is time since an arbitary epoch, and Δf is the remixing frequency given approximately by (1/13.66 – 1/365.25) cycles per day.

In addition to estimation of near diurnal and semidiurnal signal using the spectral techniques just discussed, high frequency Earth rotation variations can studied through the use of intensive measurement programs which run continuously over extended intervals of time. One such session, the Extended Research and Development Experiment (ERDE) was carried out by NASA/GSFC in cooperation with NOAA/LES and Haystack Observatory in October 1989. This series of experiments which was originally scheduled to run continuously for about three weeks

but was interrupted by the Loma Prieta earthquake. Nevertheless, it produced some the best VLBI data ever collected. To analyze the subdaily variations in UT1 from these data, we modeled UT1 as a stochastic process and its time variation was estimated using the VLBI Kalman filter described in *Herring et al.* [1990]. Figure 5 shows the resultant differences between the Kalman filter estimates of UT1 and an a priori of table of values (IERS bulletin B) plus the tidal contributions to UT1 given in Table 1. No continuity conditions have been placed on the estimates between successive days of data and yet the sequence is continuous within the estimated uncertainties of about 20 μs. More surprising is that these results still show diurnal signals. The reason for the existence of these variations is still under investigation, but they could be related to unmodeled tidal displacements (presumably due to ocean loading) or to diurnal signals in atmospheric delay modeling errors.

Table 1. Estimates of the amplitudes of the tidally induced UT1 variations.

Tide Doodson Code	Period (hrs)	Alias period (solar days)	Fundamental Argument†						UT1 amplitude	
			l	l'	F	D	Ω	γ	cos (mas)	sin (mas)
165.555 (K_1)	23.94	∞	0	0	0	0	0	-1	0.15	0.24
163.555 (P_1)	24.07	182.62	0	0	2	-2	2	-1	0.02	-0.13
145.555 (O_1)	25.82	13.66	0	0	2	0	2	-1	-0.20	-0.38
135.655 (Q_1)	26.88	9.13	1	0	2	0	2	-1	-0.05	-0.07
275.555 (K_2)	11.97	∞	0	0	0	0	0	-2	-0.03	0.04
273.555 (S_2)	12.00	182.62	0	0	2	-2	2	-2	0.03	0.19
255.555 (M_2)	12.42	13.66	0	0	2	0	2	-2	-0.13	0.39
245.655 (N_2)	12.66	9.13	1	0	2	0	2	-2	-0.04	0.08

†The fundamental arguments are given by Brown's lunar theory and γ is Greenwich sidereal time $(GST)+\pi$. (The addition of π here is for consistency with the conventional definitions of tidal arguments.) The alias period refers to the period of the signals as seen in the VLBI analysis. These results were obtained from the analysis of 1171 VLBI experiments. The standard deviation of the estimates is 0.03 mas for all components.

From our studies of the high-frequency spectrum of the Earth's rotation, we conclude that much of the variation in the diurnal and semidiurnal bands is tidally driven, although there are still signals in the diurnal band which do not appear to be consistent with this explanation. We have shown that day-to-day continuity of UT1 can be determined with 20 μs uncertainties using existing (although probably the best) VLBI data. The coefficients of the tidally coherent variations in UT1 and polar motion can be determined with standard deviations of 0.03 mas, and these estimates can be obtained from the complete VLBI data set by determining the coefficients of the signals with precisely 1 and 2 cpsd and analyzing the spectral content of these signals.

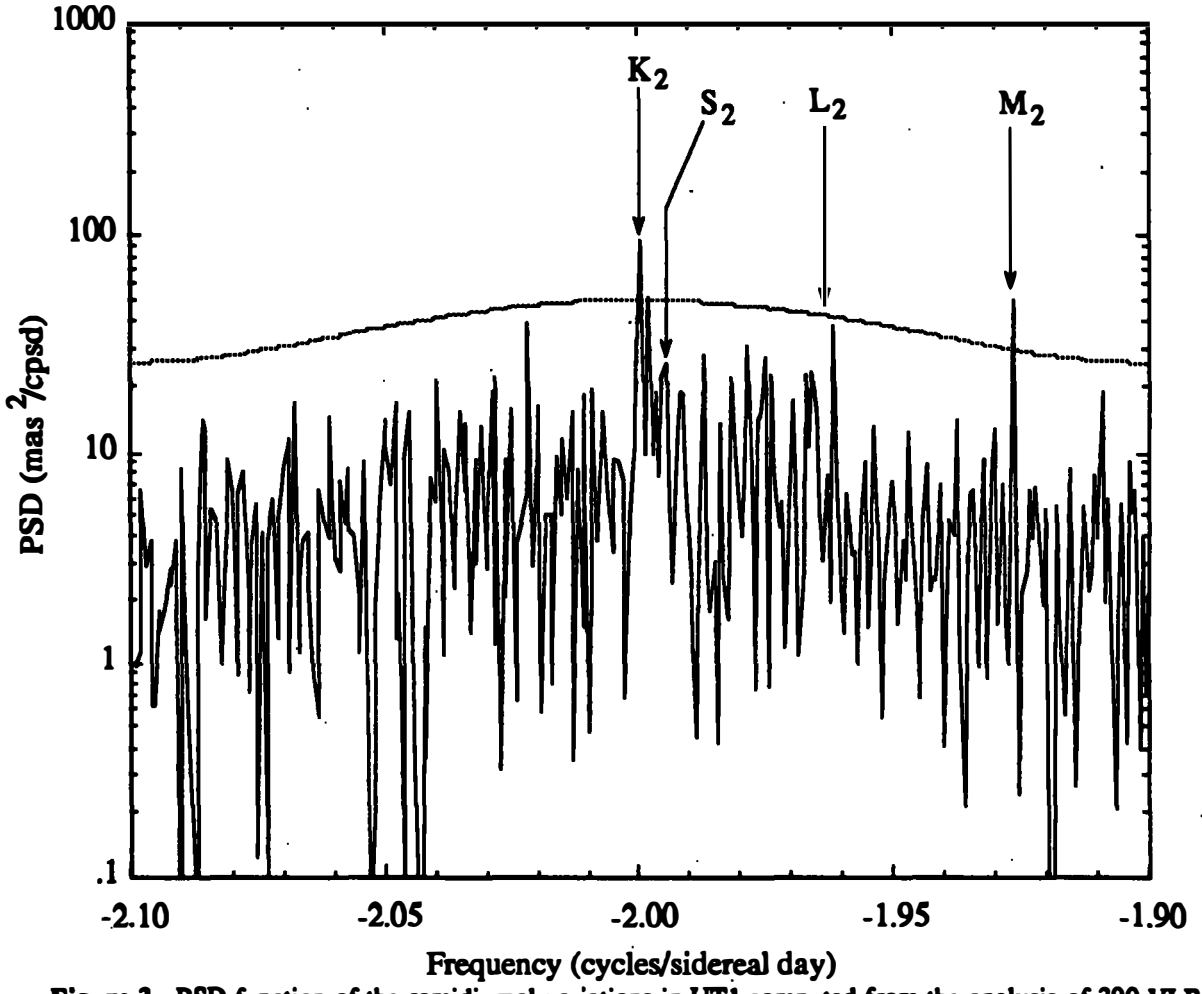

Figure 3. PSD function of the semidiurnal variations in UT1 computed from the analysis of 390 VLBI experiments carried out between January 1985 and February 1989. The dotted line gives the 99.5% confidence interval in the PSD. The fall off of the PSD and the confidence interval with increasing frequency away from -1 cpsd is due the Gaussian smoothing we have used to produce a uniformly spaced data set from the original non-uniformly spaced VLBI data. The full-width-at-half-maximum (FWHM) of the filter was 4 days. The 99.5% confidence interval gives the limit on PSD values expected from the original noise in the VLBI estimates of the UT1 diurnal components. The frequencies of the main tidal lines are also marked on the PSD.

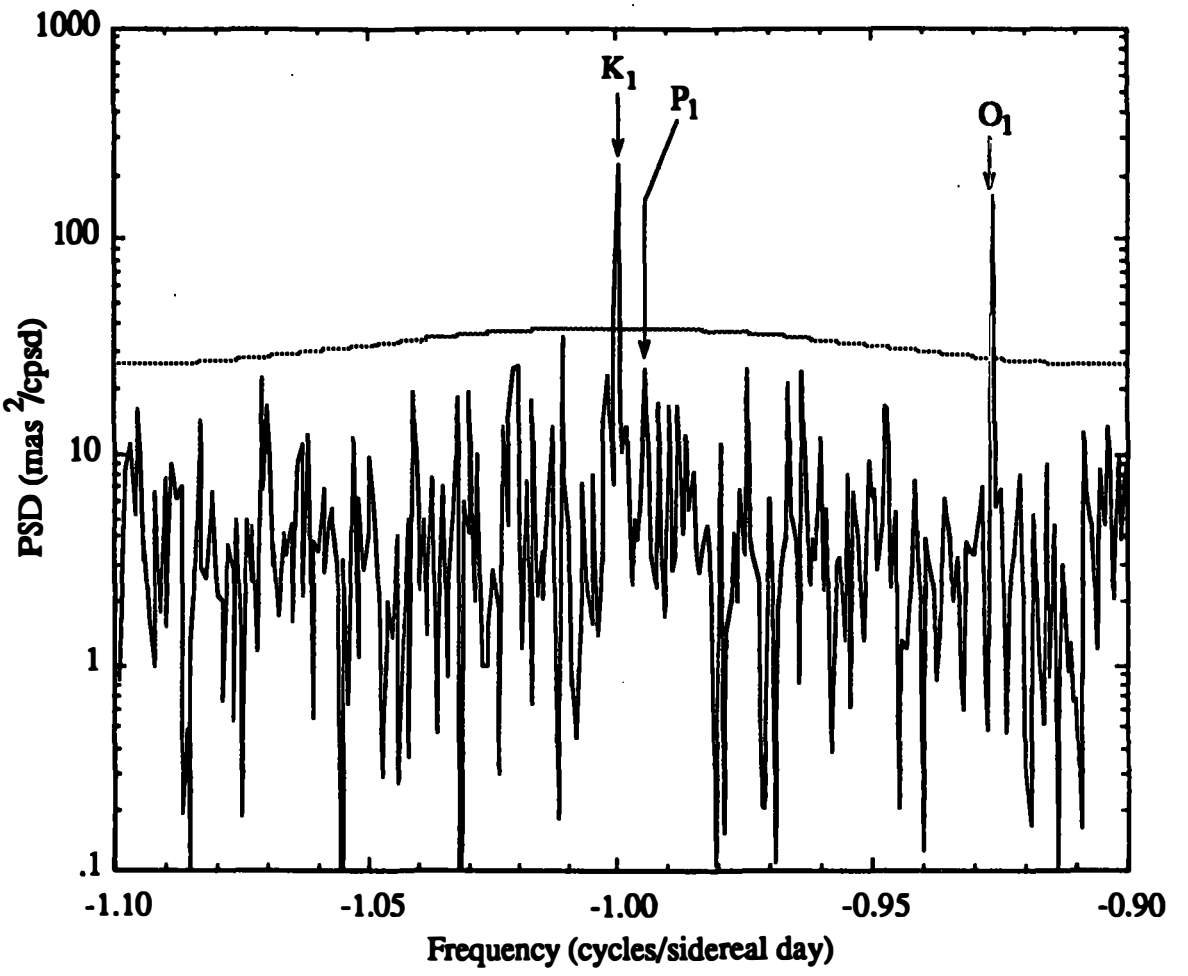

Figure 4. Similar to Figure 3 except the PSD of the semidiurnal variations of UT1 are shown.

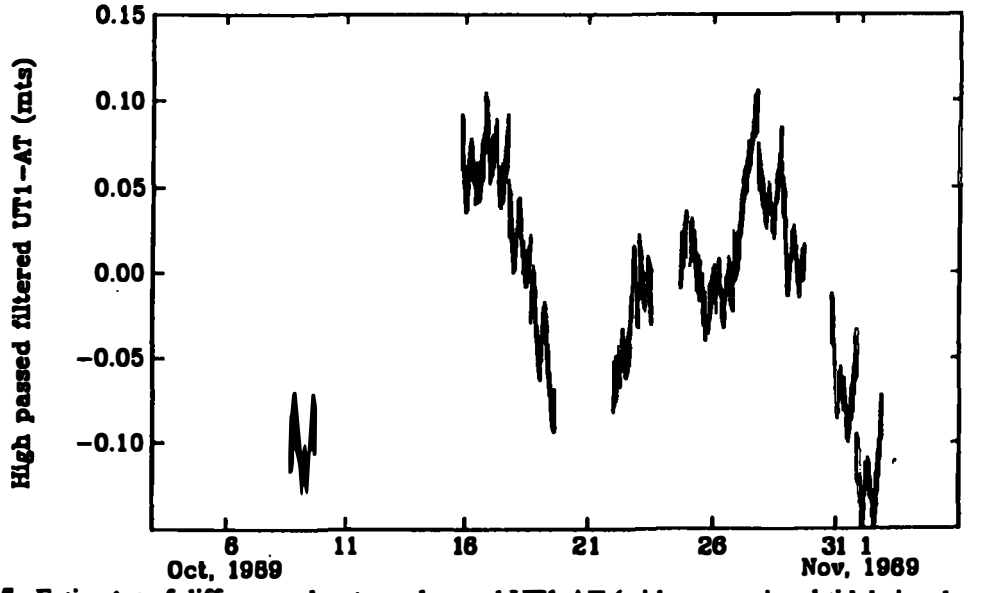

Figure 5. Estimates of differences bewteen observed UT1-AT (with conventional tidal signals removed) and IERS Bulletin-B obtained from the analysis of the Extended R&D VLBI experiments from October, 1989. For this analysis, UT1 was estimated as a stochastic process, and the ocean-current induced changes in UT1 (given in Table 1) were removed before filtering. The error bars shown are one standard deviation, and the data set has been decimated by a factor of ten for the plot.

3. STABILITY OF EARTH ROTATION MEASUREMENTS

For studying the slowly varying processes of global change, stability of the coordinate system in use becomes critical. We address here two issues associated with this stability: (1) the structural integrity of radio telescopes, and (2) the implied stability of the Earth itself inferred from variations in the chord distances between sites (this latter quantity is chosen since it is independent of the stability of current realization of the terrestrial coordinate system).

Over the past 15 years, the relative locations of two radiotelescopes in Westford, Massachusetts, have been determined 36 times using the very precise VLBI phase-delay observable [*Rogers et al.*, 1976; *Carter et al.*, 1980]. The results for the relative positions of the two telescopes are shown in Figure 6. The resolution of the phase delay ambiguities for the Mark III VLBI experiments (those results after 1980) was achieved by selecting the number of phase delay delay ambiguities that would bring the phase delay within one ambiguity of the group delay. Any remaining ambiguities (usually due to low signal-to-noise ratio group delays) were resolved visually. The analysis of the 15-year data set yields weighted root-mean-squares (WRMS) scatters about the mean locally-horizontal coordinates of 1.0 and 2.0 mm in the North and East directions, respectively. The vertical coordinate scatter over this same duration is 3.2 mm. The measurements made during the last decade yield WRMS scatters of 0.7, 0.8, and 2.3 mm, for the north, east and vertical coordinates, respectively. The estimates rates of change of the coordinates of the baselines are -0.12±0.04, -0.09±0.07, and -0.26±0.11 mm/yr for the 15 year analysis, and -0.11±0.05, 0.08±0.06, -0.15±0.15 mm/yr for the last decade. From these results, the maximum admissible rate of change of this baseline, either from geophysical causes or from telescope deformation, can be bounded to be less than 0.5 mm/yr (95% confidence interval) in all coordinate directions. We conclude from these studies that VLBI antennas, of at least of the structural quality of the pair in Westford, satisfy the necessary but not sufficient condition for being able to maintain a global reference system with submillimeter per year accuracy for intervals in excess of a decade. The results presented here are discussed in more detail in *Herring* [1991].

Long term stability of a global reference frame may be assessed by the examination of the time evolution of the baseline lengths. This quantity has the advantage of being essentially independent of the coordinate system used to analyze the data and is thus not affected by any existing problems in maintaining a stable global reference frame. In any well defined reference frame, the evolution of baseline lengths must be a known function of time, and therefore the correct prediction of the evolution of baseline lengths is a necessary, but not sufficient, condition for defining a global reference frame. The disadvantage of using length is that the contributions of each of the components of the baseline (i.e., the locally horizontal and vertical coordinates at each site in the baseline) can not be separately determined. We show in Figures 7 and 8 the evolution of two frequently measured baselines—Westford, Ma to Ft. Davis, Tx, and Westford, Ma to Wettzell, Germany. The first of these clearly shows large amounts of not-understood variations which at times deviate by as much as 40 mm from the mean. Analysis of these data (for example, by estimating the position of Ft. Davis in a reference frame defined by all of the other sites in the network) indicates that these variations are due mainly to height changes at Ft. Davis. Errors in

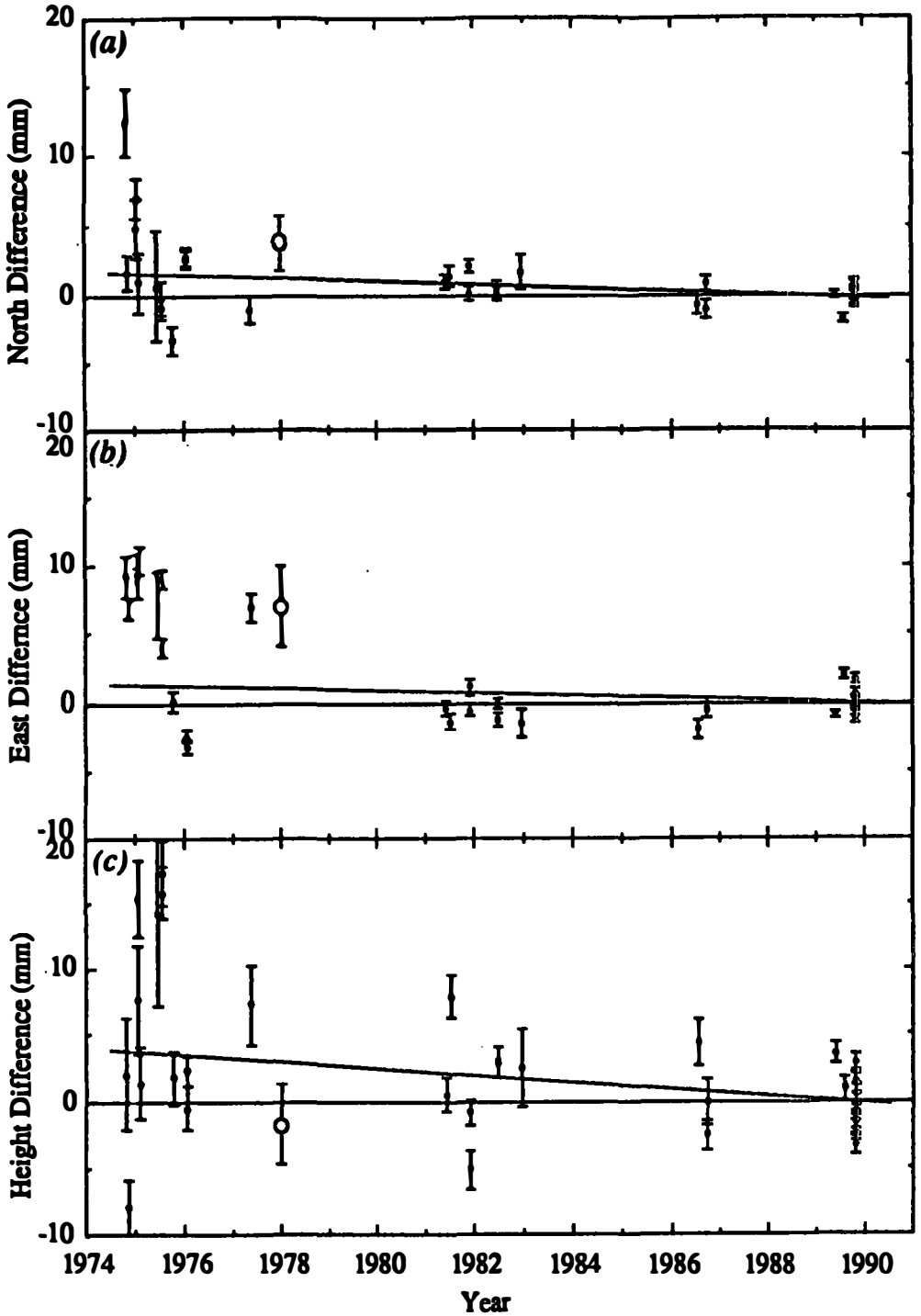

Figure 6. Deviations from the mean of the north, east and height components of the Westford antenna position relative to the Haystack antenna for the past 15 years (small closed circles). The large open circle is the conventional survey results given in *Carter et al.* [1981]. These results were obtained from the analysis of VLBI phase delay measurements. Group delay results for the Mark III experiments (those after 1980), show about twice the amount of scatter in the horizontal directions and about the same scatter in the vertical. The results in the 1970's used the Mark I VLBI system, and are taken from *Rogers et al.* [1978]. Differences are from the values determined from the combined analysis of the Mark III phase delay data in an analysis in which no data below 15° elevation angle were used and no differential atmospheric delay parameters were estimated. The resultant coordinates for Westford from this analysis were in a righted-handed cartestian, approximatley geocentric coordinate system, X = 1,492,208.5497 m, Y = -4,458,131.3288 m, and Z = 4,296,015.8751 m. In this system, the a priori adopted position of the Haystack antenna were X = 1,492,406.6910 m, Y = -4,457,267.3300 m and Z = 4,296,882.1020 m. The chord difference between the reference points of the two telescopes (see *Carter et al.* [1980]) is 1,239.3962 m.

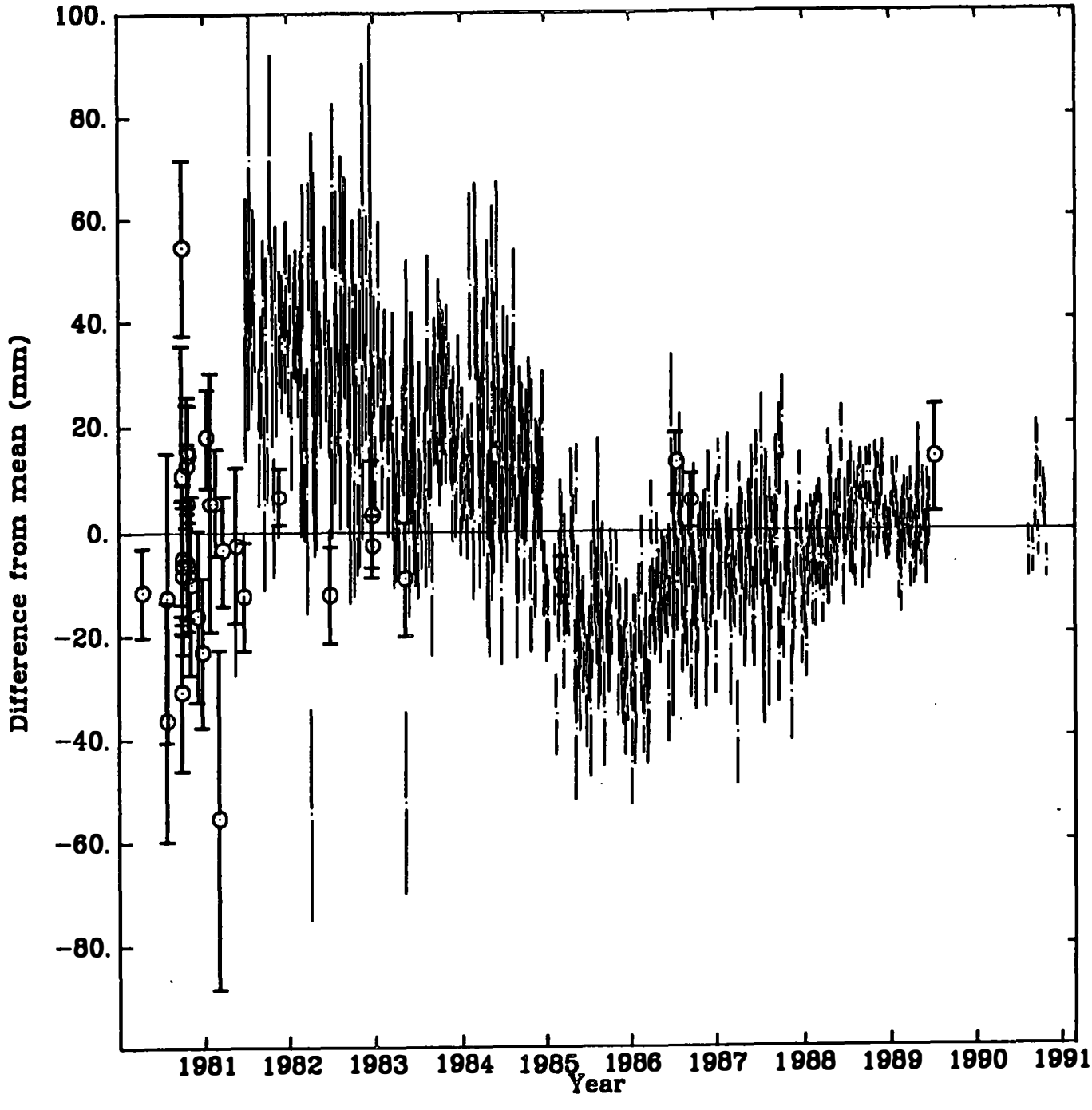

Figure 7. Evolution of the Westford–Ft. Davis baseline length shown as differences, with one standard deviation error bars, from the mean length. We have combined the measurements using the Haystack and Westford radio telescopes in this plot, with the Haystack values shown with open circles and horizontal tics on the error bars. The differential position of Haystack and Westford is known to the sub-millimeter level from phase-delay measurements between these two telescopes. The gap in the sequence between 1989 and 1990 occurs because the International Radio Interferometric Surveying (IRIS) Earth orientation service shifted its operation from Ft. Davis to Mojave (Ca) in mid-1989. In the summer of 1990, a mobile VLBI system was moved to Ft. Davis and its electronics van used (with the Ft. Davis antenna) to conduct the sequence of experiments shown. It is expected that these summer measurements will be continued until the Very Long Baseline Array (VLBA) antenna at the same location becomes operational within the next few years. For this baseline, about 25% of height changes project into the baseline length.

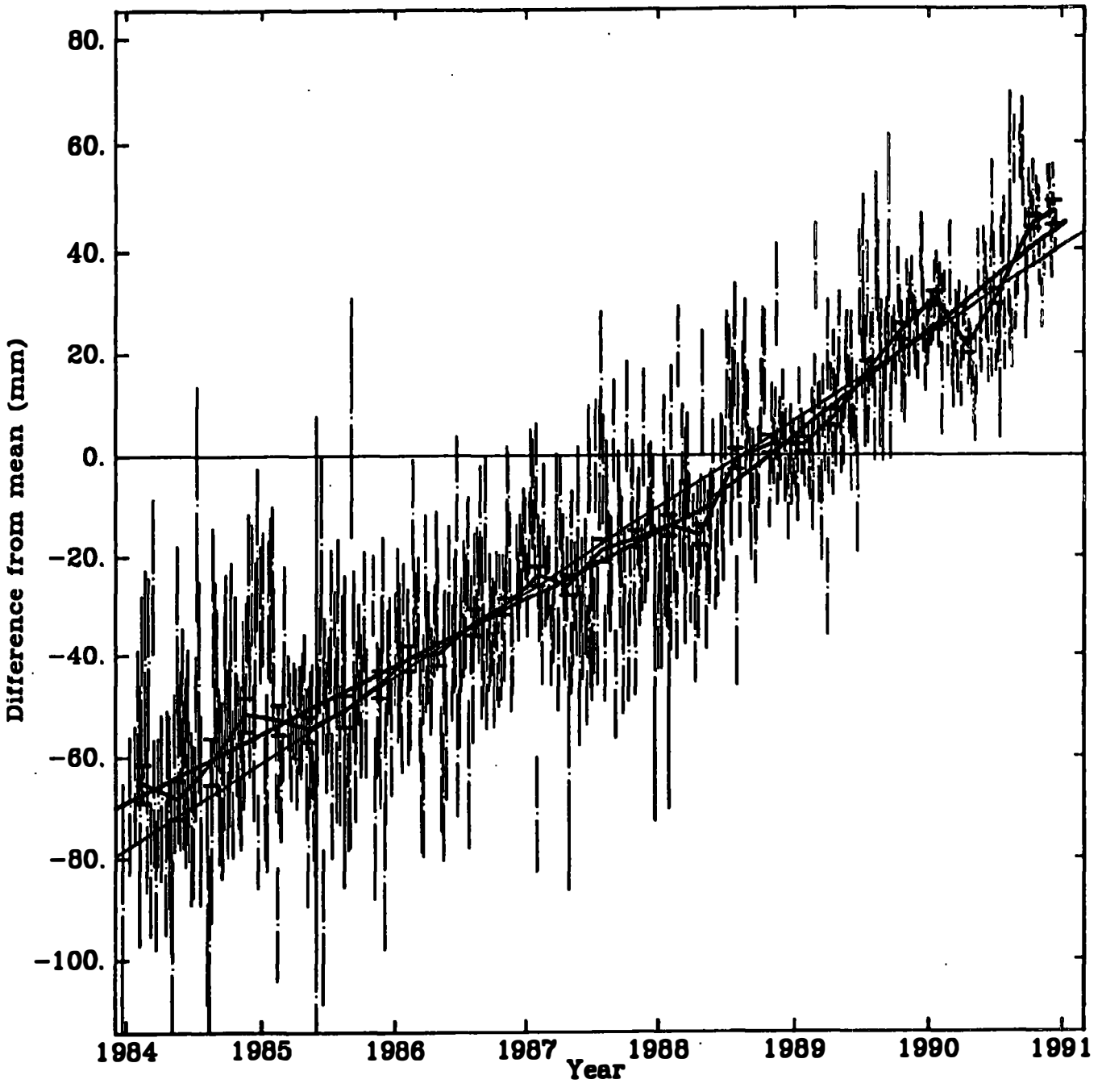

Figure 8. Evolution of the Westford-Wettzell baseline length shown as differences, with one standard deviation error bars, from the mean length. The dark solid squares with horizontal bars on the error bars give the independent 90-day averages of the baseline lengths. The light sloping line is the average rate of change of the baseline length based on 548 determinations (17.0±0.3 mm/yr). The weighted root mean square (WRMS) scatter about this best-fit rate is 12 mm. The two dark solid lines (one between 1984 and 1988.5, and the other between 1988.5 and 1991) show the estimates of the rates of change for these two intervals of data. For the first interval the rate is 13.4±0.6 mm/yr (346 measurements, WRMS scatter 13 mm); for the second interval the rate is 20.6±0.9 mm/yr (202 measurements, WRMS scatter 10 mm). No continuity condition has been applied across the division of data. The discontinuity is 1.2 mm. The NUVEL-1 estimate of the rate of change of this baseline is 18.8 mm/yr.

modeling atmospheric delays seem an unlikely cause for the variations because of the long duration of the variations and the absent of any strong annual signature in the results.

The other baseline (Figure 8) shows more subtle changes. Careful analysis of these data indicates that in about 1988 the rate of increase of the baseline length increased from 13.4 ± 0.6 mm/yr (346 measurements) to 20.6 ± 0.9 mm/yr (202 measurements), where the standard deviations are computed assuming independent data samples. In this case, we cannot easily rule out a possible atmospheric delay modeling error as the cause of the change in rate. After 1988, a distinct annual signal appears in the results, suggesting a deficiency in modeling the atmospheric delay. (The development of this annual signal is not unique to our analysis of this data. Similar signals are seen in both the NOAA Laboratory for Earth Sciences (LES) and NASA Goddard Space Flight Center (GSFC) analyses [D. S. Robertson and J. W. Ryan, private communications, 1991].) The growth of this annual signal may be related to the inclusion at about this time of more low-elevation angle observations. With lower-elevation angle observations included, the VLBI height estimates are more sensitive to atmospheric modeling errors (see e.g., *Herring* [1986b]), and the variations in Figure 8 may be due to the changing "projection" of atmospheric delay errors into baseline length. However, until the origin of the annual signal is isolated, it will not be known whether or not the change in rate is real or an artifact.

The analysis of both of the indicates that there may be unmodeled variations of station positions on times scales of decades which will complicate the definition of a stable global reference system. At this time it is not clear how much of the variations is local (i.e., coherent over distances of about 10 km) and how much represents much longer wavelength features. One method for addressing these issues by densifying the global network is addressed in the next section. Until such variations are understood it will be necessary to maintain the global reference frame with a relatively large number of stations so that no one site greatly affects the reference frame.

4. ANALYSIS OF THE IERS GIG–91 DATA

In January and February 1991, the International Earth Rotation Service (IERS) carried out a trial experiment to test the utility of the Global Positioning System (GPS) for determining variations in the Earth's rotation [*Freedman et al.*, 1990]. The experiment lasted 23 days and included over 80 stations. We present here a preliminary analysis of results obtained using data from collected at twenty globally distributed sites equipped with Rogue receivers [*Thomas*, 1988]. Rapid analysis of the Rogue data was possible for three primary reasons: (1) the data were collected and distributed in RINEX format [*Gurtner et al.*, 1989] within 50 days of the experiment by the coordination team at the Jet Propulsion Laboratory [*Yunck and Lockhart*, 1991]; (2) the Rogue measures precise pseudorange at both GPS frequencies, allowing nearly automatic removal of cycle slips from the carrier phase observations [*Blewitt*, 1990]; and (3) by processing carrier phase data from individual days and then combining in the geodetic results from the indivuals days in a sequential fashion, our processing software could handle efficiently a network of this size.

We carried out our analysis in two steps. In the first step we performed a least squares solution of the carrier phase observations for each of the 23 days separately using the MIT GPS Analysis Program (GAMIT). Tables (ephemerides) for the motions of the satellites were generated by numerical integation of initial conditions for two 8-day and one 7-day arcs, using as a force model lunar and solar perturbations, the GEM L2 gravity model truncated to degree and order eight, and a three-parameter model for non-gravitational forces. At the same time, we numerically integrated the partial derivatives (variational equations) for the satellites' positions and velocities with respect to the initial conditions and non-gravitational force parameters [*Ash* 1972]. Because we used a common orbital arc for each week of observations, we were able, at a later stage in the analysis, to allow stochastic variations of the satellites' motions from day to day or to constrain initial conditions such that one set of initial conditions was used for each satellite in each of the weekly orbital arcs. Using these satellite ephemerides, along with nominal values for the site coordinates, values of Earth rotation parameters interpolated from IERS Bulletin B, and standard expressions for the precession and nutation, we computed theoretical values for the carrier phase observations at both the L1 and L2 frequencies and formed residuals (observed – computed) for each station-satellite combination. We then combined these "one-way" residuals as double differences (between satellites and between sites) in a least squares analysis using the algorithm described by *Schaffrin and Bock* [1988]. Our "observable" was the linear combination (LC) of L1 and L2 that eliminates the inverse-squared-frequency part of the dispersive delay due to the ionosphere. The least squares analysis of each day's data was performed with weak constraints on all of the estimated parameters in order that the adjusted values of the parameters along with their full variance-covariance matrix could be used as input for the second step in our processing.

In the second step we combined the adjustments and variance-covariance matrices from all 23 days using GLOBK, a Kalman filter developed for the combination of VLBI experiments (see *Herring et al.* [1990] for description of the basic algorithms used). At the time of the analysis, we did not know precisely where the GPS receivers were located and therefore we estimated all site positions except for the longitude of the receiver located at Algonquin, Ontario. To define the orientation of the coordinate system, we held the pole position and UT1-AT on the first day fixed at the IERS Bulletin B value. For succesive days, we estimated the pole position and UT1 variations as random walk stochastic processes with the power spectral density of the white noise driving the random walk (see *Herring et al.* [1990]) set such that changes in the orientation parameters were constrained to ±10 mas per day (one standard deviation). Since these parameters were determined to less than 0.5 mas for each day of data, the weak constraint imposed by the random walk effectively allowed independent estimates of the orientation parameters from each day of data. During the IERS campaign, five of the GPS satellites were being eclipsed by the Earth (PRN's 6, 12, 15, 17, 19). For these satellites, we treated the satellite state vector (initial Cartesian position and velocity) as a random walk with the stochastic process noise set such that the position and velocity were allowed to change each day by ±10 m and ±1 mm/sec respectively. These constraints were sufficiently weak that these orbits were effectively treated as single-day arcs. The orbits of the remaining satellites were treated in two different ways. In one analysis, we treated the state vector of each satellite orbit as a deterministic parameter, and estimated one state

vector, along with a direct radiation pressure scaling factor and a Y-bias scaling factor, for each of the near weekly arcs. In the other analysis, we allowed the state vector of all non-eclipsing satellites to vary as a random walk during each of the weekly arcs such that the state vector (referred to a common epoch) could change by 100 mm/day and the velocity by 0.1 mm/day. Figures 9 and 10 give the estimates of the differences, relative to IERS Bulletin-B, of the pole position and UT1-AT obtained from these two analyses. For comparison, we also show our estimates of the Earth orientation parameters obtained from the analysis of the IRIS VLBI data collected during this interval. (IERS Bulletin-B is constructed from a smooth combination of IRIS VLBI data and Satellite Laser Ranging results with approximately equal weights, and therefore does not perfectly track the VLBI results).

Overall the agreement between the VLBI estimates and the GPS estimates of the pole position variations is impressive. For both of the analyses, the root-mean-square (RMS) difference between the VLBI pole position estimates and the GPS results interpolated to the epoch of the VLBI determination is less than 1 mas after a mean difference is removed. (The mean difference arises because we have made no attempt to align the GPS and VLBI coordinate systems.) The analysis which allowed stochastic variations in all orbital parameters agrees best with the VLBI solution, and also shows the smoothest variation of the pole position estimates, suggesting that even for the non-eclipsing satellites the dynamic models are not adequate for accurately representing the orbits of the GPS satellites. This conclusion is similar to that reached by *Lichten and Bertiger* [1989]. The comparison of UT1 between VLBI and GPS is far less satisfactory. While there are some hints that both systems are seeing similar signals (i.e., each have local minimum and maximum at the same time), the GPS results appear to be dominated by long-period (relative to a few days) effects which cause large drifts between the VLBI and GPS results. The comparison is further complicated by the "resetting" of the UT1 origin at the beginning of each orbital arc; since the arcs are 7–8 days long, there are only one or two VLBI determinations per orbital arc. Unlike the comparisons of pole position estimates, for UT1 the more constrained orbital solution seems to agree better with VLBI. It is clear that more analysis is needed to understand the effects of orbit modeling errors on the determination of UT1 and pole position from GPS data.

5. CONCLUSIONS: CURRENT ACCURACY AND FUTURE PROSPECTS.

Comparison of recent Earth-rotation data sets shows agreement between independent estimates of ~1 mas for pole position and ~0.1 ms for UT1 (although more strictly usually length of day is compared). Recent comparisons of Earth rotation parameters from simultaneously running, but independent, VLBI networks have shown RMS differences of ~0.3 mas for pole position and ~0.02 ms for UT1 determinations [*Eubanks*, 1991]. The recent results we have presented here show RMS differences between pole position estimates obtained from the analysis of VLBI and GPS data of less than 1 mas. The results from research and development VLBI experiments have yielded statistically determined standard deviations for pole position estimates of 0.1 mas and for UT1 of 0.01 ms; however the accuracy of such determinations is difficult to assess since there are no other techniques yet available of comparable precision. The tidally-coherent signals in Earth rotation parameters are determined extremely accurately by VLBI with typical uncertainties for the amplitudes of the coherent

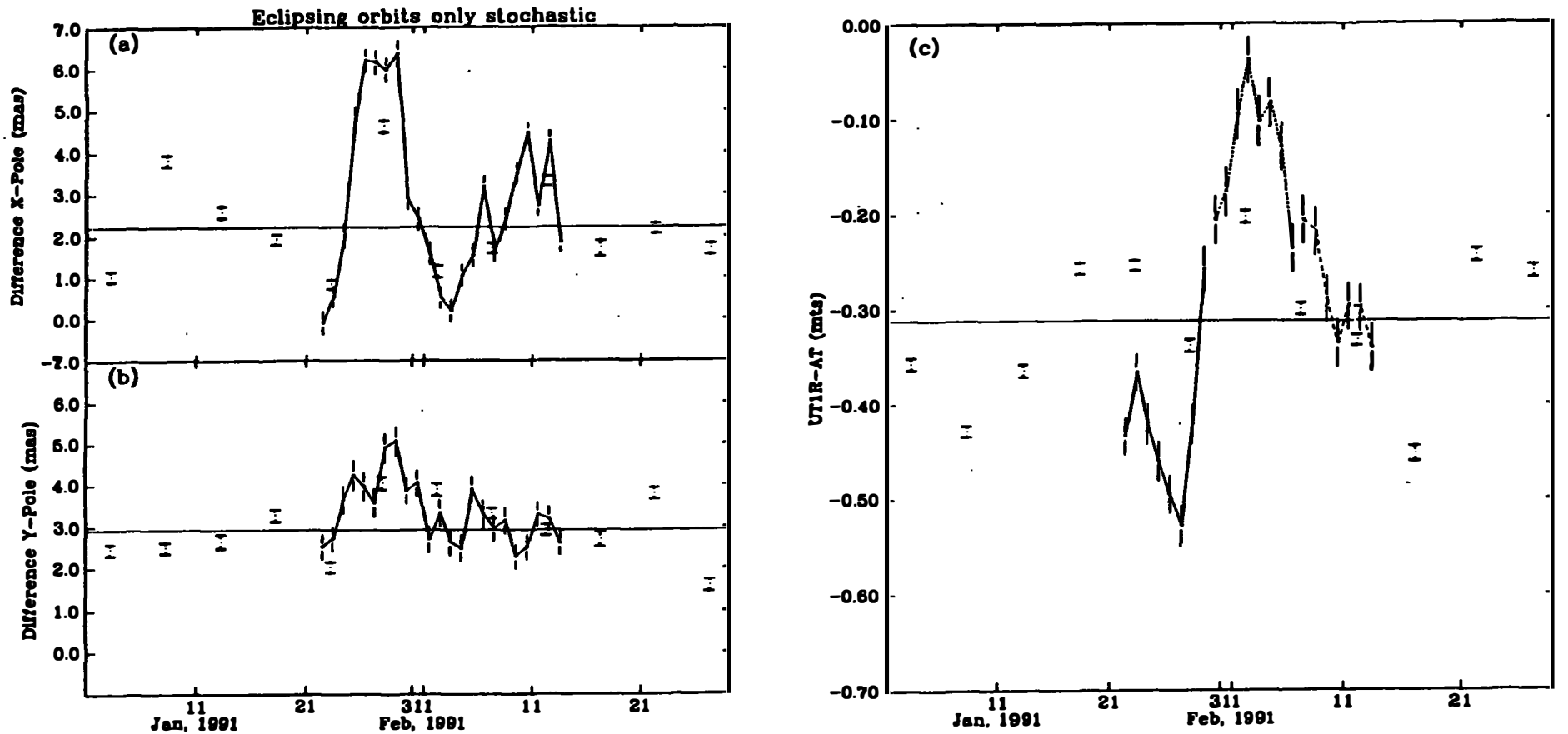

Figure 9. Earth rotation parameters determined from the analysis of the GIG-91 GPS campaign and IRIS VLBI data. Differences are shown relative to IERS Bulletin-B published values. *(a)* X pole position, *(b)* Y pole position, *(c)* UT1R–AT. In each case the points shown with horizontal lines on the (one-standard deviation) error bars are the VLBI estimates. The points connected with a line are the GPS determinations. The GPS values have been offset to agree in the mean with the VLBI estimates. For the X and Y pole positions the RMS difference between the GPS results, linearly interpolated from the two nearest measurements to the epoch of the VLBI determination (midpoint of the 24 hour-VLBI data span), are 0.9 and 0.6 mas respectively. The UT1R-AT results *(c)* are shown with three different line types indicating each of the orbital arcs. Since variations in the positions of the nodes of the satellite orbits can not be distinguished from variations of UT1, each of the segments can in principle be arbitrarily shifted. The connection between each of the segments here is determined by the stochastic models for the satellite orbital elements and UT1R. The RMS difference between the GPS and VLBI determinations (interpolated as discussed above) is 0.12 mts when the segments are not moved relative to each other. In this solution, a multiday state vector for the ~weekly orbital arcs was estimated for all non-eclipsing satellites. The five eclipsing satellites were effectively treated as signal day orbital arcs.

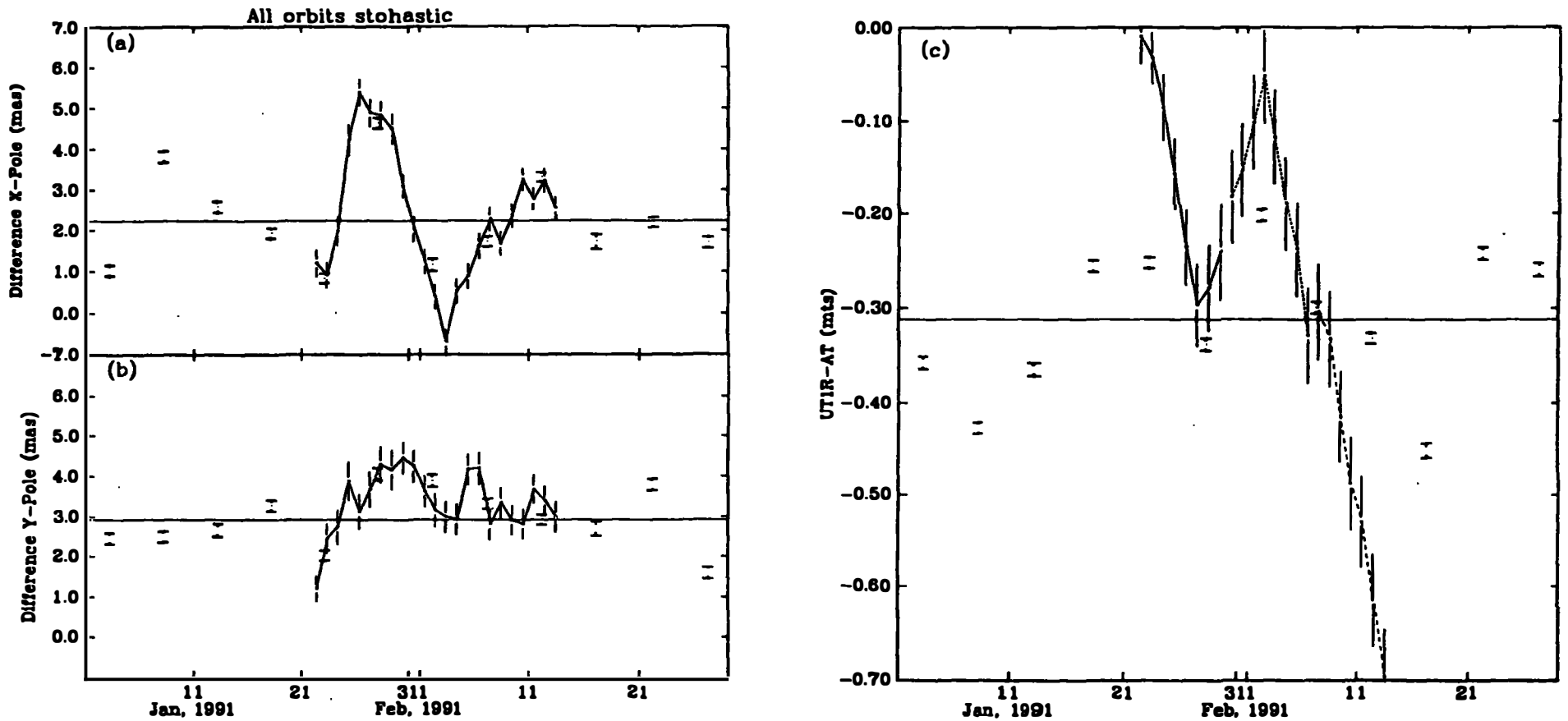

Figure 10. Similar to Figure 10 except the state vector of the non-eclipsing satellites was processed as a random walk with the stochastic model given in the text. In this case the RMS differences between the GPS and VLBI Earth rotation parameter estimates were 0.4 mas for both X pole position *(a)* and Y pole position *(b)*, and 0.19 mts for UT1R–AT *(c)*. The eclipsing satellites were treated in the same fashion as for Figure 9.

signals of 0.03 mas for nutations and other polar motion signals, and 0.002 ms for the variations in UT1 induced mainly by ocean currents.

Indications are that routine determination of Earth-rotation parameters with 0.1 mas precision for pole position (equivalent pole displacement of 3 mm) and 0.01 ms for UT1 with daily resolution should be technically possible. Analysis of a long time history of accurate VLBI measurements indicates that radiotelescopes should be sufficiently stable to support long-term (decades or more) maintenance of such precision. It is not clear at this time that the Earth itself is stable enough to maintain such precision. However, the preliminary results from global GPS experiments indicate that this technique may be accurate enough (at least for pole position determinations) to allow global densification of a primary VLBI system and thus distribute the uncertain contributions for local site motions over large number of sites and therefore minimize their impact on the determination of global reference system. For studies of long-term variations in either UT1 or the nutations of the Earth, there is currently no alternative to VLBI since this is the only technique whose inertial reference frame is stable.

Acknowledgments. This work was supported by the National Science Foundation under grant EAR-89-05560, the National Aeronautics and Space Administration under grant NAG 5-538, by the National Oceanographic and Atmospheric Administration under grant NA90AA-D-AC481, and the Kerr-McGee Foundation. We are also grateful to the researchers at the Jet Propulsion Laboratory and the institutions involved in the GIG-91 campaign for the collection and dissemination of the Rogue data.

REFERENCES

Ash, M. E., Determination of Earth satellite orbits, *Tech. Note 1972-5*, 258 pp., Mass. Instit. of Technol., Lincoln Lab., Lexington, 1972.

Baader, H. -R, P. Brosche, and W. Hovel, Ocean tides and periodic variations of the Earth's rotation, *J. Geophys., 52,* 140-142, 1983.

Brosche, P., U. Seiler, J. Sundermann, and J. Wunsch, Periodic changes in Earth's rotation due to oceanic tides, *Astron. Astrophys., 220,* 318–320, 1989.

Carter, W. E., A. E. E. Rogers, C. C. Counselman III, and I. I. Shapiro, Comparison of geodetic and radio interferometric measurements of the Haystack–Westford base line vector, *J. Geophys. Res., 85*,2685–2687, 1980.

Dong, D., and T. Herring, Observed variations of UT1 and polar motion in the diurnal and semidiurnal bands, *EOS, Trans. Am. Geophys. Union, 71*, 482, 1990.

Eubanks, T. M., J.A. Steppe, J. O . Dickey, R. D. Rosen, and D. A. Salstein, Causes of rapid motions of the Earth's pole, *Nature, 334,* 115–119, 1988.

Eubanks, T. M., this volume, 1991.

Friedman, A. P., S. M. Lichten, W. G. Melbourne, and S. Pogorelec, A GPS campaign to assess high frequency Earth rotation variability, *EOS, Trans. Am. Geophys. Union, 43,* 1272, 1990.

Gwinn, C.R., T.A. Herring, and I.I. Shapiro, Geodesy by radio interferometry: studies of the forced nutations of the earth, Part II: interpretation, *J. Geophys. Res., 91*, 4755–4765, 1986.

Gurtner, W. G. Mader, D. McArthur, A common exchange format for GPS data, *CSTG GPS Bulletin, 2*(3), 1–11, 1989.

Herring, T. A., J. L. Davis, and I. I. Shapiro, Geodesy by radio interferometry: The application of Kalman filtering to the analysis of VLBI data, *J.Geophys. Res., 95*, 12561–12581, 1990.

Herring, T.A., C.R. Gwinn, and I.I. Shapiro, Geodesy by radio interferometry: studies of the forced nutations of the earth, Part I: data analysis, *J. Geophys. Res., 91*, 4745–4755, 1986; —, *ibid., 91*, 14165, 1986.

Herring, T. A., Submilleter horizontal position determination using very long baseline interferometry, in preparation, 1991.

Herring, T. A., and D. Dong, Detection of diurnal and semidiurnal variations in the rotation of the Earth, in preparation, 1991.

Lichten, S. M. and W. J. Bertiger, Demonstration of sub-meter GPS orbit determination and 1.5 parts in 10^8 three dimensional baseline accuracy, *Bull. Geod., 63*, 167–189, 1989.

Melchior, P., Precession-nutations and tidal parameters, *Celestial Mech., 4*, 190–212, 1971.

Rogers, A. E. E., C. A. Knight, H. F. Hinteregger, A. R. Whitney, C. C. Counselman III, I. I. Shapiro, S. A. Gourevitch, and T. A. Clark, Geodesy by radio interferometry: Determination of a 1.24-km base line vector with ~5-mm repeatability, *J. Geophys. Res., 83*, 325–334, 1978.

Rosen, R. D., D. A. Salstein, and T. M. Wood, Discrepancies in the Earth-atmosphere angular momentum budget, *J. Geophys. Res., 95*, 265–279, 1990.

Schaffrin, B., and Y. Bock, A unified scheme for processing GPS phase observations, *Bull. Geod., 62*, 142–160, 1988.

Thomas, J. B., Functional description of signal processing in the Rogue GPS receiver, *JPL Pub. 88-15*, Jet Propulsion Laboratory, Pasadena, June, 1988.

Wahr, J. M., The Earth's rotation, *Annual Review of Earth and Planetary Sciences, 16*, 231–249, 1988.

Yoder, C. F., J. G. Williams, and M. E. Parke, Tidal variations of Earth rotation, *J. Geophys. Res., 86*, 881–891, 1981.

Yunck, T. P., T. G. Lockhart, IERS/CASA analysis working group memo AWG-5, Jet Propulsion Lab., April 1, 1991.

The Superfluid Helium Gyroscope; An emerging technology for Earth rotation studies

James C. Davis and Richard E. Packard,
Ultra Low Temperature Laboratory,
Physics Department,
University of California, Berkeley CA 94720

Introduction

Superfluid Helium is a system described by a macroscopic quantum mechanical wavefunction[1] of the form $\Psi=|\Psi|e^{i\phi}$. The phase ϕ of this wavefunction can be modified by the absolute rotation of a container containing the superfluid. It has been recognized for some time that the observation of the rotationally induced changes in the wavefunction could lead to the development of a sensitive detector of rotation[2]. The purpose of this report is to describe the basic principles of the superfluid Helium gyroscope[3] (SHEG) and to report progress toward developing demonstration devices at the University of California at Berkeley. Our research programs are investigating the rotation induced effects in both superfluid ^{4}He and ^{3}He. Our ultimate goal is to see if the technology can be extended to a limit useful for the study of variations in the Earth's rotation rate. The first section of the paper contains a discussion of the development of the ^{4}He based device while the second section relates to the ^{3}He gyroscope.

Superfluid ^{4}He

We consider below an N turn, superfluid ^{4}He filled, toroidal container, partitioned at some point by a thin wall containing a small hole. The temperature of the device is below 2.2K where ^{4}He becomes a superfluid. If the torus is at rest, the fluid velocity everywhere is zero and the wavefunction of the superfluid has its phase constant in space. However if the torus is now rotated slowly, velocity fields will be established throughout the container.

The superfluid velocity, v_s, is related to the phase gradient through the relation,

$$\nabla \phi = (m_4/h)v_s \qquad (1)$$

where h is Plank's constant and m_4 is the atomic mass of ^{4}He. Since the wavefunction must be single valued at a given point, v_s is

restricted to values which will quantize the fluid circulation[4] $\kappa_4 = h/m_4$ round the torus. If the fluid is in a state with n (integer) quanta of circulation when the torus is at rest, a subsequent slow rotation forces the velocity within the hole v_h to have the value given by[3],

$$V_h = \frac{2}{\pi r}\left[\frac{n\kappa_4 - 2\pi NR^2\,\vec{\Omega}\cdot\vec{\alpha}}{1 + \frac{4\pi NRr}{\sigma}}\right] \tag{2}$$

where N is the number of turns in the torus, R is the torus radius, r is the radius of the small hole, σ is the cross sectional area of the torus, Ω is the angular velocity vector characterizing the rotation and α is a unit vector perpendicular to the plane of the torus. Inspection of the numerator of Eq. 2 shows that the flow velocity within the orifice can be substantial even for very slow rotation rates. For instance if n=0, $r=10^{-7}$m, N = 10 and R = 0.5m the velocity within the hole is on the order of 0.01 ms^{-1} when $\Omega = 10^{-6}\Omega_E$. (Here and in the following we will use the rotation rate of the Earth, $\Omega_E = 7\times10^{-5}s^{-1}$, as a basic unit of rotational angular velocity.)

It has been known for many years that when the superfluid velocity reaches a critical value v_c, energy dissipation will commence in the otherwise frictionless flow. The fundamental dissipation process was analyzed by Anderson[5]. He predicted that when the fluid reaches the critical velocity, v_c, it would be energetically favorable for a quantized vortex line to move across the orifice, removing an amount of energy $E=\rho\kappa_4 v_c s$ (where s is the orifice area, and ρ the density of the superfluid) from the flow. Such a discrete process changes the quantum phase difference across the orifice by 2π.

These so called 2π phase slip events were first seen by Avenel and Varoquaux[6] using an oscillator technique invented by W. Zimmerman. In a pioneering series of experiments they have demonstrated many of the fundamental features of the phase slip events. Their apparatus possesses the same topology as the divided torus which we have been discussing. Figure 1, below, shows the torus connected in parallel to a diaphragm pump, of area S, which can force fluid, in a transient fashion through the torus. The restoring force of the diaphragm coupled to the inertia of the fluid in the torus create a simple harmonic oscillator (we call it a ZAV oscillator) whose resonant frequency ω is given by,

$$\omega^2 = \left[2r + \frac{\sigma}{2\pi R}\right]\frac{k}{S^2\rho} \tag{3}$$

where k is the stiffness of the diaphragm, 2r is the hydrodynamic area to length ratio of the phase slip weak link and $\sigma/2\pi R$ is the area to length ratio of the torus .

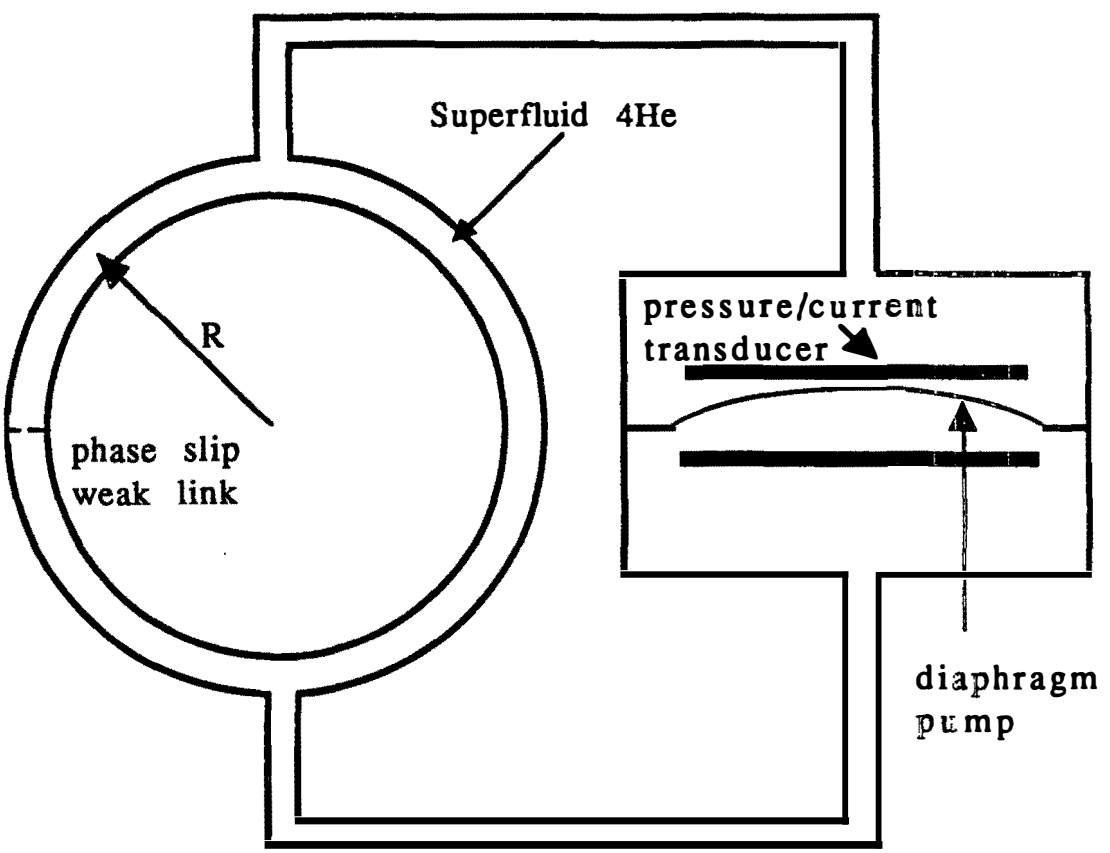

Figure 1. A torus which is interrupted by a phase slip weak link is connected to a diaphragm superfluid pump and a pressure/current transducer.

AV have demonstrated that when the oscillator is driven at resonance, if the hole is characterized by only 2π phase slip processes, a graph of oscillation amplitude vs. driving amplitude displays a characteristic staircase pattern[7]. The velocity amplitude of the first step corresponds to the hole's critical velocity, v_c. They also demonstrated that if a persistent current is trapped within the torus

the level of the first step can be modulated.

A steady rotation of the ZAV oscillator will create a persistent current in the torus. For small rotation rates the velocity within the orifice will change by the amount given in Eq. 2. This rotation induced current will shift the levels of the staircase pattern and lead to a measurement of the rotational state of the torus.

Our laboratory has been progressing toward a demonstration of this phenomenon. The essential requirement for the experiment is to develop a small orifice which exhibits only 2π phase slip events. Our approach has been to construct an apparatus which has the sensitivity needed to detect the individual phase slip events and then to use it to characterize the behavior of various microfabricated orifices.

We fabricate the micro-holes using electron beam lithography on Silicon Nitride (SiN). Presently we can produce holes of 100nm radius in membranes of 100nm thickness[8]. Figure 2a shows an SEM photograph of a typical orifice; this one was nominally intended to be rectangular, and has the general shape as that used by AV.

To study the phase slip events in the orifice we place it in a diaphragm driven oscillator which does not have a parallel flow path (i.e. the torus is blocked on the right hand side in Figure 1). This renders the critical velocity insensitive to rotation or to spuriously trapped persistent currents. When the oscillator is driven at resonance, the amplitude develops in time as shown in Figure 3. One clearly sees here the phase slip events. This is the first experiment to confirm this feature of the AV results. The quality of this data and the repeatability of the phase slips are very encouraging steps forward in the development of the ^{4}He SHEG.

In experiments thus far conducted[9] , we find that the slips are 2π when the flow is in one direction but are of larger size (although still quantized) when the flow is in the opposite direction. These multiple phase slip events will cause the AV staircase pattern to "washout" and cannot be used in a rotation sensor.

The microscopic physics which determines whether or not a given slip is 2π has not yet been determined. However the insight gained from our experiments thus far leads us to believe that smaller holes inhibit multiple phase slips. We are following an empirical approach by using orifices of various shapes and sizes to determine what are the relevant parameters for the simplest slip events.

When we secure an orifice characterized by 2π slips in both directions, we will install a parallel flow path to make the apparatus sensitive to the Earth's rotation. The entire apparatus can be

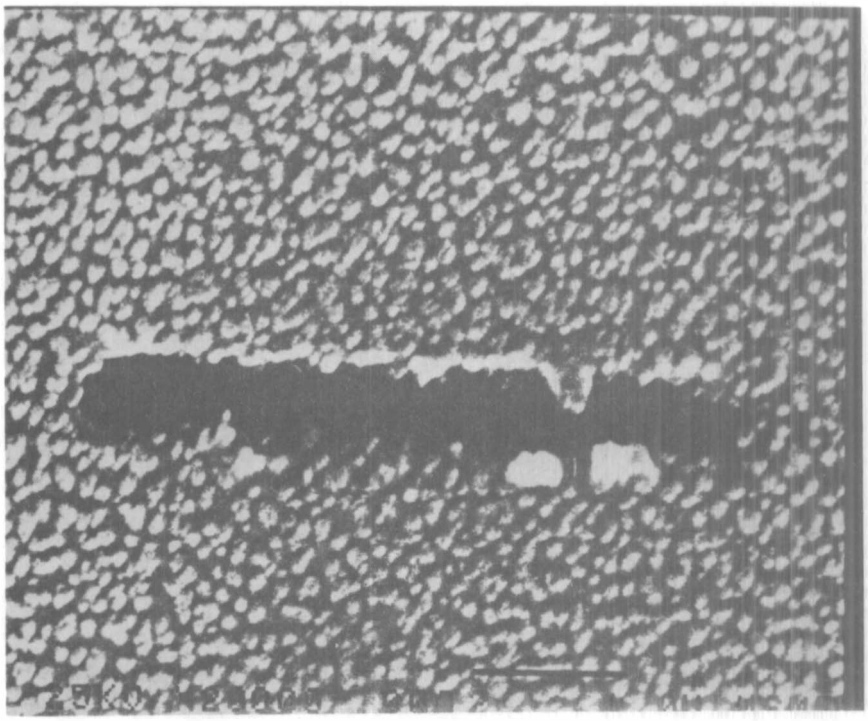

Figure 2a. A scanning electon micrograph (SEM) picture of the orifice used in 4He experiments described in this paper. It has length ~ 5 μm and width ~ 0.4 μm.

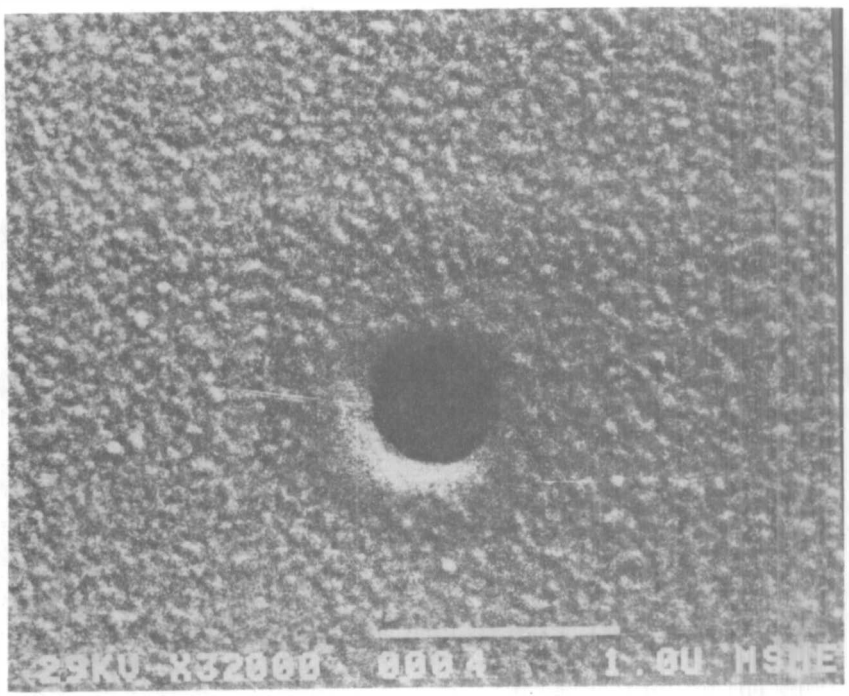

Figure 2b. A SEM picture of an orifice in a 0.1 μm SiN membrame whose side is about 0.4 μm. This type of hole is used for research in ^{3}He-B.

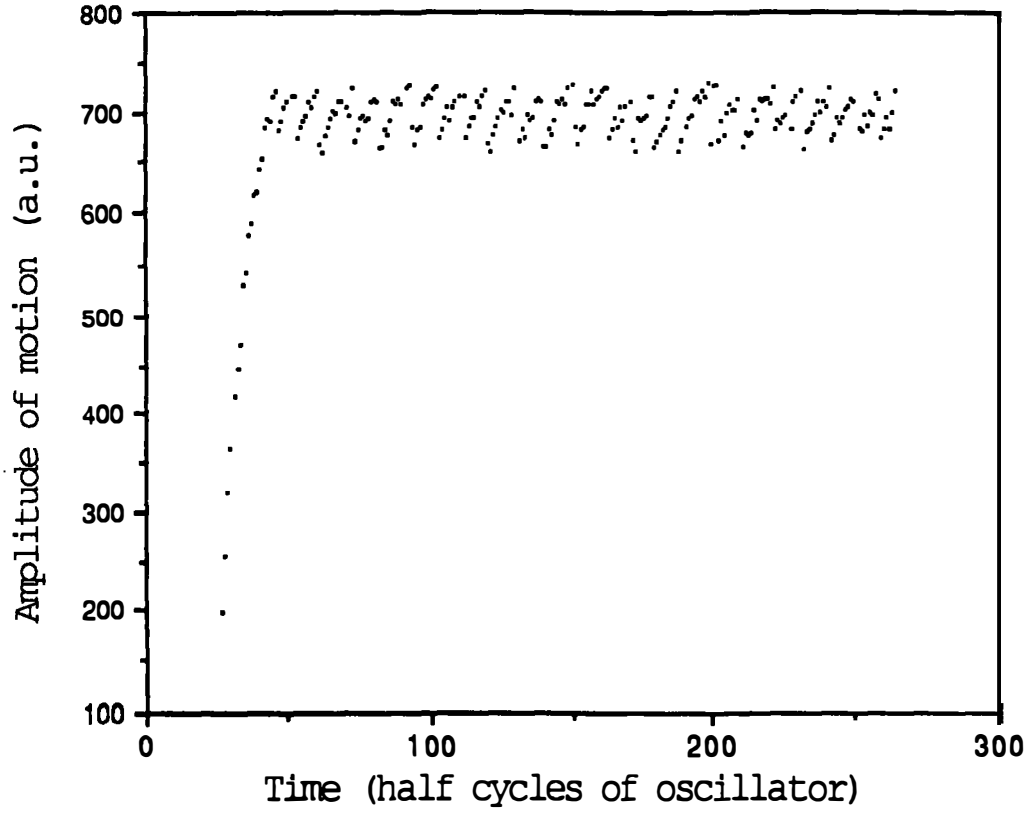

Figure 3. The amplitude of motion as a function of time for our ZAV oscillator containing the orifice shown in Fig. 2a. The critical amplitude for the onset of phase slips and the 2π slips themselves are clearly seen.

reoriented with respect to the Earth's rotation vector. The experiment is designed so that reorientation of the apparatus by 90° will cause the apparent critical velocity (i.e. the level of the first "step") to cycle between minimum and maximum levels about three times.

The rotation resolution $(\delta\Omega)_{min}$ of the ^{4}He SHEG is given by[3]

$$(\delta\Omega)_{min} = \left[\frac{\pi r^2}{\sigma R}\right](\Delta V_c)\left(\frac{1}{\sqrt{f\tau}}\right) \tag{4}$$

where ΔV_c is the spread in the measurements of the critical velocity, $f=\omega/2\pi$ is the frequency at which the device is operated and τ is the time for which a measurement is taken.

The ultimate rotation resolution of the ^{4}He SHEG depends in a fundamental way on statistical fluctuations in the phase slip critical velocity. The information which we now have about this process comes from the data of AV and from that in our own laboratory. The AV data suggests that the phase slip events are triggered by a thermally activated process which creates a finite spread in the measured value of v_c. Their analysis suggests that the v_c distribution function should be on the order of T/E_0 where T is the absolute temperature and E_0 characterizes an energy barrier which appears empirically to be about 106K. The physics underlying the magnitude of this barrier is unknown at present.

In our own preliminary data the statistical width of observed v_c is about 1% (about the same as seen by AV) but a simple temperature dependence is not yet apparent. Only future research will reveal the processes underlying the precision of the phase slip critical velocity.

Eq. 4 implies that the sensitivity of the SHEG is affected by the frequency of the ZAV oscillator. Since only one oscillator (that of AV) has thus far displayed the staircase pattern it is not yet known what factors put an upper limit on ω.

Superfluid ^{3}He

In the second program we have developed an apparatus for superfluid ^{3}He-B, which will allow us to study phase slip processes, and also the details of the current phase relationship, in a very different type of superfluid. ^{3}He-B, which exists at temperature near 10^{-3} K, has long been thought to be described by a macroscopic quantum wavefunction whose phase varies with position as

$$\nabla \phi = (2m_3/h)v_s \qquad (5)$$

where m_3 is the mass of the ^{3}He atom. We have recently demonstrated[10], for the first time, that circulation is quantized in this superfluid in the units predicted by Eq. 5. This circulation quantization is a feature that is a necessary condition for the creation of a SHEG.

The properties of ^{3}He-B are believed to be such that a hole, of radius r and length l ,where both r and l are of the same order as the coherence length ξ (= 70 nm at P= 0), forms a Josephson junction for this superfluid[11]. This means that the current through the hole I

is related to the phase difference across it, $\Delta\phi$, by the equation

$$I = I_c \sin\Delta\phi \tag{6}$$

where I_c is the critical current of the junction. Holes of this size are again made by e-beam lithography on SiN and an example is shown above in Figure 2b.

Consider an N turn torus containing two of these superfluid Josephson junctions whose topology is shown below in Figure 4. This torus is again connected with a diaphragm pump and the effect of rotation on this whole apparatus is measured.

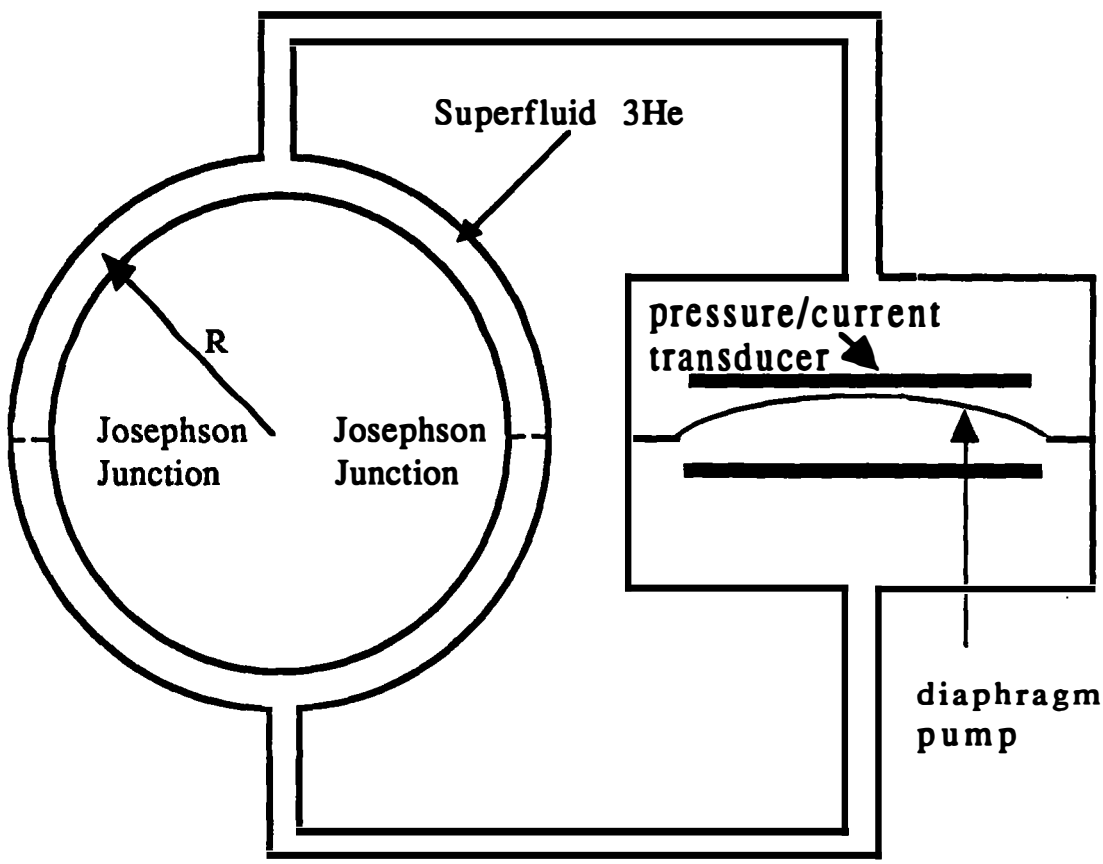

Figure 4. A torus which is interrupted at two points by ^{3}He Josephson Junctions is connected to a diaphragm superfluid pump and a pressure/current transducer.

It can be shown[3] that the maximum current through the

two junctions in parallel, I_0, is related to the rotation speed of the gyroscope by

$$I_0 = 2I_c \left| \cos \left[\frac{2\pi N R^2 \vec{\Omega} \cdot \vec{\alpha}}{\kappa_3} \right] \right| \tag{7}$$

where $\kappa_3 = h/2m_3$ is the circulation quantum in ^{3}He and the other symbols are as before. Thus a measurement of I_0 provides information on Ω.

The operation of such a device requires temperatures below 1 mK, holes with size $r \approx 0.1$ μm and a very sensitive current/pressure transducer. We have constructed, at Berkeley, a reorientable millikelvin cryostat[12] for the purpose of testing the ^{3}He SHEG by modulating the Earth's rotation field threading the sensing area. This machine is one of only two of its type in the world. A current/pressure transducer of the type used for the ZAV oscillators[13] has also been constructed for this experiment.

The fundamental sensitivity limits of this device are as yet unknown. However, Eq.7 indicates that[3]

$$(\delta\Omega)_{min} = \frac{\kappa_3}{4I_0\pi^2R^2}(\delta I)_{min} \tag{8}$$

where $(\delta I)_{min}$ is the minimum resolvable current. Both the value of I_c for a ^{3}He Josephson junction and the limits on $(\delta I)_{min}$ remain unmeasured. Earlier work[14] at our laboratory has given indications that thermal processes dominate the measurement of very small mass currents in narrow channels containing superfluid ^{3}He. Experiments are now under way at Berkeley to characterize single Josephson junctions and to find the sensitivity limits for measurement of current through them before fabrication of the complete ^{3}He-SHEG.

Conclusion.

The potential of devices, based on the macroscopic quantum properties of the Helium superfluids, to allow a new type of extemely sensitive absolute rotation measurement, is now recognised in a number of laboratories around the world. Efforts to develop this idea into a system which can be used by geodesists, geophysicists and also physicists interested in general relativistic effects are under way at Berkeley. This effort is based on our long history of research

into the macroscopic quantum properties of these superfluids and over the last two years we have seen steady progress towards the realization of a demonstration device.

Acknowledgements

We would like to acknowledge A. Amar and Y. Sasaki for their preliminary data shown in Fig 3. We thank S. Vitale for useful conversations. This work is supported in part by Air Force Geophysical Lab. contract #F19628-90-K-0013 P00004, the National Oceanic and Atmospheric Administration (N.O.A.A.) and by the Institut fur Angewandte Geodasie, Frankfurt, Germany.

References

1. D.R. Tilley and J. Tilley, *Superfluidity and Superconductivity 2nd-ed.*, Published by Adam Hilger and Sons 1986, p. 39.
2. M. Cerdonio and S. Vitale, Phys. Rev. B **29**, 481 (1984); M. Bonaldi, S. Vitale and M. Cerdonio Phys. Rev. B **42**, 9865 (1990); J. Anandan, J. Phys. A. Math Gen. **17**, 1367 (1984); R. Y. Chiao, Phys. Rev. B **25**, 1655 (1982); O. Avenel and E. Varoquaux , Jpn. J. Appl. Phys. **26-3**, 1798 (1987); R.E. Packard, N.O.A.A proposal 1988.
3. A tutorial article on superfluid rotation sensors will be published by R.E. Packard and S. Vitale in Phys. Rev.
4. The superfluid circulation κ is defined as the integral around a closed loop within the superfluid of the superfluid velocity v_s i.e. $\kappa = \oint \vec{V_s} \cdot \vec{dl}$
5. P.W. Anderson, Rev. Mod. Phys. **38**, 298 (1966).
6. O. Avenel and E. Varoquaux, Phys. Rev. Lett. **55**, 2704 (1985)
7. O. Avenel and E. Varoquaux, Phys. Rev. Lett. **60**, 416 (1988)
8. A. Amar, R. Lozes, J.C. Davis and R.E. Packard to be published.
9. A. Amar, Y Sasaki, J.C. Davis and R.E. Packard to be published.
10. J.C. Davis, J.D. Close, R.J. Zieve and R.E. Packard, Phys. Rev. Lett. **66**, 399 (1991)
11. J.R. Hook, Jpn. J. Appl. Phys. **26-3**, 159, (1987); E.V. Thuneberg, Europhys. Lett. **7**, 441,(1988); J Kurkijarvii, Phys. Rev. B **38**, 11184 (1988); Ref. 7 above.
12. J.C. Davis, R.J. Zieve, J.D. Close and R.E. Packard, Physica B **165&166**, 57 (1990).
13. O. Avenel and E. Varoquaux, in Proc. XIth I.C.E.C. (Butterworths, Guilford, 1986), p. 587.
14. J.P. Pekola, J.C. Davis and R.E. Packard, J. Low Temp. Phys. **71**, 141

THE STABILITY OF THE TERRESTRIAL REFERENCE FRAME INFERRED FROM EARTH ORIENTATION SERIES

R. S. Gross and J. A. Steppe
Jet Propulsion Laboratory
California Institute of Technology
4800 Oak Grove Drive
Pasadena, CA 91109-8099
USA

ABSTRACT. A terrestrial reference frame (TRF) is defined in practice by the specification of the coordinates of a set of observing stations located on the Earth's surface. These station locations are currently determined from observations by the modern, space-geodetic techniques of very long baseline interferometry (VLBI), satellite laser ranging (SLR), and lunar laser ranging (LLR). Each determination defines, in general, its own TRF, although analysis centers attempt to place their results within a common TRF by imposing constraints during their data reduction procedures. Besides station locations, observations by these techniques are also able to determine the Earth's orientation in space, the results being given within the TRF defined by the station location results. Comparisons of Earth orientation series determined by independent techniques and/or observations are undertaken in this study in order to infer the level of agreement (in bias and rate) of the TRFs within which the Earth orientation results are given.

The Earth orientation data sets studied were specifically chosen as having been determined by use of the same plate tectonic motion model, without adjustment. Corrections for bias and rate were determined by an iterative, round-robin scheme in which each data set is compared to a combination of all others. The data's stated uncertainties were adjusted at the same time by a factor such that the residual, upon differencing with a combination of all other data sets, has a reduced chi-square of one. After convergence of this iterative scheme, the relative corrections and uncertainty scale factors that have been determined (making the data sets agree with each other in bias, rate, and uncertainty) are applied to the data sets prior to forming a combination of them all. This combination was then compared to a UTPM series [EOP(IERS) 90 C 02] derived by the International Earth Rotation Service (IERS) in order to obtain the additional bias-rate correction that must be applied to each data set in order to place it within the same IERS reference frame in which this IERS UTPM series is given. The scatter in the rate corrections that must be applied to the data sets so that they agree with each other (in rate) is about 0.3 mas/yr, or about 1 cm/yr. This value, although representing the scatter in the rate corrections that must be applied to independent determinations of Earth orientation series in order for them to agree with each other, should also represent the scatter in the rate at which the underlying TRFs are drifting away from each other, regardless of the direction of that drift, and can therefore be taken as a measure of the stability of the terrestrial reference frame as it is capable of being currently defined.

1. Introduction

One consequence of global change is a possible rise in sea level, either due to thermal expansion of water, or to the addition of new water to the ocean basins from melting of continental glaciers and ice sheets (e.g., *DOE*, 1985; *JOI*, 1990; *NRC*, 1990). The level of the seas has been, and continues to be, monitored by tide gauges which measure the sea level relative to a benchmark

located on land (e.g., *Pugh*, 1987). Thus, the change in sea level recorded by a tide gauge can be caused not only by a changing water level, but also by vertical crustal motions due to, for example, tectonic motions or postglacial rebound. If the location and motion of the tide gauge benchmarks were accurately determined within a stable terrestrial reference frame (TRF), then the absolute change in sea level within that TRF could be recovered. For long-term monitoring of sea level change from tide gauge data it therefore becomes important to know how accurately a terrestrial reference frame can be defined, particularly in terms of its long-term stability.

A terrestrial reference frame is a right-handed Cartesian reference frame that is attached to the solid Earth in some prescribed manner so that the motion in inertial space of the TRF represents the spatial motion of the solid Earth (in some globally averaged sense depending upon the details of how the TRF is actually tied to the solid Earth). A terrestrial reference frame is realized in practice by specifying the coordinates and secular motions of a globally distributed set of observing stations that are located on the surface of the Earth (e.g., *Kovalevsky et al.*, 1989). For purposes of terrestrial reference frame definition, these station locations and secular motions are currently determined by the modern space-geodetic techniques of very long baseline interferometry (VLBI), satellite laser ranging (SLR), and lunar laser ranging (LLR). Each solution for the station locations and secular motions determined by these modern space-geodetic techniques defines its own unique TRF, and TRFs defined by different solutions will, in general, differ from each other by being offset from each other and/or drifting away from each other.

In addition to determining the locations and secular motions of observing stations (e.g., *Lambeck*, 1988), the modern techniques of VLBI, SLR, and LLR are also able to determine (among other parameters) the orientation of the terrestrial reference frame with respect to either a space-fixed, celestial reference frame (defined by the locations of radio sources in the case of VLBI), or a quasi-inertial reference frame defined by the orbital motions of the Moon (in the case of LLR) or of artificial satellites (in the case of SLR). Each solution for the Earth orientation parameters is given in a unique terrestrial reference frame defined by the station locations and secular motions used in obtaining that solution. Different Earth orientation solutions will, in general, be given within different TRFs, although analysis centers attempt to place their results within a common TRF by imposing constraints during their data reduction procedures. The different Earth orientation solutions can be offset from each other (exhibit differences in bias) and can drift away from each other (exhibit differences in rate) reflecting differences between the TRFs within which the Earth orientation solutions are given.

The topic of this paper is the accuracy with which terrestrial reference frames are currently being defined. As a measure of this accuracy, differences in bias and rate between independent solutions of the Earth's orientation are determined. These bias-rate differences of the Earth orientation series reflect offset-drift rate differences between the TRFs within which the Earth orientation series are given, and can therefore be used as a measure of the stability of the underlying TRF. In order to interpret bias-rate differences of independently determined Earth orientation series in terms of the stability of the underlying TRF, it is important to study only Earth orientation series that have been determined as similarly as possible. In particular, only Earth orientation series have been studied herein that were determined by applying without adjustment the plate tectonic motion model AM0-2 of *Minster and Jordan* (1978) as a model for the secular motions of the observing stations.

2. Data Sets and Approach

The data sets that have been used in this study are identified in Table 1. In order to directly interpret observed bias-rate differences between Earth orientation series in terms of TRF stability, it is important that the Earth orientation series be given within the same TRF, or at least in TRFs that are as similarly defined as possible. In particular, in order to address the question of the long-term stability of the TRF, it is important that each Earth orientation series be determined by a solution technique that accounts in the same way for the secular motions of the stations. At the time that this study was undertaken, most Earth orientation solutions available to us were solely determined

TABLE 1. DATA SETS STUDIED

DATA SET NAME	DATA TYPE	ANALYSIS CENTER	DATA SPAN	NUMBER POINTS	PLATE MODEL
LLR (L1707; ΔΦ, UT0)					
McDonald 2.7m	LLR	JPL	4/15/70 – 6/29/85	810	AM0–2
McDonald LRS	LLR	JPL	3/2/85 – 1/27/88	35	AM0–2
McDonald LRS (New Site)	LLR	JPL	3/28/88 – 12/9/89	20	AM0–2
CERGA	LLR	JPL	4/7/84 – 12/20/89	271	AM0–2
Haleakala	LLR	JPL	11/14/84 – 12/17/89	105	AM0–2
TEMPO (90 R 01; T, V)					
CA (12) – Spain (63)	VLBI	JPL	7/18/82 – 8/25/84	57	AM0–2
CA (14) – Spain (61)	VLBI	JPL	9/19/82 – 8/1/87	42	AM0–2
CA (14) – Spain (63)	VLBI	JPL	11/26/79 – 12/10/89	142	AM0–2
CA (15) – Spain (63)	VLBI	JPL	10/4/87 – 7/8/90	42	AM0–2
CA (12) – Australia (43)	VLBI	JPL	7/2/82 – 7/22/84	58	AM0–2
CA (14) – Australia (42)	VLBI	JPL	2/15/83 – 9/20/87	34	AM0–2
CA (14) – Australia (43)	VLBI	JPL	10/28/78 – 3/3/90	170	AM0–2
CA (15) – Australia (43)	VLBI	JPL	11/8/87 – 7/9/90	36	AM0–2
CDP (EOP.629)					
Multi-Baseline	VLBI	GSFC	8/4/79 – 12/29/89	700	AM0–2
Westford – Ft. Davis	VLBI	GSFC	6/25/81 – 1/1/84	103	AM0–2
NAVNET (NAVY 1990-2)					
Multi-Baseline	VLBI	USNO	9/11/88 – 2/21/90	38	AM0–2
CSR (89 L 02; PMX, PMY)					
LAGEOS	SLR	U. Texas	5/15/76 – 1/3/89	970	AM1–2
IRIS (28SEP90)					
Multi-Baseline	VLBI	NGS	9/27/80 – 9/15/90	558	Adjusted
Intensive (UT1 Only)	VLBI	NGS	4/2/84 – 8/10/90	1357	Adjusted

by applying without adjustment a plate tectonic motion model as a model for the secular motions of the stations. It was therefore decided to study only those Earth orientation series that had been determined in this manner, namely, by applying without adjustment the plate tectonic motion model AM0-2 of *Minster and Jordan* [1978]. As it was also desirable to only study independently determined Earth orientation series, only one LLR series was chosen, namely, that determined at the Jet Propulsion Laboratory (JPL) by *Newhall et al.* [1990], and only one SLR series was chosen, namely, that determined at the Center for Space Research (CSR) at the University of Texas at Austin by *Schutz et al.*[1989]. Three different data sets derived from independent VLBI observations were chosen, namely, that determined from the approximately twice-a-week single baseline observations made using the radio telescopes of the Deep Space Network (DSN) of NASA [*Steppe et al.*, 1990], that determined from the approximately weekly multi-baseline observations made using the U.S. Naval Observatory's VLBI network (NAVNET; *Eubanks et al.*,

1990), and that determined by the VLBI group of NASA's Crustal Dynamics Project (CDP) at Goddard Space Flight Center (GSFC) from both their own VLBI observations, and from their reduction of the multi-baseline observations made under the auspices of the International Radio Interferometric Surveying (IRIS) subcommission [*Ma et al.*, 1990]. Note that the particular CDP VLBI solution chosen (EOP.629) was determined by applying the plate tectonic motion model AM0-2 without adjustment [*C. Ma*, personal communication, 1990].

Also listed in Table 1 as having been studied are an IRIS multi-baseline solution, and an IRIS "Intensive" (UT1 only) solution [*IRIS Earth Orientation Bulletin No. 80*, October, 1990]. Bias-rate corrections have been determined and will be presented for these IRIS series, although these corrections were determined separately and in a different manner from how they were determined for the other series listed in Table 1. The IRIS multi-baseline solution is not completely independent of the CDP solution since the same raw VLBI observing data were used in determining both solutions, at least through the end of 1989 which is the terminating date of the CDP series. The IRIS "Intensive" series is independent of the other series listed in Table 1, but it was determined by a technique in which the station velocities were adjusted, and hence the IRIS "Intensive" UT1 values are likely to be given within a TRF that is very different from that within which the other series are given. Thus, neither IRIS series was included in the iterative, round-robin technique (see below) that was employed in determining the bias-rate corrections of the other series.

Prior to computing the bias-rate corrections that must be applied to each series in order for them to agree with each other, the SLR-derived series (the CSR entry in Table 1) was first analytically corrected to be in the AM0-2 frame (from the AM1-2 frame) by applying a rate adjustment of –0.52 mas/yr to the x-component of polar motion (PMX), and of –0.24 mas/yr to the y-component of polar motion (PMY; *IERS Annual Report for 1989*, pp. II-26). Note that the SLR-derived UT1 values were not used in this study due to problems separating the UT1 component from effects of unmodelled forces acting upon the satellite causing the node of its orbit to drift.

The approach used in this study to determine the bias-rate corrections that must be applied to the series in order for them to agree with each other (in bias and rate), and hence to be within the same terrestrial reference frame, was designed to be as free as possible of the need to make any subjective decisions during the process. It was decided not to use a reference series for comparison purposes since a subjective decision would need to be made as to what series to use for the reference series. Each series was specifically chosen to be independent of the others so that no set of observations would be given undue weight. Each series was also treated in the same manner so that no series would be given preferential treatment. The approach that was finally chosen for purposes of determining the bias-rate corrections was an iterative, round-robin approach wherein each series was compared to a combination of all others. The combination was obtained by use of a Kalman filter that was developed at JPL for the express purpose of combining Earth orientation series [*Eubanks*, 1988; *Morabito et al.*, 1988; *Gross and Steppe*, 1990, 1991]. At each iterative step, each series was differenced with a combination of all other series in order to determine the incremental bias-rate corrections that must be applied to that series in order for it to have the same bias and rate as the combination to which it is being compared. At the same time, the stated uncertainties of each component of each series were adjusted by determining and applying an uncertainty scale factor such that the residual (i.e., the differenced series) had a reduced chi-square of one. After this had been done for each series during a given iterative step, the incremental bias-rate corrections and uncertainty scale factors thus determined for each series were applied to each series and the process repeated until convergence was attained (convergence being indicated by the incremental bias-rate corrections approaching zero, and the incremental uncertainty scale factors approaching one). After this process converged, all the incremental bias-rate corrections for each series were summed, and all the incremental uncertainty scale factors were multiplied, in order to obtain the final values for the bias-rate corrections and uncertainty scale factors that must be applied to the original series in order for them to be consistent with each other in bias, rate, and uncertainty.

TABLE 2. ADJUSTMENTS TO DATA SETS (RELATIVE)

DATA SET NAME	BIAS (mas)		RATE (mas/yr)		UNCERTAINTY (σ) SCALE FACTOR	
LLR (L1707; ΔΦ, UT0)	ΔΦ	UT0	ΔΦ	UT0	ΔΦ	UT0
McDonald 2.7m	−1.954 ±0.601	3.994 ±0.751	—	—	1.086	1.199
McDonald LRS	0.170 ±0.482	0.634 ±0.869	—	—	0.917	1.687
McDonald LRS (New Site)	−0.260 ±0.441	3.822 ±0.495	—	—	0.716	1.001
CERGA	0.479 ±0.201	2.998 ±0.138	0.328 ±0.125	0.650 ±0.086	1.204	1.104
Haleakala	−1.308 ±0.400	3.262 ±0.276	0.801 ±0.279	0.269 ±0.202	1.204	1.192
TEMPO (90 R 01; T, V)	T	V	T	V	T	V
CA (12) – Spain (63)	−1.877 ±0.553	4.293 ±0.876	—	—	1.240	1.181
CA (14) – Spain (61)	−0.123 ±0.549	2.827 ±1.024	—	—	1.196	0.991
CA (14) – Spain (63)	−0.344 ±0.151	2.109 ±0.377	0.258 ±0.073	−0.524 ±0.133	1.295	1.144
CA (15) – Spain (63)	−0.879 ±0.231	1.193 ±0.744	—	—	1.021	1.130
CA (12) – Australia (43)	−2.495 ±0.222	−4.004 ±0.744	—	—	1.142	1.160
CA (14) – Australia (42)	−1.842 ±0.250	−3.651 ±0.872	—	—	1.168	1.143
CA (14) – Australia (43)	−1.767 ±0.113	−2.529 ±0.273	0.103 ±0.042	−0.014 ±0.110	1.456	1.114
CA (15) – Australia (43)	−1.085 ±0.184	−4.028 ±0.409	—	—	1.139	0.852
CDP (EOP.629)	T	V	T	V	T	V
Westford – Ft. Davis	−0.947 ±0.329	−4.687 ±0.558	—	—	1.649	1.021
CDP (EOP.629)	PMX	PMY	UT1	PMX	PMY	UT1	PMX	PMY	UT1
Multi-Baseline	1.402 ±0.051	−1.465 ±0.047	−1.616 ±0.099	0.009 ±0.027	0.775 ±0.025	0.559 ±0.060	1.567	1.540	2.181
NAVNET (NAVY 1990-2)	PMX	PMY	UT1	PMX	PMY	UT1	PMX	PMY	UT1
Multi-Baseline	0.971 ±0.168	−0.569 ±0.187	−1.475 ±0.204	—	—	—	1.278	1.436	1.274
CSR (89 L 02; PMX, PMY)	PMX	PMY	UT1	PMX	PMY	UT1	PMX	PMY	UT1
Satellite Laser Ranging	−2.176 ±0.059	3.512 ±0.055	—	−0.025 ±0.032	0.412 ±0.029	—	0.838	0.835	—

REFERENCE TIME FOR RATE ADJUSTMENT IS 1988.0

3. Results

The bias-rate corrections and uncertainty scale factors that have been determined by the above iterative, round-robin approach are given in Table 2. These are labelled "relative" corrections since they are the corrections that must be applied to each series in order for them to be in agreement

TABLE 3. ADJUSTMENTS TO IRIS DATA SETS (RELATIVE)

DATA SET NAME	BIAS (mas)			RATE (mas/yr)			UNCERTAINTY (σ) SCALE FACTOR		
IRIS (28SEP90)	PMX	PMY	UT1	PMX	PMY	UT1	PMX	PMY	UT1
Multi-Baseline	−7.421	4.442	−2.821	0.161	0.840	0.331	1.357	1.250	1.913
	±0.030	±0.028	±0.038	±0.016	±0.016	±0.020			
Intensive (UT1 Only)	—	—	−2.857	—	—	0.445	—	—	1.308
			±0.037			±0.025			

REFERENCE TIME FOR RATE ADJUSTMENT IS 1988.0

relative to each other. The values for the bias-rate corrections in Table 2 are the sum of all the incremental corrections for each series, and the values for the uncertainty scale factors are the products of all the incremental scale factors for each series. The errors for the bias-rate corrections given in Table 2 are the formal errors in determining the incremental correction during the last iterative step. For each series, these results have been determined and reported in the natural reference frame for that series. For single baseline VLBI observations this is the transverse (T), vertical (V), degenerate (D) frame [*Eubanks and Steppe*, 1988], for single station LLR observations this is the variation of latitude (ΔΦ), UT0, degenerate frame, and for SLR and multi-baseline VLBI observations this is the usual PMX, PMY, UT1 frame. There are no entries in Table 2 for components that were either not used (in the case of the CSR UT1 values) or whose overlap with the other series was not sufficiently long that a reliable rate correction could be determined. As can be seen, the bias corrections range from −4.687 mas to 4.293 mas with a mean value of −0.262 mas, a median value of −0.724 mas, and a standard deviation of 2.430 mas. The rate corrections range from −0.524 mas/yr to 0.801 mas/yr with a mean value of 0.277 mas/yr, a median value of 0.269 mas/yr, and a standard deviation of 0.374 mas/yr.

The IRIS data sets listed in Table 1 were not included in the above iterative, round-robin scheme since they were either not independent of the other series, or had been determined in a different manner from the other series. However, it is still of interest to know how well the bias and rate of the IRIS series agree with those of the other series. This was determined by comparing the IRIS series to a combination of all the other series after the bias-rate corrections and uncertainty scale factors listed in Table 2 for the other series had been applied to them. The "relative" corrections listed in Table 3 for the IRIS series are therefore the corrections that must be applied to them in order for them to agree (in bias, rate, and uncertainty) with a combination of all the other series listed in Table 1 (after the other series had been corrected to agree with each other by applying to them the corrections listed in Table 2). The errors listed in Table 3 for the bias-rate corrections are simply the formal errors in determining those corrections. Note that in determining the corrections for the IRIS series, the bias-rate corrections were determined first, and then the uncertainty scale factors were determined. Thus, the bias-rate corrections were determined before the uncertainties had been adjusted. This probably has little effect upon the values for the bias-rate corrections, but is likely to have a larger effect upon the formal errors of those corrections. This is probably one reason why the bias-rate errors given in Table 3 for the IRIS series are less than the corresponding errors given for the CDP series in Table 2.

The International Earth Rotation Service (IERS) is responsible for, among other things, defining and maintaining a terrestrial reference frame based upon the modern, space-geodetic observing techniques of VLBI, SLR, and LLR [e.g., *IERS Annual Report for 1989*, 1990, pp. I-1]. It is of interest to know how well a terrestrial reference frame determined by some individual solution agrees with that maintained by the IERS. This is studied herein by comparing the Earth orientation series identified in Table 1 with the Earth orientation combination [EOP(IERS) 90 C 02]

TABLE 4. COMMON BIAS-RATE CORRECTION APPLIED TO EACH SERIES IN ORDER TO PLACE IT WITHIN AN IERS REFERENCE FRAME

BIAS (mas)			RATE (mas/yr)		
PMX	PMY	UT1	PMX	PMY	UT1
−2.627	−0.591	4.244	−0.044	−0.588	−0.439
±0.031	±0.029	±0.040	±0.017	±0.016	±0.025

REFERENCE TIME FOR RATE ADJUSTMENT IS 1988.0

determined by the IERS. It is accomplished by determining an additional bias-rate correction, common to all series, that when added to those given in Tables 2 and 3 makes each series not only agree with each other in bias and rate, but also be in the same TRF within which the IERS combination [EOP(IERS) 90 C 02] is given. This additional, common, bias-rate correction is obtained by first combining all of the series given in Table 1, including the independent IRIS series (consisting of the "Intensive" series and the post-1989 multi-baseline values), after applying to them the corrections given in Tables 2 and 3 for them. This combination is then compared to the IERS combination in order to obtain the additional, common, bias-rate correction that must be applied to the series so that they not only agree with each other in bias, rate, and uncertainty, but are also in the same TRF as the IERS combination. The additional, common, bias-rate correction thus determined is given in Table 4. The error listed in Table 4 for this correction is simply the formal error in its determination.

By adding the common correction given in Table 4 to the relative corrections given in Table 2 for each series, the absolute corrections given in Table 5 are obtained. These corrections are termed "absolute" since they are the corrections that must be applied to the original series in order for them to not only agree with each other in bias, rate, and uncertainty, but also be in that particular TRF within which the IERS combination [EOP(IERS) 90 C 02] is given. The values in Table 5 are the sum of the values in Tables 2 and 4, but given in the natural reference frame for each series. No entry is given for the CSR UT1 values as these were not used in this study. If no relative rate correction is given in Table 2 for some series, then the corresponding entry in Table 5 for that series is just the common rate correction (but given, of course, in the natural reference frame for that series). The errors listed in Table 5 are the square root of the sum of the squares (rss) of the errors given in Tables 2 and 4 (but determined and given in the natural reference frame for each series). As can be seen, the absolute bias corrections range in value from −4.802 mas to 9.017 mas, with an average value of 0.626 mas, a median value of 0.263 mas, and a standard deviation of 3.388 mas. The absolute rate corrections range in value from −0.474 mas/yr to 0.605 mas/yr, with an average value of 0.005 mas/yr, a median value of −0.035 mas/yr, and a standard deviation of 0.286 mas/yr. Note that the rate statistics given here were computed by excluding those rate entries in Table 5 for series for which no relative rate corrections were determined.

Table 6 gives the absolute corrections for the IRIS series which are obtained by summing the entries in Tables 3 and 4. The errors given in Table 6 are the rss of the errors given in Tables 3 and 4.

TABLE 5. ADJUSTMENTS TO DATA SETS (ABSOLUTE)

DATA SET NAME	BIAS (mas)			RATE (mas/yr)		
LLR (L1707; ΔΦ, UT0)	ΔΦ		UT0	ΔΦ		UT0
McDonald 2.7m	−1.891		9.017	−0.559		−0.284
	±0.602		±0.752	±0.016		±0.023
McDonald LRS	0.232		5.657	−0.559		−0.284
	±0.483		±0.870	±0.016		±0.023
McDonald LRS (New Site)	−0.197		8.845	−0.559		−0.284
	±0.442		±0.496	±0.016		±0.023
CERGA	−2.057		5.450	0.355		−0.074
	±0.203		±0.142	±0.127		±0.088
Haleakala	0.858		7.797	0.605		0.053
	±0.401		±0.279	±0.279		±0.203
TEMPO (90 R 01; T, V)	T		V	T		V
CA (12) – Spain (63)	0.349		0.294	−0.226		0.486
	±0.554		±0.876	±0.022		±0.020
CA (14) – Spain (61)	2.110		−1.172	−0.227		0.484
	±0.550		±1.024	±0.022		±0.020
CA (14) – Spain (63)	1.889		−1.890	0.031		−0.039
	±0.155		±0.379	±0.076		±0.135
CA (15) – Spain (63)	1.354		−2.806	−0.227		0.484
	±0.234		±0.745	±0.022		±0.020
CA (12) – Australia (43)	−3.799		0.689	−0.576		−0.401
	±0.224		±0.745	±0.016		±0.021
CA (14) – Australia (42)	−3.134		1.043	−0.577		−0.399
	±0.251		±0.873	±0.016		±0.021
CA (14) – Australia (43)	−3.060		2.165	−0.474		−0.413
	±0.117		±0.275	±0.045		±0.112
CA (15) – Australia (43)	−2.378		0.666	−0.577		−0.399
	±0.186		±0.411	±0.016		±0.021
CDP (EOP.629)	T		V	T		V
Westford – Ft. Davis	−0.429		−0.482	−0.294		−0.548
	±0.331		±0.559	±0.020		±0.021
CDP (EOP.629)	PMX	PMY	UT1	PMX	PMY	UT1
Multi-Baseline	−1.225	−2.056	2.628	−0.035	0.187	0.120
	±0.060	±0.055	±0.107	±0.032	±0.030	±0.065
NAVNET (NAVY 1990-2)	PMX	PMY	UT1	PMX	PMY	UT1
Multi-Baseline	−1.656	−1.161	2.769	−0.044	−0.588	−0.439
	±0.171	±0.190	±0.208	±0.017	±0.016	±0.025
CSR (89 L 02; PMX, PMY)	PMX	PMY	UT1	PMX	PMY	UT1
Satellite Laser Ranging	−4.802	2.921	----	−0.069	−0.176	----
	±0.067	±0.062		±0.036	±0.033	

REFERENCE TIME FOR RATE ADJUSTMENT IS 1988.0

TABLE 6. ADJUSTMENTS TO IRIS DATA SETS (ABSOLUTE)

DATA SET NAME	BIAS (mas)			RATE (mas/yr)		
IRIS (28SEP90)	PMX	PMY	UT1	PMX	PMY	UT1
Multi-Baseline	−10.048	3.851	1.423	0.117	0.252	−0.108
	±0.043	±0.040	±0.055	±0.023	±0.023	±0.032
Intensive (UT1 Only)	----	----	1.387	----	----	0.006
			±0.054			±0.035

REFERENCE TIME FOR RATE ADJUSTMENT IS 1988.0

4. Conclusions

The results given in Tables 2 and 5 are the main results of this study. For the question of the long-term stability of the terrestrial reference frame, the rate correction results are the most important. If the standard deviation of these rate corrections is used as a measure of how stably the terrestrial reference frame can be currently determined, then it is seen that it can be determined to within about 0.3 mas/yr to 0.4 mas/yr, or about 1 cm/yr. This value, although representing the scatter in the rate corrections that must be applied to independent determinations of Earth orientation series in order for them to agree with each other in rate, should also represent the scatter in the rate at which the underlying TRFs are drifting away from each other, regardless of the direction of that drift. As planned improvements to the hardware and software of the observing systems are implemented, these rate discrepancies should diminish, with concomitant improvement in the determination of the terrestrial reference frame.

ACKNOWLEDGMENTS. The work described in this paper was performed at the Jet Propulsion Laboratory, California Institute of Technology, under contract with the National Aeronautics and Space Administration.

References

DOE, Glaciers, ice sheets, and sea level: Effect of a CO_2-induced climatic change, Report of a workshop held in Seattle, Washington September 13-15, 1984, *Department of Energy, DOE/ER/60235-1*, 343 pp., National Technical Information Service, Springfield, VA, 1985.

Eubanks, T. M., Combined Earth orientation series smoothed by a Kalman filter, in *Bureau International de l'Heure Annual Report for 1987*, pp. D85-D86, Observatoire de Paris, Paris, France, 1988.

Eubanks, T. M., and J. A. Steppe, The long term stability of VLBI Earth orientation measurements, in *The Impact of VLBI on Astrophysics and Geophysics*, edited by M. J. Reid and J. M. Moran, pp. 369-370, D. Reidel, Dordrecht, Holland, 1988.

Eubanks, T. M., M. S. Carter, F. J. Josties, D. N. Matsakis, D. D. McCarthy, and J. Russell, Earth orientation results from the U.S. Naval Observatory VLBI program, in *IERS Technical Note 5: Earth Orientation and Reference Frame Determinations, Atmospheric Excitation*

Functions, up to 1989 (Annex to the IERS Annual Report for 1989), pp. 33-39, Observatoire de Paris, Paris, France, 1990.

Gross, R. S., and J. A. Steppe, Tectonically-induced divergences of Earth rotation series, paper presented at IAU Colloquium 127: Reference Systems, Inter. Astron. Union, Virginia Beach, VA, October 14-20, 1990.

Gross, R. S., and J. A. Steppe, A combination of Earth orientation data: SPACE90 (in press), *IERS Annual Report for 1990*, Observatoire de Paris, Paris, France, 1991.

JOI, Towards an integrated system for measuring long term changes in global sea level, Report of a workshop held at Woods Hole Oceanographic Institution, May 2-4, 1990, 194 pp., Joint Oceanographic Institutions Incorporated, Washington, D.C., 1984.

Kovalevsky, J., I. I. Mueller, and B. Kolaczek (eds.), *Reference Frames in Astronomy and Geophysics*, 474 pp., Kluwer, Norwell, Mass., 1989.

Lambeck, K., *Geophysical Geodesy: The Slow Deformations of the Earth*, 718 pp., Oxford University Press, Oxford, 1988.

Ma, C., J. W. Ryan, and D. S. Caprette, Earth orientation parameters with estimated site velocities from the NASA Crustal Dynamics Project, in *IERS Technical Note 5: Earth Orientation and Reference Frame Determinations, Atmospheric Excitation Functions, up to 1989 (Annex to the IERS Annual Report for 1989)*, pp. 1-4, Observatoire de Paris, Paris, France, 1990.

Minster, J. B., and T. H. Jordan, Present-day plate motions, *J. Geophys. Res.*, **83**, 5331-5354, 1978.

Morabito, D. D., T. M. Eubanks, and J. A. Steppe, Kalman filtering of Earth orientation changes, in *The Earth's Rotation and Reference Frames for Geodesy and Geodynamics*, edited by A. K. Babcock and G. A. Wilkins, pp. 257-267, D. Reidel, Dordrecht, Holland, 1988.

NRC, Sea level change, *National Research Council, Studies in Geophysics*, 246 pp., National Academy Press, Washington, D.C., 1990.

Newhall, X X, J. G. Williams, and J. O. Dickey, Earth rotation (UT0–UTC) from lunar laser ranging, in *IERS Technical Note 5: Earth Orientation and Reference Frame Determinations, Atmospheric Excitation Functions, up to 1989 (Annex to the IERS Annual Report for 1989)*, pp. 41-44, Observatoire de Paris, Paris, France, 1990.

Pugh, D. T., *Tides, Surges, and Mean Sea-Level*, 486 pp., Wiley, New York, 1987.

Schutz, B. E., B. D. Tapley, R. J. Eanes, and M. M. Watkins, Earth rotation from LAGEOS laser ranging, in *IERS Technical Note 2: Earth Orientation and Reference Frame Determinations, Atmospheric Excitation Functions, up to 1988 (Annex to the IERS Annual Report for 1988)*, pp. 53-57, Observatorie de Paris, Paris, France, 1989.

Steppe, J. A., S. H. Oliveau, and O. J. Sovers, Earth rotation parameters from DSN VLBI, in *IERS Technical Note 5: Earth Orientation and Reference Frame Determinations, Atmospheric Excitation Functions, up to 1989 (Annex to the IERS Annual Report for 1989)*, pp. 13-24, Observatorie de Paris, Paris, France, 1990.

POLAR MOTION OBSERVED BY DAILY VLBI MEASUREMENTS

A. Nothnagel, J. Campbell

Geodetic Institute of the University of Bonn
Nussallee 17
D-5300 Bonn 1
Federal Republic of Germany

ABSTRACT. In 1986 and 1987 the Hartebeesthoek Radio Astronomy Observatory in South Africa and the Wettzell Geodetic Fundamental Station in Bavaria, FRG, performed two short series of daily VLBI experiments for polar motion monitoring. The two series were scheduled for periods of about 35 days with each session lasting only 2 hours. The purpose of these short daily sessions was to demonstrate the potential of the VLBI technique to monitor polar motion by relatively short and inexpensive experiments on a long north-south baseline. Furthermore, this first daily pole position monitoring project should allow to investigate short period fluctuations of the pole.

Here we present the final results of the two series. Small scale fluctuations in the path of the pole are discernible and were analysed with spectral analysis techniques. The raw data shows accuracies of about 1 mas for each pole component. Considering the reduced observing requirements compared with present day earth orientation monitoring networks, these results demonstrate the high sensitivity of north-south baselines for both components of polar motion.

1. INTRODUCTION

In January and February 1986 and 1987 the Hartebeesthoek Radio Astronomy Observatory (HartRAO) in South Africa was temporarily equipped with a Mark III data acquisition terminal and a wide band dual frequency receiver on loan from the US National Geodetic Survey (NGS), National Oceanographic and Atmospheric Administration of the U S Department of Commerce (NOAA). The installation of this equipment for the first time permitted measurements of highest accuracy with a station in the southern hemisphere .

With the Hartebeesthoek Radio Astronomy Observatory and the Wettzell Geodetic Fundamental Station in the Federal Republic of Germany a long north-south baseline was formed which is almost equally sensitive to changes in both components of polar motion as compared to a single east-west baseline which - with restrictions - can only be sensitive to one component. The baseline between the Wettzell Geodetic Fundamental Station and HartRAO has a z component of 7580 km. This is about eight times its x component and five times its y component which results in large values for the partial derivatives of the pole components and thus a high sensitivity for changes in these parameters.

In order to exploit the sensitivity of this baseline, daily polar motion measurements of short duration were initiated in 1986, complementary to those routinely observed in the IRIS-Intensive project for UT1 determinations (Robertson et al., 1985). Two series of daily measurements spanning periods of 30 to 36 days were prepared using any day where the stations were not occupied by multi-station measurements. The main purpose of the daily sessions was to demonstrate the potential of the VLBI technique to monitor

polar motion by relatively short and inexpensive measurements on a long north-south baseline. Furthermore, the first daily pole position measurements would allow a search for short period fluctuations of the pole.

2. OBSERVATIONS

In 1986 25 sessions were scheduled in the period of January 12 to February 11. Most of them took place at the same sidereal time in the morning (7h UT) while six measurements had to be shifted to the evening hours (20h UT) because the Wettzell observatory was occupied by other commitments in the morning. In 1987 only 24 sessions but all at the same sidereal time were scheduled between Januray 21 and February 27.

For practical reasons the sessions of the single baseline observations were restricted to use no more than two magnetic tapes for data recording per station in 1986 and three magnetic tapes in 1987. About 200 to 400 seconds integration time were used to receive signals from the radio sources for each delay observable resulting in 10 to 15 observations for a single session.

The small number of individual delay observables in a session puts severe restraints on the geometric configuration of the observations. Unlike short term UT1 determinations, for example the IRIS Intensive series, short polar motion measurements are strongly affected by intrinsic high correlations between one polar motion component and the clock offset between the two stations. In order to reduce correlations and achieve well conditioned normal equations it is important to use a distinct configuration of observations relative to the baseline which we shall discuss later.

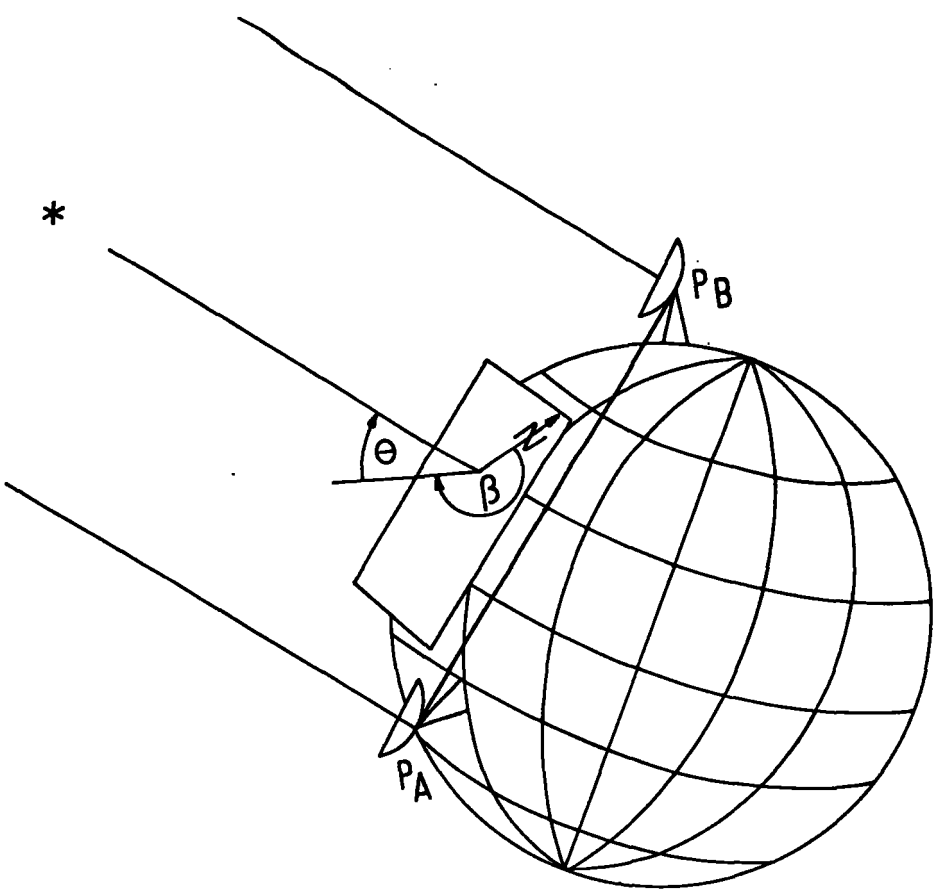

Figure 1. Location and Orientation of Baseline Reference System

Conventional scheduling programs, like SKED, display the instantaneous source positions relative to each station and do not disclose any information about the position of the source relative to the baseline. In order to select the observations according to special requirements a procedure was developed which graphically displays the geometric configuration of each observation relative to a fictitious baseline reference point. This reference point is defined as the projection of the baseline midpoint onto the ellipsoid and serves as the origin of a topocentric system with the tangential plane being the equatorial plane of this system (Figure 1).

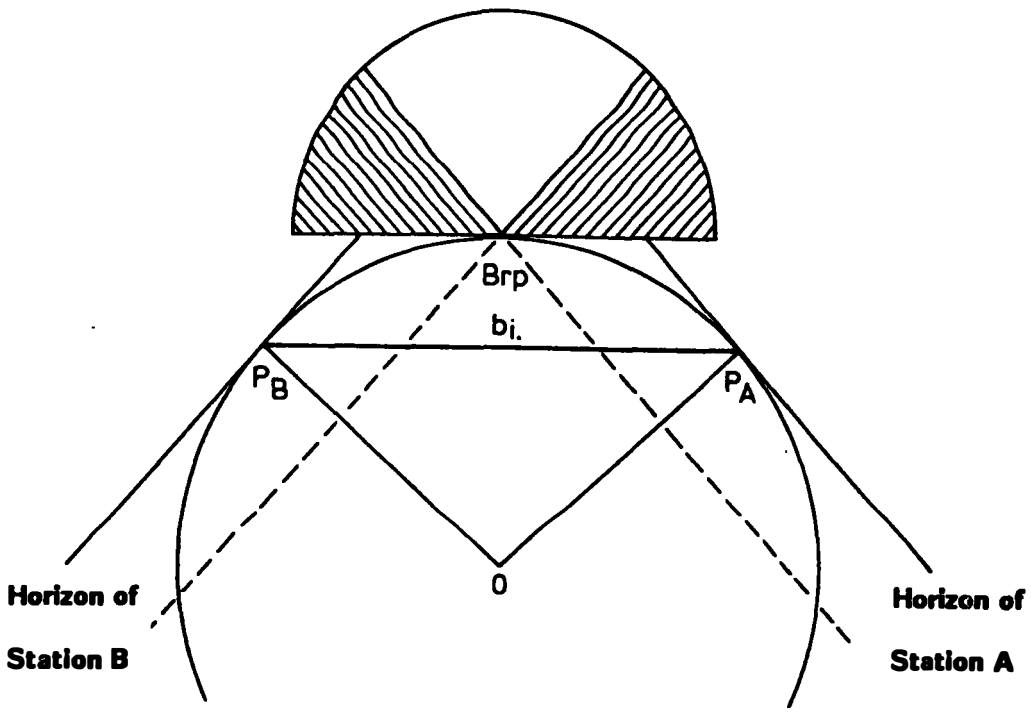

Figure 2. Geometry of Baseline Reference System and Horizon Mask

In a different projection the baseline system can be interpreted as a hemisphere put on top of the ellipsoid at the baseline reference point. Figure 2 gives an impression how the sky available for observations is limited depending on the baseline length. Perpendicular to the baseline, however, the areas are narrowed but the depth of these valleys remains unchanged. Both, the horizon limits of the two stations and the observations are best displayed in a stereographic projection (Figure 3). The solid line is the natural horizon while the dashed line is a 10° elevation limit.

The observing schedule of 1986 consisted of 11 observations with a maximum hour angle separation of 126° and a minimum elevation of 10°. Simulations have shown that part of the observations should span as wide an hour angle as possible and part of them should be placed in the zenith of the baseline reference point in order to reduce correlations and to increase the accuracy of the pole position results (Nothnagel et al., 1988). In 1987 the schedule was prepared using the display method explained above and provided 15 observations with a maximum hour angle separation of 139° and an elevation cut-off of 20° to reduce atmospheric refraction effects.

It should be emphasised here that the observations in the valleys perpendicular to the baseline are most important for a good constitution of the normal equations for all types of experiments. Independent of the purpose of the experiment the angular separation of these observations affects the degree of correlation between the clock offset and the vertical component in this system and thus the overall accuracy.

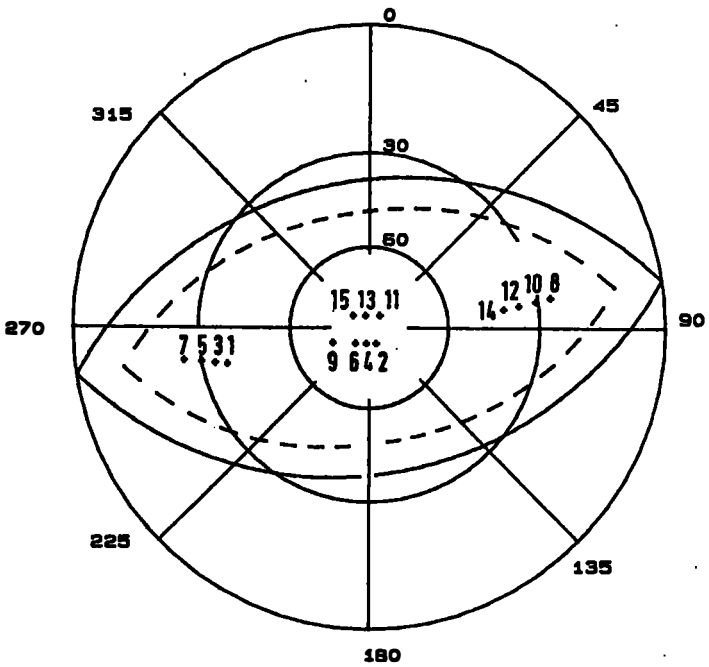

Figure 3. Stereographic Projection of Baseline Reference System (Observing Schedule of 1987 with 20° Elevation Limit)

3. DATA ANALYSIS

The analysis of short duration measurements for the estimation of the components of polar motion has to rely on externally determined terrestrial and celestial reference frames as well as on the precession, nutation and spin matrices to be able to establish the relationship between the reference frames. For the final analysis of the daily polar motion observations all necessary information to define the reference frames was taken from the NASA CDP627 global VLBI solution (Ma et al., 1990). This data set contains the data of all available Mark III network measurements between 1980 and 1989 including 24 IRIS-S network observing sessions of 24-hour duration in which HartRAO participated for the last four years. This time span was necessary to gather enough data to ensure that this solution provides an adequate foundation for the HartRAO station coordinates relative to Wettzell.

All sessions of the intensive polar motion campaign were individually reduced using the CALC 7.0/SOLVE software system. The use of the terrestrial and celestial reference frames from the global solution CDP627 for our analysis made it necessary to also apply the respective nutation corrections. Therefore, we performed spectral analyses of the nutation offset results of CDP627 similar to the technique used by Herring et al. (1986). In the reduction of the daily polar motion measurements we then introduced nutation corrections which we computed analytically from the coefficients of the spectral analyses. For the tropospheric corrections we used the CfA 2.2 model (Davis et al., 1985) based on surface meteorological data. The ionospheric refraction was calibrated by dual frequency observations.

In the least squares adjustments only the two polar motion components x_p, y_p, and the offset and rate between the two station clocks were estimated. Higher order clock terms were neglected in these short observing sessions as were estimates for atmospheric excess path delays.

The formal errors of the pole coordinates were based on observation weights adjusted so that the Chi-square (χ^2) per degree of freedom ratio are

close to unity. In 1986 an average of about 100 psec was added quadratically to each a priori sigma of the delay observables. These contributions to the a priori variances should account for unmodelled effects in the data reduction (Herring et al., 1986). As has been mentioned the observing schedules of 1987 were prepared with a more sophisticated strategy which further reduced the sensitivity of the observations to atmospheric modelling errors. This resulted in a reduced scatter of the residuals and thus a χ^2 of about 1 was achieved by adding only about 50 psec to each a priori sigma.

4. RESULTS

Figures 4 and 5 depict the pole paths of early 1986 and 1987 according to the daily measurements together with the results from 5-daily multi-station IRIS experiments. The average formal errors of the 1986 results are 0.73 mas for the x component and 0.38 mas for the y component while in 1987 the formal errors are 0.43 mas and 0.27 mas, respectively. Since the error bars are too small to be seen in this scale the data points are depicted as crosses of a fixed size. The daily pole position results show a smooth path within the pole positions fixed by the results of the 24 hour IRIS-A measurements. Differences between an interpolated pole path of the IRIS-A results and the actual measurements do not exceed five sigma. There may, however, be a small offset in the y component of about 1 mas between the IRIS-A and the intensive series. This offset may be due to inconsistent HartRAO station coordinates of the order of 3 cm.

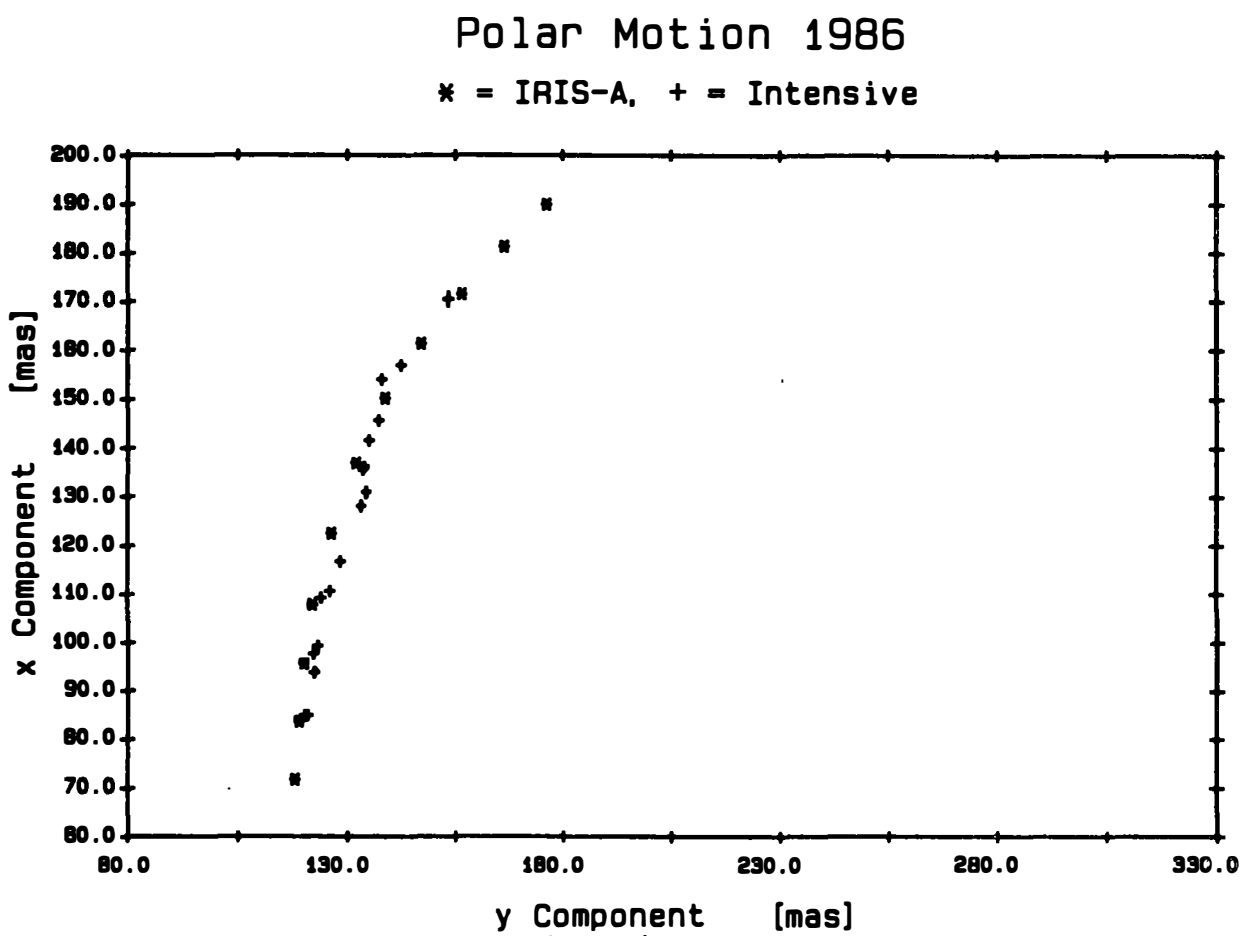

Figure 4

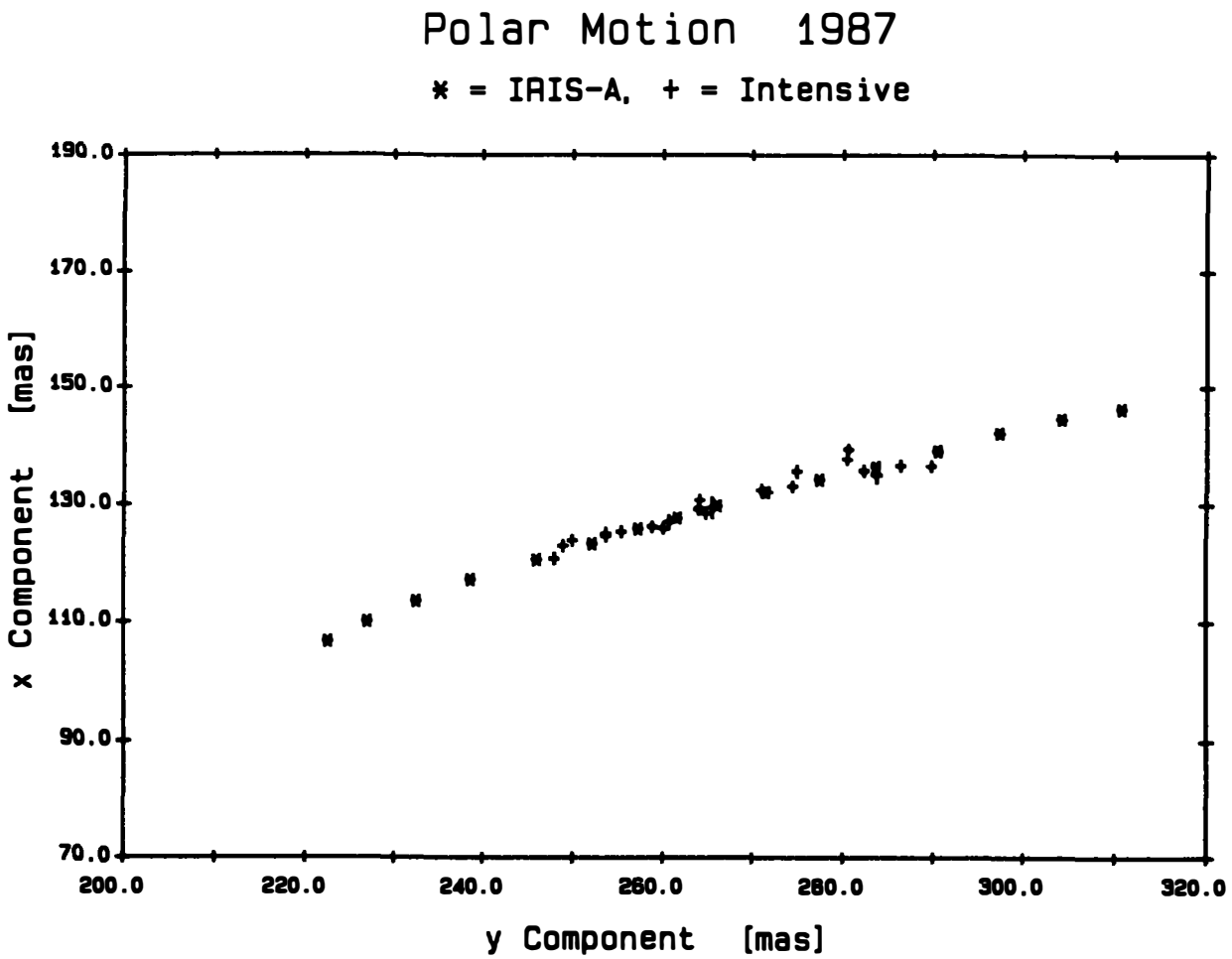

Figure 5

5. ERROR ANALYSIS

The analysis of the daily VLBI measurements may be affected by several systematic error sources. In order to estimate the influence of these possible systematic error sources calculations were performed changing the magnitude of these effects and comparing the results. The most uncertain part in the analysis of VLBI measurements is the tropospheric correction. The influence of the tropospheric corrections is dependent on the schedule and thus changes between 1986 and 1987 owing to the change in the elevation limit from 10° to 20°.

The imperfections in the analytical model for the nutation corrections introduces small errors in the pole positions as well. In UT1 there are small differences between the values interpolated from the 5-daily IRIS-A measurements and results of daily UT1 measurements performed within the IRIS-Intensive campaign (Robertson et al., 1985). The combined effect of these systematic error sources is determined by forming the root sum squared (RSS) of the errors.

The results indicate that in 1986 the major contribution to the error budget is the tropospheric refraction. A comparison between the RSS error and the standard deviation of this year shows that the formal errors of the pole position results may be too optimistic. In 1987 the influence of the tropospheric refraction has been reduced considerably and possible systematic errors are at the same level as the measurement noise. In both years the scatter of the results about a mean pole path which can also be interpreted as a measure of repeatability seems to confirm the validity of this estimate.

Estimate of Systematic Errors

ERROR SOURCE		x_p [mas]	y_p [mas]
Nutation $d\psi$		0.12	0.12
$d\epsilon$		0.32	0.20
DUT1		0.35	0.20
Troposphere	1986	0.80	0.60
	1987	0.12	0.09
RSS	1986	1.0	0.5
	1987	0.5	0.3
Av. Standard Deviation	1986	0.73	0.38
	1987	0.43	0.27

Table 1

6. SPECTRAL ANALYSIS

One of the goals of the polar motion intensive series was to investigate possible short period fluctuations of the pole path which are hardly to be detected by 5-daily observing intervals. Therefore, a spectral analysis was performed with the data. The two data sets with x and y components were first transformed into along-track (tangential) and cross-track (radial) components as described by Schuh (1989).This was achieved by fitting circles to the data (Figure 6) and subsequently calculating residuals to the average radii and angles. Equally spaced data is required for the spectral analysis and missing data points were interpolated linearly.

Table 2 contains the results of our analysis. The signal-to-noise-ratio (SNR) is calculated by dividing the amplitudes through the respective sigma. The spectral analyses of the polar motion data of both years yielded several periods with significant amplitudes exceeding the 3-sigma threshold. More periods are found in the 1987 data owing to the improved observing strategy and thus smaller standard deviations in the polar motion results.

In 1987 the 13.7 day period has the largest amplitude and the highest signal-to-noise-ratio of all periods detected. In 1986 the only period which may correspond to this is a 12.3 day period. However, this deviation may result from the observing schedule which was somewhat worse in 1986 than that in 1987. The period found is very close to the theoretical earth tide frequency of 13.66 days which is a sound indication of real detection. A similar degree of agreement between the data of the two years can be found in the 23.1 day period in the radial component of 1986 and the one of 20.2 days in the 1987 data which have similar amplitudes in the range of about 1 mas.

There are a few periods with cycles shorter than the 10 day Nyquist frequency detectable by the regular 5-daily IRIS-A observations. Although their signal-to-noise-ratios seem to confirm a high probability of real existence some of the amplitudes of the short periods are at the same level as possible systematic effects. Therefore, much longer observing periods with daily observations are required to make full use of the high temporal resolution and to achieve doubtless detections.

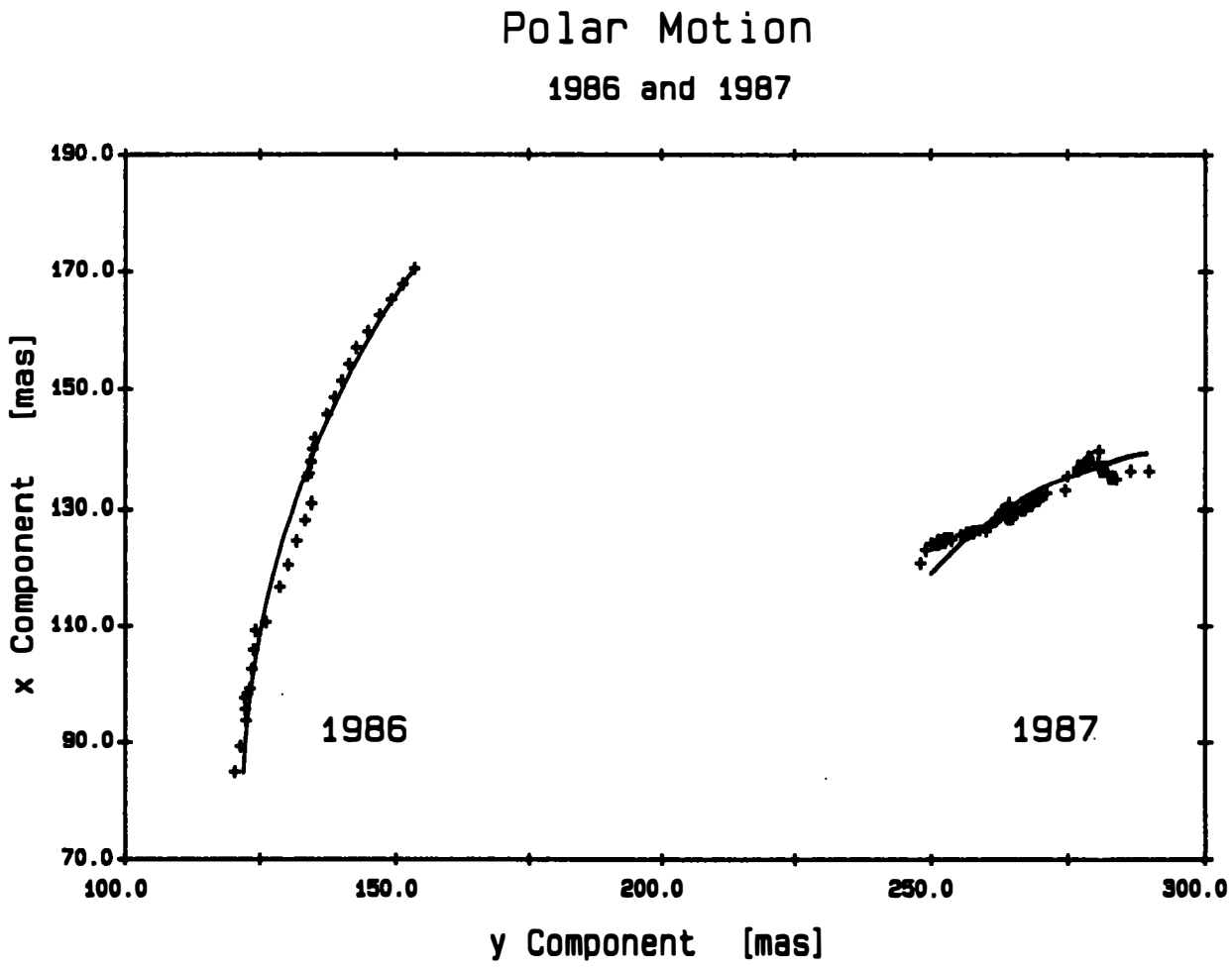

Figure 6. Pole Positions with Fitted Circles

Results of the Spectral Analysis

Data set	Component	Period [days]	Amplitude [mas]	SNR
1986	radial	4.2	0.32 ± 0.08	4.2
		8.5	0.49 ± 0.08	6.4
		12.3	0.65 ± 0.08	8.2
		23.1	1.39 ± 0.08	17.4
	tangential	6.3	1.46 ± 0.61	2.5
		7.4	1.71 ± 0.60	2.8
1987	radial	2.9	0.21 ± 0.07	3.1
		7.2	0.59 ± 0.07	8.3
		9.6	0.33 ± 0.08	4.4
		13.3	1.15 ± 0.08	14.4
		20.2	0.80 ± 0.09	9.1
	tangential	3.8	0.06 ± 0.02	2.7
		5.1	0.11 ± 0.02	5.0
		6.5	0.08 ± 0.02	3.4
		14.9	0.12 ± 0.02	5.5

Table 2

CONCLUSION AND OUTLOOK

This series of short daily pole position measurements on a single baseline has shown that the technique of geodetic VLBI is capable of monitoring polar motion with very high temporal resolution. The basis for the success of this project was the north-south baseline between Hartebeesthoek in South Africa and Wettzell in the Federal Republic of Germany which is particularly sensitive to polar motion. The design of the observing schedules plays an important role in achieving these remarkable results.

In the polar motion data presented here significant periods shorter than 30 days were identified. A period of 13.7 days was found in both the 1986 and 1987 intensive series with a high degree of reliability. However, signal-to-noise-ratios of most other periods are comparably small and thus need further confirmation through longer observing periods. In addition, some of the amplitudes of the short periods detected in this analysis are at the same level as possible systematic effects.

The internal accuracy of these 2 - 3-hour measurements is only slightly worse than the 24h sessions using the 4 or 5 station IRIS-A network. Nevertheless, observations with networks of stations and observing sessions of 24-hour duration will always be necessary to provide the required information about the terrestrial and celestial reference frames.

The ideal setup for checking the absolute accuracy of such polar motion observations is a configuration with two parallel north-south baselines. This idea was partly realised by a network of four stations (Wettzell, HartRAO, Kashima and Hobart) which performed short daily observations for a period of 1 month from February 13 to March 13, 1991. The schedules were prepared so that two independent solutions with either the triangle Wettzell - HartRAO - Kashima or the triangle Kashima - HartRAO - Hobart will be possible in addition to a combined solution. The total observing time was roughly three hours and each station recorded three full passes. We anticipate that these observations will allow a rigorous determination of the absolute accuracy of such short term observations.

REFERENCES

Carter, W.E., D.S. Robertson, J.R. MacKay; Geodetic Radio Interferometric Surveying: Applications and Results: JGR, Vol. 90, No. B6, p. 4577; May 1985

Davis, J.L., T.A. Herring, I.I. Shapiro, A.E.E. Rogers, G.K. Elgered; Geodesy by Radio Interferometry: Effects of Atmospheric Modelling Errors on Estimates of Baseline Lengths; Radio Science, Vol. 20, p. 1593; 1985

Eubanks, T.M., J.A.Steppe, J.O. Dickey; Atmospheric Excitation of Rapid Polar Motions; Proceedings of IAU Symposium No. 128, The Earth's Rotation and Reference Frames for Geodesy and Geodynamics; Coolfont, West Virginia, USA; October 1986; Kluwer Academic Publishers, Dordrecht, Netherlands, 1988

Herring, T.A., I.I. Shapiro, C.R. Gwinn; Geodesy by Radio Interferometry: Studies of the Forced Nutations of the Earth, 1. Data Analysis; JGR, Vol. 91, No. B5, p. 4745; April 1986 (a)

Herring, T.A., I.I. Shapiro, T.A. Clark, C. Ma, J.W. Ryan, B.R. Schupler, C.A. Knight, G. Lundqvist, D.B. Shaffer, N.R. Vandenberg, B.E. Corey, H.F. Hinteregger, A.E.E. Rogers, J.C. Webber, A.R. Whitney, G.K. Elgered, B.O. Rönnäng, J.L. Davis; Geodesy by Radio Interferometry: Evidence for Contemporary Plate Motion; JGR, Vol. 91, No. B8, p. 8341, July 1986 (b)

Kaplan, G.H.; The IAU Resolutions on Astronomical Constants, Time Scales and the Fundamental Reference Frame; USNO Circular No. 163; Washington D.C.; 1981

Lieske J.H., T. Lederle, W. Fricke, B. Morando; Expressions for the Precession Quantities Based upon the IAU (1976) System of Astronomical Constants; Astron. Astrophys., Vol. 58, p. 1; 1977

Ma, C.; Very Long Baseline Interferometry Applied to Polar Motion, Relativity and Geodesy; Ph.D. Thesis; NASA Technical Memorandum 79582; Greenbelt, USA; 1978

Melbourne, W., R. Anderle, M. Feissel, R. King, D. McCarty, D. Smith, B. Tapley, R. Vicente; Project Merit Standards; United States Naval Observatory, Circular No. 167, Washington D.C., December 1983

Nothnagel, A., G.D. Nicolson, H. Schuh, J. Campbell, H. Cloppenburg, R. Kilger; Radiointerferometric Polar Motion Determination Using a Very Long North-South Baseline; Proceedings of IAU Symposium No. 128, The Earth's Rotation and Reference Frames for Geodesy and Geodynamics; Coolfont, West Virginia, USA; October 1986; Kluwer Academic Publishers, Dordrecht, Netherlands, 1988

Robertson, D.S., W.E. Carter, J. Campbell, H. Schuh; Daily Earth Rotation Determinations from IRIS Very Long Baseline Interferometry; Nature, Vol. 316, No. 6027, p. 424; Aug 1985

Ryan, J.R., D. Gordon, C. Ma; CALC 6.0 Memorandum; Goddard Space Flight Center; Greenbelt, MA, USA; 1985

Schuh, H.M.; Earth Rotation Parameters Determined by VLBI Within Project IRIS; IEEE Trans. on Instr. and Measurement, Vol. 38; April 1989

ON THE DAMPING OF THE NEARLY DIURNAL FREE WOBBLE

E. Groten and S.M. Molodenski*)

Institut für Physikalische Geodäsie,
Technische Hochschule
Petersenstraße 13, D-6100 Darmstadt
*) on leave from USSR Acad. Sci., Moscow

The spectral analysis of modern VLBI measurements allows us, first, to obtain reliable data concerning the period, amplitude and attenuation of the nearly diurnal free wobble (NDFW). The value of the period of NDFW gives mainly information about the flattening of the core-mantle boundary, whereas the value of the quality factor Q is connected with (1) the anelastic properties of the mantle, (2) dissipation of tidal enery in the ocean as well as with (3) the viscous and electromagnetic dissipation in the liquid core. We consider here the influence of the first two effects. It is found, that the dissipation of the tidal energy in the anelastic mantle and in the ocean results in the attenuation of the NDFW with the value of $Q \sim 1.5 \cdot 10^5$, which corresponds to the time of attenuation of the order of 150 years. This means, that the amplitude and phase of NDFW may preserve some invariable values during the time intervals, which are comparable or even essentially longer than all the time where modern VLBI-measurements are available. The comparison of the theoretical values of Q with the results of VLBI - as well as of modern tidal gravity measurements gives us the new possibilities to estimate the upper bounds of the mantle's anelastic properties, liquid core's viscosity and core-mantle electromagnetic coupling at the range of diurnal frequencies.

1. INTROCUCTION

Modern VLBI-measurements allow us, first, to obtain reliable data for period. amplitude and attenuation of free core nutation (FCN). After the spectral analysis of 234 series of measurements which were performed during ~ 4 years, Herring, Gwinn and Shapiro (1986) have discovered FCN with an amplitude of $(5,1 \pm 1,8) \cdot 10^{-4}$ mas and with a period of 432,2 mean solar days in space. The simple analysis of these new data (Gwinn, Herring, Shapiro, 1986) led to the important conclusion that the agreement between the results of measurements and Wahr's (1981) theory may be reached after replacing the hydrostatic value of the core-mantle flattening $e_h = (2,53 \text{ to } 2,56) \cdot 10^{-3}$ by $\tilde{e} \approx 1,67 \cdot 10^{-3}$. The different possible explanations of new VLBI-data (including the new values of the forced nutation amplitudes) were considered in a number of papers. Wahr & Bergen (1986) and Dehant (1986; 1988; 1989; 1990) have compared the effects of the mantle's inelasticity which were calculated based on the Anderson & Minster (1979) and Zschau & Wang (1985) rheological models with discrepancies between observed and theoretical (Wahr, 1981) nutation amplitudes. They concluded, that these effects are too small and that they cannot explain the main dis-

crepancies. They used rheological models for the mantle which were mainly based on the extrapolation of the comparatively well-known inelastic properties of the mantle in the range of the periods τ of the Earth's free oscillations (from a few seconds to one hour) and the insufficient and perhaps not very reliable data, of the mantle's inelasticity at Chandler's period (τ=14 month) up to the significantly different nutation periods $\tau \approx 1$ day. Obviously, such extrapolation may not be exact and reliable enough. Moreover, it is possible that the superposition of different perturbing factors (such as uncertainties of our knowledge of the mantle's inelastic properties, core-mantle boundary flattening e, the value of the moment of inertia C_1, of the liquid core etc.) can give some alternative explanations of the aforementioned disagreement. To exclude these uncertainties Molodenski & Kramer (1987) have calculated the nutation amplitudes for a large number (~10000) of Earth's models with different values of e, C_1 and with different mantle's rheological properties, which were described by an arbitrary frequency-dependent function $f(\sigma)$, varying in a sufficiently wide range. As a result, the region of the possible values of the parameters (e, C_1, f) was constructed for which the nutation amplitudes and the period of FCN are in sufficient agreement with their theoretical values.

It was found that there is a closed region of possible values of e within a comparatively short interval

$$2{,}63 \cdot 10^{-3} \leq e \leq 2{,}68 \cdot 10^{-3} \tag{1}$$

which is practically independent of the adopted values of C_1. At the same time, the possible values of f are strongly dependent on C_1. Thus for C_1/C = 0,11; 0,115 and 0,12 (where C is the total moment of inertia of the Earth) the limitations of f are

$$-18 \leq f \leq -4{,}5; \quad -3 \leq f \leq 9{,}5 \text{ and } 13{,}5 \leq f \leq 24, \tag{2}$$

respectively. In case of the model of inelasticity, adopted by Wahr & Bergen (1986) and described by the relation

$$Q_\mu(\sigma, r) = \tilde{Q}_\mu(r)(\sigma/\sigma_0)^n, \tag{3}$$

(where σ is the frequency, r is the radius, $Q_\mu(\sigma, r)$ are the parameters of the mantle's mechanical quality and $\tilde{Q}_\mu(r)$ is the known distribution of Q_μ with depth at the frequencies of the Earth's free oscillations σ_0) the limitations (3) are reduced to the conditions

$$n < 0{,}2 \text{ for } T = \frac{2\pi}{\sigma_0} = 1_s \tag{4a}$$

$$\text{and } n < 0{,}5 \text{ for } T_0 = \frac{2\pi}{\sigma_0} = 100_s. \tag{4b}$$

These restrictions are not as rigid as those which follow from the

analysis of the Chandler wobble; nevertheless, they are of interest because they correspond to the essentially different range of frequencies.

Moreover, some effects were considered which may be connected with the existence of a rigid inner core, core-mantle topography and with the possible influence of small errors in the adopted system of nutation constants for a rigid Earth.

Vries & Wahr (1990) and Buffett, Herring & Shapiro (1990) have estimated that the influence of the rigid inner core on the amplitude of the retrograde annual nutation is extremely weak (of the order of (3 to 4) $\cdot 10^{-5}$ arc seconds only) and that it can, consequently, not explain the disagreement between measurements and theory.

Kinoshita & Souchay (1988) and Zhu & Groten (1989) have recalculated the nutation amplitudes of the rigid Earth, taking into account the higher order effects in the motion of Moon and Sun. It was found, that these effects, too, are comparatively small.

The influence of the core-mantle boundary (CMB) topography on the amplitudes of the forced nutations was considered by Dehant (1990) and Bykova (1991). Dehant (1990) has estimated that the nutation amplitudes are sensitive enough to the CMB topography. Bykova (1991) has obtained the possible values of the corresponding effects, by taking into account modern results (Morelli & Dziewonski, 1987), of the core-mantle boundary. It was shown, that the influence of CMB on the nutation amplitudes depends mainly on the resonant excitation of the inertial waves in the liquid core. From a formal view point this effect may be large enough even for the very small amplitudes of CMB topography, provided that the CMB is close enough to some "resonant" forms (which are described by a single spherical harmonic $Y_n^m(\theta,\lambda)$ with different values of n,m, which depend on the frequency).

But a more detailed analysis shows that the probability of such coincidence is extremely low. Using the assumption about Gaussian distribution of the CMB coefficients in the spherical harmonics expansion and taking into account the limitation of (Morelli & Dziewonski, 1987) on the total amplitude of the CMB topography, Bykova has estimated that this probability is only equal to $\sim 10^{-5}$. Thus, the discrepancy between theoretical and observed nutation amplitudes can certainly not be attributed to the influence of CMB topography.

Summarizing we may conclude that all sets of modern data of forced nutation amplitudes give mainly (1) information on the flattening of the core-mantle boundary and (2) not very rigid restrictions on the possible rheological properties of the mantle for the nearly-diurnal range of frequencies.

The situation is quite different for the data interpolation in the damping of FCN. The main sources of the FCN energy dissipation should be (1) in the ocean; (2) in the inelastic mantle and (3) in the liquid core. In the last case, the dissipation may be caused by two possible sources: (a) viscous friction on the core-mantle boundary or (b) electromagnetic dissipation.

The modern information on the Earth's core viscosity and lower mantle's electroconductivity is very poor and is mainly based on some physical limitations. Frenkel (1950) has estimated that the viscosity ν of melted metals for temperatures and pressures which exist in the Earth's liquid core, is of the order of 0.1 Poise, while the viscosity of the silicates is of the order of $10^{10}-10^{13}$ Poises under the same conditions. The estimation $\nu \sim 0{,}1$ Poise was confirmed by Gans (1972). Up to now this value of viscosity is usually considered as most probable. The data for the attenuation of seismic waves which penetrate the liquid core result in the restriction $\nu \leq 10^{9}$ Poise (Zharkov, Trubitzin, 1980); the attenuation of the Earth's free oscillations practically does not depend on the value ν (MacDonald, Ness, 1961). Thus, up to now the estimates of the Earth's core viscosity which are based on physical considerations, have not yet found an experimental geophysical confirmation. Obviously, if the main cause of the FCN attenuation is the dissipation in the liquid core, then the data of the FCN damping can fill in this gap. At the same time, if the attenuation of FCN is mainly connected with the dissipation in the inelastic mantle, then the measurements of the quality factor Q_{FCN} will permit us to certainly obtain essentially more rigid restrictions for the possible values Q_{μ}. The basic aim of this report is the consideration of the effects (1) and (2), i.e. the estimation of the influence of the dissipation in the real ocean and in the inelastic mantle on the attenuation of free core nutation.

2. THE GOVERNING EQUATIONS

The influence of the real ocean on free and forced nutations of the Earth was earlier considered in (Wahr, Sasao, 1981; Molodenski, 1981) and the effects of the mantle's inelasticity were considered in (Molodenski, 1981; Wahr & Bergen, 1986; Dehant, 1986, 1988, 1989, 1990). We shall use here the system of governing equations of Molodenski (1981), which give the possibility to take into account the influence of both the inelastic mantle and the real ocean on the forced nutation as well as FCN in a similar way, in terms of the effective rigidity coefficients $\lambda_1 \ldots \lambda_4$ of the mantle which describe the reaction of the system (inelastic mantle plus real ocean) on the action of the volume forces and surface loads on the core-mantle boundary.

We shall use here the system of cartesian coordinates (x,y,z), which are described by the following system of conditions:

(1) At some initial moment of time t_0 the axes (x,y,z) coincide with the principal axes of the Earth's ellipsoid of inertia A and C, (including mantle, liquid core and ocean), correspondingly; and

(2) the motion of this reference frame at any subsequent time is described by the condition

$$\int_{\tau_2} \rho \, \vec{r} \times \vec{v} \, d\tau_2 = 0 \tag{5}$$

where τ_2 is the volume which is occupied by the system of mantle plus

ocean only, $\vec{v}$ is the velocity of the mass element $\rho d\tau_2$ with respect to the mobile reference frame (x,y,z), ρ is density and $\vec{r}$ is the radius vector.

In this system of coordinates the relation between the components of the Earth's angular momentum vector M_i and the vector of our reference frame angular velocity $\vec{\omega}$ reads as follows:

$$M_i = (I_{ik}^{(1)}+I_{ik}^{(2)})\omega_k + \iiint_{\tau_1} \rho\, \vec{r} \times \vec{v}\, d\tau_1, \tag{6}$$

where $I_{ik}^{(1)}$ and $I_{ik}^{(2)}$ are the inertia tensors of the liquid core and the system mantle plus ocean, respectively, which are defined by the relations:

$$I_{xx}^{(1)} = I_{yy}^{(1)} = A_1; \qquad I_{zz}^{(1)} = C_1;$$

$$I_{xx}^{(2)} = I_{yy}^{(2)} = A_2; \qquad I_{zz}^{(2)} = C_2;$$

$$I_{xz}^{(1)} = -\iiint_{\tau_1} \rho xz\, d\tau_1; \qquad I_{yz}^{(1)} = -\iiint_{\tau_1} \rho yz\, d\tau_1; \tag{7}$$

$$I_{xz}^{(2)} = -\iiint_{\tau_2} \rho xz\, d\tau_2; \qquad I_{yz}^{(2)} = -\iiint_{\tau_2} \rho yz\, d\tau_2;$$

where (A_1, C_1) and (A_2, C_2) are the principal moments of inertia of the liquid core and of the system (mantle plus ocean), respectively.

Let us suppose here that the liquid core is incompressible and homogeneous. In this case it is possible to use the well known Poincare's solution for the liquid core which describes the spatial destribution of the pressure P and displacements $\vec{u}$ as follows:

$$P = \rho\left(\Psi+\Phi_0 - \frac{\sigma+\omega}{\omega}\Phi_1 - V_t - V_i\right) \tag{8a}$$

$$(\sigma^2-4\omega^2)\,\vec{u} = \nabla\Psi + \frac{2\omega}{\sigma^2}\vec{k}\times\nabla\dot{\Psi} + \left(1-\frac{4\omega^2}{\sigma^2}\right)\left[\vec{k},\nabla\left(\Psi + \frac{2\sigma}{\omega}\Phi_1\right)\right], \tag{8b}$$

where σ is the angular frequency in the mobile reference frame, ω is the angular velocity of the Earth's rotation, $\vec{k}$ is a unit vector, which is oriented along the axis z,

$$\Phi_0 = \frac{\omega^2}{2}(x^2+y^2) \tag{9}$$

is the potential of the centripetal force for the case of the Earth's uniform rotation,

$$\Phi_1 = -\frac{r^2}{a^2} \sin\theta \cos\theta \, \mathrm{Re}(\epsilon e^{i(\sigma t-\lambda)}) \tag{10}$$

is the variation of Φ_0, which is connected with the nutational motion; a is the Earth's mean radius; θ is colatitude; λ is the longitude; ϵ is a complex number which defines the amplitude and phase of nutational motion of $\vec{\omega}$ with respect to the mobile reference frame:

$$\omega_x + i\omega_y = \omega\epsilon e^{i\sigma t}; \tag{11}$$

V_t is the tide generating potential

$$V_t = v_t \frac{r^2}{a^2} \sin\theta \cos\theta \cos(\sigma t-\lambda); \tag{12}$$

v_t is the amplitude of V_t; V_i is the variation of the potential, which is associated with the redistribution of masses inside the Earth; in case of a laterally homogeneous inelastic mantle V_i may be given in the form:

$$V_i = \frac{r^2}{a^2} \sin\theta \cos\theta \, \mathrm{Re}(v_i e^{i(\sigma t-\lambda)}), \tag{13}$$

where v_i is the complex value which determines the amplitude and phase of V_i; Ψ is the complex-valued function, which, in accordance with (8), determines the distributions of velocities and pressure in the liquid core. In case of a homogeneous and incompressible liquid core Ψ has a simple analytical form, which is totally similar to (13):

$$\Psi = \frac{r^2}{a^2} \sin\theta \cos\theta \, \mathrm{Re}(\psi e^{i(\sigma t-\lambda)}), \tag{14}$$

where ψ is a complex constant which determines the amplitude and phase of Ψ.

The relations (8-14) connect the unknown functions P, $\vec{u}$ as well as the unknown components ω_x ω_y with the values of three complex parameters ϵ, ψ v_i. To determine their values, it is necessary to take into account the mechanical properties of the inelastic mantle and real ocean and to consider then the system of some additional conditions. These last conditions read as follows:

(1) <u>the equation of the angular momentum.</u>

Substituting (8b) in (6), we get:

$$\vec{M} = C\,\omega\vec{e}_z + \mathrm{Re}[(\vec{e}_x - i\vec{e}_y)\,(A\,\omega\epsilon + I_1 + I_2)e^{i\sigma t}] + $$
$$+ \iiint_{\tau_1} \rho\,\vec{r}\times\vec{v}\,d\tau_1 \tag{15}$$

and

$$\iiint_{\tau_1} \rho\,\vec{r}\times v\,d\tau_1 = \mathrm{Re}[m(\vec{e}_x - i\vec{e}_y)\,e^{i\sigma t}],$$

where $A = A_1 + A_2$, $C = C_1 + C_2$ are the principal moments of inertia of the whole Earth,

$$m = C_1\left[\frac{\omega^3\psi}{\sigma(\sigma+2\omega)} - \epsilon\omega\right] + (C_1 - A_1)\,\frac{\omega^2\psi}{\sigma+2\omega}; \tag{17}$$

I_1, I_2 are two complex parameters, which are connected with $I_{xz,yz}^{(1,2)}$ by the relations:

$$I_{xz}^{(1)} + i\,I_{yz}^{(1)} = I_1\,e^{i\sigma t};$$
$$I_{xz}^{(2)} + i\,I_{yz}^{(2)} = I_2\,e^{i\sigma t}. \tag{18}$$

Substituting (15) in Euler's equation for the angular momentum

$$\dot{\vec{M}} + \vec{\omega}\times\vec{M} = \frac{C-A}{a^2}\,v_e(\vec{e}_x\sin\sigma t - \vec{e}_y\cos\sigma t), \tag{19}$$

we get the first relation between our complex parameters:

$$\frac{\sigma+\omega}{\omega}\left[A\epsilon + I_1 + I_2 + \frac{m}{\omega}\right] - eC + \frac{C-A}{a^2\omega^2}\,v_e = 0 \tag{20}$$

(2) <u>The boundary condition on the core-mantle boundary.</u>

The continuity condition at the core-mantle boundary has the form:

$$(\vec{u},\vec{n}_0) = H(b) \tag{21}$$

where $\vec{n}_0$ is the outer normal of the elliptical core-mantle boundary;

$$\vec{n}_0 = \frac{\vec{r}}{r} + 2e\vec{K}\cos\theta;$$

e, as before, is the flattening of the core-mantle boundary, H(b) is the normal component of the core-mantle boundary displacements.

By taking into account that the dependence of H on the angular variables θ,λ has a form similar to (18)

$$H(b) = \sin\theta \cos\theta \, \mathrm{Re}(h\, e^{i(\sigma t-\lambda)}), \tag{23}$$

(where h is a new complex constant), it is easy to connect the values of h and I_1. For the case of incompressible homogeneous liquid core it has the form:

$$h = 2I_s/C_1 . \tag{24}$$

Substituting the expressions (23), (24) in (21) and using the representation of $\vec{u}$ in terms of ϵ, ψ, v_t, v_i (8b-14), we get:

$$(\vec{u},\vec{n}_0) - H(b) = b \sin 2\theta \, \mathrm{Re} \left\{ e^{i(\sigma t-\lambda)} \left[\psi \left(\frac{\omega^2(\sigma+\omega)}{\sigma^2(\sigma+2\omega)} + e\frac{\omega^2}{\sigma^2} \right) - \epsilon \frac{\omega}{\sigma}\left(1+2e\right) + \frac{I_1}{C_1} \right] \right\} = 0 \tag{25}$$

From (25), it follows that the expression in straight brackets, is equal to zero, too.

(3) <u>The equation for the angular momentum of the system (mantle plus ocean).</u>

This equation is reduced to the relation

$$\frac{\sigma+\omega}{\omega}(A_2\epsilon+I_2) - \epsilon C_2 + \frac{C-A}{\alpha^2\omega^2} v_t + \left(C_1-A_1\right)\left(\psi - \frac{\sigma+\omega}{\omega}\epsilon\right) + I_1 = 0. \tag{26}$$

It is easy to show that this equation is not independent of (24), (25). Multiplying the expression in straight brackets (25) of (1-2e) and subtracting (20) from it we get the equation which coincides exactly with (26). Thus, the equations (20, (25), (26) give only two restrictions on five unknown parameters ϵ, ψ, v_i, I_1, I_2.

To determine all unknown values uniquely, it is necessary to take into account the mechanical properties of the inelastic mantle and the actual ocean. To carry this out, we note that the tidal displacements in the liquid core and in the system (mantle plus ocean) are caused by two mechanisms: (1) the action of the volume tidal forces and (2) the action of the hydrodynamic pressure at the core-mantle boundary. Consequently, we may write the values I_1, I_2 in the form:

$$\frac{I_1}{C_1} = \lambda_1 \psi + \lambda_2 \frac{v_e}{ga};$$
$$\frac{I_1+I_2}{C_1+C_2} = \lambda_3 \psi + \lambda_4 \frac{v_e}{ga}, \tag{27}$$

where $\lambda_1, \ldots \lambda_4$ are dimensionless complex constants, of the "effective rigidity" which characterize the displacements of the core-mantle boundary and the tidal displacements in the system (mantle plus ocean) under the action of hydrodynamic pressure at the core-mantle boundary (λ_1, λ_3) and of the volume tidal forces (λ_2, λ_4); g is the mean gravitational acceleration at the Earth's surface which is introduced in (27) in order to reduce the values $\lambda_1, \ldots \lambda_4$ to the dimensionless form.

If the mechanical system (mantle plus ocean) is linear, the values $\lambda_1, \ldots \lambda_4$ don't depend on ψ and v_e, but only on the mechanical properties of mantle and ocean. Thus, we can assume that these values are known. By substituting (27) in (24), (25) and solving the system of algebraic equations obtained in such a way with respect to ϵ, we obtain, after neglecting some small terms, (Molodenski, 1981):

$$\epsilon \approx \epsilon_0 \left[1 + \frac{\frac{C_1}{C}(1+\alpha\lambda_2)}{(e+\lambda_1)\frac{\omega}{\sigma+\omega} + \frac{A_2}{A}} + \frac{\sigma+\omega}{\omega}\alpha\lambda_4 \right], \tag{28}$$

where

$$\alpha = \frac{C}{C-A}\frac{a\omega^2}{g} = 1{,}057$$

and

$$\epsilon_0 = -\frac{v_e}{a^2}\frac{C-A}{\omega\sigma A+\omega^2(A-C)}$$

is the nutation amplitude for the rigid Earth without liquid core and ocean. In case $\lambda_1 = \ldots \lambda_4 = 0$ the relation (28) coincides with the well known Poincare's solution; for the dissipationless models all the values λ_i are real, and relation (28) describes the influence of the mantle's elasticity at the period of FCN and on the amplitudes of forced nutation; the substitution of the complex values λ_i in (28) determines also the effects of dissipation both in the inelastic mantle and in oceans on the phase lag of the forced nutation and on the damping of FCN.

The frequency of FCN with respect to the mobile reference frame is described by using the condition that the denominator of (28) equals zero. This condition is valid if

$$\sigma = \sigma_0 = -\omega\left[1 + \frac{A}{A_2}(e+\lambda_1)\right]. \tag{29}$$

Using the well known definition of the mechanical quality parameter

$$Q_{FCN} = \frac{|\mathrm{Re}\ \sigma_0|}{2\ \mathrm{Im}\ \sigma_0}$$

and taking into account $|e+\lambda_1| \ll 1$, we get:

$$Q_{FCN} = -\frac{A_2}{2A\ \mathrm{Im}\ \lambda_1}. \tag{30}$$

Thus the value of the mechanical quality of FCN is connected only with Im λ_1. One realizes from (27) that Im λ_1 defines the phase of the core-mantle boundary displacements under the action of the pressure on it, which has the unit amplitude and is distributed proportionally to the second-order spherical harmonic $\sin\theta \cos\theta \cos(\sigma t-\lambda)$.

3. THE NUMERICAL ESTIMATIONS

3.1 The effect of mantle elasticity and inelastisity

Using the well-known MacCullagh's formula, it is easy to show that

$$\lambda_4 = -\frac{a^4 g}{3GC} k = -1{,}01\ k,$$

where G is the gravitational constant and k is the Love Number. Taking into account that for the real models of the elastic Earth without ocean k = 0,30, we have

$$\lambda_4 = -0{,}302. \tag{31}$$

Correspondingly, the corrections to λ_4, which take into account the mantle's inelastisity, have the imaginary part

$$\mathrm{Im}\ \delta\lambda_4 = \sim 1{,}01\ \mathrm{Im}\ k.$$

As it was mentioned above, the values Im k for the inelastic Earth models may be calculated only by applying some extrapolation of the known inelastic properties of the mantle at the periods of the Earth's free oscillations to the essentially lower nearly diurnal periods. Moreover, it is necessary to take into account the distributions of the mantle's inelastic properties and the shear energy densities inside the Earth. Using the method of perturbations, we can present the general relation between the variation of Love Number δk and the variations of the Lame's parameters $\delta\lambda$, $\delta\mu$ in the mantle as follows:

$$\delta k = \int_b^a (k_\mu(r)\ \delta\mu(r) + k_\lambda(r)\ \delta\lambda(r))dr, \tag{32}$$

where r is the radius, (b,a) are the radii of the liquid core and of the Earth, respectively, k_μ and k_λ are the known realfunctions of r, which depend only on the distribution of the mechanical parameters in

the elastic (unperturbed) model of the Earth. In case of the purely imaginary variations $\delta\mu$, $\delta\lambda$ the variations δk are imaginary, too, and the relations (32) determine the connections between Im k and the values

$$\delta\mu(r) = \mu_0(r)\, Q_\mu^{-1}(r),$$

and $\delta\lambda$, where $\mu_0(r)$ is the unperturbed distribution of the shear modulus and $Q_\mu(r)$ is the distribution of the parameters of the mechanical quality in the mantle.

It is usually assumed that the dissipation in the mantle is mainly connected with the shear and not with the variation of the volume. With this approximation

$$\delta\lambda = -\, 2/3\delta\mu,$$

and the relation (32) is consequently reduced to

$$\delta k = \int_b^a \mu_0(r) Q_\mu^{-1}(r)\ (k_\mu(r) - \frac{2}{3} k_\lambda(r))dr. \tag{33}$$

The numerical values of the functions $k_\mu(r)$, $k_\lambda(r)$ for the real Earth's model were calculated in (Molodenski, 1976). If we shall suppose that the values $Q_\mu(r)$ are independent of the periods not only for the range of the Earth's free oscillations frequencies, but also for the wider region of periods, including nearly diurnal periods, then the relation (33) results in

$$\text{Im}\ \delta k = (0{,}6 \div 0{,}8) \cdot 10^{-3}, \tag{34}$$

and, in accordance with (32), we have

$$\text{Im}\ \delta\lambda_4 = -\,(0{,}6 \div 0{,}8) \cdot 10^{-3}, \tag{35}$$

The valuees λ_1, λ_2 for the elastic and oceanless Earth entering in (28) were calculated by us for the model N° 508 of Gilbert & Dziewonski (1975). Their numerical values are as follows:

$$\lambda_1 = -0{,}61 \cdot 10^{-3};\ \lambda_2 = -\,0{,}57. \tag{36}$$

The corrections to these values due to mantle inelasticity were calculated by a method of perturbation which is in full length similar to the procedure described by us above. For the same rheological model the influence of mantle inelasticity leads to the corrections

$$\begin{aligned} \text{Im}\ \delta\lambda_1 &= (-0{,}6 \div -1{,}1) \cdot 10^{-6}, \\ \text{Im}\ \delta\lambda_2 &= (-0{,}7 \div -1{,}4) \cdot 10^{-3}. \end{aligned} \tag{37}$$

Substituting (37) in (30), we get:

$$Q_{FCN}^{(m)} = (5,5\pm1,5) \cdot 10^5. \tag{38}$$

It is easy to recalculate this value for rheological models which are arbitrary by dependent on frequency. Thus, in case of the dependence $Q_\mu(\sigma)$ described by (3) and for $T_0 = 1$ hour we get:

$$\begin{aligned}
Q_{FCN}^{(m)} &= (4,0\pm1,0) \cdot 10^5 \quad \text{if } n = 0,1;\\
Q_{FCN}^{(m)} &= (2,9\pm0,7) \cdot 10^5 \quad \text{if } n = 0,2;\\
Q_{FCN}^{(m)} &= (2,1\pm0,5) \cdot 10^5 \quad \text{if } n = 0,3;\\
Q_{FCN}^{(m)} &= (1,5\pm0,4) \cdot 10^5 \quad \text{if } n = 0,4;\\
Q_{FCN}^{(m)} &= (1,1\pm0,3) \cdot 10^5 \quad \text{if } n = 0,5;
\end{aligned} \tag{39}$$

3.2 The influence of the oceans

It is easy to show that the influence of the oceans on both forced and free nutation is only dependent on the values of the second order coefficients in the expansions of the ocean tides in the spherical harmonics. Indeed, using the spherical system of coordinates we have

$$I_{xz}^{(1)} = -\iiint_{\tau_1} \rho r^2 \sin\theta \cos\theta \cos\lambda \, d\tau_1;$$

$$I_{yz}^{(1)} = -\iiint_{\tau_1} \rho r^2 \sin\theta \cos\theta \sin\lambda \, d\tau_1.$$

The functions $\sin\theta \cos\theta \cos\lambda$, $\sin\theta \cos\theta \sin\lambda$ are proportional to the second-order spherical harmonics $Y_2^1(\theta,\lambda)$, $Y_2^{-1}(\theta,\lambda)$. Taking into account the orthogonality conditions for the spherical harmonics, we may conclude that only second order displacements $\sim Y_2^1(\theta,\lambda)$, $Y_2^{-1}(\theta,\lambda)$ can perturb the values $I_{xz}^{(1)}$, $I_{yz}^{(1)}$. At the same time, it is known that, in case of a laterally homogeneous (elastic or inelastic) mantle, the outer surface loading which is proportional to $Y_n^m(\theta,\lambda)$ implies desplacements of the core-mantle boundary which are proportional to the same spherical harmonic Y_n^m. Thus, only the second-order coefficients in the expansions of the oceanic tides in spherical harmonics must be taken into consideration by us.

The damping of FCN is determined by the imaginary parts of the effective rigidity parameters λ_i of the mantle with respect to the action of the pressure P (8a) for the model of a deformable mantle with the real ocean. Insofar as the value λ_3 does not enter in (28) and the value λ_4 enters only with a very small coefficient

$$\frac{\sigma+\omega}{\omega} \sim \frac{1}{400},$$

the damping of FCN does not depend on the phase of the non-diagonal

components of the ocean inertia tensor but on the phase of the core-mantle boundary oscillations. The mechanism of the damping is reduced to the following:

(1) The pressure P causes the elastic deformation of the core-mantle boundary.

(2) The elastic deformations are transmitted to the Earth's outer surface.

(3) Displacements of this surface affect, in turn, the ocean currents, which have the same nearly diurnal period, as the period of FCN with respect to the mobile reference frame. These currents are accompanied by the vertical displacements of the level of the ocean and the corresponding variations of the oceanic loads at the Earth's surface. Insofar as the real ocean at the nearly diurnal periods is described by a comparatively low values of Q, the phase of these loads lag essentially behind the phase of the pressure p and the phase of the initial displacements of the Earth's outer surface which cause the currents in the ocean.

(4) The oceanic loads cause a secondary elastic deformation of the Earth's surface, which are transmitted back to the core-mantle boundary. The phase of these secondary deformations coincides with the phase of the oceanic load and, consequently, it lags essentially behind the phase of the initial displacements. The phase lag of the second order spherical harmonics in the resulting displacements (which represent the sum of the initial displacements of the core-mantle boundary due to pressure P and the secondary displacements of the same boundary due to the oceanic loads) determines the imaginary part of λ_1 and the value Q of FCN.

The numerical calculation of this effect for the Earth's model N° 508 of Gilbert & Dziewonski (1975) leads to the following results:

1. If the amplitude of the core-mantle boundary h(b) is 1 centimeter, then the amplitude of the Earth's outer surface displacements h(a) = 0,739 cm and the amplitude of this surface displacements with respect to the equipotential surface is equal to

$\tilde{h}(a) = 0{,}388$ cm.

The oceanic currents caused by these displacements are equivalent to the currents which arise under the action of the tide generating potential with the frequency σ and with the amplitude

$\tilde{g}h(a) = 380\ cm^2/s^2$.

The second order spherical harmonic in the expansion of the corresponding gravitational potential variation is determined by the expression

$$\tilde{V} = \sin\theta \cos\theta \, Re(\tilde{v}\, e^{i(\sigma t - \lambda)}),$$

where $\tilde{v}=\tilde{k}g\tilde{h}(a)$ and $\tilde{k}$ is the correction to the Love Number k, which takes into account the influence of the ocean. The potential $\tilde{v}$ is generated by a layer of water, of desity ρ_0 and of depth h_0. Expressing $\rho_0 h_0$ in terms of $\tilde{v}$, we get:

$$\rho_0 h_0 = \frac{5}{4\pi G}\tilde{v}, \tag{40}$$

where G is the gravitational constant.

The pressure at the Earth's outer surface due to this layer of water is equal to

$$\tilde{p} = \sin\theta\cos\theta\,\mathrm{Re}(\tilde{p}e^{i(\sigma t-\lambda)}), \text{ where}$$

$$\tilde{p} = \rho_0 g h_0 = \frac{5}{4\pi G}\tilde{k}g^2\tilde{h}(a).$$

The pressure $\tilde{p}$ and the gravitational interaction between the layer (40) and the Earth result in the radial displacements of the core-mantle boundary

$$\delta H(b) = \sin\theta\cos\theta\,\mathrm{Re}(\delta h(b)\,e^{i(\sigma t-\lambda)}),$$

where

$$\delta h(b) = 0{,}24\,\tilde{k}h(b).$$

Comparing this expression with (24), (27), we get:

$$\frac{\delta h(b)}{h(b)} = \frac{\delta I_1}{I_1} = \frac{\delta\lambda_1}{\lambda_1} = 0{,}24\,\tilde{k}hb. \tag{41a}$$

Using relations (31), (24), and the solutions of the elastic equilibrium equations for the second order spherical harmonic in the real Earth it is easy to calculate also the corrections to the values λ_2, λ_4, which are connected with the influence of the ocean. Their values are

$$\delta\lambda_4 = -\frac{a^4 g}{3GC}\tilde{k} = -1{,}01\,\tilde{k}; \tag{41b}$$

$$\delta\lambda_2 = 0{,}61\,\tilde{k}. \tag{41c}$$

Substitution of (41a) in (28) yields the correction to the FCN period with respect to the mobile reference frame due to ocean:

$$\mathrm{Re}\,\frac{\delta\sigma}{\omega} = 1{,}6\cdot 10^{-4}\ \mathrm{Re}\,\tilde{k}. \tag{42}$$

Correspondingly, the correction to the period T of FCN in space is equl to

$$\delta T = -\frac{T}{\sigma+\omega}\,\mathrm{Re}\,\frac{\delta\sigma}{\omega} = 0{,}08\ \mathrm{Re}\,\tilde{k}\ T. \tag{43}$$

By substituting now (41a) in (30) we get:

$$\left(Q^{(oc)}_{FCN}\right)^{-1} = 3{,}3\cdot 10^{-4}\ \mathrm{Im}\,\tilde{k}. \tag{44}$$

Thus, we see that both δT and $Q^{(oc)}_{FCN}$ are uniquely determined by the value of the correction to the Love number $\tilde{k}$.

Taking into account that the frequency of FCN with respect to the mobile reference frame is extremely close to the frequency of the tidal Luni-Solar wave K_1; we can estimate the value $\tilde{k}$ from the known cotidal maps for this wave.

The values $\tilde{k}$ for the cotidal maps of Bogdanov & Magarik (1969) and Schwiderski (1980) were calculated by Pertzev (1987). The results for the wave K_1 are as follows:

	Bogdanov & Magarik (1969)	Schwiderski (1980)
$\mathrm{Re}\,\tilde{k} =$	$-0{,}0171$	$-0{,}0236$
$\mathrm{Im}\,\tilde{k} =$	$0{,}0078$	$0{,}0237.$

(45)

One sees that the values Re $\tilde{k}$ for the different cotidal maps are in a relatively good agreement; however, the difference of the values Im $\tilde{k}$ is significant.

Substituting these vales in (42-44) we find

$$Q^{(oc)}_{FCN} = \begin{cases} 3{,}9\cdot 10^{5} & \text{for the cotidal map B \& M (1969)} \\ 2{,}3\cdot 10^{5} & \text{for the map Schwiderski (1980)} \end{cases} \tag{46}$$

and

$$\delta T = (-0{,}8 \pm 0{,}1)\ \text{days}. \tag{47}$$

Comparing these values with (38) and (39), we may conclude that the influence of the inelastic mantle and the ocean in these effects is of the same orders of magnitude.

To obtain the more rigorous restrictions on the possible values of Q_{FCN}, it is necessary to use some analytical interpolation of the

mantle's rheological properties in the range of periods from ~ 1 hr to Chandler's period T_{CH} = 14 months. Such interpolation involves some information on the damping of Chandler wobble. It is known, that modern measurements of quality parameter Q_{CH} of the Chandler wobble lead to the conclusion, that their most probable value is of the order of

$$Q_{CH\ obs.} \sim 50 \text{ to } 100 \tag{48}$$

(see, for example, Currie, 1974, 1975; Yatskiv, 1973; Groten, 1984; Dickman, 1986). At the same time, if we use Lomnitz's rheological law as adopted in the theory of the Earth's free oscillation with the values $Q\mu(r)$ which are independent of the frequency satisfying the attenuation data of the Earth's free oscillations, then the theoretical value of Q_{CH} is equal to

$$Q_{CH\ theor.} \approx 500 \tag{49}$$

(Zharkov, Molodenski, 1977). Moreover, the influence of the mantle inelasticity leads to a lengthening of the Chandler period, which is equal to

$$\delta T \sim 2{,}9 \text{ days} \tag{50}$$

for the same rheological model (Zharkov, Molodenski, 1979). The disagreement between (48) and (49) may only be related to two possible reasons: (1) the dissipation of the tidal energy in the ocean and (2) some possibly weak dependence of $Q_\mu(\sigma)$ in the range of periods between ~ 1 hour and 14 months. It was shown by Smith & Dahlen (1981), that if one puts in (3) $n \approx 0{,}15 \pm 0{,}04$, then the theoretical values of Q and δT are equal to

$$\tilde{Q}_{CH\ theor.} \approx 50 \div 100 \tag{51a}$$

and

$$\delta\tilde{T} \sim 8 \text{ days}. \tag{51b}$$

These values are in good agreement with (50) and with Dahlen's (1976) calculation of the real ocean influence on the Chandler's period, which was found in hydrostatical approximation.

The problems associated with the validity of the hydrostatical approximation in the real ocean were considered in a large number of papers (see, for example, Carton & Wahr, 1986; Dickmen, et al., 1985, 1986, 1988; Groten et al., 1990; Molodenski, 1989; O'Connor, Starr, 1983; O'Connor, 1986a, 1986b; Okubo, 1982). From our point of view (see Groten, Lenhardt, Molodenski, 1990; Groten, Molodenski, Zwielich, 1990) there are up to now some significant difficulties in the dynamical theory of pole tides, which don't permit us to consider this problem as completely solved. That is why we shall not exclude here the case, for which the deviation of the pole tides from the equilibrium surface is great enough and most part of Chandler wobble is absorbed in the ocean. Correspondingly, we shall consider the simplest dependence

$Q_n(\sigma)$ in the form (3) with the parameter n, which is bounded by the limits

$$0 \leq n \leq 0,2. \tag{52}$$

Using our estimations (38), (39) and (45), we may conclude that in case n=0

$$Q_{FCN} = \left\{ \left[Q^{(m)}_{FCN}\right]^{-1} + \left[Q^{(oc)}_{FCN}\right]^{-1} \right\}^{-1}$$

$$= \begin{cases} 2,3 \cdot 10^5 & \text{for the cotidal map B \& M (1969)} \\ 1,1 \cdot 10^5 & \text{for the cotidal map Schwiderski (1980)} \end{cases}$$

and for n = 0,2

$$Q_{FCN} = \begin{cases} 2,0 \cdot 10^5 & \text{(B \& M, 1969)} \\ 1,0 \cdot 10^5 & \text{(Schwiderski, 1980)} \end{cases}$$

4. DISCUSSION AND CONCLUSIONS

It is interesting to note that the influence of dissipation in the inelastic mantle and in the ocean leads to extremely high values of Q_{FCN}. The time of FCN damping is

$$\tau = \frac{2}{|\sigma|} Q \sim 100 \div 200 \text{ years.}$$

This means that the amplitude and phase of FCN may preserve some invariable values during time intervals which are comparable to or even essentially longer than all the time where modern VLBI-measurements are available.

Up to now the measurements of the parameter Q_{FCN} were based mainly on the tidal measurements. Using superconducting gravimeters series (Zürn et al. (1985)) have estimated, for four different data sets at Bad Homburg:

Q_{FCN} = 3281 ± 479; 3120 ± 323; 3692 ± 7662; 3804 ± 7633;

Neuberg et al. have found Q_{FCN} = 2305 ± 673 at Brussels and Q_{FCN} = 3131 ± 826 at Frankfurt with mean value 2767 ± 529 (Melchior, et al., 1988); Sato (1990), using the measurements of tidal strains, found Q_{FCN} = 5200 ± 2500.

All these values are essentially less than the results of the calculations, given above which were based on the model fo the Earth with an inviscid liquid core, anelastic mantle and the actual ocean. From our point of view, this may be explained by two possible causes:

(1) the experimental determinations of Q_{FCN} were based on the comparison of observed tidal waves amplitudes (such as K_1, ψ_1) close to the resonance with their theoretical values. If this comparison was performed only for the Earth's model with the hydrostatical value of the core-mantle flattening $e = (2,53 \div 2,56) \cdot 10^{-3}$, then the disagreement between theoretical and observed values may rather be connected with the influence of non-hydrostatic value of this flattening, than with the influence of the dissipation. Obviously, in this case all estimations of Q_{FCN} must be reconsidered.

(2) it is possible, that the influence of the Earth's core viscosity and the electromagnetic core-mantle coupling are essential too and that these effects must be taken into account.

As it was mentioned above, in this case the determination of FCN damping can give a very important new information concerning the liquid core's viscosity and (or) the mantle's electroconductivity. Obviously, all these problems need additional consideration.

Summing up, we can conclude, that modern VLBI-measurements give a new and very valuable information concerning the problem of the Earth's mechanical properties in the range of the very low frequencies which cannot be obtained from any other sources of geophysical data.

REFERENCES

Anderson, D.L. & Minster, J.B. (1979) The frequency dependence of Q in the earth and implications for mantle rheology and Chandler wobble. Geophys. J. R. astr. Soc., 58, 431-440

Bykova V.V. (1991) On the influence of the core mantle boundary topography on the nutation of the Earth. Izv. Akad. Nauk SSR, Fizika Zemli [Solid Earth] No 3, p. 8-17

Carton J.A. and J.M. Wahr (1986) Modelling the Pole Tide and Its Effect on the Earth's Rotation. Geopys. J. R. astr. Soc. 84, 121-137.

Currie, R.G. (1974) Period and Qw of the Chandler wobble. Geophys. J. R. astr. Soc., 38, 179-185

Currie, R.G., (1975) Period Qp and amplitude of the pole tide. Geophys. J. R. astr. Soc., 43, 73-86

Dahlen F.A. (1976) The Passive Influence of the Oceans upon the Rotation of the Earth. Geophys. J. R. astr. Soc. 16, 363-406.

Dehant, V. (1986) Global Earth models and earth rotation. Proceedings of the NATO AWR Workshop on Earth Rotation: Solved and Unsoled Problems, June 1985, Bonas, France, pp. 269-275, ed. Cazenave, A., Reidel, Dordrecht

Dehant, V. (1988) Nutation and inelasticity of the earth. Proceedings of the 128th Symp. of IAUIAG on Earth Rotation and Reference Frames, 1987, Washington, pp. 323-329, eds. Babcock, A. & Wilkins, G.A., Reidel, Dordrecht

Dehant, V. (1989) Tidal parameters and nutations: influence from the Earth interior. Proc. of the 19th General Assembly of the IUGG, Symp. U4 on Earth Rotation, Vancouver, Canada, in press

Dehant, V. (1990) On the nutations of a more realistic earth model. Geophys. Journ. Int. 100, 477-483

Dickman, S.R., 1985 The self-consistent dynamic pole tide in global ocean. Geophys. J. R. astr. Soc., 81, 157-174

Dickman, S.R., 1986 The damping of the Chandler wobble and the pole tide, in "Earth rotation: solved and unsolved problems", edited by A. Cazenave, p. 203-228, D. Reidel Dodrect/Boston/Lancaster/Tokyo

Dickman, S.R. and D.J. Steinberg (1986) New Aspects of the Equilibrium Pole Tide. Geophys. J. R. astr. Soc. 86, 515-529.

Dickman S.R. (1988) The Self-Consistent Dynamic Pole Tide in Non-Global Oceans. Geophys. J. R. astr. Soc. 94, 519-543.

Frerkel, Ja. I. (1950) The introduction in the physics of metalls, Moscow (in russian)

Gans F. (1972) Viscosity of the Earth's core. J. Geophys. Res. Vol. 77, No. 2, p. 360-366

Gilbert, F. & Dziewonski, A.M. (1975) An application of normal mode theory to the retrieval structural parameters and source mechanisms from seismic spectra. Phil. Trans.R. Soc. Lond. A, 278, 187-269

Groten, E., (1984) The motion of the Earth. In "Landolt-Börnstein Zahlenwerte und Funktionen aus Naturwissenschaften und Technik. Neue Serie, Band 2 Geophysik der festen Erde, des Mondes und der Planeten, Teilband a", Herausgeber K. Fuchs und H. Stoffel, Springer-Verlag Berlin/Heidelberg/New Yor/Tokyo, 61-83

Groten, E., Lenhardt, H., Molodenski S.M. (1990) On the period and damping of polar motion. Proc. of Conf. of Math. Geophys. of IUGG, Jerusalem, in press

Groten, E., Molodenski, S.M., Zwielich J. (1990) Long-period perturbations in terrestrial reference frames. Proc. IAU Coll., Nov. 1990, Virginia Beach, (in press)

Gwinn, C.R., Herring, T.A. & Shapiro, I.I. (1986) Geodesy by radio interferometry: studies of the forced nutations of the Earth, 2. Interpretation. J. geophys. Res., 91, B5, 4755-4765

Herring, T.A. (1988) Some Remarks for the Resolutions to IAU Nutations Working Group, 21th General Assembly of the IAU, August 1988, Baltimore, USA

Herring, T.A., Gwinn, C.R. & Shapiro, I.I. (1986) Geodesy by radio interferometry: studies of the forced nutations of the Earth, 1. Data analysis. J. Geophys. Res., 91, B5, 4745-4754

Kinoshita, H. (1977) Theory of the rotation of the rigid earth, Celest. Mech., 15, 277-326

Kinoshita, H., Nakajima, K., Kubo, Y, Nakagouva, I., Sasao, T. & Yokoyence, K. (1979) Note on nutations in Ephemeris, vol. 12,no. 2, pp. 71-108, Publ. Int. Lat. Obs. Mizusawa

Melchior, P., Crossley, D.J., Dehant, V.P., Ducarme B. (1987) Have inertial waves been identified from the Earth's core? In: Structure and dynamics of Earth's deep interior. Geophys. Monograph., Eds: D.E. Smylie, R. Hide, USA

MacDonald, G.J.F., Ness, N.F. (1961) A study of the free oscillations of the Earth. J. Geophys. Res., Vol. 66, No 6, 1865-1911

Molodenski S.M., (1976) The dependance of Love numbers on the small variations of the Earth models. Izv. Akad. Nauk SSSR, Fizika Zemli [Solid Earth], No. 2, pp. 3-14

Molodenski, S.M. (1981) The influence of the ocean and anelasticity of the mantle on the Earth's nutation. Izv. Akad. Nauk, SSR, Fizika Zemli [Solid Earth], No. 6, pp. 3-17 (in Russian; in French: Bulletin d'Information, Marees Terrestres, Belgique, 1981, No. 86, p.p. 5545-5562)

Molodenski, S.M. & Zharkow, V.N. (1982) On the Chandler's wobble and the dependance of Earth mantle's values Ql from the frequency. Izv. Akad. Nauk SSSR, Fizika Zemli [Solid Earth], No. 4, pp. 3-16

Molodenski, S.M. & Kramer, M.V. (1987) Sur les propriétés mécaniques du noyau et de l'enveloppe d'apres les nouvelles données astronomiques. Bulletin Informations Marées Terrestres, No 102, 7183-7193, 1988, traduction in french of Phys. Earth, 11, 117-121, 1987 (in russian)

Molodensky S.M. (1989) Asymptotic Behaviour of Solutions to Laplace's Tidal Equations at Low Frequencies. Geophys. J. R. astr. Soc., 97, 459-469

Munk, W.H. & Mac Donald, G.J.F., 1960 The rotation of the earth. Cambridge University Press

O'Connor, W.P. & Starr, T.B., 1983 Approximate particular solutions for the pole tide in global ocean. Geophys. J. R. astr. Soc., 75, 397-405

O'Connor (1986a) The 14 Month Wind Stressed Residual Circulation (Pole Tide) in the North Sea. NASA Technical Memorandum 87800.

O'Connor (1986b) On the Application of Asymptotic Analysis to the Dynamical Theory of the Pole Tide. Geophys. J. R. astr. Soc. 85, 1-11.

Smith, M.L. & Dahlen, F.A., 1981 The period and Q of the Chandler wobble. Geophys. J. R. astr. Soc., 64, p. 223-284

Yatskiv, Ja. S., 1973 Chandler wobble and free diurnal nutation derived from latitude observations. Proc. 2nd Int. Symp. Geodesy & Physics of the Earth, Potsdam, 143-151

Wahr, J.M. (1981b) The forced nutations of an elliptical, rotating, elastic and oceanless Earth. Geophys. J. R. astr. Soc., 64, 705-727

Wahr, J.M. & Sasao, T. (1981) A diurnal resonance in the ocean tide and in the Earth's load response due to the reasonant free 'core nutation', Geophys. J. R. astr. Soc., 64, 747-765

Wahr, J.M. & Bergen, Z. (1986) The effects of mantle anelasticity on nutations, Earth tides and tidal variations on rotation rate,. Geophys. J. R. astr. Soc. 87, 633-668

Zharkov V.N. & S.M. Molodenski (1977) On the corrections for the dynamical shear moduli to Love numbers. Izv. Akad. Nauk SSSR, Fizika Zemli [Solid Earth], No. 5, pp. 17-19

Zharkov, V.N. & S.M. Molodenski, 1979 Corrections for the dynamical shear moduli for the Love numbers and Chandler's period. Izv. Akad. Nauk SSSR, Fizika Zemli [Solid Earth], No. 6, pp. 88-89

Zharkov, V.N. & S.M. Molodenski, 1980 The Love numbers of the anelastic Earth. In "Nutation and the Earth's Rotation", edited by E.P. Federov, M.L. Smith and P.L. Bender, IAU, pp. 239-242

Zhu, S.Y. & Groten, E. (1989) Various aspects of numerical determiantion of nutation constants. 1. Improvement of rigid Earth nutation. Manuscripta Geodaetica, submitted

Zschau, J. & Wang, R. (1985) Imperfect elasticity in the Earth's mantle: implications for Earth tides and long period deformations, pp. 379-384, Proc. of hte 10th Int. Symp. on Earth Tides, Madrid, Spain, eds. Vieira, R. & Consejo Superior de Investigaciones Cientificas, Madrid

Zürn, W. Schiltach, P.A., Rydelek, P.A., Richter, B. (1985) The core-resonance effect in the record from the superconducting gravimeter at Bad Homburg. Proc. of thenth Int. Symp. on Earth Tides, Ed.: Vieira, Madrid

ACKNOWLEDGEMENT

This work was performed when one of the authors (S.M. Molodenski) was invited by A. v. Humboldt foundation in Germany on a Humboldt-fellowship. The support by A. v. Humboldt foundation is gratefully acknowledged.

VLBI Reference Frames

Chopo Ma and James W. Ryan
NASA/Goddard Space Flight Center

W.E. Himwich
Interferometrics Inc./NASA

ABSTRACT

Through the end of 1990 geodetic VLBI measurements have been acquired from 36 fixed stations and 52 mobile sites (including several locations with multiple measurement points) connected by 480 baselines. The terrestrial reference frame constructed using the Goddard GLOBL VLBI analysis system from the ~688,000 observations has horizontal formal errors typically <4 mm and vertical errors typically <20 mm at 1988.0 including the adjustment of velocities for the 56 sites with sufficient data. The positions of other sites are propagated to the reference epoch, without additional covariances, using a plate motion model. Typical formal errors for horizontal velocities are <2 mm/yr while typical vertical rate uncertainties are <2 mm/yr for well-observed fixed stations and ~10 mm/yr for mobile sites. Data from both geodetic and astrometric observing programs have contributed to the 354 extragalactic radio sources forming the celestial reference frame with typical formal errors <1 milliarcsecond and negligible observed proper motion.

1. Observations

The geodetic and astrometric Mark III VLBI data used to create a unified terrestrial/celestial reference system have been acquired through a multi-agency, multinational cooperative effort spanning more than a decade. The primary geodetic contributors have been NASA's Crustal Dynamics Project (CDP), the Earth orientation monitoring programs initially organized by the NOAA's National Geodetic Survey (NGS) starting with the two-station POLARIS network and continuing with IRIS, and the U.S. Naval Observatory Navnet program, also for Earth orientation. IRIS has three regular networks - A (Atlantic), S (South Africa), and P (Pacific, sponsored by the Japanese National Astronomical Observatory at Mizusawa). Table 1 shows the distribution of observations and observing sessions by program. The mobile category includes both CDP and NGS mobile campaigns in North America, Hawaii, and Europe, while Japan comprises mobile observations by the Geographical Survey Institute in cooperation with the Communications Research Laboratory. Two special Eurasian sessions organized by the Geodetic Institute of Bonn University form the FRG (Germany) category.

Table 1. Geodetic data distribution by program

Observation counts by year

	1979	1980	1981	1982	1983	1984	1985	1986	1987	1988	1989	1990	Total
CDP	775	10667	3168	4584	1938	12184	24195	28909	34708	29688	39870	33480	224166
POLARIS	0	591	4410	7560	12537	0	0	0	0	0	0	0	25098
Mobile	0	0	0	1081	5458	7157	15001	17603	19194	28072	40747	23659	157972
IRIS-A	0	0	0	0	0	22065	25274	24522	23838	29958	28666	53219	207542
Japan	0	0	0	0	0	39	96	155	325	353	180	123	1271
IRIS-S	0	0	0	0	0	0	0	1622	2777	1489	2060	6920	14868
IRIS-P	0	0	0	0	0	0	0	0	2746	3026	3376	6621	15769
Navnet	0	0	0	0	0	0	0	0	0	1671	13983	25017	40671
FRG	0	0	0	0	0	0	0	0	0	0	0	866	866
Total	775	11258	7578	13225	19933	41445	64566	72811	83588	94257	128882	149905	688223

Session counts by year

	1979	1980	1981	1982	1983	1984	1985	1986	1987	1988	1989	1990	Total
CDP	2	17	3	8	8	24	31	40	41	38	34	34	280
POLARIS	0	3	29	47	58	0	0	0	0	0	0	0	137
Mobile	0	0	0	4	16	18	25	29	40	45	77	39	293
IRIS-A	0	0	0	0	0	72	73	73	73	73	63	73	500
Japan	0	0	0	0	0	1	1	2	3	4	2	1	14
IRIS-S	0	0	0	0	0	0	0	6	8	4	6	11	35
IRIS-P	0	0	0	0	0	0	0	0	8	12	11	16	47
Navnet	0	0	0	0	0	0	0	0	0	16	33	55	104
FRG	0	0	0	0	0	0	0	0	0	0	0	2	2
Total	2	20	32	59	82	115	130	150	173	192	226	231	1412

Table 2 shows the distribution of observations and observing sessions by site. The total observation count by site is twice that by program since each observation involves two sites. Fixed stations are marked F and mobile sites are marked M. In several places, notably the Goldstone tracking complex in California, Fort Davis in Texas, and the Haystack Observatory in Massachusetts, there are multiple measurement points close together. It can be seen that the distribution of data is extremely varied in number and time. For example, the National Crustal Motion Network sites except for Seattle (marked MN) and the European mobile sites (marked ME) have only been occupied once, although the latter had several days at each location. At the other extreme the stations of POLARIS/IRIS (HRAS, Westford, Wettzell, Richmond and Mojave) and the CDP station at Gilmore Creek have over 400 sessions each. The velocity of sites with data of little or no time span cannot be estimated, and the propagation of their positions to other epochs is dependent on the accuracy of plate motion models. Since there are significant differences between modeled and measured velocities, the reliability of such positions can degrade rapidly away from the epoch of observation.

Table 2. Geodetic data distribution by site

Observation counts by year

	1979	1980	1981	1982	1983	1984	1985	1986	1987	1988	1989	1990	Total
HAYSTACK F	490	5549	2100	1120	969	2232	1537	1173	0	233	9525	556	25484
NRAO 140 F	507	601	903	365	0	0	0	0	0	420	0	325	3121
OVRO 130 F	456	4462	1256	2562	2463	2375	4817	4733	2620	2746	0	0	28490
EFLSBERG F	97	1395	0	0	298	0	0	0	0	0	0	0	1790
HRAS 085 F	0	4838	5364	9006	12412	13419	17450	18261	21470	24670	13244	4120	144254
ONSALA60 F	0	3742	591	1824	2085	2087	5963	5961	6121	5519	5015	7709	46617
CHLBOLTN F	0	1929	0	0	0	0	0	0	0	0	0	0	1929
WESTFORD F	0	0	4786	9507	11309	14592	19644	24793	29036	28270	39402	48501	229840
GOLDVENU F	0	0	156	544	259	227	0	0	346	316	0	530	2378
MARPOINT F	0	0	0	804	123	0	0	0	305	895	2865	0	4992
JPL MV1 M	0	0	0	155	590	299	605	794	387	543	0	0	3373
MON PEAK M	0	0	0	299	541	284	1556	2254	903	1002	1115	373	8327
QUINCY M	0	0	0	264	152	200	845	607	594	1119	688	322	4791
PBLOSSOM M	0	0	0	0	174	296	365	0	505	121	0	0	1461
ROBLED32 F	0	0	0	0	97	0	0	0	0	0	0	0	97
HATCREEK F	0	0	0	0	728	1703	3865	3648	5318	5039	7774	6502	34577
PLATTVIL M	0	0	0	0	137	673	987	871	554	1032	497	556	5307
MOJAVE12 F	0	0	0	0	4777	7892	14862	16285	20727	22678	38437	53604	179262
MAMMOTHL M	0	0	0	0	112	221	0	232	0	0	0	0	565
VNDNBERG F	0	0	0	0	927	2657	7196	8242	6623	7416	8706	3985	45752
FORT ORD M	0	0	0	0	163	80	460	0	495	691	0	0	1889
PRESIDIO M	0	0	0	0	283	0	710	0	616	1012	944	303	3868
PT REYES M	0	0	0	0	185	110	376	0	557	695	993	270	3186
SANPAULA M	0	0	0	0	135	31	140	0	322	78	462	360	1528
PINFLATS M	0	0	0	0	244	347	494	1319	506	326	0	346	3582
YUMA M	0	0	0	0	221	109	667	1726	949	1032	0	0	4704
BLKBUTTE M	0	0	0	0	161	103	304	512	593	519	0	0	2192
PVERDES M	0	0	0	0	100	0	150	0	318	165	394	374	1501
WETTZELL F	0	0	0	0	221	9797	15569	15053	15527	16770	20402	28287	121626
RICHMOND F	0	0	0	0	0	7751	9461	10147	12285	15200	20856	34392	110092
KASHIMA F	0	0	0	0	0	2224	3940	6195	7133	5624	5935	3798	34849
DEADMANL M	0	0	0	0	0	72	64	0	350	143	0	0	629
OCOTILLO M	0	0	0	0	0	47	376	0	0	0	0	0	423
FLAGSTAF M	0	0	0	0	0	83	265	158	173	266	0	293	1238

ELY	M	0	0	0	0	0	126	204	202	169	933	388	231	2253
KAUAI	F	0	0	0	0	0	2458	2922	5317	5203	5901	7717	15288	44806
GILCREEK	F	0	0	0	0	0	5827	7924	11275	18811	20851	34034	39567	138289
KWAJAL26	F	0	0	0	0	0	1419	1379	1819	0	1198	0	0	5815
NOME	M	0	0	0	0	0	475	393	493	0	0	0	373	1734
SNDPOINT	M	0	0	0	0	0	49	244	218	44	708	704	443	2410
TSUKUBA	M	0	0	0	0	0	39	96	93	128	185	114	0	655
KODIAK	M	0	0	0	0	0	111	161	431	755	869	637	435	3399
SOURDOGH	M	0	0	0	0	0	537	616	798	387	822	912	0	4072
YAKATAGA	M	0	0	0	0	0	215	317	359	800	709	804	321	3525
WHTHORSE	M	0	0	0	0	0	89	0	369	0	754	723	0	1935
ALGOPARK	F	0	0	0	0	0	904	1268	0	0	0	0	5527	7699
YELLOWKN	M	0	0	0	0	0	412	416	0	0	0	0	0	828
PENTICTN	M	0	0	0	0	0	318	524	0	0	0	0	473	1315
HARTRAO	F	0	0	0	0	0	0	0	625	1535	838	767	2485	6250
VERNAL	M	0	0	0	0	0	0	0	202	198	411	407	369	1587
SHANGHAI	F	0	0	0	0	0	0	0	137	0	0	0	0	137
SEATTLE1	MN	0	0	0	0	0	0	0	258	0	0	0	291	549
MIYAZAKI	M	0	0	0	0	0	0	0	62	0	168	0	0	230
MEDICINA	F	0	0	0	0	0	0	0	0	773	2716	727	3452	7668
AUSTINTX	MN	0	0	0	0	0	0	0	0	225	0	0	0	225
CARROLGA	MN	0	0	0	0	0	0	0	0	117	0	0	0	117
BERMUDA	M	0	0	0	0	0	0	0	0	788	0	0	0	788
BLOOMIND	MN	0	0	0	0	0	0	0	0	78	0	0	0	78
LEONRDOK	MN	0	0	0	0	0	0	0	0	249	0	0	0	249
MOJ 7288	M	0	0	0	0	0	0	0	0	537	0	0	0	537
OVR 7853	M	0	0	0	0	0	0	0	0	560	0	0	0	560
DSS15	F	0	0	0	0	0	0	0	0	289	267	246	0	802
TITIJIMA	M	0	0	0	0	0	0	0	0	197	0	66	0	263
SESHAN25	F	0	0	0	0	0	0	0	0	0	1296	1071	1882	4249
MILESMON	MN	0	0	0	0	0	0	0	0	0	156	0	0	156
DSS45	F	0	0	0	0	0	0	0	0	0	678	1039	893	2610
HALEAKAL	M	0	0	0	0	0	0	0	0	0	674	0	0	674
DSS65	F	0	0	0	0	0	0	0	0	0	1161	905	2093	4159
PIETOWN	F	0	0	0	0	0	0	0	0	0	1290	9715	4068	15073
MCD 7850	M	0	0	0	0	0	0	0	0	0	602	0	0	602
FTD 7900	M	0	0	0	0	0	0	0	0	0	438	0	0	438
FORTORDS	M	0	0	0	0	0	0	0	0	0	349	2361	344	3054
NRA085 3	F	0	0	0	0	0	0	0	0	0	0	8294	12732	21026
GORF7102	M	0	0	0	0	0	0	0	0	0	0	878	0	878
NOTO	F	0	0	0	0	0	0	0	0	0	0	3225	2753	5978
HOHENFRG	ME	0	0	0	0	0	0	0	0	0	0	1024	0	1024
METSHOVI	ME	0	0	0	0	0	0	0	0	0	0	575	0	575
TROMSONO	ME	0	0	0	0	0	0	0	0	0	0	729	0	729
CARNUSTY	ME	0	0	0	0	0	0	0	0	0	0	404	0	404
BREST	ME	0	0	0	0	0	0	0	0	0	0	720	0	720
GRASSE	ME	0	0	0	0	0	0	0	0	0	0	616	0	616
HOBART26	F	0	0	0	0	0	0	0	0	0	0	643	2611	3254
NOBEY 6M	F	0	0	0	0	0	0	0	0	0	0	65	522	587
KASHIM34	F	0	0	0	0	0	0	0	0	0	0	0	4127	4127
SEST	F	0	0	0	0	0	0	0	0	0	0	0	353	353
MARCUS	F	0	0	0	0	0	0	0	0	0	0	0	461	461
VICTORIA	M	0	0	0	0	0	0	0	0	0	0	0	521	521
MATERA	F	0	0	0	0	0	0	0	0	0	0	0	1689	1689
Total		1550	22516	15156	26450	39866	82890	129132	145622	167176	188514	257764	299810	1376446

Session counts by year

	1979	1980	1981	1982	1983	1984	1985	1986	1987	1988	1989	1990	Total
HAYSTACK	2	20	9	3	6	10	4	3	0	1	17	1	76
NRAO 140	2	1	2	2	0	0	0	0	0	1	0	1	9
OVRO 130	2	16	3	13	13	12	18	20	12	11	0	0	120
EFLSBERG	1	5	0	0	1	0	0	0	0	0	0	0	7
NRAS 085	0	20	32	55	65	79	89	96	108	113	59	11	727
ONSALA60	0	18	6	13	17	13	22	22	22	19	20	19	191
CHLBOLTN	0	7	0	0	0	0	0	0	0	0	0	0	7
WESTFORD	0	0	27	55	61	72	89	106	116	109	129	133	897
GOLDVENU	0	0	1	3	1	2	0	0	1	1	0	1	10
MARPOINT	0	0	0	3	1	0	0	0	3	13	13	0	33
JPL MV1	0	0	0	2	5	4	4	4	2	3	0	0	24

MON PEAK	0	0	0	2	3	1	7	10	5	4	4	2	38
QUINCY	0	0	0	2	1	1	3	2	3	4	4	2	22
PBLOSSOM	0	0	0	0	2	2	2	0	3	1	0	0	10
ROBLED32	0	0	0	0	1	0	0	0	0	0	0	0	1
HATCREEK	0	0	0	0	5	7	13	15	26	24	34	24	148
PLATTVIL	0	0	0	0	2	4	3	4	2	4	2	2	23
MOJAVE12	0	0	0	0	22	32	45	49	55	69	118	161	551
MAMMOTHL	0	0	0	0	1	2	0	1	0	0	0	0	4
VNDNBERG	0	0	0	0	9	17	27	26	26	27	34	13	179
FORT ORD	0	0	0	0	1	1	2	0	3	4	0	0	11
PRESIDIO	0	0	0	0	2	0	3	0	3	4	6	2	20
PT REYES	0	0	0	0	1	1	2	0	3	3	6	2	18
SANPAULA	0	0	0	0	1	1	1	0	2	1	2	2	10
PINFLATS	0	0	0	0	2	2	3	7	3	2	0	2	21
YUMA	0	0	0	0	2	1	3	6	5	4	0	0	21
BLKBUTTE	0	0	0	0	2	1	2	2	3	2	0	0	12
PVERDES	0	0	0	0	1	0	1	0	2	1	2	2	9
WETTZELL	0	0	0	0	2	69	84	88	89	85	96	88	601
RICHMOND	0	0	0	0	0	55	60	73	79	87	96	112	562
KASHIMA	0	0	0	0	0	9	9	16	27	28	27	16	132
DEADMANL	0	0	0	0	0	1	1	0	2	1	0	0	5
OCOTILLO	0	0	0	0	0	1	2	0	0	0	0	0	3
FLAGSTAF	0	0	0	0	0	1	1	1	1	2	0	2	8
ELY	0	0	0	0	0	1	1	1	1	4	2	2	12
KAUAI	0	0	0	0	0	7	6	12	14	23	32	63	157
GILCREEK	0	0	0	0	0	15	15	23	47	77	101	126	404
KWAJAL26	0	0	0	0	0	7	4	4	0	5	0	0	20
NOME	0	0	0	0	0	2	2	3	0	0	0	3	10
SNDPOINT	0	0	0	0	0	1	1	1	1	3	3	3	13
TSUKUBA	0	0	0	0	0	1	1	1	1	2	1	0	7
KODIAK	0	0	0	0	0	1	1	2	2	3	3	3	15
SOURDOGH	0	0	0	0	0	2	2	4	2	3	3	0	16
YAKATAGA	0	0	0	0	0	1	1	2	3	3	3	3	16
WHTHORSE	0	0	0	0	0	1	0	2	0	3	3	0	9
ALGOPARK	0	0	0	0	0	2	3	0	0	0	0	22	27
YELLOWKN	0	0	0	0	0	1	1	0	0	0	0	0	2
PENTICTN	0	0	0	0	0	1	2	0	0	0	0	3	6
HARTRAO	0	0	0	0	0	0	0	6	8	4	6	15	39
VERNAL	0	0	0	0	0	0	0	1	1	2	2	2	8
SHANGHAI	0	0	0	0	0	0	0	1	0	0	0	0	1
SEATTLE1	0	0	0	0	0	0	0	1	0	0	0	2	3
MIYAZAKI	0	0	0	0	0	0	0	1	0	2	0	0	3
MEDICINA	0	0	0	0	0	0	0	0	5	12	3	5	25
AUSTINTX	0	0	0	0	0	0	0	0	1	0	0	0	1
CARROLGA	0	0	0	0	0	0	0	0	1	0	0	0	1
BERMUDA	0	0	0	0	0	0	0	0	4	0	0	0	4
BLOOMIND	0	0	0	0	0	0	0	0	1	0	0	0	1
LEONRDOK	0	0	0	0	0	0	0	0	1	0	0	0	1
MOJ 7288	0	0	0	0	0	0	0	0	1	0	0	0	1
OVR 7853	0	0	0	0	0	0	0	0	1	0	0	0	1
DSS15	0	0	0	0	0	0	0	0	1	1	1	0	3
TITIJIMA	0	0	0	0	0	0	0	0	2	0	1	0	3
SESHAN25	0	0	0	0	0	0	0	0	0	5	4	7	16
MILESMON	0	0	0	0	0	0	0	0	0	1	0	0	1
DSS45	0	0	0	0	0	0	0	0	0	5	4	3	12
HALEAKAL	0	0	0	0	0	0	0	0	0	3	0	0	3
DSS65	0	0	0	0	0	0	0	0	0	4	2	3	9
PIETOWN	0	0	0	0	0	0	0	0	0	3	14	10	27
MCD 7850	0	0	0	0	0	0	0	0	0	1	0	0	1
FTD 7900	0	0	0	0	0	0	0	0	0	1	0	0	1
FORTORDS	0	0	0	0	0	0	0	0	0	2	13	2	17
NRA085 3	0	0	0	0	0	0	0	0	0	0	32	51	83
GORF7102	0	0	0	0	0	0	0	0	0	0	4	0	4
NOTO	0	0	0	0	0	0	0	0	0	0	15	4	19
HOHENFRG	0	0	0	0	0	0	0	0	0	0	5	0	5
METSHOVI	0	0	0	0	0	0	0	0	0	0	5	0	5
TROMSONO	0	0	0	0	0	0	0	0	0	0	4	0	4
CARNUSTY	0	0	0	0	0	0	0	0	0	0	4	0	4
BREST	0	0	0	0	0	0	0	0	0	0	4	0	4
GRASSE	0	0	0	0	0	0	0	0	0	0	4	0	4
HOBART26	0	0	0	0	0	0	0	0	0	0	4	15	19
NOBEY 6M	0	0	0	0	0	0	0	0	0	0	1	5	6

KASHIM34	0	0	0	0	0	0	0	0	0	0	0	16	16
SEST	0	0	0	0	0	0	0	0	0	0	0	3	3
MARCUS	0	0	0	0	0	0	0	0	0	0	0	1	1
VICTORIA	0	0	0	0	0	0	0	0	0	0	0	3	3
MATERA	0	0	0	0	0	0	0	0	0	0	0	5	5
Total	7	87	80	153	230	444	540	616	704	800	952	978	5591

Table 3 shows the distribution of astrometric data by observing program. The CDP has astrometric and survey sessions to find and monitor sources suitable for geodesy. The Naval Research Laboratory (NRL) has a program to develop a radio/optical catalog of ~400 sources for fundamental astronomy. Observations are scheduled on a regular basis for the northern hemisphere and as antenna time permits in the south. Not all the NRL data acquired to date are included in Table 3. The NGS has a monthly observing program of southern hemisphere sources.

Table 3. Astrometric observations and sessions by program

	1979	1980	1981	1982	1983	1984	1985	1986	1987	1988	1989	1990	1991	Total
CDP	0	0	1322	1680	0	473	0	555	2452	1634	2155	2729	113	13113
NRL	0	0	0	0	136	0	0	0	749	2149	2415	218	0	5667
NGS	0	0	0	0	0	0	0	0	0	0	102	1316	245	1663
Total	0	0	1322	1680	136	473	0	555	3201	3783	4672	4263	358	20443

	1979	1980	1981	1982	1983	1984	1985	1986	1987	1988	1989	1990	1991	Total
CDP	0	0	2	3	0	2	0	1	5	5	4	5	1	28
NRL	0	0	0	0	1	0	0	0	5	11	9	1	0	27
NGS	0	0	0	0	0	0	0	0	0	0	1	11	2	14
Total	0	0	2	3	1	2	0	1	10	16	14	17	3	69

2. Geodetic Results

All the geodetic data have been analyzed using the Goddard CALC/SOLVE/GLOBL analysis system to produce a set of positions and velocities to define the terrestrial reference frame at any epoch. The general method is described in Ma *et al.* (1990) and Caprette *et al.* (1990). First, each observing session is analyzed separately, and calibration, editing and parametrization of station clocks and atmospheres are set. In the second step a multiyear solution is sequentially incremented using data from fixed station networks and selected long baseline mobile networks. Arc parameter elimination reduces the size of the matrices that need to be manipulated at each stage. Three-dimensional station positions and velocities are estimated as well as five Earth orientation parameters for each day. The reference frame is anchored by fixing the position and velocity of one station, the direction to another station, and the vertical rate of a third station. The third step applies the VLBI terrestrial orientation parameters and covariances as *a priori* information as the solution is incremented with the remaining mobile data.

Figure 1 shows the sites in the northern hemisphere. It can be seen that most of Eurasia is not covered, a condition that can be remedied with the QUASAR network now under construction by the Institute for Applied Astronomy in Leningrad. This network will include stations in both the European and Asian parts of the Soviet Union as well as possible collaborative efforts in China and India. Figure 2 shows the actual and prospective stations in the southern hemisphere. Mark III data have been acquired in South Africa (HARTRAO), in Australia (DSS45 and HOBART26) and in Chile (SEST), and a K-4 test was done at the Japanese Antarctic Syowa station. Sanitago, Chile and O'Higgins on the Antarctic Peninsula are being equipped for Mark III VLBI while the station at McMurdo is under discussion.

Figure 3 shows the distribution of 1σ formal errors in position for the 36 fixed stations and 52 mobile sites and in rate for the 26 fixed stations and 30 mobile sites with sufficient data. It can be seen that the formal errors are generally better for fixed stations, particularly in the vertical components. This difference arises from the higher sensitivity of the large, fixed antennas and the inability of the mobile systems to observe at the low elevations needed for good separation of the troposphere from the site vertical component.

Figure 1.

NORTHERN HEMISPHERE VLBI SITES

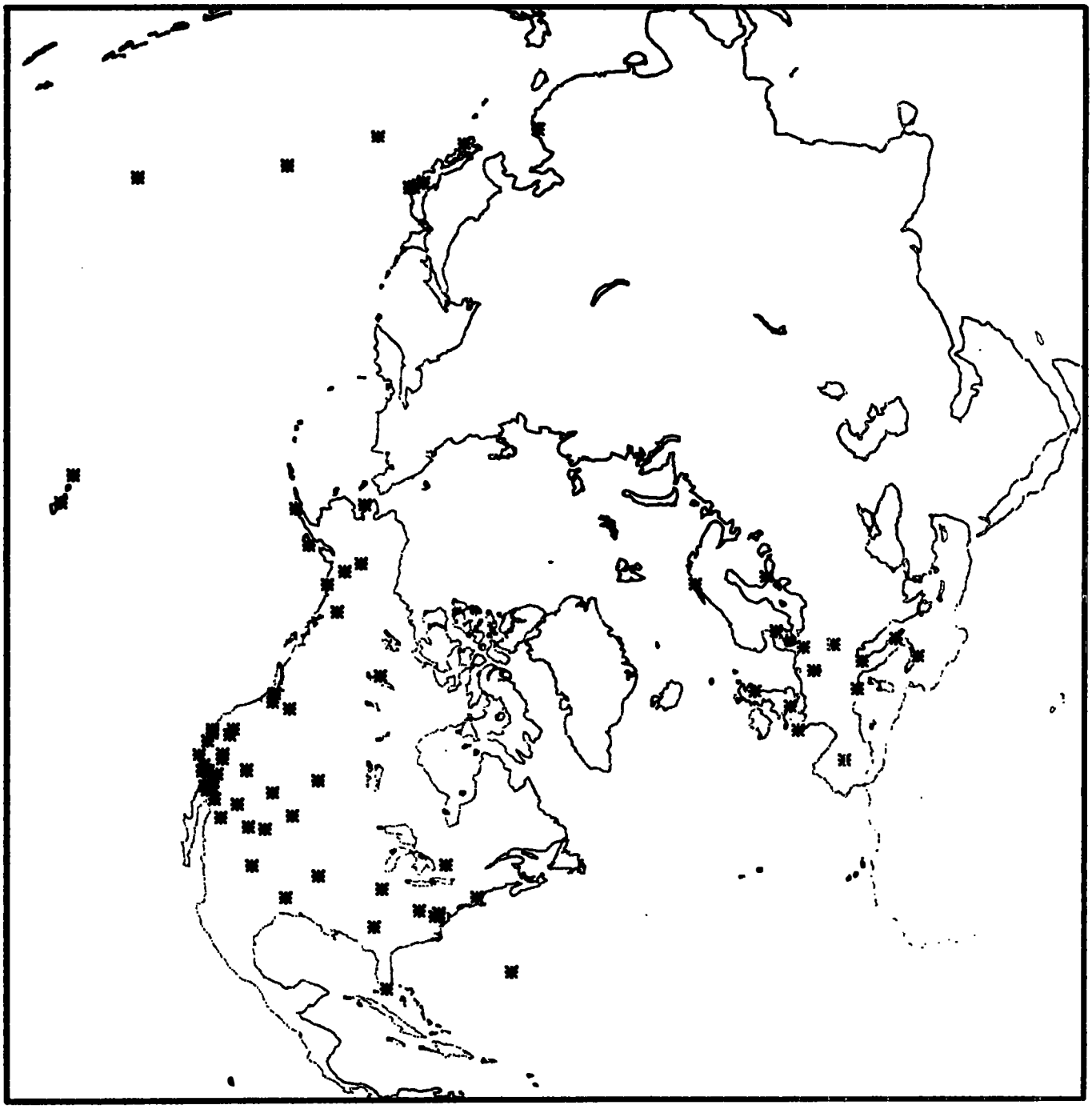

Figure 2.

SOUTHERN HEMISPHERE VLBI SITES

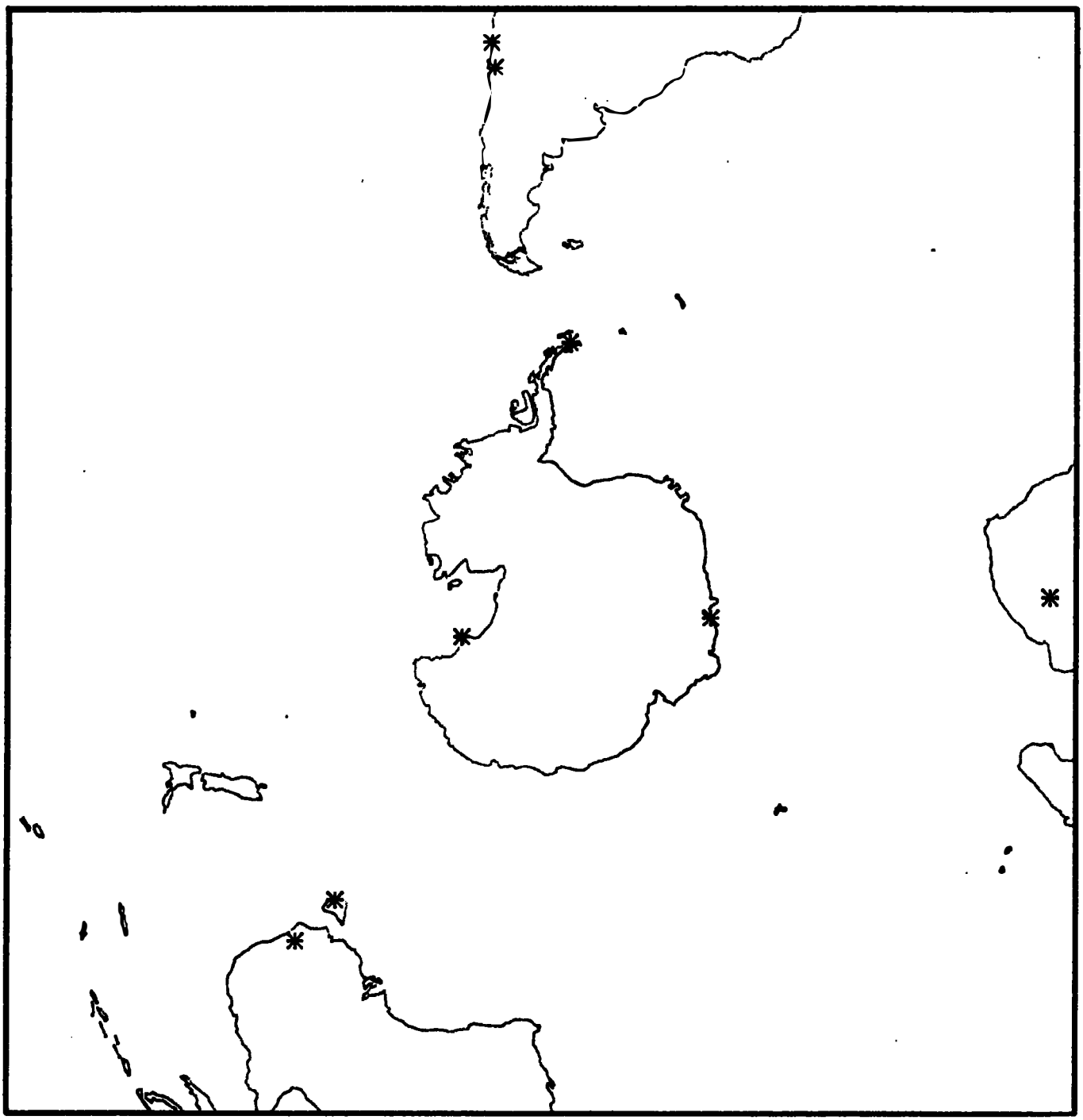

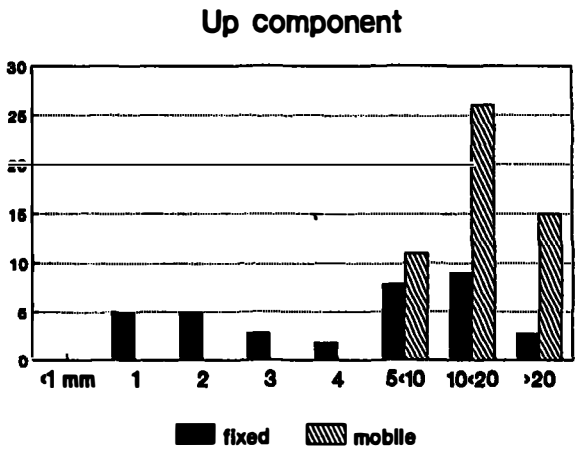

Figure 3. Distribution of 1σ formal errors in position and velocity

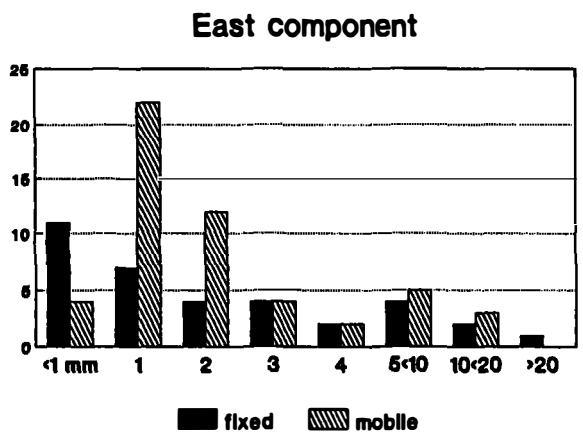

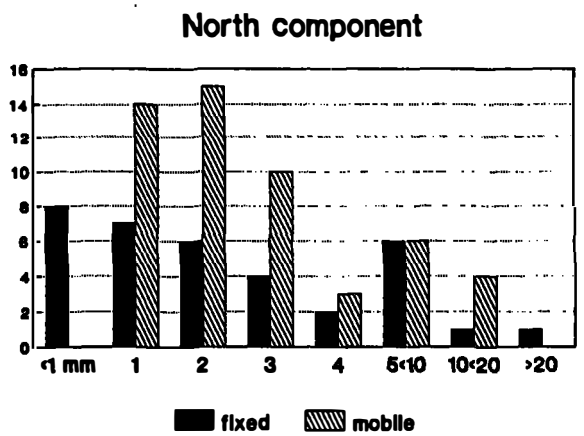

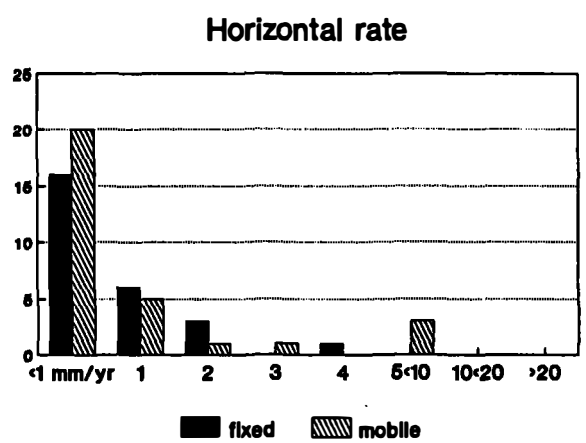

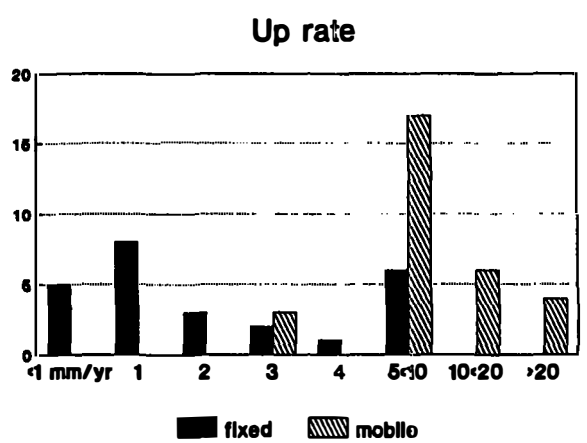

Figure 4.

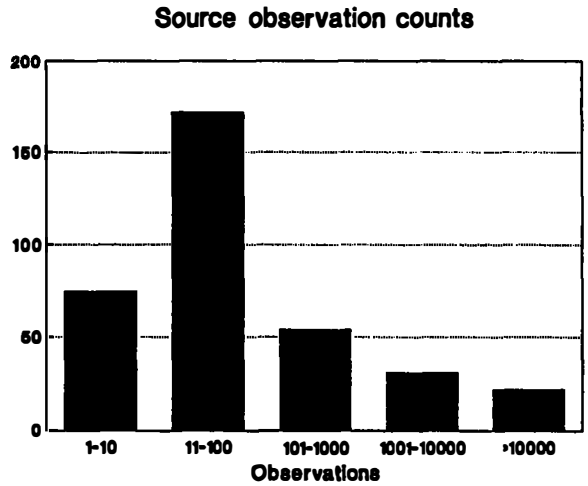

Figure 5.

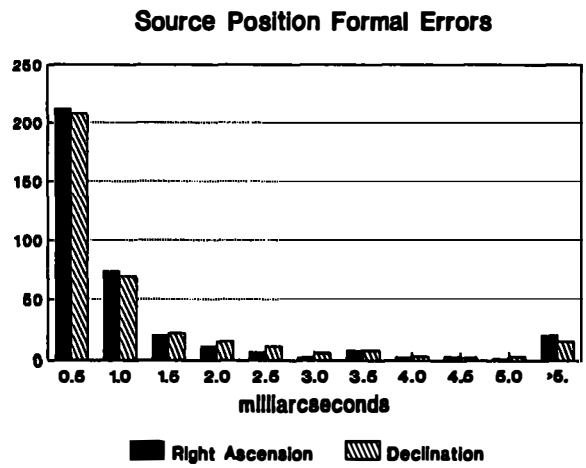

3. Astrometric Results

The celestial reference frame is derived from both astrometric and selected geodetic data. The 354 extragalactic radio sources so far observed are quite uniformly distributed in right ascension and declination. There are, however, small areas in the galactic plane where S-band observations are not possible. The distribution of observations by source is uneven. As can be seen in Figure 4, only a few sources have been extensively observed, by their use in the geodetic observing programs. These sources provide the core of the celestial reference frame. Most sources have fewer than 100 observations and a significant number have fewer than 10 observations. Nonetheless, as shown in Figure 5, the distribution of formal position errors peaks below 1 milliarcsecond for both right ascension and declination. The NRL astrometric program is planning to make repeated measurements of all sources over the next few years to improve the reliability and precision of the positions.

4. Sources of Error

The chief sources of error in the terrestrial reference frame are the modeling of the troposphere and possible nonuniform motion of the sites. The troposphere model enters in two ways. Long term, largely seasonal errors cause both periodic biases and random noise in the determination of the geodetic parameters. Since the temporal distribution of data for most sites is not uniform within or between years, these can lead to biased estimates of site velocities. In addition, to the extent that troposphere model errors are elevation-dependent, a systematic change of elevation distribution in the observing schedules over time can have a systematic effect on baseline lengths and consequently on the inferred site velocities. Such a change in elevation distribution has occurred in the IRIS-A schedules. See Kuehn *et al.* (this volume).

Figure 6 shows the evolution of the Fort Davis (HRAS) - Westford baseline. Both length and vertical clearly show nonuniform rates of change. Modeling the motion of Fort Davis as uniform causes a complex parceling of its real motion among the other sites depending on the observing networks and temporal distribution of data. The proper geodynamic model for Fort Davis remains to be determined. One extreme is to treat its position as an arc parameter estimated for each day, a choice that should cause the least distortion of the rest of the frame. The resulting velocities are systematically affected in some regions, notably in the northward rate of the western U.S. sites. Giving Fort Davis so many degrees of freedom also significantly weakens the Earth orientation parameters derived from the POLARIS/IRIS programs. A similar but smaller nonuniformity may be present at Wettzell.

The celestial reference frame is probably less subject to systematic errors although the troposphere model may have some effect on source declinations. The primary weaknesses are structure in some of the stronger sources

Figure 6. Fort Davis - Westford baseline components

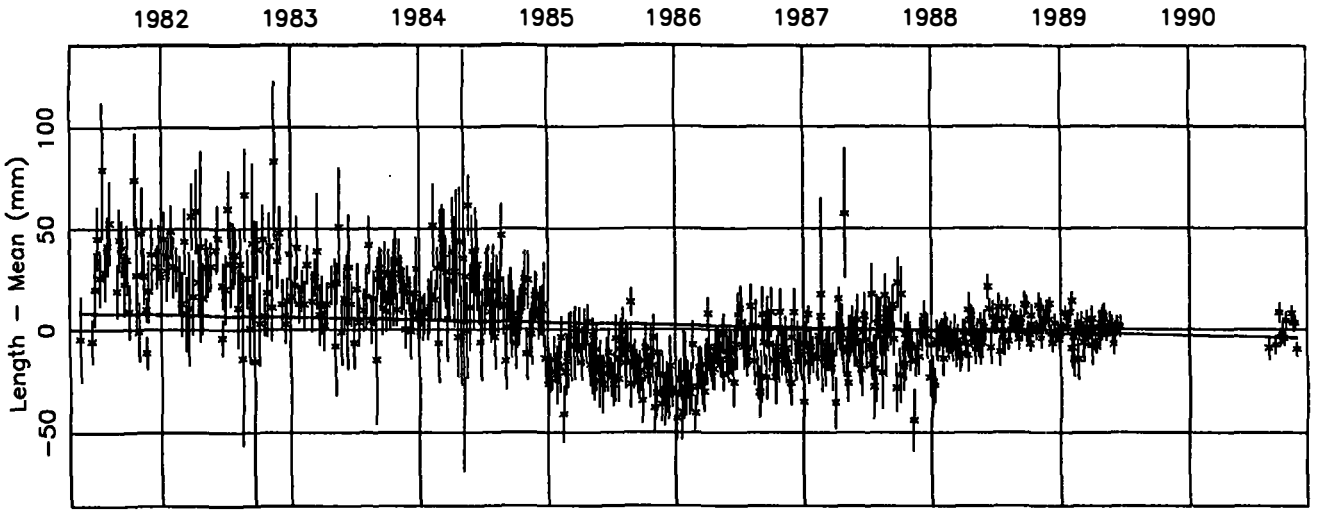

Rate = −1.3 +/− .2 mm/yr (scaled 1−sigma) Wrms of fit = 12.0 mm Reduced Chi−square = 2.47

Weighted mean length = 3134928010.9 mm

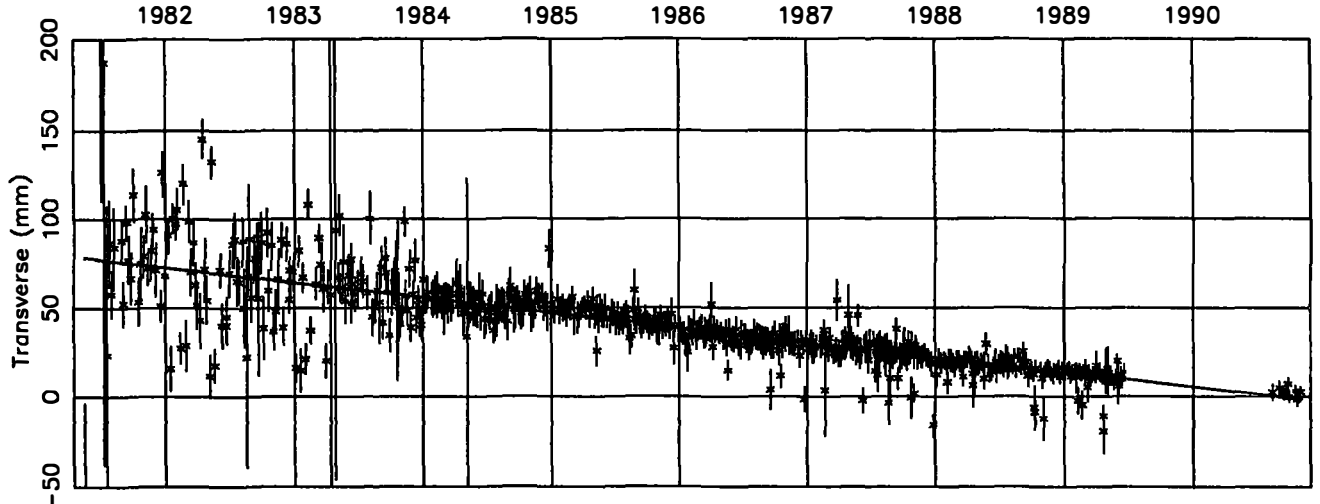

Rate = −8.4 +/− .2 mm/yr (scaled 1−sigma) Wrms of fit = 8.5 mm Reduced Chi−square = 1.75

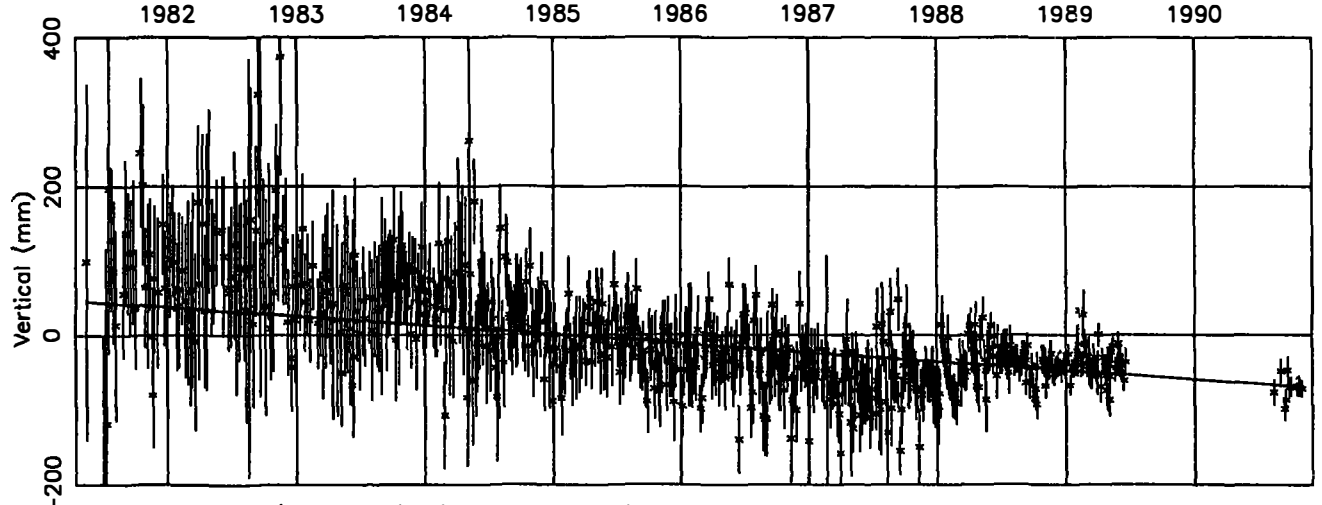

Rate = −12.1 +/− .8 mm/yr (scaled 1−sigma) Wrms of fit = 32.3 mm Reduced Chi−square = 1.21

Solution 721a

and uneven distribution of data. No significant (<5mas/century) proper motion has been detected for the few sources with long histories and many observations (Ma, in press).

The authors wish to thank Dave Gordon for Figures 1 and 2.

References:

Caprette, D.S., C. Ma, and J.W. Ryan, Crustal Dynamics Project Data Analysis--1990: VLBI Geodetic Results 1979-1989, *NASA Tech. Memo., TM 100765*, 378 pp., 1990.

Ma, C., J.M. Sauber, L.J. Bell, T.A. Clark, D. Gordon, W.E. Himwich, and J.W. Ryan, Measurement of Horizontal Motions in Alaska Using Very Long Baseline Interferometry, *J. Geophys. Res., 95*, 21991-22011, 1990.

Ma, C., Stability of the Extragalactic Reference Frame Realized by VLBI, in Proc. IAU Colloq. 127, J. Hughes, ed., US Naval Observatory, in press.

(This page intentionally left blank)

COMPARISON OF VLBI OBSERVATIONS

Dennis D. McCarthy
Brian J. Luzum
U. S. Naval Observatory
Washington, DC 20392 USA

Different series of Very Long Baseline Interferometry observations of Earth orientation were compared. The results show that the different series, in general, agree with each other at the millisecond-of-arc level. There are a few individual differences which are noteworthy because they appear to be caused by differences in models and possible errors in reduction.

1. INTRODUCTION

Very Long Baseline Interferometry (VLBI) is one of the most accurate techniques used for determining Earth orientation. However, it is suspected that VLBI observations, like other techniques, may be subject to systematic errors which degrade its true accuracy to many times that of its formal errors (McCarthy and Luzum, 1991). A simple way to check this, is to compare solutions produced by different analysis centers currently reducing VLBI observations. The series chosen for this comparison are the International Radio Interferometric Survey (IRIS) 5-day and 1-day values, the Crustal Dynamics Project (CDP) data, and the Navy Network (NAVNET) data. The IRIS data are provided by the National Geodetic Survey, the CDP data by the National Aeronautics and Space Administration (NASA), and the NAVNET data by the U. S. Naval Observatory. Each analysis center does independent solutions of their VLBI data although the stations, sources, and reduction software are similar.

The comparisons of the different solutions were performed by interpolating one series to match the epochs of the another series, when necessary, and then differencing the two Earth orientation values. After some preliminary analysis, it became apparent that a linear interpolation is not sufficient to represent the high- frequency variations found in the data. Stirling's method was then used instead to provide interpolation based on higher order terms. The interpolated series were compared with one another and differences computed and plotted.

Amplitude spectra of the differences were calculated to determine if there were any systematic errors which were consistent across all data sets. All amplitude spectra for a particular Earth orientation parameter (e.g. x, y, UT1-UTC) were plotted together.

2. VLBI OBSERVATIONS

Different VLBI solutions provide different sets of parameters. The IRIS data provide both a 5-day and a 1-day intensive series (NEOS Annual Report for 1989). The 5-day series provides a full complement of Earth orientation data (x, y, UT1-UTC, $d\Psi$, and $d\epsilon$) while the 1-day data provide only UT1-UTC. The IRIS 5-day series started on 27 September 1980 (MJD 44509) and continues to the present. The 1-day values start on 2 April 1984 (MJD 45792) and continue to the present. The system of observing site motions used by NGS is an internal system.

The CDP solution GLB716 is very similar to that of the IRIS series since many of the raw data come from the same experiments. As a result, many of the points occur at the same epoch. However, the reduction process is different from that of the NGS. The CDP data provide all 5 Earth orientation parameters (x, y, UT1-UTC, $d\Psi$, and $d\epsilon$) with the data set beginning in 4 August 1979 (MJD 44089) (IERS Annual Report for 1990). The CDP data set has recently included the observations made by NAVNET. Once again, the reduction of the CDP and the NAVNET are different thereby providing an alternate time series that can be used in this comparison. The CDP provided two versions of their data set. In the "free" solution, the station coordinates are treated as a "solve-for" parameter. The "fixed" solution constrains the station coordinates to follow the AM0-2 no-net-rotation model.

The NAVNET experiments started as "GNUT" experiments. The first 24-hour experiment was held on 11 September 1988 (MJD 47415). Since then, the NAVNET experiments have been run on a weekly basis. They provide a full set of Earth orientation parameters (x, y, UT1-UTC, $d\Psi$, and $d\epsilon$). The NAVNETs use the AM0-2 model to describe station motions (NEOS Annual Report for 1989).

3. INTERPOLATION METHOD

Initially, it was thought that a simple linear interpolation might be sufficient to compare various VLBI solutions. However, after preliminary analyses, it was found that a linear interpolation would not suffice to account for the effects seen at high frequencies which are found in VLBI. With this in mind, a higher order interpolation method was chosen to model more completely the high frequency variations found in VLBI data. Stirling's method was chosen because it could provide as high an order term as required to interpolate. Tests showed that all terms beyond the quadratic were insignificant.

4. ANALYSIS

Each VLBI solution was compared to all other solutions for the various Earth orientation parameters. This was done by interpolating the VLBI series that had the smallest spacing between the data points to minimize the interpolation error. For example, in the comparison between the NAVNET weekly data and the IRIS 5-day data, the IRIS points were interpolated.

A simple difference between the two VLBI solutions was made for each epoch. Comparisons were compiled between the NAVNET and IRIS data sets, the NAVNET and CDP data sets, the IRIS and CDP data sets, the NAVNET and intensive data sets, and the CDP and intensive data sets. Differences were plotted to determine if any systematic differences could be detected.

Some plots show differences with a distinct slope, particularly in polar motion (Figures 1-6). A plot of the difference between the CDP and the intensives in UT1-UTC shows a noticeable bump (Figure 7).

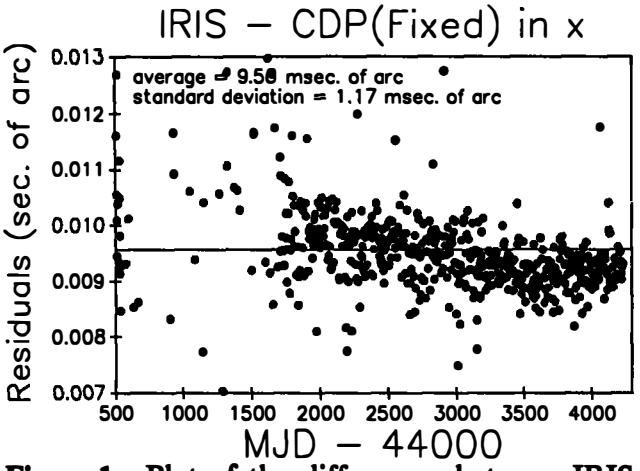

Figure 1. Plot of the differences between IRIS and the CDP fixed solution in x.

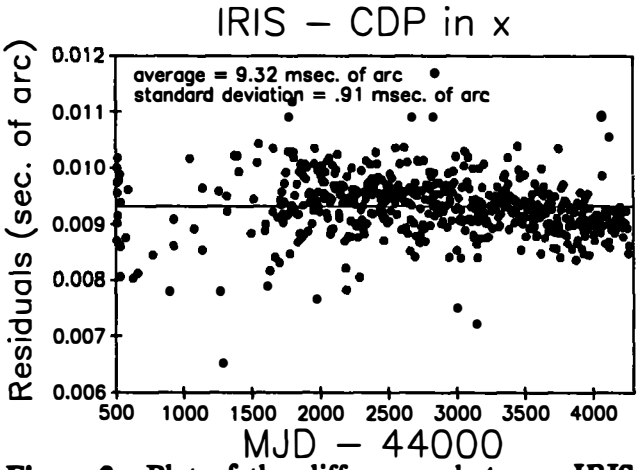

Figure 2. Plot of the differences between IRIS and the CDP free solution in x.

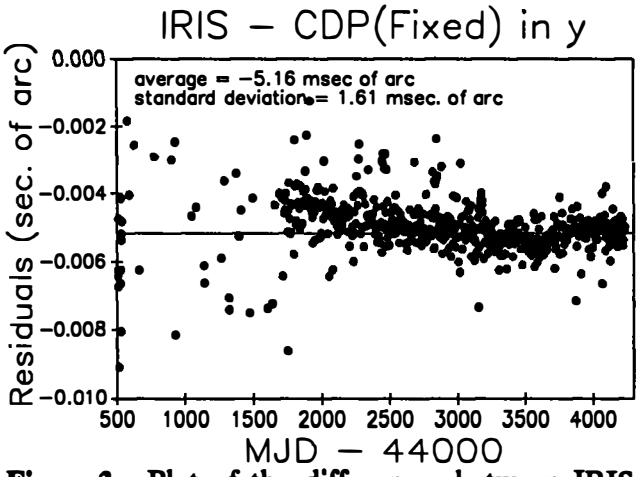

Figure 3. Plot of the differences between IRIS and the CDP fixed solution in y.

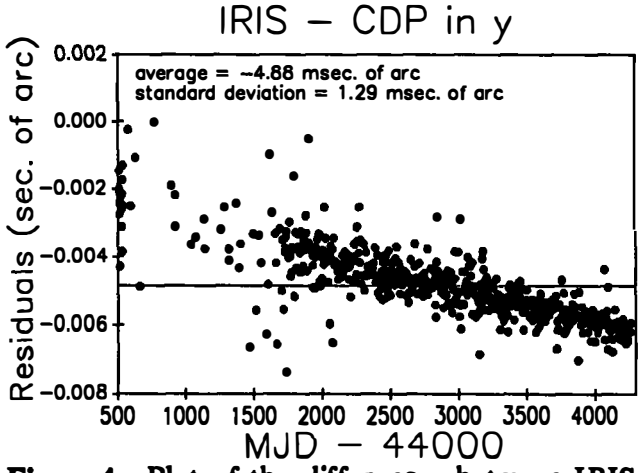

Figure 4. Plot of the differences between IRIS and the CDP free solution in y.

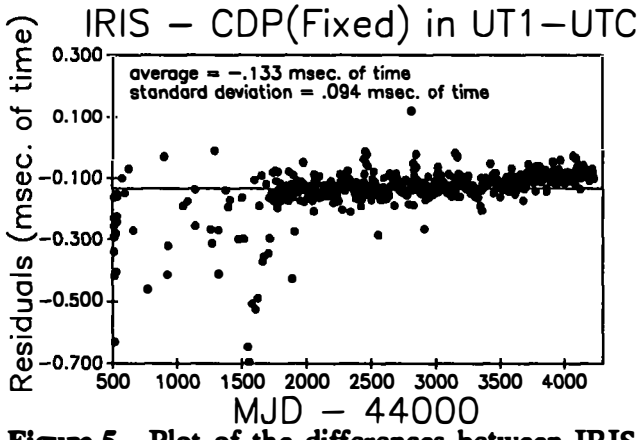

Figure 5. Plot of the differences between IRIS and the CDP fixed solution in UT1-UTC.

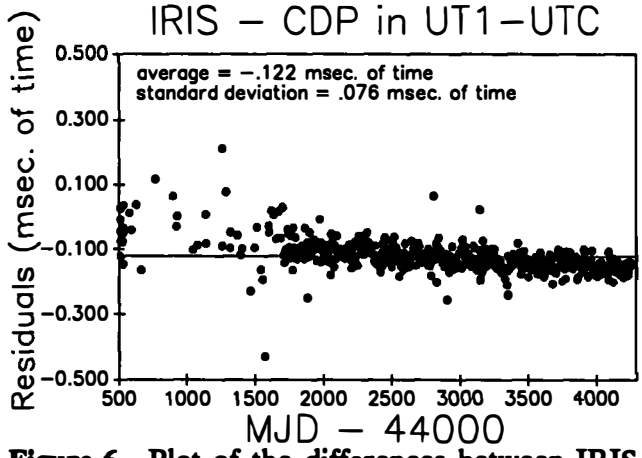

Figure 6. Plot of the differences between IRIS and the CDP free solution in UT1-UTC.

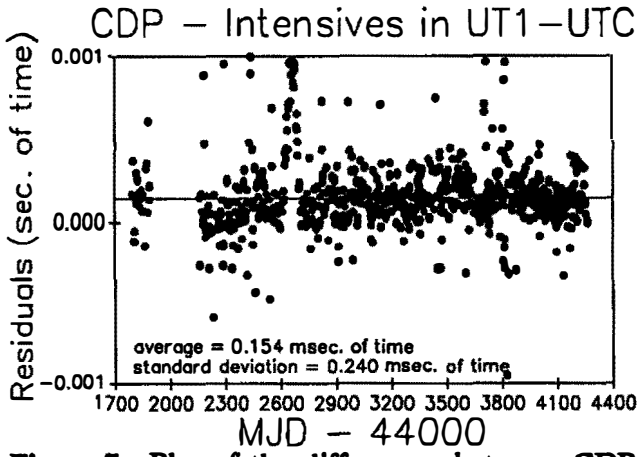

Figure 7. Plot of the differences between CDP free and the intensive solution in UT1-UTC.

Amplitude spectra were constructed to examine the possible periodic nature of the differences between the solutions.

The amplitude spectra showed no significant signature. The most noticeable feature of the amplitude spectra was that the spectra with the highest noise level were the spectra which involved solutions requiring the most interpolation (Figure 8).

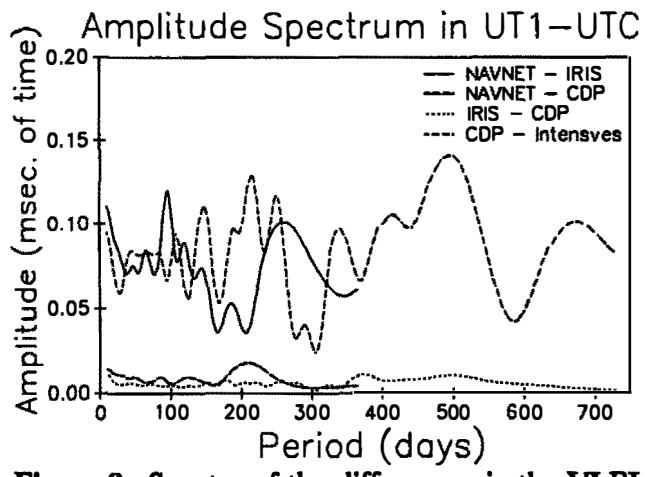

Figure 8. Spectra of the differences in the VLBI solutions in UT1-UTC.

5. DISCUSSION

The slopes that are apparent in the residual plots may be caused by a difference in the models of the station motion used by the various analysis centers. The slopes change depending on the station motion model used (e.g. the CDP fixed and free plate motion).

The "spike" that is present in the plot of the differences between the CDP and the intensive data in UT1-UTC has been traced to a previous error in the intensive reduction.

The difference in noise levels in the amplitude spectra appears to be a problem associated with the interpolation of the data. For instance, between the CDP and the IRIS data, which have the lowest noise level, there is little or no need for interpolation since most of the observations fall at the same epoch. Conversely, in most instances when a NAVNET is compared to an IRIS or a CDP point, an interpolated point must be calculated in order to provide a difference.

6. CONCLUSION

Systematic differences do exist between different VLBI solutions. Most of the differences appear to be based on the different plate motion models that are being used by the analysis centers. Other systematic differences are caused by reduction errors. The VLBI estimates of Earth orientation are accurate to approximately ± 1 millisecond of arc.

It is important to note that estimates of the level of accuracy are limited by the interpolation schemes used to intercompare data. Higher frequency observations may be required to evaluate more fully the true accuracy of the VLBI technique.

8. ACKNOWLEDGEMENTS

It is a pleasure to thank Dr. Brent Archinal and Mr. Marshall Eubanks for their helpful discussions in preparing this document, Dr. Chopo Ma for providing the CDP data sets, and Dr. Doug Robertson for his explanation of the NGS reduction procedure.

9. REFERENCES

IERS Annual Report for 1990, (1991), Paris Observatory.

McCarthy, D. D. and Luzum, B. J., 1991, "Combination of precise observations of the orientation of the Earth," *Bull. Geod.*, **65**, pp. 22-27.

NEOS Annual Report for 1989, (1990), National Geodetic Survey.

MONITOR OF OCEANIC ACTIVITIES FROM OBSERVATIONS OF EARTH ROTATION

Dawei Zheng and Shifang Luo (Both at Shanghai Observatory, Chinese Academy of Sciences, 80 Nandan Road, Shanghai 200030, P.R.China)
Zhiren Xie (Department of Geo and Ocean Science, Nanjing University, Nanjing 210008, P.R.China)

The interannual variation of the length of day is derived in the analysis of the data of Earth rotation from 1962 through 1988 by using the new techniques in time series analysis. Comparing the series of length of day with the data of departures of the sea surface temperature in the equatorial area of eastern Pacific (180°-80°W, 5°S-5°N), we found that the deceleration and acceleration of the interannual rate of Earth rotation are consistent with the warming up and down of sea surface temperature in the equatorial area very well. It is shown in our analysis that the minimum of the interannual LOD series, which is deduced from the observations of Earth rotation, can predict the occurrence of El Nino events for long range forecast about one year. In addition, the relationship between the sea level changes and LOD series from the historical data is preliminarily drawn in this paper.

Since last stronger El Nino event in 1982-83, which was characterized by the anomalous warming up of the sea surface water in the equatorial area of the eastern Pacific, the study on the relationship between the variation of the rate of Earth rotation and the El Nino events has got significant progress[1-8]. At first, the evidence of 1982-83 El Nino event from the change of the Length Of Day (ΔLOD) was revealed by Carter et al.[1] and Rosen et al.[2], the correlation between the El Nino event and ΔLOD has been presented by Chao[3], Ren et al.[4], Enbanks et al.[5] and Zheng et al.[6] by using the various analysis methods, respectively. The possibility of predicting El Nino events from ΔLOD was suggested successively by Eubanks et al.[5] and Zheng et al.[6-7].The dynamical analysis on the interannual variation in ΔLOD has been preliminarily made by Song et al.[8].

When the El Nino event happens, the destructive climate with the global scale will cause serious damage to human being. In this study,

the approach to forecast the El Nino event from ΔLOD data analysis is explored further.

By adopting the data of UT1-UTC from 1962 through 1988 observed with astronomical techniques a series of ΔLOD in a 5-day interval could be reduced[9-11]. According to the theoretical expression provided by Yoder et al.[12], the influence of all zonal tidal terms upon the ΔLOD is removed. Then the series obtained by averaging over each span of 30-day is adopted as the fundamental one in our analysis of the interannual variation of Earth rotation.

The variation of Earth rotation is influenced by many factors both astronomically and geophysically[13,14]. It is very important question in the analysis of data how to remove from the series of ΔLOD what does not relate to the El Nino event. The new techniques of Multi-Stage Filter(MSF) and Leap-Step Autoregression(LSAR) provided by Zheng Dawei et al.[15] have been applied. Not only is the MSF a narrower truncation band in frequency response function, but also it significantly reduces the error induced by the separation of instantaneous signals in the series of ΔLOD on the various frequency bands. In the process of filtering the LSAR could weaken or eliminate the end effects of the series of output signals and enhance the reliability of prediction.

According to the frequency band scale (from 2 yr. through 7 yr.) of seven El Nino events since 1962, the series of ΔLOD is processed with the band-pass filtering by adopting the MSF and LSAR. The results are shown at the top of Fig.1 and the monthly departures of the sea surface temperature (SST) in the equatorial eastern Pacific (180°-80°W, 5°S-5°N) from 1962 through 1988 are shown at the bottom of Fig.1.

The plot of ΔLOD after filtering clearly shows that the interannual variation of Earth rotation, which is in the time scale of several years but not quasi-periodic terms, exists in the long term fluctuations. The interannual variations of Earth rotation and the departures of the sea surface temperature in the equatorial eastern Pacific area are well consistent with each other. The interannual rate of Earth

ratation decelerates when the sea water warms up (referred to as the duration forming the El Nino events), while the interannual rate of Earth rotation accelerates when the sea water cools down (referred to as the duration of non-El Nino events). It means that every El Nino event usually occurs after the acceleration of the interannual rate of Earth ratation turns to deceleration. It is also found in Fig.1 that the amplitudes of the interannual change in ΔLOD are correlated with the strength of El Nino events. Since 1962, the two stronger El Nino events, i.e., the higher warming up of sea water, occurred in 1972 and in 1982-83, and the amplitudes of interannual variation in ΔLOD were bigger in the periods mentioned above. In the two durations, the increase in the length of day was close to 0.3ms, i.e., the variation in the rate of Earth rotation was about -2.5×10^{-13} rad/s.

As the interval between the El Nino events in 1963 and 1965 is very close to the truncation frequency band of the filter used in the data analysis, the differences between the epochs of maximum in warming up of the equatorial sea surface water in 1969, 1972, 1976, 1982, 1987 and epochs of minimum in interannual variation of ΔLOD series in 1968, 1970, 1974, 1981, 1985, respectively, are used, by which the average of 25-month lead of the minimum in ΔLOD is estimated. The curve of crosscorrelation between the interannual ΔLOD and SST series is given in Fig.2. The correlation coefficient at zero lag is derived to be 0.65. However,the maximum negative correlation is 0.69 when the interannual ΔLOD is shifted by 24 months forward relative to SST.

The results derived above have substantiated and provided the possibility and way to forecast the El Nino events by using the observations of Earth rotation. As data UT1-UTC can be reduced in time (about within one month) from determination with several techniques globally, such as VLBI, SLR, and LLR, it is feasible to predict the El Nino events by deriving and monitoring the extremes of the interannual variation in the series ΔLOD. If the delay in collecting and processing data is taken into account, the prediction could be made one year before, which belongs to the long range forecast in meteorology.

In addition, the relationship between the sea level changes and ΔLOD series is preliminarily analysed from the historical data in this paper. In order to investigate into the sea level changes in different latitudes, 162 series of annual mean heights of sea level was selected from the gauge records of more than six hundreds tidal stations all over the world during 1900 to 1970. They were divided into 12 groups by an interval of 10 degrees latitude. The result of preliminary analyses revealed that in the sea level fluctuations at the decade time scale there has been a certain mirror image relationship between high and low latitudes since the present century. It is most interesting that the phase of sea level fluctuations has correlated closely with the phase of the variation of Earth rotation. As shown in Fig.3, when the Earth rotation was accelerated, the sea level rose in low latitudes and fell in high latitudes. Conversely, as the Earth rotation was decelerated, the sea level fell in low latitudes and rose in high. Therefore it might be infered from the recent observations of Earth rotation that the sea level is rosing in low latitudes and felling in high latitudes since the beginning of 1970's.

We sincerely thank Drs. Z.Q.Ren and J.Y.Chen of the Academy of Meteorological Science, State Meteorological Administration, China for sending SST data. Cordial thanks are expressed by us to Prof. S.H.Ye, Director of Shanghai Observatory, for her support to this work.

References:

1. Carter,W.E.et al., Science, **224**, 957-961(1984).
2. Rosen,R.D.et al., Science, **225**, 411-414(1984).
3. Chao,B.F., Geophys.Res.Lett., **11**, 541-544(1984).
4. Ren,Z.Q. and Zhang,S.G., Kexue Tongbao, 6, 444-447(1985).
5. Eubanks,T.M.et al., Earth Rotation: Solved and Unsolved Problems, D.Reidel Publishing Company,163-187(1986).
6. Zheng,D.W.,Luo,S.F.and Song,G.X., Science in China(series B), **32**,6, 729-736(1989).
7. Zheng,D.W.,Song,G.X., and Luo,S.F., Nature,**348**, 119(8 November,1990).
8. Song,G.X.,Zheng,D.W. and Luo,S.F., Acta Astronomica Sinica, **30**,3, 310-314(1989).
9. Li,Z.X., in Annual Report for 1984, D31-63, Bureau international de l'Heure(1985).
10. BIH Annual Report for 1982-1987, Observatoire de Paris(1983-1988).
11. IERS Annual Report for 1988, Observatoire de Paris(1989).
12. Yoder,C.F.et al., J.Geophys.Res., **86**, 881-891(1981).
13. Lambeck,K., The Earth's Variable Rotation, Cambridge University Press, New York(1980).
14. Luo,S.F. et al., Acta Astronomica Sinica, **15**, 1, 79-84(1974).
15. Zheng,D.W.,and Dong,D.N., Acta Astronomica Sinica,**27**,4,368-375(1986).

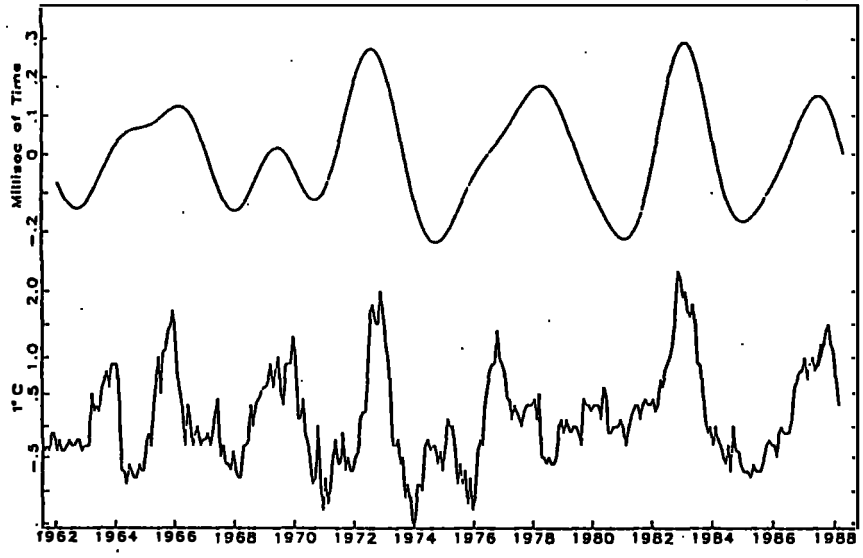

Fig.1. The interannual variationa of LOD (in the top part) and the monthly departures od sea surface temperature in the equtorial eastern Pacific area (in the bottom part) during 1962 to 1988.

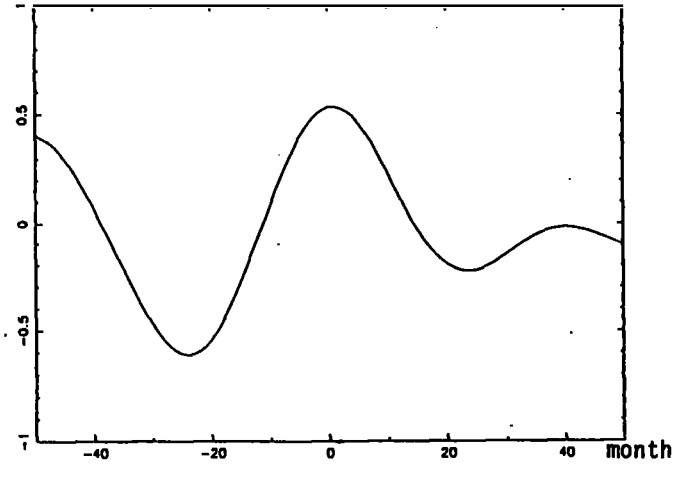

Fig.2. Cross-correlation between the interannual LOD and SST.

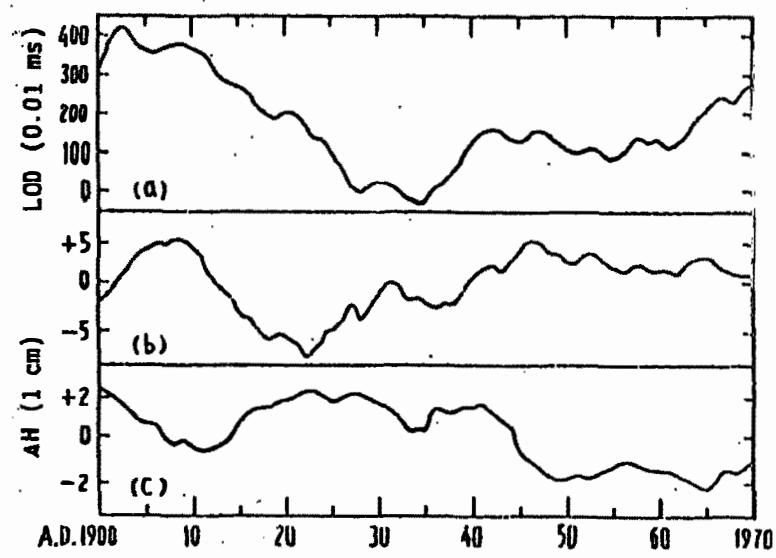

Fig.3. The relationship between the sea level changes and LOD. (a). The LOD curve of annual mean variation. (b). The change of mean sea level in 60°-70°N. (c). The change of mean sea level in 10°-20°N.

Geodetic VLBI: Monitoring Global Change

W E Carter and D S Robertson
Laboratory for Geosciences, Office of Ocean and Earth Sciences
NOAA, Rockville, Maryland 20852

Abstract:

For more than a decade the international geodetic community has been working cooperatively to develop a global network of very long baseline interferometry (VLBI) observatories. The purposes of the network include the regular monitoring of Earth orientation (precession, nutation, polar motion, and Universal Time) and the measurement of contemporary plate motion and glacial rebound, to learn about the structure and dynamics of the Earth. Recent concerns about the effects of global warming have raised questions about the current rate of rise of sea level and the possibility of a dramatic increase in the rate caused by melting of the Greenland and Antarctic ice caps. Geodetic VLBI can contribute to the monitoring of global sea level by providing a terrestrial reference frame accurate to the sub-centimeter level to which the positions of tide gauge can be referred, by accurately mapping glacial rebound and other vertical crustal motions, by placing bounds on changes in the building or destruction of the Greenland and Antarctic ice caps (inferred from the secular polar motion), and by providing the fundamental reference frame for generating accurate orbits of artificial satellites, including the Global Positioning System (GPS) and altimetric satellites. The current status of the global VLBI network, initial results, and goals for the next 3 to 5 years will be discussed.

Introduction

The role of Very Long Baseline Interferometry (VLBI) in monitoring Climate and Global Change (C&GC) may not be immediately apparent. The end product of VLBI measurements is a set of accurately determined baseline vectors between radio telescopes (fixed or mobile) around the world, at the times of the observations. The key phrase of course is "at the times of the observations." The changes in the solid earth, oceans, atmosphere system that are collectively referred to as C&GC essentially all involve movements of mass that result in deformations of the Earth and changes in the vectors observed with VLBI. For example, on an interannual time scale the El Niño - Southern Oscillation which strongly affects climate along the western coastal regions of both North and South America, involves an exchange of angular momentum between the atmosphere and solid earth that modulates the rotation of the Earth, changing the orientation of the VLBI vectors with time. On much longer time scales the melting of glaciers and polar ice caps and the redistribution of the mass over the oceans causes shifts in the location of the pole, changes in the length-of-day (lod), and crustal deformations that affect the components of VLBI interstation vectors. These changes can be all detected by a series of VLBI observations. Detecting and separating the different effects of C&GC will require long uninterrupted time series from a global network of properly distributed observatories.

Separating the causes of observed changes in the vectors measured with VLBI may prove extremely difficult or even impossible without independent information from other observing techniques such dense networks of vectors determined from Global Positioning System (GPS) satellite observations, airborne and satellite altimetry profiles of the oceans and ice masses, and vertical crustal motions and mass relocations obtained from absolute gravimetry. Appropriately for this conference, this

paper will focus primarily on the role of VLBI in monitoring C&GC but does address other techniques both from the points of view of the support they derive from VLBI and how the information obtained from them may improve the interpretation of VLBI measurements.

Major goals of the NOAA C&GC program are to determine the long term trends of climate change, to determine the causes of those changes (particularly the possible effects of human activities such as atmospheric pollution), to explore techniques that might be used to mitigate the undesirable consequences of climate change, and to provide the best possible information to those officials responsible for setting national policy. One of the predicted effects of global warming is a general rise in global sea level. The early detection of an increase in the rate of rise of sea level would confirm the predictions from computer climate models and provide important information for coastal planning activities. VLBI, along with other geodetic measurements, can contribute to the measurement of the change in global absolute sea level. Two approaches to the problem have been identified: the direct monitoring of sea level, and the indirect approach of monitoring ice masses that contain the water that could cause sea level to increase rapidly. Certain VLBI observations, such as the establishment and maintenance of an accurate global terrestrial reference frame, are fundamental to the success of both approaches.

Background Information

In 1977 the National Oceanic and Atmospheric Administration (NOAA) began to develop a three station network of Very Long Baseline Interferometry (VLBI) observatories. This was several years before the term Climate and Global Change came into common usage, and the immediate scientific goal of the project [Carter, 1978; Carter and Strange, 1979] was to replace the antiquated optical observatories that NOAA had operated since the turn of the century, as part of the International Latitude Service, with a more accurate Earth orientation monitoring system to support modern global geodetic measurements. A second important goal of the NOAA project was to demonstrate the feasibility of using VLBI operationally. By 1984 NOAA and a consortium of German geodetic organizations, led by the Institute for Applied Geodesy (IFAG), had joined efforts and the International Radio Interferometric Surveying (IRIS) network consisting of the three NOAA observatories and the newly built Wettzell Observatory, in Germany, was routinely producing polar motion, UT1 and nutation determinations at 5 day intervals. The VLBI results were two orders of magnitude more accurate than those of the classical optical networks. The success of the IRIS observations stimulated several other nations to develop geodetic VLBI facilities. Today there are more than 20 observatories around the world that regularly participate in geodetic VLBI observing programs and several more, most notably in the USSR and the southern hemisphere, are under construction or planned. See Figure 1.

The Hartebeesthoek, South Africa, and Hobart, Australia observatories utilize VLBI instrumentation loaned by NOAA explicitly for joint C&GC monitoring. The station planned for Natal, Brazil, is also being developed jointly by NOAA and a consortium of Brazilian scientific organizations led by the University of Sao Paulo for C&GC monitoring. The more tentative plans for a station at McMurdo, Antarctica, are based on a project currently under consideration by the National Science Foundation and the National Aeronautics and Space Administration (NASA) to develop a synthetic aperture radar (SAR) station. The Japanese and German stations at Syowa and O'Higgins are designed for both SAR and VLBI operations. The station at Santiago is being funded by IFAG, with technical assistance by NASA. The station planned for Tahiti, will be developed by French space research and geodetic organizations.

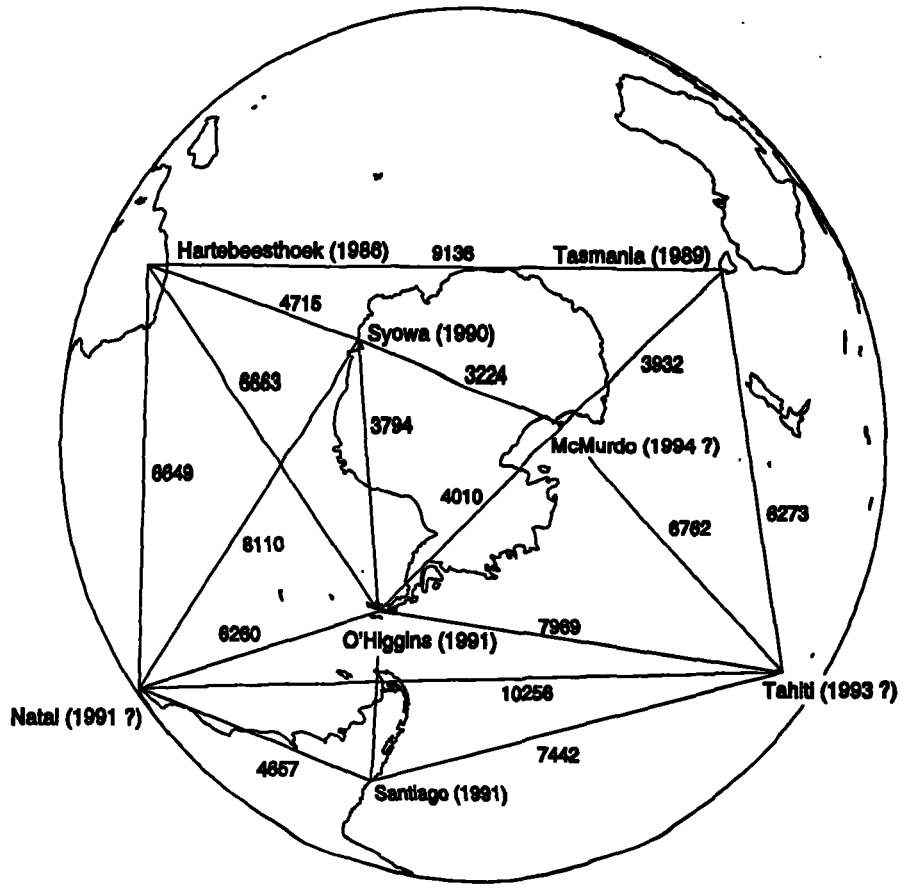

Figure 1. Map showing the locations of southern hemisphere geodetic VLBI stations. Distances are in kilometers.

Monitoring Global Sea Level

NOAA, along with other agencies from around the world, has operated tide gauges in most harbors for many decades. Some tide gauge records are more than 100 years long and a few exceed 150 years. These records show a global increase in sea level of 10 to 25 centimeters over the past century. The uncertainty is large because the rates observed at the various gages disagree markedly, even in sign, and different researchers have taken different approaches in attempting to get the "best" estimate of global sea level change. It has long been recognized that the apparent change in sea level in certain regions seen in the tide gauge records is caused by vertical crustal motion at the tide gauge rather than by an increase or decrease in the volume of water in the oceans. In the Hudson Bay region of Canada and along the Baltic Sea coastline of Fennoscandia, glacial rebound causes a drop of relative sea level by about one centimeter per year. It is now known that the isostatic readjustments associated with the melting of the Laurentide and Fennoscandian ice sheets causes positive or negative vertical crustal motions of a good fraction of a millimeter per year over the entire planet. All tide gauge measurements are corrupted to some extent by glacial rebound effects.

The direct approach to measuring sea level change is to use modern geodetic techniques (VLBI, GPS, absolute gravity) to establish and maintain a global terrestrial reference frame accurate to the subcentimeter level, and then to regularly resurvey to tide gauge stations to determine the rate of

vertical motions of the gauges. To be useful the crustal rates need to be accurate to no worse than a fraction of a millimeter per year. This is a very challenging geodetic problem at sites with constant rates and currently not possible at sites with frequent episodic motions. NOAA has established two networks, in Hawaii and along the Atlantic Coast of the U.S. (including a station in Bermuda) to develop and test the techniques for surveying the tide gauge stations. The results of the initial surveys have been reported by Carter *et al.*, [1988] and will not be repeated here. However, it was clear from the first tests that all three techniques (VLBI, GPS, and absolute gravity) had to be improved about one order of magnitude before the required accuracies could be achieved.

Progress on VLBI has been dramatic. NASA and Haystack Observatory have already performed engineering experiments with improved instrumentation that achieved one millimeter repeatability in the horizontal and three millimeters in the vertical on baselines of 800 kilometers and longer [T.A. Herring, private communication, 1990]. Haystack Observatory has recently completed the specifications and preliminary designs for a new generation, Mark 4, VLBI system that will be initially capable of recording at 10 times the data rate of the Mark 3, with upgrade capability to 20 times [Rogers, 1991]. The increased recording bandwidth and other calibration and observing techniques should achieve the few millimeter level in a routine operational mode about 1994.

A major breakthrough was made in absolute gravimetry in 1990, when Klopping *et al.*, [1991] developed data collection, reduction and analysis techniques to remove the largest known systematic error in the Joint Institute for Laboratory Astrophysics (JILA) absolute gravimeter. Comparison of determinations from absolute and cryogenic gravity meters at the Richmond VLBI observatory show agreement within one microgal in measuring a change of 11 microgals in the gravity caused by changes in the water table and soil moisture content. A joint gravity monitoring program in North America, concentrated in Canada where the glacial rebound rates are the largest has been initiated by NOAA and the Canadian Bureau of Energy and Mines. NOAA C&GC program funds are being used to fund a joint NOAA-National Institutes of Science and Technology-JILA-private industry transfer of technology and manufacture of a new generation absolute gravimeter. Absolute gravity may provide a relatively inexpensive alternative method with different error sources with which to check VLBI vertical motion results.

Progress on GPS has been good but slower than the other techniques. Delays in launching new satellites have limited the observing periods and resulted in less than optimal sky coverage. Refraction anomalies along coastlines appear to be a more challenging problem than anticipated. Rather than repeat the Hawaiian and Atlantic Coast tide gauge surveys, focus has shifted to the collection of long time series of observations at the Richmond VLBI and Haulover tide gauge sites. The repeatability of the horizontal components is currently 2-3 millimeters, RMS, while the vertical component is approximately 1.5 centimeters. The vertical repeatability represents a recent improvement of about a factor of 3 achieved through better atmospheric modelling and improved orbits. A factor of 5 or more is still needed to make the GPS tide gauge surveys useful.

Analysis of historical tide gauge data by several researchers (see for example Douglas, 1991) has revealed difficulties in the interpretation of water level measurements. There are large (ten centimeter level) interdecadal variations in relative sea level that are probably driven by basin-scale winds that currently make it impossible to extract sea level rise values at the submillimeter per year level of accuracy. Such effects will have to be removed before the benefits of the improved geodetic results can be realized. The direct measurement of sea level must and will continue to be a major component of the NOAA global sea level project, but the indirect approach of monitoring ice

masses is likely to take on increasing importance with time, assuming that the planned observing campaigns prove successful.

Ice Monitoring

The ice masses that contain enough water to cause significant increases in global sea level are concentrated in a few areas of sub-continental scale. Approximately 85 percent of the ice mass is contained in the Antarctic, 12 percent in Greenland, and 3 percent in mountain glaciers.

The large difference between the surface areas of the ice masses and that of the oceans means that the changes in the surface elevations of the ice sheets will be many times larger than the rise or fall of the oceans. For example, for the Greenland ice cap to yield sufficient water to raise global sea level by 1 millimeter, uniformly distributed melting would decrease the surface elevation by about 16 centimeters. If the melting were restricted to the southern portions the surface change would be 2 to 3 times larger. This enhanced signal suggests that it may prove easier to detect changes in the ice masses than the resultant changes in sea level.

At least three approaches to monitoring ice masses, which vary in degree of directness, have been suggested. In chronological order they are: monitor earth rotation (polar motion and length of day (lod)) to detect the effects of the redistribution of mass caused by melting or building of ice caps [Munk and MacDonald, 1960]; make repetitive measurements of the surface elevations of the icecaps and compute changes in volumes based on changes in the surface elevations [Zwally, 1989]; and measure vertical and horizontal crustal deformations at stations near the peripheries of major ice masses, caused by changes in the weight of ice resting on the crust [Hager, 1991]. The references cited do not necessarily represent the first or only papers to suggest the particular approach, but they serve as sources of more detailed discussions of the techniques and results.

Munk and MacDonald noted that displacement of the pole of rotation is potentially "a remarkably sensitive indicator of the source of melted water." Using reasonable estimates of simplified excitation functions they pointed out that melting of ice on Greenland would displace the pole toward Greenland, while melting of ice in Antarctica would displace the pole toward Chicago. If melting of ice were the only cause of changes in earth rotation we would indeed already have an exquisite monitoring system. The development of an earth orientation monitoring system based on Very Long Baseline interferometry (VLBI) during the past decade has led to at least two orders of magnitude improvement in our knowledge of polar motion and lod. The IRIS VLBI earth orientation monitoring system routinely tracks the location of the pole to 2.0 millisecond of arc (6 centimeters) or better, as verified by comparison with satellite laser ranging results [Robertson *et al.*, 1985], at 5 day intervals (Figure 2). More recent intercomparisons with a 23-day test series of GPS pole determinations during January and February, 1991, indicate agreement at better than 0.5 millisecond (1-2 centimeters) in both components of the pole position [Herring, 1991]. The IRIS network also produces daily values of Universal Time (UT1) the time integral of lod, accurate to a tenth of a millisecond of time (Figure 3). Improvements approaching another order of magnitude are anticipated in the next 3-5 years as the next generation Mark 4 VLBI instrumentation becomes operational and methods for correcting the observations for atmospheric refraction and other sources of systematic error are developed.

Unfortunately, variations in earth rotation are not caused only by changes in the ice masses, but by several other phenomena as well. For example, the entire secular motion of the pole from 1900 to present shown schematically by the irregular line in figure 2, approximately 10 centimeters per year

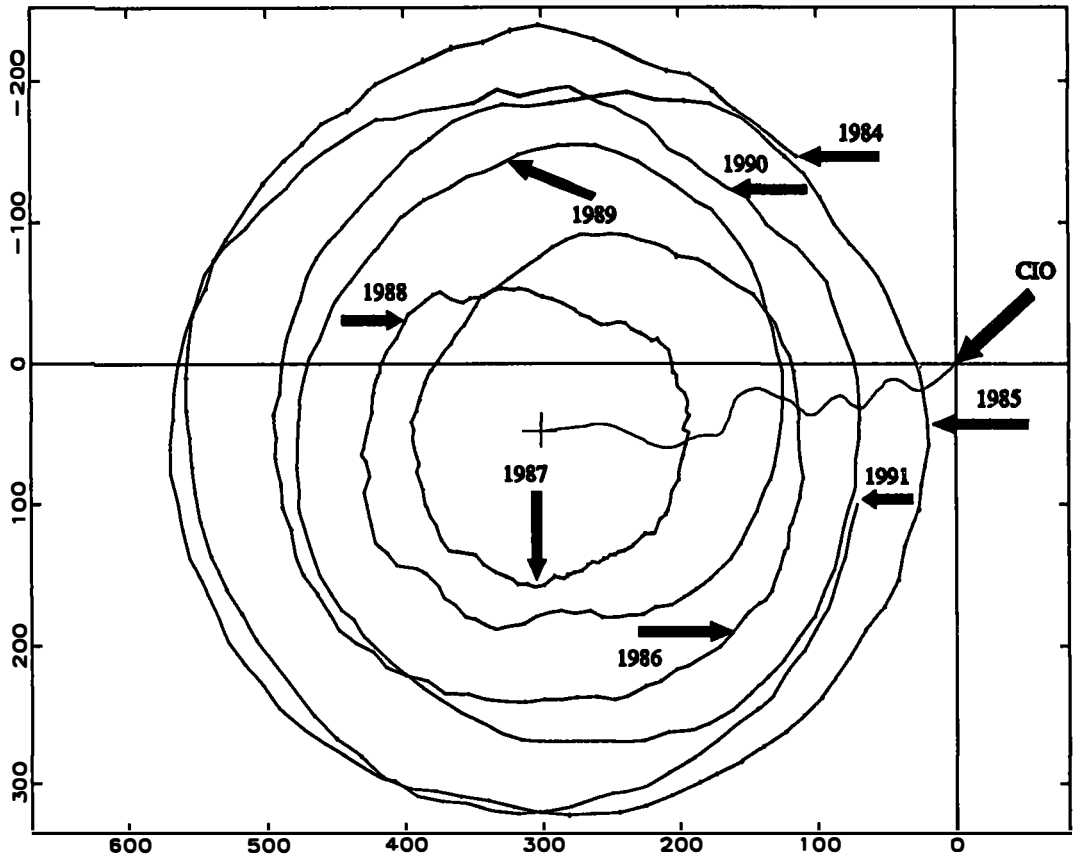

Figure 2. VLBI determinations of the pole position, 1984-1990. Scales are in milliseconds of arc. The origin is the conventional international origin (CIO) which was determined by averaging measurements made in about 1900.

toward Newfoundland, may be the result of relocation of mass within the solid earth associated with glacial rebound [Peltier and Tushingham, 1989]. On time scales of a decade or less the apparent motion of the pole is irregular at the level of several centimeters per year. The cause of the irregularities has been attributed to meteorological effects as well as tectonic effects including earthquake displacements. Chao and Gross [1977] concluded that, "The computed changes in the Earth's global geodetic/gravitational parameters induced by the earthquakes during 1977-1985 are in general two orders of magnitude smaller than the observed values that are available." Meteorological shifts of atmospheric masses are another possible source of the excitation mechanism that has received extensive study [Munk and Hassan, 1961; Wilson and Haubrich, 1976; Wahr, 1982; 1983; Barnes *et al.*, 1983; Hide, 1984]. A related possibility involves changes in the distribution of surface and ground water resulting from changes in rainfall and snow cover [Wilson and Hinnov, 1985; Hinnov and Wilson, 1987; Chao *et al.*, 1987; 1988; Chao and O'Connor, 1988; Chao 1988]. The problem is at least equally bad with the changes in lod. The winds associated with weather patterns cause several tenths of milliseconds variations in lod on time scales of weeks to years. Attempts to use meteorological data to correct for these effects have been relatively successful [Langley, *et al.*, 1981; Rosen and Salstein, 1983; Carter *et al.*, 1984; Rosen *et al.*, 1984; 1990; Chao, 1989]. However, there are equally large unexplained variations in lod on decadal time scales that are thought to derive from fluid core - mantle interactions that cannot currently be determined by other methods. For the foreseeable future we will not be able to interpret earth

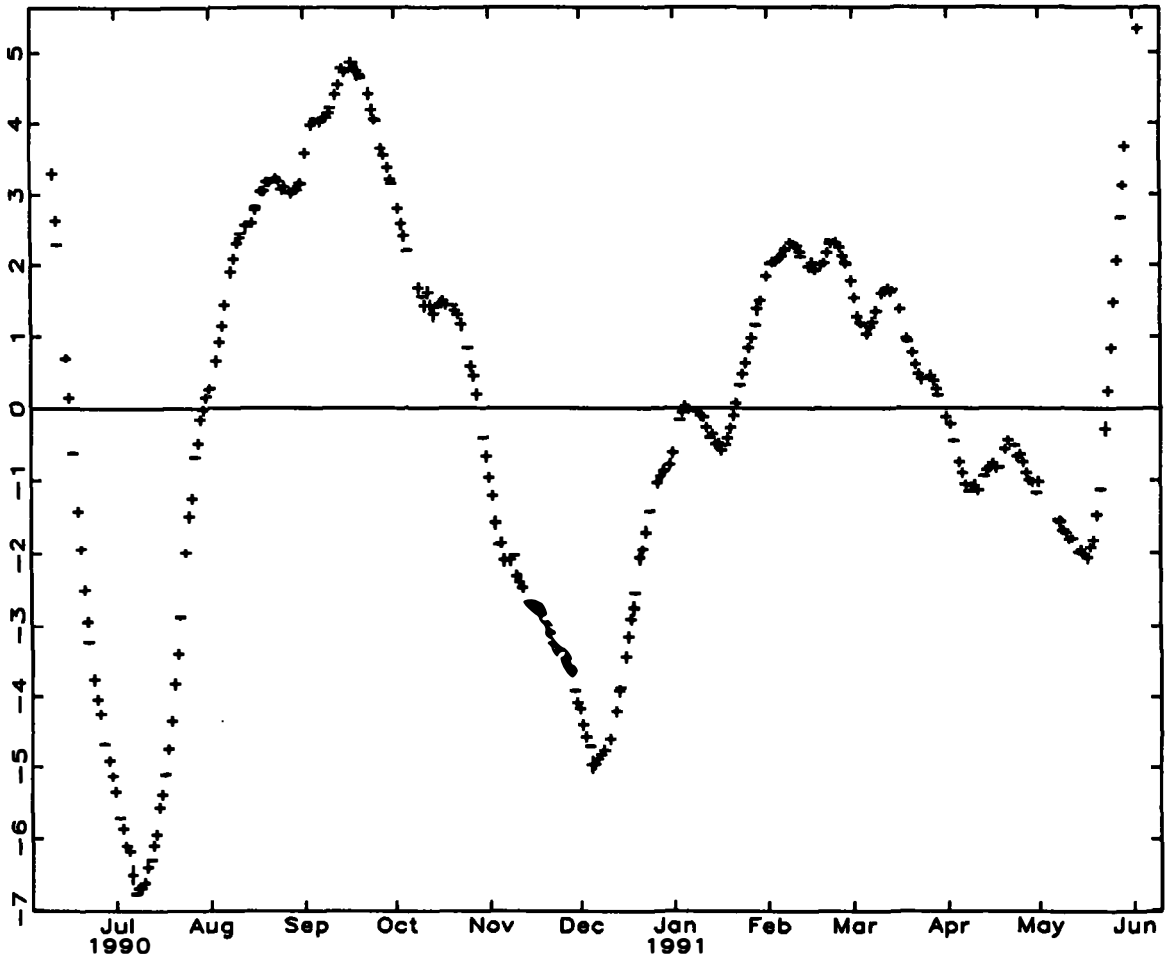

Figure 3. Daily UT1 determinations from the IRIS VLBI project. The vertical scale is in milliseconds of time. Tidal variations and a fifth-order polynomial have been removed.

rotation data to unambiguously determine if specific ice masses are melting or accumulating at certain rates, but the earth rotation data will provide constraints that will help us evaluate purported changes in the ice masses. For example, the absence of change in motion of the pole makes the accumulation of more than 20 centimeters per year of ice on Greenland reported by Zwally [1989] very unlikely [Douglas *et al.*, 1989].

Repeat measurements of the elevations of the surfaces of the major ice masses, such as the Greenland ice cap, have been technologically possible for many decades using spirit leveling. However, acquiring sufficiently dense levelling profiles to compute the volume of the ice would have required very costly observing campaigns in remote and hostile environments. Within the past few decades technological developments have brought remote sensing techniques closer to being able to achieve the accuracy and coverage required. Laser and microwave altimeters on aircraft and artificial satellites now are routinely used to make repeat profiles of the ocean surfaces, and satellite altimetry is now competitive in accuracy and far superior in coverage for interannual monitoring of sea level compared to tide gauge networks [Cheney *et al.*, 1989; Cheney and Miller, 1990; Miller and Cheney, 1990]. Satellite microwave altimetry data have also been successfully collected over southern Greenland and parts of Antarctica, and attempts have been made to derive changes in

surface elevations from these data [Zwally, 1989]. Orbit errors are still at a level that they can introduce significant errors in the ice profiles. However, continued development of the Global Positioning System (GPS) satellite constellation, receivers, and observing and data analysis techniques are reaching a level where airborne and satellite altimetry may soon achieve the required accuracy and coverage at acceptable costs.

During the summer of 1991 NOAA researchers will participate in two separate airborne ice profiling experiments in Greenland, one jointly with researchers at the Naval Research Laboratories (NRL) and the second with National Aeronautics and Space Administration (NASA) researchers at the Wallops Island Space Center. In both experiments P-3 aircraft instrumented with laser and microwave altimeters, and navigated by differential kinematic GPS techniques, will make initial epoch measurements of ice profiles across the Greenland ice cap, including lines that will be profiled repeatedly by the ERS-1 satellite to be launched during 1991 by the European Space Agency (Figure 4). The portion of the ERS-1 track drawn in solid line beginning a Sondre Stromfjord and extending northeastward onto the icecap will be the primary focus of the airborne altimeter flight during the 1991 observing campaign. Comparison of the NRL-NOAA, NASA-NOAA, and the ERS-1 profiles should provide a reliable estimate of the current state of the art in ice profiling. Decimeter accuracy is expected, and profiles of that accuracy would make a valuable contribution to monitoring ice caps. There remain questions about how well ice profiles can be converted to ice volume. Fresh snow falls may cause difficulties. Variations in the penetration into the snow and ice of microwave altimetry signals could result in significant errors. Voids in the ice masses, changes in density of the ice, and difficulties in mapping the steep edge areas are other concerns. But this approach is perhaps the most direct method devised for monitoring changes in the ice masses, the prospects for improvements in the accuracy achieved are good in the near future, and ultimately remote sensing of the ice caps using GPS positioned altimetric satellites may prove the least costly method to achieve the spatial coverage and temporal resolution needed for climate change studies.

The third approach to monitoring changes in ice masses has been described by Hager as "weighing the ice." On short time scales (decades) the earth responds to changes in surface loading elastically. If ice is added or subtracted from an existing ice mass there will be an immediate response in the elevation of the surface of the crust under the load, which will extend significantly beyond the edge of the load (Figure 5). Using a simplified model Hager has estimated that the addition of 21 centimeters of ice over Greenland would result in approximately 1 centimeter vertical (downward) and 3 millimeters of horizontal (toward the ice) displacement of a point located on bed rock at the edge of the ice cap. If points on opposite sides of the ice mass can be observed the horizontal "signal" can be effectively doubled, i.e., the horizontal displacements of points A and B in figure 4 would be toward one another and the distance between points A' and B' would be reduced by twice the horizontal displacement of each station. This is an "instantaneous" response associated with the elastic deformation of the earth and should not be confused with the long term pattern of deformation that eventually would result from the viscous response of the earth if the load persisted over long time scales. If the vertical and horizontal displacements of points around the periphery of ice masses can be measured with sufficient accuracy changes in the weight of the ice mass can be determined in much the same way as if it were to be placed on a spring scale at the local fruit market.

In well designed and carefully executed experiments both VLBI and GPS have already achieved, and even exceeded, the requisite precision to detect the crustal deformations expected from decimeter changes of the Greenland and Antarctic ice caps. Improvements in both systems currently underway should make the required precision well within routine operations within the

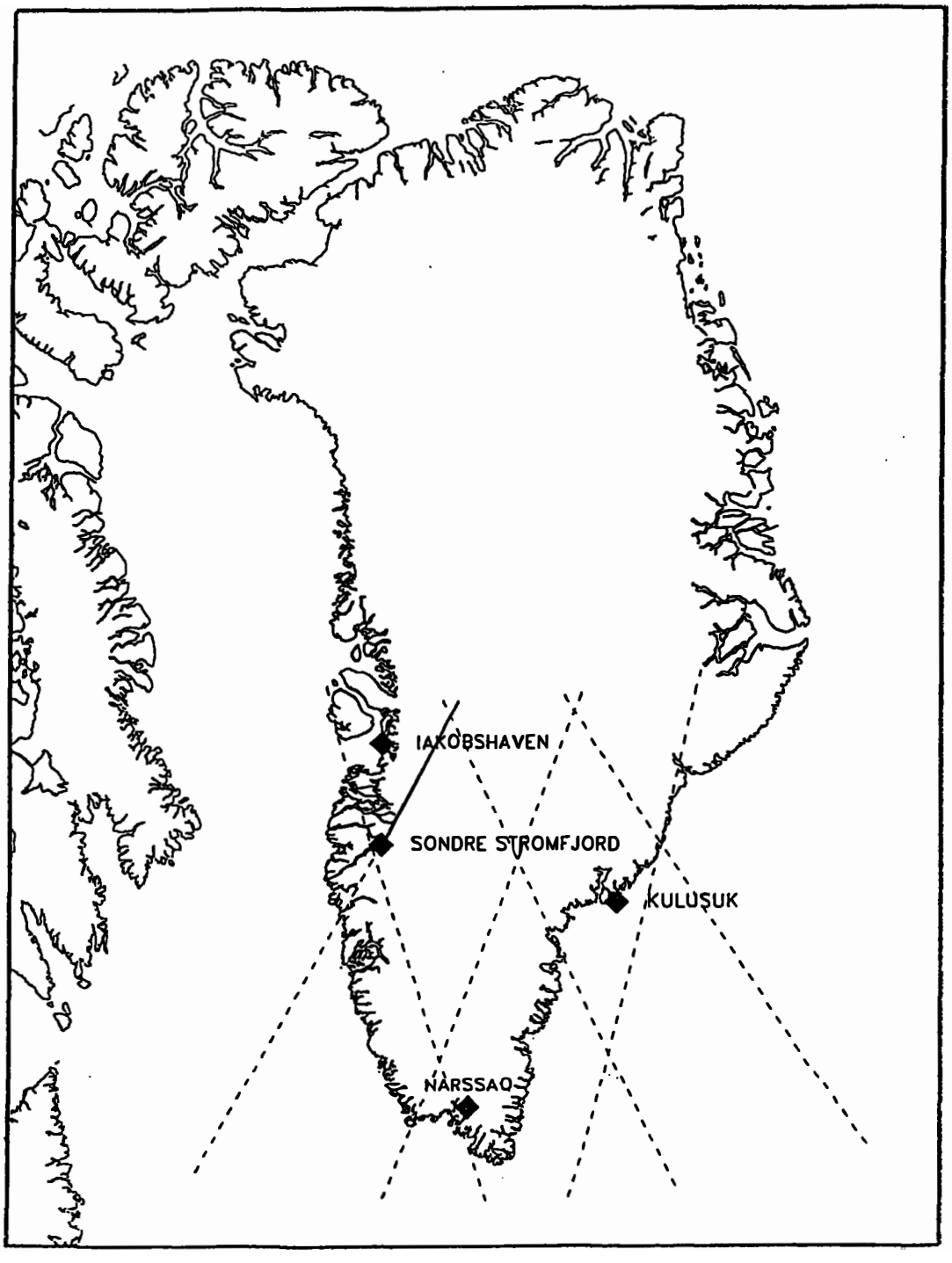

Figure 4. Map showing the locations of the GPS ground stations and ERS-1 satellite tracks over southern Greenland.

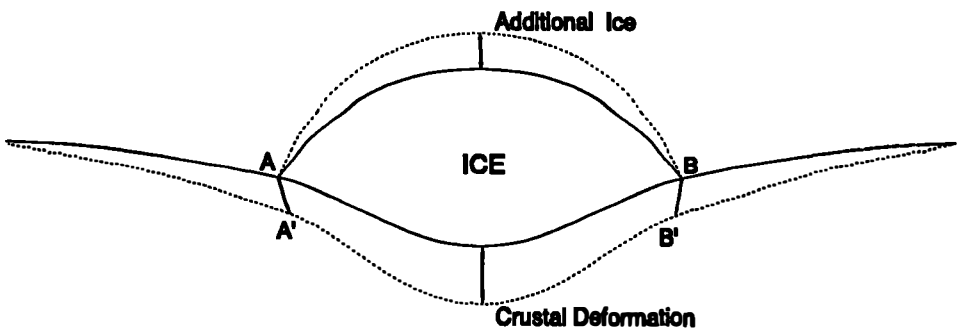

Figure 5. Sketch (not to scale) showing effects of increased loading of ice on the crust. The elastic deformation will cause instantaneous displacements, both vertically and horizontally, of points under and around the ice.

next few years. However, because atmospheric refraction tends to limit the vertical accuracy of GPS and VLBI to a factor of 3 to 5 worse that the horizontal accuracy, the horizontal component of the displacement may actually prove more useful than the larger vertical component. The base stations to be used for phase difference kinematic GPS observations during the ice profiling tests scheduled for Greenland in 1991 may yield observations of sufficient quality to serve as initial epoch measurements. Tentative plans for to make mobile VLBI observations in Greenland during 1992, as part of the NOAA C&GC program, are also being explored. In the longer term the most cost effective approach may be to establish permanent regularly observing GPS stations near the ice margins in Greenland and Antarctica.

The crustal displacements and changes in attraction of the ice caused by decimeter level changes in major ice masses would also result in a significant changes in the absolute gravity at nearby stations. The changes caused by the two mechanisms would be of opposite signs, but preliminary estimates of the expected change if two decimeters were added to the Greenland ice cap indicate that absolute gravity measurements may be a relatively inexpensive complementary observing technique to GPS and VLBI.

The method of weighing ice masses using VLBI, GPS, and absolute gravity to detect the elastic deformation of the crust near the periphery of the ice, is not limited to the very large Greenland and Antarctic ice caps. For example, Hager has pointed out that regions of southeast Alaska are

undergoing rapid emergence as mountain glaciers shrink. The combination of airborne profiling from a light aircraft and ice weighing with GPS and absolute gravity might prove particularly cost effective for monitoring such limited areas.

Concluding Remarks

When the geodetic community first began to consider the feasibility of exploiting the new technologies of VLBI, GPS, and absolute gravity to attack long standing scientific problems, determining the contemporary rate of rise of global absolute sea level was one of the first goals identified [Carter *et al.*, 1986; 1989]. At first the most feasible approach appeared to be to utilize the existing array of tide gauge stations to determine the relative rate of sea level rise and to use geodetic measurements to cleanse the records of vertical crustal motions. This approach is still a fundamental component of the NOAA sea level project, but there is now a greater awareness of the complexity of the problem. Even assuming that the challenging accuracy requirements for the geodetic measurement can be met, there remain at least equal challenges in determining the water level with sufficient accuracy and adequate spatial sampling. Relative sea level changes of tens of centimeters occur at time scales from interannual to interdecadal. Ocean dynamics may pose more of a problem than crustal dynamics, and it appears there is now a consensus that tide gauges alone are not adequate for monitoring the water level. Satellite altimetry is the only hope for gathering the required water level data.

The NOAA sea level project has always included the concept of attacking the problem from the point of view of monitoring the sources of the water causing changes in sea level. But the remoteness and severe weather conditions in Greenland and Antarctica made this approach rather forbidding. Advances in kinematic GPS, satellite and airborne altimetry, and new ideas such as inferring changes in the ice masses from nearby crustal deformations are making ice monitoring appear ever more tractable. It appears that direct measurements at the source of the water, where the signal to noise level is more favorable, may yield the earliest and most accurate measurement of global sea level change.

The basic components of both the water level and ice monitoring approaches are the same. We must establish a global terrestrial reference frame accurate to the sub-centimeter level over time scales of decades. We must use GPS to determine the locations of water/ice surface level sensors (tide gauges or airborne/satellite altimeters) in the terrestrial reference frame. This will require accurate orbits for the GPS satellites, high quality GPS receivers, and accurate fixed and kinematic GPS observing procedures and data reduction software. Reliable data archiving will also be required. The difference in the two approaches is largely the focus of the GPS activities, *i.e.*, positioning tide gauges or airborne/satellite remote sensing systems. The balance is clearly shifting in favor of the latter. The 1991 tests of airborne/satellite profiling of the Greenland ice cap may well mark a major turning point in the NOAA sea level project. If this approach proves successful, more of the resources may be focussed on ice monitoring in the future.

References:

Barnes, R.T.H., R. Hide, A.A. White, and C.A. Wilson, Atmospheric Angular Momentum Fluctuations, Length-of-Day Changes and Polar Motion, *Proc. Roy. Soc. Lond.*, **A387**, 31-73, 1983.

Carter, W.E., Modern Methods for the Determination of Polar Motion and UT1, Proceedings of Tenth Annual Precise Time and Time Interval Applications and Planning Meeting, NASA Memorandum #80250, 1978.

Carter, W.E. and W.E. Strange, The National Geodetic Survey Project "POLARIS," *Tectonophysics*, **52**, 39-46, 1979.

Carter, W.E., D.S. Robertson, J.E. Pettey, B.D. Tapley, B.E. Schutz, R.J. Eanes, and Miao Lufeng, Variations in the Rotation of the Earth, *Science*, **224**, 957-961, 1984.

Carter, W.E., D.S. Robertson, T.E. Pyle, and J. Diamante, The Application of Geodetic Radio Interferometric Surveying to the Monitoring of Sea Level, *Geophys. J. R. Astron. Soc.*, **87**, 3-13, 1986.

Carter, W.E., D.G. Aubrey, T. Baker, C. Boucher, C. LeProvost, D. Pugh, W.R. Peltier, M. Zumberge, R.H. Rapp, B.E. Schutz, K.O. Emery, and D. Enfield, Geodetic Fixing of Tide Gauge Bench Marks, *Woods Hole Oceanographic Institute Technical Report, WHOI-89-31*, 1989.

Carter, W.E., M. Chin, J.R. Mackay, G. Peter, W. Scherer, and J. Diamante, Global absolute sea level: the Hawaiian network, *Marine Geodesy*, **12**, 247-257, 1988.

Chao, B.F., Excitation of the Earth's Polar Motion Due to Mass Variations in Major Hydrological Reservoirs, *J. Geophys. Res.*, **93**, 13811-13819, 1988.

Chao, B.F., Length-of-Day Variations Caused by El Niño-Southern Oscillation and Quasi-Biennial Oscillation, *Science*, **243**, 923-925, 1989.

Chao, B.F., and R.S Gross, Changes in Earth's Rotation and Gravity by Earthquakes, *Geophys. J. R. Astron. Soc.*, **91**, 569-596, 1987.

Chao, B.F., and W.P. O'Connor, Global Surface-water Induced Seasonal Variations in the Earth's Rotation and Gravitational Field, *Geophys. J. R. Astron. Soc.*, **89**, 263-270, 1988.

Chao, B.F., W.P. O'Connor, A.T.C. Chang, D.K. Hall, and J.L. Foster, Snow-load Effect on the Earth's Rotation and Gravitational Field, *J. Geophys. Res.*, **92**, 9415-9422, 1987.

Chao, B.F., W.P. O'Connor, and A.T.C. Chang, Snow-load Excitation of the Earth's Annual Wobble, in *The Earth's Rotation and Reference Frames for Geodesy and Geodynamics*, A.K. Babcock and G.A. Wilkins, (eds.), Kluwer, Dordrecht, Holland, 373-380, 1988.

Cheney, R.E., B.C. Douglas, and L. Miller, Evolution of Geosat Altimeter Data with Application to Tropical Pacific Sea Level Variability, *J. Geophys. Res.*, **94**, 4737-4747, 1989.

Cheney, R.E., and L. Miller, Recovery of the Sea Level Signal in the Western Tropical Pacific from Geosat Altimetry, *J. Geophys. Res.*, **95**, 2977-2984, 1990.

Douglas, B.C., R.E. Cheney, L. Miller, R.W. Agreen, W.E. Carter, and D.S. Robertson, Greenland Ice Sheet: Is It Growing or Shrinking?, *Science*, **248**, p. 288, 1990.

Hager, B.H., Weighing the Ice Sheets Using Space Geodesy: A Way to Measure Changes in the Ice Sheet Mass, *EOS, Transactions of the AGU*, supplement to the Apr 23, 1991 issue.

Herring, T.A., Current and Future Accuracy of Earth Orientation Measurements, this volume, 1991.

Hide, R., Rotation of the Atmospheres of the Earth and Planets, *Phil. Trans. R. Soc. Lond.*, **A 313**, 107-121, 1984.

Hinnov, L.A., and C.R. Wilson, An Estimate of the Water Storage Contribution to the Excitation of Polar Motion, *Geophys. J. R. Astron. Soc.*, **88**, 437-459, 1987.

Langley, R.B., R.W. King, I.I. Shapiro, R.D. Rosen, and D.A. Salstein, Atmospheric Angular Momentum and the Length of the Day: a Common Fluctuation with a Period Near 50 Days, *Nature*, **294**, 730-733, 1981.

Klopping, F.J., G. Peter, D.S. Robertson, K.A. Berstis, R.E. Moose, and W.E. Carter, Improvements in Absolute Gravity Observations, *J. Geophys. Res.*, **96, B5**, 8295-8303, 1991.

Miller, L., and R.E. Cheney, Large-Scale Meridional Transport in the Tropical Pacific Ocean During the 1986-1987 El Niño from Geosat, *J. Geophys. Res.*, **95**, 17905-17919, 1990.

Munk, W.H., and G.J.F. MacDonald, *The Rotation of the Earth*, Cambridge University Press, London, 1960, p 232.

Munk, W.H., and E.S.M. Hassan, Atmospheric Excitation of the Earth's Wobble, *Geophys. J. R. Astron. Soc.*, **4**, 339, 1961.

Peltier, W.R., and A.M. Tushingham, Global Sea Level Rise and the Greenhouse Effect: Might They Be Connected?, *Science, 244*, 806-810, 1989.

Robertson, D.S., W.E. Carter, B.D. Tapley, B.E. Schutz, R.J. Eanes, Polar Motion Measurements: Sub-Decimeter Accuracy Verified by Intercomparison, *Science,* **229**, 1259-1261, 1985.

Rogers, A.E.E., Instrumentation Improvements to Achieve Millimeter Accuracy, this volume, 1991.

Rosen, R.D., and D.A. Salstein, Variations in Atmospheric Angular Momentum on Global and Regional Scales and the Length of Day, *J. Geophys. Res.*, **88**, 5451-5470, 1983.

Rosen, R.D., D.A. Salstein, T.M. Eubanks, J.O. Dickey, and J.A. Steppe, An El Niño Signal in Atmospheric Angular Momentum and Earth Rotation, *Science*, **225**, 411-414, 1984.

Rosen, R.D., D.A. Salstein, and T.M. Wood, Discrepancies in the Earth-Atmosphere Angular Momentum Budget, *J. Geophys. Res.*, **95**, 265-279, 1990.

Wahr, J.M., The Effects of the Atmosphere and Oceans on the Earth's Wobble - I. Theory, *Geophys. J. R. Astron. Soc.*, **70**, 349-372, 1982.

Wahr, J.M., The Effects of the Atmosphere and Oceans on the Earth's Wobble and on the Seasonal Variations in the Length of Day - II. Results, *Geophys. J. R. Astron. Soc.*, **74**, 451-487, 1983.

Wilson, C.A., and R.A. Haubrich, Meteorological Excitation of the Earth's Wobble, *Geophys. J. R. Astron. Soc.*, **46**, 707-743, 1976.

Wilson, C.A., and L. Hinnov, Water Storage Effects on the Earth's Rotation, in *Proc. Int. Conf. Earth Rotation and the Terrestrial Reference Frame*, Dept. Geod. Science, Ohio State University, Columbus, Ohio, 415-433, 1985.

Zwally, H.J., A.C. Brenner, J.A. Major, R.A. Bindschadler, and J.G. Marsh, Growth of Greenland Ice Sheet: Measurement, *Science,* **246**, 1589-1591, 1989.

IfAG-Plans to support VLBI in the Southern Hemisphere

Hermann Seeger, IfAG-Frankfurt a. M. (D)

1. General Aspects:

Monitoring global change and global geodynamics requires a global distribution of VLBI-and SLR-stations at distances of approximately 5000 km. In the Southern Hemisphere there are presently only a few permanent stations available: 3 VLBI-sites and 2 SLR-systems; 4 other stations are operated only 6 months per year. Due to the economic situations in many countries in the Southern Hemisphere it is unrealistic to assume that this situation might improve during the coming years if the US, European Countries and Japan are not granting the necessary support.

2. The German ERS-1/VLBI Facility at O'Higgins/Antarctica:

The German Federal Ministry of Research and Technology has funded a German Ground Station on the Antarctic Continent through the IfAG. This is intended as a contribution to the use of ERS-1 in the Antarctic and the system was designed as a combined ERS-1(SAR)/VLBI Facility. The telescope has been installed during the Antarctic Summer 1990/1991 and is ready for the ERS-1 Service (figure 1 and 2). The last components of the VLBI-System (VLBA/MKIII Terminal and Maser) will be shipped in October 1991; first VLBI experiments are foreseen for late 1991. The overall responsibility for the O'Higgins Observatory will be assumed by the DLR or AWI; the operation of the geodetic components will remain with IfAG. The basic design of this telescope is as follows:

- Environment
  - Temperature: -30...+15 Deg.Cel.
  - Windvelocity: up to 300 km/h
- Time and Frequency system
  - Time HP "high performance" cesium std.
  - Time sync.: GPS-receiver
  - Frequency: EFOS active H-maser

Fig. 1 and 2.: The ERS-1/VLBI-Telescope in O'Higgins

- ERS-Equipment
  - G/T: 31 dB
  - ERS Tracking receiver
  - ERS SAR-datareceiver
  - SAR Data HDTR recorder
  - SAR Quick look processor
- VLBI-Equipment
  - Kryogenic LNA and downconverter
  - VLBA/VLBI compatible receiver, 14 ch. (NRAO-Interferometrics)
  - VLBI-HDT recorder

Mount:

- Special 3-axis mount, completely covered backstructure
- 1. Axis: azimuth ±270 deg. from north
- 2. Axis: tilt 0 deg. or 8 deg. from vertical (2 possible positions)
- 3. Axis: oblique 45 deg. (instead of elevation axis)
- Azimuth velocity 0.0017 deg./sec. – 11 deg./sec., acceleration 7 deg./sec.^{2}
- Pseudo-elevation velocity 0.001...5 deg./sec., acceleration 5 deg./sec.^{2}

Antenna:

- Type: On-axis Cassegrain
- Main reflector
  - Diameter: 9.0 m
  - Shape: true rot. Paraboloid
  - Focal length: 3.6 m
  - Surface acc. 0.5 m rms
- Sec. reflector:
  - Diameter: 1.3 m
  - Shape: true rot. Hyperboloid
  - Surface acc. 0.1 mm rms

- Feed
  - Type: corrugated horn
  - Frequency 2.0–2.3 GHz and 8.0–8.6 GHz
  - Polarisation RHC and LHC

O'Higgins and the Japanese telescope in Syowa will form, together with stations in South-Africa (Hartebeesthock), Tasmania (Hobart), South America (Natal or Santiago de Chile) and perhaps at Tahiti, a new Antarctic VLBI-Network as it was designed by Carter et. al., NGS; the configuration in figure 3 may even be improved by an additional (US) telescope at Mc Murdo.

3. The TIGO-Concept

The optimal design for a space-oriented geodetic-geodynamical observatory still follows the philosophy of "fundamental stations" which include all the modern precise observation techniques such as Laser Ranging, VLBI, GPS etc. One of the few places where these ideas have really been put into action is the German observatory in Wettzell. In order to transfer this concept to the Southern Hemisphere the TIGO-concept has been developed in the German Research Group for Satellite Geodesy (FGS = Forschungsgruppe Satellitengeodäsie). "TIGO" stands for "Transportable Integrated Geodetic (or Geodynamic) Observatory". The complete system will be made transportable by installing it in several containers of standard size. All the different modular observation and support units will be controlled from one central computer and a communication processor, but for special tasks it may be necessary that selected (modular) components can be operated as a single system, so that every subsystem will include its own processor.

Based on agreements with the host agencies in Southern Hemisphere countries TIGO should be installed at selected places for periods of about one year. Ground support and routine observers should be made available by the host agencies with training and maintenance support from at least two IfAG engineers who will travel with the system.

Using the best technology available TIGO will include the following components:

- SLR
- VLBI
- GPS- PRARE? - GLONASS?
- Reflector for GLRS
- Absolute Gravimeter
- Superconducting Gravimeter

Antarctic VLBI Sites

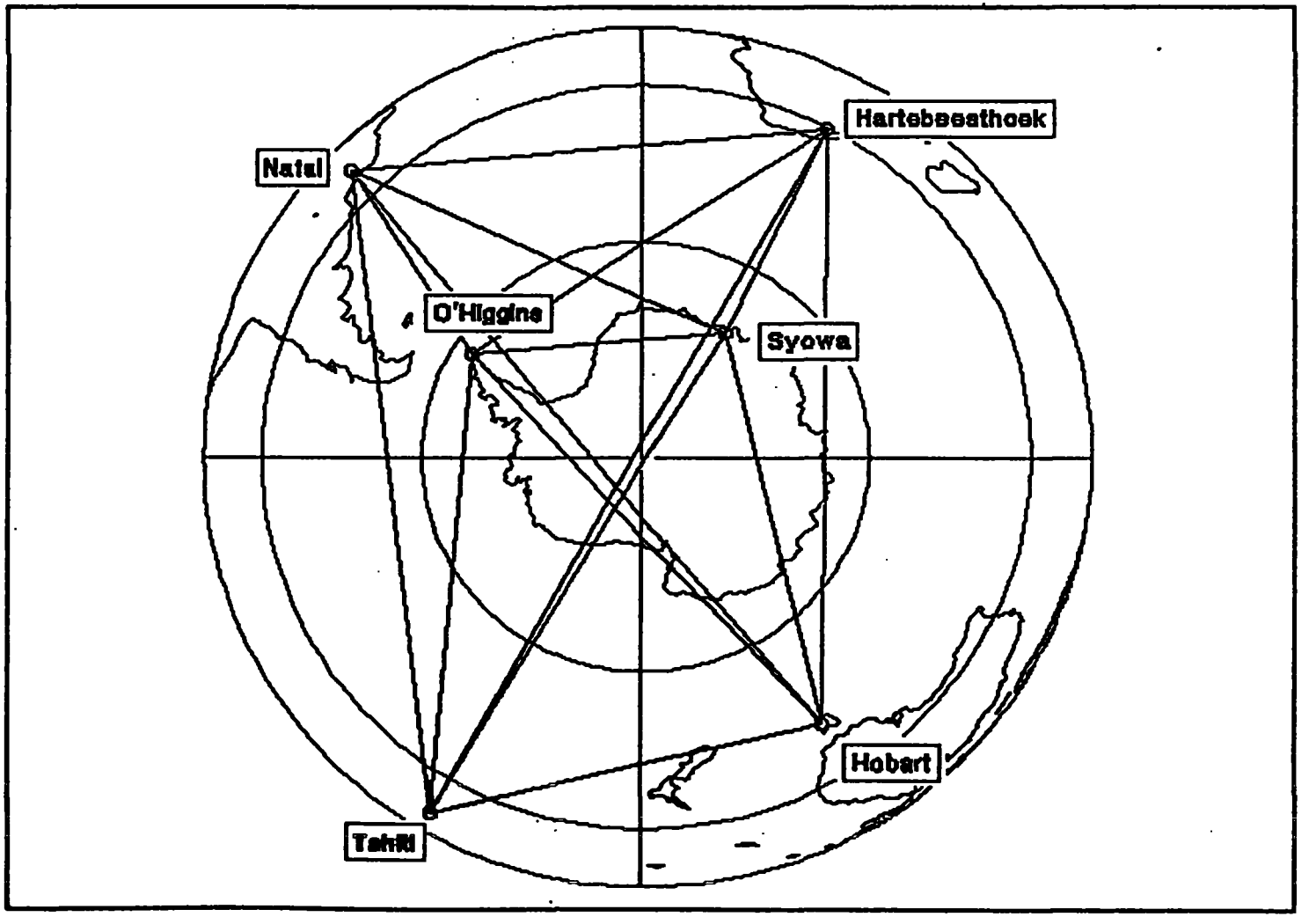

DGFI-ABT.2
IFAG

Proposed Network

DATE: 04/17/91
TIME: 15:27:17

Figure 3

- Seismometer
- Magnetometer
- Time + Frequency (2 Masers, Cs-standards, GPS-time)
- Met. Data aquisition
- Computer-network for:
- operation (automatic operation)
- system control
- data aquisition
- testing/maintenance
- communication
- data processing
- data transfer

Figure 4 includes a graph showing the TIGO components and the ties between the various components.

4. The TIGO SLR-Module

The TIGO SLR-module should fullfill all the modern requirements of a highly mobile SLR-unit and make use of the latest technology. Its main characteristics will be

- subcentimeter
- 500 km to 40.000 km range
- multicolour ?
- day/night capability
- automatic operation
- alt./azim.-mount
- a single telescope for transmit and receive functions
- high efficiency in transmission
- precise pointing
- Nd:YAG or Titan-Saphir laser
- pulse less than 30 picosec.

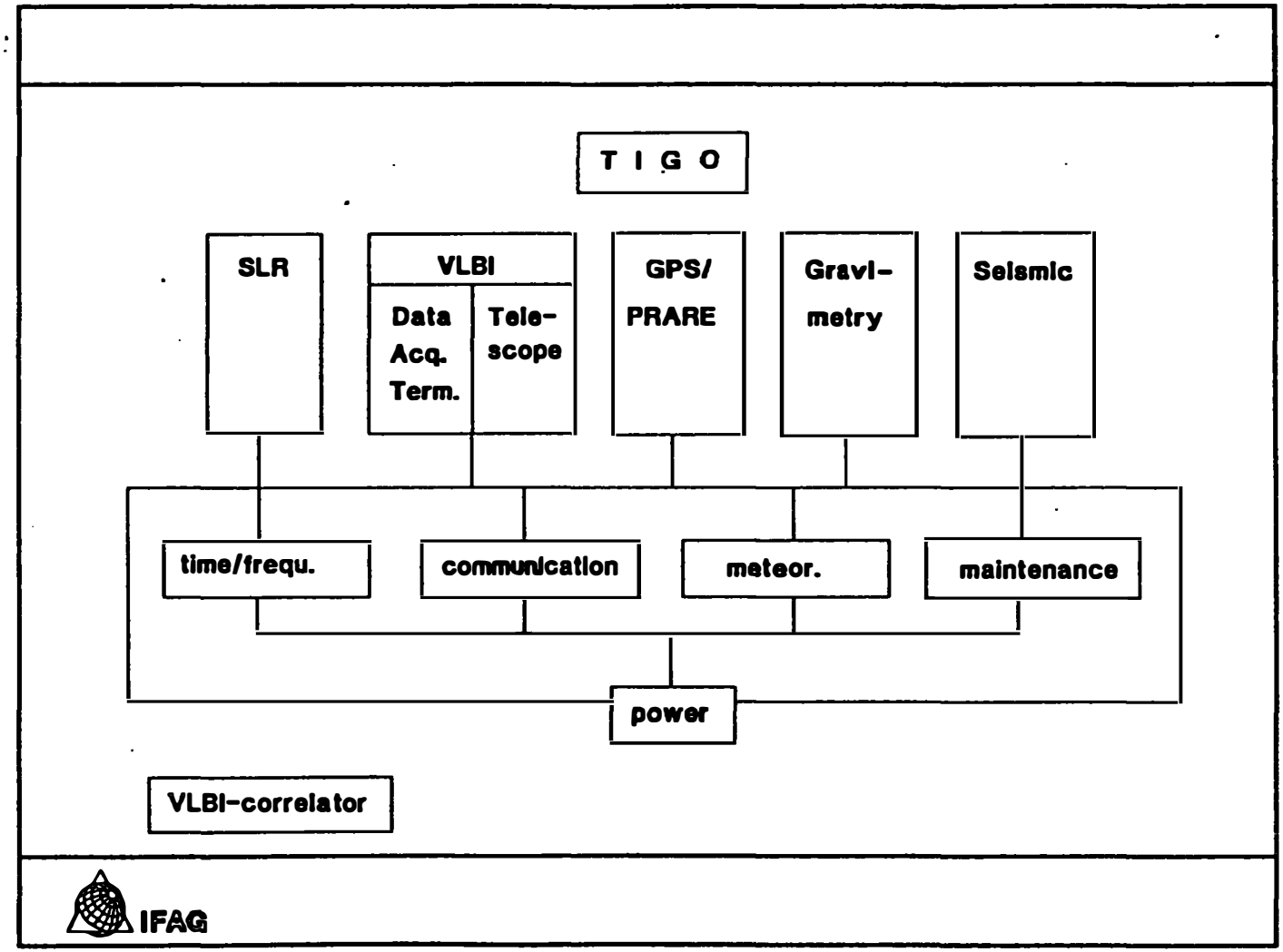
T I G O
SLR
VLBI
Data Acq. Term.
Tele-scope
GPS/ PRARE
Gravi-metry
Seismic
time/frequ.
communication
meteor.
maintenance
power
VLBI-correlator
IFAG

Figure 4

- repetition rate 10...20 Hz
- avalanche diode, and/or MCP detector
- set-up time 1-5 days
- highly reliable operation

5. The TIGO VLBI-Modul

The VLBI-System will be based on the recent results of research and development experiments which due to the high sensivity of the new receiving techniques and the data aquisition terminals may allow us to use much smaller telescopes. Some of the future characteristic may be

- 5...8 m antenna (alt./azim.)
- S/X horns
- helium cooled S/X receiver
- MK IV date aquisition terminal
- highly reliable automatic operation
- setting up: 1...5 days

Future and ongoing VLBI-activities such as the 6 station MKIII European Geodetic VLBI-Network (Onsala, Wettzell, Medicina, Matera, Noto and Madrid), the Antarctic Network and TIGO require more correlator capacity. As a result a TIGO-VLBI-Correlator is under discussion which will either be

- designed as a MPIfR/IfAG project to be installed in Bonn having 50% of the total time available for geodesy, sharing the costs (investment and operation) 50:50 between MPIfR and IfAG and establishing an IfAG-Correlator-Group in Bonn

or

- installed and operated as a 100% IfAG facility at the new branch of the IfAG in Leipzig.

6. The TIGO-Schedule

IfAG expects that the budget for TIGO will be accepted for 1992-1997. The necessary staff is available as result of the German reunification. Base-station will be Wettzell where the TIGO-Management will be established with Dr. Schlüter as its head, Dr. Sperber, Dr. Schreiber, Dr. Dassing, Dipl.-Ing. Kilger and Dr. Nothnagel as well as 4–5 additional project scientists to be contracted in late 1991 as members of staff. The different components will be produced by private industry.

The Results of the Test VLBI Experiments with the Syowa Station in Antarctica and its Future Plans

by

N. Kurihara, T. Kondo, Y. Takahashi, and F. Takahashi
(Kashima Space Research Center, CRL, 893-1 Hirai, Kashima, Ibaraki, 314 Japan)

and
M. Ejiri
(National Institute of Polar Research, Itabashi, Tokyo, 173 Japan)

ABSTRACT

The position of Syowa Station in the Antarctica was measured with an error of decimeters by a Very Long Baseline Interferometer (VLBI) experiment carried out in January, 1990. This is the first VLBI experiment that connects the Antarctica with other continent. Kashima, Japan and Tidbinbilla, Australia participated in the experiment in conjunction with Syowa Station. The K-4 data acquisition terminal used at the Syowa Station was transported from Kashima for a temporary use. The data at Syowa Station and Tidbinbilla were gathered to Kashima for data processing. All data were correlated at Kashima and analyzed to obtain a precise position of the Syowa Station. This paper summarizes an outline of the test VLBI experiments and its future plans.

1. Introduction

Geodetic VLBI stations are mainly distributed in the northern hemisphere, but it is important to extend the networks to include stations in the southern hemisphere not only for measuring precise plate motion but also for monitoring the earth rotation. Many efforts have been, therefore, devoted for extending networks to the south. However no VLBI experiment had been conducted with an Antarctic station until the first experiment reported here, because there had been no antenna available for VLBI experiment. In 1989, the 30th Japanese Antarctic Research Expedition (JARE-30) organized by the National Institute of Polar Research (NIPR), Japan, built a multipurpose satellite data receiving antenna with 11m in diameter at Syowa Station (69.0S,39.6E) in

the Antarctica[1]. This antenna is also designed to have a capability for VLBI and radio astronomy. Fig.1 shows the position of the Syowa Station in the Antarctica. Communications Research Laboratory(CRL), Japan conducted a test VLBI experiments between 11 m antenna at Syowa Station and a 26 m antenna at Kashima (35.8N,140.7E), Japan, in January 1990 in cooperation with the JARE-30. The main purpose of the test experiments is to the detection of the fringes, in order to check the feasibility for future regular Antarctic VLBI experiments. A 34 m antenna at Tidbinbilla (35.2S,149.0E), Australia, was also participated in the experiment to improve the mutual visibility limitation.

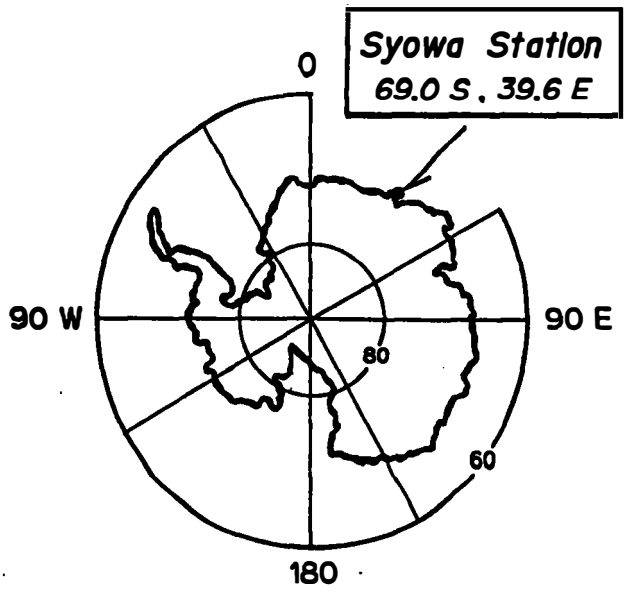

Fig. 1 The Antarctic Continent and position of the Syowa Station

2. Experiments

2.1. An environments of the experiments and instruments

The experiment was scheduled to be carried out within a month during the yearly exchange of personnel at Syowa Station in austral summer season. All equipments necessary for the VLBI experiment at Syowa Station were transported by members of the JARE-31 and Japanese ice-breaker "Shirase".

In these experiments newly developed and highly transportable recorders dedicated to VLBI data acquisition named "K-4 recorder" [2] were employed both at Syowa Station and Kashima. By adopting a helical scanning head with a 3/4 inch wide cassette tape, the K-4 recorder becomes much more compact (approximately one-fourth both in size and in weight) compared with a conventional K-3 or Mark-III recorder for VLBI use. Consequently the K-4 recorder can be easily transported and diminishes the operator's work load. Hence, it would have been impossible to perform the experiment without this transportable K-4 recorder at

Syowa Station.

Moreover a use of the highly stable crystal oscillator with its phase locked to a cesium clock[3] at Syowa Station as a frequency standard enabled us to perform the experiment promptly, in spite of the lack of a transportable H-maser oscillator. Fig.2 shows the block diagram and signal flow of the data acquisition system at Syowa Station. Clock synchronization at the microsecond level at Syowa Station, which is necessary for correlation processing, was achieved both by a GPS receiver and by a portable clock technique using the cesium clock transported from Japan.

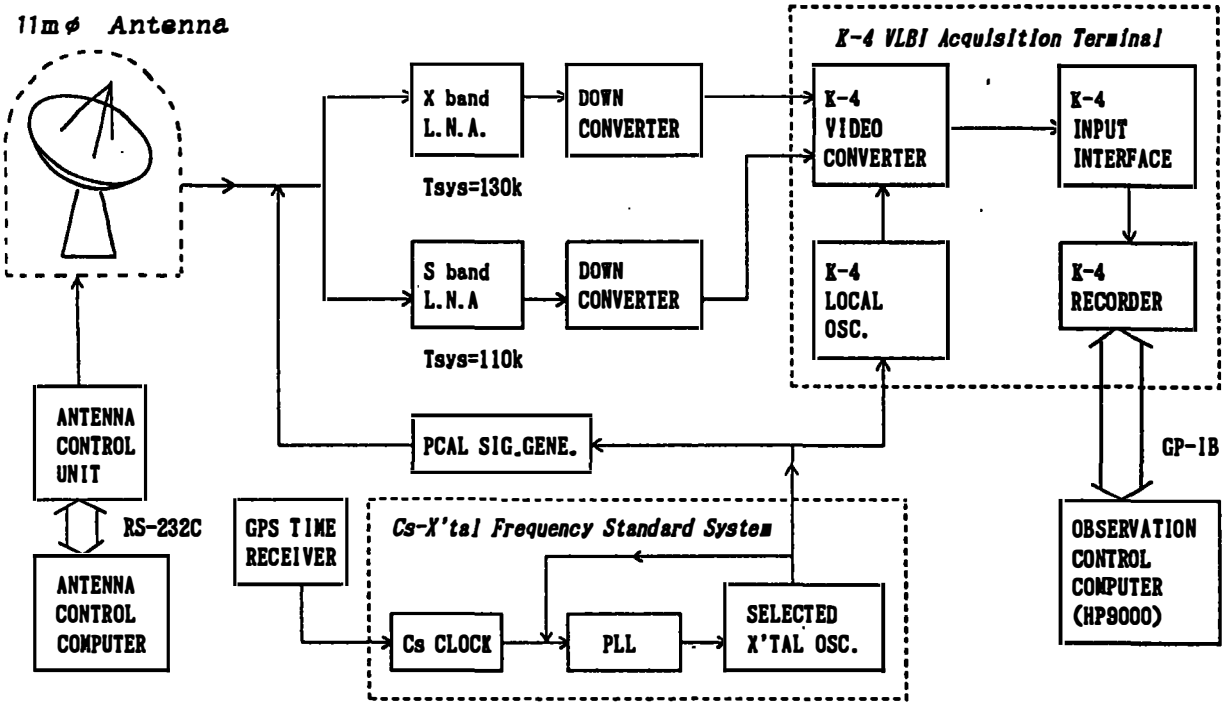

Fig. 2 The block diagram and signal flow of the data acquisition system at Syowa Station

2.2. Observations

A total of three experiment sessions were carried out in January, 1990, according to the schedule shown in Table 1. One session is here defined to be a set of scans where a scan observes a radio source (quasar) for 196 sec. we used the 31 radio sources listed in Table 2. The first session was a rehearsal session consisting of 12 scans and was performed on Jan. 16 between Kashima and Syowa Station. The second and the third sessions were carried out on Jan. 20 and 25 and lasted for about 24-hours in which more than 150 scans were included. In the latter two sessions, Tidbinbilla participated to improve the restriction on observations arising from the very limited mutual visibility area in the sky in the case of a Kashima-Syowa Station baseline, which is the longest VLBI baseline (about 11400km) on the earth at present time. The quasar signals were recorded at

dual frequency bands (S band:2GHz and X band:8GHz) at each station in order to calibrate the ionospheric excess delays. Table 3 summarizes the performances of the antenna and receiving system in the Syowa Station.

Table 1. The schedule of the test VLBI experiments

Exp. Name	Date	Time (UT)	Station
Test experiment	16 Jan. 1990 16 Jan. 1990	09:00 - 09:30 23:00 - 23:30	Syowa Kashima
1st 24-hour experiment	20 Jan. 1990 21 Jan. 1990	03:00 - 03:03	Syowa Kashima Tidbinbilla
2nd 24-hour experiment	25 Jan. 1990 26 Jan. 1990	19:20 - 19:23	Syowa Kashima Tidbinbilla

Table 2. Observed source list of 24-hour VLBI experiments

0104-408,	0308-611,	0402-362,	0420-014,	0454-234,
0537-441,	0607-157,	0637-752,	0727-115,	1034-293,
1057-797,	1101-325,	1104-445,	1206-399,	1226+023,
1251-713,	1253-055,	CENT-A,	1334-127,	1424-418,
1510-089,	1548+056,	1549-790,	1730-130,	1741-038,
1831-711,	1921-293,	2134+00,	2145+067,	2223-052,
2355-534				

Table 3. Performance of the receiving system in the Syowa Station

Distance from Kashima:	11400 km
Antenna Diameter:	11 m
Radome Diameter:	17 m
Receiving Frequency	
S band:	2200 - 2320 MHz
X band:	7860 - 8600 MHz

Aperture Efficiency	
S band:	57 %
X band:	59 %
System Noise Temperature	
S band:	111 k
X band:	126 k
Fringe Detectability	
S band:	1.77×10^{-4} Jy^{-1}
X band:	1.61×10^{-4} Jy^{-1}

2.3. Correlation Processing

The "Shirase" brought back the observation data from Syowa Station, in April 1990. The data were cross-correlated at the Kashima K-3 correlator immediately in order to form cbservables, such as delay time, delay rate and fringe amplitude. Delay time is defined as the time difference between the arrival of a certain wave front at one end of baseline and its arrival at the other end. Delay rate is rate of change of the delay time. By correlating two station's data, good fringes were detected at both S and X band. (One of them is shown in Fig. 3). In order to correlate the data obtained with different recording systems, i.e., K-4 type and Mark-III type, new correlating software had to be developed.

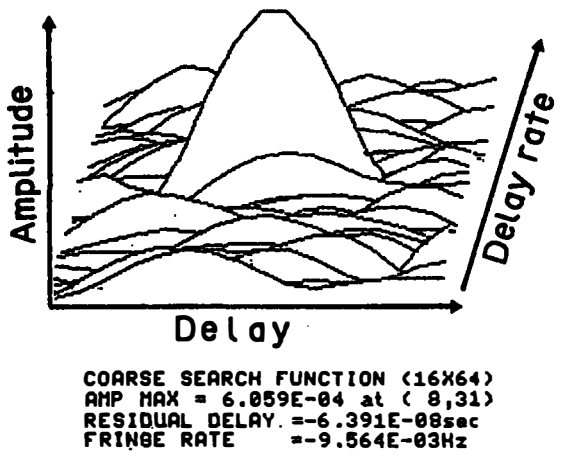

Fig. 3 The detected fringe at X band signal from 3C273B for Syowa Station-Kashima baseline

2.4. Analysis and Geodetic Results

After correlation processing, the positions of Syowa Station and Tidbinbilla were obtained by means of parameter adjustment in the least squares estimation using the delay observables. By that estimation, the position of Kashima was fixed at the posi-

tion on Jan. 20, 1990, whose x,y, and z components are -3997890.354m, 3276580.512m, and 3724118.800m, respectively, in the VLBI coordinate system[4]. The major radio source positions were also fixed at the values given by the VLBI group at Goddard Space Flight Center,NASA. But some of the source positions in the southern hemisphere, which are not included in the radio source catalog of the GSFC VLBI group, were adjusted in the analysis. Other characteristics of the least squares analysis process were identical to the normal international procedure for geodetic VLBI data analysis[5]. The positional coordinates obtained for the stations are summarized in Table 4, together with their one sigma formal errors.

Table 4. Position of Syowa Station and Tidbinbilla obtained by VLBI experiment in January, 1990

Station		1st 24-hour experiment (20 January)	2nd 24-hour experiment (25 January)
Syowa Station	x	1766198.06 +/- 0.08 m	1766197.93 +/- 0.08 m
	y	1460404.00 +/- 0.08 m	1460403.91 +/- 0.08 m
	z	-5932268.45 +/- 0.17 m	-5932268.17 +/- 0.18 m
Tidbinbilla	x	-4460933.56 +/- 0.05 m	-4460933.47 +/- 0.06 m
	y	2682764.82 +/- 0.03 m	2682764.77 +/- 0.04 m
	z	-3674381.21 +/- 0.06 m	-3674380.92 +/- 0.07 m

2.5. Discussion

The adjusted results show considerably larger errors than those common in current geodetic VLBI experiments, especially in the z-component of the Syowa Station position. This is thought to be due to an observing schedule unsuitable for precise geodesy, that is, an imperfect sky coverage of the observed sources. Participation of Tidbinbilla was intended to improve the mutual visibility limitation. This was not entirely successful, in part because of machine time restrictions on the Tidbinbilla antenna (approximately 15 hours for the session on Jan. 20 and 21 hours for that on Jan. 25), and partly because of the imperfect radio source catalog in the southern hemisphere (we had to use the sources in a limited declination range). Unsuitable observing schedules, especially in the case of limited sky coverage, elongate the error ellipsoid of estimated station positions in the baseline direction. Furthermore, the errors of vertical component are usually larger than those of horizontal components. Both of these effects result in an increase of the error in the z-component of position, especially that of Syowa Station. Another

possible contribution to the larger errors is the inferior stability of the frequency standard at Syowa Station, compared to the H-maser oscillators used at other stations. Fig. 4 shows the station locations and baseline lengths obtained by VLBI experiment in January, 1990.

3. Conclusion

We presented the results of the test VLBI experiment with an Antarctic station, for the first time in the world. We successfully got a lot of good S and X band fringes on the baseline among Syowa Station in Antarctica, Kashima in Japan and Tidbinbilla in Australia. From the delay observations, we determined the position of Syowa Station in Antarctica, whose estimated error are less than 8 centimeters for x and y components, less than 18 centimeters for z component. Although the station positions derived from the experiment have larger errors than the accuracy expected from a conventional geodetic VLBI experiment, We can conclude that this first VLBI experiment connecting Antarctica with other continents was successful. The results is initial value of future measurement of Antarctic plate by fixed VLBI system.

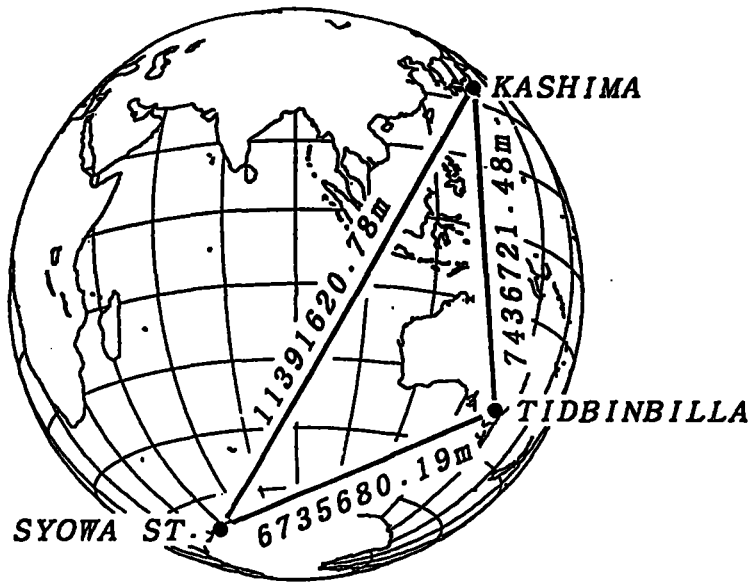

Fig. 4 The station configurations and baseline length obtained by test VLBI experiments

4. Future plans

Now, Syowa Station doesn't have any VLBI data acquisition terminal. We are planning to have a permanent VLBI data acquisi-

tion terminal at Syowa Station in cooperation with National Institute of Polar Research (NIPR), Japan. Japanese antarctic research program has been organized by NIPR. NIPR is an institute responsible for requesting the budget relating to antarctic research for Japanese government. CRL will support the construction of VLBI system (H-Maser frequency standard, K-4 data acquisition terminal) at Syowa Station. In a few years later (Jan. 1994?), Japanese antarctic VLBI program will be start. When the fixed VLBI station at Syowa Station will be completed, we will conduct the VLBI experiments with Syowa Station regularly. The regular experiments will produce very useful data for

(a) Antarctic plate motion,
(b) Monitoring the earth rotation,
(c) Radio astronomy in the southern hemisphere,
(d) Research of the ionospheric propagation.

References

(1) M.Ejiri, S.Tamagawa,K.Endo, R.Kuzuya, and M.Chiba, "Multi purpose Satellite Data Receiving Antenna", Proceedings of ISAP'89, pp.655-658, 1989.

(2) H.Kiuchi, S.Hama, J.Amagai, Y.Abe, Y.Sugimoto, and F. Takahashi, "Present status of the K-4 VLBI system", in this issue, 1991.

(3) H.Kiuchi, J.Amagai, and N.Kawaguchi, "A Highly Stable Crystal Oscillator Applied to Geodetic VLBI", J.Commun. Res.Lab., 36, 148, pp.107-124, Jul.1989.

(4) D.S.Caprette, C.Ma, and J.W.Ryan, "Crustal Dynamics Project Data Analysis - 1990", NASA Technical Memorandum 100765,1990

(5) K.Heki, Y.Takahashi, T.Kondo, N.Kawaguchi, F.Takahashi, and N.Kawano, "The Relative Movement of the North American and Pacific Plates in 1984-1985,Detected by the Pacific VLBI Network", Tectonophysics,144,151-158 (1987)

A New Transportable VLBI System

T A Clark (Code 926.9, NASA/GSFC, Greenbelt MD 20771; clark@tomcat.gsfc.nasa.gov)
D B Shaffer (Interferometrics & NASA/GSFC, Greenbelt MD 20771)
R M Allshouse (Bendix Field Engineering Corp., Columbia MD 21045)

Through the last decade, mobile VLBI systems have been used to obtain cm-level accuracy geodetic measurements in support of several scientific and operational programs. The *modus operandi* has been to move a mobile system (consisting of two large trailers, one with a 3-5 m diameter antenna and another filled with expensive electronics) to a site for a few days of observing, and then to rapidly move to another site. Low-cost and easily transportable GPS systems are now proving to be a cost-effective alternative to VLBI for regional scale (*i.e.*, < 1000 km) measurement campaigns. The scientific problems of the next decade (post-glacial rebound, monitoring changes in sea level, etc.) still require VLBI systems which can be installed at remote locations but with the more stringent demand for mm-level performance--comparable to the "best" achieved by VLBI with larger, fixed antennas now in use.

We envision a new class of VLBI system which would be transported to a remote location and operated within the global VLBI network for periods of several months (vs. days for the present mobile VLBI systems); the need for high mobility becomes a low priority when weighed against system accuracy, ease of transportation, ease of assembly, reliability and costs of remote operations. Such a system would provide high accuracy measurements at the remote location and serve as a fiducial station for a dense local GPS network.

Since VLBI sensitivity is of over-riding importance for such operations, the Mark-4 VLBI system is being developed with data recording capabilities of $\approx$1 GBit/sec (a 4-fold increase over the present Mark-3 system), which halves the diameter of the antenna required to achieve a given level of performance. Further system sensitivity improvements can be achieved through the use of high-efficiency microwave optics with off-axis shaped antenna reflectors and new low-less dual frequency antenna feeds, and with improved cryogenic microwave receivers. With the improved optics and electronics, performance comparable to (or better than) that achieved by Mojave (12 m antenna) VLBI station during the NASA CDP's ERDE (Extended R&D Experiment) could be achieved with a 3-5 m diameter transportable antenna system.

The NASA CDP, in cooperation with NOAA and USNO, has embarked on the development of just such a system. The existing MV-3 mobile VLBI system is being relocated to the NASA Goddard Optical Research Facility (GORF) and will serve as the development "test bed" with the goal of having the prototype operating within about two years.

Current Precision of VLBI Vertical Determinations

DANIEL S. MACMILLAN & JIM R. RAY

Interferometrics Inc./Goddard Space Flight Center, Greenbelt, Maryland

The precision of NASA Crustal Dynamics Project R&D experiments was examined to derive the current precision of VLBI vertical determinations. Observed length scatter was decomposed into modeled (based on formal errors) and unmodeled (excess scatter) errors. These errors were further decomposed into average local station vertical and horizontal errors. Inferred vertical scatter of 11.0 mm for the two-year ATD series is about twice the 6.8 mm for the three-week long ERDE burst. This difference occurs primarily because the short-term ERDE campaign did not sample the full range of unmodeled atmospheric errors experienced by the longer-term ATD set. Some reduction in error was produced by increased number of observations and better group delay precision. R&D precision is better than the average of all Mark III VLBI data by more than a factor of two.

INTRODUCTION

Over the last two decades, better instrumentation, observing strategies, and data analysis methods have improved VLBI baseline length precision from 1 meter to better than 1 centimeter [*Clark et al.*, 1989]. This improvement is shown in the average performance of the ensemble of all VLBI stations [*Caprette et al.*, 1990]. Since 1984, NASA's Crustal Dynamics Project (CDP) has conducted a series of R&D sessions using the best VLBI stations with sensitive fixed antennas and the most advanced observing techniques. These R&D experiments have produced significantly better geodetic precision than the average VLBI session.

It is important to reassess the precision of VLBI vertical determinations in light of current consensus in the geodynamics community that vertical motions of the earth's surface are related to critical geophysical problems, for example, global sea level rise, post-glacial rebound, and volcano monitoring. The purpose of this study was to evaluate the current precision of VLBI vertical determinations by analyzing state-of-the-art R&D experiments. We have studied two series of R&D experiments to obtain measures of both long- and short-term VLBI precision. Baseline length repeatability results were used to derive an empirical VLBI error budget. To obtain the magnitudes of different sources of error, we have decomposed VLBI errors into broad source categories as well as into average local station (vertical and horizontal) errors.

An underlying motivation for this study was to assess the significance of atmospheric error on geodetic VLBI by analyzing the R&D experiments. The R&D schedules were specifically designed to observe to low elevation in order to better model the effect of atmospheric delay. When low elevation observations are made, the correlation between estimates of vertical site position and the zenith atmospheric delay decreases so that the formal errors of the geodetic estimates are reduced. However, atmosphere model errors increase as elevation angle decreases, thus producing a potential for increased scatter in geodetic estimates. This is because the atmospheric thickness increases rapidly as elevation angle decreases. This fact combined with the true variability of the atmospheric profile (site and season) implies that the unmodeled atmospheric error (variance) should also increase as elevation angle decreases. The atmospheric delay using the standard mapping functions (that relate zenith path delay to the delay at arbitrary elevations) does not deviate significantly above 5° from the model (or actual) atmosphere profile delays that were used to generate (for example, by fitting) the mapping functions. However, the atmospheric profile parameters of standard dry mapping functions are held fixed in most current VLBI geodetic analysis, independent of site location and season. (In addition, the effect of inversions has been ignored in standard analyses, although both of these shortcomings could be addressed. For instance, there is a Lanyi inversion height parameter that could be used [*Lanyi*, 1984].) Other atmospheric conditions like gradients are not generally modeled. In this study, we have estimated the size of the total unmodeled atmospheric error.

METHODOLOGY

Choice of Data Sets

For this study, we were interested in estimating both long- and short-term precision of geodetic VLBI. This is because the performances over different time scales presumably reflect properties of the unmodeled errors. If atmospheric error sources predominate, as is widely expected [*Herring et al.*, 1990, *Davis et al.*, 1991], then the long-term geodetic repeatability will likely be poorer because of exposure to a wider range of atmospheric conditions. Two data sets ideal for this study are the ATD (Advanced Technique Development) and ERDE (Extended R&D Experiment) experiment series conducted by NASA's CDP. The ATD experiments used a high-quality network of stations with fast slewing (except Ft. Davis) antennas: Mojave (CA), Westford (MA), Fairbanks (AK), and Ft. Davis (TX). This series of 18 experiments consisted of monthly sessions during 1987 and bimonthly sessions in 1988. (The series is nearly homogeneous: 5 sessions used

modified networks; Ft. Davis was not used in the February, November, and December 1987 sessions; Goldstone-DSS13 (CA) was substituted for Ft. Davis in July 1988; and Pie Town (NM) was substituted for Fairbanks in September 1988.) By spanning a two-year period, the ATDs were designed to uniformly sample seasonal variations. The experiment schedules (designed by A. Niell, Haystack Observatory) were nearly azimuthally symmetric in sky coverage down to the lowest observation angles (4.5° at Westford), and made use of extensive subnetting. This network has long enough baselines (> 2000 km) to sense vertical errors, correlated with atmospheric effects, in baseline lengths.

In contrast to the ATDs, ERDE was a burst of 12 sessions over only 17 days in October 1989. ERDE used basically the same North American network of the ATDs with the substitution of Pie Town for Ft. Davis and the addition of Haystack (MA). The aim of ERDE was to achieve the best geodetic precision possible at the time. In part, ERDE was also designed to sample a short period of time to eliminate seasonal variations (principally atmospheric) or long-term systematic errors. In addition, the spanned bandwidth and channel bandwidth (data sampling rate) at X-band were twice that of the ATDs (standard). In this way, the group delay precision of individual observables was improved as expected over the ATDs [*Ray and Corey*, 1991]. The observation schedules were similar to the ATDs but with the addition of even lower elevation coverage at Pietown and Haystack, down to 2.5°. More than twice as many observations were scheduled (more than 2000 observations per day over 10 baselines) than for the ATDs.

Solution Procedure

The experiments were analyzed in a standard manner with the Kalman filter (SOLVK) [*Herring et al.*, 1990]. In the analysis, all positions were referenced to Westford. The reference clock was Fairbanks for the ATDs and Westford for ERDE. At each remote station in each experiment, the stochastic clock model consisted of a random walk plus integrated random walk with Allan standard deviation of 10^{-14} at 50 minutes. *Herring et al.* found this value to be optimal by comparing Kalman filter solutions using simulated and real VLBI data over a wide range of atmospheric and clock conditions. The value is also consistent with reasonable behavior for masers plus Mark III instrumentation.

The *a priori* dry (hydrostatic) zenith delay was given by the Saastamoinen dry zenith delay. For the ATDs, the CfA2.2 mapping function [*Davis et al.*, 1985] was used for the dry atmosphere. (For the ATDs, results are not very dependent on the dry mapping function.) Since observations at Pietown and Haystack were made down to elevations of 2.5° in ERDE, the MIT dry mapping function (*Herring*, MIT, private communication) was used since it was fit to ray tracings below 5°. Surface meteorological data (pressure, temperature, and relative humidity) was input data for these dry mapping functions. For all of these dry mapping functions, the lapse rate was held fixed at -5.6 K/km and the tropopause height at 10 km. The residual wet troposphere delay component was estimated with the Chao wet mapping function.

The Kalman filter estimates the wet zenith delay (total atmospheric delay - hydrostatic delay) as a random walk process. Site-dependent atmospheric variances were determined independently for each experiment from the delay rate residuals by the KALAN procedure [*Herring et al.*, 1990]. The random walk variances determined in this way were usually less than 0.3 ps^2/s and range from about 0.05-0.6 ps^2/s. There is some evidence for seasonal dependence of the atmosphere variances obtained from the rate residuals. For example, Figure 1 shows the atmosphere variances for Westford as a function of time of year. There is a clear tendency for the atmospheric variances at Ft. Davis, Westford, and Fairbanks to be greatest from May to September. (The Mojave variation is more complicated than this.) For each station, most of the points from 1988 are very close to or are consistent with the trend from 1987. This implies that the seasonal trends are real and provides some confidence that the rate residuals do contain information about atmospheric fluctuations as expected [*Treuhaft and Lanyi*, 1987].

Error Estimate Methodology

We have chosen to study baseline length estimates because length measurements are independent of the secondary uncertainties associated with the orientation of the coordinate system [*Herring*, 1986]. Errors in determinations of the local vertical coordinates contribute increasingly to length scatter as baseline length increases and dominate baseline length errors for baselines greater than about 2000 km. This is important since it is preferentially the vertical coordinate that we are trying to distinguish from zenith atmospheric delay by observing at low elevations.

For each baseline, the repeatability of length estimates was determined. For the ATDs, this is the weighted rms scatter (wrms) about the best fit line through the lengths versus time; and for ERDE, this is the wrms about the mean length over the 3 week burst. The wrms (observed scatter) is a measure of total random error and can be decomposed into modeled (expected scatter) and unmodeled (excess scatter) components

$$\mathrm{wrms}^2 = (\sigma^{\mathrm{model}})^2 + (\sigma^{\mathrm{unmodel}})^2. \qquad (1)$$

The modeled error is simply the formal error of the length estimate. This arises from the propagation of measurement noise and the atmospheric and clock model process noise through covariances with the geodetic parameters. The nonatmospheric modeled component was estimated by performing a filter run with the atmosphere model turned off so that the zenith wet delay was not estimated. The resulting formal error of the length estimate (from the

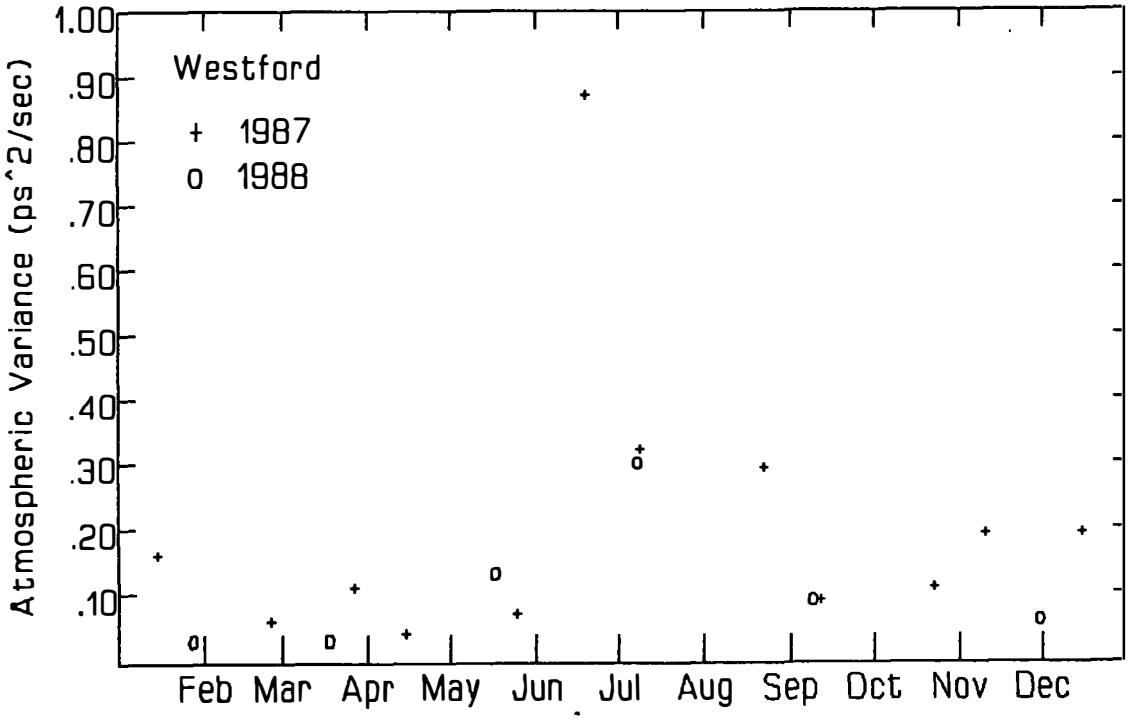

Figure 1. Atmosphere variance (ps^2/s) for Westford plotted versus time of the year. These variances were computed for the ATD experiment series (1987-1988) from delay rate residuals.

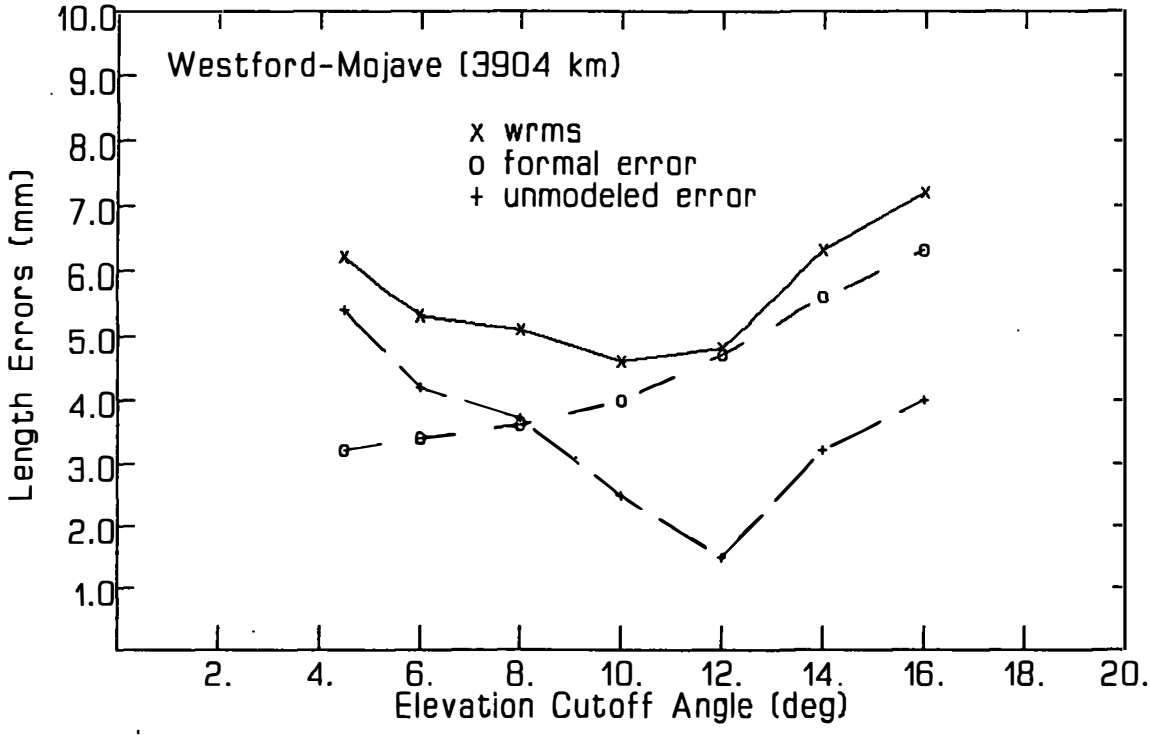

Figure 2. Westford-Mojave baseline length errors for the ATD series plotted against elevation cutoff angle. Observed scatter is shown along with the formal (modeled) error and excess scatter (unmodeled error).

covariance matrix) is produced from the measurement noise and clock model process noise propagated through correlations with nonatmospheric parameters, which allows the portion of the modeled error due to the additional estimation of atmospheric parameters to be determined, that is

$$(\sigma^{model}{}_{atm})^2 = (\sigma^{model})^2 - (\sigma^{model}{}_{nonatm})^2. \qquad (2)$$

This difference includes contributions from correlations of the atmosphere parameters with all the nonatmosphere parameters (including clock parameters). One would also like to estimate how much of the length scatter is produced by atmospheric effects that have been modeled inadequately or incorrectly. In principle, one can decompose the unmodeled error into atmospheric and nonatmospheric components.

$$(\sigma^{unmodel})^2 = (\sigma^{unmodel}{}_{atm})^2 + (\sigma^{unmodel}{}_{nonatm})^2 \quad (3)$$

Several of the most important possible sources of unmodeled error are atmospheric delay, antenna deformation, atmosphere loading, and ocean loading. The atmosphere component should vary with elevation angle and season. However, given the uncertainty in decomposing the unmodeled error, it is simply taken as an upper bound on the unmodeled atmosphere error.

$$(\sigma^{unmodel}{}_{atm})^2 \leq (\text{wrms})^2 - (\sigma^{model})^2 = (\sigma^{unmodel})^2$$

The elevation cutoff tests [*Herring*, 1986; *Davis et al.* 1991] described in the next section are a technique for distinguishing between different unmodeled errors assuming they have different elevation angle dependences.

RESULTS

Cutoff Tests

One of the most sensitive ways of revealing elevation angle dependence is through elevation cutoff tests where data are excluded below a certain elevation cutoff threshold. In this way, the effect of unmodeled atmospheric errors is reduced, although the formal modeled error will increase. One can then study the behavior of the unmodeled error as a function of elevation cutoff threshold. Elevation cutoff tests were performed for the ATD and ERDE series at cutoff angles between 0° (no observations were excluded for this case) and 16°. The 0° cutoff corresponds to the lowest observing angle at a given antenna: Westford (4.5°), Fairbanks (6°), Ft. Davis (7°), Mojave (10°), Haystack (2.5°), and Pietown (2.5°) Each elevation cutoff threshold was applied at all stations. For the ATD series, this is nearly the same as applying the cutoff only at Westford; Westford made about 2 to 3 times as many observations below 10° as Fairbanks.

The elevation cutoff test is a method for detecting the presence of atmosphere model errors. The wrms length scatters were computed for all baselines as a function of elevation cutoff angle. For all the ATD Westford baselines, the wrms actually decreases with increasing elevation cutoff angle and reaches a minimum between 10° and 12°. This is shown in Figure 2 for the Westford-Mojave baseline for which the modeled (formal) error as well as the inferred unmodeled error determined with equation (1) are also plotted. Since the formal error reflects the geometric correlation between the vertical and the zenith atmospheric delay, it increases monotonically as low elevation points are eliminated from the solution. The unmodeled component of the wrms scatter also has a minimum between 10° and 12° for the Westford baselines. Most importantly, the unmodeled error increases as the elevation cutoff decreases below 10° to 12°. The large increase of unmodeled error below 10° indicates that there is probably a random error in the atmosphere modeling for elevations less than 10°. Assuming that the formal errors are accurate, the size of the unmodeled error implies a large potential for improvement in baseline length estimation by improved atmospheric calibration.

There are several observations one can make about the nature of this unmodeled error. A large part of the excess scatter for Westford baselines is produced by a few outlier experiments. The most distinct example is in the Westford-Mojave baseline length scatter, which is shown in Figure 3. Removing the three outlier experiments essentially removes the elevation cutoff dependence of the excess scatter below 10° and brings the total scatter as a function of elevation cutoff angle down to the level of the formal error. The three Westford-Mojave outliers are also elevation-cutoff-dependent outliers for the other Westford baselines, although not so pronounced. This implies that it is likely that there were atmosphere model errors associated with Westford on these days.

Since atmosphere errors increase as elevation decreases, it can be argued that the outlier experiments, which are elevation-cutoff sensitive, are produced by improperly modeled atmospheric conditions. Possible candidates for such conditions are gradients or large deviations of the atmosphere profile from that assumed by the mapping functions. Other possible contributors to unmodeled scatter are seasonal behavior at Fairbanks and nonatmospheric errors at Ft. Davis. Seasonal behavior of Fairbanks baseline lengths has been observed and is attributed to deep thermal inversions that occur in the winter [*A. Niell*, 1990].

Similar cutoff tests were also done for the ERDE series. A typical example of the observed length scatter as a function of elevation cutoff is given in Figure 4 for the Westford-Pietown baseline. Most of the elevation cutoff dependence is below 5°. The ERDE elevation cutoff dependence of the excess (unmodeled) scatter is reduced to about half that of the ATDs. A smaller excess scatter is expected since ERDE sampled the atmosphere for less than three weeks; whereas, the ATDs sampled a two-year period that could include seasonal variations as well as extreme atmospheric conditions.

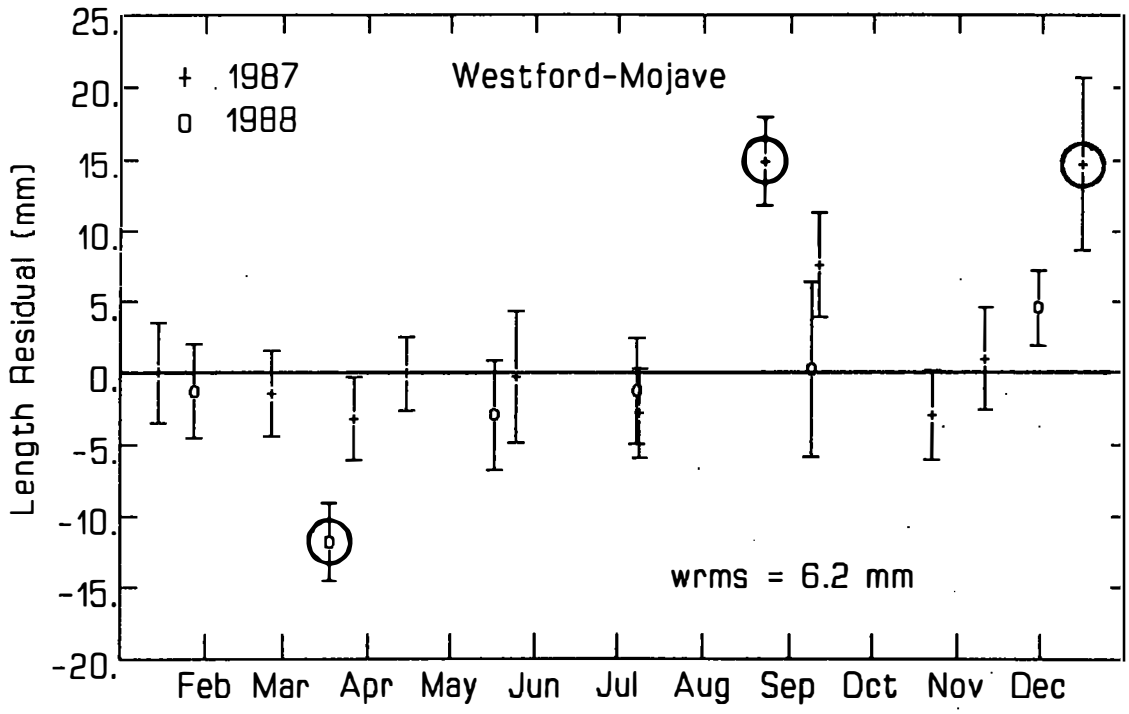

Figure 3. Westford-Mojave ATD baseline length residuals from a best fit line through the experiment lengths. Three outlier experiments (circled) produce most of the excess scatter above the formal error.

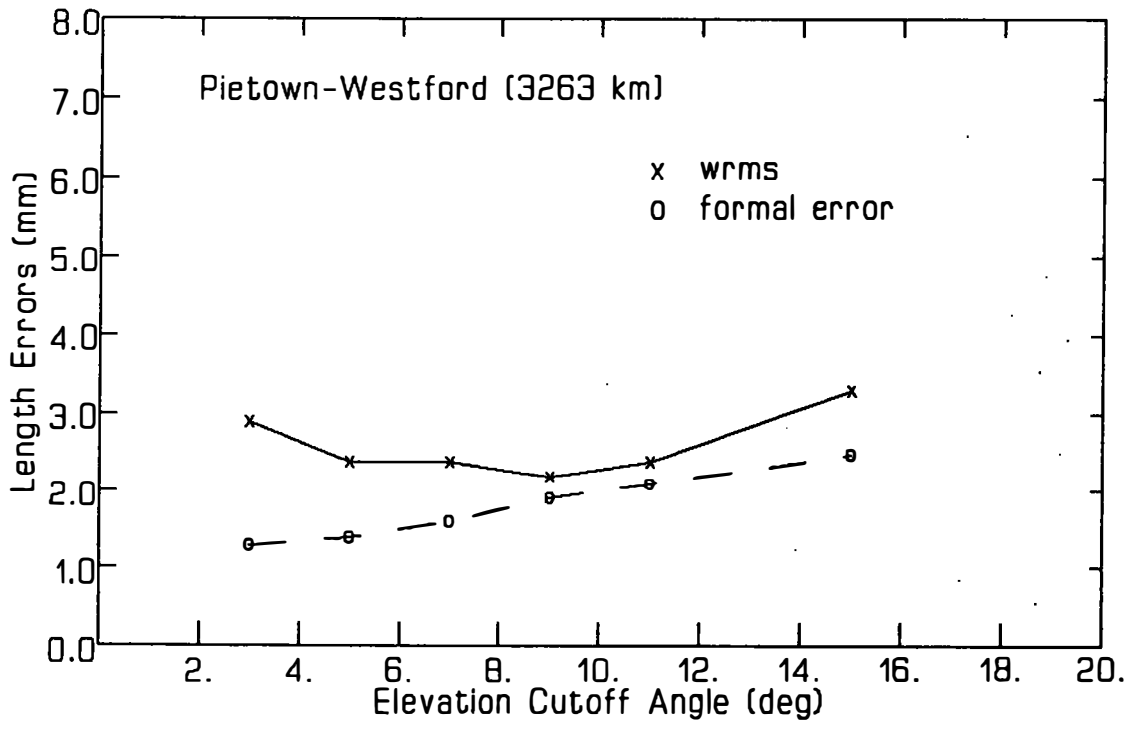

Figure 4. Pietown-Westford (ERDE) baseline length errors are plotted against elevation cutoff angle. Observed scatter is shown along with the formal error and excess scatter.

Station Coordinate Errors

From baseline length precision results we derived average station coordinate errors. This was done by decomposing baseline length errors into average local station vertical and horizontal errors

$$\sigma_L^2 = (2 - f_L)\,\sigma_H^2 + f_L\,\sigma_V^2, \qquad (4)$$

where σ_L is the baseline length error, σ_H is the site horizontal error, σ_V is the site vertical error, $f_L = L^2/2R^2$, R is the earth's radius, and L is the baseline length. This relation is purely geometric and assumes the station coordinate errors are Gaussian and uncorrelated. This local vertical error is free of secondary earth orientation uncertainty since it is derived from length uncertainties. This approach is desirable in order to assess model errors (e.g., atmospheric delay model errors) independently from earth orientation effects.

The repeatability should scale approximately with baseline length according to equation (4). The observed length scatters (repeatabilities) have been computed using all of the observations (down to 4.5° at Westford) for the ATDs without elevation cutoff and applying a 4.5° cutoff for the ERDE series to eliminate differential effects due to observations below 4.5°. Figure 5 shows the observed length dependence for these experiments. The best fit quadratics through the points are

$$\text{wrms(ATD)} = [(3.3\ \text{mm})^2 + (1.2\ \text{ppb} * L)^2\,]^{1/2}$$

$$\text{wrms(ERDE)} = [(1.4\ \text{mm})^2 + (0.75\ \text{ppb} * L)^2\,]^{1/2}.$$

Observed scatter has been decomposed into modeled and unmodeled components according to equations (1-3) and then into local station errors by equation (4). The latter decomposition was performed by fitting the observed scatters for all baselines but solving for separate vertical and horizontal errors for Ft. Davis versus non-Ft. Davis sites. Ft. Davis was treated separately from the other ATD stations since it is thought to have peculiar station-dependent errors that are unlikely to be related to atmospheric effects. The fit in Figure 5 for the ATDs corresponds to non-Ft.Davis baselines. Figure 5 shows that the Ft. Davis baseline length repeatabilities are systematically higher than for the non-Ft. Davis baselines.

The resulting ATD error budget in Table 1 is an empirical decomposition of VLBI errors over a relatively long time span. The inferred average uncertainties for the local ATD station (non-Ft. Davis) coordinates are

$$\sigma_V \approx 11.0\ \text{mm} \ \text{ and } \ \sigma_H \approx 2.3\ \text{mm}.$$

The modeled vertical error of 4.4 mm is largely atmospheric; only about 1 mm is from instrument noise and clocks. The remaining 4.3 mm is the additional error from estimating atmospheric parameters. Observed VLBI vertical uncertainties are 4 to 5 times worse than horizontal uncertainties. This is qualitatively consistent with *Herring* [1986], although the level of error here is much smaller than at that time. However, the level of modeled error is only 2 to 3 times greater in the vertical than in the horizontal. The sensitivity of the repeatability to minimum elevation angle shown in Figure 1 for the Westford-Mojave baseline implies that the excess scatter (unmodeled error) of 10.1 mm beyond the modeled (formal) error is dominated by atmospheric effects. At Ft. Davis, there is an additional unmodeled vertical error of 19.2 mm, which is nonelevation cutoff dependent and probably of nonatmospheric origin.

TABLE 1. ATD ERROR BUDGET
(millimeters)

	σ_V	σ_H	σ_L 1000 km	σ_L 5000 km
wrms (non-Ft. Davis)	11.0	2.3	3.5	6.8
modeled error	4.4	1.7	2.5	3.5
atmospheric	4.3	1.4	2.1	3.2
noise+clocks	0.9	0.9	1.3	1.3
unmodeled error (mostly atmospheric)	10.1	1.5	2.4	5.8
[Ft. Davis	19.2	1.1	2.6	10.6]*

* peculiar additional unmodeled error at Ft. Davis

A measure of short-term geodetic precision of VLBI technique is given by the ERDE series. The observed length scatters yield average local coordinate errors shown in Table 2 of

$$\sigma_V \approx 6.8\ \text{mm} \ \text{ and } \ \sigma_H \approx 1.0\ \text{mm},$$

which are about half the level of the ATDs. Further decomposition yielded an unmodeled vertical component of 5.9 mm, which is again about half that of the ATDs. The modeled (formal) error for ERDE is also less than that of the ATDs. One can see from Table 2 that most of the modeled vertical error arises from estimating atmospheric parameters. The reduction in ERDE of observational noise does not produce a commensurate reduction in the formal error of all the geodetic coordinates. While some of the observed reduction of the modeled error for ERDE is explained by more observations per session and more precise observables, most of the difference in both modeled and unmodeled error is probably due to the shorter time span of ERDE. Additionally, we note that the atmospheric variances derived from delay rate residuals are relatively small for all the ERDE sessions and are roughly in agreement with those derived for the September-October ATDs. Compared with the ATDs, both the observed and

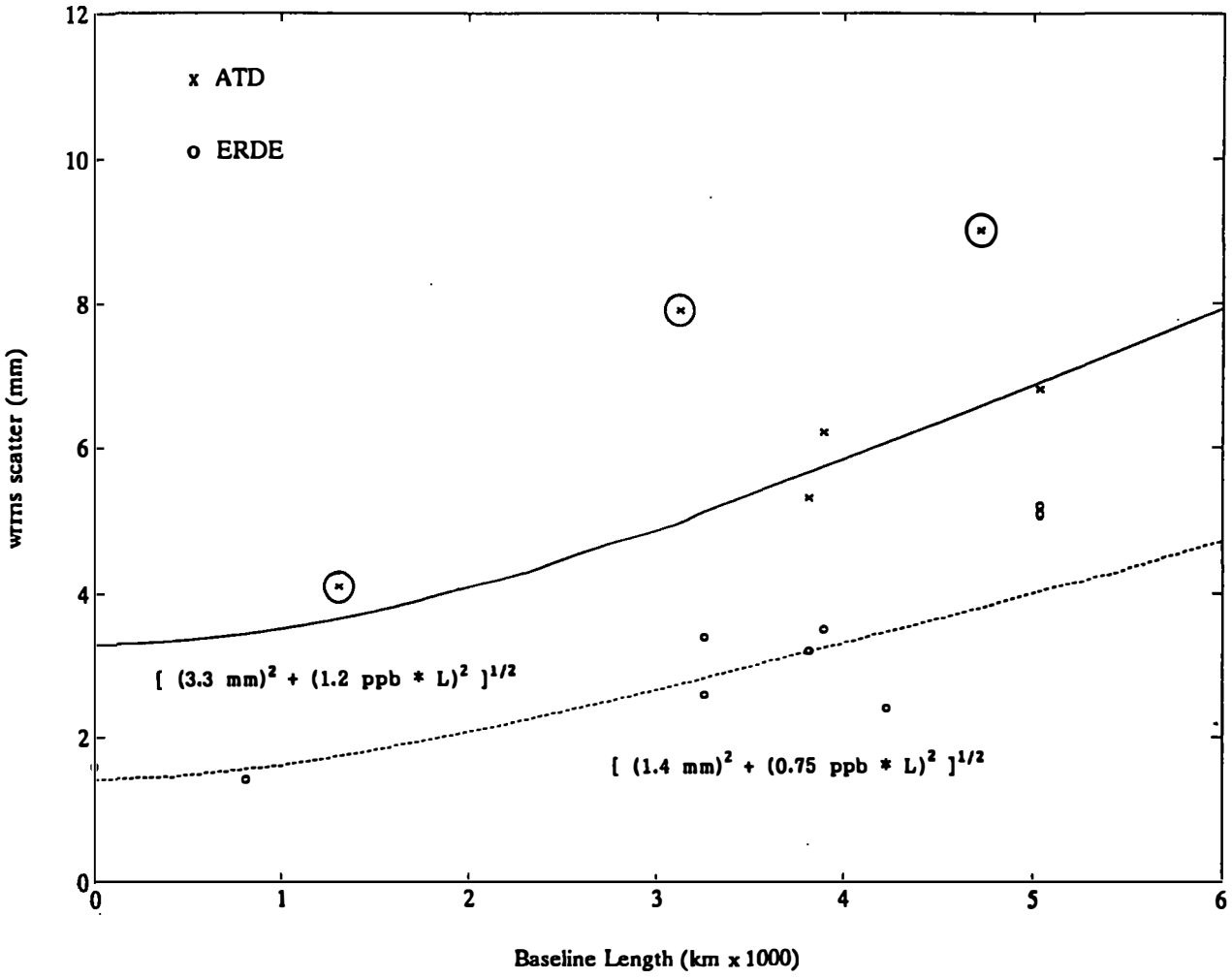

Figure 5. Observed length scatter (repeatabilities) for ATD and ERDE series plotted versus baseline length. Ft. Davis baseline length repeatabilities (circled) are systematically higher than for non-Ft. Davis baselines. The fit through the ATD points corresponds to non-Ft. Davis baselines.

TABLE 2. ERDE ERROR BUDGET
(millimeters)
4.5° elevation cutoff

	σ_V	σ_H	σ_L 1000 km	σ_L 5000 km
wrms	6.8	1.0	1.6	4.0
modeled error	3.4	0.6	1.0	2.0
atmospheric	3.3	0	0.6	1.8
noise+clocks	0.6	0.6	0.8	0.8
unmodeled error (mostly atmospheric)	5.9	0.9	1.2	3.5

modeled horizontal inferred errors are reduced by a factor of about 2 to 3, consistent with a combination of about twice the group delay precision and about twice as many observations ($\sim 2\sqrt{2}$). There is not a comparable improvement in the vertical because of the predominant effect of atmosphere errors.

In Table 3, the performance of various VLBI data sets are compared in order to put the errors derived for the R&D experiments into perspective. The average of all Mark III data [*Caprette et al.*, 1990] for baseline lengths less than 8500 km (148 baselines) yields an inferred vertical error of 26.4 mm. This number includes the effects of mixed networks and includes experiments that used small mobile antennas with minimum elevation limits of 20°. This is close to the level of unmodeled error for the ATD Ft. Davis baselines given in Table 1. An example of long-term repeatability for an operational network with high-quality fixed stations is provided by the IRIS-A network. For

TABLE 3. INFERRED PRECISIONS FOR VARIOUS DATA SETS
(millimeters)

	σ_V	σ_H	σ_L 1000 km	σ_L 5000 km
	long-term repeatabilities			
average of all Mark III data •	26.4	4.9	7.5	16.0
IRIS 1990	13.3	3.5	5.1	8.6
ATDs	11.0	2.3	3.5	6.8
	short-term repeatability			
ERDE	6.8	1.0	1.6	4.0

• for baseline lengths ≤ 8500 km (148 baselines)

1990 on baselines sampled by more than fifty sessions, IRIS-A had an inferred vertical scatter of 13.3 mm, which approaches the level of 11.0 mm for the ATDs.

DISCUSSION AND CONCLUSIONS

Given the increasing geophysical emphasis on problems involving the vertical, we have derived an error budget for the VLBI determination of local station vertical and horizontal coordinates. The ATDs provide a measure of long-term state-of-the-art VLBI performance. As expected, the observed ATD scatter of 11.0 mm as well as the excess scatter of 10.1 mm is larger than (by almost twice) that of the short-term ERDE series, but less than half the observed scatter of the full Mark III data set. This error budget also gives a broad category decomposition of VLBI error. The formal (modeled) error is produced by instrument noise and process noise introduced through the atmosphere and clock models. We find that the observed scatter is much larger than the formal error and that this is likely to be caused by mismodeling of atmospheric propagation. For example, standard analysis uses mapping functions that fix the lapse rate and tropopause height at average values appropriate for mid-latitudes. Additionally, we have seen that the observed length scatter for the ATD experiments contains a large contribution from a few outlier experiments. The cause of these outliers appears to be atmosphere related, since the length residuals for these experiments are elevation cutoff dependent, but specific mechanisms to account for their behavior have not been identified.

Acknowledgements. The Pie Town data were made possible by the Very Long Baseline Array and the National Radio Astronomy Observatory, which is operated by Associated Universities, Inc. under cooperative agreement with the National Science Foundation. Tom Herring provided the MIT dry mapping function. Arthur Niell made helpful suggestions during the course of this work.

REFERENCES

Caprette, D.S., C. Ma, J.W. Ryan, Crustal Dynamics Project data analysis - 1990, VLBI geodetic results 1979-1989, *NASA TM-100765*, 1990.

Clark, T.A., W. G. Melbourne, Ch. Reigber, L.E. Young, and T.P Yunck, Instrumentation: Microwave techniques, in *Proceedings of an International Workshop held at Erice, The Interdisciplinary Role of Space Geodesy, Lecture Notes in Earth Sciences* (I.I. Mueller and S. Zerbini, eds.), vol. 22, Springer-Verlag, Berlin, 148-162, 1989.

Davis, J.L., T.A. Herring, I.I. Shapiro, A.E.E. Rogers, and G.Elgered, Geodesy by radio interferometry: Effects of atmospheric modeling errors on estimates of baseline length, *Radio Sci.*, *20*, 1593-1607, 1985.

Davis, J.L., T.A. Herring, and I.I. Shapiro, Effects of atmospheric modeling errors on determinations of baseline

vectors from VLBI, *J. Geophys. Res.*, *96(B1)*, 643-650, 1991.

Herring, T.A., Precision of vertical estimates from very long baseline interferometry, *J. Geophys. Res.*, *91(B9)*, 9177-9182, 1986.

Herring, T.A., J.L. Davis, and I.I. Shapiro, Geodesy by radio interferometry: The application of Kalman filtering to the analysis of VLBI data, *J. Geophys. Res.*, *95(B8)*, 12561-12582,1990.

Lanyi, G.E., Tropospheric delay effects in radio interferometry. *Tracking and Data Acquisition Prog. Rept.* 42-78 (JPL, Pasadena, CA), 152-159, 1984.

Niell, A., VLBI troposphere estimation using radiosonde data, *Eos Trans. AGU*, *71(43)*, 1276, 1990.

Ray, J.R., and B.E. Corey, Current precision of VLBI multiband delay observables, this volume, 1991.

Treuhaft, R.N., and G.E. Lanyi, The effect of the dynamic wet troposphere on radio interferometric measurements, *Radio Sci.*, *22*, 251-265, 1987.

D.S. MacMillan and J.R. Ray, Interferometrics Inc., GSFC/NASA, Code 926.9, Greenbelt, MD 20771 (dsm@bootes.gsfc.nasa.gov and jrr@bootes.gsfc.nasa.gov)

Global Warming signals in Earth Rotation

T M Eubanks (U.S. Naval Observatory, Washington, DC 20392)

Geodetic measurements of the Earth's rotation rate can be used as a proxy index for changes in the meridional temperature gradient in the atmosphere. Most global warming models do not predict a uniform global temperature rise, but instead typically a warming of higher latitudes in winter, while the meteorological data suggest that the warming is concentrated at low latitudes. These data suffer, however, from a number of problems, including undersampling and the urban "heat island" effect. The geodetic data thus have the potential for resolving some important issues in the global warming debate.

Close agreement is found between changes in the Length of the Day (δLOD) as measured by methods such as Very Long Baseline Interferometry, and zonal atmospheric angular momentum changes, caused by zonal wind variations, over time scales less than a few years. Global scale zonal winds are nearly geostrophic and are thus related to the meridional gradients of the atmosphere temperature. If the atmosphere is assumed to be geostrophic and barotropic, then changes in δLOD can be directly related to changes in T_2^0, the second zonal spherical harmonic of the atmospheric temperature distribution, through

$$\delta\mathrm{LOD} = 0.3458\ T_2^0 \qquad (1),$$

Where T_2^0 is in °C and δLOD is in milliseconds. The accuracy of the modern δLOD data is such that, in principle, long term temperature changes could be monitored at the 0.1 °C level using geodetic data. Changes in δLOD caused by the core will limit the ability of δLOD data to monitor changes in T_2^0, however the seasonal T_2^0 cycle can be accurately monitored. This talk will describe an analysis of a proxy T_2^0 index derived from δLOD data.

Appendix: List of Participants

Michael D. Abell, NOAA, N/CG114, 11400 Rockville Pike, Room 420, Rockville, MD, 20852
Keith Aldridge, Dept. of Earth and Atm. Sci., York University, 4700 Keele Street, North York, Ontario, Canada
Roger L. Allshouse, Bendix Field Engineering, One Bendix Road, Columbia, MD, 21045
Allen J. Anderson, NASA Headquarters, 600 Independence Ave., S.W., Washington, DC, 20546
Brent A. Archinal, U.S. Naval Observatory, Earth Orientation Division, Washington, DC, 20392
Knute Berstis, NOAA, N/CG114, 11400 Rockville Pike, Rockville, MD, 20852
Bruce B. Bills, NASA/GSFC, Geodynamics Branch, Greenbelt, MD, 20711
John M. Bosworth, NASA/GSFC, Code 901, Greenbelt, MD, 20711
Roger J. Cappallo, Massachusetts Institute of Technology, Haystack Observatory, Westford, MA, 01886
Tim S. Carroll, U.S. Naval Observatory, 11800 SW 166 St., Miami, FL, 33177
Merri Sue Carter, U. S. Naval Observatory, 34th St. and Massachusetts Ave., N.W., Washington, DC, 20392
William E. Carter, NOAA, N/CG114, 1400 Rockville Pike, Room 420, Rockville, MD, 20852
Benjamin Fong Chao, NASA GSFC, Mail Code 921, Greenbelt, MD, 20771-0001
Miranda Chin, NOAA, N/CG114, 11400 Rockville Pike, N/CG114, Rockville, MD, 20852
Thomas A. Clark, NASA GSFC, Mail Code 926.9, Greenbelt, MD, 20771-0001
Robert J. Coates, NASA/GSFC/Ret., 529 Whittingham Drive, Silver Spring, MD, 20904
Brian E. Corey, Massachusetts Institute of Technology, Haystack Observatory, Westford, MA, 01886
Aracy Mendes Da Costa, University of Sao Paulo, Center of Radio, Astronomy and Space App., Polytechnic Inst., P.O. Box 8174, Sao Paulo 05508, Brazil
James C. Davis, Physics Department, University of California, Berkeley, Berkeley, CA, 94720
Gregory L. DeAngelo, NOAA, N/CG114, 11820 SW 166 Street, Miami, FL, 33177
Jean O. Dickey, JPL/Mail Stop 238-332, 4800 Oak Grove Dr., Pasadena, CA, 91009-8099
Steven R. Dickman, State University of New York, Department of Geological Sciences, Binghamton, NY, 13901
William H. Dillinger, NOAA, N/CG114, 11400 Rockville Pike, Room 420, Rockville, MD, 20852
Danan Dong, Massachusetts Institute of Technology, P.O. Box 313, Kendall Square, Cambridge, MA, 02142
Bruce C. Douglas, NOAA, N/CG114, 11400 Rockville Pike, Room 420, Rockville, MD, 20852
C. Everett Dutton, NOAA, N/CG114, 11400 Rockville Pike, Room 420, Rockville, MD, 20852
Joseph F. Engeln, NASA Headquarters, Code SEP-05, Washington, DC, 20546
Bjorn Engen, Statens Kartverk, Monservdveien, Honefoss 3500, Norway
Martin N. England, Interferometrics/NASA-GSFC, Code 926.9, Greenbelt, MD, 20771
T. Marshall Eubanks, U.S. Naval Observatory, 34th and Massachusetts Ave., Washington, DC, 20392-5100
David R. Florkowski, U.S. Naval Observatory, 34th St. and Massachusetts Ave., N.W., Washington, DC, 20392
Adam P. Freedman, JPL/Mail Stop 238-332, 4800 Oak Grove Dr., Pasadena, CA, 91009-8099
Frank D. Ghigo, National Radio Astronomy Observatory, P.O. Box 2, Green Bank, WV, 24944
David Gordon, STX/GSFC, Code 926.9, Greenbelt, MD, 20771
Richard S. Gross, JPL/Mail Stop 238-332, 4800 Oak Grove Dr., Pasadena, CA, 91009-8099
Erwin Groten, Technical University Inst. of Phy. Geodesy, Petersenstr .13, D-6100 Darmstadt, Germany

Shin'ichi Hama, 610 Campbell Hall/R.A. Lab, University of California, Berkeley, Berkeley, CA, 94720
Donald E. Haw, NOAA, N/CG114, 11400 Rockville Pike, Room 420, Rockville, MD, 20852
Ronald W. Hellings, JPL, 4800 Oak Grove Dr., Pasadena, CA, 91009-8099
Thomas A. Herring, MIT, Room 54-618, 77 Massachusetts Avenue, Cambridge, MA, 02139
William E. Himwich, Interferometrics, Inc./GSFC, 8150 Leesburg Pike, Vienna, VA, 22182
Larry D. Hothem, U.S. Geological Survey, Reston, 510 National Center, Reston, VA, 22092
Christopher S. Jacobs, JPL/Mail Stop 238-700, 4800 Oak Grove Dr., Pasadena, CA, 91009-8099
Lillian Jensen, Statens Kartverk, N-3500 Honefoss, Norway
Frederick J. Josties, U.S. Naval Observatory, 3400 Massachusetts Ave., N.W., Washington, DC, 20392
Eugenia Kalnay, NMC/NWS/NOAA, W/NMC3, WWB, Room 204, Washington, DC, 20233
Deirdre Kann, PRL/CAC, 1406 Madison, NE, Albuquerque, NM, 87110
Pierre Kaufmann, CRAAE/EPUSP, C.P. 8174, Sao Paulo 05508, Brasil
Richard Kilger, Technical University, Munich, Wettzell Observatory, 8493 Kotzting, Germany
Kerry A. Kingham, U.S. Naval Observatory, 34th and Massachusetts Ave., N.W., Washington, DC, 20392
Hiroshi Kiuchi, Kashima Space Center, CRL, 893-1, Hirai, Kashima, Ibaraki 314, Japan
Sergei A. Klioner, Institute of Applied Astronomy, 197042 8 Zhdanovskaya ul., Leningrad, USSR
John A. Knauss, Department of Commerce, NOAA, Herbert C. Hoover Building, 14th and Constitution Ave., N.W., Washington, DC, 20230
Curtis A. Knight, Interferometrics, Inc., 8150 Leesburg Pike, Vienna, VA, 22182
Clara E. Kuehn, Interferometrics, Inc./GSFC, Mail Code 926.9, Greenbelt, MD, 20771-0001
Madhav H. Kulkarni, Department of Geodetic Science and Surveying, Ohio State University, 404 Cockins Hall, 1958 Neil Avenue, Columbus, OH 43210
Noriyuki Kurihara, Kashima Space Center, CRL, 893-1, Hirai, Kashima, Ibaraki 314, Japan
Stephen T. Lowe, JPL/Mail Stop 238-700, 4800 Oak Grove Dr., Pasadena, CA, 91009-8099
Shifang Luo, ST Systems Corporation, 4913 Blackfoot Road, College Park, MD, 20740
Chopo Ma, NASA GSFC, Mail Code 926.9, Greenbelt, MD, 20771-0001
J. Ross MacKay, NOAA, N/CG114, 11400 Rockville Pike, Room 420, Rockville, MD, 20852
Daniel S. MacMillan, Interferometrics, Inc./GSFC, Mail Code 926.9, Greenbelt, MD, 20771-0001
Gerald L. Mader, NOAA, N/CG114, 11400 Rockville Pike, Room 420, Rockville, MD, 20852
Seiji Manabe, National Astronomical Observatory, Mizusawa, Iwate, 023 Japan
James O. Martin, U.S. Naval Observatory, 34th & Massachusetts Ave., N.W., Washington, DC, 20390
Demetrius Matsakis, U.S. Naval Observatory, 34th & Massachusetts Ave., N.W., Washington, DC, 20375
Shigeru Matsuzaka, Geographical Survey Institute of Japan, 11400 Rockville Pike, Room 420, Rockville, MD, 20852
Dennis D. McCarthy, U.S. Naval Observatory, Time Service Department, 34th and Massachusetts Ave., Washington, DC, 20392-5100
John F. Meekins, Naval Research Laboratory, Code 4210, Washington, DC, 20375-5000
William G. Melbourne, Jet Propulsion Lab/CalTech, 4800 Oak Grove Drive, Pasadena, CA, 91109
Arvid Meyers, U.S. Naval Observatory, 34th and Massachusetts Ave., N.W., Washington, DC, 20392
Charles C. Mitchell, Mojave Base Station, Goldstone Deep Space Network, P.O. Box 997, Barstow, CA, 92311
Jerry X. Mitrovica, Harvard-Smithsonian Center for Astrophysics, 60 Garden Street, Cambridge, MA, 02138
Alice K.B. Monet, U.S. Naval Observatory, Flagstaff Station, P.O. Box 1149, Flagstaff, AZ, 86002

Arthur E. Niell, Massachusetts Institute of Technology, Haystack Observatory, Westford, MA, 01886
Axel Nothnagel, Geodetic Institute, University of Bonn, Nussallee 17, D-5300 Bonn 1, Germany
William T. Petrachenko, Geological Survey of Canada, Geophysics Division, EMR, 1 Observatory Crescent, Ottawa, Ontario, K1A OY3 Canada
Richard J. Podgorny, NOAA/National Ocean Service, 1825 Connecticut Ave., N.W., Suite 615, Washington, DC, 20009
Rui M. Ponte, AER, Inc., 840 Memorial Drive, Cambridge, MA, 02139
Joseph Popelar, Geodetic Survey of Canada, 615 Booth Street, Ottawa, Ontario, Canada
Robert L. Potash, Interferometrics Inc./GSFC, Code 926.9, Greenbelt, MD, 20771
Robert E. Price, Bendix Field Engineering Corp., One Bendix Road, Columbia, MD, 21045
James R. Ray, Interferometrics, Inc./GSFC, Mail Code 926.9, Greenbelt, MD, 20771-0001
Douglas S. Robertson, NOAA, N/CG114, 11400 Rockville Pike, Room 420, Rockville, MD, 20852
Alan E.E. Rogers, Massachusetts Institute of Technology, Haystack Observatory, Westford, MA, 01886
Jonathan D. Rommey, National Radio Astronomy Observatory, Edgemont, Charlottesville, VA, 22903
Richard D. Rosen, AER, Inc., 840 Memorial Drive, Cambridge, MA, 02139
Jane L. Russell, Naval Research Laboratory, Code 4210, Washington, DC, 20375
James A. Ryan, NASA GSFC, Mail Code 926.9, Greenbelt, MD, 20771-0001
David A. Salstein, AER, Inc., 840 Memorial Drive, Cambridge, MA, 02139
Tetsuo Sasao, National Astronomical Observatory, Mizusawa, Iwate, 023 Japan
Mark S. Schenewerk, NOAA, N/CG114, 11400 Rockville Pike, Room 420, Rockville, MD, 20852
Gernod Schindler, Project Scientist, IFAG, Karl-Rothe-Strabe 10-14, Leipzig D-7072, Germany
Bruce R. Schupler, Bendix Field Engineering Corporation, One Bendix Road, Columbia, MD, 21045
Hermann Seeger, IfAG, Richard Strauss-Allee 11, D-6000 Frankfurt Main 70, Germany
David B. Shaffer, Interferometrics Inc./GSFC, 1742 Saddleback Court, Henderson, NV, 89014
Irwin I. Shapiro, Harvard-Smithsonian Center for Astrophysics, 60 Garden Street, Cambridge, MA, 02138
Michael H. Soffel, Lehrsteul fur Theoretische Astrophysic, Auf der Morgenstelle 12, D-7400 Tübingen, Germany
John H. Spencer, Naval Research Laboratory, Code 4214, Washington, DC, 20375
Heinz Steufmehl, Geodetic Institute, University of Bonn, NuBallee 17, 5300 Bonn 1, Germany, Fujinobu Takahashi, Communications Research Laboratory, 2-1, Nukui-Kitamachi, 4-Chome Koganei-shi, Tokyo, 184, Japan
Guogiang Tang, CfA/Onsala Space Observatory, 60 Garden Street, Cambridge, MA, 02138
Nina D. Umbaraeva, Institute of Applied Astronomy, 197042 8 Zhdanovskaya ul., Leningrad, USSR
Tonie M. VanDam, University of Colorado, CIRES, Campus Box 216, Boulder, CO, 80309
Nancy R. Vandenberg, Interferometrics/GSFC, 8150 Leesburg Pike, Vienna, VA, 22182
Grazia Verrone, Department of Physics, University of Bari, Via Amendola, 173, Bari 70126, Italy
R. Craig Walker, National Radio Astronomy Observatory, Post Office Box 0, Socorro, New Mexico, 87801
John C. Webber, Interferometrics, Inc., 8150 Leesburg Pike, Vienna, VA, 22182
Glenn H. White, NMC/NWS/NOAA, W/NMC3, WWB, Washington, DC, 20233
Alan R. Whitney, Massachusetts Institute of Technology, Haystack Observatory, Westford, MA, 01886
James D. Williams, Harvard College Observatory, P.O. Box 978, Fort Davis, TX, 79734
Clark R. Wilson, University of Texas, Austin, Department of Geological Sciences, Austin, TX, 78713
Nikita Zelensky, ST Systems, 4400 Forbes Boulevard, Lanham, MD, 20706
Gunter Zeppenfeld, Geodetic Institute, University of Bonn, NuBalle 17, 5300 Bonn 1, Germany
Dawei Zheng, Shanghai Observatory, Academia Sinica, Shanghai, Peoples Republic of China